KEK Report 90-10
July 1990
H

Proceedings of the International Workshop on Solenoidal Detectors for the SSC

April 23-25, 1990
KEK, Tsukuba, Japan

Edited by

Fumio Abe,
Katsuo Hasegawa

KEK, National Laboratory for High Energy Physics

KEK Reports are available from:

Technical Information & Library
National Laboratory for High Energy Physics
1-1 Oho, Tsukuba-shi
Ibaraki-ken, 305
JAPAN

Phone: 0298-64-1171
Telex: 3652-534 (Domestic)
(0)3652-534 (International)
Fax: 0298-64-4604
Cable: KEKOHO

Foreword

The International Workshop on Solenoidal Detectors for the SSC was held at KEK from April 23 through 25, 1990. The SSC which is planned in the United States will be the highest energy accelerator during the period from the end of this century to the first decade of the 21's century. We believe a general purpose solenoidal detector will be the most powerful apparatus to explore multi-TeV physics providing a deeper understanding of the profound particle physics. This workshop is the first SSC workshop which is held outside the United States. More than 120 persons came from US, Japan, and Europe and discussed about the physics, detectors, data acquisition, and computing problems. This workshop is the first step of the international collaboration for the SSC.

The construction of the Solenoidal Detector is a big technical challenge and a long way to the physics goal. Each detector component as well as electronics, data acquisition and computing has severe problems to achieve stable high performance in the extremely high luminosity operation. Furthermore, there are several system wide problems: design of the detector system, cost optimization, electron ID, and how to detect signals of the new physics. To discuss these problems deeper, we arranged 5 parallel sessions and 5 plenary sessions each of which had about 20 minutes free discussion. The detector specific problems, data acquisition, and computing problems were discussed in parallel sessions. The system wide problems were discussed in plenary sessions.

This workshop was held just a month before the deadline of the submission of the Expression of Interest (EoI). Due to the increase of the interest, lively discussion was made during the workshop toward EoI and post EoI studies. We expect this workshop is the first step to the success of the experiment and physics at the SSC.

The timely publication of this proceedings, hopefully, will help those who are involved in advancing the detector design as well as physics study for the SSC. We wish to take this opportunity to thank those speakers who have prepared the manuscript for publication promptly. We acknowledge with thanks, the help of the Local Organizing Committee and the KEK

Administration Department. Among others, the help by Mr. H. Kitagawa and Mr. T. Aizawa of the Research Cooperation Section was indispensable. Finally we would like to thank H. Sugawara, KEK Director General and S. Iwata, KEK Physics Department Chairman for providing us an opportunity of holding this Workshop at KEK.

Workshop Chairman
Takahiko Kondo

Workshop Organizer:

H. Yuta	(Tohoku University)
K. Amako	(KEK)
T. Kondo	(KEK)
A. Maki	(KEK)
Y. Takaiwa	(KEK)
Y. Asano	(University of Tsukuba)
K. Kondo	(University of Tsukuba)
S. Mori	(University of Tsukuba)
Y. Nagashima	(Osaka University)
T. Ohsugi	(Hiroshima University)
G. Trilling	(LBL)

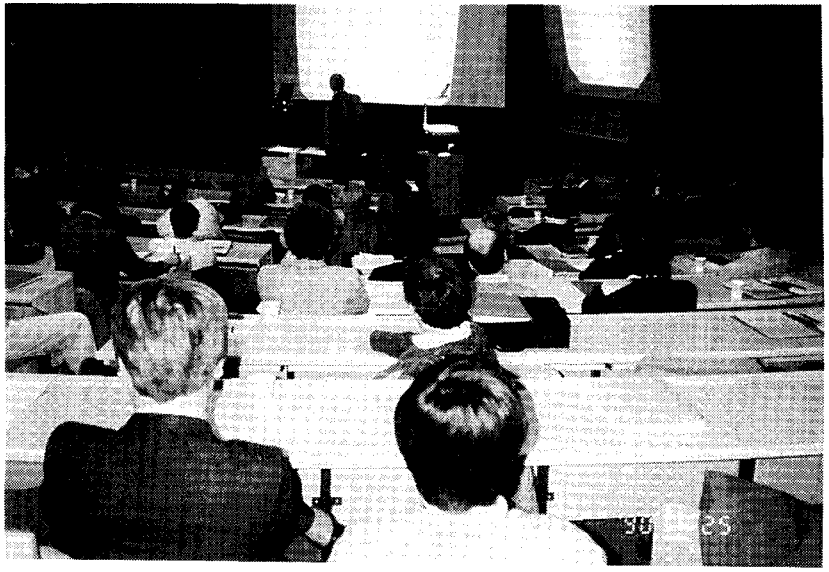


'90 4 23


'90 4 25


'90 4 24


'90 4 25

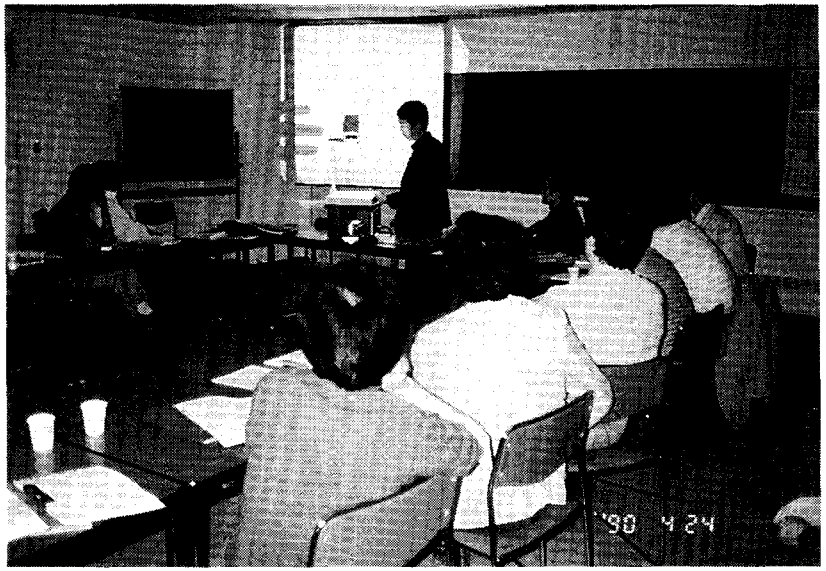
'90 4 24

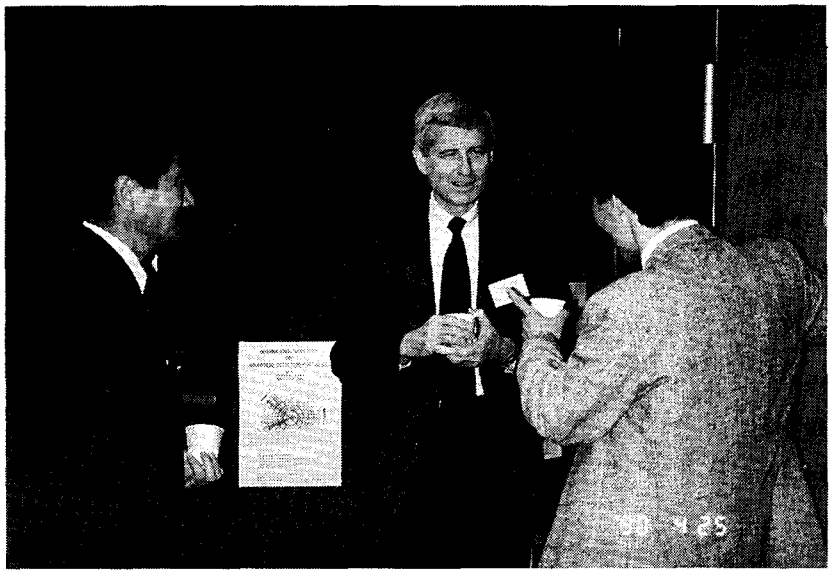
'90 4 25


'90 4 23


'90 4 25


'90 4 23


'90 4 23


'90 4 23

CONTENTS

Electron ID

Integrated Tracking System

Parallel Session: Tracking

Parallel session: Calorimeter

Parallel Session: Muon System

Plenary Sessions

Opening Session

Detector Design and Cost Optimization

Short Solenoid versus Long Solenoid

Electron ID

Integrated Tracking System

Parallel Sessions, Summary talk

Tracking

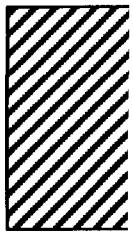

Calorimeter

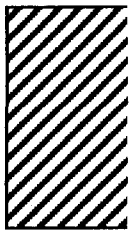

Muon System

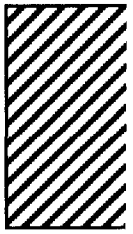

Electronics, Trigger, and Data Acquisition

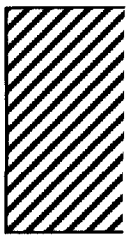

Physics, Computing, and Simulation

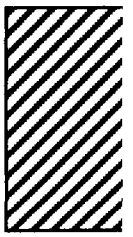

Summary talk

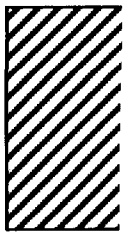

Opening Session

April 23, 9:00-12:05

April 24, 11:15-12:15

Welcome address

Hirotaka Sugawara

Welcome to KEK and to the SSC Solenoidal Group Workshop. It is very nice that SSC workshop of this kind is held not just in one place but in various places in the whole world. But I hope that your studies will eventually lead to a single detector design instead of endlessly oscillating among various designs or converging to several distinct designs. Completed detector will be the largest particle detector on earth for the largest particle accelerator on earth. Texans will certainly like it. What do we expect you to discover with this detector? I hope that you will not find the Higgs bosons. I hope that you will not find the super particles. These cannot possibly be true because they are mere invention of theorists. I hope that you will find something that nobody ever expected. Only with such discoveries can we anticipate that physics of 21st century will be an exciting me? Only with such discoveries can the true collaboration of theorists and experimentalists start again? In this sense I hope that you will make the first important scientific discovery of the 21st century rather than the last important discovery of the 20th century. I am sure that not only Texans but entire world will like it.

Thank you.

Status, Accelerator and Experimental Program of the SSC

Fred Gilman
SSC Laboratory

******** This summary is written by the proceeding **********
******** editor based on the transparencies presented. ********

- **When formed in January, 1989 SSC Laboratory began major activities**

  - Mobilize effort near site
  - Develop baseline design, schedule, and cost estimate
  - Perform geotechnical investigations
  - Specify footprint
  - Support preparation of environmental impact statement
  - Select architect-engineer / construction manager
  - Continue magnet development
  - Initiate scientific programs

- **Near-term Objectives**

  - Magnet industrialization
  - Accelerator system string test by October, 1992
  - Campus planning, design, and construction
  - Continue strengthening SSC Laboratory management

- **SSC Project Cost Estimates**

20 TeV "SCDR" w/5 cm aperture	$ 7830M
20 TeV recommended design	$ 7235M

- **Physics of the SSC**

  - Uncover the nature of electroweak symmetry breaking
    Higgs : single or multiple, elementary or composite
    more generally, discern what happens in W_LW_L scattering
  - Look at physics inside the Standard Model, e.g. b's, t's, QCD
  - Look for physics beyond the Standard Model
    Larger gauge sector : W', Z'
    SUSY
    Compositeness
    etc

  The SSC is a powerful probe for surprises at enormous energies.

- **The SSC Experimental Program**

  - The 1st PAC meeting was held on February 9-10, 1990.
  - Guidelines for Expressions of Interest due May 25, 1990.
  - SSCL, with PAC advice, will work to determine the initial program.
  - SSCL will maximize both the physics capabilities and the participation of the HEP community.
  - Funds for support of engineering design.
  - PAC June 7-9 EoI public presentation
    July 14-20 Snowmass PAC meeting
    Nov 1-3 Recommendations on subsystem R&D and EoIs

- **Foreign Participation**

  - Traditional, expected and desired in experimental program.
  - "In-kind" contribution is expected in construction.
  - Collaboration with CERN about accelerator system (?)

Physics at SSC

Kaoru Hagiwara
KEK

******** This summary is written by the proceeding **********
******** editor based on the transparencies presented. ********

1. Physics Goals of the SSC

Physics of electroweak gauge symmetry breakdown (SB) is the KEY to go beyond.

2. How to attack the goal ?

In order to probe the dynamics behind the symmetry breaking, we should study

$$W_L^{\pm} W_L^{\mp} \to Z_L Z_L$$
$$W_L^{\pm} Z_L \to W_L^{\pm} Z_L$$
$$W_L^{+} W_L^{-} \to W_L^{+} W_L^{-}$$
$$W_L^{\pm} W_L^{\pm} \to W_L^{\pm} W_L^{\pm}$$

In the absence of new particles, this is the only way to probe the symmetry breaking physics!

General properties of the $V_L V_L$ scattering amplitudes are described by 3 independent amplitudes a_{00}, a_{02} and a_{11}[1]. At low energies, these amplitudes behave linearly with s. It is the high energy behavior of these amplitude that tells us about physics of the symmetry breaking. Two extreme cases are

1. $|a_{JI}| \sim O(1)$ Strong scattering $\Lambda_{S.B.} \geq 1$ TeV
2. $|a_{JI}| << 1$ Weak scattering $\Lambda_{S.B.} < 1$ TeV

independent of models. Thus SSC should at least allow us to decide our future direction of accelerator physics:

if $\Lambda_{S.B.} \geq 1$ TeV $\rightarrow\rightarrow\rightarrow\rightarrow\rightarrow$ pp ($\sqrt{s} > 200$TeV) or e^+e^- ($\sqrt{s} > 4$TeV)

if $\Lambda_{S.B.} < 1$ TeV $\rightarrow\rightarrow\rightarrow\rightarrow\rightarrow$ e^+e^- ($\sqrt{s} = 1$TeV).

This is the physics goal of the SSC.

3. Can we pass the goal ?

I could not find a convincing study which demonstrates that in fact this physics goal is reached by a realistic detector at the SSC.

Five purely leptonic processes are considered to be detectable :

A	$W_L^+W_L^-$, $Z_LZ_L \rightarrow Z_L Z_L \rightarrow 4l$	2 events/year
B	$W_L^+W_L^-$, $Z_LZ_L \rightarrow Z_LZ_L \rightarrow 2l\ 2\nu$	10 events/year
C	$W_L^{\pm} Z_L \rightarrow W_L^{\pm} Z_L \rightarrow 3l\ 1\nu$	13 events/year
D	$W_L^+W_L^- \rightarrow W_L^+W_L^- \rightarrow l^+l^-2\nu$	140 events/year
E	$W_L^{\pm} W_L^{\pm} \rightarrow W_L^{\pm} W_L^{\pm} \rightarrow l^{\pm}l^{\pm}\ 2\nu$	8.5 events/year

where the event rates are taken from Chanowitz-Gaillard for 10000pb^{-1}. Background processes such as $q\bar{q}\rightarrow t\bar{t}$, $gg\rightarrow t\bar{t}$, $q\bar{q}\rightarrow ZZ$, $gg\rightarrow ZZ$, $qq\rightarrow qqZZ$,..... can be grouped into 6 categories in terms of coupling strength, namely α_s^2, α_w^2, $\alpha_s^2\alpha_w$, α_s^4, $\alpha_s^2\alpha_w^2$,, and α_w^4. These backgrounds must be studied more.

Some comments on signal properties are

1. angular distribution of $V_L\rightarrow l+l'$ is $\dfrac{d\Gamma(V_L)}{d\cos\theta^*} \sim \sin^2\theta^*$
2. $V_LV_L\rightarrow V_LV_L$ processes give coplanar events at very high mass.

Therefore, at very high mass (Mvv $\geq$ 2 TeV), the processes

$ZZ \rightarrow l^+l^-$ j j

$ZW \rightarrow l^+l^-$ j j

could be used because of 1. very small m_{jj}^2/E_{jj}^2

2. very small $p_t^2(VV) / m_{VV}^2$ (acoplanarity)

and 3. small jet activities ($p_{tj} \sim \alpha_s m_W$)

4. Conclusion

SSC has a unique possibility of detecting model independently

" the Physics of Electroweak Symmetry Breaking "

whose understanding is the key for us to go beyond the standard model. However, to my knowledge, no convincing demonstration has been made that this physics goal can in fact be achieved by a realistic detector at SSC. Dedicated efforts are needed to predict details of all the signal and background processes, and a detector performance should be set to ensure achievement of this physics goal. Once this is insured, you can have a good dream!

[1] Chanowitz-Gaillard, NP B261(1985) 379,
Chanowitz-Golden-Georgi PR D36,1490

SDC AT HIGH LUMINOSITY

by

Dan Green
Fermi National Accelerator Laboratory

1.0 Introduction

Why is it prudent to plan for a luminosity (L) of $> 10^{34}/(cm^2 sec)$ from the beginning? First, the SSC is easily capable of attaining high luminosity. In comparison, for $\bar{p}p$ machines such as the Tevatron, increases in L are difficult. Second, after early runs at design luminosity, the only simple upgrade to a general purpose detector is an increase in luminosity. Third, and most important, the only known model independent physics goal of SSC is in the electroweak sector; the ZZ scattering amplitude reaches the unitarity bound[1] for $\sqrt{\hat{s}} \simeq 3$ TeV. In order to reach this mass range, and assure that some new physics is found, high luminosity running is needed. Since high luminosity running is desirable and easily attainable, it is inevitable. Therefore, one should build the "hooks" for upgrades to high L into the SDC from the beginning. The experience of CDF is that if this is not done, upgrades can be painful. Specifically, if possible, SDC should make sure that the chosen technologies allow high L operation. The time to plan for the whole useful lifetime of SDC is from the beginning.

2.0 Physics Reach

A generic partonic cross section is[2]:

$$d\sigma/dM \sim \alpha^2_{EFF}(1 - - M/\sqrt{\hat{s}})^{\beta}/M^3$$
$$\langle x \rangle \simeq M/\sqrt{s},\ \beta \sim 12. \qquad (1)$$

The physics reach for a 10 fold increase in L depends on the process. For Higgs searches, $\alpha_{EFF} \simeq \alpha_w$ and the weakness of the coupling means that search limits at design luminosity are at $M \lesssim 0.8$ TeV or $\langle x \rangle \lesssim 0.02$. The source distributions are then, $(1 - \langle x \rangle)^{\beta} \sim 1$ so that a 10 fold increase in L leads to a $(10)^{1/3} \simeq 2$ fold increase in mass reach.

For dijets, with strong coupling $\alpha_{EFF} \sim \alpha_s$, one can reach $M_{JJ} \simeq 10$ TeV ($\langle x \rangle \sim 0.25$) at design luminosity. A 10 fold increase in L only leads to a factor 1.3 increase in M_{JJ}, since one is now limited by the source functions. Thus, the two gauge boson search gains most with L

since one is limited by statistics, but is at low <x>. By comparison, dijet physics is likely to be best done at or below design luminosity.

Where in phase space is the multi-TeV physics scale? The central (wide angle) region is the discovery region. For example, a 2 TeV mass object has a kinematic limit of $y_{MAX} \sim 3.0$

$$y_{MAX} = \ln (1/\langle x \rangle). \tag{2}$$

Clearly, allowing two units of rapidity to fall off the "plateau," multi-TeV masses populate only the central region. Figure 1 shows that there is little loss in cross section due to sources even with soft gluons if $M \lesssim 4$ TeV, while for $M \gtrsim 2$ TeV only the central (barrel) $\pm$ 1.0 unit of y is populated. Therefore, only the central barrel region needs to function at high luminosities since the forward region is depopulated for these high mass objects.

3.0 Radiation Dose

A crucial issue for high luminosity detector performance is obviously the radiation dose. The maximum dose comes in the electromagnetic calorimeter, since the energy deposition is most concentrated there. The energy deposited by one m.i.p. crossing a plane of material of density ρ, volume V is roughly:

$$\text{e.m.i.p.} = (\sigma_I \, LT) \; (1/\sigma_I \, d\sigma/dy) \; (1/2\pi R_\perp^2) \Delta E \rho V. \tag{3}$$

where σ_I = inelastic cross section, L = luminosity, T = dose time, $R_\perp$ = transverse distance, and $\Delta E \simeq 1.8$ MeV/(gm/cm^2). Approximating $P_\perp \simeq \langle P_\perp \rangle \simeq 0.5$ GeV, then $P \simeq \langle P_\perp \rangle / \sin\theta$. The number of shower m.i.p.s. at shower maximum in the EM detector is $\equiv n_e^{MAX} P = n_e^{MAX} \langle P_\perp \rangle / \sin\theta$. The maximum energy deposit, and dose are:

$$\begin{aligned} E_{MAX} &= (\text{e.m.i.p.}) \; n_e^{MAX} \langle P_\perp \rangle / \sin\theta \\ \text{dose} &= (E_{MAX})/(V\rho). \end{aligned} \tag{4}$$

Numerically, for $\sigma_I = 100$ mb, $L = 10^{34}/(\text{cm}^2\text{sec})$, $T = 10^7$sec/yr, $(1/\sigma_I \, d\sigma/dy) = 3\pi^0$/unit of rapidity, $n_e^{MAX} = 10$ e/(GeV incident),[3] the dose is $\simeq$ 21 krad for $\theta = 90°$, $R_\perp = 2.0$m, and 3.4 Mrad for $y = 3$, $z = 5.0$m, $R_\perp = 0.5$m for plastic scintillator. These limits are almost attainable, in that samples of scintillator (green) exposed to 1 Mrad suffer only modest changes in light output.[4] The goal of preserving the operation of the central barrel over the roughly 10

year life of SDC, operated at high luminosity, seems almost possible. In what follows one assumes that the "discovery" region is not impaired for calorimetry. However, the $1/(R_\perp^2 \sin\theta)$ behavior of Eq. 4 means that $y \geq 3$ is problematic for calorimetry. Hence the missing E_T measurements will be compromised.

Tracking will exist at lower $R_\perp$, but will not suffer the increase in m.i.p.s. due to an electromagnetic shower. Ignoring neutron albedo leaking back into the tracking detectors,[5] one finds that at 90°; $R_\perp$ = 1.5m, dose ~ 21 krad $(2.0/1.5)^2(2)/5$ ~ 15 krad/year. It seems plausible that radiation hard tracking could be made to work in this radiation field. Clearly, from Eq. 3, the dose goes as $1/R_\perp^2$. By comparison, the momentum resolution is proportional to $1/R_\perp^2$ in the barrel. Much optimization of dose vs. resolution clearly needs to be done. The stable operation of both detectors and readout electronics becomes problematic for detector radii much less than 1.5m.

As a simple example of a system at large radii consider a set of scintillating fibers 1mm x 1mm x 4m in two superlayers (xx'uv + xx'uv). Such a minimal system has 150,000 channels of readout. In the case of fibers, there is neither gain (heat) nor electronics (heat and radiation damage) within the solenoid volume; all power is dissipated outside the calorimeter volume - which also acts as a radiation shield. This layout also offers a potential commonality of tracking and calorimeter readout-pipeline and triggering. As noted above,[5] the "sea" of albedo neutrons has not been discussed. Clearly, the response of scintillating fibers, or any other tracking detector, immersed in this "sea" is a crucial problem to be given detailed study.

4.0 Quark, Lepton, and Boson Identification

Increasingly, one can think of the task of general purpose collider detectors to be that of detecting partons. The gauge bosons to identify are γ, $W^\pm$, Z^0, and g. The fermions are leptons (e, μ, τ, and ν) and quarks (u, d, s, c, b, and t). The main question is if, indeed, the possible necessity of operating tracking detectors only at $R_\perp \gtrsim$ 1.5m has severly compromised the physics. Specifically, have we lost the 2 gauge boson physics which we raised the luminosity in order to gain?[6]

For tracking, assume two superlayers at $R_\perp$ = 1.5m to 2.0m. The radiation dose seems tolerable at $L = 10^{34}/(\text{cm}^2\text{sec})$. For Δy = 2 length elements, there are roughly 480 charged tracks. Assuming 1mm diameter elements, the occupation level is only 2.5% (1 track every 5 cm of azimuthal distance). Clearly pattern recognition appears possible at least in principle. Given two layers separated by 50 cm, one can resolve angles of ~ 1 Mrad. In a 2T field, a 1 TeV track bends 1 Mrad in 1.5m, or $(dP_\perp/P_\perp^2)$ ~ $(1\ \text{TeV})^{-1}$. This value for the resolution assumes

that the vertex is known from accelerator scans. The tracking "stubs" then give a redundant measurement of energy to compare to the electromagnetic calorimeter, $dE/E \simeq 0.15/\sqrt{E} \oplus 0.01$.

At this point, detailed studies of particle identification at high L have not been made. However, some obvious and superficial comments can still be made. To lowest order, high $P_\perp$ jets (in the multi-TeV range) are not seriously altered by high luminosity; u, d, s, c, b, t; g are still usable. Since γ and e (and hence W, Z) are detected primarily by calorimetric means, they too will be largely uneffected. Since calorimetry will be difficult for $y \geq 3$, missing $E_\perp$, or ν tagging will be compromised. Secondary vertices (c, b, t) are probably impossible at high L. Conversely, these processes occur inclusively at high rate and will be well studied at low L. Finally, muon momentum measurement, but <u>not</u> identification, is compromised by the loss of momentum resolution. The proposed SDC muon system has some "stand alone" capability with room for added detector planes as part of a high L upgrade. The mass resolution for $Z \to \mu\mu$ is degraded, but if the S/N is acceptable a constrained fit to $M_{\mu\mu} \equiv M_Z$ can be made.

5.0 Z, ZZ Resolution at High L

A major physics emphasis of SDC is on 2 gauge boson scattering up to the unitarity limit at $\sqrt{s} \sim 3$ TeV. A one year run at design luminosity will only yield a handful of events of the "gold plated" variety, $H \to ZZ \to 4l$, $l = e, \mu$ for Higgs masses above 600 GeV. It is primarily for this reason that high luminosity running is considered. What compromises are made in detector performance?

Let us begin with the Z natural width. $\Gamma_Z/M_Z \sim \alpha_w$, $\alpha_w \equiv \alpha/\sin^2\theta_w \sim 1/30$. This width sets a natural scale for detector resolutions.

$$\begin{aligned} \Gamma_Z/M_Z &\sim \alpha_w \\ dM_Z/M_Z &= 1/\sqrt{2}(dP_l/P_l). \end{aligned} \tag{5}$$

The comparison is shown in Fig. 2. Clearly, in the e^+e^- final state calorimetry supplies a resolution dM_Z comparable to $\Gamma_Z/2$. In contrast, the tracking has $dM_Z > \Gamma_Z/2$ for all rapidity of interest, as does the toroids. Therefore, signal/noise is degraded. However, with isolation cuts, for example, to reject $t\bar{t}$ background, the S/N for dimuons appears to be acceptable.[7] That being true, one can impose the constraint $M_{\mu^+\mu^-} \equiv M_Z$ and improve the errors on the muon track parameters. In Fig. 2, tracking with $dP_\perp/P_\perp^2 = (1\ \text{TeV})^{-1}$, calorimetry with $dE/E = 0.15/\sqrt{E} \oplus 0.01$, and toroids with $dP_\perp/P_\perp = 0.2$ was assumed.

What about H → ZZ? The scale for the detector resolution is again set by the natural width;

$$\Gamma_H/M_H \sim \alpha w(M_H/M_w)^2$$
$$\Gamma_H \sim 0.5 \text{ TeV } (M_H/\text{TeV})^3 \quad (6)$$
$$dM_H/M_H = 1/2\sqrt{2}\ (dP_l/P_l).$$

The relevant curves are shown in Fig. 3. A constrained fit was assumed for tracking and toroids, but not for calorimetry, since $dM_Z \leq \Gamma_Z/2$ in this latter case. It appears that, in the heavy Higgs regime where one wants high L, resolution on the physics (Γ_H) is not compromised for $M_H \geq 0.4$ TeV. Thus, the main goal of high L running is preserved. However, it must be noted that calorimetry and toroids (steel) have a resolution improving with or independent of y, while tracking resolution deteriorates as P ~ cosh y. Thus, at y = 3 the tracking resolution will be perhaps 10 times worse, and the muon system will need to rely on external toroids (perhaps air core). A detailed cost/benefit study needs to be made since the region y = 3 is precisely that region largely depopulated by high mass states (see Fig. 1).

6.0 Pileup Effects

6.1 Minbias:

A serious potential difficulty for high luminosity running is caused by the overlap of ~20 minbias events per bunch crossing. Assuming $\langle P_\perp \rangle \sim 0.6$ GeV and 6 tracks per unit of rapidity, 20 events yield 72 GeV of $P_\perp$ in $|y|<3$ per minimum resolving time of one bunch. Obviously, a global E_T trigger needs a rather higher threshold at higher L.

What about towers? For granularity of $\Delta y \sim 0.05$, $\Delta\phi \sim 0.05$ (10 x 10cm @ 90°, $R_\perp$ = 2.0m), there is only 30 MeV of $P_\perp$/tower in minbias overlap. However, a typical jet of interest has a size at least $R_{cone} \equiv \sqrt{\Delta y^2+\Delta\phi^2} \sim 0.2$. This means 16 towers in a cluster trigger or ~ 0.5 GeV of $P_\perp$ in minbias. With discovery level at $P_\perp \sim M_{JJ}/2 \sim 5$ TeV (see Section 2.0), the fluctuations in the minbias background cause little problem. High L raises the "underlying event" by 10x in $P_\perp$ scale, but that scale is still very low w.r.t. the SSC discovery scale of multi TeV.

What about triggering on jets? The minbias events have a cross-section which goes as $d\sigma/dP_\perp^2 \sim \exp(-bP_\perp)$, while jets have a power law, hard scattering spectrum, $d\sigma/dP_\perp^2 \sim 1/P_\perp^4$. Therefore, the hard scattering physics will always prevail over the soft minbias triggers at suficiently high $P_\perp$. To set the scale, $\langle P_\perp \rangle \sim 2/b \sim 0.6$ GeV per minbias track. The high luminosity overlap level is ~ 0.5 GeV/cluster (1/16 track per tower). Thus, one might apply a

threshold cut of 1 GeV per cluster in order for a cluster to add to the jet $P_\perp$ sum. This threshold, on average, subtracts out the underlying pileup of minbias events. The conclusion of an early Snowmass study[8] was that one could simply raise the jet-trigger threshold by a few GeV at high luminosity.

6.2 W → JJ Mass Resolution:

If possible, one wants to preserve the dijet mass resolution at high luminosity. A benchmark for detector performance is $W^- \to \bar{u}d$. Given that the quark fragments uniformly in y, the major problem is in confusing slow fragments of the quarks with the underlying (overlapped) minbias events. The scale is set by the momentum at which that confusion exists;

$$dM_{\bar{u}d} \sim P_{Slow}$$
$$[M^2_{\bar{u}d} \sim 2\sum_{F,S} P_{Slow}\ P_{Fast}\ (1-\cos\theta_{FS})]. \qquad (7)$$

The slow fragments make a large contribution to the dijet mass since they contribute to $M_{\bar{u}d}$ multiplied by fast fragments, and θ_{FS} is large (since at fixed $P_\perp$ fragmentation, the slow fragments make large angles w.r.t. the quark direction). Thus, high L, which raises P_{Slow}, could make a major impact on dijet spectroscopy. A study of this problem has recently been made.[9] The idea was to study the resolution $dM_{\bar{u}d}$ as a function of calorimeter segmentation Δy, $\Delta\phi$ for various levels of pileup. In Fig. 4 is shown dM_W for 1 and 10 overlapped minbias events as a function of $\Delta y = \Delta\phi$. Clearly segmentation, $\Delta y = \Delta\phi \lesssim 0.05$ is preferable. Just as clearly, the jet algorithim confusion level (P_{Slow}) is greater than the intrinsic width $\simeq \Gamma_W/2 \sim 1.2$ GeV by a large factor.

The overlap of 10 events is not a factor 10 worse in dM_W, because (as in jet triggers, section 6.1) a $P_\perp$ threshold is placed on the cluster before it goes into the M_W calculation. This cut worsens dM_W by cutting out real quark fragments, but protects against pileup. More study is needed to optimize this procedure. At present, the tentative conclusion is that high L does not dramatically worsen the W mass resolution.

6.3 Z Pairs and Pileup

Does pileup hurt the Higgs search? In order to make a cursory examination, one notes that, as shown in Fig. 5, σ (ZZ) ~ 30 pb and $d\sigma/dM_{zz} \sim 1/M^3_{zz}$. A possible background comes from accidental Z overlaps from different events. Since $\sigma(Z) \sim 100$ nb, the overlap ZZ background at $L = 10^{34}/(cm^2 sec)$, if the live time is 50 nsec, is;

$$\sigma_{EFF}(ZZ) = \sigma(Z)\ [\sigma(Z)\ L\Delta t]=5\ \text{pb}. \tag{8}$$

which is comparable to σ (ZZ).

Clearly, the scale of $P_{\perp Z}$ for single Z production is O (M_Z), while that for continuum ZZ production is O (M_{ZZ}). The overlap ZZ mass spectrum is, however, harder than the continuum spectrum.

$$\begin{aligned} M_{ZZ}^2 &\sim 2\ M_Z^2[1 + \cosh(\Delta y)] \\ \Delta y &= |y_{z1}-y_{z2}| \\ d\sigma/dM_{ZZ} &\simeq d\sigma/d(\Delta y)\ [d(\Delta y)/dM_{ZZ}] \sim 1/M_{ZZ}. \end{aligned} \tag{9}$$

The overlap spectrum (from ISAJET) is shown in Fig. 6a. For 1000 (5 pb) overlaps there are 150 events with $M_{ZZ} > 1$ TeV, which is indicative of the long $1/M_{ZZ}$ tail. For $M_{ZZ} = 1$ TeV, Eq. 9 yields $\Delta y = 4$, which is within the barrel region ($|y| < 2$). Assuming $1/M^3$ and $1/M$ behavior respectively, one has $\sigma(ZZ)/\sigma_{EFF}$ (ZZ) ~ 0.24 at M_{ZZ} ~ 1 TeV.

Even so overlap ZZ events are not a problem if the $P_\perp$ spectrum of the Z is well understood. Since $P_{\perp Z}$ is limited, $\langle P_{\perp Z}\rangle$ ~ 26 GeV in ISAJET for overlap ZZ, the overlap events look like very asymmetric decays. Real H → ZZ decays have $P_{\perp Z} \sim M_H/2$ for symmetric ($\cos\theta^* = 0$) decays. In Fig. 6b is plotted the c.m. decay angle, $\cos\theta^*$, for all overlap events treated as H → ZZ decays. Clearly a modest cut of $|\cos\theta^*| < 0.75$ removes almost all overlap events while preserving the majority of the real H → ZZ decays.

7.0 Summary

High luminosity appears to be feasible from an accelerator viewpoint, and desirable in that the electroweak mass reach doubles. Hence, it is probably inevitable and SDC should plan for high L operation from its inception. Upgrades should be provided for ab initio.

At the mass scales of interest, the central barrel region is populated, while the end caps are not. The radiation dose is such that forward calorimetry is difficult. In the barrel region tracking seems feasible in the outer 50cm directly proceeding the solenoid coil. This tracking lever arm can yield "stubs" which aid electron identification, muon momentum measurements, and give energy measurements at reduced (w.r.t. design luminosity) resolution.

Calorimetry in the barrel is not at radiation risk, although the loss of high y means that the neutrino trigger is compromised. Thus e, μ, and jets will continue to be detectable, although muons will have reduced momentum resolution of $dP_\perp \sim P_\perp^2/(1\text{TeV})$, $dP_\perp \sim 0.2\ P_\perp$.

The loss of y range and μ resolution does not hurt $ZZ \to 4l$ physics for ZZ masses ≥ 0.4 TeV. The lower mass scales will be well studied at the design luminosity of the SSC in any case.

The overlap of minbias events does not appear to severely compromise either the jet trigger or the jet $P_\perp$ measurements. Dijet masses appear not to be ruined by pileup, but more realistic studies need to be made. Overlap ZZ events are controlled, if the $P_{\perp Z}$ distribution is limited.

In summary, quite to the authors surprise, high luminosity running looks plausible. Clearly, this is an extremely tentative conclusion and much more detailed studies are required.

References

[1]M. Chanowitz, Ann. Rev. of Nuc. and Part. Sci. 38 323, (1988).

[2]D. Green, $\bar{p}p$ Collider Physics, Fermilab-Conf-89/70.

[3]S. Iwata, DPNU-3-79.

[4]F. Takasaki, High Energy Physics in the 1990's, Snowmass 88.

[5]D.E. Groom, SSC-SR-1033.

[6]T. Skesson et al., The Feasibility of Experiments at High Luminosity at the LHC, CERN 88-02.

[7]L. Nodulman et al., $\bar{t}t$ backgrounds for $H \to \mu^+\mu^-\mu^+\mu^-$ at the SSC. SSC Lab Preprint.

[8]H. Gordon et al., Proceedings of the 1982 DPF Summer Study, Snowmass 82.

[9]A. Bay et al., High Energy Physics in the 1990's, Snowmass 88.

Figure Captions

1.a. Source factor for soft gluons (β=12) as a function of mass.

1.b. Plateau half width as a function of mass for $\sqrt{s}$ = 40 TeV.

2. Reconstructed width of Z bosons as a function of rapidity using calorimetry, (e^+e^- solid curve) tracking (l^+l^- dashed curve) and muon steel toroids ($\mu^+\mu^-$ dot-dashed curved). Natural width scale is cross hatched.

3. Reconstructed width of Higgs bosons as a function of Higgs mass for $y_H = 0$ using calorimetry (solid curve), tracking (dashed curve) and steel toroids (dot-dashed curve). Natural width scale is cross hatched.

4. W mass resolution for W → JJ as a function of segmentation for 1 and 10 overlap minbias events.

5.a. ZZ continuum cross section vs. $\sqrt{s}$.

5.b. $d\sigma/dM_{zz}$ for longitudinal and transverse polarizations of ZZ bosons.

6.a. ZZ overlap mass distribution for "accidentals."

6.b. ZZ decay angle, $\cos\theta^*$, assuming H → ZZ.

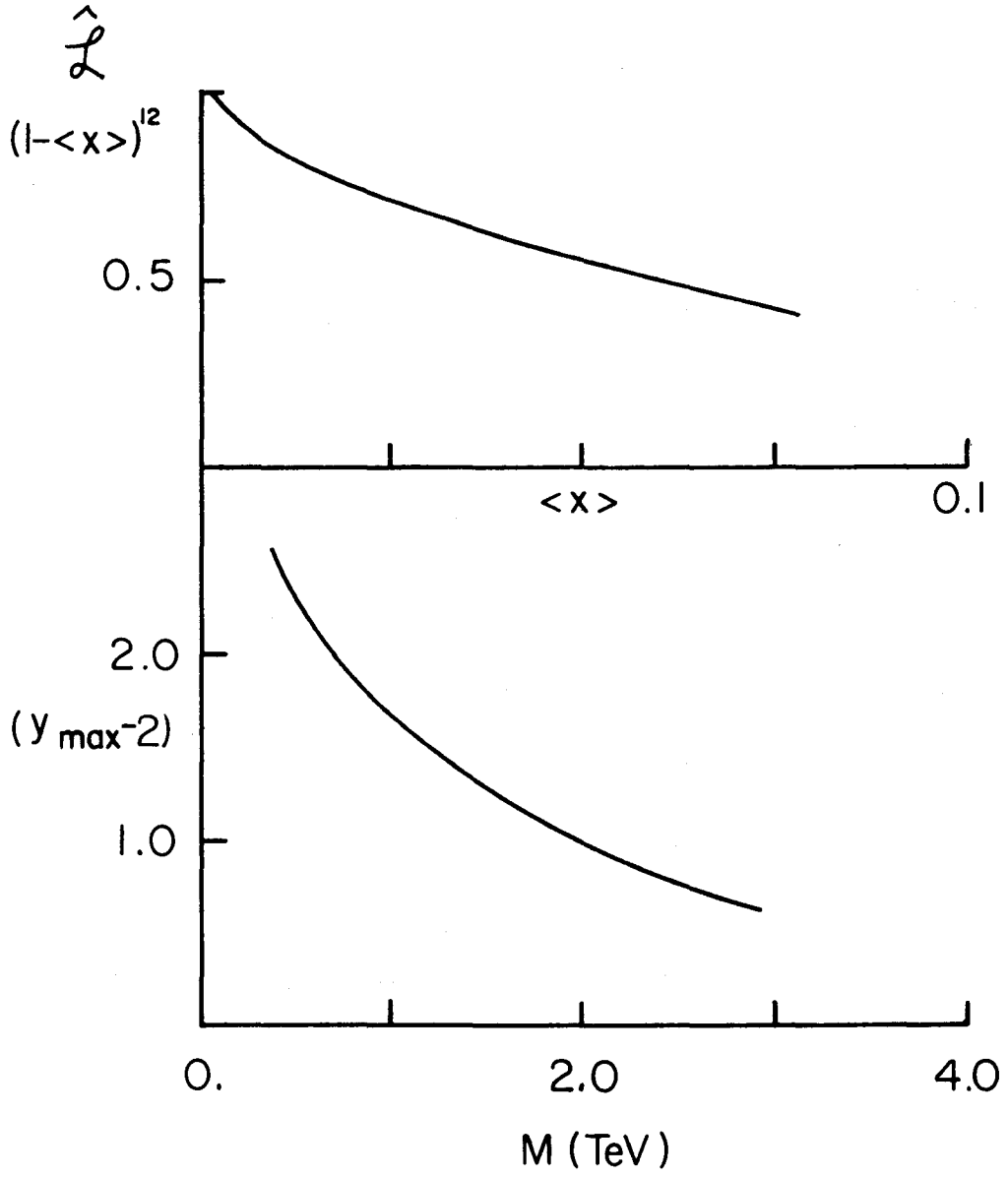

1.a. Source factor for soft gluons (β=12) as a function of mass.

1.b. Plateau half width as a function of mass for $\sqrt{s}$ = 40 TeV.

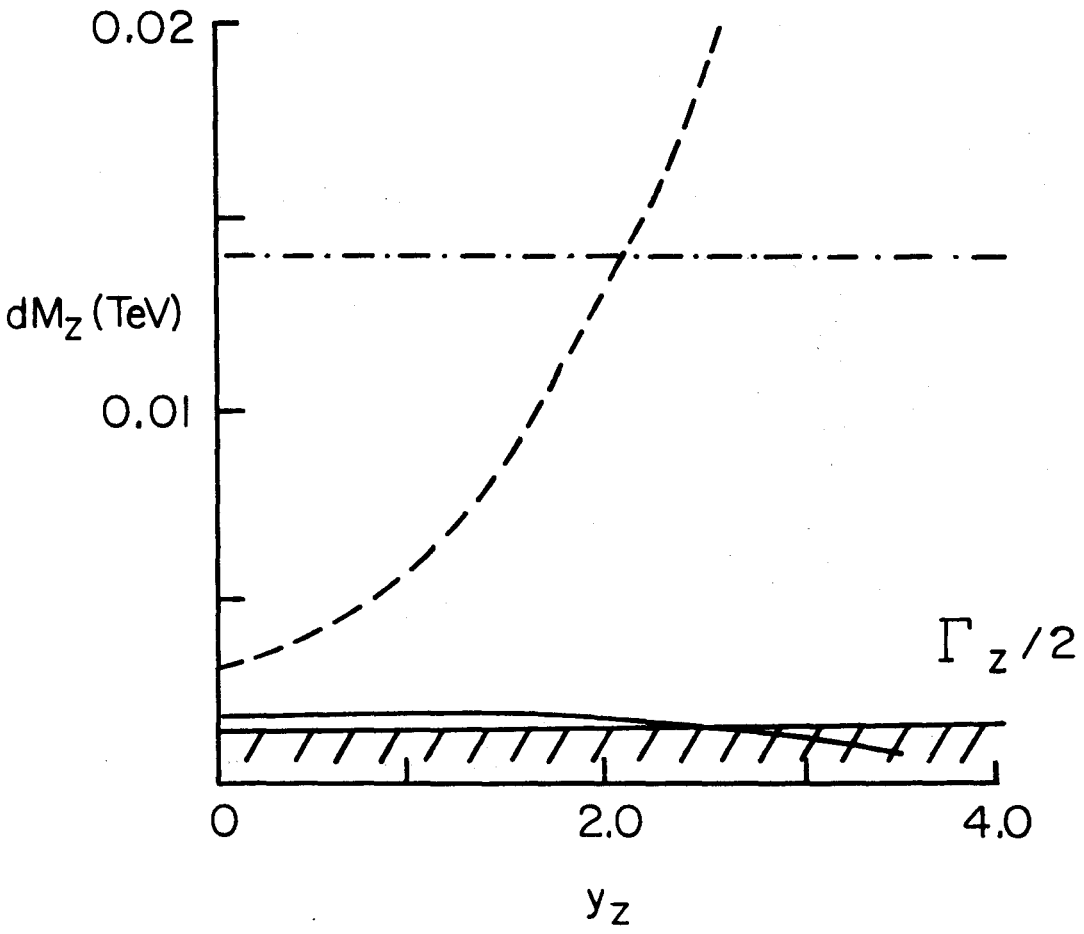

2. Reconstructed width of Z bosons as a function of rapidity using calorimetry, (e^+e^- solid curve) tracking ($\ell^+\ell^-$ dashed curve) and muon steel toroids ($\mu^+\mu^-$ dot-dashed curved). Natural width scale is cross hatched.

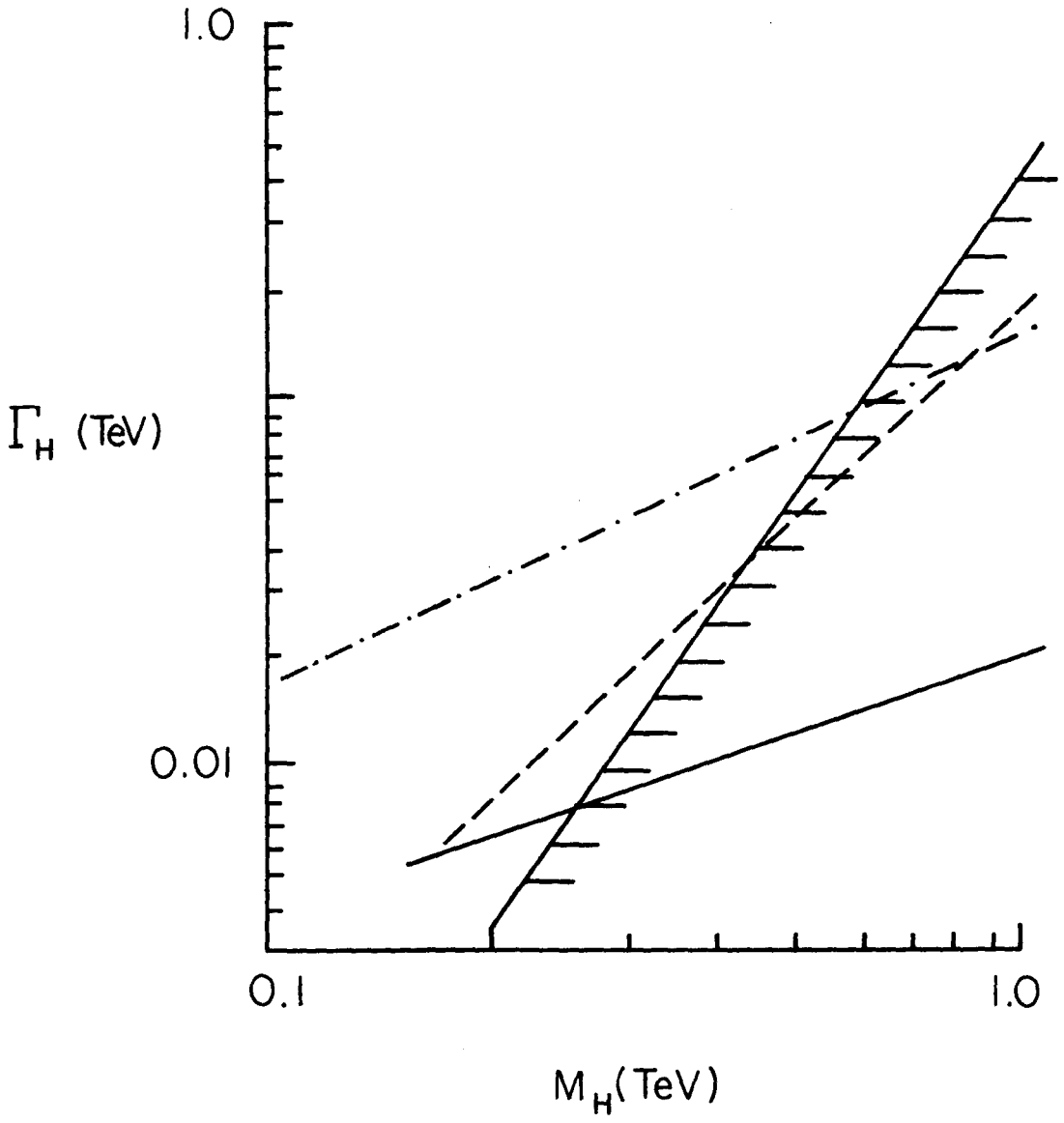

3. Reconstructed width of Higgs bosons as a function of Higgs mass for $y_H = 0$ using calorimetry (solid curve), tracking (dashed curve) and steel toroids (dot-dashed curve). Natural width scale is cross hatched.

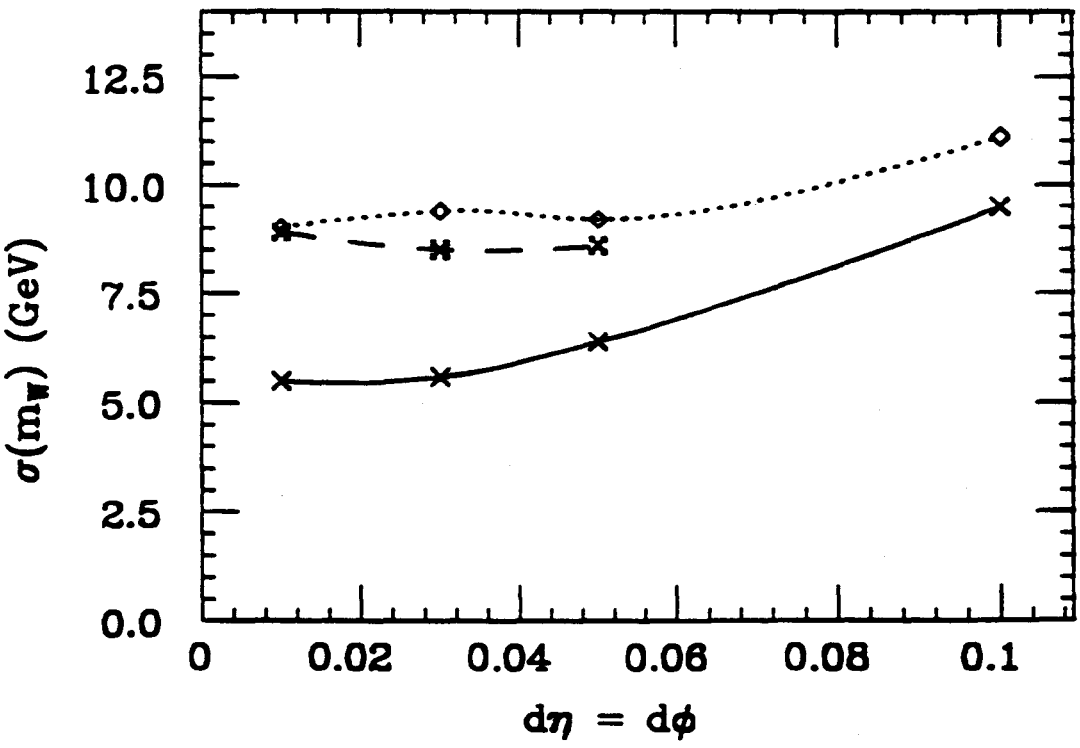

4. W mass resolution for W → JJ as a function of segmentation for 1 and 10 overlap minbias events.

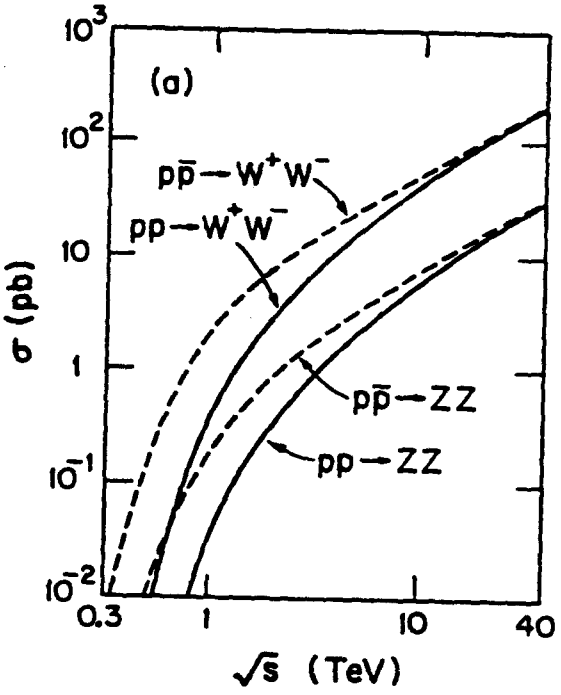

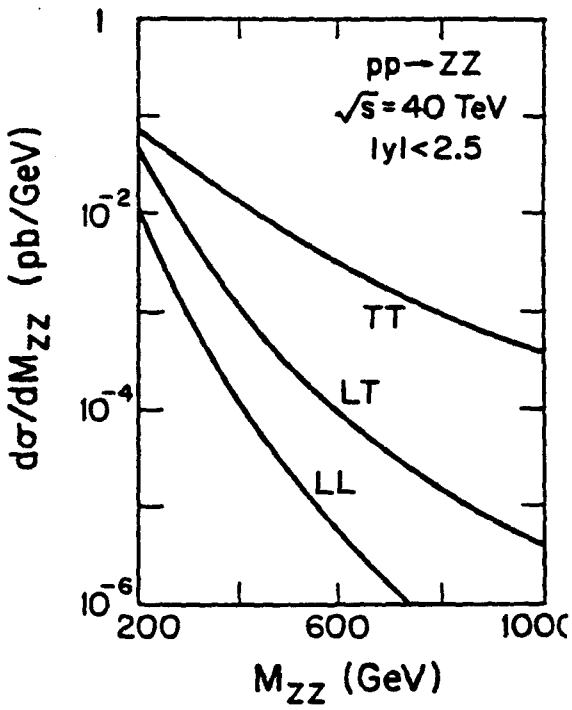

5.a. ZZ continuum cross section vs. $\sqrt{s}$.

5.b. $d\sigma/dM_{zz}$ for longitudinal and transverse polarizations of ZZ bosons.

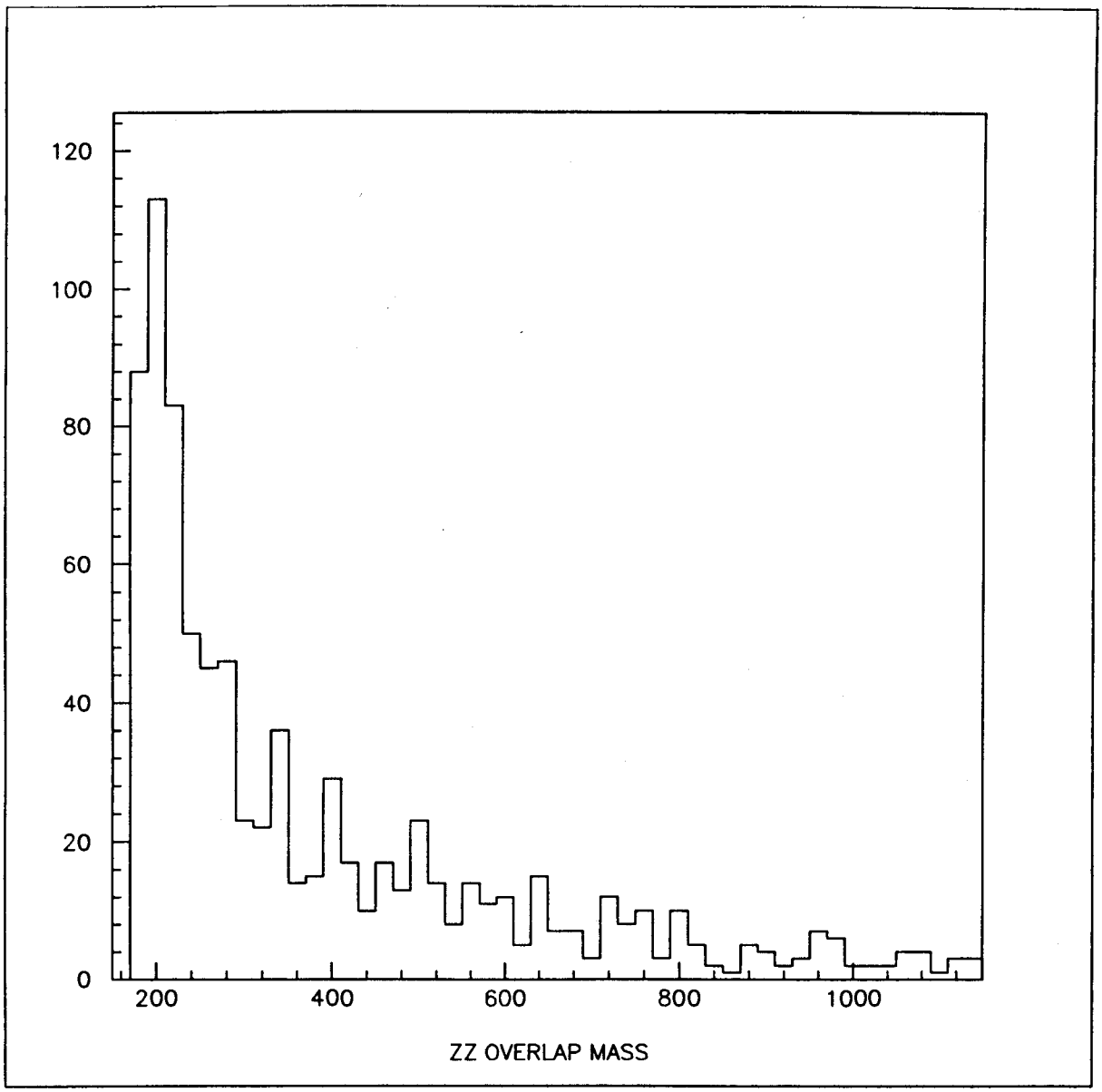

6.a. ZZ overlap mass distribution for "accidentals."

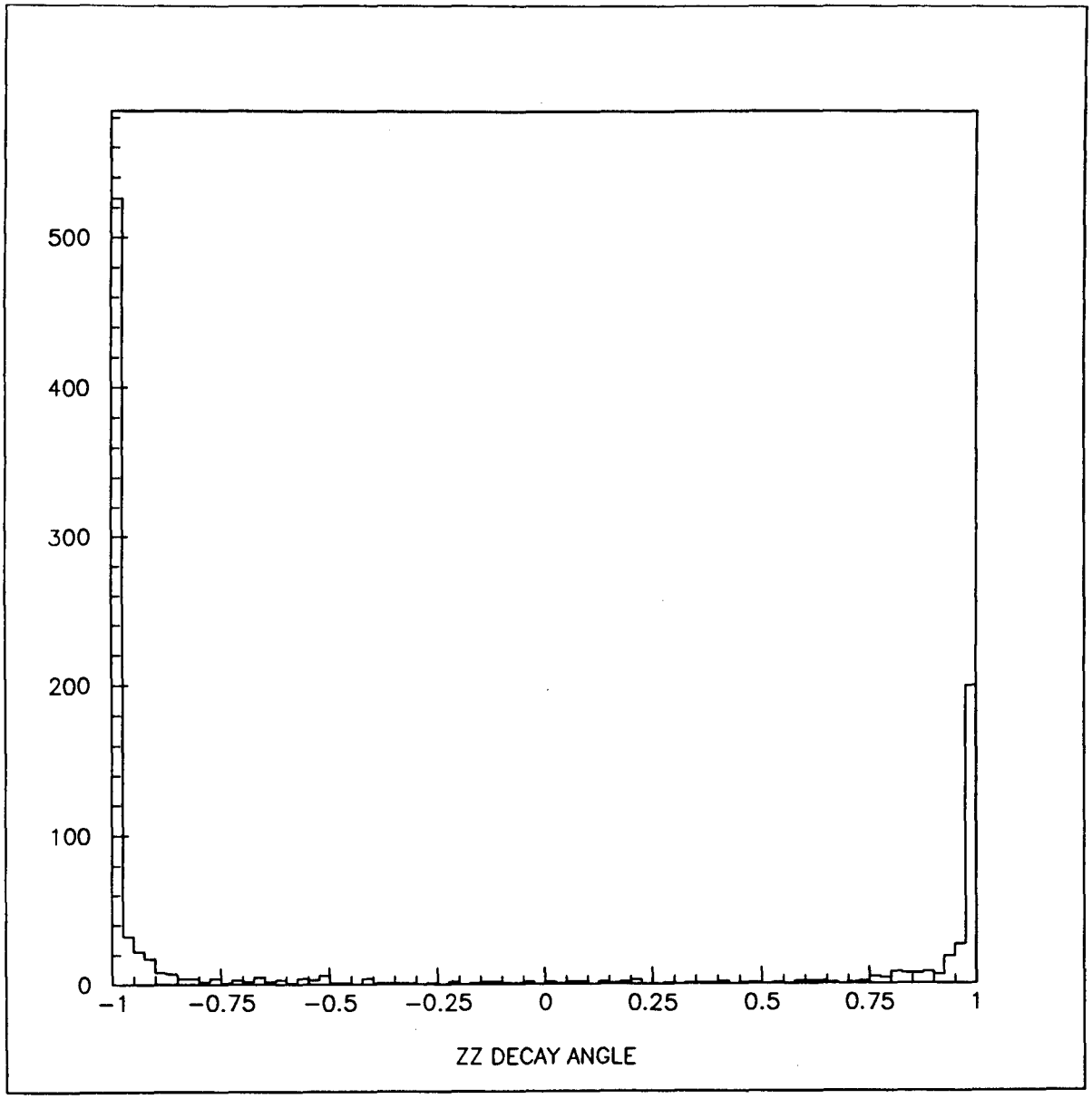

6.b. ZZ decay angle, $\cos\theta^*$, assuming H → ZZ.

SDC - overview and physics goals

G. Trilling
LBL

******** This summary is written by the proceeding **********
******** editor based on the transparencies presented. ********

Benefits of a Solenoidal Detector

1. Almost all e^+e^- detectors, the CDF detector, and both ep detectors are solenoidal. In a program which studies new phenomena, it seems inconceivable not to have at least one solenoid magnet detector.

2. The momentum information makes the detector a fine exploratory tool, adapted to study a wide range of physics at all Pt and at a wide range of luminosities.

3. The field permits determination of electron signs up to 1-2 TeV Pt. Direct applications include like-sign W production, and some supersymmetric signatures. Indirect applications include improved understanding of potential backgrounds. At Pt<100 GeV momentum precision is comparable to calorimeter precision.

4. Muons can be accurately measured over the rapidity region covered by the tracking and magnet.

5. Reconstructed segments in outer layers can help provide an effective high Pt electron trigger. Momentum/calorimetry provide effective electron ID.

6. Momentum measurements are necessary to properly interpret information from vertex detectors. Measurements of impact parameters can be used both to detect B-jets, or to recognize prompt leptons.

7. The solenoid tracking can provide in-situ monitoring of the calorimetry.

8. Jet fragmentation at high Pt can potentially be studied (provided that the fine resolution provides by silicon can be achieved).

9. Charged particle multiplicity for tracks above a minimum value of Pt can potentially be useful for removing some backgrounds, especially in the study of heavy Higgs.

10. Tracking technology may well undergo continuing technological development. It is quite conceivable that in a future upgrade the tracking chamber may be replaced by one with improved technology. With a coil in place, this possibility remains a real option.

Conclusions

1. A Solenoid Detector appears to be well-matched to the opportunities presented by the exploration of a totally new energy range.

2. An SSC detector is a large extrapolation from existing detectors. Engineering and cost/benefit considerations will necessarily play a more important role.

3. A large and dedicated group will be required to put it together , but the scientific prospects are extremely exciting.

Knife edge chamber and parallax spectrometer

P. McIntyre
Texas A&M

******** This summary is written by the proceeding **********
******** editor based on the transparencies presented. ********

Two problems for magnetic spectroscopy :

Chamber technology

Need 1. $\sigma \sim 20\mu m$, 2. $t_{live} \sim 15$ nsec, 3. Mrad radiation hardness

No existing technology has all three.

Spectrometer design

> 200 track/events are extremely difficult to reconstruct, prone to "fake" high pt solutions.

Tracking Specifications and Technology

	Spatial Resolution	2-track Resolution	Live Time	Radiation Hardness
Need	< 50 μm	< 1 mm	16 nsec	~ Mrad
Straw Tube	> 150 μm	~ 3 mm	~ 60 nsec	?
Si strip	~ 20 μm	~ 100 μm	~ 100 nsec	X
Sci Fi	~125 μm	250 μm	~ 10 nsec	?
KEC	~ 25 μm	~ 100 μm	~ 10 nsec	√

Progress of R&D of KEC to date

- sputter deposition of metals and dielectrics
- evaporation deposition of metals and dielectrics
- photolithography to submicron dimensions
- plasma etching of metals of dielectrics and semiconductors
- ODE of silicon

- a class 100 clean room with 18MΩ deionized water
- diffusion oxide film growth
- scanning electron microscope (SEM) capability

READY TO MAKE A CHAMBER.....

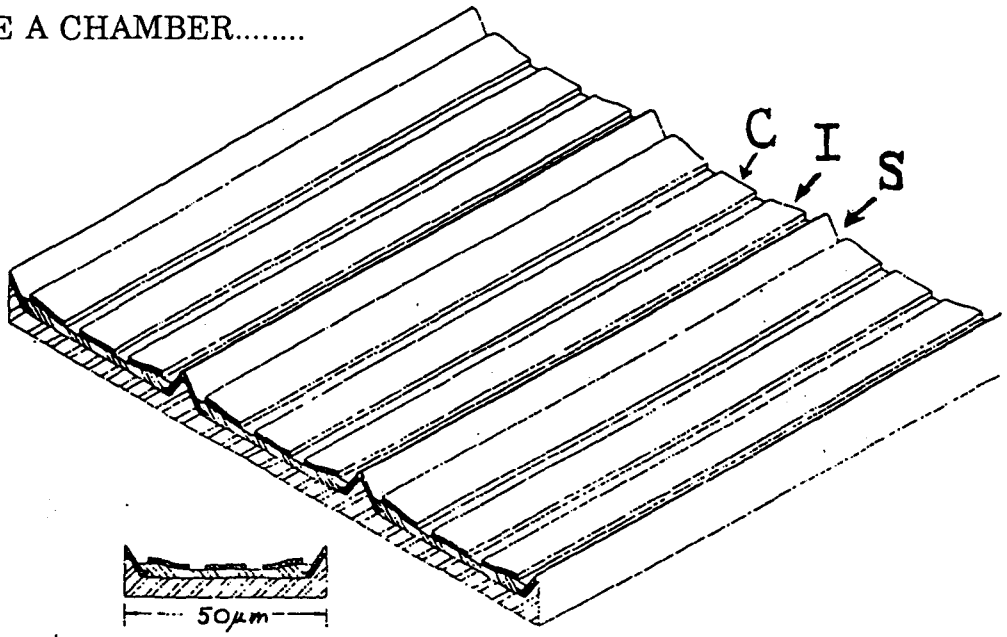

The Parallax Spectrometer

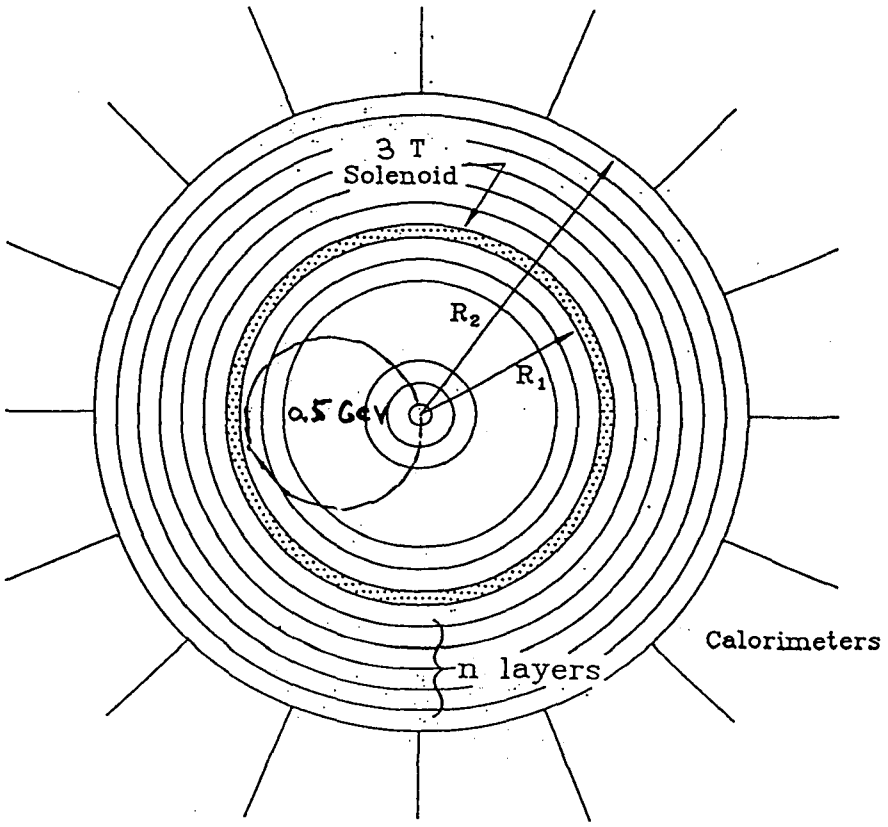

B	magnetic field	3 T
R_1	magnet radius	1 m
R_2	max. chamber radius	2 m
σ	spatial resolution	20 μm
n	number of layers	5
$\sigma_{P_\perp}/P_\perp^2$	statistical momentum resolution	8.7×10^{-5} GeV^{-1}
$\sigma_{P_\perp}/P_\perp$	mult. scat. momentum resolution	0.7 %

High Luminosity Solenoidal Detector for Higgs

Richard L. Lander, Physics Department and IIRPA
University of California Davis

Abstract

A detector incorporating a 4m diameter, 6 Tesla solenoid and a large absorber is described. The multiple scattering contribution to the transverse momentum resolution is shown to be a few percent for absorbers as thick as 15 to 20 interaction lengths, even for iron absorbers. It is less if the absorber is carbon or beryllium. Other contributions to the resolution probably can be significantly smaller. Trigger rates and occupancy are likely to be acceptable. A detailed study needs to be performed.

Introduction

The study of prompt muons has been fruitful in the past, as evidenced by the experiment that discovered the upsilon (B quark). Muons at the SSC can also be expected to provide insights into the behavior of elementary particles. Beam dump style detectors for collider accelerators have, in fact, been studied in the past[1]. None has been built, to our knowledge. One of the main problems in such detectors is the effect of multiple scattering on the momentum resolution. Detectors that rely for momentum analysis on the magnetic field produced by iron are limited to about 2 Tesla in field strength and have a momentum-independent resolution that decreases inversely as the square root of the the path length in iron. For 2 or 3 meter lengths, this resolution is about 10 percent or more.

We avoid this limitation by placing the absorber inside a very high field supeconducting magnet, and placing the momentum-measuring trackers outside the solenoid, using the beam interaction point to fix the other end of the track. Fig. 1 illustrates the geometry. The two main factors in determining the momentum resolution are the multiple scattering in the absorber and the accuracy of the angle measurement. We will show that for a 6 Tesla field in a solenoid of 2 meter radius (If iron is used as the absorber, the field is then about 8.0 Tesla.) the multiple scattering contribution to the momentum resolution is a

[1]See the 1974 and 1975 PEP Summer Study reports.

few percent (independent of momentum) even for 15 interaction lengths of absorber, unless one uses high Z materials like tungsten or uranium. The requirement on the angle measurement will depend on the momentum, varying from about one milliradian or less at 100 GeV to a tenth of a milliradian or less at 500 GeV, for a 2% angle measurement.

Multiple Scattering

Studies of punch-through fluxes[2] suggest that 10 to 15 absorption lengths will be needed to reduce the punch-through at the SSC to levels that can be tolerated. For iron, this thickness is about 2 meters. For carbon and beryllium, it is about 5 meters. We consider here an absorber that fills the solenoid (iron) or which may extend outside the coil (carbon or beryllium) as shown in Fig. 1.

In the R-ϕ plane, a track from the interaction point will travel in a curved path through the absorber inside the solenoid, and thereafter follow a straight line through any remaining absorbing material. The direction outside the solenoid is determined by the transverse momentum of the track. A track of infinite momentum will lie along a radius (point back to the beam line). Tracks of lower momentum will lie at an angle Φ_B to the radial line drawn to the point where the track exits the magnetic field. The larger the angle, the lower the momentum. Thus a measure of the track direction determines the momentum.

The bend angle, Φ_B , is determined by the intergral of the magnetic field strength through the solenoid. The momentum resolution in the bend plane, dPt/Pt , is deterimined by $d\Phi_B/\Phi_B$. Multiple scattering will contribute to the error in this angle measurement. At a polar angle, Θ,

multiple scattering is defined by $\Phi_{ms} = (0.0141/P_t)\sqrt{R_2/X_o \sin\Theta}$

where P_t is in GeV/c. The bend angle is defined by $\Phi_B = (0.3/P_t)\int B\, dl$

where B dl is in Tesla-meters and P_t is in GeV/c. The ratio gives the multiple scattering contribution to the momentum resolution. For the arrangement of Figure 1, the ratio is

$$dP_t/P_t = \Phi_{ms}/\Phi_B = (.0141/0.3BR_1)\sqrt{R_2/X_o \sin\Theta},$$

---

[2]D. Hedin, p.169, Workshop on Major SSC Detectors, Tucson, Arizona,1990.

which becomes, for B = 6 Tesla and R_1 = 2 meters,

$$dP_t/P_t = 0.39\%\sqrt{R_2/X_0 \sin\Theta}.$$

Now $R_2 / X_0 \sin\Theta = N \lambda_{abs} / X_0$, where N is the number of absorption lengths. Once N is chosen, the momentum resolution depends on the square root of the ratio of the absorption length to the radiation length for the absorber used. Thus the square root of this ratio is the figure of merit for the material. A smaller value improves the momentum resolution. Table I shows X_0 and λ_{abs} and the square root of their ratio. Several values of X_0 and λ_{abs} are given for carbon, depending on the density, but the ratio is independent of density. It is clear that beryllium is a factor 2 better than iron, and carbon is almost as good. For iron, the values in parentheses reflect the effect of an additional 2 Tesla from the magnetization of the iron. The advantage of iron over carbon and beryllium is compactness.

The multiple scattering contribution to the resolution is shown in Fig. 2 as a function of N. For any absorber length likely to be required, the effect of multiple scattering in this spectrometer will be close to 2% for beryllium, less than3% for carbon, and less than 4% for magnetized iron.

Tracking

The tracking system that is used to determine the bend angle will itself contribute to the error in this angle measurement, and hence to the error in dP_t/P_t. For the 16 Tesla-meter magnet considered (magnetized absorber), the bend angle is 45 milliradians at P_t = 100 GeV. If we take the multiple scattering contribution to be 3.5% and want not to increase that value appreciably, then the contribution from this source should be held to 2% or less (which would give 4.0% in quadrature). At 100 GeV this requires that the exit track angle be known to an accuracy of 0.5 mr over a 1.5 meter tracking distance. At P_t = 500 GeV, 0.1 mr is needed. And the angle must be referenced to the beam line, some 2.5m or more away. This is probably not out of the question, but it will require some care. For absorbers other than iron, the bend is 36 mr at P_t = 100 GeV. Table II indicates the accuracy needed to keep the tracking contribution to dP_t/P_t below a specified percentage in the case of a non-magnetic or magnetic absorber.

Example Detector

Two very rough examples to illustrate what such a detector might look like are given in Figs. 3 and 4. The first uses magnetized iron as the absorber,while the second employs carbon. The carbon device is considerably larger than the iron, but even so, is not large by SSC standards.

One advantage of carbon (or beryllium) is that the radiative processes (bremsstrahlung and pair production) that lead to unwanted tracks accompanying the muon are less of a problem. The 1990 Tucson workshop[3] indicated that the number of muons that traverse more than two absorption lengths of material and emerge without any other accompanying track is about 90% for iron and 96% for carbon at 300 GeV. Thus 85% of the 4-muon events would have four "clean" muons. For iron, the number is 66%. However, an outer layer of low-Z material might reduce this effect. (The thick aluminum coil might serve this purpose.)

Radiative Losses

The muons will lose energy by ionization in traversing the absorber, as well as by the radiative processes. These losses of a few GeV can be corrected for, but their fluctiations will introduce an error in the correction. The Tucson workshop proceedings seem to indicate[3] that the variation in total energy loss for 316 GeV muons traversing 14 absorption lengths of Pb is 1 or 2 percent (sigma) of the most probable loss. The 90% upper limit seems to be about 4% of the most probable. Since the long tail on the high end comes mostly from radiative processes, it should be reduced in carbon and iron. A proper computation needs to be done for carbon and iron, but the results for lead encourage one to think that an overall 4 percent dP_t/P_t will not be precluded by these energy loss fluctuations.

Trigger

Triggering is likely to be on muons of 50 GeV or more. Total charged particle rates as a function of P_t reported at the Tucson workshop[2] indicate that above a P_t of 50 GeV the rate integrated between eta = +- 3 will be a few Hertz at 10^{34} $cm^{-2}sec^{-1}$. For these tracks, the stray magnetic field should be small enough that the tracks will be essentially straight. This makes for a fast angle measurement, and thereby a fast trigger. It may be necessary to use a second tracking measurement after the iron return flux to eliminate soft punch-through tracks. This measurement will be much less precise, but a 20% dP_t/P_t may be

[3]R. Adair, p. 474, Workshop on Major SSC Detectors, Tucson, Arizona, 1990.

adequate for triggering purposes, especially since there are two independent measurements. These tracks outside the iron return yoke will also be straight.

The Tucson workshop also reported[2] results on rates for punch-through and prompt decays as a function of angle for absorbers of 14, 24, and 40 absorption lengths. While the total charged-particle rates are fairly high if one has only 14 lambda in the forward direction (10 megaHz/deg at 10^{o} for 10^{34} cm^{-2} sec^{-1}), they do not, at first glance, seem prohibitive for detectors with no more than a one-microsecond memory time and reasonable granularity.

Physics Requirements

As mentioned in the introduction, muons are good candidates for a signature of new physics, but is our resolution good enough? We take, as a typical example for the SSC, a heavy Higgs decay into 4 muons via a pair of Z^{o} bosons. What is needed in the way of momentum resolution to observe this reaction? We know that we must be able to see the Z^{o}, and that, in order to retain most of the Z^{o} bosons, the dimuon mass cut about the Z^{o} mass must be about +-2 σ, where σ is the dimuon mass resolution. Also, the narrower this dimuon mass selection, the smaller the background contribution under the Higgs in the Z^{o}-Z^{o} mass spectrum. A 1988 Snowmass report[4], reproduced here as Fig. 5 (b), showed that a dilepton mass spectrum that gave an 8 GeV full width at the Z^{o} mass (sigma = 3.4 GeV, or 3.7%) would provide an observable 400 GeV Higgs signal (Fig. 5(e)) after a cut of +- 10 GeV on the Z^{o}. The effect of dP_t/P_t on dm/m for a muon pair is $1/\sqrt{2}$ times dp/p, so the 3.7% sigma of Fig. 5 (b) corresponds to what one would observe for dP_t/P_t = 5.2%. Fig. 5(b) seems quite reasonable for observing the Z^{o}. Of course, further reduction of the mass resolution would reduce the background under the Z^{o} when making the Z^{o} mass cut, and thereby improve the signal-to-background ratio in the mass spectrum of the Z^{o} pairs (the Higgs mass spectrum). The natural width of the Z^{o} (full width = 2.4 GeV) has a sigma equal to 1% of the Z mass, so a 1.4% resolution in dp/p would be required to match the Z^{o} natural width. Detailed studies are needed to detemine more precisely the signal to background in a Higgs search, but the 4 percent dP_t/P_t that seems to be obtainable with an iron, carbon, or beryllium absorber in a 12 Tesla-meter solenoid looks promising. Considering the higher luminosity that can be obtained (a factor of ten or more), this "beam dump" spectrometer appears to be an attractive option.

[4] 1988 Snowmass Summer Study, p. 115.

Summary

If a large (2 m), high-field (6 T), solenoid can be built (of any coil thickness), then rather good momentum resolution can be obtained for muons traversing quite thick absorbers. Part or all of the absorber could be replaced by a calorimeter, if sufficiently radiation hard materials (diamond?) can be found. While a good deal of detailed work is needed to define the parameters of a practical detector of this kind, and to determine with confidence just what resolutions can be obtained, the analysis presented here suggests that such a study would be well worth the effort. This sort of detector may be the only one that can handle the available luminosity at the SSC.

Table I. Parameter values for various absorbing materials.

	X_0, cm	λ_{abs}, cm	ρ g/cm3	λ_{abs}/X_0	$\sqrt{\lambda_{abs}/X_0}$	$0.39\sqrt{\lambda_{abs}/X_0}$, %
Be	35.3	40.7	1.85	1.15	1.07	0.42
C	18.8	38.1	2.27	2.03	1.42	0.55
C'	21.3	43.2	2.00	2.03	1.42	0.55
C'	25.0	50.8	1.70	2.0	1.42	0.55
Fe	1.76	16.8	7.87	9.52	3.09 (2.31)	(0.90)
W	0.35	9.6	19.3	27.8	5.27	2.05
Pb	0.56	17.1	11.35	30.3	5.50	2.15

Table II. The angular accuracy, in milliradians, required in the measurement of O in order to keep $d\phi/\phi$ below 2%, for various values of P_t.

Pt , GeV/c	$d\phi$, mr (Magnetized Fe)	$d\phi$, mr (Non-magnetic absorber)
100	0.48	0.36
300	0.16	0.12
500	0.10	0.07

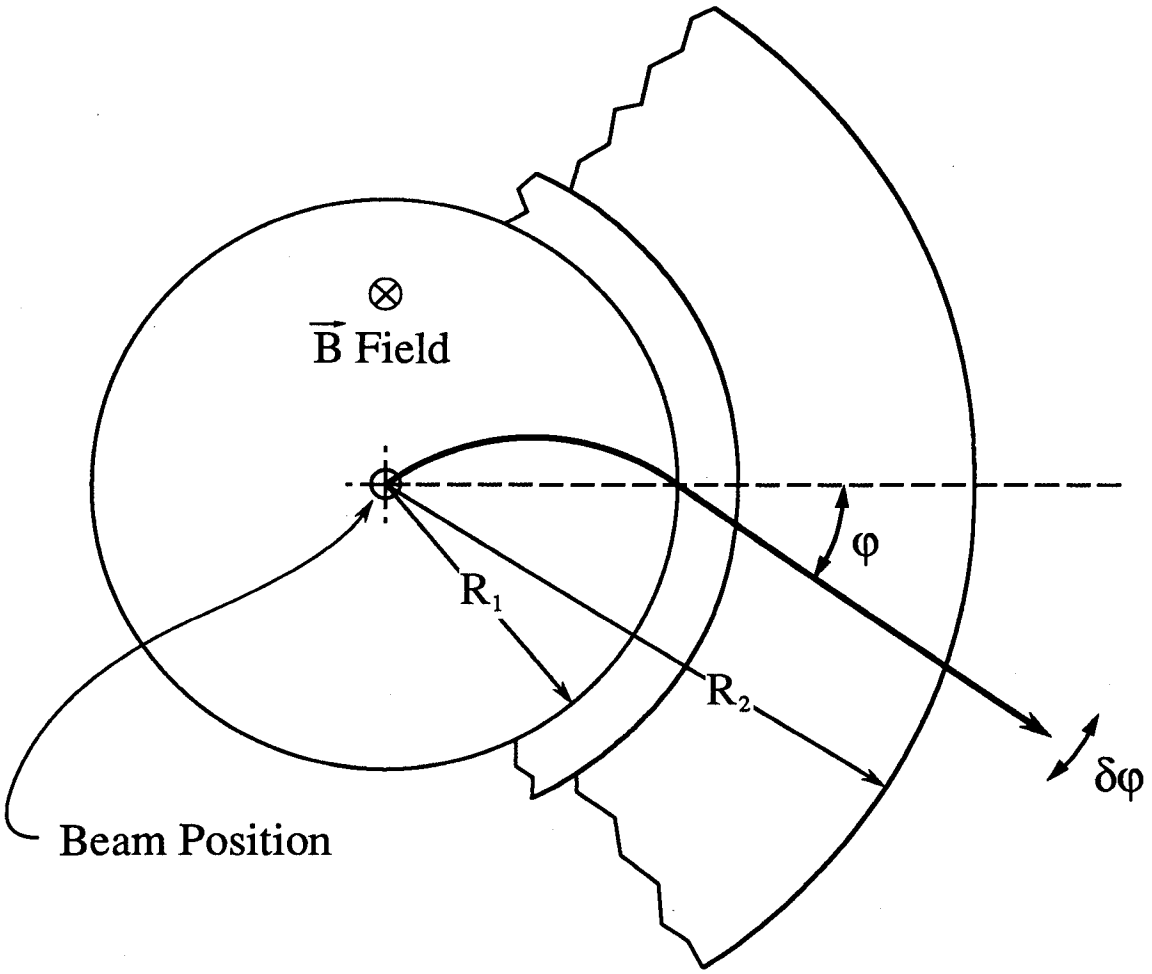

Fig. 1. Cross section of solenoid and cylindrical absorber, showing path of particle.

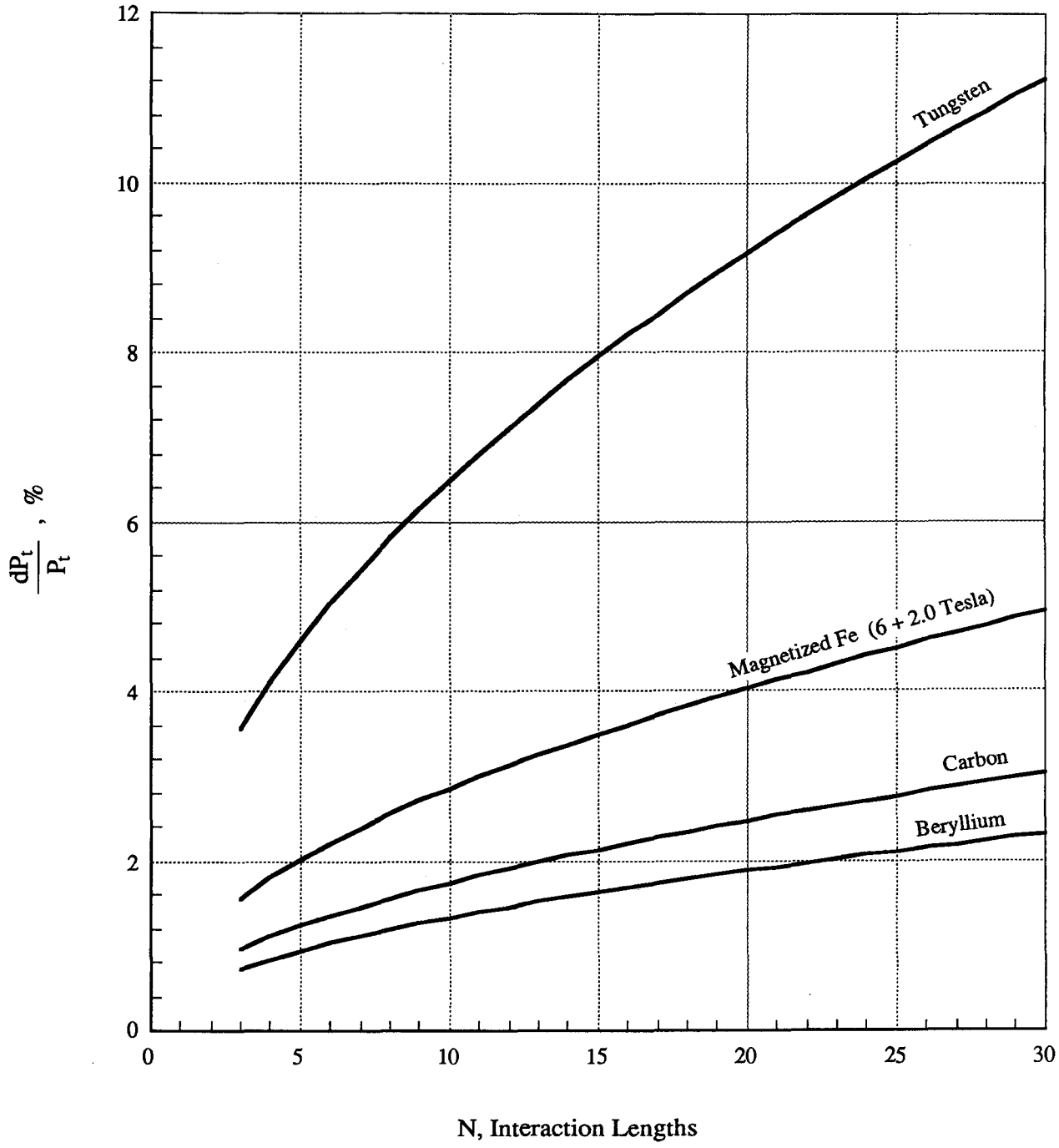

Fig. 2. The multiple scattering contribution to dP_t / P_t as a function of length of absorber traversed.

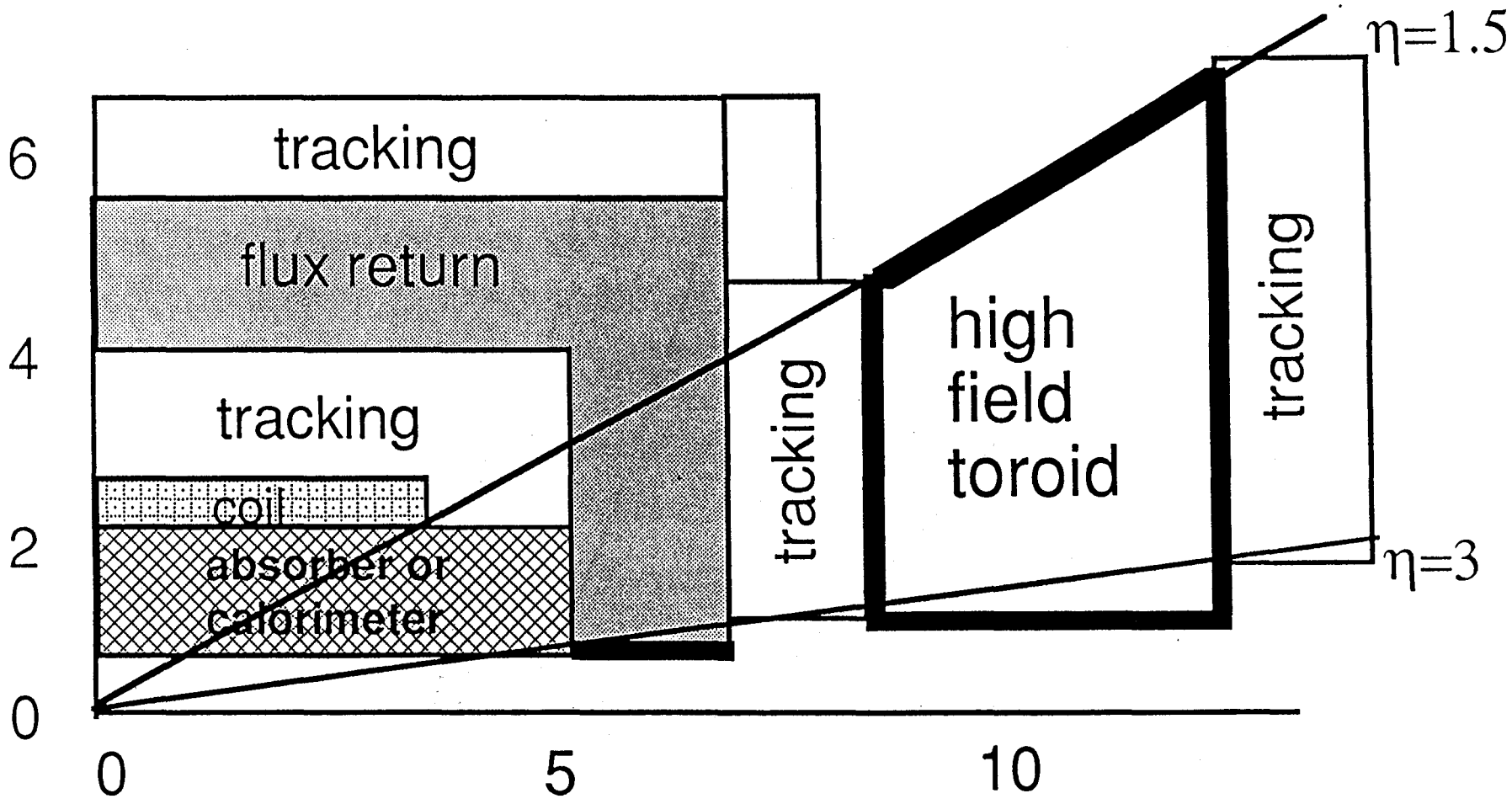

Fig. 3. Example detector using iron absorber.

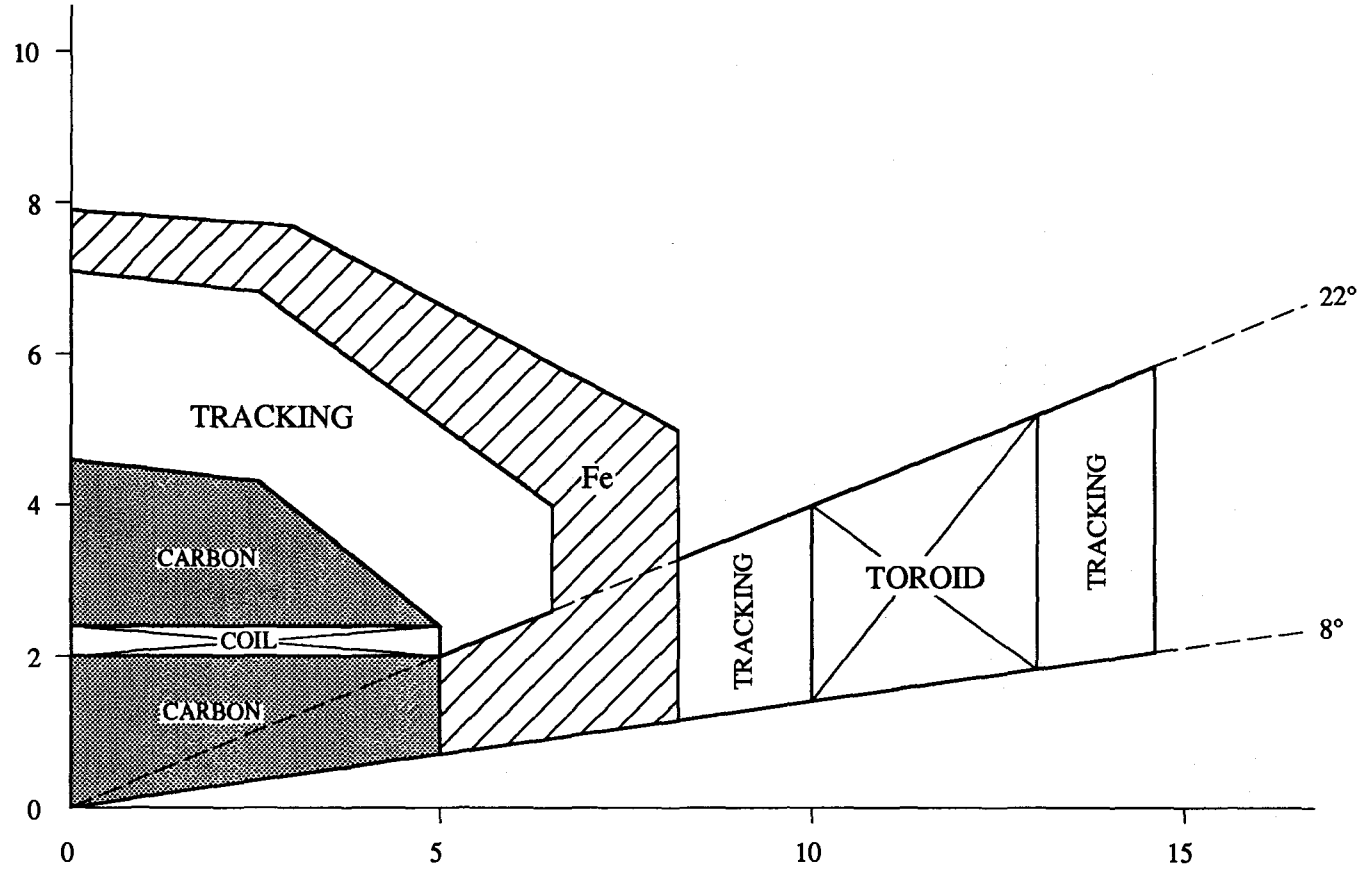

Fig. 4. Example detector using carbon as absorber.

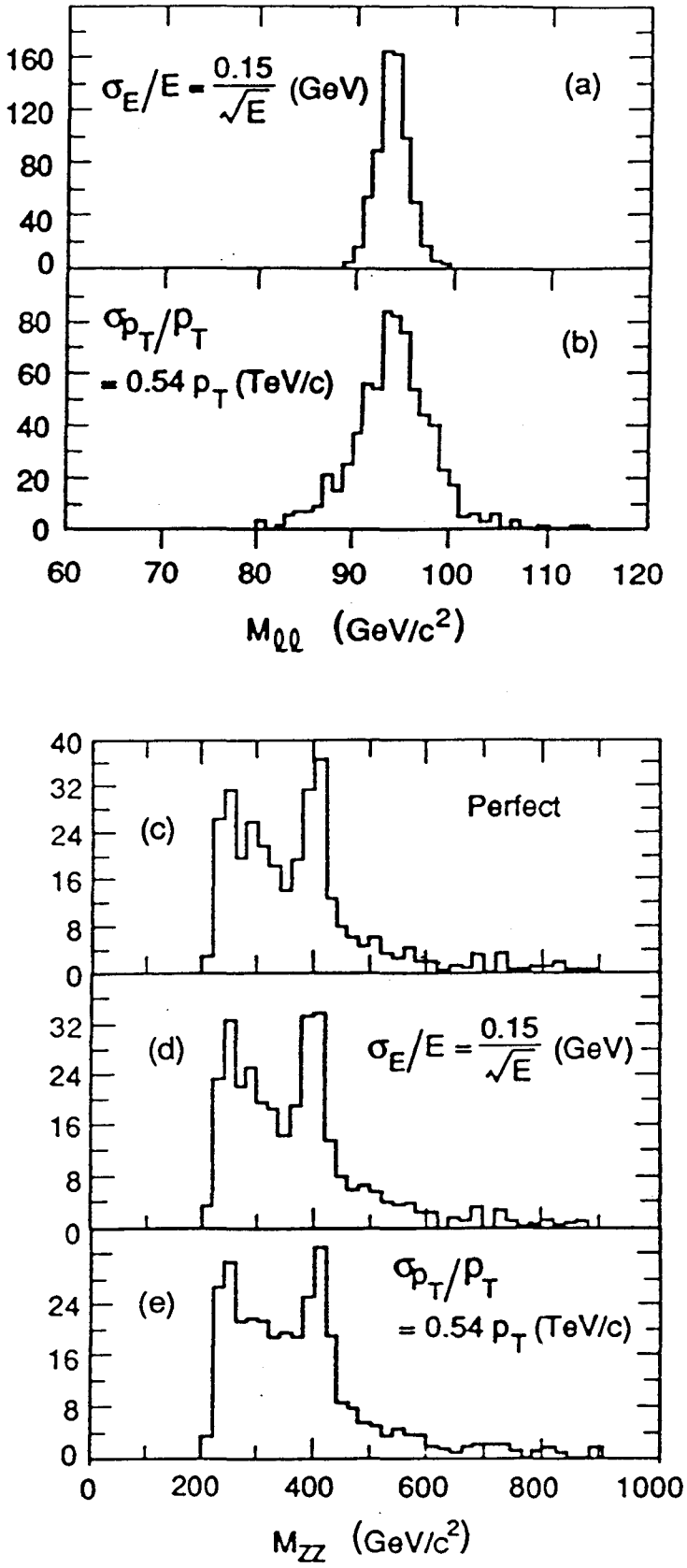

Fig. 5. Dilepton mass resolution effect on Higgs mass spectrum, as reported at Snowmass 1988 (p. 115).

Detector Design and Cost Optimization

April 23, 13:40-14:10

and

April 25, 11:00-11:50

EXPERIENCE AT CDF

M. Mishina
KEK

We review 10 year span of CDF activity and discuss distinctive milestones and sociological aspects of the successful large scale international collaboration of physicists from US, Italy, and Japan.

We emphasize the importance of *in situ* calibration of calorimeter and discuss the technique used by CDF which uses signals of isolated electrons whose momenta are measured by central tracking chamber within 15 k Gauss solenoid in an absolute scale.

We argue that after a careful corrections to the tracking chamber based on measured quantities, without any arbitrary assumptions, one can establish the absolute scale of the momentum in good precision. As a proof we present dimuon spectra which exhibit clean J/Ψ peak and 1s, 2s, and 3s state peaks of upsilon whose mass values are right at the masses of those particles within small but finite uncertainties. K^0_S peak in $\pi^+\pi^-$ mass spectrum is an additional proof.

After the absolute scale of the momentum measurement was established, we calibrated central calorimeter using isolated electron signals. Then the mass and the width of Z^0 was determined using both e^+e^- decay mode and $\mu^+\mu^-$ mode. These values were later confirmed by LEP experiments within our quoted uncertainty.

We conclude that momentum measurement by tracking chamber in a solenoidal field is a vital tool for establishing an absolute scale of the calorimeter response in a hadron collider experiment in which collision energy is not the initial beam's center-of-mass energy and there is no Bhabha event.

One of the lessons we have learned is that the detector has to evolve in order to take advantage of ever evolving luminosity of the accelerator. We are anticipating to accumulate more than 1 fb^{-1} in foreseeable future. With an established analysis technique, we will be able to search for top quark signal in the entire range of what standard model predicts, namely a range up to 300 GeV.

CDF CHRONOLOGY

We start with a chart of CDF chronology, as shown in TABLE 1, which spans a decade from 1978 to 1989. In 1978 there was still a debate on whether to push a 1 TeV x 1 TeV pp collider or to take 1 TeV x 150 GeV pp collision option using superconducting TEVATRON and Main Ring. This was an era when there was not enough confidence in the feasibility of superconducting synchrotron and also there was a significant worry on antiproton accumulation in enough number with small enough phase space. Electron cooling was the choice for antiproton cooling and the test was under way with a collaboration with Novosibirsk.

We spent significant fraction of time at Fermilab's M-5 test beam in 1979 and 1980 to test various calorimeter ideas including lead glass, gas calorimeter and scintillator calorimeter. By the time we wrote down CDF design report (dated August 1981), major decision had been taken and the detector configuration was quite similar to what we have now. The central calorimeter was decided to be a scintillator based calorimeter in which scintillator plates were interleaved with absorber panels and read out by wave shifter bar or rods. The absorber material was lead for the front e.m. segment and steel plates for the hadron calorimeter. The end wall calorimeter also uses scintillator.

Comparing with the present CDF detector[1], as shown in **Fig. 1** , significant differences can be noticed in the detector configuration described in the design report . The Main Ring beam pipe is penetrating the center of the system only 50 cm apart from the Tevatron Ring and there is a pair of muon toroids in front of the forward calorimeters on either of forward and backward directions. These were not realized and the forward calorimeter and the muon

toroids behind it are pushed closer to the central system.

TABLE 1

CDF CHRONOLOGY

1978	Argument on 1-TeV pp or 1-TeV - 400-GeV pp	
1979		
1980	Beam Test at M-5	Pb Glass, Scintillator Calorimeter
1981	TeV I Project approved	6x6 bunches, $10^{30}cm^{-2}sec^{-1}$
	Design Report :9 US , 2 Italian, 2 Japanese Institutions	
	1 m^D x 1 m^L Solenoid Prototype Tested	
	Beam Test at M-5	Proportional Chamber Calorimeter
1982	B0 building Construction Started	
1983	512 GeV Energy Saver Complete	
	p Source Construction Started	
	Wedge Calorimeter Production Started	
	Solenoid Fabrication	
	Beam Test at NW	Central Calorimeter
	Beam Test at MBottom	End Plug Calorimeter Prototype
		Forward Calorimeter Prototype
1984	Solenoid Delivered	
1985	1.6 TeV Collider Completed	
	CDF Central System (Calorimeter, CTC, VTPC, Muon) Completed	
	CDF Test Run	
	Beam Calibration	End Plug Calorimeters
		Forward Calorimeters
1986		
1987	Main Ring Overpass Completed	
	CDF Completed	
	CDF 1st Data Taking/Engineering Run	: 4 Months
	Total $L_{ACCELERATOR}$	$74\ nb^{-1}$
	Total L_{TAPE}	$34\ nb^{-1}$
	L_{MAX}	$10^{29}\ cm^{-2}sec^{-1}$
1988	CDF 2nd Data Taking Run	: 10 Months
|	Total $L_{ACCELERATOR}$	$9.8pb^{-1}$
1989	Total L_{TAPE}	$4.7\ pb^{-1}$
	L_{MAX}	$2x10^{30}cm^{-2}sec^{-1}$
	MEMBERSHIP	: 17 U.S., 2 Italian, 3 Japanese Institutions

If we count the number of the collaborating institutions, there were nine U.S. institutions

including three national laboratories, Fermilab, Argonne, and LBL, two Italian institutions, and two Japanese institutions. Today we count 17 U.S. institutions, 2 Italian institutions, and just recently, we unanimously welcomed Osaka City University in addition to the original Japanese members, KEK
and University of Tsukuba.

In 1981 the funding for 1-TeV x 1-TeV antiproton-proton collider project was approved under a title of TEVATRON-I and the construction of the CDF detctor-assembly/collision hall, B0 building, was started. Also the construction of the antiproton accummullator ring was started.

It should be noted that the design luminosity was 10^{30} $cm^{-2}sec^{-1}$ with 6 x 6 bunch operation and anything beyond such a luminosity was not discussed because it was felt in those days that it was not quite useful to argue without a real experience on the superconducting synchrotron and anti proton accumulator both of them were totally new technology.

By that time antiproton cooling scheme was switched from electron cooling to stochastic cooling because of the delay in electron cooling test and also due to the fact that CERN accumulator ring was successfully operated with stochastic cooling.

One of the major milestones was the construction of the solenoid. A 1 meter diameter and 1 meter long prototype was successfully tested in 1981 with the current exceeding the design value without any spurious quenching. The final solenoid was completed and delivered to Fermilab in 1984 summer and eventually tested half a year later successfully. This was the very first major component of CDF that was completed and it was a quite encouraging accomplishment.

1983 was memorable because the Energy Saver, the version which was only to save the electricity by using superconducting ring instead of the iron magnet ring with the same energy, was completed and reached 512 GeV.

In 1985, the energy was raised to 800 GeV, and the very first collision was observed by then completed central system, central calorimeter, solenoid, central tracking chamber, central drift tubes, vertex TPC, and muon detector. The run was only for a few hours. The Main Ring beam pipe was still penetrating through the middle of the detector and the end plug and forward calorimeter could not be installed. The overpass of the main ring beam pipe was completed by the time of 1987 run.

4-month run in 1987 was the first data taking run defined as an engineering run with the major fraction devoted to debugging the hardware and the software though many physics results were produced. All the detector components were completed and installed by this time. Major concept on the multi-layer structure of the complicated triggering specific to hadron collider, among other practices, was established in this run. The maximum luminosity was $10^{29}cm^{-2}sec^{-1}$ with 3 x 3 bunch operation and about half, 34 nb^{-1}, of the total integrated luminosity 74 nb^{-1} delivered by the Tevatron was recorded on tape.

In 10-month run continued from 1988 and 1989, the luminosity was consistently increased and the maximum reached near the end of the run was 2 x 10^{30} $cm^{-2}sec^{-1}$, exceeding the original design value by a factor of 2. Again about half, 4.7 pb^{-1}, out of 9.8 pb^{-1} delivered from TEVATRON was recorded onto tape. Although TEVATRON was operated with 6 x 6 bunches with 3.5 μ sec bunch crossing intervals as originally designed, whenever there was a trigger from the beam-beam counter around the beam pipe, the next bunch was skipped accepting a small, $\leq$15 %, inefficiency.

Both from 1987 run and 1988-89 run, many papers have been published on the physics topics in a domain of the world highest energy.

Two notions are to be pointed out here. It took four to five years to build individual components after the basic design was chosen. It should be reminded that the total weight of CDF detector including the magnet return yoke and the forward muon toroids is about 4000 tons. About half, 2000 tons, is for the calorimeter.

Then the accelerator has been evolving and so has the detector.

THIN WALL SUPERCONDUCTING SOLENOID

The thin wall solenoid designed and built for CDF was 1.5 Tesla, 3 meter in diameter,

and 5 meter long, and 30 M Joule in stored energy. This solenoid is worth of special mention for various reasons. Also I find relevance of this subject in this occasion of the Solenoidal Detector Workshop.

Before the decision was made, there was a lively debate about the solenoid what type it should be and under whose responsibility. Finally it was decided that University of Tsukuba would take the responsibility of the funding and the construction operation. It should be reminded that this was after the troubles encountered on all three largest solenoids build by that time, CELLO, CLEO, and TPC. The parameters of these solenoids are listed in Table 2. These are all a factor of 3 smaller than the solenoid for CDF in terms of the stored energy. The causes of the initial failure of these are all different but it aroused legitimate concerns over the feasibility of the conceived, then the world largest, thin wall solenoid for high energy physics.

TABLE 2

CDF SOLENOID

PARAMETERS : 1.5 Tesla, 3 meter^{D}, 5 meter^{L}, 30 M J

SPECIFIC FEATURES : 1) Ni-Ti conductor extruded with pure Al stabilizer.
2) Outside aluminum bobbin.

FABRICATED BY : Hitachi Works, Ltd.

1982 : 1 meter^{D} x 1 meter^{L} prototype
1983~1984 : Final design and fabrication
1984 : Delivery to Fermilab : Very first large component completed.
Full current test

LARGEST THIN WALL SOLENOIDS BEFORE CDF SOLENOID

	CELLO	CLEO	TPC
NOMINAL FIELD	1.5 Tesla	1.5 Tesla	1.5 Tesla
DIAMETER	1.66 m	2.06 m	2.18 m
LENGTH	3.42 m	3.15 m	3.4 m
STORED ENERGY	7 M J	9.4 M J	10.9 M J

IMMEDIATE SUCCESSOR OF CDF DESIGN

TOPAZ	VENUS	AMY
1.21 Tesla	0.75 Tesla	3 Tesla
2.86 m^{D}	3.54 m^{D}	2.38 m^{D}
5.1 m^{L}	5.27 m^{L}	1.54 m^{L}
19.5 M J	12 M J	40 M J

In my understanding there were two distinctive innovations which led to the success of CDF solenoid. The first key element was the cable extrusion technique specially developed for this project. Ni-Ti superconductor was extruded with pure, on the order of 99.999%, aluminum stabilizer guaranteeing perfect metallic bonding between the superconductor and the stabilize. The quality of the bonding have been substantiated by electronmicroscopy. Pure aluminum is an

order of magnitude better than copper at helium temperature in terms of electrical conductivity. The second point is that the bobbin, or aluminum bandage, was on the outside of the winding. When the coil is energized, the magnetic force is in the direction of expanding the coil. The outer bobbin prevents the coil to expand and make no chance of the coil being separated from the bobbin. This technique was originally proposed by Cornell people for CLEO solenoid but was never realized. In case of CDF solenoid, the cable winding was pushed into the bobbin by shrink fit method taking advantage of the different thermal expansion coefficient between aluminum bobbin and the winding with insulator.

With a slight exaggeration, the success of this solenoid changed the perception on thin wall solenoid by the high energy physics community from a very difficult technology to a perfectly manageable one.

All three solenoids for TRISTAN detectors, VENUS, TOPAZ, and AMY, adopted these basic techniques, namely the extruded cable and the outside bobbin, and have been in operation without any failure. These two techniques became standard in thin wall solenoid and are adopted by further larger solenoids for LEP experiments. It is obvious that this is a very important factor for the success of a solenoid based detector if one imagine how annoying it would be if it does not function properly.

The solenoid has been operated without any spurious quenching or training from the very first time of the operation. For completeness we report two minor and inessential troubles. When the polarity of the solenoid was reversed, there were a few times of quenching at current level lower than the specification and training like behavior was observed before it reached the specified 4500 A. Since the CDF solenoid has to be operated in a definite polarity due to the fact that the wire cells of the central tracking chamber has 45° inclination to one direction with respect to the radial lines, we decided not to investigate the cause thoroughly. When we switched the polarity back to the normal operating condition, the current reached 4500 A again without any quenching.

The second problem was a minute leak of He into vacuum insulation layer found in the course of 1988-89 run. We kept the current several % lower than the nominal value for precaution and pumped down the vacuum cell whenever we had enough beam-off pause. An effort is going on to locate the troubled spot and the indication so far is that the leakage is from the cold-warm transition point outside of the solenoid winding and can be fixed soon.

The construction of the solenoid was itself an intriguing operation.

First, it was done by a close cooperation among physicists from U.S. side and Japan side not only within CDF but also including experts from KEK. R. Kephart, D. Theriot, and R. Yamada from Fermilab flew many times to Japan to discuss the design in detail with H. Hirabayashi and A. Yamamoto from KEK, and K. Kondo and S. Mori from University of Tsukuba. It should be mentioned that the cryogenic system to support the solenoid was Fermilab's responsibility.

Then the construction, including the prototype, was done by Hitachi Works, Ltd. Since the team decided to adapt completely new technologies, as mentioned earlier, it was far from a catalog item. Therefore involvement of the Hitachi's engineer team headed by R. Saito in the design from the very beginning was essential.

As can be noticed the construction of the solenoid was done rather fast. The prototype was made within a year and two year was spent for the final solenoid including the period for finalizing the design. This reflects the advantage of mobilizing a powerful resources in a large industry. Also the technique of shrink fit was made possible by taking advantage of Hitachi's expertise and facility which is routinely manufacturing large objects, although outside bandage was done by simply winding the coil inside a bobbin in case of TOPAZ solenoid and there is an argument that it was a better way to control the tolerance.

When the solenoid was completed, it was decided to airlift it rather than transporting by surface, although a fair amount of expense was incurred. The decision stemmed from a caution to avoid a possible risk of damaging the delicate structure in the course of repeated loading-unloading and long distance hauling by a truck. A large cargo plane was chartered. The solenoid barely fit in the large cargo bay which was capable of carrying a mid size military tank. A G-force gauge was mounted on the solenoid to monitor possible shock. A special flight permit was granted from US Aviation Agency through DOE and also a special permit was needed from local authority for transporting an oversized object via road from O'Hare airport to Fermilab. No damage was detected and the very first operation with full 4500 A current was

successfully made after steel return yoke was completed half a year later.

CALORIMETER DESIGN

The types of calorimeters built in the CDF detector are summarized in Table 3.

The central calorimeter which subtends a region of $|\eta| < 1.1$ is made of scintillator plates read out by wave length shifter bars/rods. The interleaved absorber panels are lead for e.m. segment and steel plates for hadronic segment.

The end wall calorimeter is also a scintillator-WLS bar combination.

All the calorimeter components, end plug and forward, in $|\eta|$ region between 1.1 and 4.2 are based on gas proportional tubes. Absorber materials are lead for e.m. segment and steel plates for hadronic segment.

TABLE 3

TYPES OF CALORIMETERS IN CDF

		$\lvert\eta\rvert$		$\Delta\eta \times \Delta\phi$
CENTRAL E.M. & HAD	:	<1.1	Scintillator + WLS Bar/Rod + P.M. Strip Chamber at Shower Max.	0.1 x 15°
END WALL	:		Scintillator + WLS Bar + P.M.	
END PLUG E.M. & HAD 0.1 x 5°	:	1.1~2.4	Conductive Plastic Proportional Tube with Pads Strips at Shower Max.	
FORWARD E.M. & HAD	:	2.4~4.2	Proportional Tube with Resistive Coating with Pads	

Among basic requirements for calorimeter,
1) good lateral segmentation,
2) projective tower geometry,
3) good hermeticity.
4) unity e/h ratio,
5) good energy resolution,
and
6)longitudinal segmentation for e/π separation,
e/h compensation was not quite a common terminology at the time and hermeticity was not an established concept although we perfectly realized the importance of it especially for missing E_t measurement for $W \rightarrow e\nu$ signals.

Therefore we were quite successful in segmenting the calorimeters laterally with almost adequately small segmentation. **Fig. 2** is an illustration of the lateral segmentation in a space of η and ϕ. The central calorimeter was segmented into 0.1 x 0.26 (15°) in $\Delta\eta$ x $\Delta\phi$. Also the side view is shown in **Fig. 3** illustrating a perfect projective tower geometry. The segmentation was quite adequate for our measurement so far although it is much coarser than what has been discussed for SSC for which the interaction diamond is much shorter than what we have, σ_z =

31 cm, along the beam axis.

In the end plug, as shown in **Fig. 4**, and the forward region, as shown in **Fig. 5**, $\Delta\eta$ is about the same but $\Delta\phi$ is 5°. As a result the physical tower size is unnecessarily small, much smaller than the shower size, in the very forward region. A segmentation constant in $\Delta\Theta$ might be adequate for SSC taking account of the importance in physics and the economy in channel count. It should be reminded that heavier mass objects are created near at rest and therefore the acceptance in the forward region for decay products diminishes. Only the minimum bias events are distributed uniformly over the entire rapidity interval.

As an inevitable consequence of the reasonably fine lateral segmentation in the central calorimeter with ordinary scintillator-WLS bar/rod combination, there is a sizable crack at every 15° in ϕ. As shown in **Fig. 6** the steel walls of the wedges and the gap between the wall and the WLS bar make dead spots and if particles hit the WLS bars, they generate excessive signals. Eventually such ϕ–cracks were partially hidden by "crack filler", patching calorimeter blocks, but still these cracks are removed from fiducial volume for sensitive measurement.

Since the effect of such cracks were fairly large, these were intentionally made projective from the interaction vertex so that they could be removed from the fiducial volume cleanly. For SSC, the design should be that the cracks be minimal and if the effect is mild, there would be a choice to incline the cracks so that they can be essentially smeared.

Since the projective towers in the central calorimeter were rectangular and relatively large in their transverse cross section, it was relatively easy to realize them. However some difficulty is met in the end plug to the forward region where the towers has to be defined by explicit polar coordinate system. Furthermore the end plug calorimeter was a part of the flux return of the solenoid. Therefore we chose gas proportional tube calorimeter out of two possible alternatives with another choice being liquid argon calorimeter. Fine lateral segmentation was exactly realized by segmenting cathode pads behind resistive wall of proportional tubes without introducing any crack among them. The same design was taken in all of the end plug and the forward calorimeters. An example of how electron signal is measured by such projective towers **Fig. 7** in which a LEGO plot of an electron signal in the end plug e.m. calorimeter is shown.

In the algorithms in electron identification matching of the shower centroid with pointing track in the central tracking chamber, CTC hereafter, and the agreement of the shower profile with what was observed by beam test are important ingredients. To measure these quantities, there is a strip chamber, with perpendicular cathode strips with respect to anode wires strung in z direction, was embedded at $6\,X_0$ in the e.m. segment of the wedges and also 10 layers around the shower maximum, out of 34 layers in total, of the end plug e.m. calorimeter chambers were instrumented with strips stretched in Θ - and $r\,\phi$ -directions with about 4 to 5 times finer segmentations, as shown in **Fig. 8.** These are capable to measure the shower centroid to an accuracy of a few mm.

The price paid for the choice of fine segmentation taking gas calorimeter option in the end plug and the forward region was the rather low density. In case of the end plug calorimeter, 50 cm in the depth was only enough to accommodate $18\,X_0$. As a result transition region, $|\eta| = 1.1 \sim 1.3$, between the central calorimeter and the end plug does not have enough thickness in front of the solenoid and is causing a loss of electron signals. Also the thickness is not enough to hide a crack between the end wall, or return yoke, and the end plug due to a 1-inch gap needed for cabling including the cables of the CTC and the VTPC, the vertex time projection chamber, and for the necessary structure. This might be fixed in near future once we decide to replace the gas calorimeter system with scintillator based calorimeters which are 3 to 4 times denser, $0.7 \sim 1.2$ cm / X_0, and the transition region will be well covered by a thickness enough to contain e.m.shower in front of the solenoid. For SSC, any of the proposed calorimeter has similar density to scintillator based calorimeter and will not cause such a problem.

CALORIMETER CALIBRATION AND MONITORING

Calibration and monitoring is a very important issue for calorimeter for hadron collider in

contrast to e^+e^- collider. The colliding partons' c.m.s. energy $\sqrt{s}$ is not equal to the laboratory-rest c.m.s. energy of the initial beam particles. Nor there are Bhabha electron pairs each of which can be used as a convenient source for direct calibration.

At CDF, all the calorimeters were exposed to test beam, whose energy was carefully calibrated before being installed into the detector system.

All the central calorimeter modules ($\Delta\phi = 15°$ and $\Delta z = 2.5$ meter each) were calibrated tower by tower by 50 GeV electron beam. Also five modules, 15° in ϕ each, were completely mapped within towers with the beam. Mapping of the rest was done with cosmic ray muons.

These calibration constants were normalized by monitoring signals. The primary monitoring was done by Cs^{137}, 3 m Ci, source which can be driven through a gap right behind the strip chamber. Since it is at the shower maximum , it is a reasonable way of sampling the calorimeter response.

Xenon flasher and LED are used as additional, local however, quick method to be repeated in shorter time intervals. Xenon flasher shines every WLS bar through optical fibers and LED's were mounted on every phototube.

Such a set was also used to monitor the central hadronic calorimeter. Through such monitoring it has learned that scintillator based calorimeters are quite stable in long term.

The end plug and the forward calorimeter have a quite different nature. The gain of the proportional tubes is a sensitive function of gas composition, temperature, and pressure. However we have been successful in monitoring the gain to about 1% or better by measuring 5.9 keV peak of Fe^{55} source routinely. These sources were embedded within the same gas atmosphere as the calorimeter. The calibration procedures and the monitoring method is summarized in **Table 4** .

TABLE 4

CALORIMETER CALIBRATION & MONITORING

$\sqrt{s}_{\text{COLLIDING PARTONS}} \neq \sqrt{s}_{\text{BEAM}}$

No Bhabha event

CENTRAL E.M.

CALIBRATION	1) Test Beam : 50 GeV e Tower by tower 2) Cosmic Ray: Mapping within each tower
MONITORING	1) Cs^{137} Source (3 m Ci) at shower max 2) Xenon Flasher / PIN Diode (0.06%/°C) - Fiber on WLS Bar 3) LED Flasher on Phototube

END PLUG & FORWARD CALORIMETERS

CALIBRATION	100 GeV e : Tower by tower	
MONITORING	Fe^{55} source (1 ~ 100 m Ci) 5.9 keV peak	: ≤ 1 %

With such elaborate monitoring systems, it turned out that there was a shift of the energy

scale for unknown cause. We needed some other means which can calibrate the calorimeters *in situ.*

A method was developed for such a purpose in which energies of isolated electrons were compared with the momenta measured by CTC. The momentum measurement is an absolute measurement as far as the following conditions are fulfilled:

1) Solenoid current is measured.
2) Field mapping was done for known solenoid current.
3) Properties of CTC, namely the geometry of the wires and the electron drift velocity,are established.

These were measured in an absolute scale and in good accuracy.

The current was measured to 0.02 % and the field mapping was estimated to be accurate to 0.05%.

Then careful corrections were made to the wire geometries and the drift velocity using the tracks from the collisions and also high energy cosmic ray tracks.

After all these corrections the momentum scale was established with the nominal resolution

$$\sigma_{P_t} / P_t = 0.2\ \%\ P_t$$

based on 1-meter path length from the innermost layer at radius of 31cm to the outermost layer at 1.3 meter as shown in **Fig. 9** and **Table 5** . This gives about 5% momentum resolution for typical 25 GeV electrons. This is not good enough.

TABLE 5

PARAMETERS OF CENTRAL TRACKING CHAMBER

WIRE LENGTH	: 321.4 cm
INNERMOST SENSE WIRE RADIUS	: 30.1 cm
OUTERMOST SENSE WIRE RADIUS	: 132.0 cm
NUMBERS OF SENSE WIRE LAYERS	: 84
NUMBER OF SUPER LAYERS	: 5 axial + 4 stereo
CELL TILT ANGLE	: 45°
DRIFT FIELD	: 1350 V/cm ± 1.5 % (rms)
GAS	: Argon - Ethane - Ethanol, 49.6 % - 49.6 % - 0.8 %

Then it was found that the beam position was very stable in time and could be used as a stringent constraint for fitting the tracks.

As mentioned before the interaction vertices distribution along the beam axis is rather long. **Fig. 10** is the measured distribution[2] with σ_z = 31 cm and a small, -1.5 cm, offset of the centroid from the nominal CDF center.

However the transverse beam profile is extremely small being squeezed by a pair of low beta quadrupoles. **Fig. 11** is the transverse beam profile measured by flipping wires at two places in TEVATRON orbit, one at a normal lattice point and another at the center of CDF. The beta value was 1 m. The r.m.s. radius of the interaction vertex must be $1/\sqrt{2}$ times the value . 87 μm shown in the figure, of the single beam and therefore 61 μm. While CDF detector is in place such a flipping wire setup is incompatible. Therefore the vertex profile is calculated by "transporting" the beam through an accelerator lattice in a calculation with the beam profile measured at normal lattice point as the input. The vertex profile is 50 to 60 μm by such calculation and the calculated luminosity based on such vertex profile is in good agreement with

the luminosity derived from the rate of the beam-beam counter placed at $|\eta|= 3.2\sim5.9$ at the forward and the backward of the CDF center and the measured total cross section within ~7 %. The uncertainty is mainly from the uncertainty in the total cross section used in the calculation.

What about our own measurement? We extrapolate the tracks measured by CTC to the beam axis to find out the impact parameters. The impact parameter distribution is measured to a σ of 200 μm which is limited by the resolution of CTC. However since an enormous number of charged tracks can be used in such a measurement, one can determine the centroid of the impact parameter to 1 μm accuracy as far as the distribution is stable. To demonstrate that the transverse vertex distribution is stable run by run, the horizontal and vertical component of the impact parameters are plotted in **Figs. 12** a and b. Also are plotted the angles of the impact parameter distribution with respect to the beam axis in **Figs. 12** c and d. These are plotted against the run numbers for the entire 10 month period of 1988 ~ 1989 run. As is clearly observed, there is a walk of the centroids in time but the amplitude is small, ~160 μm horizontally and ~220 μm vertically peak-to-peak. The angles of the distribution is also small, in a scale of tenth of m radian. Furthermore the walk is a slow function of fill number of the stored beam and within each fill in which the accelerator lattice tuning is not changed one can easily assume that the beam position does not move. Then we can use such measured beam position with the assumed σ of 50 μm as the constraint for fitting the tracks.

With such a constraint, the path length of the CTC is essentially stretched to full 1.3 meter as indicated in the $r\,\phi$ view of the CTC for a typical event in **Fig. 13** and as a result the momentum resolution becomes

$$\sigma_{P_t} / P_t = 0.11\ \%\ P_t.$$

Thus we have improved the resolution by almost a factor of two.

After such corrections and vertex constraint we need to check the validity of the whole procedure. The check comes from observed dimuon mass spectra. Dimuons have sharper peaks than e^+e^- due to the fact that they do not suffer from smearing due to the external bremsstrahlung.

Dimuon mass spectrum is shown in **Fig. 14** up to 10 GeV. The solid line for $\mu^+\mu^-$ pairs clearly exhibit J/Ψ and upsilon peaks. The shape of the base line continuum is consistent with the background random pairs of like sign dimuons indicated by the broken line.

An expanded view of J/Ψ region is shown in **Fig. 15**. The mass value of the peak determined by fitting is 3.0962 GeV with width $\sigma = 24.6$ MeV is in excellent agreement with the mass value found in the Particle Data Booklet (3,096.9 ± 0.1 MeV, $\Gamma = 0.068 \pm 0.010$ MeV) within the uncertainty of 0.0007 GeV we calculate.

Upsilon region is also in **Fig. 16** in an expanded horizontal scale. $1s$, $2s$, and $3s$ states of upsilon are well identified above the continuum, which is again consistent in shape with random pairs as seen in like sign pairs shown in broken line. The masses obtained from fitting, 9.469, 10.01, and 10.37 GeV, are in good agreement, within an uncertainty of 0.010 GeV, with the masses found in Particle Data Booklet (9.4603, 10.0233, and 10.3553 GeV).

K^0_S peak seen in $\pi^+\pi^-$ pairs[3], as shown in **Fig. 17**, is an additional check. The mass measured is 0.4986 ± 0.002 GeV to be compared with one in Particle Data Booklet , 0.497671 GeV.

These are the proof of our capability of measuring the momentum in an absolute scale using a solenoidal field and a tracking chamber with an *in situ* calibration using real events.

Now armed with such evidences we turn to a real physics objective which is the measurement of the mass and width of Z^0 [4]. In this case e^+e^- pairs measured by the calorimeter are of equal or better quality as muon pairs measured by CTC because the energy by the associated bremsstrahlung are mostly not lost and the energy resolution is superior to the CTC measurement based on the nominal energy resolution of the calorimeter 14% /$\sqrt{E}$. The remaining task is the tower by tower absolute calibration of the calorimeter. For this we can use isolated high energy electrons and normalize the energy measured by the calorimeter by the momentum measured by CTC. First we identify isolated electrons by the criteria listed in **Table 6** .

We are left with 17,000 electrons over 480 towers of the central calorimeter. Therefore an

average of 35 electrons can be used to calibrate each tower. Combined with the energy resolution of 14 % / $\sqrt{E}$, the final statistical uncertainty in the calorimeter energy scale is estimated to be 1.7 %.

TABLE 6

CALORIMETER CALIBRATION WITH ISOLATED ELECTRONS

(*IN SITU* ABSOLUTE CALIBRATION)

E/P MEASUREMENT USING INCLUSIVE ELECTRONS

ELECTRON IDENTIFICATION	COMMENT
$E_t > 15$ GeV	: High energy electrons
HAD/EM < 0.04	: Most of the energy is dumped in e.m. segment
Shower Profile on Strip Chamber	
: $\chi^2 < 10$ ($N_f = 9$)	: Consistency with electron signal seen at test beam
Track Matching btwn CTC & Strip Chamber	
: $\Delta(r\phi) \leq 1$ cm	
$\Delta z \cdot \sin\theta \leq 8$ mm	: Pointing charged track
$0.7 \leq E/P < 1.3$	: Correspondence btwn calorimeter and CTC
Strip chamber Wire-Strip Pulse Height Matching	
: Δ (Wire/ Strip) $\leq$ 40 %	
	: Correspondence btwn wire and strip signals

17, 000 e candidates within 480 CEM towers => 35 / Tower
(B.G. 4 %)

Δ (Energy Scale) $_{\text{Statistical}}$ = 1.7 %*

*Note: $\sigma_E/E = 14\ \% / \sqrt{E}$

Thus at last we have made *in situ* calibration of the calorimeter in an absolute scale. The result is seen in **Fig. 18** which is a mass spectrum of e^+e^- pairs in Z^0 range. The mass thus obtained is 91.1 GeV with an estimated uncertainty of ±0.3 ±0.4 GeV(statistical + systematic and scale, respectively). This is in good agreement with the value obtained from muon pairs, 90.7±0.4±0.2 GeV, and combined with the mass value derived from electron pairs whose momenta were measured by CTC, 91.5±0.8±0.4 GeV, we determine the mass of Z^0 to be 90.9 ±0.3±0.2 GeV. The width was determined to be 3.8 ±0.8±1.0 GeV. Later LEP experiments confirmed these values within our quoted uncertainty.

In the above the electron acceptance was limited to the central calorimeter of $|\eta| \leq 1$ which is entirely covered by CTC. However once the mass of Z^0 is established, electron pairs identified within Z^o peak can be used as a convenient calibration source for the calorimeters which are not covered by CTC as far as one of each pair is within the coverage of the central calorimeter. This assertion relies on the fact that the continuum background electron pairs, from Drell-Yang process, is quite small. This technique was used to calibrate the end plug e.m. calorimeter below 20° combined with the same technique as described above using isolated single electrons for the angles above 20°. For the forward calorimeter electrons from Z^0 is the only such calibration source.

In case of SSC, it is amusing to calculate how many Z^0 is produced in a year. The unit can be used to measure is in the range of femtograms, or more appropriately femto-carats.

Therefore electron pairs from Z^0 will be a powerful source for *in situ* calorimeter calibration as far as one of each pair is in the acceptance of barrel calorimeter which in turn calibrated by central tracking chamber in an absolute scale.

FUTURE PROSPECT OF CDF

As has been reported elsewhere CDF has established a technique to look for top quark signals by looking at all combinations of lepton pairs, $e^{\pm}$ and $\mu^{\pm}$, and also lepton-jet combinations. We have pushed the mass limit close to 90 GeV already. On the other hand low energy electroweak interaction results and our own data of Z^0/W mass ratio limit the upper bound of top mass within the framework of the standard model. Furthermore if vertex silicon chamber which is soon to be implemented in the coming 1991 run, or its next generation version, works, 50% of the B decay will be tagged further cleaning the candidate events. Therefore CDF has a rare promising opportunity of finding a new fundamental particle or possibly, more intriguingly, proving the absence of top quark in the mass range consistent with the standard model.

There are many other topics like compositeness and SUSY particle search, for example, in addition to furthering the precision of electroweak parameters like W mass and $\sin^2\theta_W$. We will enjoy whatever we could do at the highest energy hadron collider in the world until SSC becomes operational.

Fortunately TEVATRON has a vigorous and realistic plan of pushing up the luminosity in near future including ongoing upgrade of the lineac and new construction plan of Main Injector. If the entirety of such a plan is funded as endorsed by HEPAP recently, we expect a total integrated luminosity of more than 1000^{-1}pb by the year 2000 as shown in **Fig. 19**. **Fig. 20** is the accumulated number of lepton pairs, without b-tagging, expected against the mass of top quark on the horizontal scale based on TEVATRON upgrade scenario. Then, depending on how many events one needs to claim/approve the discovery, it is obvious that the day to leave no stone unturned ,within the standard model, will not be too far.

On the part of the detector to take full advantage of such high luminosity, a significant upgrade is needed. Though it is still an order of magnitude slower than the expected SSC operation, the beam crossing will be 395 ns (36 x 36 bunches) instead of the present 3.5 μsec (6 x 6 bunches) from the run in 1993 on. Therefore slow component, especially the data acquisition system including the front end electronics and the triggering system and possibly gas proportional tube calorimeter which are essentially slow system designed for 6 x 6 bunch operation, have to be upgraded/replaced. There are vigorous R&D programs in various front under way. Naturally much faster and more powerful on-line and off-line computing is necessary to keep up with the vast increase in the amount of data to be processed.

Needless to say, even though there is a vast difference in dealing with 16 nsec bunch crossings and with 395 ns, still this is the nearest kin of SSC in every aspect and we are sure to learn a lot from TEVATRON collider.

This is another lesson we have learned. The accelerator keeps evolving and so does the detector. except for the central calorimeter which was the major investment. It does not seem to be necessary to upgrade the main body of the central calorimeter because it is an intrinsically fast scintillator-phototube system. Such a scenario may well be true for SSC. As far as the most expensive barrel part remains usable, minor system in the forward angles can be replaced without much pain, in terms of the human effort and the cost, if necessary.

CONCLUSION

1) CDF has been an example of very successful, large scale international collaboration. Collaboration among physicists from U.S., Italy, and Japan, has been very fruitful in a) bringing talented physicists and engineers of different background together, b) exchanging information, in physics and technical, c) making use of the resources of different institutions which have different expertise, and d) making use of the resources of advanced industries in different part of the globe.

2) CDF has been very successful in cooperating with large industries at various stages. As an

example we discussed the case of solenoid construction.
3) Central tracking chamber within solenoidal magnetic field is a mean of measuring momenta of charged particles in an absolute scale if a careful calibration, using particle tracks from real events without any arbitrary adjustment, is done.
4) It has been demonstrated that full track length from the beam axis could be counted on because the vertex distribution established by many charged tracks was found to be very stable to be used as a very tight constraint at the beam axis.
5) Calibration and monitoring of calorimeter are very important for hadron collider. CDF has demonstrated that *in situ* calibration can be done in good precision and in an absolute scale using a tracking chamber within a solenoidal magnetic field. As a proof we have presented dimuon mass spectra which exhibit J/Ψ and upsilon peaks of correct mass values. We were successful in measuring the mass and the width of Z^0 after calibrating the central calorimeter by isolated electron signals whose momenta were measured by CTC.

Electron pairs from Z^0 will be a bountiful source for calibration at SSC for the calorimeters beyond the coverage of the tracking chamber if one of each electron pair is measured by the central calorimeter within the tracking chamber coverage, as demonstrated by CDF.
6) CDF has a bright prospect of searching top quark signals within the framework of the standard model in foreseeable future, among many other topics. TEVATRON will evolve continuously to push up the luminosity and the detector will be upgraded to take full advantage of the higher luminosity.

REFERENCES

1) Articles published in Nucl. Instr. Meth. in Physics Research, A267 (1988) 249-366, A268 (1988) 24-104, A269 (1988) 33-100, and A271 (1988) 387-403.
2) Report by H. Edwards.
3) F. Abe et al., Phys. Rev. D, Rapid Communications 40(1989)3791.
4) F. Abe, et al., Phys. Rev. Lett., 63 (1989) 720.

FIGURE CAPTIONS

Fig. 1 : Cross sectional view of CDF detector.
Fig. 2 : Lateral segmentation of calorimeter in η - ϕ space.
Fig. 3 : Cross sectional view of projective tower geometry of the calorimeter.
Fig. 4 : Isometric view of the projective towers in the end plug e.m. calorimeter.
Fig. 5 : Lateral segmentation of the forward e.m. calorimeter.
Fig. 6 : Cross sectional view of the ϕ-cracks between $\Delta\phi = 15°$ central calorimeter modules.
Fig. 7 : LEGO plot of electron signal observed by the end plug e.m. calorimeter.
Fig. 8 : θ - and ϕ - strips implemented in the chambers around shower maximum of the end plug e.m. calorimeter compared with the pad pattern.
Fig. 9 : View of the central tracking chamber end plate.
Fig. 10 : Vertex distribution along the beam axis.
Fig. 11 : Transverse beam profiles measured by flipping wire at a) CDF center with low beta quadrupoles ($\beta = 1$ meter) and at b) a normal lattice point. From report by H. Edwards.
Fig. 12 : Impact parameter distribution measured by extrapolating the charge tracks measured by the central tracking chamber , a) horizontal, b) vertical, c) horizontal angle with respect to the beam axis, and d) vertical angle.
Fig. 13 : Vertex constrained $r\phi$-view of the tracks in central tracking chamber .
Fig. 14 : Dimuon mass distribution. Solid line represents opposite sign pairs and broken

line is for like sign pairs.

Fig. 15 : Dimuon mass spectrum around J/ψ peak.

Fig. 16 : Dimuon mass spectrum around upsilon peaks.

Fig. 17 : $\pi^+\pi^-$ pair mass spectrum around K^0_S peak.

Fig. 18 : Z_0 peak in e^+e^- pair mass spectrum.

Fig. 19 : Expected integrated luminosity to be recorded onto tape based on TEVATRON upgrade scenario.

Fig. 20 : Expected number of dilepton events, without B-tagging, plotted against the mass of top quark based on the TEVATRON upgrade plan.

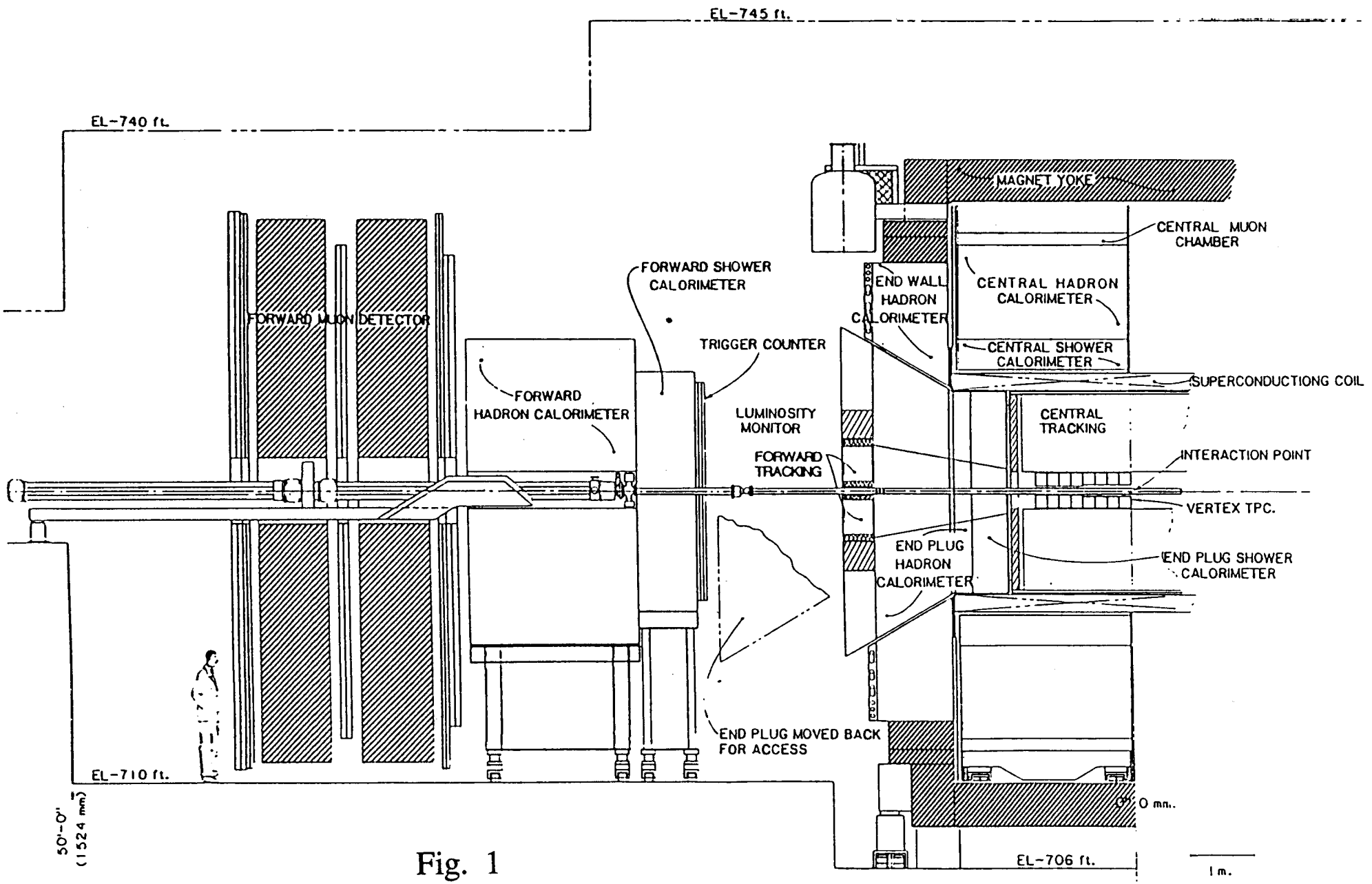
EL-745 ft.
EL-740 ft.
MAGNET YOKE
CENTRAL MUON CHAMBER
FORWARD SHOWER CALORIMETER
END WALL HADRON CALORIMETER
CENTRAL HADRON CALORIMETER
FORWARD MUON DETECTOR
TRIGGER COUNTER
CENTRAL SHOWER CALORIMETER
SUPERCONDUCTIONG COIL
FORWARD HADRON CALORIMETER
LUMINOSITY MONITOR
CENTRAL TRACKING
FORWARD TRACKING
INTERACTION POINT
VERTEX TPC.
END PLUG HADRON CALORIMETER
END PLUG SHOWER CALORIMETER
END PLUG MOVED BACK FOR ACCESS
EL-710 ft.
0 mm.
50'-0" (1524 mm)
EL-706 ft.
1 m.

Fig. 1

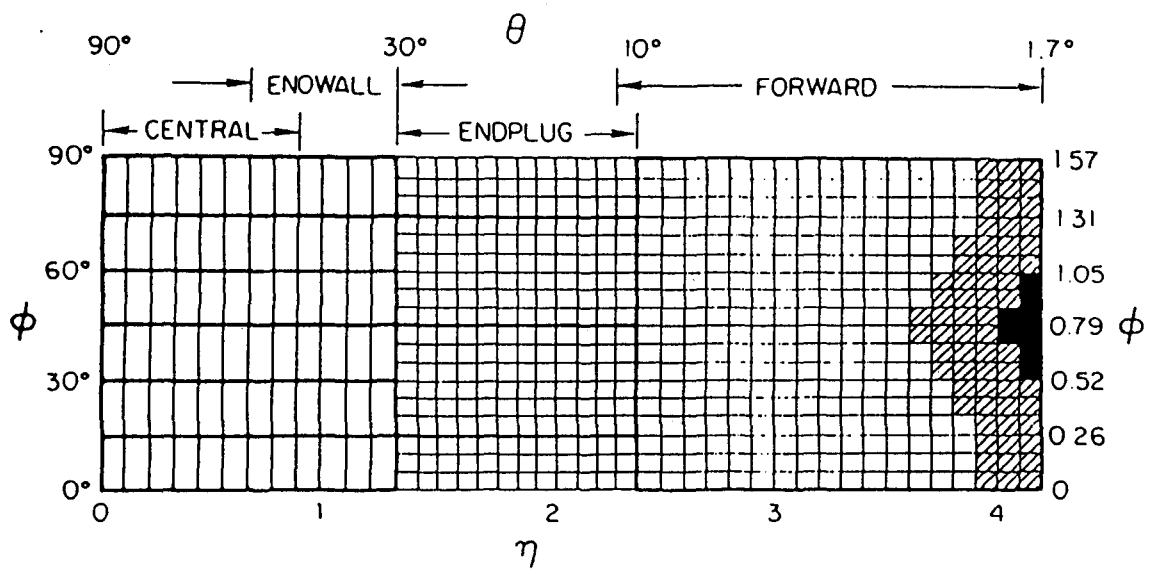
θ
90°
30°
10°
1.7°
ENOWALL
FORWARD
CENTRAL
ENDPLUG
90°
60°
30°
0°
φ
0
1
2
3
4
η
1 57
1 31
1.05
0.79
0.52
0 26
0
φ

Fig. 2

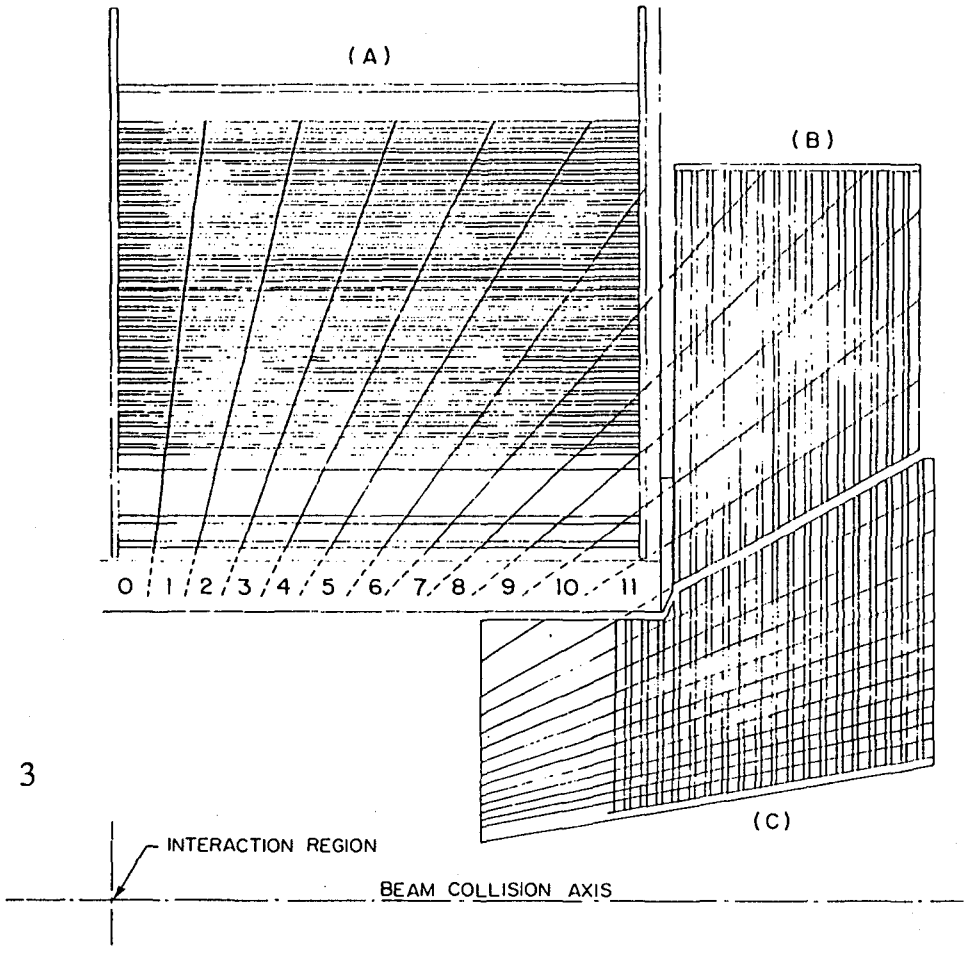
(A)
(B)
(C)
0 1 2 3 4 5 6 7 8 9 10 11
INTERACTION REGION
BEAM COLLISION AXIS

Fig. 3

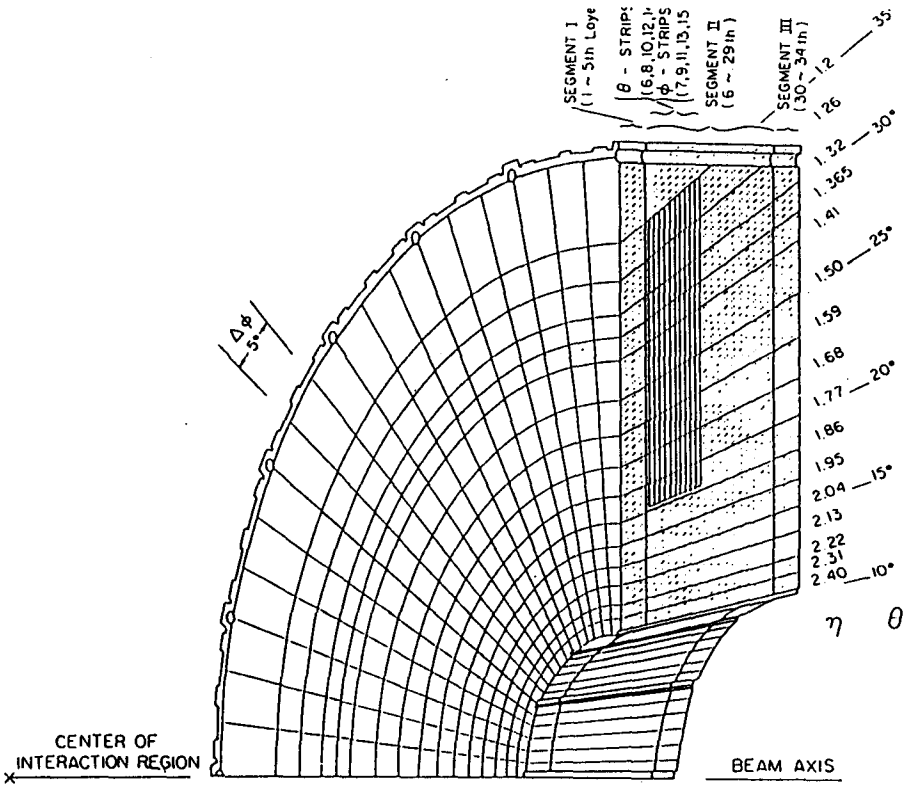
SEGMENT I
(1 ~ 5th Layer
θ - STRIPS
(6,8,10,12,1
φ - STRIPS
(7,9,11,13,15
SEGMENT II
(6 ~ 29th)
SEGMENT III
(30 ~ 34th)
35°
30°
25°
20°
15°
10°
1.2
1.26
1.32
1.365
1.41
1.50
1.59
1.68
1.77
1.86
1.95
2.04
2.13
2.22
2.31
2.40
Δφ
5°
η θ
CENTER OF
INTERACTION REGION
BEAM AXIS

Fig. 4

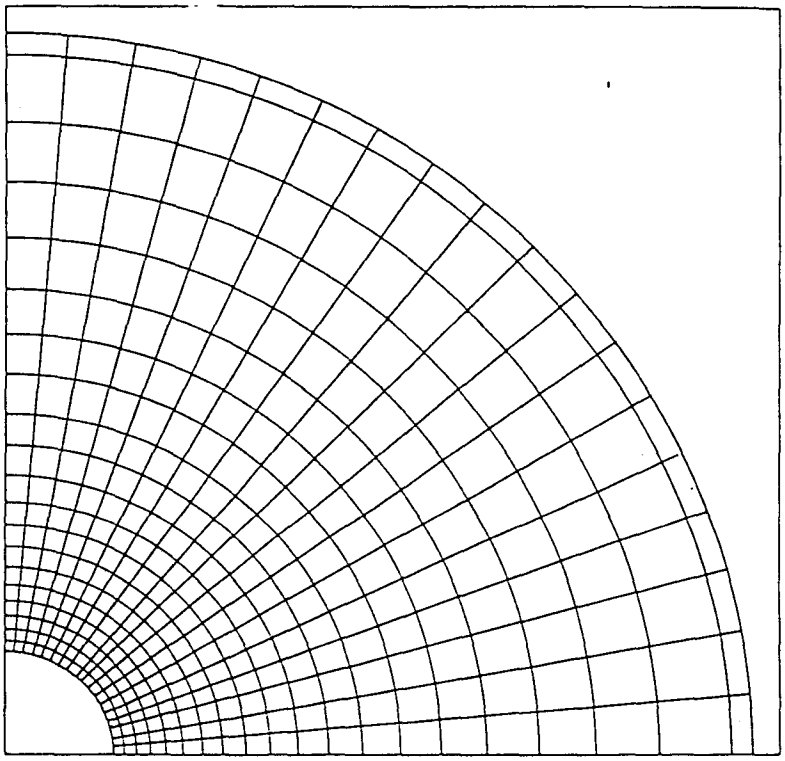

Fig. 5

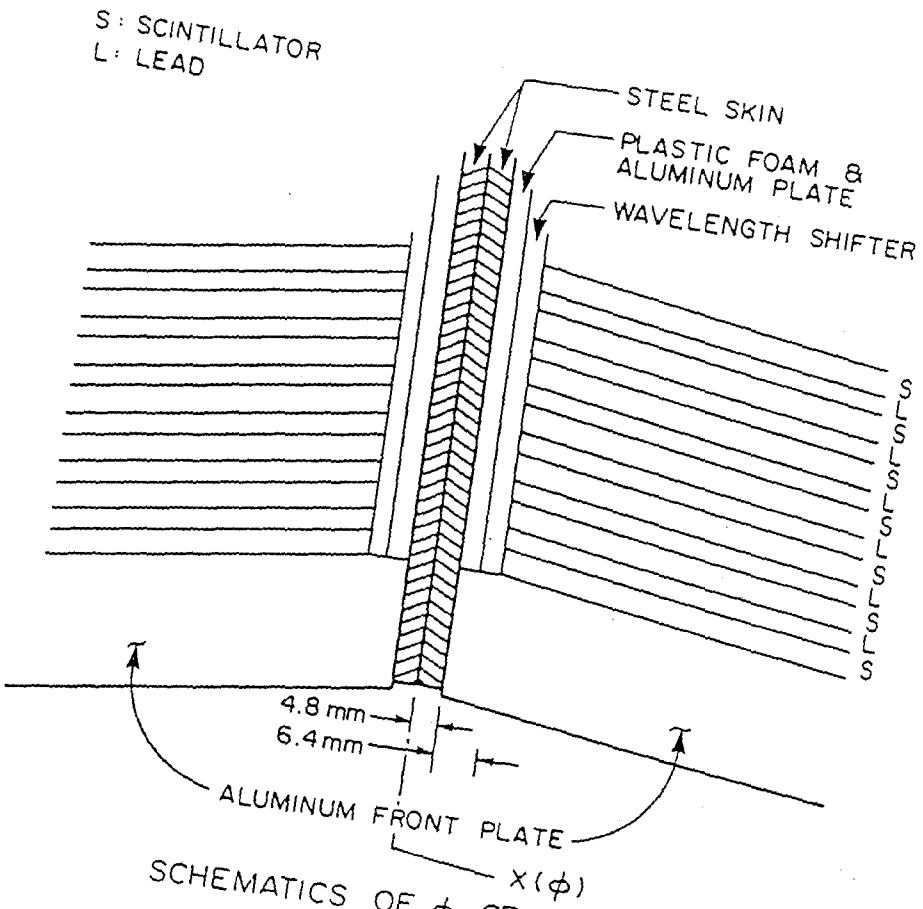

SCHEMATICS OF ϕ-CRACK REGION

Fig. 6

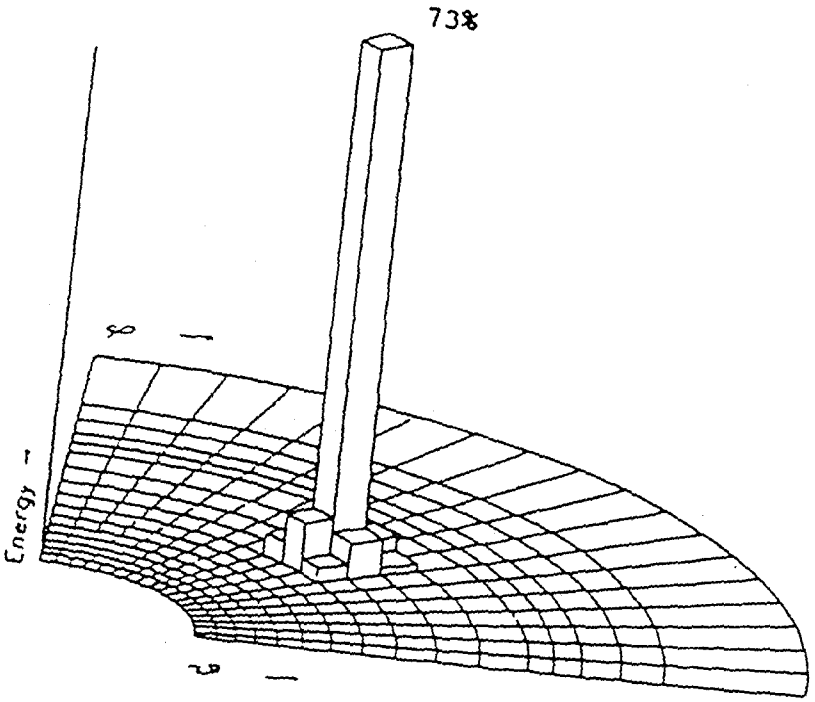

Fig. 7

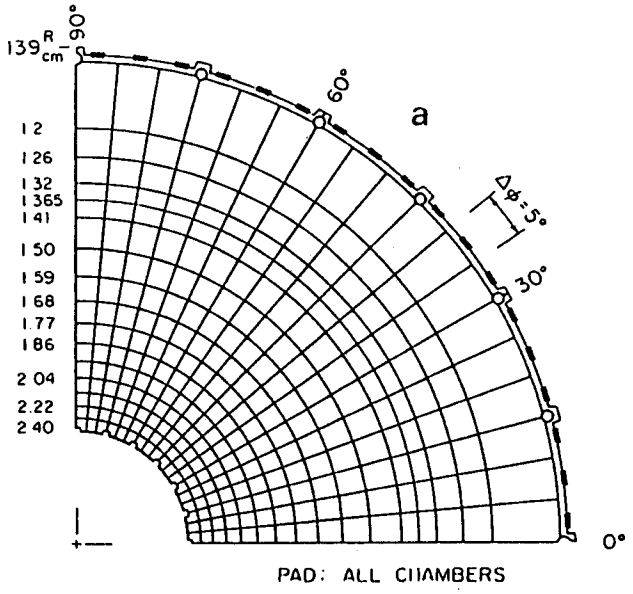
90°
139^{R}_{cm}
60°
a
12
126
132
1365
141
150
159
168
177
186
204
222
240
30°
$\Delta\phi = 5°$
0°
PAD: ALL CHAMBERS

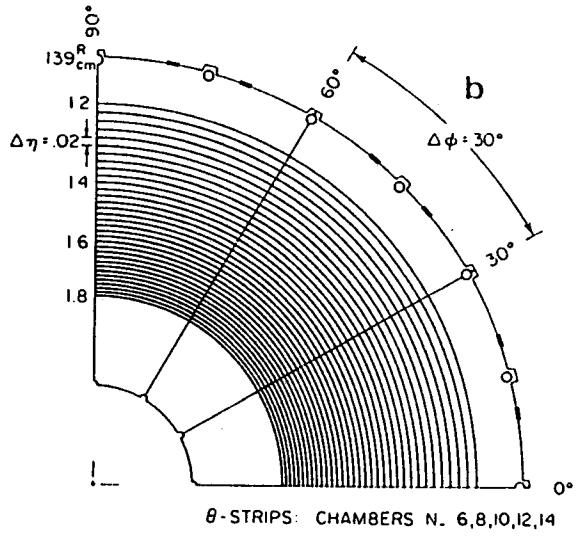
90°
139^{R}_{cm}
60°
b
12
$\Delta\eta = .02$
14
16
18
$\Delta\phi = 30°$
30°
0°
θ-STRIPS: CHAMBERS N. 6,8,10,12,14

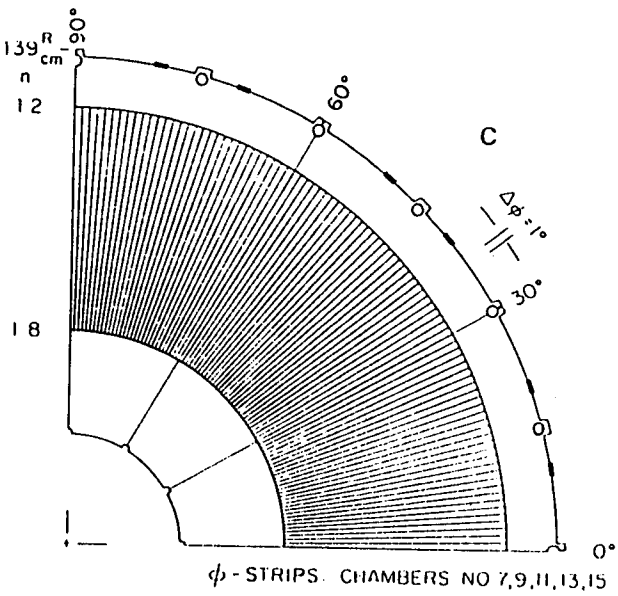
90°
139^{R}_{cm}
n
12
60°
c
18
$\Delta\phi = 1°$
30°
0°
φ-STRIPS: CHAMBERS NO 7,9,11,13,15

Fig. 8

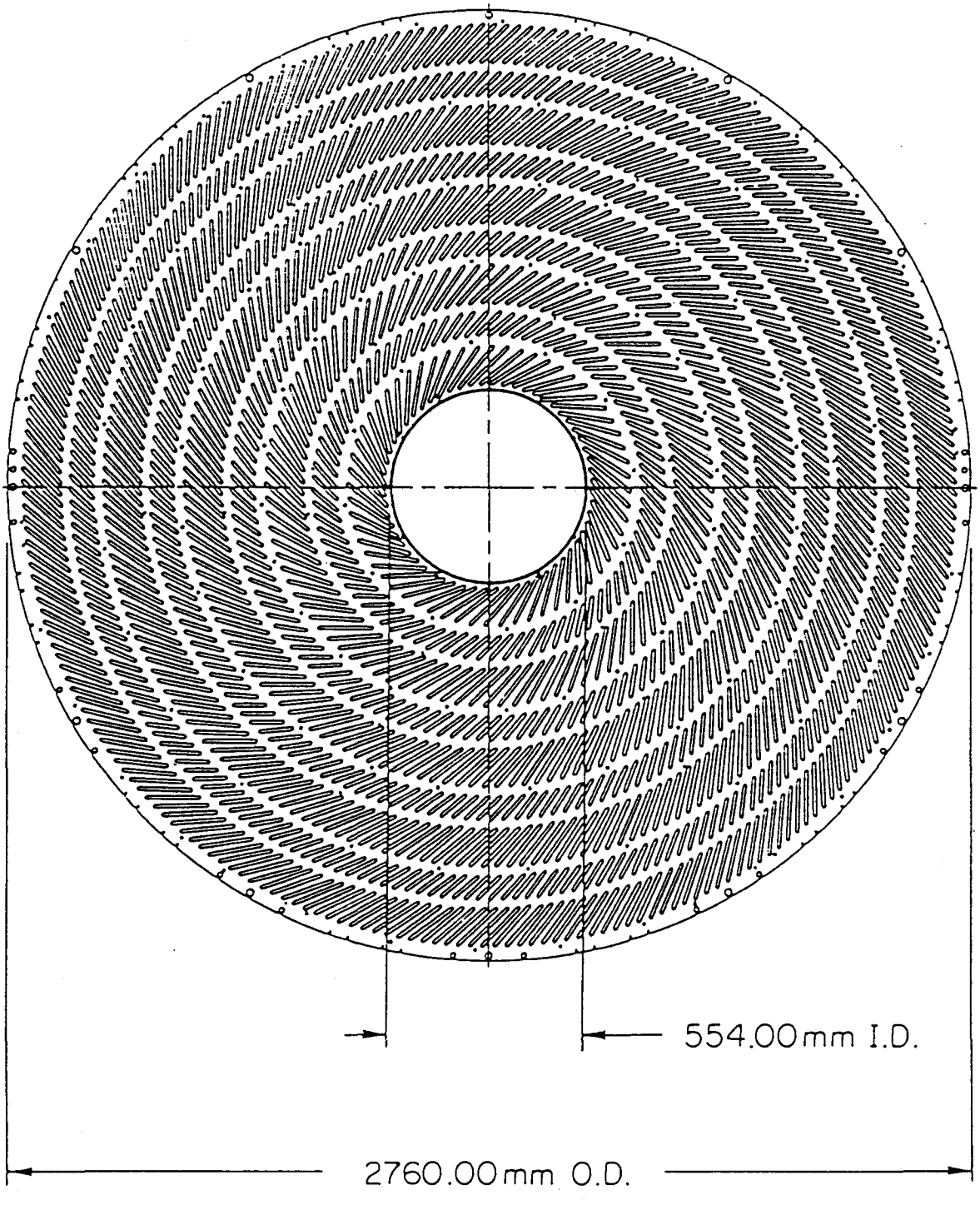

Fig. 9

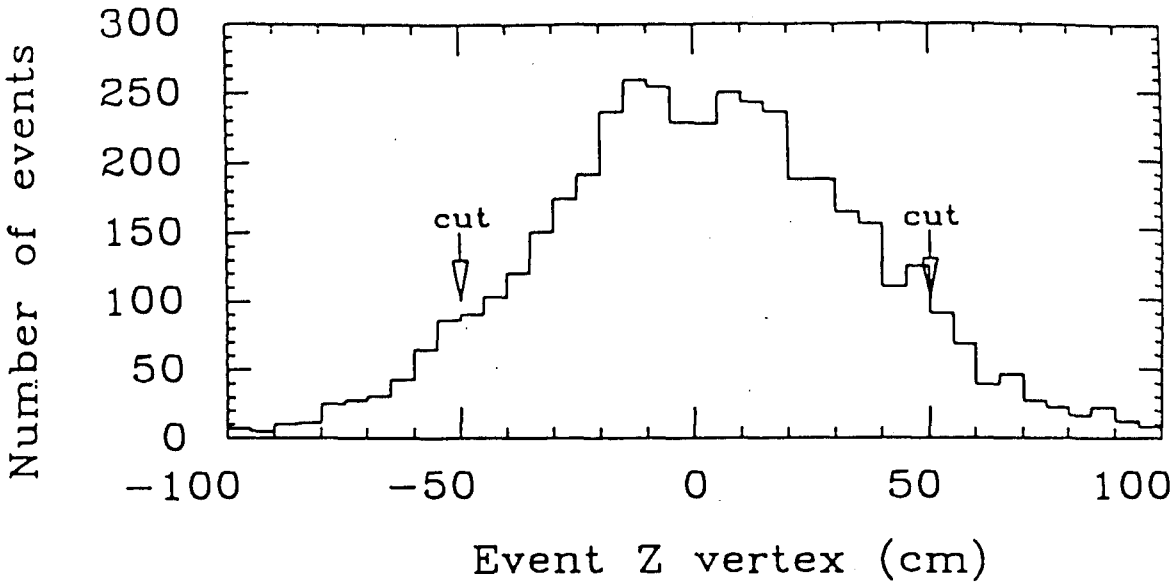

Fig. 10

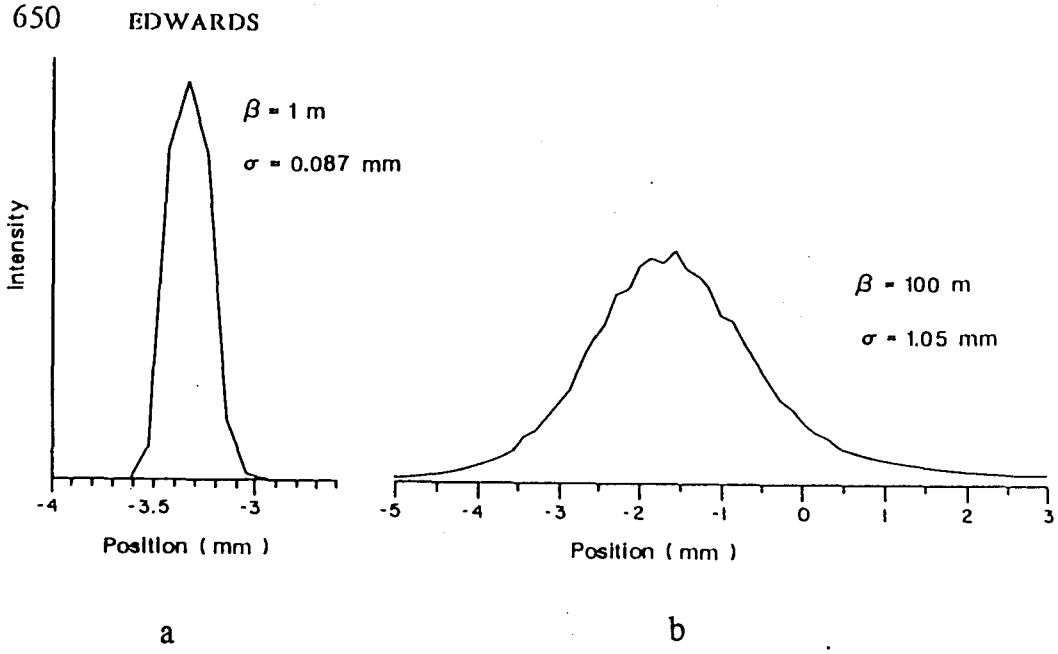

a b

Fig. 11

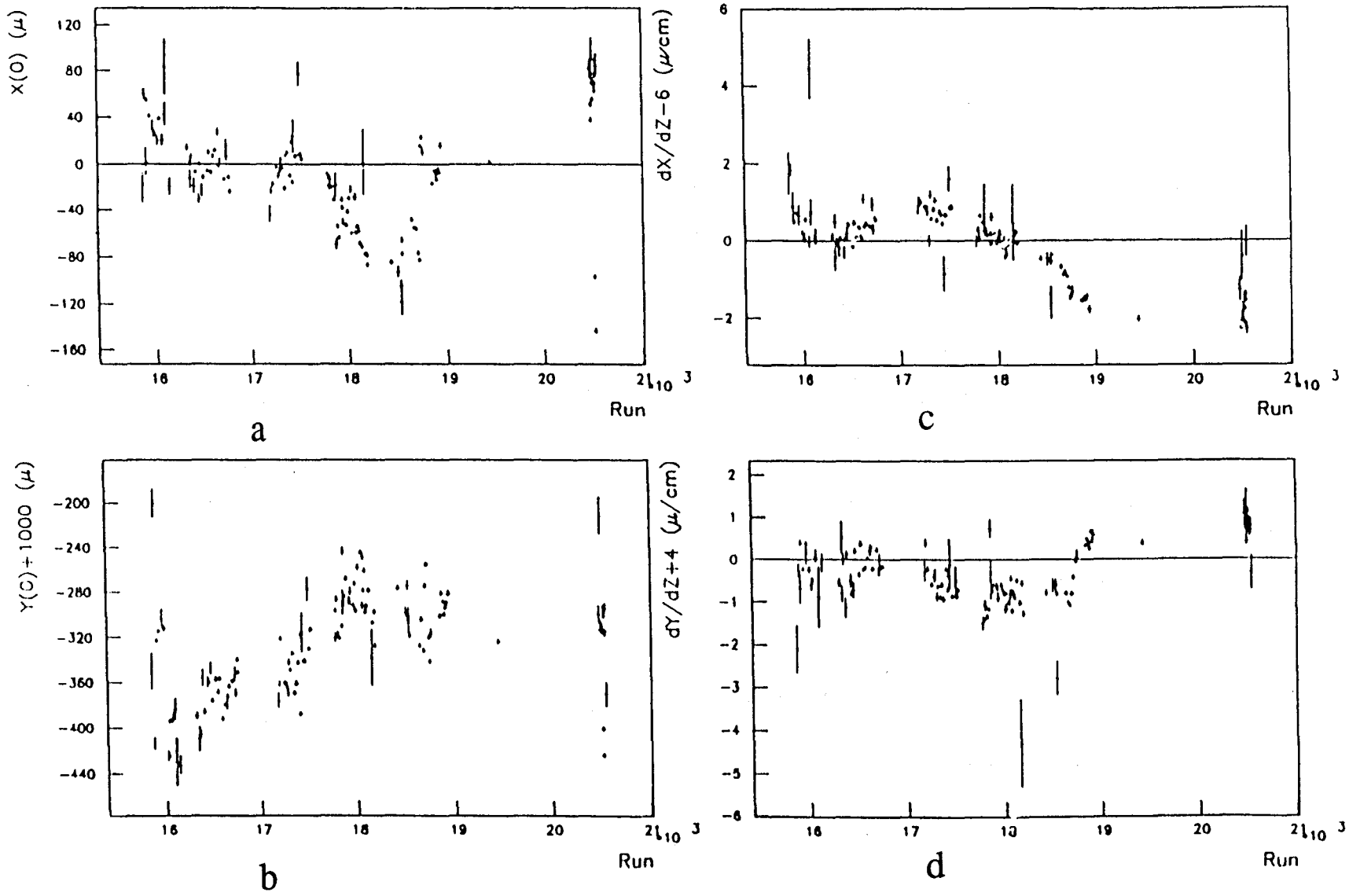

Fig. 12

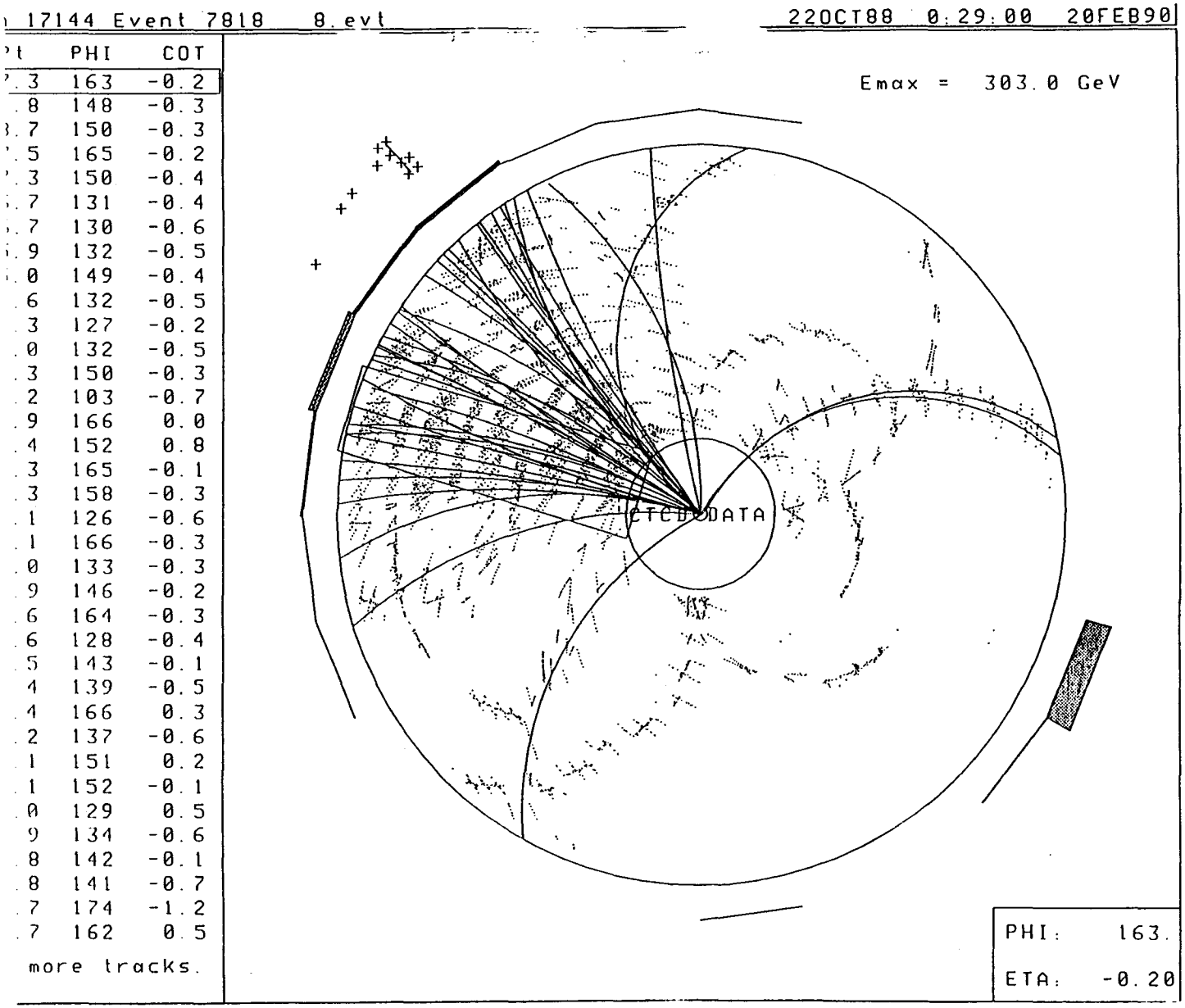
17144 Event 7818 8.evt
22OCT88 0:29:00 20FEB90
PHI COT
.3 163 -0.2
.8 148 -0.3
.7 150 -0.3
.5 165 -0.2
.3 150 -0.4
.7 131 -0.4
.7 130 -0.6
.9 132 -0.5
.0 149 -0.4
.6 132 -0.5
.3 127 -0.2
.0 132 -0.5
.3 150 -0.3
.2 103 -0.7
.9 166 0.0
.4 152 0.8
.3 165 -0.1
.3 158 -0.3
.1 126 -0.6
.1 166 -0.3
.0 133 -0.3
.9 146 -0.2
.6 164 -0.3
.6 128 -0.4
.5 143 -0.1
.4 139 -0.5
.4 166 0.3
.2 137 -0.6
.1 151 0.2
.1 152 -0.1
.0 129 0.5
.9 134 -0.6
.8 142 -0.1
.8 141 -0.7
.7 174 -1.2
.7 162 0.5
more tracks.
Emax = 303.0 GeV
CTCHODATA
PHI: 163.
ETA: -0.20

Fig. 13

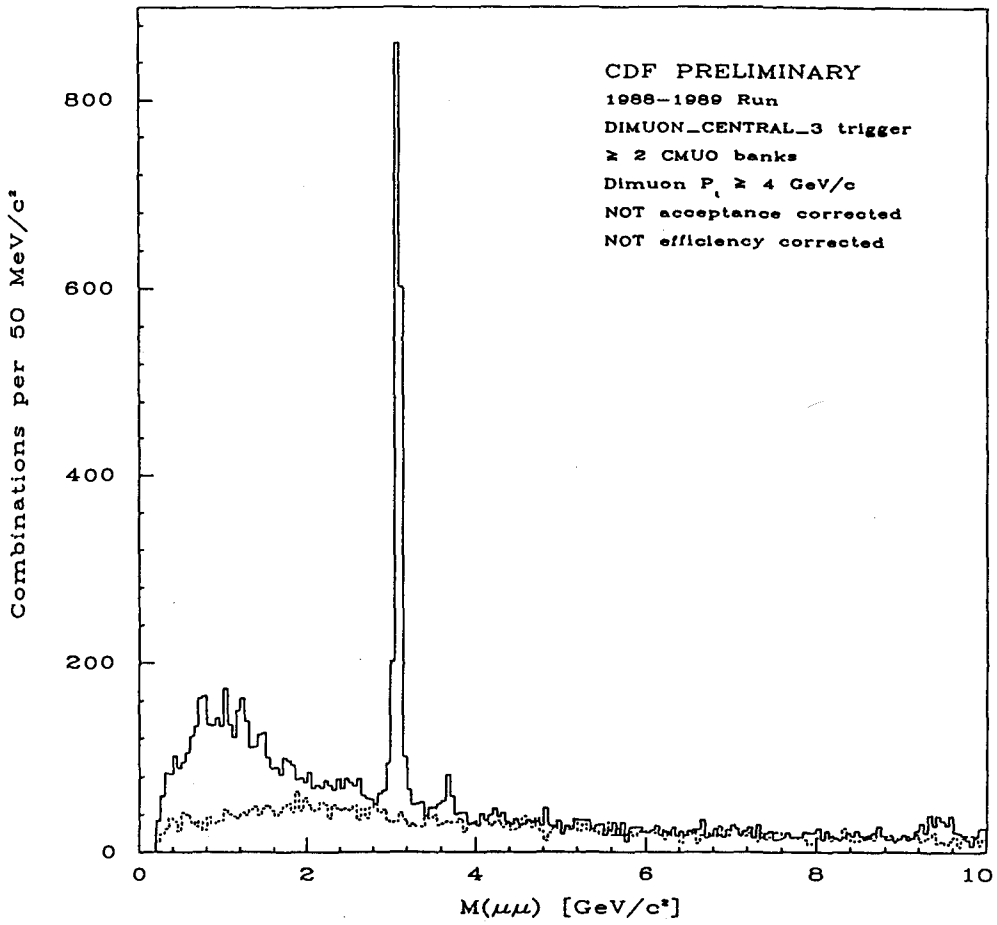
CDF PRELIMINARY
1988–1989 Run
DIMUON_CENTRAL_3 trigger
≥ 2 CMUO banks
Dimuon P_t ≥ 4 GeV/c
NOT acceptance corrected
NOT efficiency corrected
Combinations per 50 MeV/c²
M(μμ) [GeV/c²]
0
200
400
600
800
0
2
4
6
8
10

Fig. 14

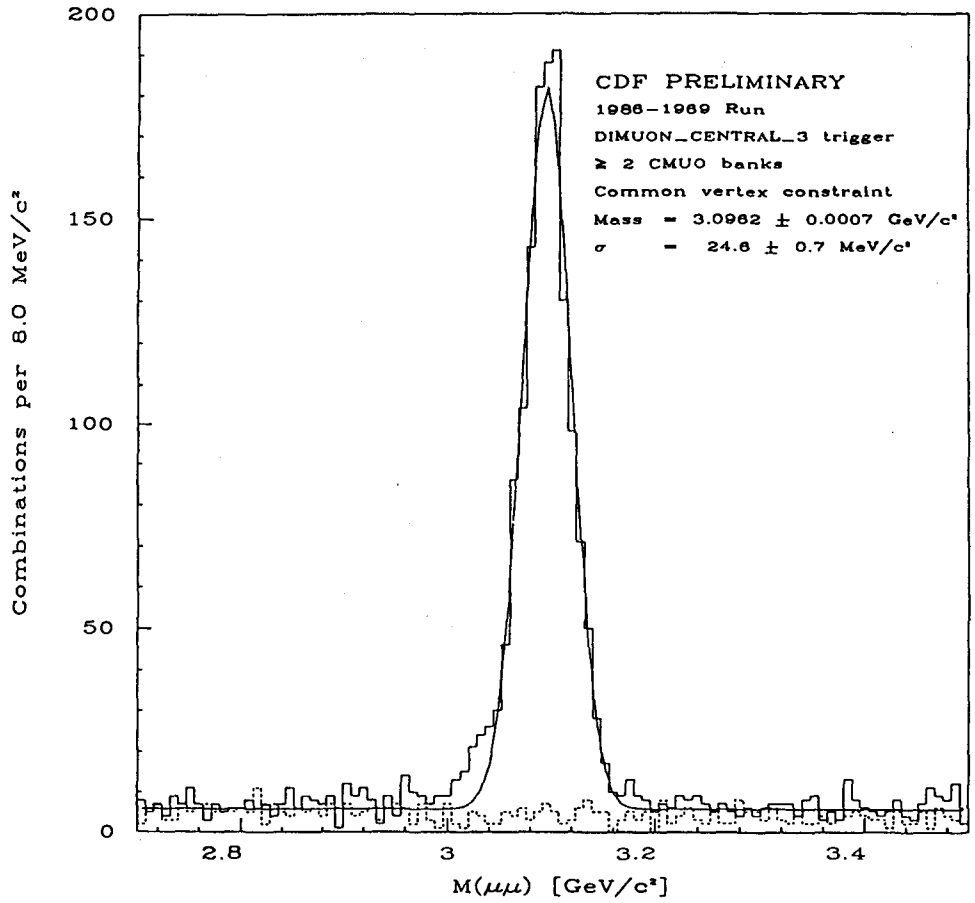
CDF PRELIMINARY
1988–1989 Run
DIMUON_CENTRAL_3 trigger
≥ 2 CMUO banks
Common vertex constraint
Mass = 3.0962 ± 0.0007 GeV/c²
σ = 24.6 ± 0.7 MeV/c²
Combinations per 8.0 MeV/c²
M(μμ) [GeV/c²]
0
50
100
150
200
2.8
3
3.2
3.4

Fig. 15

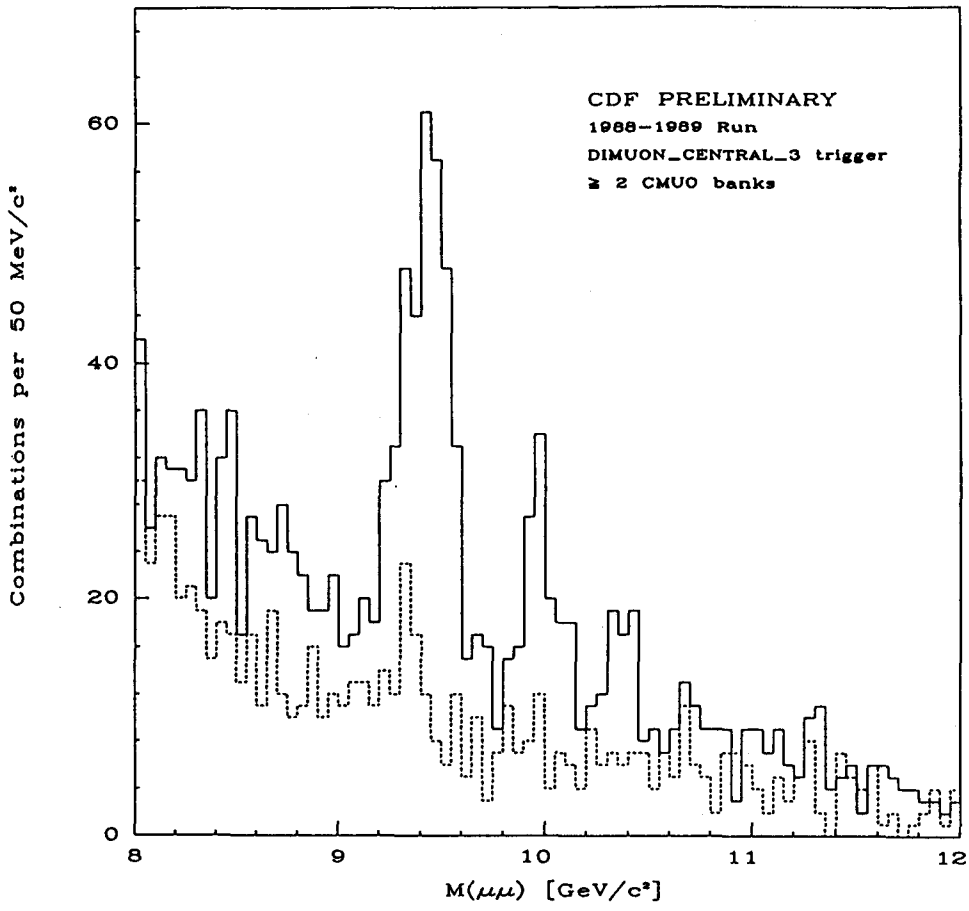
CDF PRELIMINARY
1988-1989 Run
DIMUON_CENTRAL_3 trigger
≥ 2 CMUO banks
Combinations per 50 MeV/c²
M(μμ) [GeV/c²]
0
20
40
60
8
9
10
11
12

Fig. 16

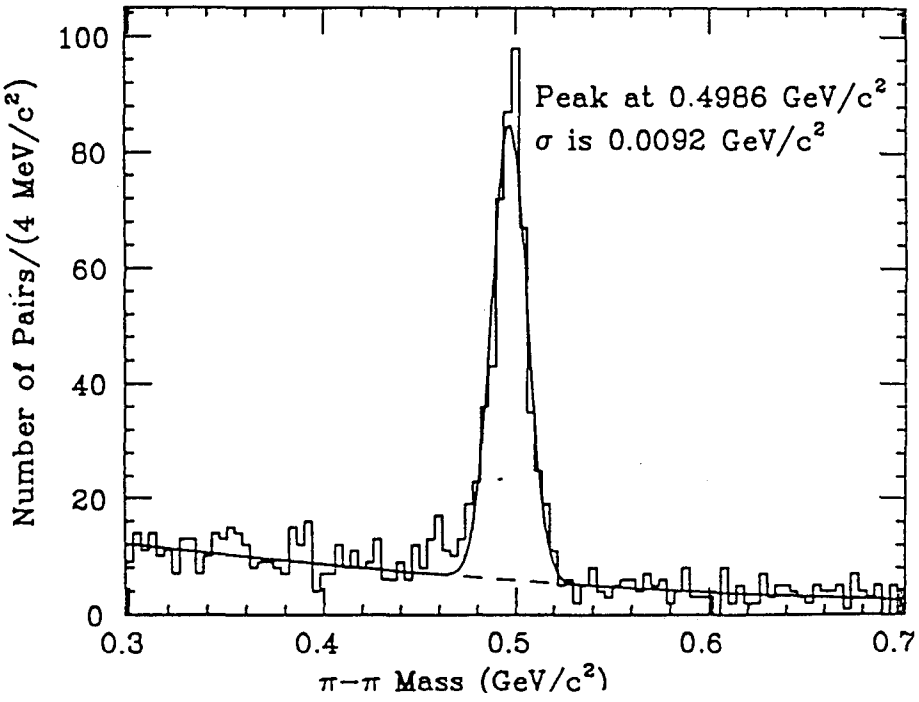
Peak at 0.4986 GeV/c²
σ is 0.0092 GeV/c²
Number of Pairs/(4 MeV/c²)
π−π Mass (GeV/c²)
0
20
40
60
80
100
0.3
0.4
0.5
0.6
0.7

Fig. 17

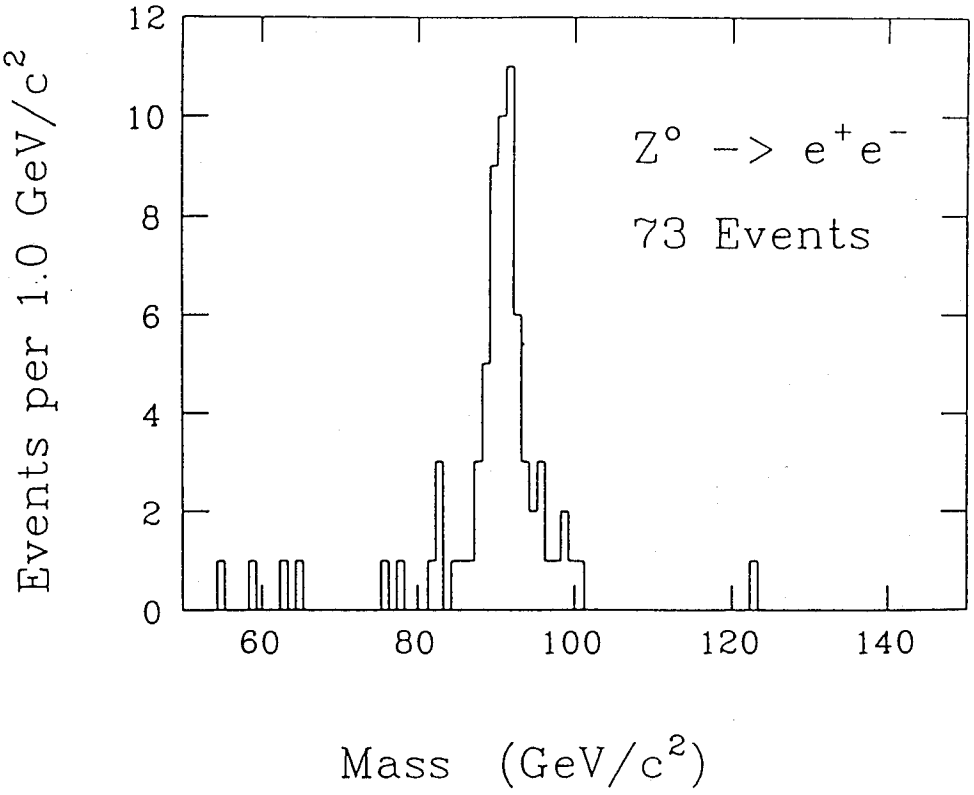
Events per 1.0 GeV/c^2
12
10
8
6
4
2
0
60
80
100
120
140
Z° -> e$^+$e$^-$
73 Events
Mass (GeV/c^2)

Fig. 18

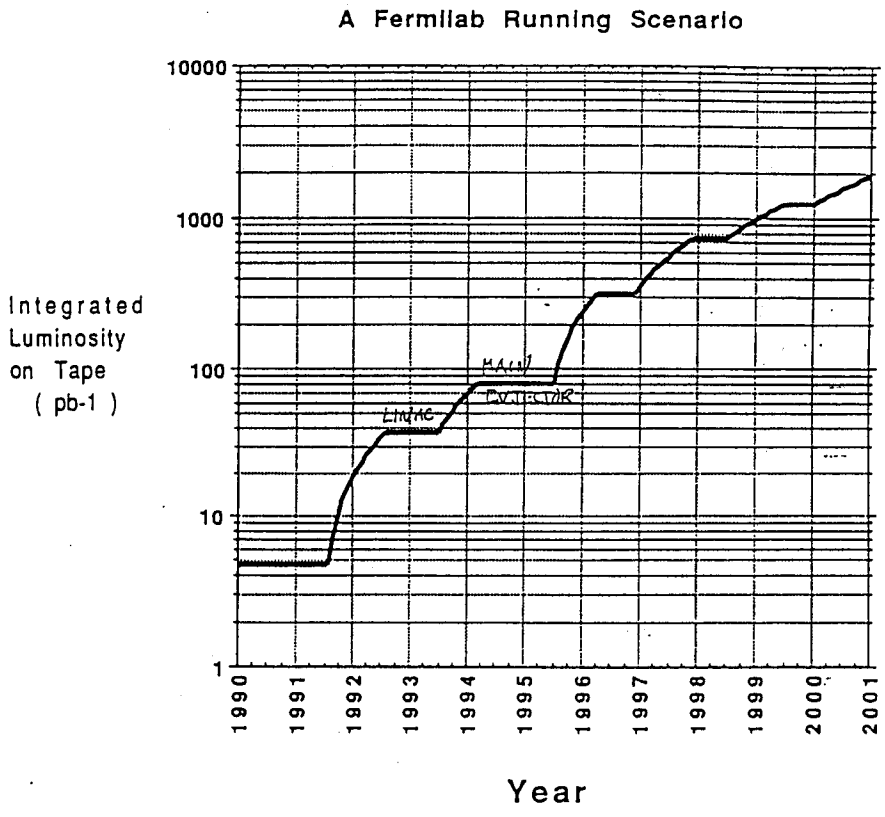
A Fermilab Running Scenario
Integrated Luminosity on Tape (pb-1)
10000
1000
100
10
1
1990
1991
1992
1993
1994
1995
1996
1997
1998
1999
2000
2001
Year

Fig. 19

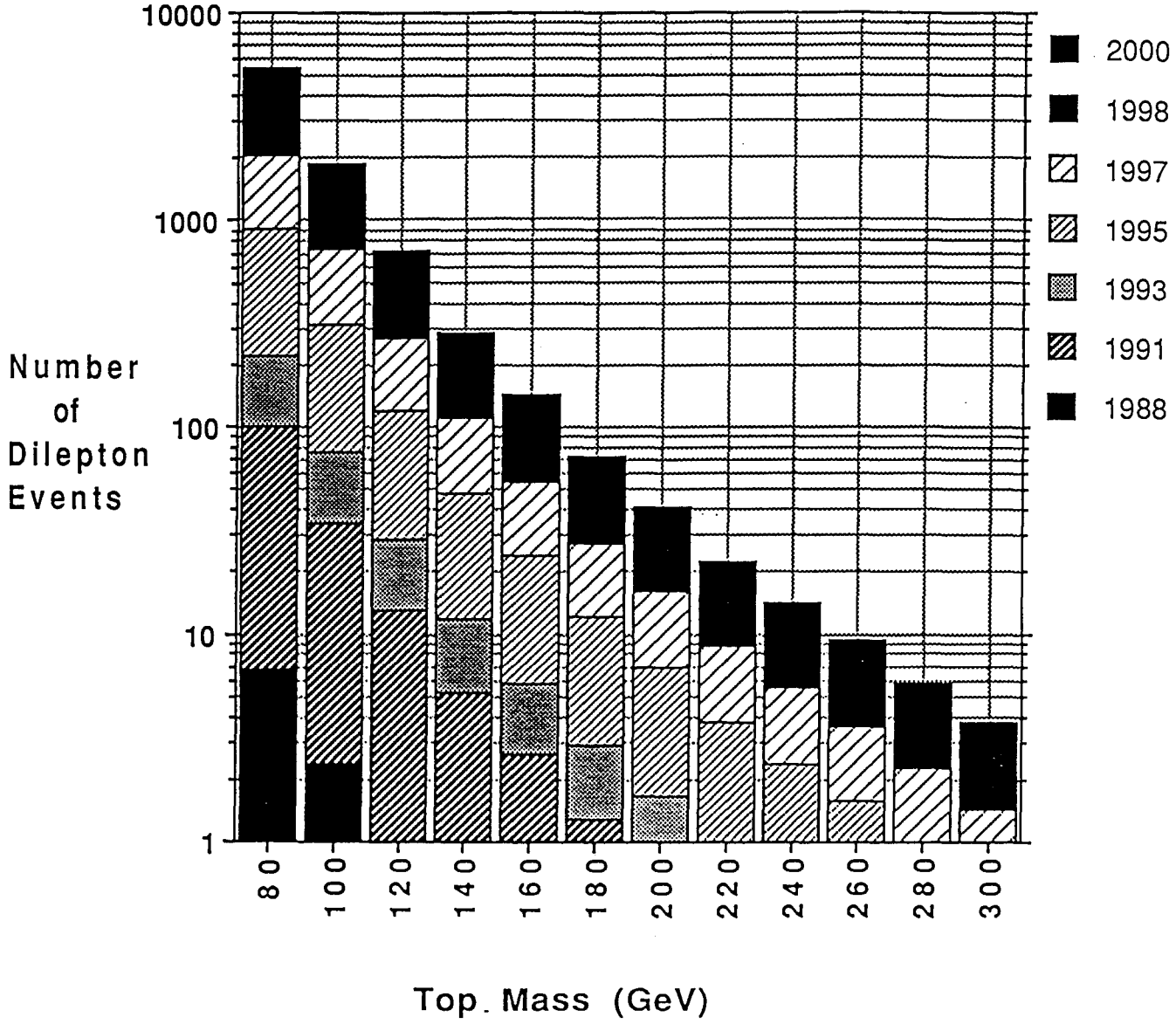
10000
1000
100
10
1
Number of Dilepton Events
80
100
120
140
160
180
200
220
240
260
280
300
Top Mass (GeV)
2000
1998
1997
1995
1993
1991
1988

Fig. 20

A Detector Design

David Bintinger
Superconducting Supercollider Laboratory
Dallas, Texas 75237, USA

J. R. Bensinger
Brandeis University/SSCL
Waltham, Mass 02254, USA

R. W. Kadel
Lawrence Berkeley Laboratory
Berkeley, California 94720, USA
June 7, 1990

Abstract: We have begun to study the dynamics of assembling a large SSC detector in a underground hall using a particular model for a solenoidal detector to improve our understanding of detector tolerances and construction specfications. We have established floor space needs; schedule, power, HVAC and utility requirements.

As we will show below the design and construction time for an SSC detector is about seven to eight years. This includes one year of hall design work, 3 years to construct the hall and 3 to 4 years to assemble the detector in the completed hall. The hall design must take into account the specifics needs of the detector. Given a target date for SSC operation in late 1998, these times imply that the final design of the hall must begin with the submission of the proposal, now scheduled for late 1991. Any major detector sub-systems which require special facilities in the hall must be identified and their needs included in the specification for the hall design. Hence, the hall design must be sufficiently flexible to accomodate facilities for any detector subsystem for which there is more than one option. We describe here an effort to try and develop the tools and information needed to effectively design an interaction hall and surface facilities for a large SSC Detector.

The work described here was done in collaboration with the engineering firm 'RTK' [1], of Oakland, California. This firm is under contract to the SSCL to perform geotechnical and cost studies of the underground interaction regions. The goals of the project were to:

1) Study the construction procedure for a detector to obtain an appreciation of the degree of difficulty of fabrication, assembly, disassembly and maintenance in an underground hall;
2) Define the hall configuration and the space requirements for the equipment, construction equipment access, operating access, personnel access, laydown areas, assembly procedure and assembly device storage;
3) Simulate the construction sequence to improve scheduling of the construction operations;
4) Specify needed utilities, such as electrical power, HVAC, and cooling water;
5) Estimate required above ground facilities and space requirements.
6) Compare above ground assembly with below ground assembly of major subsystems from a cost and schedule point of view.

We chose a simple detector design, but with sufficient complexity so that realistic studies could be made. The intent was not only to study 'a' particular detector, but to begin to develop tools

and collect information that could be applied to a broad range of detectors based on solenoidal magnets. In order to concentrate our efforts on hall design, rather than detector design, we chose a baseline detector configuration which minimized the mechanical interaction between sub- systems. Figures 1 is a cross sectional view of the detector; the plan view of the detector is shown in Figure 2. The solenoid coil design was based on 'air-core' or short solenoid [2]. This magnet does not use iron near the ends of the coil and hence the external forces on the coil cryostat and the calorimeter are dominated by gravity. Any electromagnetic forces between the calorimeter and coil have been ignored. The tracking system selected was a silicon inner tracker with an outer tracker. The outer tracker is further divided into a central and intermediate regions. The calorimeter was loosely based on the Warm Liquid design by EG&G [3] , but the results described here would apply equally to any self-supporting calorimeter built from 'modules' of order 20 to 50 Tons. The calorimeter modules are assembled into 5 cylindrical bays: 3 cental bays and two endcap bay. Each bay is about 3 meters long along the beam line and weighs of order 1200T.

The calorimeter is surrounded by magnetized iron muon toroids, 1.2 meters thick in the barrel region ($|\eta| < 1.5$) and about 4 meters thick in the intermediate region between $2.5 > |\eta| > 1.5$. There are four planes of muon chambers in the barrel region, and six in the intermediate angle regions. A major concern for the configuration of the muon steel is access to the calorimeter, and we considered two alternatives: 1) the barrel muon steel fixed in the hall with sufficient space inside to allow personnel access between the muon steel and calorimeter for electronics repairs; 2) movable barrel muon toroids.

Before proceeding with the hall design, we first considered the geography in which the hall is situated. Table I lists a number of parameters for the hall location, and our design is appropriate for IR1 or IR2 of this table. At this point the beam line is about 52 m (175 ft) underground. Note that because the accelerator is not parallel to the local direction of gravity, the beam-line passes through the interaction point at an angle of 0.09° with respect to the vertical. This corresponds to a change in height of 12.5 cm over 80 meters (the approximate size of an underground hall).

Based on previous work for the LSD detector [4], we looked at the cost of changing the width and length of the hall. The results are shown in Figure 3. For a hall of nominal width 28 meters and length 80 meters the cost of the hall is about \$27M. From the slope of the curves, one can derive that for adding a small area, it is marginally cheaper to make the hall wider (\$4.2K/m^2) than it is to make it longer (\$5.0 K/m^2). However, the usefulness of the area is probably maximized if the hall is made longer, and we have generally made the hall as narrow as possible perpendicular to the beam line to accommodate the detector (plus access space) and added length to the hall if additional floor space is necessary.

One concern was the amount of floor movement as heavy pieces of the detector are moved about. We suggested a combined nominal tolerance of 2.5 mm of non-elastic or elastic floor motion for short duration ($\sim$ 1 Week) motions of heavy (1200T) objects. Over the period of a year settling of order 2-3 cm could be tolerated. To gain some insight into the 'scale' of the deformation of the floor, we considered a simple ANSYS model for the soil motion. Figure 4 shows the result for the soil motion at the bottom of the excavation when the overburden of the soil is removed. The total motion or heave of the soil at the floor of the hall is 18 cm (7 in). More importantly, the net heave of the soil between the middle of the hall and the corner is 6.5 cm (2.7 inches), assuming laboratory values for the Young's Modulus and Poissons ratio of the soil. Since these values are large compared to our tolerances, some care will have to be taken in the design of the floor of the hall to insure that our tolerances can be met. A large boring (approx 2.5 m diameter) near the site

of the interaction regions is in progress at the SSCL to obtain better numbers to characterize the soil properties.

After some initial investigations, we quickly learned some general lessons about the hall and the detector that should be applicable to any of the solenoidal detector options:

1) Hall designs from the SSCL had the construction shaft (the major vertical access shaft for large objects) directly centered over the beam line. Once the accelerator is installed, the construction shaft is then rendered relatively useless since the floor under the shaft is occupied by accelerator components. We have located the shaft to one side of the hall.
2) The area of the construction shaft should be minimized: For safety reasons the area under the construction shaft is not useable except for temporary storage. Personnel and experimental equipment must be moved away from under the shaft to avoid falling objects.
3) Given that most of the assembly sequence and maintenance procedures require the motion of large detector components along the beam line, it seems prudent that the long dimension of the hall is parallel to the beam, not perpendicular.
4) In a similar vein, it seems clear that the detector does not want to be centered in the hall, either along the length or in the transverse dimension. Keeping the beam line to one side of the hall in the transverse dimension means that large objects can be moved from the construction shaft to the opposite end of the hall without disturbing the detector or making the hall too wide. Keeping the detector towards one end of the hall in the beam direction means that a relatively large, independent area can be created for the assembly of major subsystems, such as the calorimeter bays. If most of the muon steel is fixed in the hall, this is the most appropriate place for the assembly space. This space can be used later in the life of the experiment for maintenance or disassembly when older subsystems are replaced with new technology. The design of the accelerator provides for operation of the accelerator in a by-pass during major upgrades or repairs.
5) The amount of floor motion is still uncertain, and the muon system requires chamber placement accuracy of order 100 microns. It therefore seems prudent to keep most of the muon iron toroid fixed in place in order to minimize displacements of the floor. We considered an assembly scenario with moving steel, and discovered that at no time during the assembly sequence did we actually need to move the steel as long as we maintained an access space between the calorimeter and the muon steel. This access space is used for maintenance of calorimeter, tracking system and the muon system electronics inside the toroids. Hence, our current judgment would be to keep the steel of the barrel muon toroids to be fixed in place.

Figure 5 shows a 3-dimensional view of the empty Hall. The final location of the detector is evident in the lower half of the figure. OHSA regulations require emergency exit tunnels about every 90 ft. These emergency shafts are located at each end of the hall along the top edge of the picture. These vertical shafts are dug outside the excavation area for the hall proper. They are located 34 meters away from the hall and connect to the hall via lateral tunnels. Keeping these two shafts outside the main excavation allows access to the hall for installation of conventional electrical systems, HVAC, etc before the excavated soil is replaced. This allows access to the hall about one year earlier than if the shafts are within the area excavated for the Hall.

One of these two shafts ('personnel shaft') on the left side of the figure contains a stairwell, elevator, HVAC duct work and fire protection systems. The shaft at the far right side of the figure ('equipment shaft') also contains a stairwell, a shaft for lowering smaller pieces of apparatus (up to 35 T) and air handling ducts. Trigger and Data-acquisition cables are routed to the surface via a

third small shaft centered on the detector. A forth shaft, also near the center line of the detector is used for carrying major utilities to and from the surface: liquid and gaseous Nitrogen and Helium, low conductivity water, industrial chilled water, speciality gases for detector sub-systems, as well as current leads for superconducting and conventional magnets. All of these shafts are located on the same side of the hall to keep the above ground areas well organized; minimize the underground area used for traffic lanes and avoid interference with the accelerator bypass. Cross sections of these four shafts are shown in figure 6.

The last and largest shaft is the construction shaft located in the bottom left of figure 5. It is through this shaft that large pieces of apparatus are lowered into the hall. Examples are the muon steel, superconducting coil, and mechanical supports for the calorimeter. Note that the construction shaft is not centered above the beam line, and with the detector located to one side of the hall, we have generated a wide lane along the side of the detector for transporting material from the construction shaft to the opposite end of the hall. This shaft is also used in conjunction with a duct system on the roof of the hall for smoke removal in case of a fire.

During the initial assembly of the detector the hall is partition into two volumes 1) a large volume centered on the final position of the detector where the muon steel is assembled and 2) a calorimeter assembly area. These two volumes have independent air systems to reduce contamination between the muon steel assembly area and the relatively clean area needed to assemble the calorimeter.

In the course of our work we have created a sequential set of drawings for the construction of the detector showing the activity in the hall at roughly 3 month intervals for the entire 42 month assembly process. Figures 7, 8, 9 and 10 are examples from this work showing the state of the hall at the 9th month, 18th month, 30th month and 42nd month of the construction schedule, respectively. The 3 dimensional model of the detector has been used to verify that sufficient room exists in the hall to perform all of the work needed, including space for two large assembly fixtures needed to construct the calorimeter, as well as fixtures for installation of the coil and tracking.

We also considered an assembly scenario where the calorimeter bays are assembled above ground and lowered as five 1200 ton units into the hall. The assumption here is that tasks are more efficiently performed above ground versus below ground and that in an above ground facility one could consider building two calorimeter bays at a single time. This could reduce the assembly time for the detector. One might also imagine that some cost savings could apply since the below ground hall could be made smaller. At present we do not favor this scenario for two reasons:

1) The cost of a large crane was estimated at \$75,000 setup, \$50,000 per month operating charges and \$75,000 to disassemble. We would need such a crane for about a year. It was found to be cheaper (on the basis of figure 3) to add additional space to the hall.
2) In the event of a major repair or upgrade to of the detector, one would require sufficient below ground area for disassembly of the detector. This disassembly space is about the same needed for construction.

Further study of above ground assembly is in progress to test these impressions.

One of the issues for this project was to collect as best as possible information on the electrical power and facilities needed to operate the detector. We have developed a relatively detailed EXCEL spreadsheet to estimate the total power, HVAC, LHe, LN2 and other utilities used by the detector. Table II, taken from this spread sheet, summarizes the electrical power requirements for the detector. The total power required by this detector is estimated to be about 15MW. One important parameter is the fraction of the total power load dissipated inside the steel of the muon

toroids, either from the electronics or the coils on the muon steel. If 1% of the power in the toroid coils is transferred to the air inside the toroids, 20KW of heat must be removed in air conditioning or a thermal shield. Assuming that most of the electronics is water cooled, the dominate heat load on the air-conditioning could be heat dissipated by the coils. It is difficult to remove large, diffuse heat loads inside this enclosed volume without high air velocities and the thermal management of the heat loads and cooling sources inside the muon steel will be an engineering challange.

Finally, in Figure 11 we show an abbreviated schedule for the assembly of the detector. As noted earlier, after occupancy of the hall, about 3 and 1/2 years is needed to assemble the detector. According to the schedule, the first 60 (of about 350) calorimeter modules are needed about 6 months after occupancy of the hall and the last calorimeter module is installed one year before beam is available.

To conclude, we have identified several interesting features concerning the assembly procedures of a large detector in an underground hall. Given the long assembly time for the detector and an estimated three year construction time for the hall itself, it is advisable that major technology choices be made as early as possible so that hall design can be finalized. Some aspects of the hall design still need study, even at this general level of work described here. The first of these are the definition of special safety requirements for the detector subsystems. Of particular concern are liquid calorimeters, either Liquid Argon, liquid scintillator or warm liquids, which have either ODH or flammable liquid safety issues. A second concern is any detector subsystem that might require a shielded room at roughly beam level that can be occupied when the SSC is in operation. We have not as yet identified a need for such a room in our particular design example, but the need for such a room might arise. As this work progresses we hope to attack these and related issues.

References

1. 'RTK', a joint venture: Kaiser Engineers, Inc, Tudor Engineering, and Keller & Gannon-Knight.
2. Y. Doi, et al, "Design Study of a Short Solenoid for the SDC Detector", Proceedings , "International Workshop on Solenoidal Detectors for the SSC", KEK, April, 1990.
3. T. Ballinger, et. al, "Engineering Design Study of a Warm Liquid Calorimeter Concept for a Detector at the SSC", EG&G Energy Measurements, Report AVO-395, Sept, 1989.
4. See, for example, G. Hansen, et. al., "Report of the Large Solenoid Detector Group", in R. Donaldson, G. Gilchriese, editors "Proceedings of the International Workshop on Experiments,Detectors and Experimental Areas for the Supercollider", Berkeley, Ca., 1987, page 340.

Table Captions

1) Detailed geotechnical Parameters of the SSCL Halls. This detector was designed assuming the parameters of IR-1 or IR-2. "Depth to Material interface" is the depth to the boundary between the "Austin Chalk (AC)" and "Eagle Ford Shale (EFS)" strata.

2) Power requirements for the detector. The detector electronics are assumed to be powered via 400 Hz low voltage power supplies. Some conventional 60Hz power is used for the detector. An example is any high voltage power supply. In the computation of the total 'line power' we have taken the total power from the 400Hz, 60 Hz detector and 60 Hz (other) columns and included effects due to power supply efficiency, spare capacity, diversity and power factors.

Figure Captions

1) Cross section of the "RTK Baseline" Detector.

2) Plan view of the "RTK Baseline" detector.

3) Cost of the hall as a function of its length and width. Included in the estimate are excavation, concrete, conventional electrical power, HVAC, cranes, backfill, etc. The hall priced here had three shafts: a) a personnel shaft ($2.3M incl elevator and services), b) a construction shaft for large objects ($0.50 M) and c) an equipment shaft ($0.58M) for smaller pieces of equipment and personnel access.

4) ANSYS simulation for the net vertical heave of the soil at the floor of the hall when the overburden is removed. The element size is 5 Meters in both directions and the vertical displacement has been exaggerated for clarity. Several cases were run assuming different soil properties. Values for the soil properties as measured in the laboratory on the basis of a small test boring at the SSCL site are indicated.

5) Three dimensional view of the detector hall showing the location of the access shafts. The final detector location is centered above the support structures shown in the left-half of the hall.

6) Cross section of four shafts: a) personnel shaft, b) equipment shaft, c) DAQ/Trigger cable shaft, d) Utility shaft.

7) State of the hall at 9 months into construction.

8) State of the hall at 18 months into construction.

9) State of the hall at 30 months into construction.

10) State of the hall at 42 months into construction.

11) Simplified schedule for the detector assembly.

Table I: Experimental Halls Geotechnical Parameters
(West Cluster)

	IR1	IR2	IR3	IR4
Depth To Beam Line (ft)	178	171	137	143
Depth to Bottom of Excavation (ft)	219	210	197	174
Depth to Material Interface(ft)	218	211	168	180
Depth to limiting Load Countours (ft)	260	259	266	207
Excavated Volume (MCY)	0.25	0.57	0.48	0.55
Excavated Materials (per cent)	AC 100	AC 99 EFS < 1	AC 99 EFS 1	AC 100
Hall Volume (MCY)	0.04	0.10	0.24	0.03
Detector Axial Slope (deg)	0.09	0.09	0.09	0.09

Draft 02/08/90
Cut and Cover Construction
MYC = Million Cubic Yards

Table II: Power Consumption

Source	400 Hz	60 Hz Expt	60 Hz (other)	DC	Line Power
INSIDE COIL					
Silicon Tracking	20.0	0.5			
Straw Tracking	12.4	0.3			
Total Inside Coil	32.4	0.8			
INSIDE μ TOROID					
Calorimeter	160.0				
μ Chamber	1.4				
μ Trigger Scint.	12.0				
Trk LV Power Supplies	32.4				
Total Inside Toroid	205.8				
OUTSIDE μ TOROID					
μ Toroid Coils				2500.0	
μ Chamber	8.1				
μ Triggger Scint.	84.0				
Forward Calorimeter	11.2				
Level 1 Trig	240.0				
HV + Utilities		103.2	595.0		
Total Outside Toroid	343.3	103.2	595.0	2500.0	
UTILITY SHAFTS					
Power Bus				240.0	
Total Shafts				240.0	
SURFACE					
Data Acquisition	1200.0				
Level 2 Trigger	400.0				
Level 3 Trigger		400.0			
Control Room		400.0			
Cryogenics			190.0		2535.0
HVAC			1443.0		
Misc power		500.0	207.5		
μ Toroid pwr supplies					4212.0
400 Hz M/G Set					2212.0
60 Hz Detector					1423.0
60 Hz Other					4265.0
Total Surface	1600.0	1300.0	1890.5		14647.0
GRAND TOTAL	2181.5	1404.0	2485.5	2740.0	14647.0

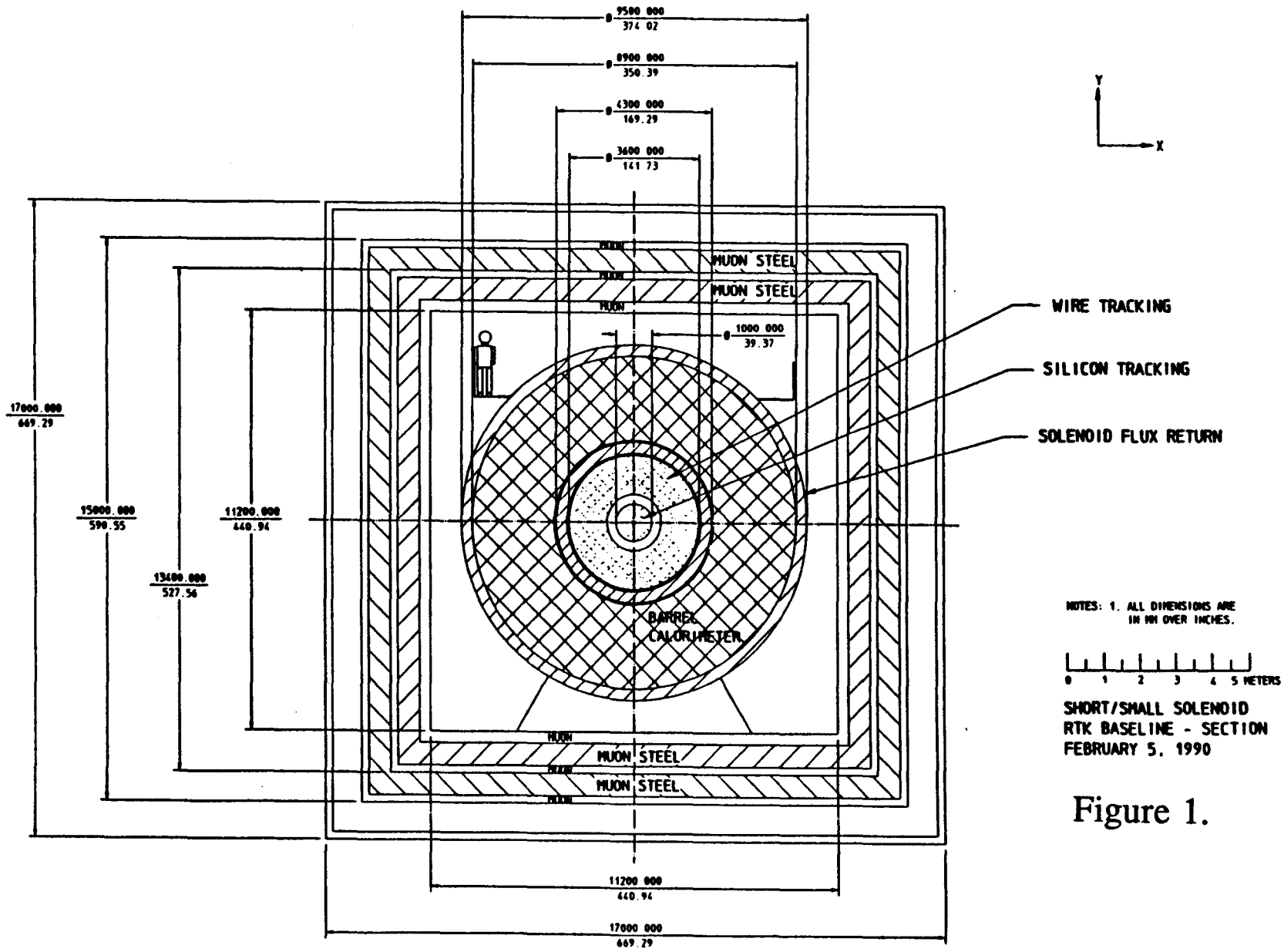
9500.000
374.02
8900.000
350.39
4300.000
169.29
3600.000
141.73
MUON STEEL
MUON STEEL
MUON
1000.000
39.37
WIRE TRACKING
SILICON TRACKING
SOLENOID FLUX RETURN
17000.000
669.29
15000.000
590.55
13400.000
527.56
11200.000
440.94
BARREL
CALORIMETER
MUON STEEL
MUON STEEL
11200.000
440.94
17000.000
669.29
Y
X
NOTES: 1. ALL DIMENSIONS ARE
IN MM OVER INCHES.
0 1 2 3 4 5 METERS
SHORT/SMALL SOLENOID
RTK BASELINE - SECTION
FEBRUARY 5, 1990

Figure 1.

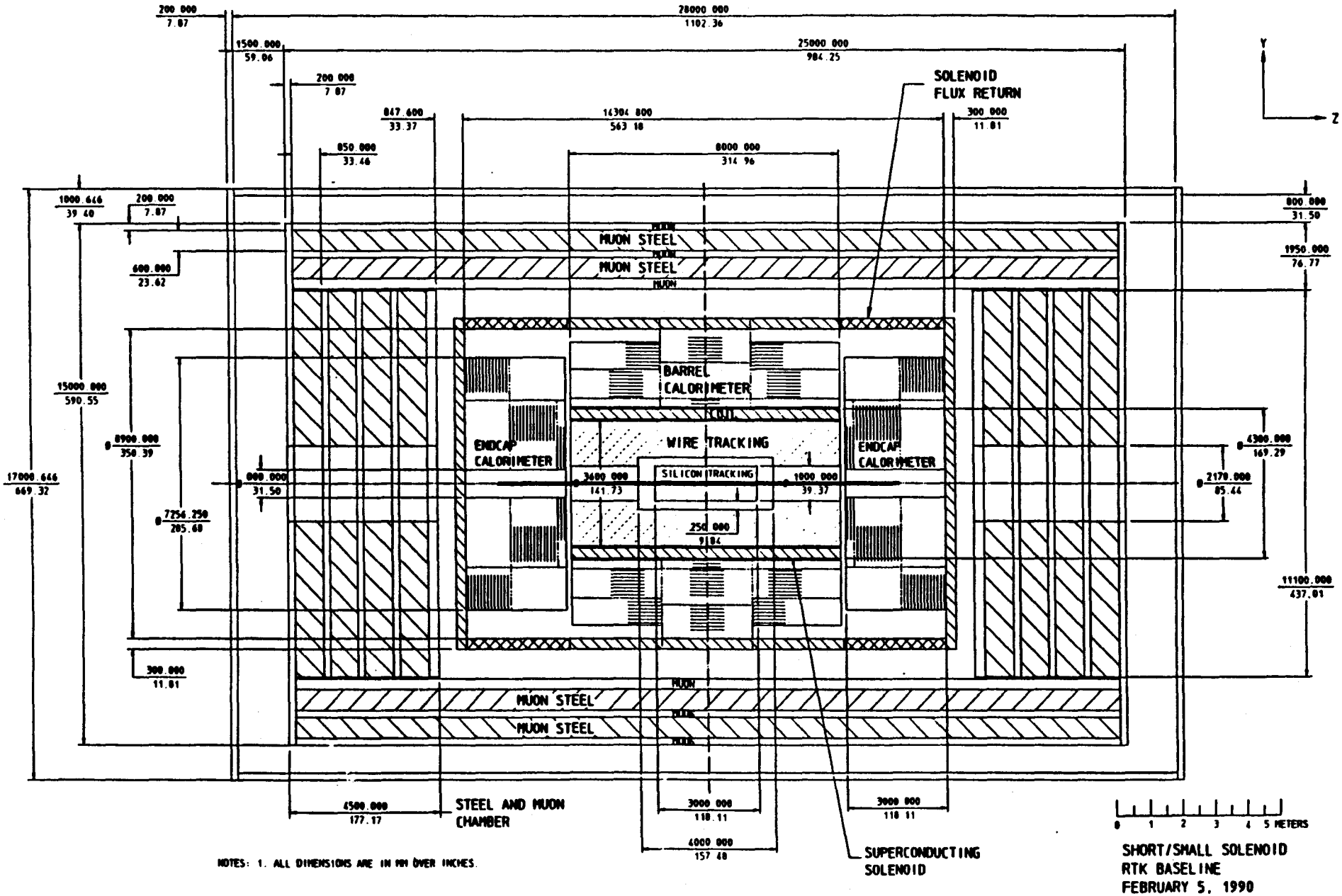
SOLENOID
FLUX RETURN
MUON STEEL
MUON STEEL
BARREL
CALORIMETER
COIL
ENDCAP
CALORIMETER
WIRE TRACKING
SILICON TRACKING
ENDCAP
CALORIMETER
MUON STEEL
MUON STEEL
STEEL AND MUON
CHAMBER
SUPERCONDUCTING
SOLENOID
Y
Z
0 1 2 3 4 5 METERS
NOTES: 1. ALL DIMENSIONS ARE IN MM OVER INCHES.
SHORT/SMALL SOLENOID
RTK BASELINE
FEBRUARY 5, 1990

Figure 2.

Figure 3.

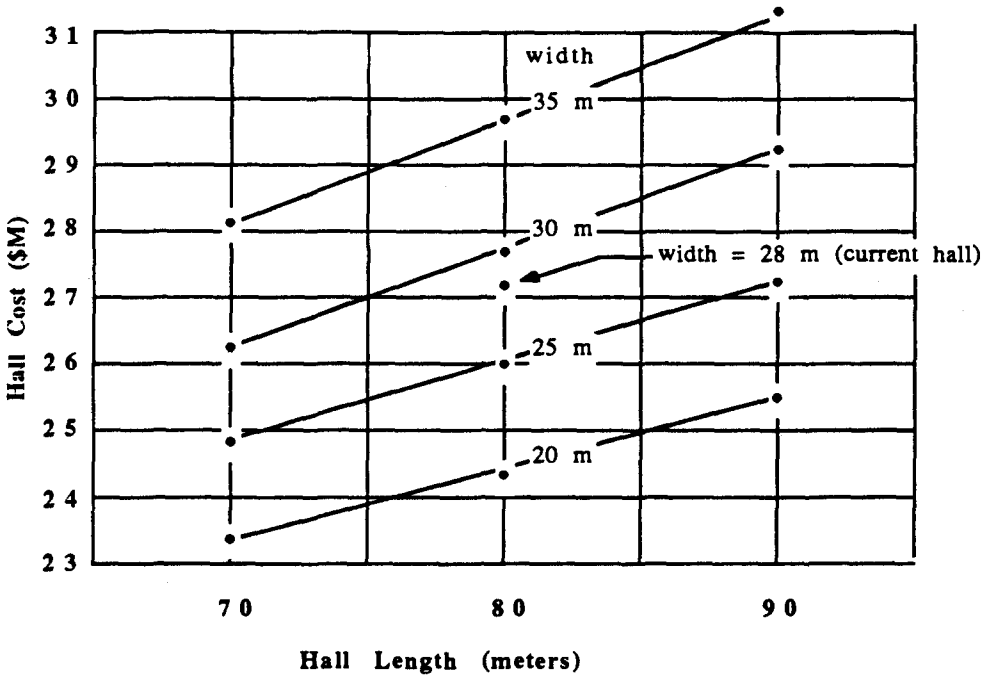
31
30
29
28
27
26
25
24
23
Hall Cost ($M)
width
35 m
30 m
width = 28 m (current hall)
25 m
20 m
70
80
90
Hall Length (meters)

Figure 4.

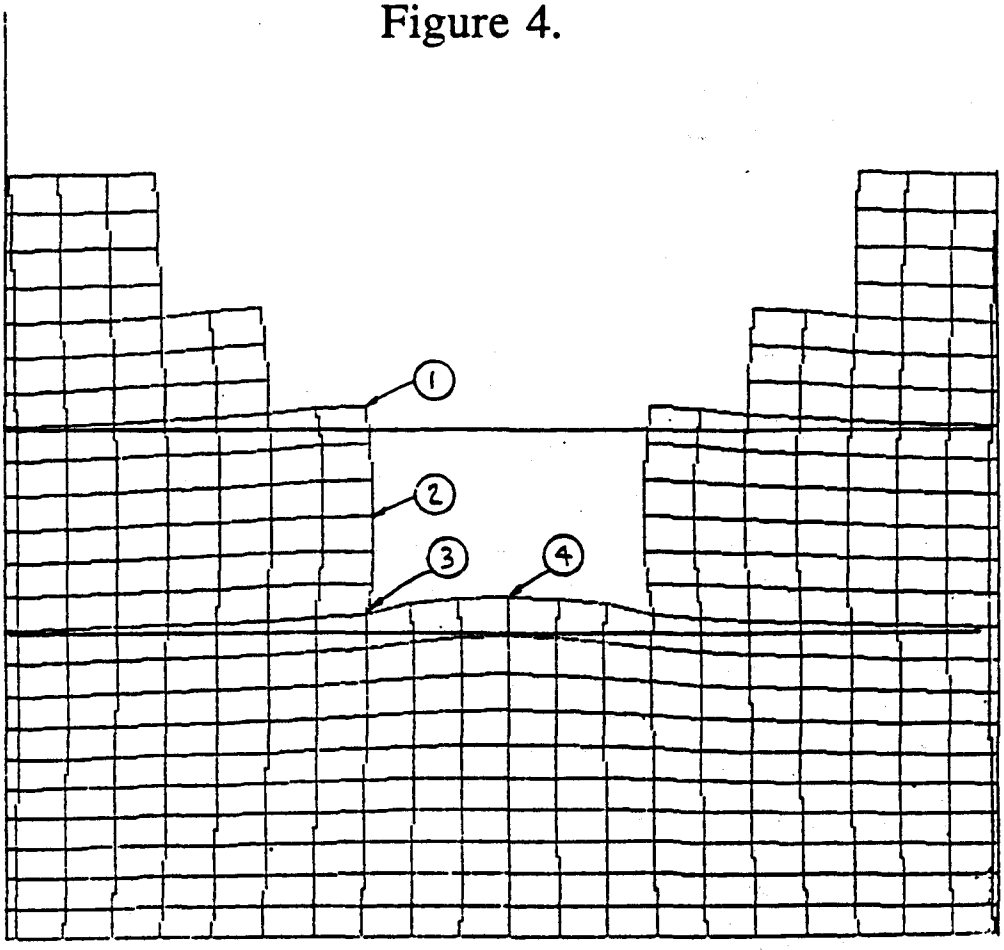

Estimated Rock Movements (inches)

Rock Properties		Movement	Location				Net Heave
E(ksi)	Poisson		1	2	3	4	(4-3)
17.5	0.35		5.7	4.3	8.8	14.2	5.4
35.0	0.35	Vertical	2.8	2.2	4.4	7.1	2.7
35.0*	0.40		5.5	4.1	4.3	7.0	2.7
17.5	0.35		1.7	3.5	1.2	0.0	
35.0	0.35	Horizontal	0.8	1.7	0.6	0.0	
35.0	0.40		1.1	2.0	0.8	0.0	

*Lab Values

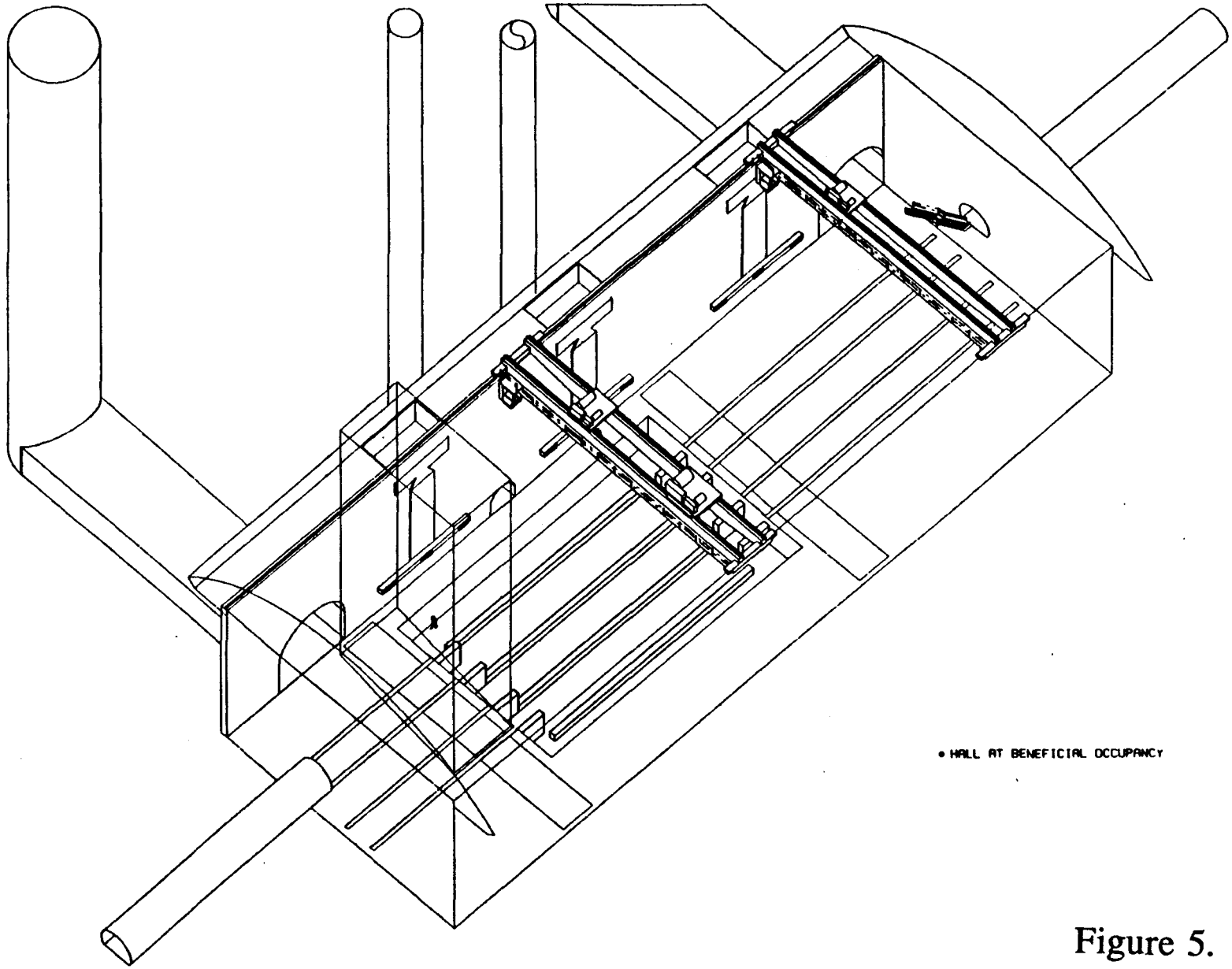

Figure 5.

RTK BASELINE DETECTOR CONSTRUCTION SEQUENCE
HALL AT 0 MONTHS

Figure 6.

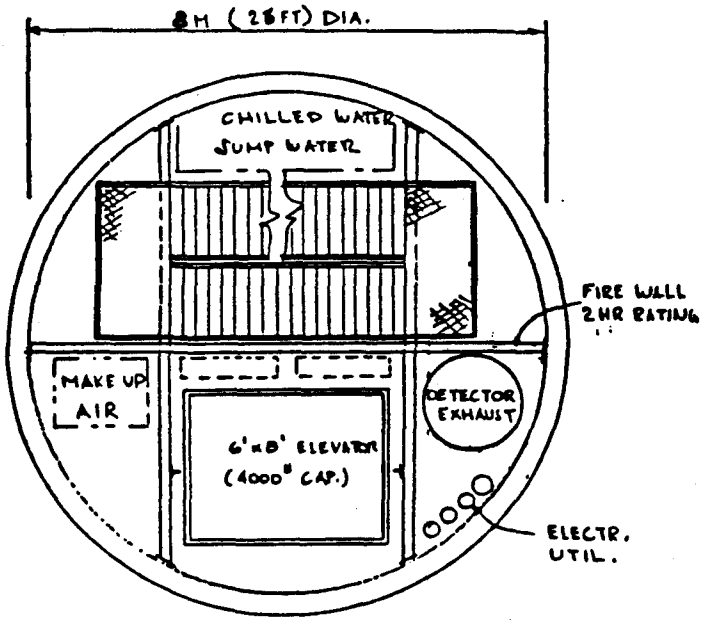

(a) PERSONNEL SHAFT

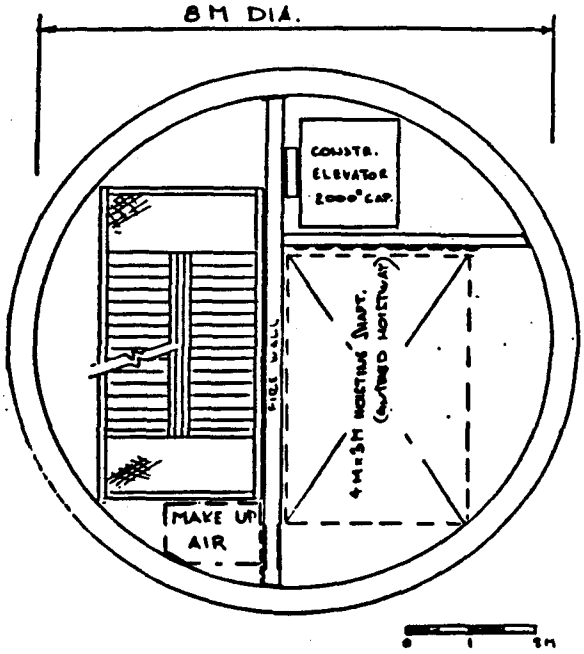

(b) EQUIPMENT SHAFT

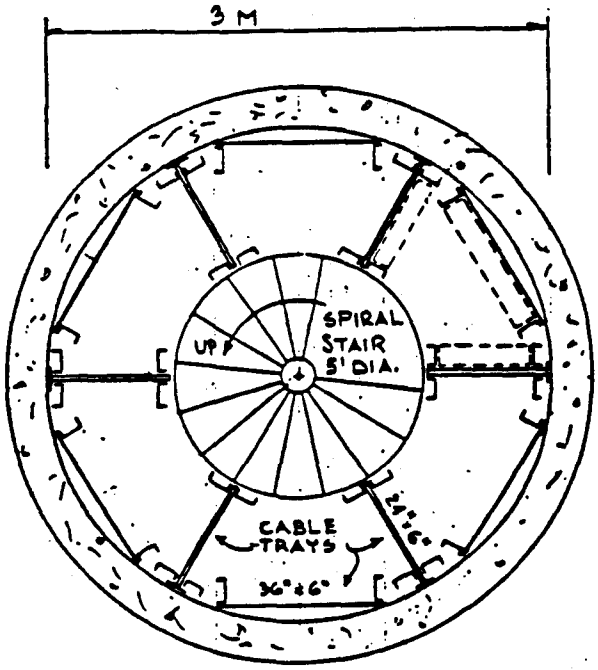

(c) CABLE SHAFT PLAN

TOTAL AREA IN TRAYS = 1.95 M²

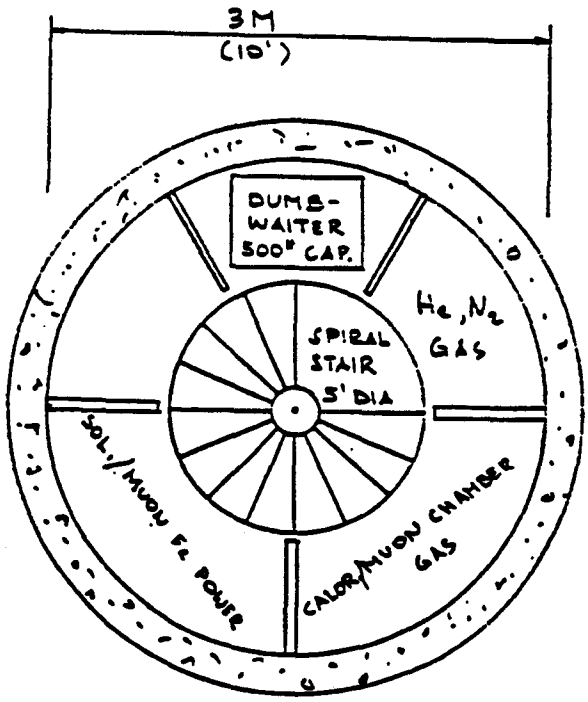

(d) UTILITY SHAFT

TOTAL NET UTILITY AREA = 35 FT²

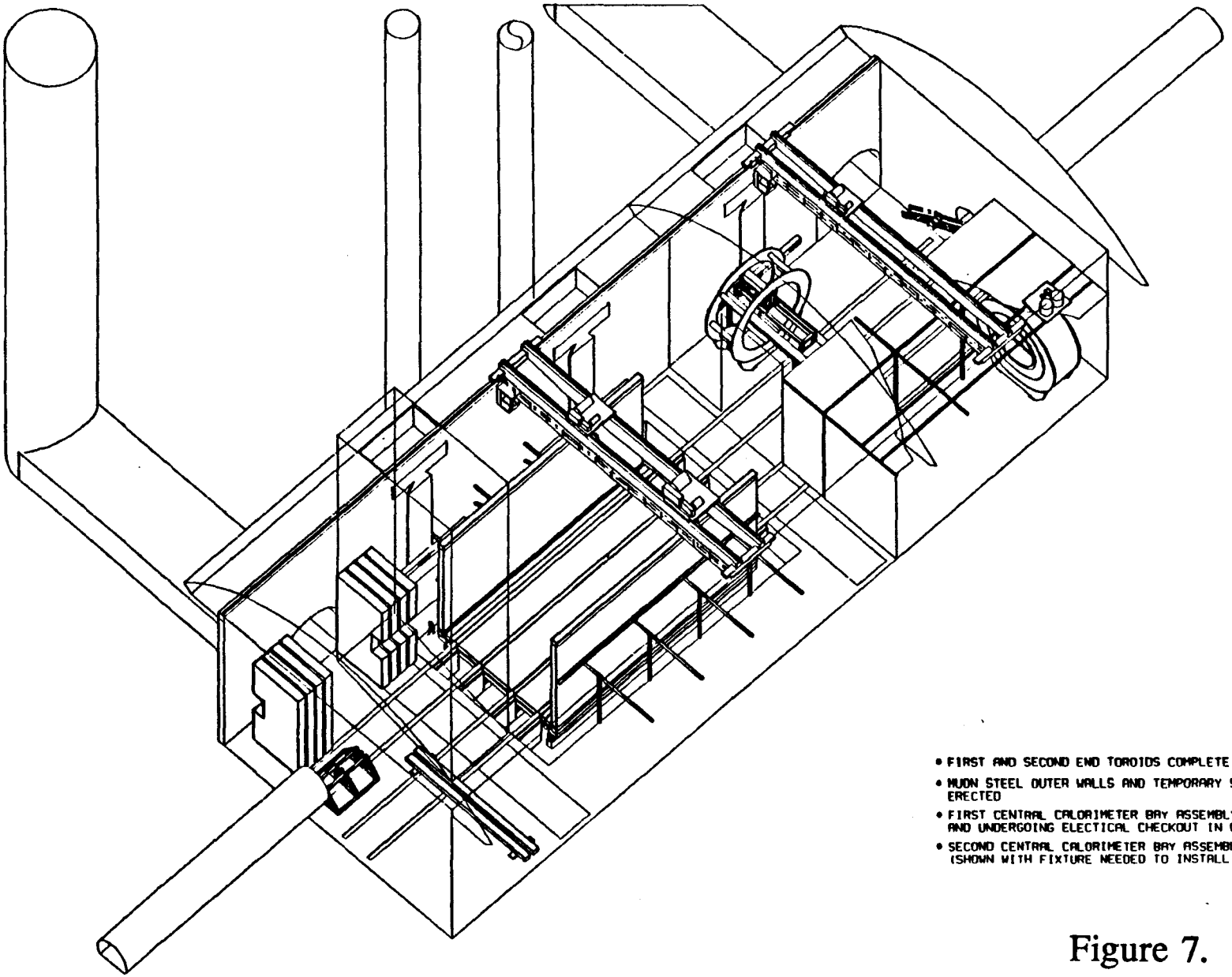

- FIRST AND SECOND END TOROIDS COMPLETE
- MUON STEEL OUTER WALLS AND TEMPORARY SUPPORTS ERECTED
- FIRST CENTRAL CALORIMETER BAY ASSEMBLY COMPLETE AND UNDERGOING ELECTICAL CHECKOUT IN CLEAN ROOM
- SECOND CENTRAL CALORIMETER BAY ASSEMBLY IN PROGRESS (SHOWN WITH FIXTURE NEEDED TO INSTALL MODULES)

Figure 7.

RTK BASELINE DETECTOR CONSTRUCTION SEQUENCE
HALL AT 9 MONTHS

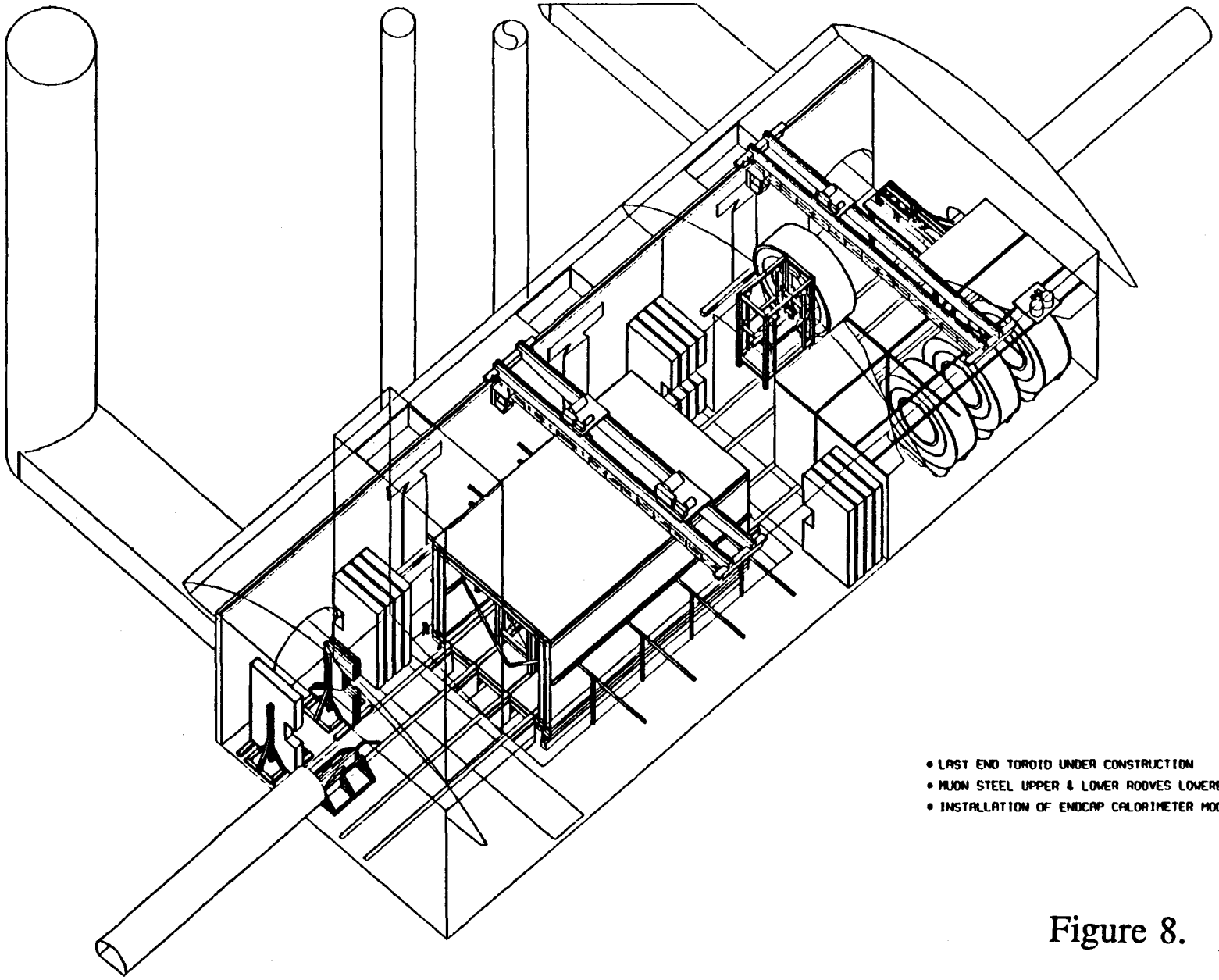

Figure 8.

RTK BASELINE DETECTOR CONSTRUCTION SEQUENCE
HALL AT 18 MONTHS

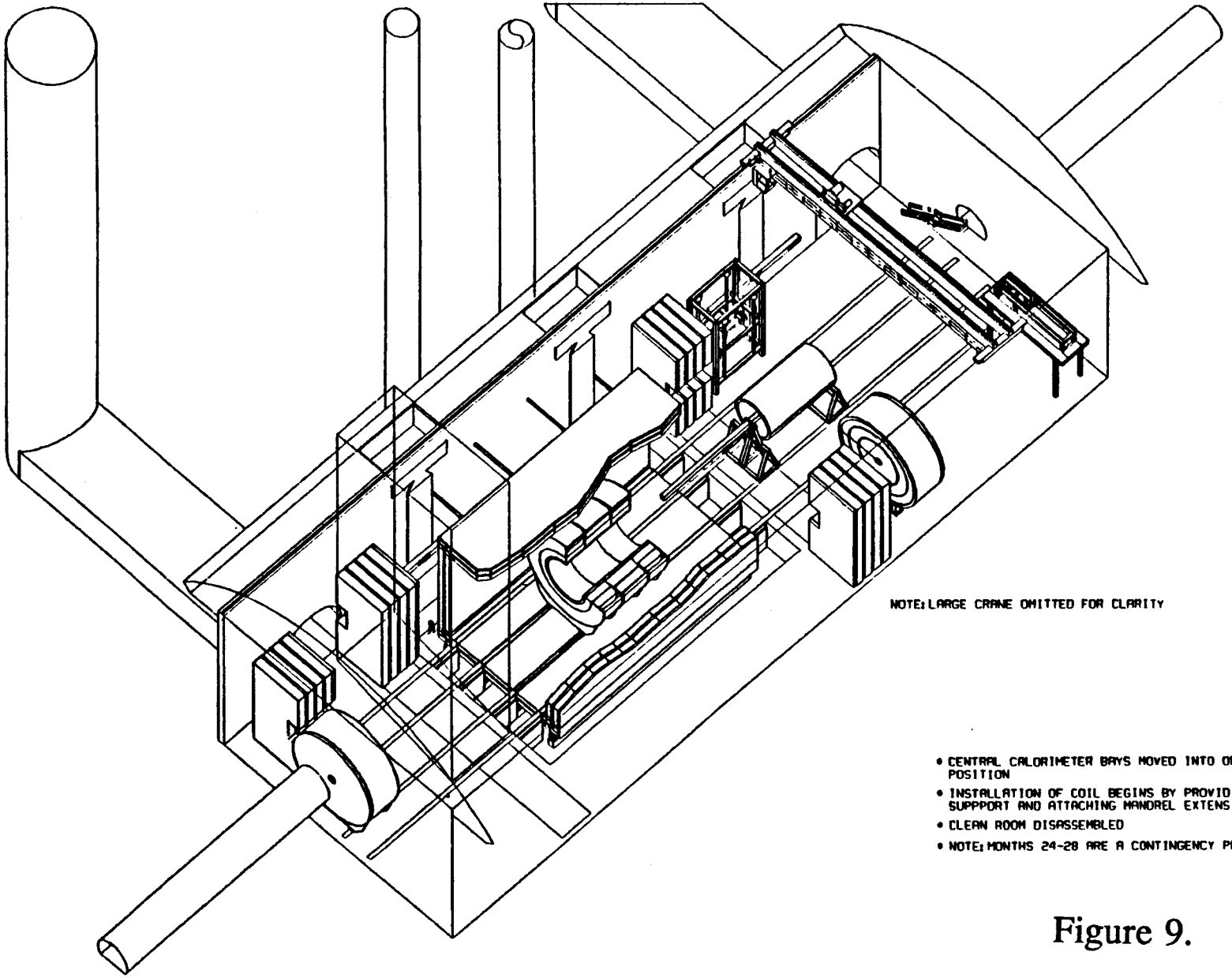

Figure 9.

RTK BASELINE DETECTOR CONSTRUCTION SEQUENCE
HALL AT 30 MONTHS

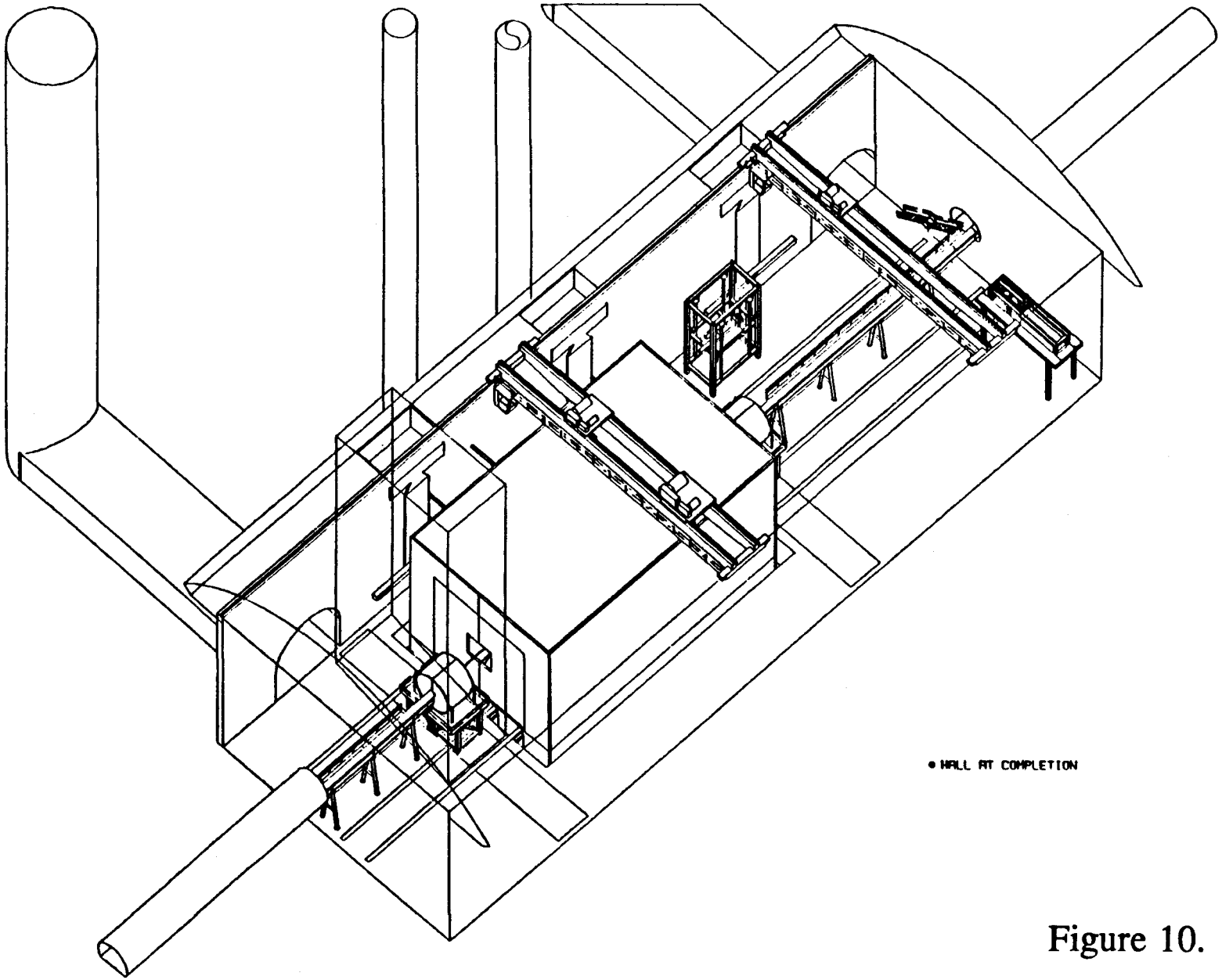

Figure 10.

RTK BASELINE DETECTOR CONSTRUCTION SEQUENCE
HALL AT 42 MONTHS

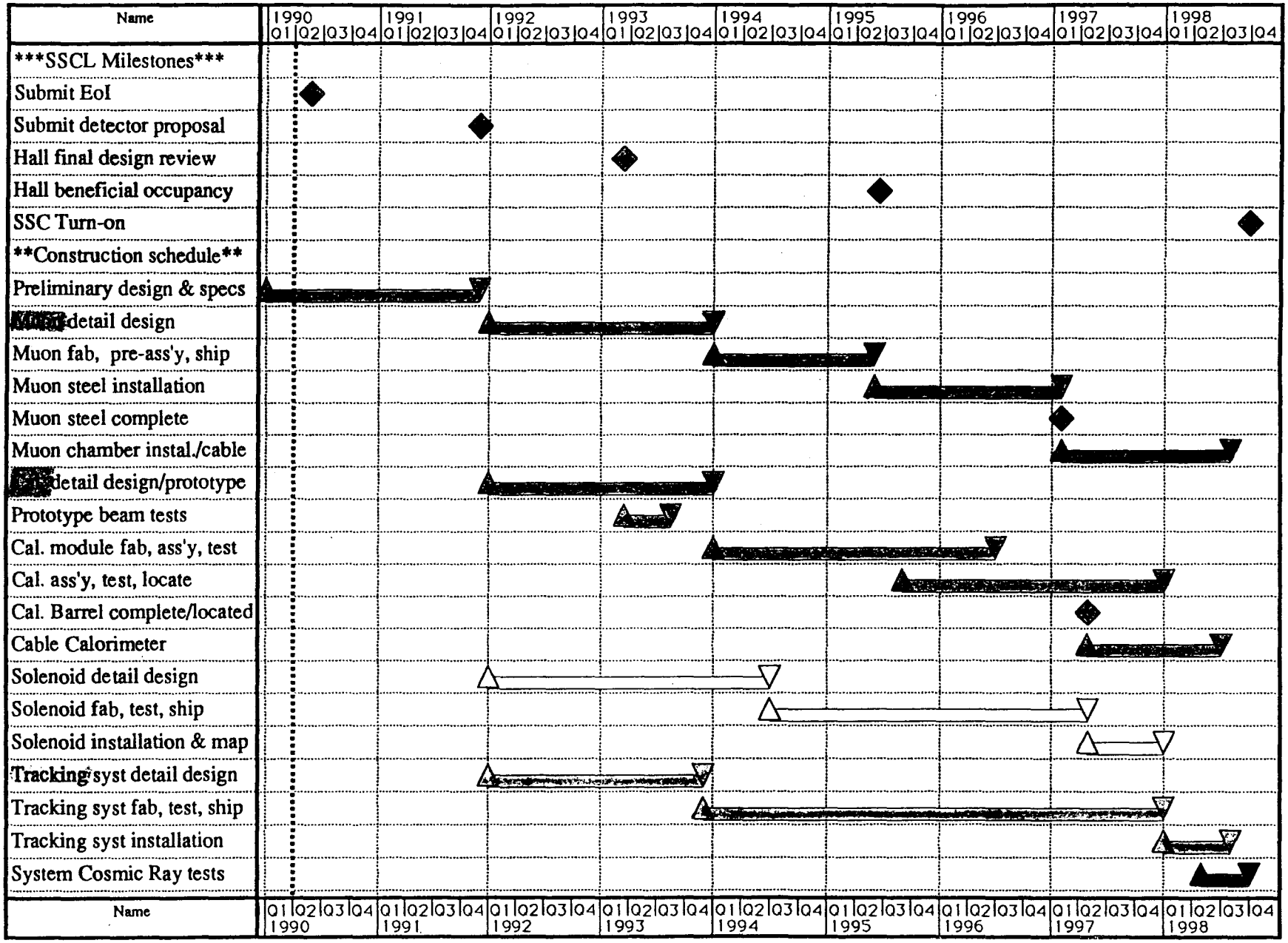
Name
1990 Q1 Q2 Q3 Q4
1991 Q1 Q2 Q3 Q4
1992 Q1 Q2 Q3 Q4
1993 Q1 Q2 Q3 Q4
1994 Q1 Q2 Q3 Q4
1995 Q1 Q2 Q3 Q4
1996 Q1 Q2 Q3 Q4
1997 Q1 Q2 Q3 Q4
1998 Q1 Q2 Q3 Q4
SSCL Milestones
Submit EoI
Submit detector proposal
Hall final design review
Hall beneficial occupancy
SSC Turn-on
Construction schedule
Preliminary design & specs
detail design
Muon fab, pre-ass'y, ship
Muon steel installation
Muon steel complete
Muon chamber instal./cable
detail design/prototype
Prototype beam tests
Cal. module fab, ass'y, test
Cal. ass'y, test, locate
Cal. Barrel complete/located
Cable Calorimeter
Solenoid detail design
Solenoid fab, test, ship
Solenoid installation & map
Tracking syst detail design
Tracking syst fab, test, ship
Tracking syst installation
System Cosmic Ray tests
Name
Q1 Q2 Q3 Q4 1990
Q1 Q2 Q3 Q4 1991
Q1 Q2 Q3 Q4 1992
Q1 Q2 Q3 Q4 1993
Q1 Q2 Q3 Q4 1994
Q1 Q2 Q3 Q4 1995
Q1 Q2 Q3 Q4 1996
Q1 Q2 Q3 Q4 1997
Q1 Q2 Q3 Q4 1998

Figure 11.

May 31, 1990

A conceptual design study of a general purpose solenoidal detector for the SSC

T.Doi[1], M.Fujita[1], H.Kakui[1], T.kondo[2], K.Ogawa[2], T.Ohba[1], I.Ohno[1], Y.Watanabe[3], and A.Yamamoto[2]

1)Ishikawajima-Harima Heavy Industries Co., Ltd., Tokyo, Japan
2)KEK,Laboratory for High Energy Physics, Tsukuba, Ibaraki, Japan
3)Tokyo Institute of Technology, Tokyo, Japan

ABSTRACT

This is a report on the study made on a conceptual design of a general purpose solenoidal detector for the SSC. The main issue was how to build a detector weighing about 30k tons, maximizing hermeticity while satisfying good support, easy access, enough space for cables and pipes etc. We also investigated a possibility of toroidally magnetizing iron.

1. Introduction

It is not at all trivial to construct a general purpose detector for the SSC. The size is inevitably big, weighing about 30k tons, and the requirements are stringent and are often contradicting. For example, the requirement of hermeticity is hard to satisfy, while allowing good support, easy access, space for cables and pipes etc. We felt it important to start a study of a conceptual design of a detector as a whole for the SSC at an early stage, even though none of the detector components have been decided yet. We focus our attention to common issues that arise in constructing such a detector, disregarding details of each detector component. In this study, we have simply picked reasonable values for the size and the weight of each detector component.

Main issues of the study are as follows.

1) Maximize hermeticity, while allowing sufficient mechanical strength, good support, space for cables and pipes, an easy access etc.
2) Optimize structural elements, taking into account machining, transportation, assembly etc.
3) Find implications to the design of an experimental hall.
4) Find a realistic design of iron toroids.

An interim report was given in January this year[1], and the present report is the final one, even though we have certainly not fully answered to the issues listed above.

2. Overall design considerations

We intended this study to be as general as possible to be applicable for most choices of detector components. But we had to specify a starting geometry, and we have adopted the "ACS design", where ACS stands for air core solenoid, meaning that the superconducting solenoidal coil is placed at some distance from end return yoke. This choice creates some non-uniform field in the tracking volume and leakage field outside of the solenoid, but the main advantage is that a calorimeter can be built outside of the solenoid, allowing smooth transition between barrel and endcap calorimeter, and thus allowing more hermetic calorimetry. It has been shown to be possible to construct such a magnet with 2T field with sufficiently thin material[2].

The overall design of the detector is shown in Fig.1 and Fig.2. For each detector component, we have specified its approximate size and weight as summarized in Table 1, and we have allowed reasonable space for cables and pipes. The main structure is three-layer octagonally shaped iron cylinder, whose size is about 18m in diameter and 24m in length, weighing about 22k tons. This serves both as return yoke of the inside solenoid and muon filter. This is to be directly constructed in an experimental hall, and never moves. For a purpose of study, we have investigated the possibility of magnetizing the iron. This would give an additional momentum measurement for muons and may help triggering on muons. Whether we choose to do so or not depends on the physics requirements and cost optimization. Each layer is toroidally magnetized, excited by coils wound in the axial direction at each octant. Muon chambers are placed in front, in between and at the back of the iron layers. How to install and assure the alignment of chambers is a nontrivial question requiring much harder study and has not been done here. In this design, every other detector component is installed from one of the open ends, slided along the axis as shown in Fig.3.

3. Assembly of the barrel iron structure

The choice of the octagonal shape seems to be optimum, when requirements of hermeticity, ease of assembly and the structural solidness are considered. One layer of iron is made in turn of 3 layers of iron plates. A convenient unit to transport and to handle is a hot-rolled iron plate of about 8m in length, 3m in width and 0.3m in thickness, weighing about 50 tons. All four sides of a plate are machined. One of the sides is cut and machined as shown in Fig.4, in order to support the weight of the plate directly above and to position it precisely. These plates are either bolted or welded each other in place. It is desirable to minimize the amount of welding to be done in the experimental hall, in order both to keep the hall clean and to shorten the construction period. But then, the cost of machining will go up. Thus, we must balance the two carefully.

The assembly proceeds as shown in Fig. 5. The lower half of the structure is assembled from outer to inner layers. The upper

half is assembled using a jig shown in Fig. 6. Three layers of octagonal cylinders are separated and held in place by 15cm-thick spacers placed every 3m or so along the axis and near each apex of the octagon as shown in Fig. 7. These spacers are placed carefully such that there are no completely dead regions when looked from the interaction point to guarantee good hermeticity for the muon detection. This choice of spacers creates a problem of how to install muon chambers between two spacers. We may prefer other design of spacers, or may simply give up inserting muon chambers in between iron plates.

It is probably a good idea to use the walls of the experimental hall for the support of the whole structure. This would ease the design of the support to hold the whole detector depicted in Fig. 1. Thus the experimental hall should be made just wide enough to contain the detector. We discuss more about requirements on the experimental hall in section 6.

4. Magnetizing the barrel and endcap iron

Three layers of barrel cylinders are toroidally magnetized by winding coils as shown in Fig. 8. A coil is a hollow conductor made of copper with the cross section of 30mm by 70mm. The hole at the center is 20mm in diameter and is for water cooling. A convenient piece that allows transportation is about 12m in length and is made in extrusion technique. An inevitable consequence is that coil joints come at the half way into the barrel cylinder. Care must be taken in joining coils to keep the water path open and not to cause water leak. This can be done with a well established technique of inserting a sleeve and welding outside the joint. A joint at an end may be done as shown in Fig. 8. Coils are supported loosely so that they can slide along the axis of the cylinder, when they expand because of the heat dissipation. The height required for the coil placement is 37mm.

An endcap toroid consists of 4 layers of iron plates as shown in Fig.9. Again muon chambers are placed in front, in between and at the back of these layers. A convenient unit to handle is a trapezoidal piece made of three layers of hot-rolled iron plates, weighing about 60 tons. All of the sides are precisely machined for the purpose of accurate assembly. Four of these units are assembled first, each separated by spacers, making an octant. Then a coil is wound around these units. This choice of design, instead of e.g. assembling disk shaped iron plates, is made to obtain more uniform field by inserting wedge shaped non-magnetic material as discussed in section 8.

5. Installation and access of detector components

Once the three-layer octagonal cylinders are constructed, the other detector components are installed from one of the open ends as shown in Fig.3. As the construction of the calorimeter will take equally long time, they are assembled separately in an assembly area, which should be close to or within the

experimental hall. The completed calorimeter is moved into the beam line on a cart, then slided into the detector as shown in Fig.3.

A sliding mechanism is provided by a plastic plate called "oilless fiber freon". It has a good mechanical strength as well as a low friction coefficient as summarized in Table 2. Table 3 gives a comparison of this and an ordinary tirtank method. A pair of these plates are used as shown in Fig.10. It is clear that this sliding mechanism is well suited for this application, requiring less space for the moving mechanism. When an access-need arises to an inner detector component, the outer components are slided out and put aside if necessary.

6. Implications to an experimental hall

We assume that an experimental hall is about 100m below ground. A possible design of an experimental hall is shown in Fig.11. As the cost to dig an experimental hall increases linearly with the area to be excavated[2], the area needed for assembly, maintenance and drop hatch is all to be fit in along the beam line. We discarded the original idea of having an assembly area perpendicular to the beam line for the sake of cost saving. A drop hatch is about 10m by 10m. The space needed for the assembly area will depend on the choice of calorimeter technique and has to be optimized taking into the excavation cost as well. The design of the support that holds the whole structure would simplify greatly, if the walls of the hall can be used for the support as well. For the crane capability, we need at least two cranes of about 100 ton each for a parallel effort of assembly work. Utility area depends on the type of the detector technology chosen, but a good size area near the detector is surely needed.

7. Structural analysis

A structural analysis of the iron structure was done with a program MSC/NASTRAN, a standard program for a finite element method. In modeling three-layer iron plates of an octagonally shaped cylinder, each layer of iron plates are allowed to slide. This approximation certainly gives an overestimation for the deformation. Thus the integrity of the structure is proven if the calculated stresses are within the allowed value. The calculated deformation due to the self-weight of the barrel cylinder is shown in Fig. 12. The maximum is at the top, amounting to 0.8mm. It is essential that the structure is supported also from both sides. The amount of deformation due to the weight of the inside detector is smaller as shown in Fig. 13. Probably, we do not have to worry about earthquakes in Texas, but we also calculated the effect by applying a side way static force of 0.2g. The result due to the self-weight is shown in Fig.14, where the maximum deformation is seen to occur also at the top. Figure 15 shows the effect due to the weight of the inner detector. Table 4 shows the calculated stresses at various points. They are well within the allowed stress for iron.

8. Calculation of the toroidal field

Magnetic field within iron is calculated using mostly a program called JMAG2D, which allows field calculation of two dimensional configuration. Some checks were made with three dimensional calculation using JMAG3D, whose results agreed well with that of two dimensions. The calculation utilizes the symmetry of the system. For the barrel part, a 1/16 section is enough for the calculation. Figure 16 explains the mesh size for the calculation and the notation of the coil placement. For iron material, special grade suited for magnetic application is selected, and compared with normal grade, SS41. The B-H curves for the two materials are shown in Fig. 17. From this figure alone, it is seen to be increasingly difficult to obtain higher field. For example, it requires three to five more currents (or power) to obtain 2T field instead of 1.8T field.

A result of calculation for the barrel toroid is shown in Table 5. The coil placement at the center of each octant seems to be good enough for the uniformity of the field. Figure 18 shows the field obtained vs. the number of amp-turns necessary for the third layer, as a typical example. As the power required to excite the coil increases rapidly beyond the field of about 1.8T, it is nontrivial to obtain higher field. There, the difference between special and normal grade of iron seems to diminish. The return flux of 2T solenoid field gives little influence to the toroidal field.

For the endcap toroid, it is well known that the field is the highest at the smallest radius, decreasing rapidly toward larger radius. Because of saturation, the deviation from the well known 1/r dependence is rather large, but the field at the outermost radius is still rather low as seen in the first row of Table 6. One way to increase the uniformity is shown in Fig.19, where a wedge shaped non-magnetic material (SUS304) is inserted to push out the field. Note that the non-magnetic material acts as a vacuum for the field calculation, but we need the same thickness of absorber material for the purpose of muon detection. The toroidal field is continuous enough to create little azimuthal dependence of the field. Results are summarized in Table 6. A uniformity within a few percent can be achieved. Figure 20 shows the field vs. amp-turns for two typical thicknesses of nonmagnetic material.

Table 7 summarizes the calculation of the heat dissipation of the coil. By using a copper coil with cross section of 30mm by 70mm, the total power consumption is limited to about 3MW for 1.8T field. As expected, most of the power is consumed in the barrel toroid, we have to optimize the requirements of physics and cost limitation to decide whether or not to magnetize the barrel part. Cooling is provided by flowing water through 20mm diameter hole bored at the center of a coil. The allowed pressure drop and the temperature rise are 5atm and 10°C, respectively. Table 8 summarizes the result of calculation for the cooling. It is well within the reasonable range.

9. Summary

This is a report on the study we have made on a conceptual design of a general purpose detector for the SSC.

The main part, the octagonal 3-layer iron cylinder has to be built directly at an experimental hall. A part of support should be provided from the walls of the experimental hall. Every other detector components are slided from one of the open ends. A good way to provide the sliding mechanism is to use a pair of plastic plates "oilless fiber freon".

Barrel and end cap iron can be magnetized up to 1.8T field, where the power consumption is 3MW. The field in the endcap iron can be made fairly uniform by inserting non-magnetic material. Obtaining higher field is increasingly difficult.

Implications to the design of an experimental hall are derived, such as the size of the hall, the assembly hall, the crane requirements etc.

ACKNOWLEDGEMENTS

The authors would like to express their sincere gratitude to Prof. S. Mori, who encouraged them to pursue this work. They are indebted to many people who injected good ideas here and there in this work.

REFERENCES

Ref. 1 "Status report on a conceptual design study of a hermetic detector for the ssc", T. Doi et al, in "Design Studies and Detector R&D for Super High Energy Hadron Colliders in Japan", March 1990, edited by T.Ohsugi and T.Kondo.

Ref. 2 "Short solenoid design", talk by A.Yamamoto, this workshop proceedings.

Ref. 3 "A solenoid detector design", talk by R.Kadel, this workshop proceedings.

FIGURE CAPTIONS

Fig. 1. Overall design of the detector ;bird's eye view.

Fig. 2 Cross sectional views of the detector.

Fig. 3. Installation of detector components.

Fig. 4. Assembly of an octagonal cylinder and a unit iron piece.

Fig. 5. Assembly of the barrel cylinder.

Fig. 6. A jig to assemble the upper part of the cylinder.

Fig. 7. Placement of spacers.

Fig. 8. Design and placement of coils for barrel and endcap toroids

Fig. 9. Assembly of an endcap toroid.

Fig.10. Sliding mechanism using a pair of plastic "oilless fiber freon".

Fig.11. Layout of an experimental hall, areas for assembly, maintenance and utility and a drop hatch.

Fig.12 Deformation of barrel cylinder due to the self-weight.

Fig.13 The same due to that of the inner detector.

Fig.14 The same due to a side way force of 0.2g (self-weight only)

Fig.15 The same as above due to the weight of the inner detector.

Fig.16. Mesh division for the calculation of the barrel toroidal field and the positioning of coils.

Fig.17 B-H curves of normal and special grade steel plates.

Fig.18. Magnetic field calculated vs. amp-turns for barrel toroid (for the third layer).

Fig.19 Mesh division for the calculation of the endcap toroidal field.
A method to increase the field uniformity by inserting a wedge-shaped non-magnetic material(SUS304).

Fig.20. Magnetic field calculated vs. amp-turns for endcap toroid with SUS304.

Table 1a Parameters of detector components (barrel part)

Element	material	shape	size(m) Rmin	Rmax	Zmax	weight (tons)	supported by
tracking	Al etc.	Cyl.	0.2	1.65	2.5	3	calorimeter
solenoid	Al etc.	Cyl.	1.7	1.95	3.8	15	calorimeter
calorimeter	Pb-LA?	Cyl.	2.0	4.50	3.8	2900	mu-filter
mu chamber	Al etc.	Oct.	4.5	5.0	11.85	45	" "
mu-filter	pure Fe	Oct.	5.0	5.85	"	6100	" "
mu chamber	Al etc.	Oct.	5.85	6.0	"	25	" "
mu-filter	pure Fe	Oct.	6.0	6.85	"	7200	" "
mu chamber	Al etc.	Oct.	6.85	7.0	"	25	" "
mu-filter	pure Fe	Oct.	7.0	7.85	"	8300	" "
mu-chamber	Al etc.	Oct.	7.85	8.35	"	120	" "

Table 1b Parameters of detector components (an endcap part)

Element	material	shape	size(m) Rmin	Rmax	Zmin	Zmax	weight (tons)	supported by
calorimeter	Pb-LA?	Cyl.	0.4	4.0	4.0	7.0	1300	mu-filter
mu-chamber	Al etc.	Oct.	0.7	4.3	7.0	7.5	40	"
toroid	pure Fe	Oct.	0.75	"	7.5	8.35	630	"
mu-chamber	Al etc.	Oct.	0.85	"	8.35	8.5	20	"
toroid	pure Fe	Oct.	"	"	8.5	9.35	630	"
mu-chamber	Al etc.	Oct.	0.95	"	9.35	9.5	20	"
toroid	pure Fe	Oct.	"	"	9.5	10.35	630	"
mu-chamber	Al etc.	Oct.	1.05	"	10.35	10.5	20	"
toroid	pure Fe	Oct.	"	"	10.5	11.35	630	"
mu-chamber	Al etc.	Oct.	"	"	11.35	11.85	40	"

Table 2 Physical properties of "oilless fiber freon"

strength	
tensile force	>1000 kgf/cm
compress force	>2000 "
impact (Idot method)	>18 cm/cm
hardness	>80HRM
Young's modulus	$>6 \cdot 10^{4}$ kgf/cm
Thermal properties	
expansion coefficient	$2 \sim 3 \cdot 10^{-5}$ /°C
conductivity	$4 \sim 7 \cdot 10^{-4}$ cal/sec/°C/cm
sliding coefficient of friction	
static	0.08～0.09
dynamic	0.03

Table 3 Comparison of two sliding mechanisms
tirtank vs. "oilless fiber freon"

item	tirtank	"oilless fiber freon"
coefficient of friction	excellent (0.04～0.02)	good (0.08～0.03)
space needed for installation		
along the axis	impossible	excellent
width	good(>300mm)	excellent(110mm)
fore-treatment	greasing	none
deterioration	rust	none
overall evaluation	poor (compact tirtank must be developed)	good (need more power to move but o.k.)

Table 4 Calculated stresses

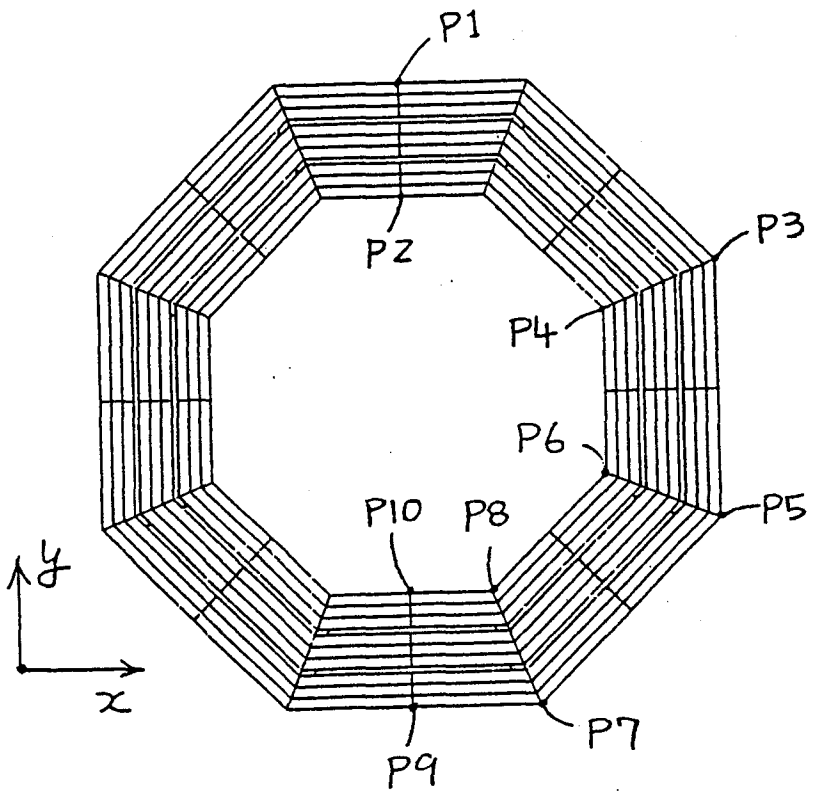

Points where stresses are evaluated

unit : kg/mm²

weight / point		SELF-WEIGHT	SELF-WEIGHT +0.2g VERTICAL	SELF-WEIGHT +0.2g HORIZ.
P 1	inner	0.21	0.23	0.21
	outer	-0.31	-0.33	-0.31
P 2	inner	0.43	0.48	0.45
	outer	-0.17	-0.18	-0.17
P 3	inner	-0.46	-0.52	-0.58
	outer	0.44	0.48	0.54
P 4	inner	-1.62	-1.78	-1.99
	outer	1.44	1.58	1.81
P 5	inner	-0.32	-0.34	-0.39
	outer	0.22	0.24	0.27
P 6	inner	0.78	0.87	1.91
	outer	-0.94	-1.03	-2.03
P 7	inner	-0.33	-0.37	0.05
	outer	0.17	0.19	-0.05
P 8	inner	1.83	2.00	2.19
	outer	-2.11	-2.32	-2.45
P 9	inner	-0.52	-0.57	-0.51
	outer	0.38	0.41	0.37
P 10	inner	-0.56	-0.62	-0.55
	outer	0.28	0.30	0.29

allowed stress
(special grade steel) = 6.6kg/mm²

Table 5 Calculated field (barrel)

No.	coil pos.	iron type	1st layer 14000AT			2nd layer 21000AT			3rd layer 28000AT			
			$Bc^{(172)}$	$Bo^{(252)}$	$Be^{(318)}$	$Bc^{(178)}$	$Bo^{(258)}$	$Be^{(324)}$	$Bc^{(184)}$	$Bo^{(264)}$	$Be^{(330)}$	
1	A	1	1.800	(+0.17) 1.803	(-6.67) 1.680	1.837	(-1.09) 1.817	(-7.73) 1.695	1.898	(-4.43) 1.814	(-10.96) 1.690	J1415
2	F	1	1.800	(+0.44) 1.808	(-7.28) 1.669	1.819	(+0.44) 1.827	(-6.76) 1.696	1.822	(+1.59) 1.851	(-6.70) 1.700	J5448
3	J	1	1.799	(+0.11) 1.801	(-7.17) 1.670	1.813	(+0.33) 1.819	(-5.79) 1.708	1.813	(+0.55) 1.823	(-3.36) 1.752	J6840
4	A	2	1.729	(+0.17) 1.732	(-11.74) 1.526	1.772	(-1.19) 1.751	(-11.85) 1.562	1.834	(-4.69) 1.748	(-15.54) 1.549	J1678

note 1; iron grade 1 = special.
2 = normal(SS41)

note 2; ( ) indicates the uniformity of field in % $\frac{Be - Bc}{Bc} \times 100\%$

Table 6 Calculated field (endcap) (SUS inserted)

No.	coil pos.	SUS width (mm)	Lower part 15000AT			Middle ——			Upper part 15000AT			
			Bc (25)	Bo (30)	Be (34)	Bc (85)	Bo (90)	Be (94)	Bc (135)	Bo (140)	Be (144)	
1	A	0	2.159	(+0.32) 2.166	(+0.79) 2.176	1.985	(-3.27) 1.920	(-11.34) 1.760	1.950	(-5.38) 1.845	(-21.33) 1.534	J3887
2	A	50	0.595	(-5.21) 0.564	(-14.96) 0.506	1.109	(-0.09) 1.108	(-0.45) 1.104	1.337	(+16.08) 1.552	(+47.79) 1.976	J4037
3	A	20	1.279	(-2.35) 1.249	(-6.49) 1.196	1.469	(+1.16) 1.486	(+5.92) 1.556	1.520	(+11.45) 1.694	(+29.34) 1.966	J3864
4	A	10	1.840	(-0.71) 1.827	(-1.79) 1.807	1.779	(-0.89) 1.765	(-0.73) 1.766	1.778	(+0.62) 1.789	(+5.51) 1.876	J4422
5	A	10	1.798	(-0.72) 1.785	(-1.84) 1.765	1.718	(-0.81) 1.704	(-1.16) 1.698	1.717	(+0.35) 1.723	(+5.36) 1.809	J6417

note 1; No. 1 - 4; for special grade, No.5; normal grade (SS41).

note 2; ( ) indicates the uniformity of field in %

Table 7 Heat dissipation of coil

material ; C1020

No.	symbol	unit	endcap	barrel		
				1st layer	2nd layer	3rd layer
1	r	Ω・m	1.55×10^{-8}	1.55×10^{-8}	1.55×10^{-8}	1.55×10^{-8}
2	S	m^2	0.0053	0.0071	0.0089	0.0107
3	I	A	5000	5000	5000	5000
4	n	—	3	4	5	6
5	ρ	m^2	1.78×10^{-3}	1.78×10^{-3}	1.78×10^{-3}	1.78×10^{-3}
6	ℓ	m	300	850	850	850
7	L	m	900	3400	4250	5100
8	R	Ω	0.0078	0.0295	0.0369	0.0443
9	V	V	39.1	147.5	184.4	221.3
10	Q	W	19.5×10^{4}	73.8×10^{4}	92.2×10^{4}	110.7×10^{4}
	n I	A・T	15000	22000	27000	32000
	A	cm^2	17.8	17.8	17.8	17.8
	J	A／cm^2	281	281	281	281
	Q	M W	0.195	0.738	0.922	1.107
	m	ℓ ／S	4.7	17.8	22.2	26.7

Symbols
- r ; electric resistivity (Ω・m)
- S ; cross section of coil (m^2)
- I ; current (A)
- n ; no. of turns
- ρ ; cross sectional area/turn (m)
- l ; length of coil/turn (m)
- L ; total length of coil (m)
- R ; total resistance (Ω)
- V ; maximum voltage (V)
- Q ; total power (MW)
- J ; current density (A/m^2)
- m ; flow rate of water (l/s)

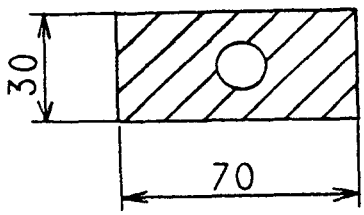

cross section of coil

Table 8 Cooling characteristics of coil

No.	symbol	unit	endcap	称		
				1st layer	2nd layer	3rd layer
1	P	M W	0.195	0.738	0.922	1.107
2	m	ℓ / S	4.7/8	17.8/32	22.2/32	26.7/32
3	D	m	0.02	0.02	0.02	0.02
4	L	m	115	110	135	160
5	U	m / S	1.870	1.771	2.208	2.656
6	R e	—	5.36×10^4	5.07×10^4	6.32×10^4	7.61×10^4
7	Δ P	MPa	0.208	0.181	0.326	0.534
8	No. lines		8	32	32	32

symbols

P ; heat dissipation(W)
m ; flow rate (l/m)
D ; tube dia.(m)
L ; total length(m)
U ; velocity(m/s)
Re ; Reynolds number
ΔP ; Press. loss (Pa)

---

the formula for the pressure loss is given by;

$$\Delta P = \frac{L}{D} \cdot \frac{\rho}{2} \cdot U^2 \times 0.3164 \times \frac{1}{Re^{0.25}}$$

$$Re = \frac{U \cdot D}{\nu}$$

assumptions

	inlet	outlet
pressure	7 atm.	2 atm.
temperature	30°C	40°C

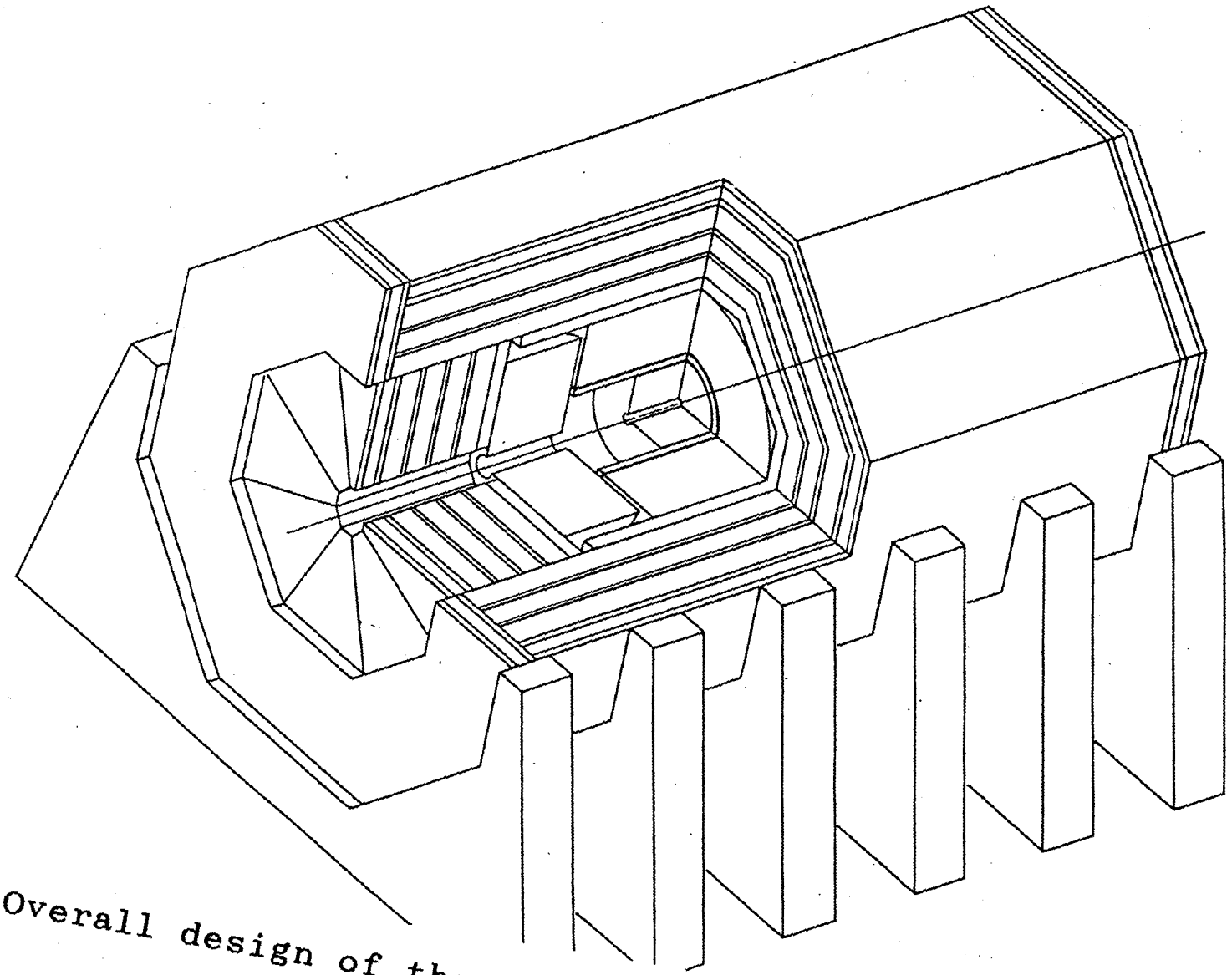

Fig. 1. Overall design of the detector ;bird's eye view.

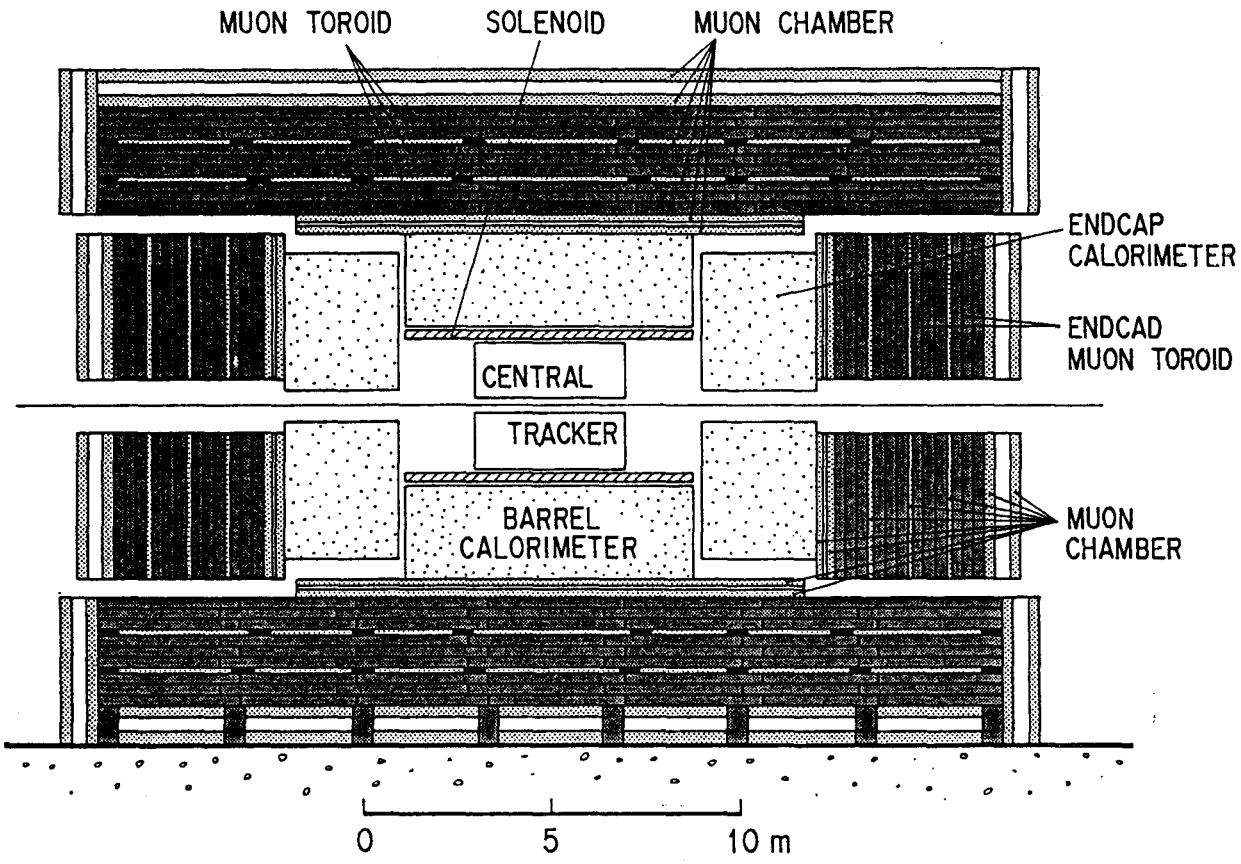

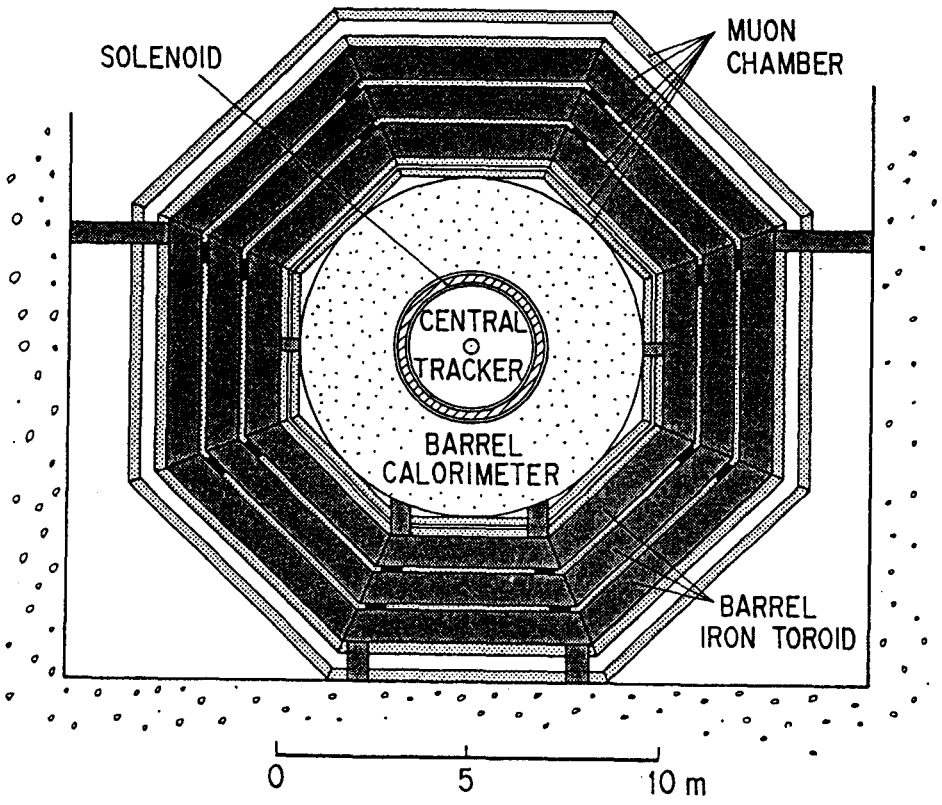

Fig. 2 Cross sectional views of the detector.

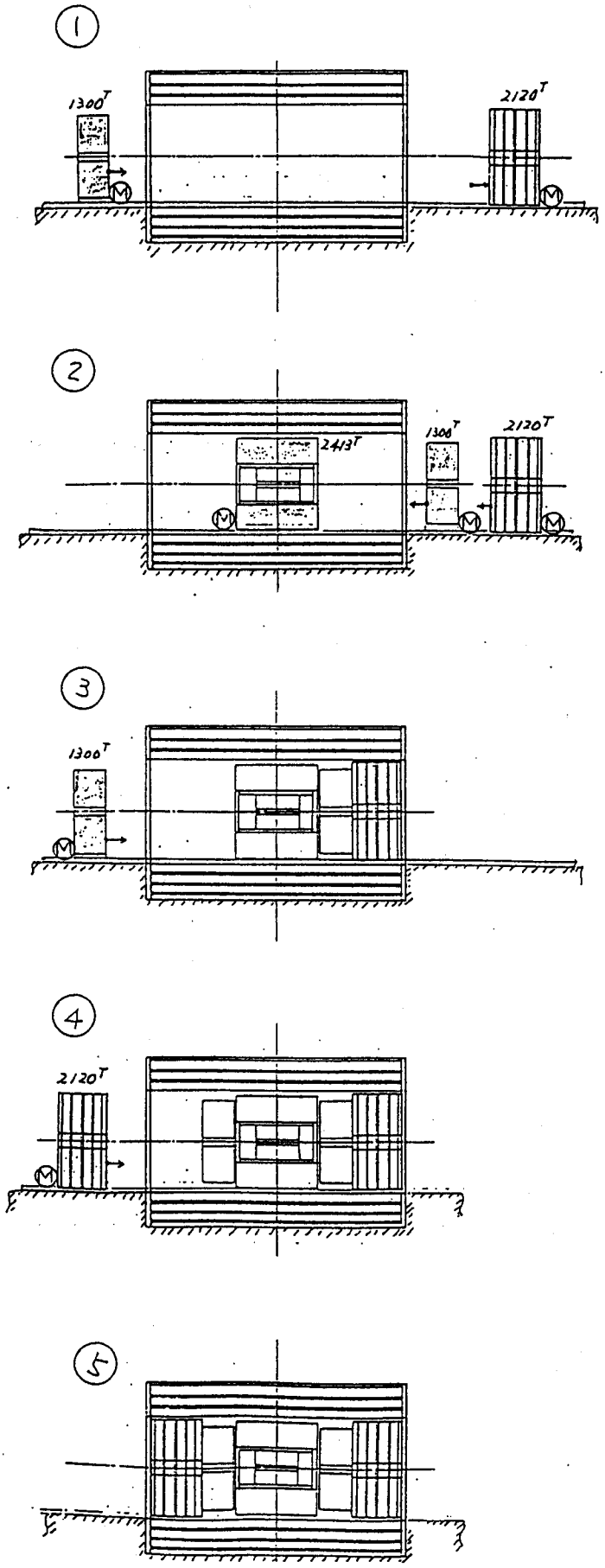

Fig. 3. Installation of detector components.

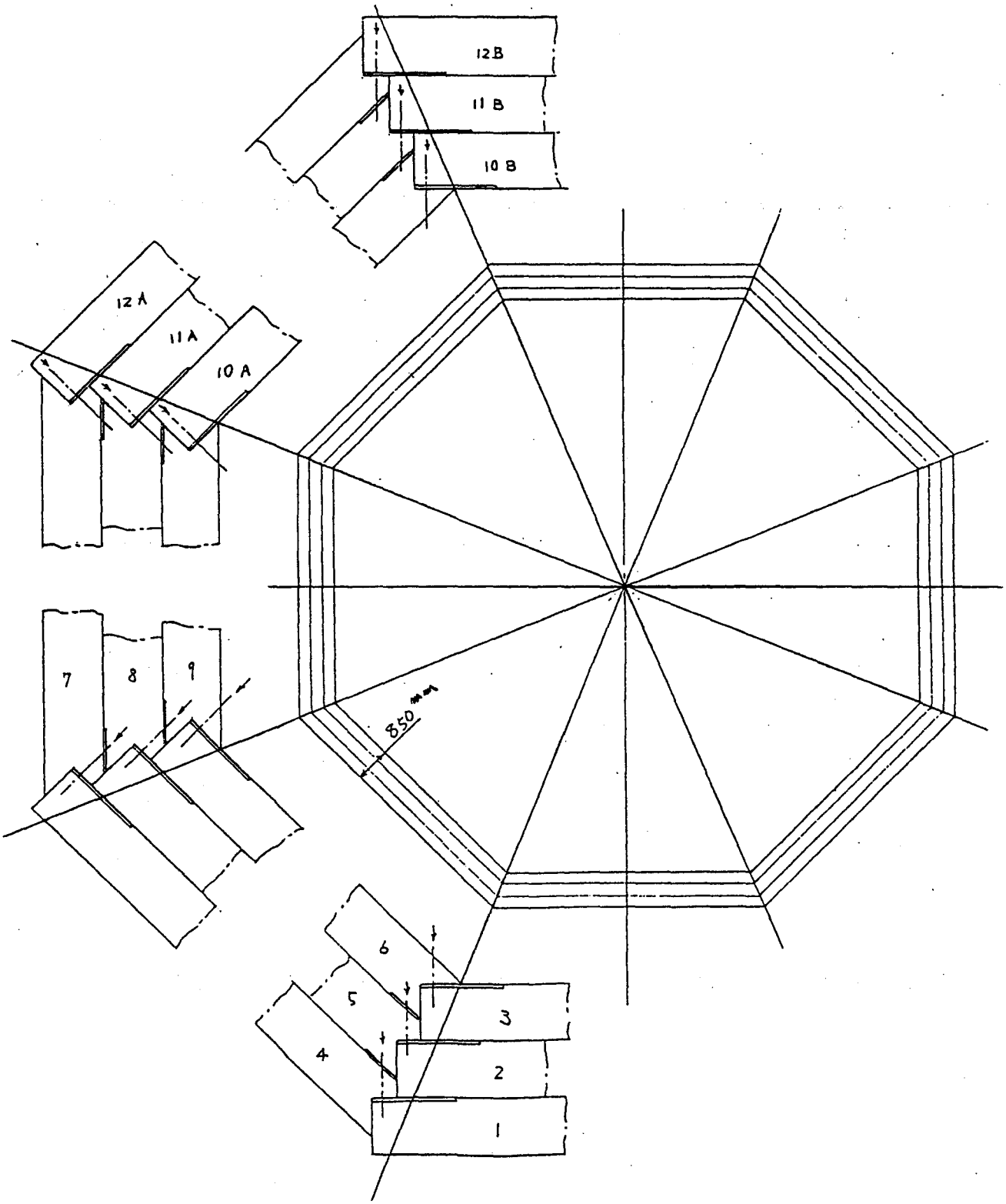

Fig. 4. Assembly of an octagonal cylinder and unit iron pieces.

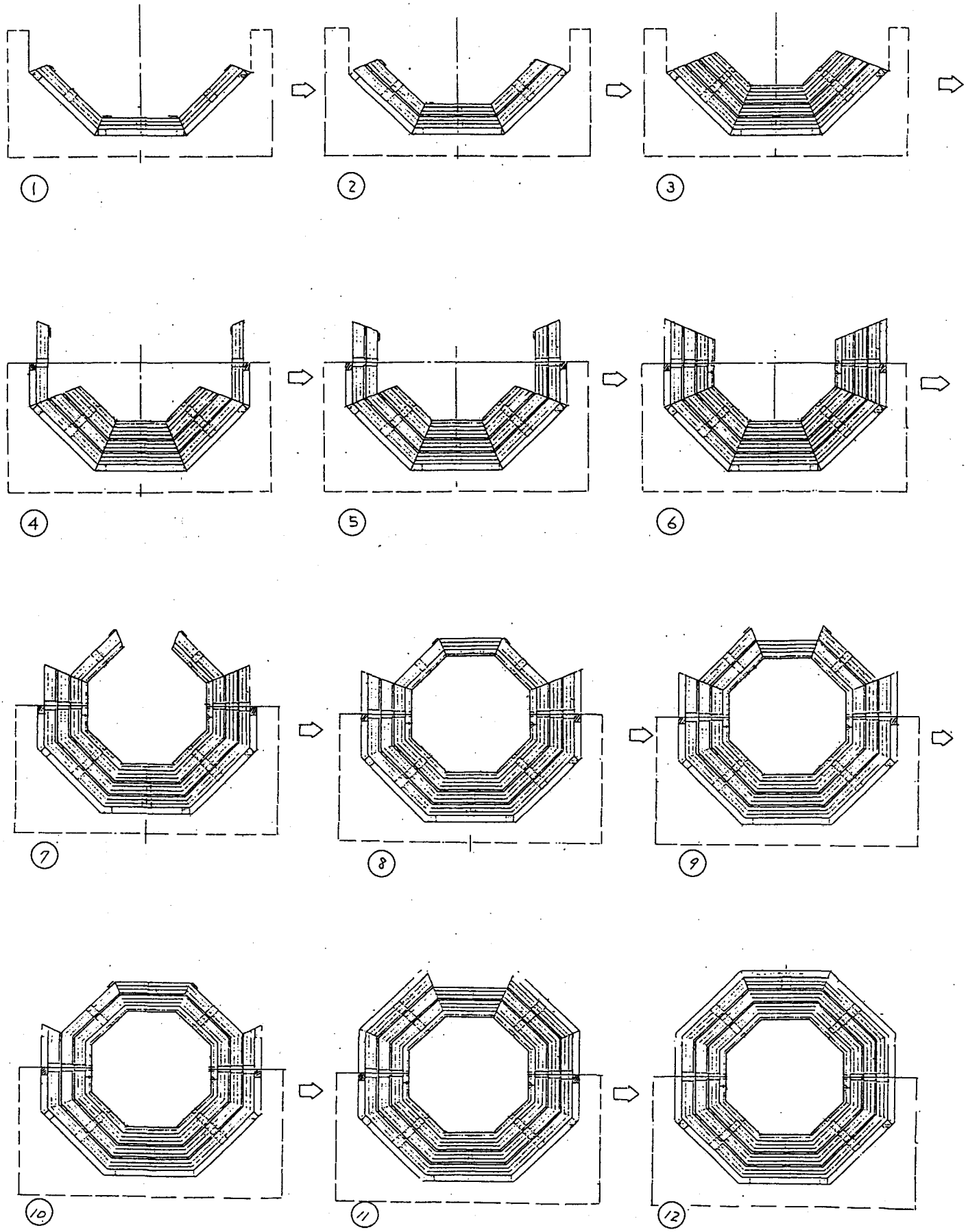

Fig. 5. Assembly of the barrel cylinder.

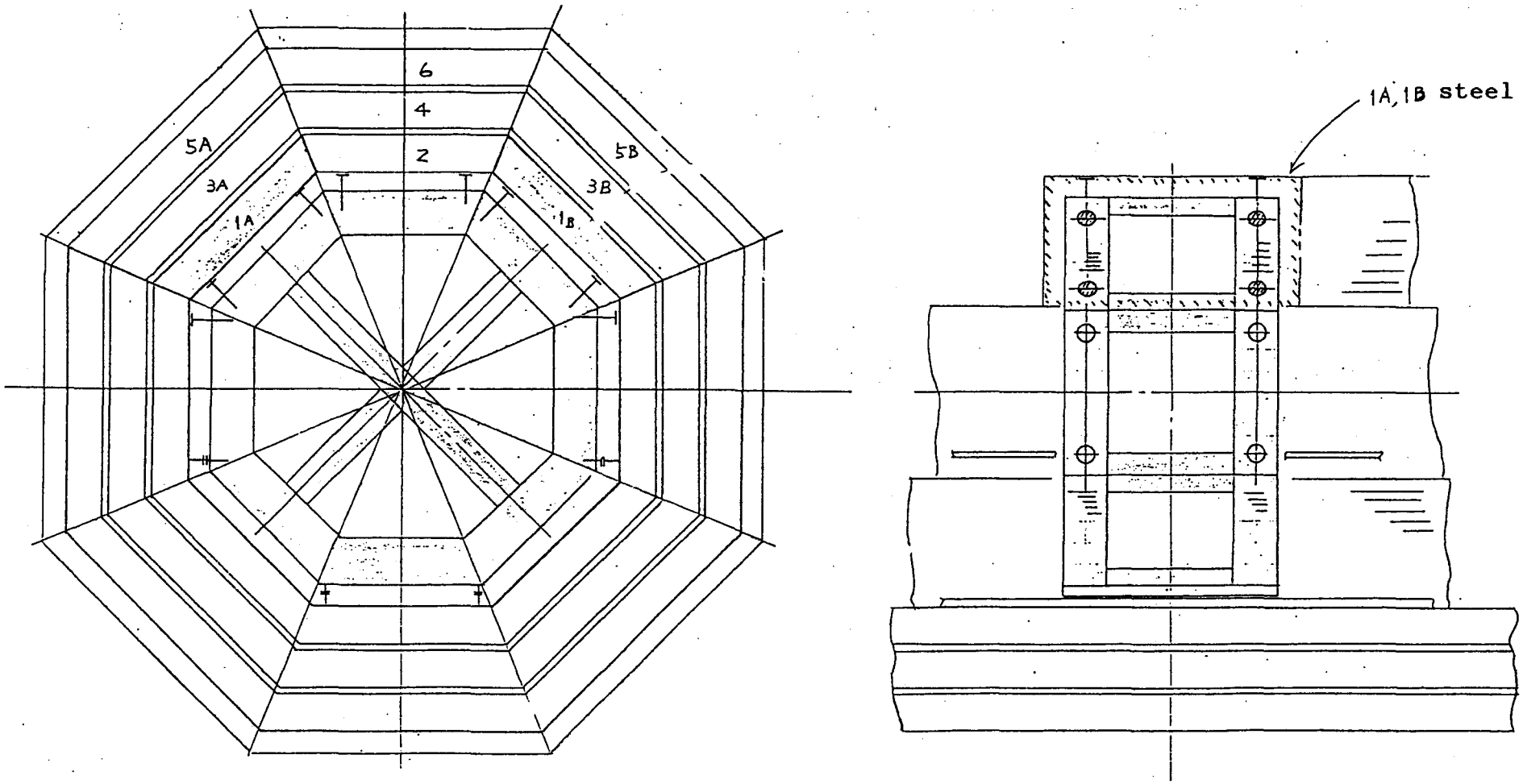

Fig. 6. A jig to assemble the upper part of the cylinder.

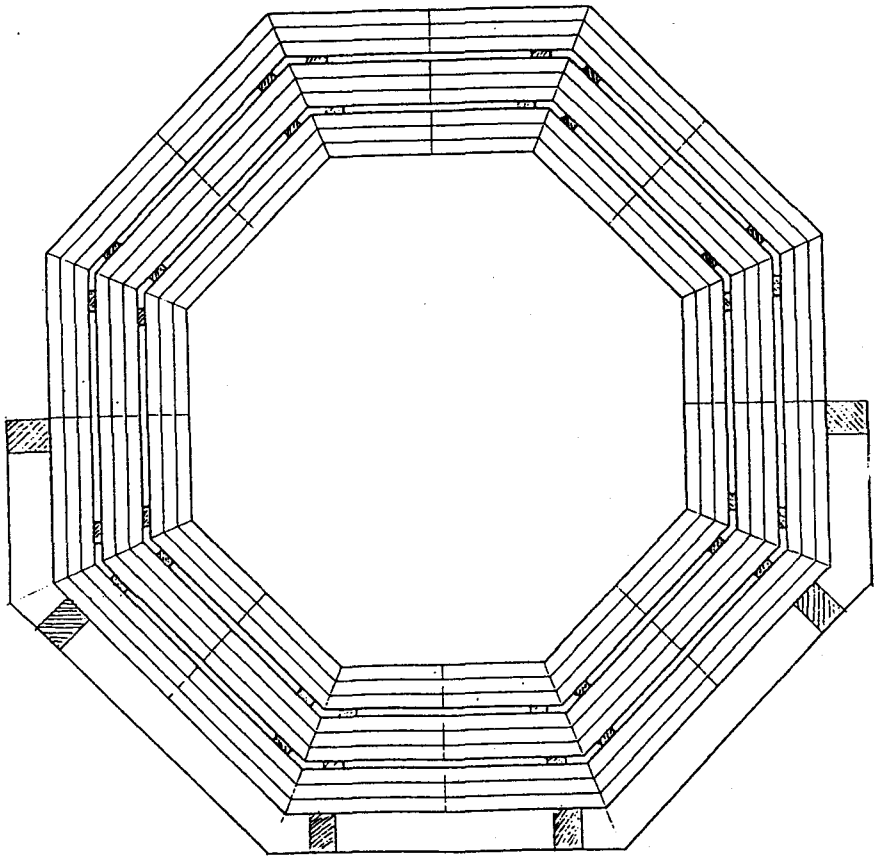

R-θ cross section

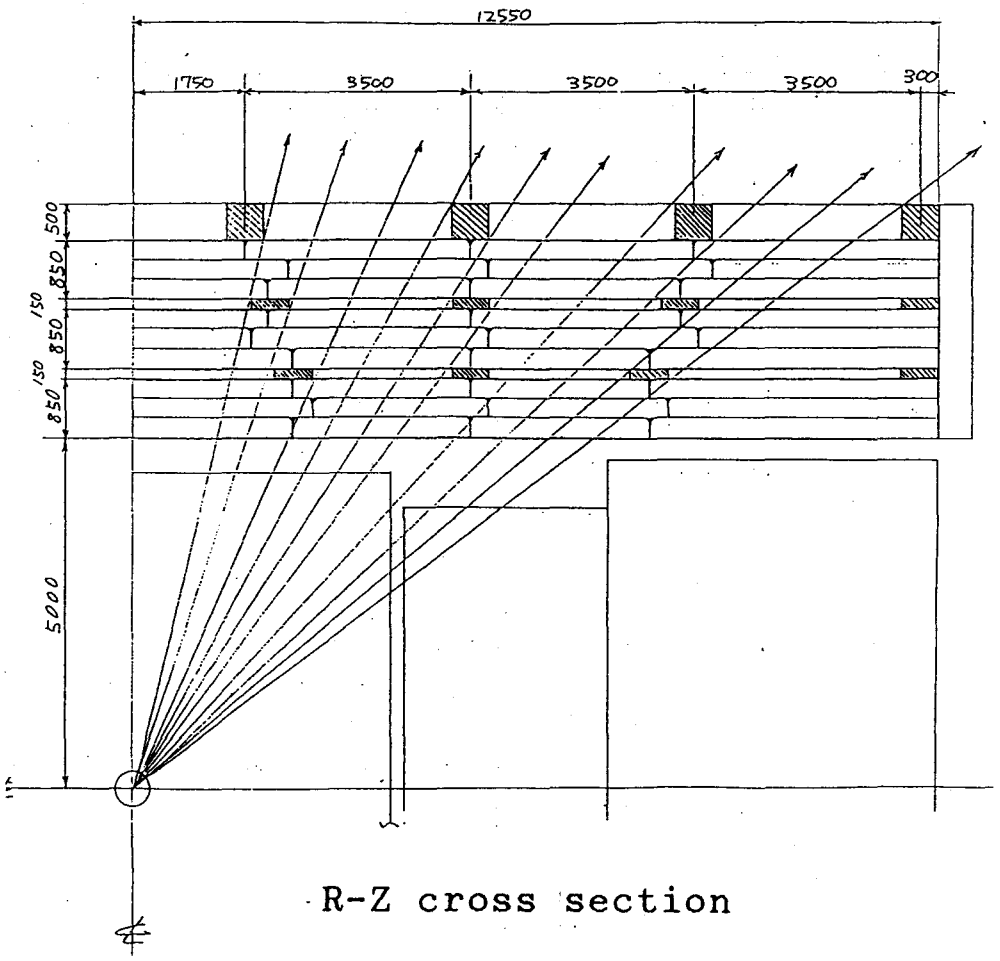

R-Z cross section

Fig. 7. Placement of spacers.

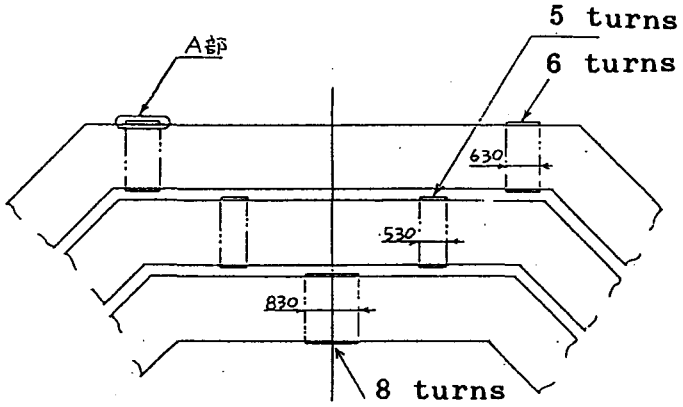

coil placement for barrel toroid

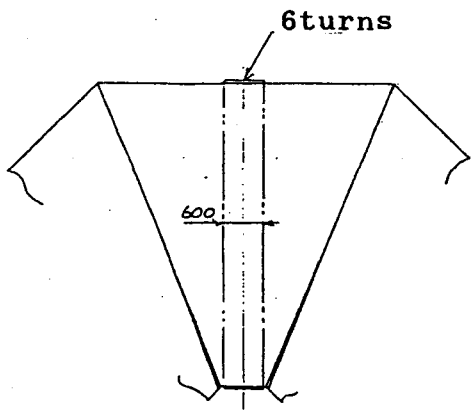

coil placement for endcap toroid

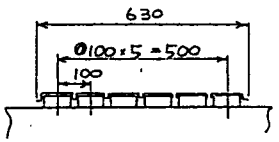

A detail

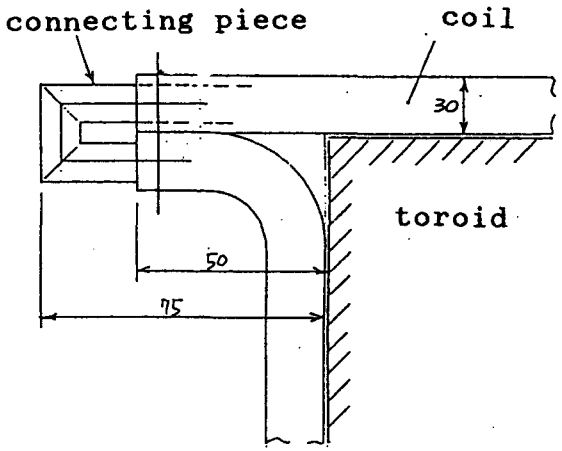

coil joint at an end

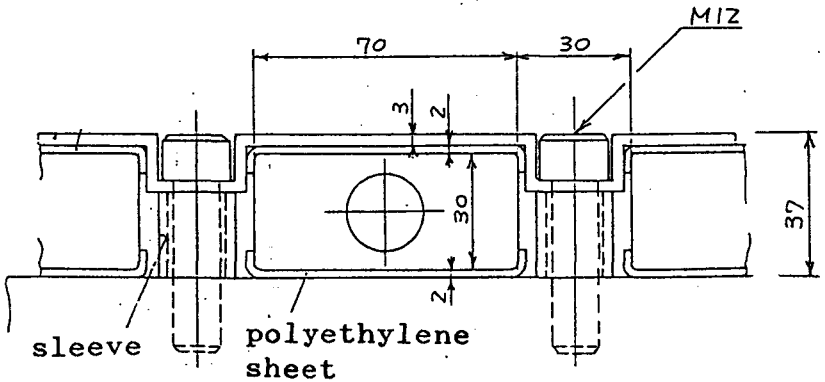

Fig. 8. Design and placement of coils for toroidal magnet.

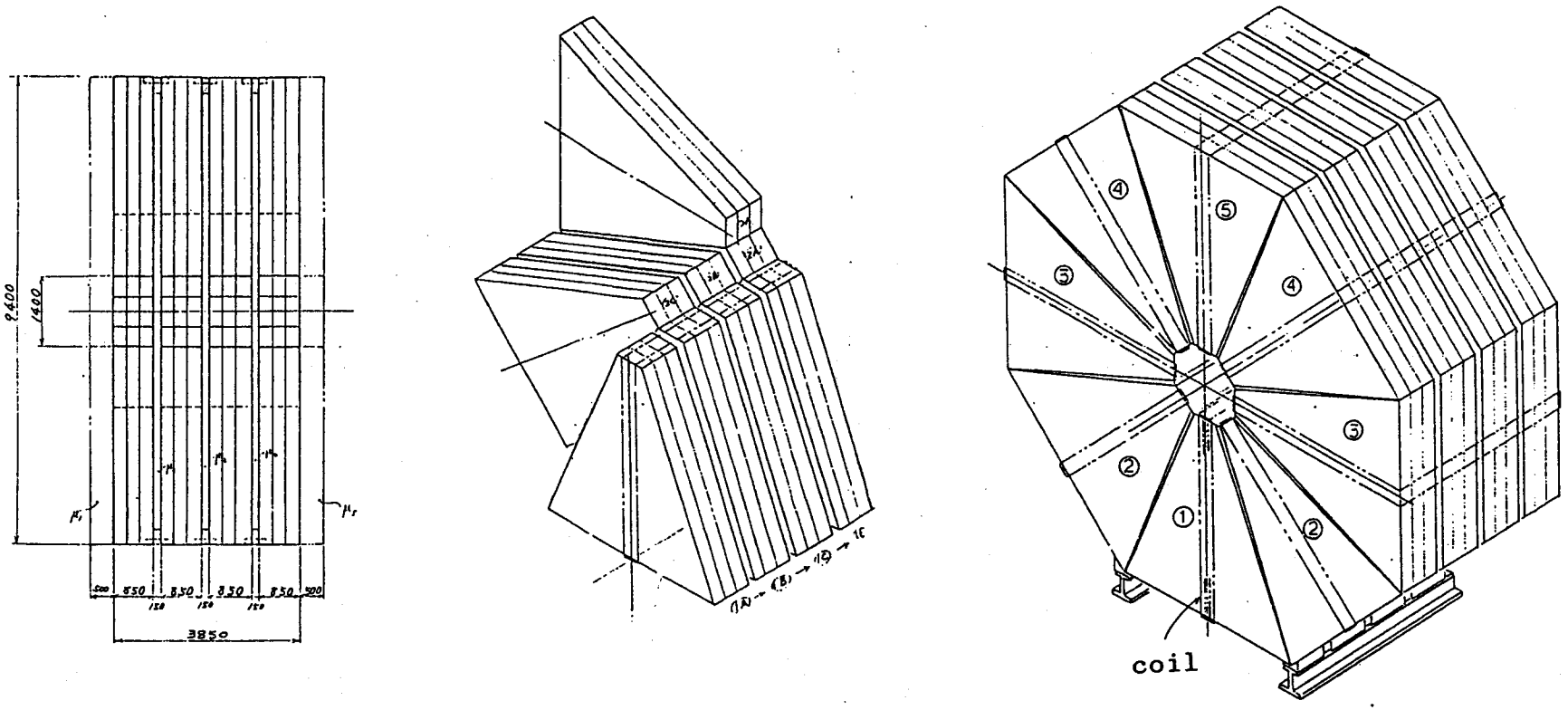

Fig. 9. Assembly of an endcap toroid.

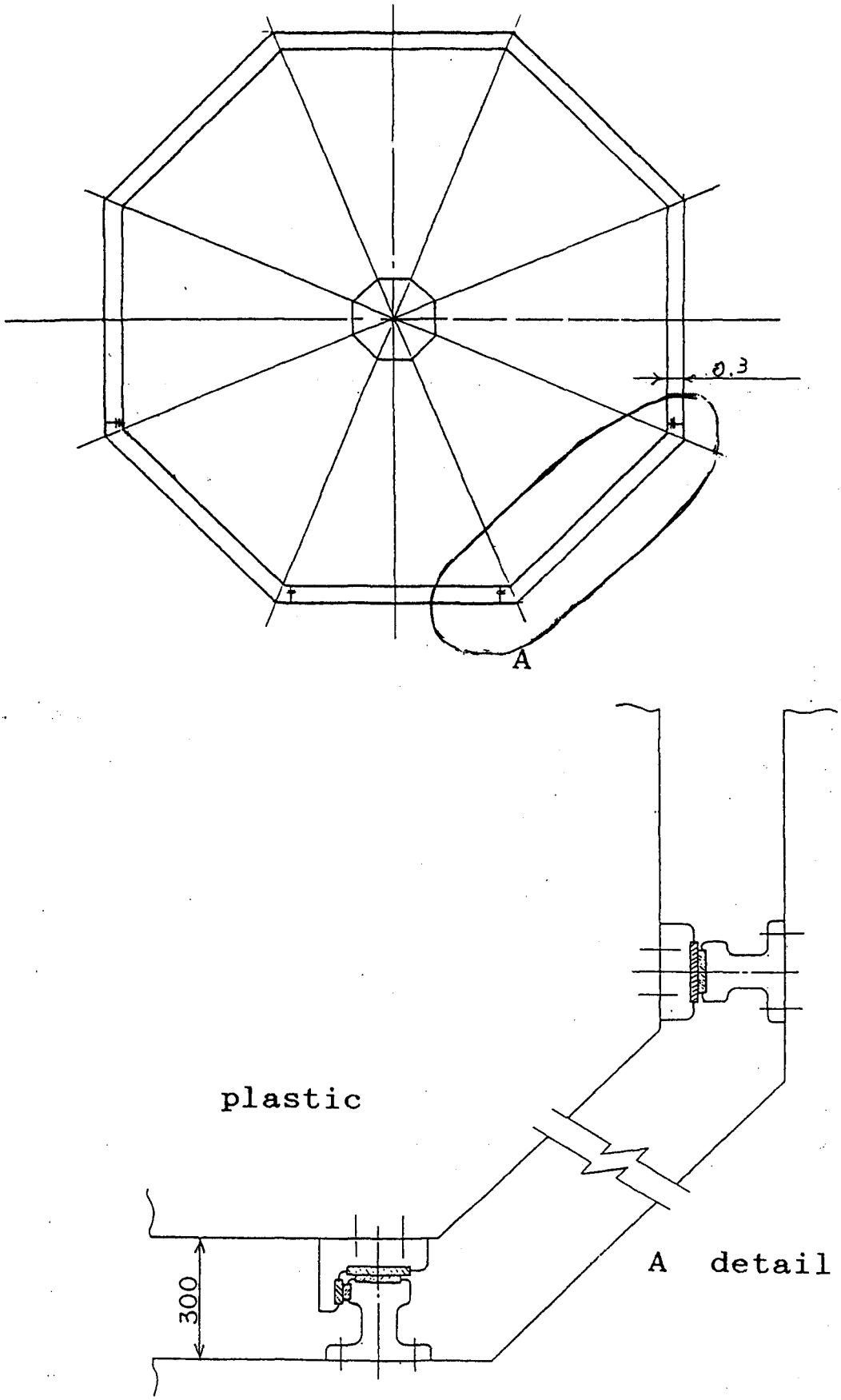

Fig.10. Sliding mechanism using a pair of plastic "oilless fiber freon".

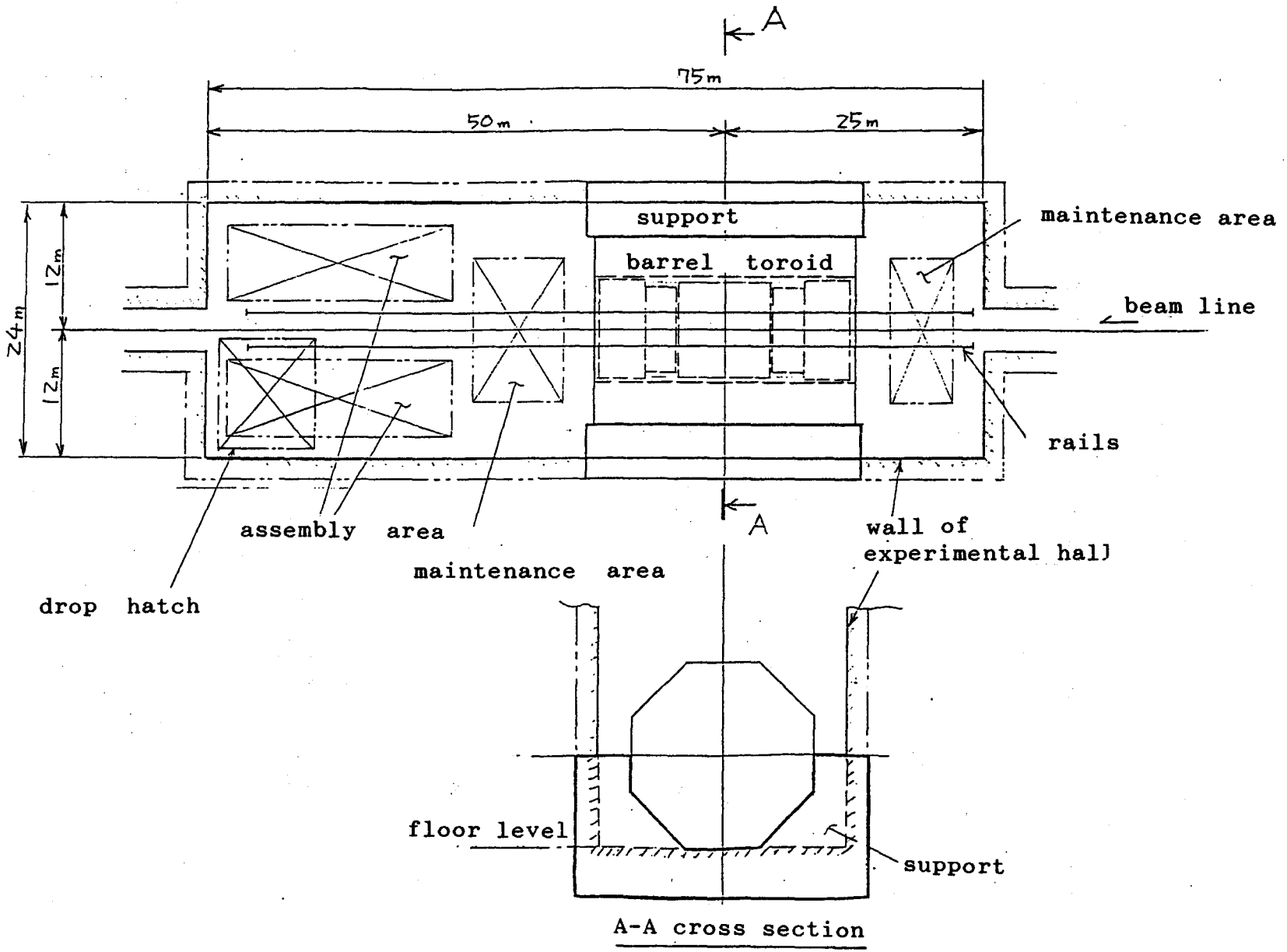

Fig.11. Layout of an experimental hall

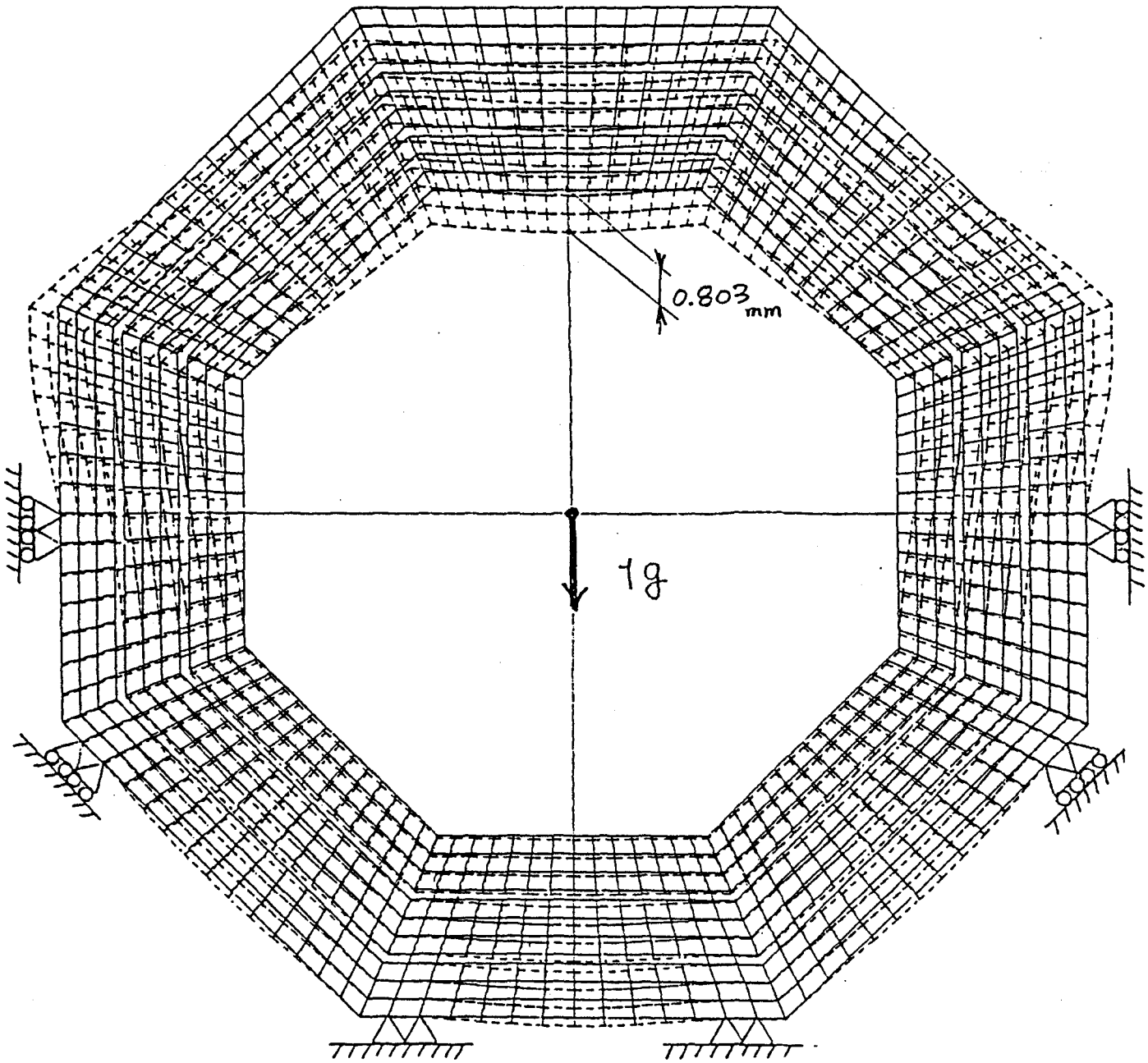

Fig.12 Deformation of barrel cylinder due to the self-weight.

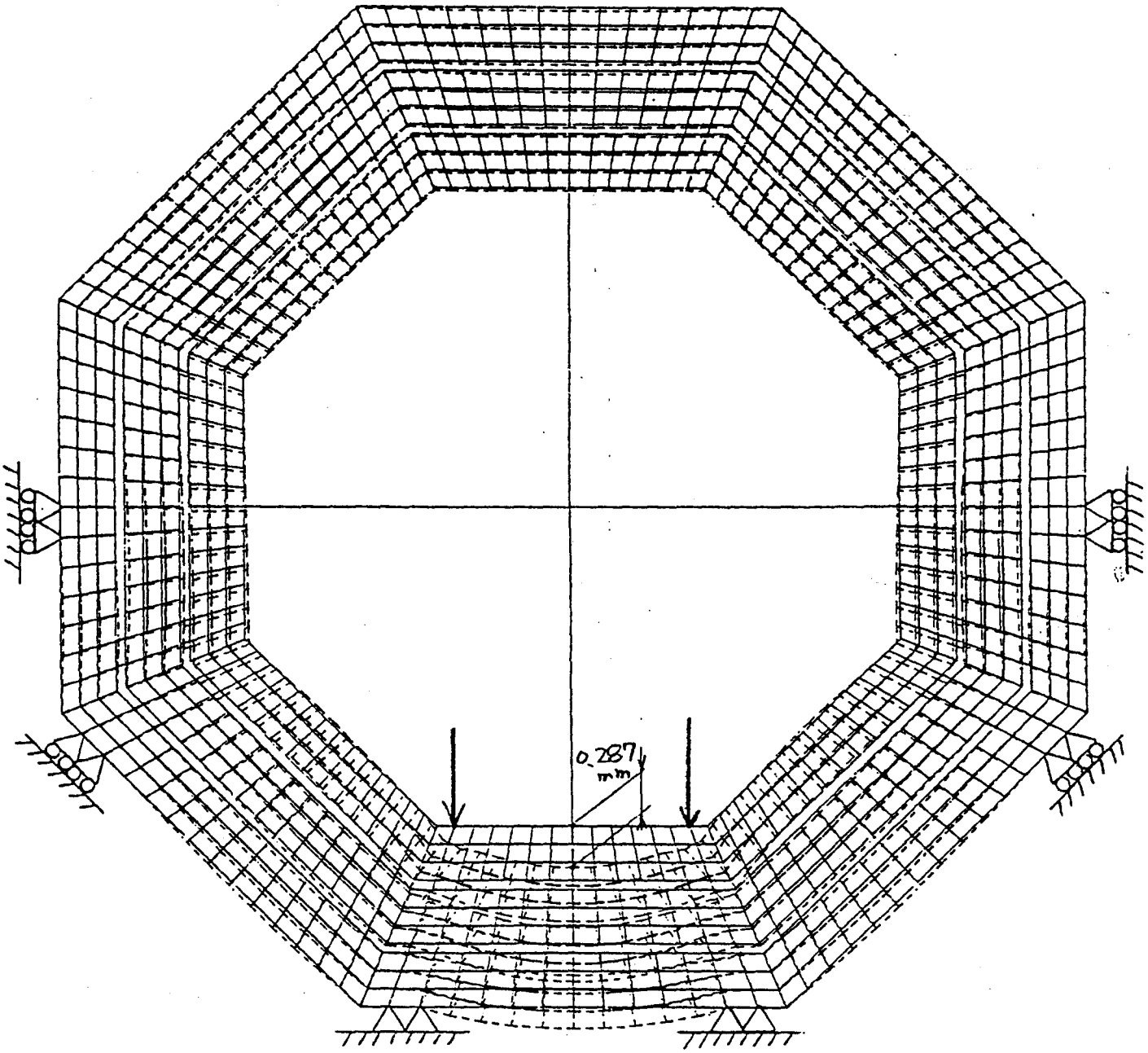

Fig.13 Deformation of barrel cylinder due to the weight of the inner detector.

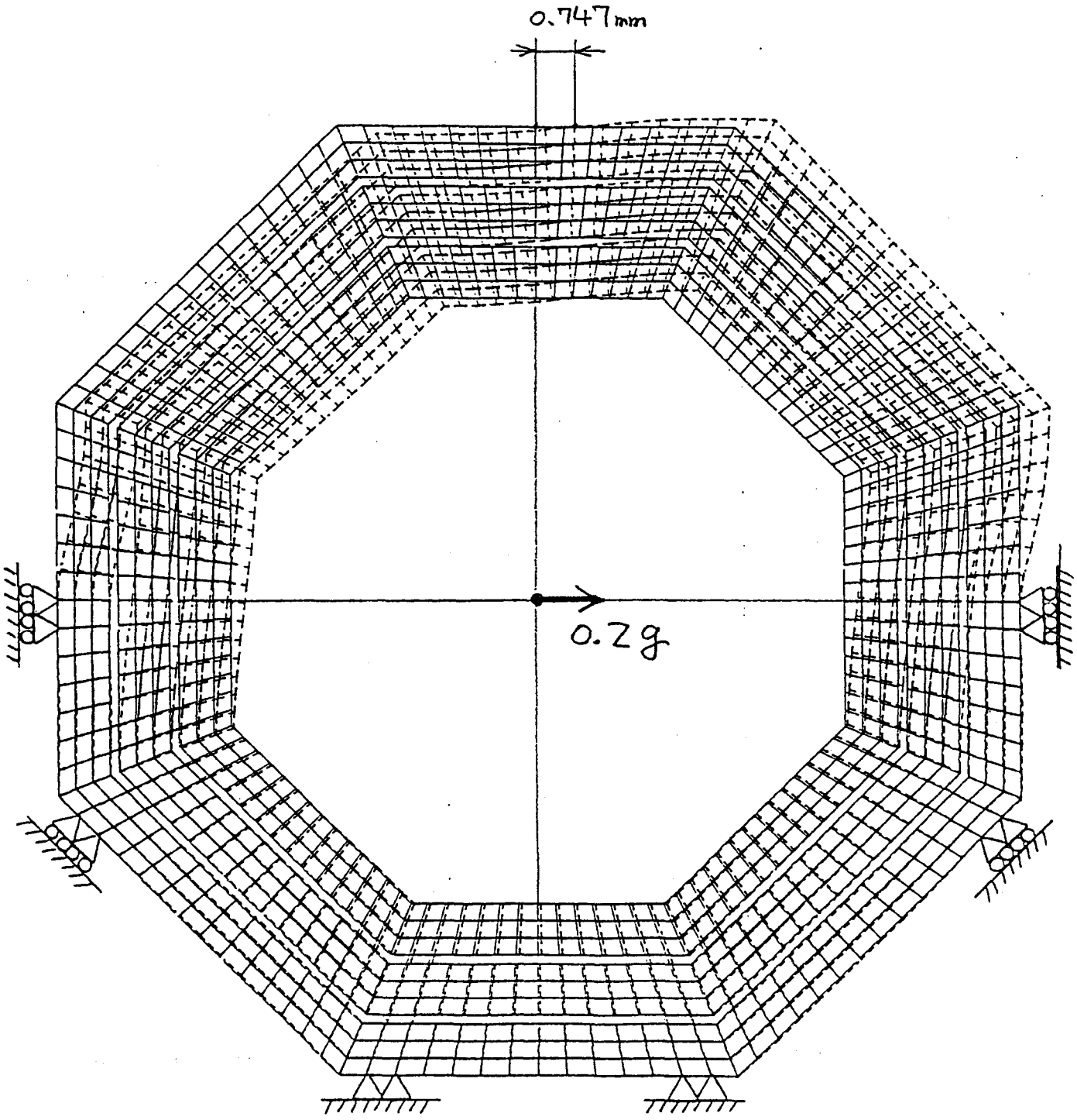

Fig.14 Deformation of barrel cylinder due to a side way static force of 0.2g (self-weight only)

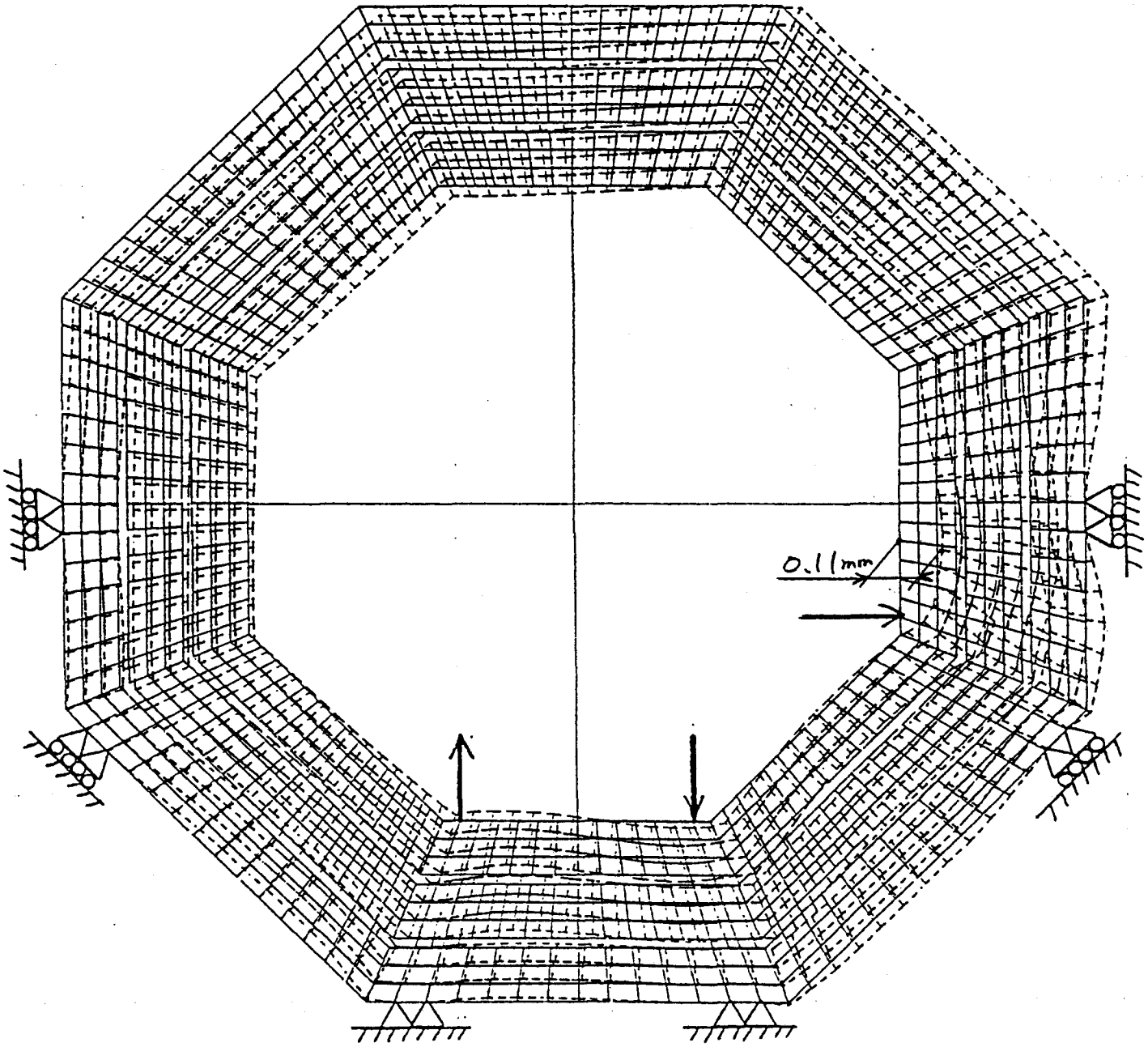

Fig.15 Deformation of barrel cylinder due to a side way static force of 0.2g (weight of the inner detector).

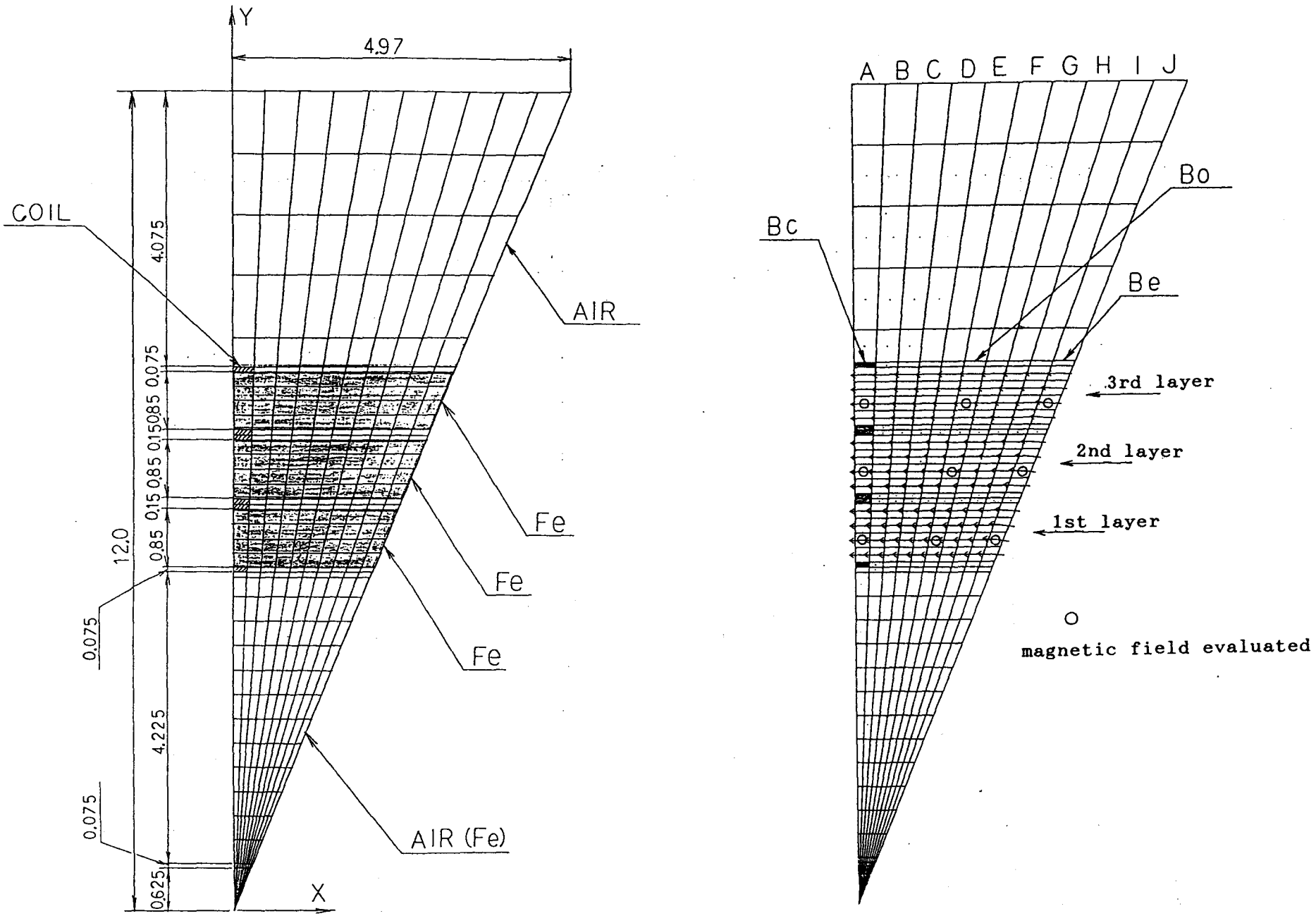

Fig.16. Mesh division for the calculation of the barrel toroidal field and the positioning of coil.

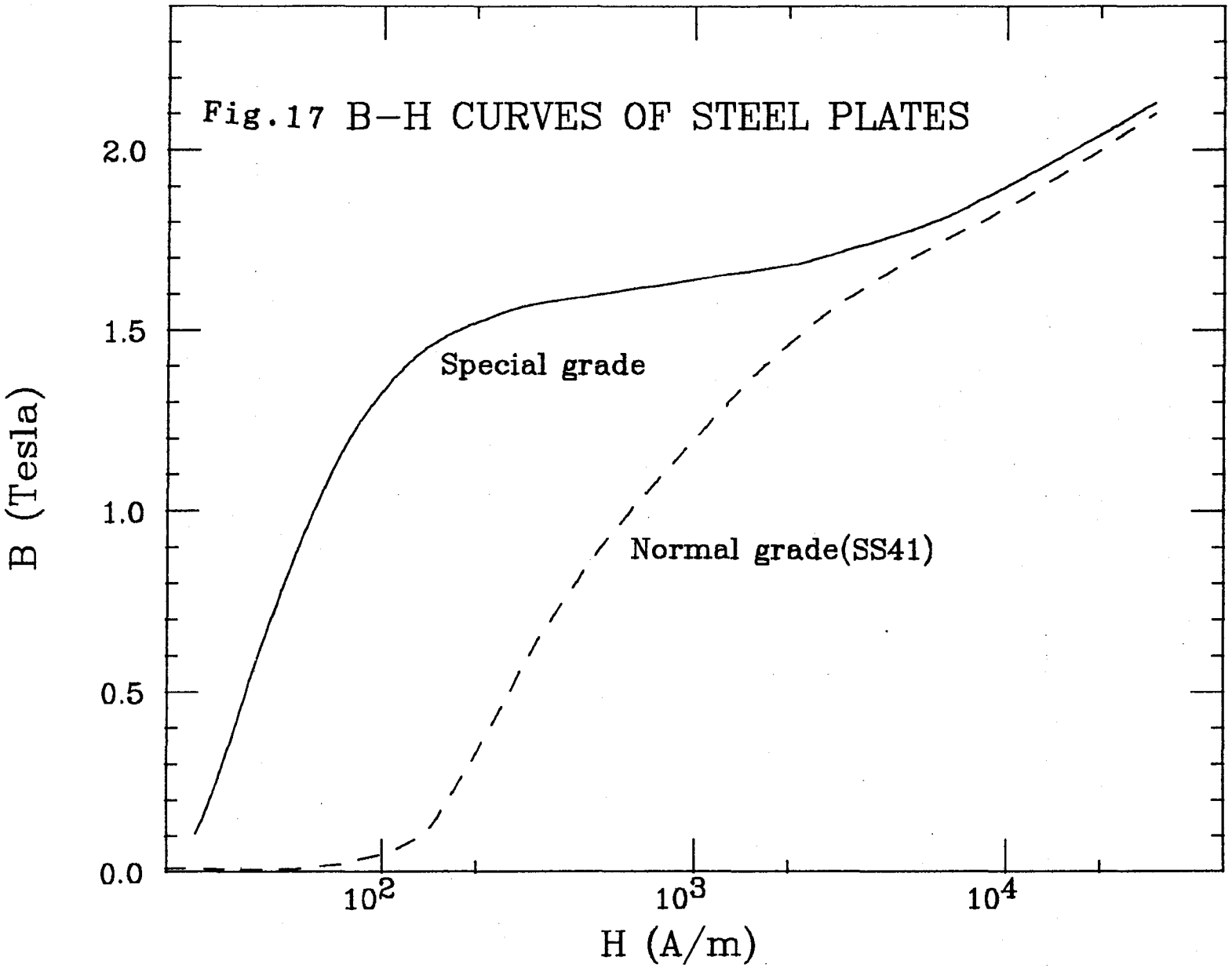
Fig.17 B–H CURVES OF STEEL PLATES
2.0
1.5
1.0
0.5
0.0
B (Tesla)
Special grade
Normal grade(SS41)
10^2
10^3
10^4
H (A/m)

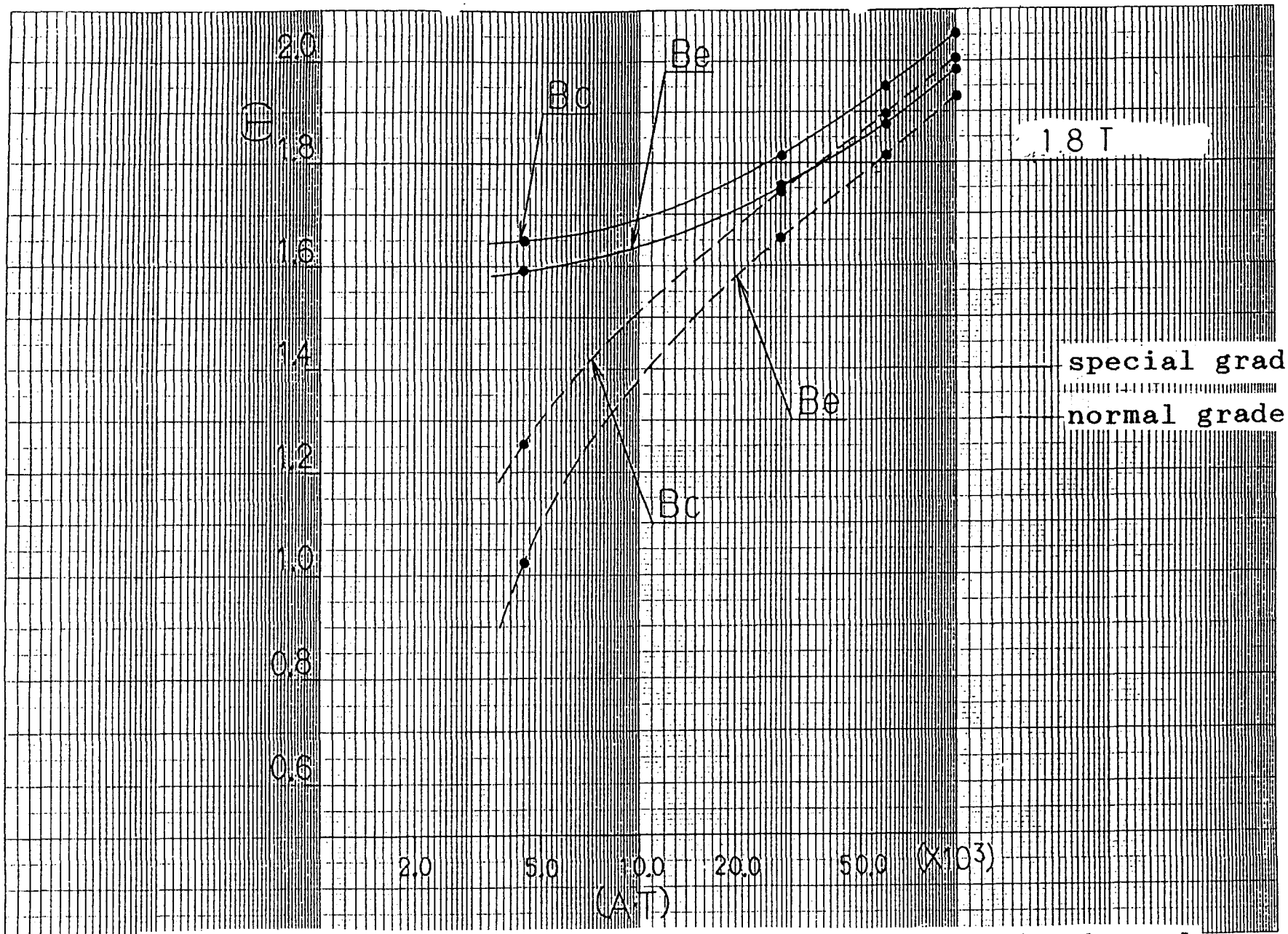

Fig.18. Magnetic field calculated vs. amp-turns for barrel toroid (for the third layer).

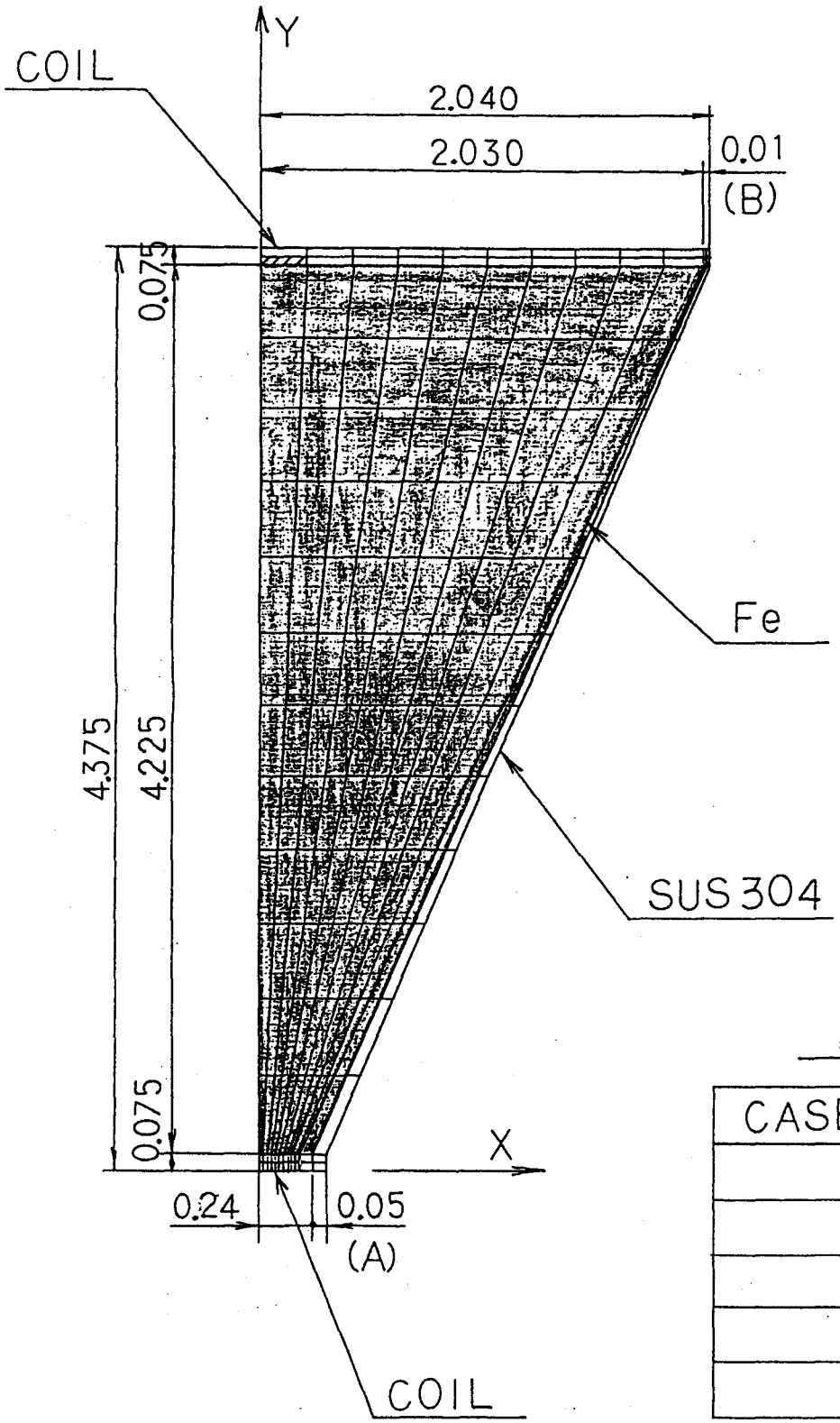

PARAMETER (m)

CASE	A	B
1	0	0
2	0.05	0.01
3	0.02	0.004
4	0.01	0.002

Fig.19 Mesh division for the calculation of the endcap toroidal field.

A method to increase the field uniformity by inserting a wedge-shaped non-magnetic material(SUS304).

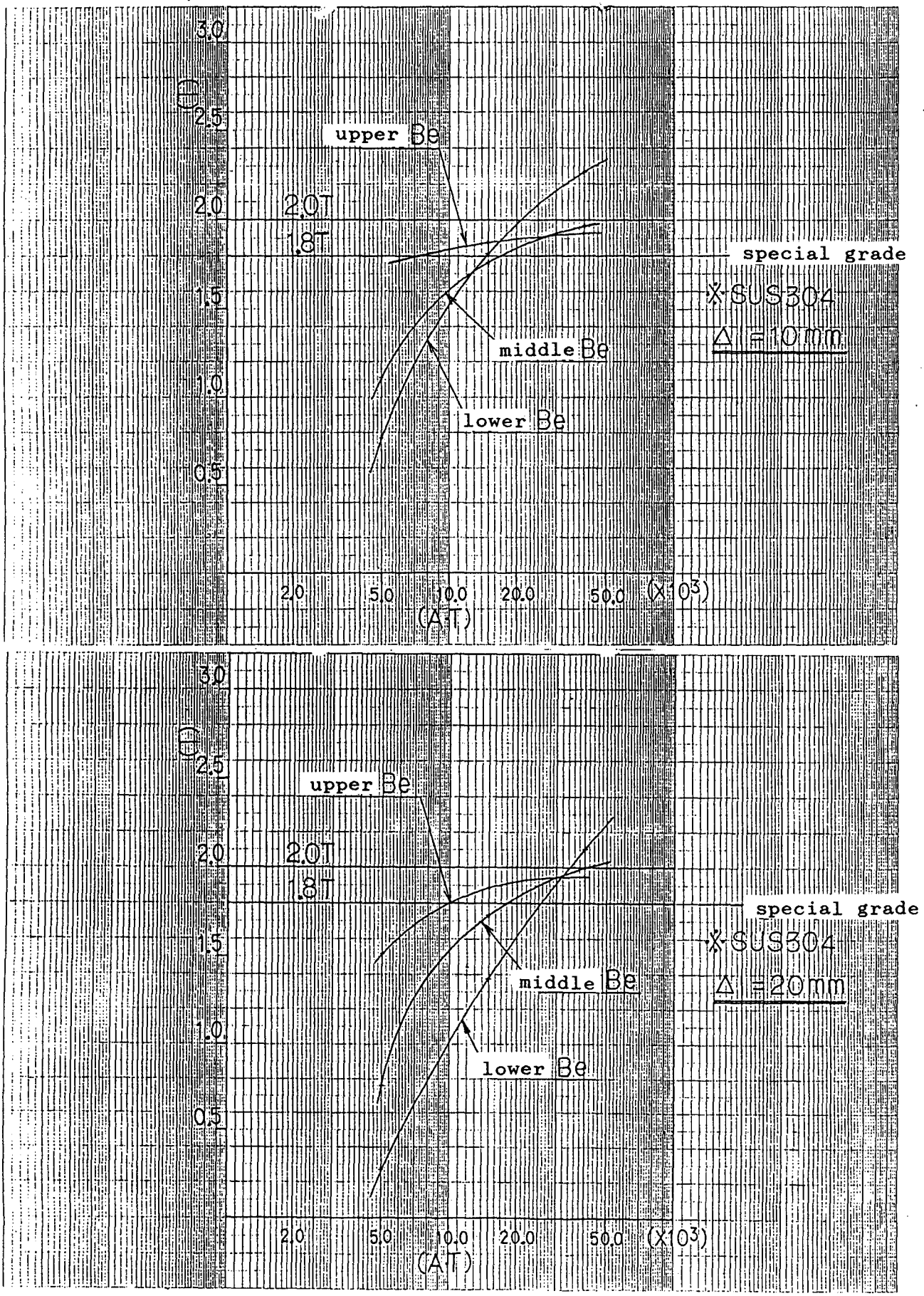

Fig.20. Magnetic field calculated vs. amp-turns for endcap toroid with SUS304.

Cost and detector scale

M. Gilchriese
LBL

******** This summary is written by the proceeding **********
******** editor based on the transparencies presented. ********

SDC Detector Costs

	$M
Silicon Vertex Detector	53
Tracking (Mech)	28
Calorimetry (Mech)	149
Muon System (Mech + Magnet)	163
Solenoid + Cryogenics	28
Electronics system	105
On-line computing	12
Engineering, design	108

TOTAL $646M

Note : contingency is substantial ($173M of the $646M), covers cost uncertainty AND scope uncertainty.

Cost and Detector Scale

Suppose change solenoid radius and/or length

Results depends on how you change channel counts but

roughly $\Delta R \sim 20$ cm $\rightarrow$ $\Delta\$ \sim 30M$
$\Delta L \sim 1m \rightarrow \Delta\$ \sim 20M$

so

$\Delta R \sim 20cm + \Delta L \sim 1m \rightarrow \Delta\$ \sim 50$ M

Cost estimates are limited by lack of design. Much work to be done to estimate cost more accurately.

Short Solenoid versus Long Solenoid

April 23, 15:40-17:20

May 1990

Solenoids with Iron Return Yokes for SDC

S. Mori

Institute of Applied Physics
University of Tsukuba

Parameter optimization of the solenoids with iron return yokes under consideration for the SDC spectrometer was carried out by keeping the momentum analyzing power of the central tracking system constant. It was shown that a solenoid with a lower magnetic field has more desirable characteristics in various ways, particularly regarding the coil thickness and operational safety. A reasonable magnetic field seems to be about 1.5 Tesla that requires the solenoid inner radius to be about 2.25 m. It is concluded that a CDF-type solenoid of interest can not be destroyed with thermal loads during quenches in any conceivable circumstances. Around 1.5 Tesla the Type-I and Type-L coil designs proposed in the EoI are almost identical regarding the solenoid construction technique. Above 1.7 Tesla extensive studies on aluminum-stabilized superconductors are required.

I. Introduction

We proposed in the EoI three alternative solenoid designs for a 4π magnetic spectrometer of the SDC [1]; i.e. an "air-core" solenoid magnet (Type-S) [2] and two solenoids with magnetic flux return. In the latter cases the magnetic flux is returned via an explicit iron return yoke (Type-L) [3] and by adding iron to the calorimeter (Type-I) [4].

Type-L and Type-I solenoids can provide relatively uniform magnetic field in the central tracking volume with essentially null magnetic field at the barrel calorimeter section. Calorimeters at the barrel and endcap sections in these solenoid designs are most likely to be built with different technologies. On the other hand, Type-S solenoids can in principle allow a continuous coverage of the calorimetry of a

single technology in both barrel and endcap sections although the magnetic field in the central tracking volume is non-uniform.

Although construction of solenoids of any types discussed above seems to be technically feasible, the Type-L coil design can be regarded very conservative, whereas the Type-S coil design very aggressive. It is not straightforward to evaluate quantitatively the degree of technical difficulty with various solenoid designs. It seems, however, very useful to make parameter optimization of a solenoid design from the standpoint of construction safety.

In the present study we focus on the Type-L solenoid design and optimize the main parameters of the solenoid. It will be shown that the lower the magnetic field, the safer the coil will be when the analyzing power of the transverse momentun by the central tracking system is kept constant. The design parameters for a central magnetic field of 1.5 Tesla will be given. At 1.5 Tesla effects of field saturation at the end plug iron calorimeter become less critical and the Type-I coil design is essentially identical to the Type-L coil design as far as the technical design considerations of large, thin superconducting solenoids are concerned.

II. Superconducting Solenoids of Collider Detectors

Table I lists the main parameters of superconducting solenoids which have been used successfully in colliding beam experiments [5] and also the three solenoid designs under consideration for the SDC detector. The schematic drawings of the geometrical arrangements for the three solenoids are shown in Fig.1. Compared with the existing solenoids the proposed SDC solenoids have a high magnetic field of 2 Tesla and large stored magnetic energies of 190 MJ or more. In most of the solenoids aluminum-stabilized NbTi/Cu superconductors are used with cryostat arrangements of the forced-flow cooling method. Since aluminum with high purity is used as stabilizer, the mechanical strength of the conductors is limited. It should be noted that the magnetic fields of the existing thin solenoids

are 1.5 Tesla or less except for the small ZEUS solenoid. Extensive studies on aluminum- stabilized superconductors must be carried out for solenoids with a magnetic field of about 2 Tesla.

In a Type-I solenoid design effects of field saturation in iron end plug calorimeters can become serious for magnetic fields above 1.7 Tesla. As demonstrated in the case of the CDF solenoid, a magnetic field of 1.5 Tesla is still tolerable in such configurations [6].

III. Parameter Optimization

A. Transverse momentum resolution

The transverse momentum resolution by the central tracking system has the following relation:

$$\frac{\sigma p_T}{p_T^2} \propto \frac{1}{B L^2} \qquad (1)$$

where L is the tracking length in the transverse direction, B is the axial component of the magnetic field, and the number of measurements by the tracking system is assumed to be constant regardless of L. If we assume that the number of measurements is proportional to the tracking length, then the transverse momentum resolution is given by

$$\frac{\sigma p_T}{p_T^2} \propto \frac{1}{B L^{2.5}} \qquad (2)$$

In the EoI we assume B = 2 Tesla and the tracking outer radius, R_t, to be 1.90 m. In general, L is much shorter than R_t because of the finite tracking inner radius. We require that the product BR_t^2 should be kept constant. This requirement corresponds to an equal transverse momentum resolution given by Eq.(1) in the extreme case of $L = R_t$. For B < 2 Tesla the resolution becomes better because $L < R_t$.

B. Magnetic stored energy

The magnetic stored energy, E_0, is given by

$$E_0(J) = \frac{B^2(T)}{8 \times 10^{-7}} R_c^2(m)\, L_c(m) \qquad (3)$$

where R_c is the coil radius, given by $R_c = R_t + 0.15$ m, and L_c is the coil length. The stored energy is proportional to the square of the product of the field and coil radius when the coil length is fixed. Furthermore, if BR_c^2 and L_c are fixed, then the stored energy is proportional to the field. This is the case that approximately satisfies the requirement of BR_t^2 to be constant.

Figures 2(a) and (b) show the stored energy and the tracking outer radius as a function of the magnetic field under the condition of $BR_t^2 = 7.22$ Tesla.m^2. The ordinate scale in (a) is shown for $L_c = 9$ and 15 m. The closed circles correspond to the EoI design field of 2 Tesla. The vertical bar in (b) indicates an increment of the tracking outer radius by 20 cm which corresponds to approximately one interaction length of the longitudinal dimension for a typical calorimeter. It is a very obvious fact, but it must be emphasized that a small increment in tracking radius can reduce the field strength and stored energy almost proportionally to the square of the fractional increment.

C. Material thicknesses

The effective material thickness of the solenoid at the polar angle θ is given by

$$T(\theta) = T_0 / \sin\theta \qquad (4)$$

where T_0 is the material thickness in the coil radial direction. Since the factor $1/\sin\theta$ is 2.35 at the rapidity y = 1.5, T_0 must be kept about 1 X_0 or less.

Support cylinder and hoop stress

If we assume that the outward magnetic pressure is supported solely by the outer support cylinder, the outward pressure and the hoop stress at the support cylinder are respectively given by

$$P(kg/mm^2) = 0.0406\ B^2(Tesla) \quad (5)$$

$$\sigma = P\ R_c/t_s \quad (6)$$

where t_s is the radial thickness of the support cylinder. For the allowed stress of 22.7 kg/mm^2 for 2219-T851 aluminum alloy we have the relation

$$t_s(mm) \geq 1.79\ B^2(Tesla)\ R_c(m). \quad (7)$$

Although the support cylinder with the thickness given by Eq.(7) can hold the whole magnetic hoop stress by itself, the strain of the aluminum-stabilized superconductor must be kept within a reasonable limit. In the fabrication process a preload is applied between the coil and support cylinder in order to reduce the hoop stress at the conductor when the coil is excited. Let the allowed stress of the conductor σ_1 and σ_2 at room and liquid helium temperatures, respectively. In the case of the CDF-type aluminum-stabilized conductor we have σ_1 = 2.0 kg/mm^2 and σ_2 = 2.5 kg/mm^2 [7]. Therefore, the preload pressure on the conductor should not exceed the stress of 2.0 kg/mm^2 and the stresses at the coil and support cylinder should be kept less than 2.5 and 22.7 kg/mm^2, respectively, when the coil is excited.

The upper limit of the preload pressure P_1 can be given by

$$P_1(kg/mm^2) = \sigma_1\ t_c(mm)/R_c(mm) \quad (8)$$

where t_c is the conductor height and will be optimized in the following section. The radially outward magnetic pressure must be shared approximately proportionally to the thicknesses of the coil and support cylinder. Therefore, the net outward pressures at the coil and support cylinder should satisfy respectively the following relations:

$$P_c(kg/mm^2) = (t_c/(t_c + t_s))P - P_1 \leq \sigma_2\ t_c/R_c \quad (9)$$

$$P_s(kg/mm^2) = (t_s/(t_c + t_s))P + P_1 \leq 22.7\ t_s/R_c. \quad (10)$$

Eqs.(8) and (9) yields the relation

$$t_c + t_s \geq P R_c/(\sigma_1 + \sigma_2) \qquad (11)$$

In general, Eq.(10) is much weaker constraint than the others. Eq.(11) is one of the most important requirements and must be satisfied. The sum of the coil and support cylinder thicknesses given by Eq.(11) is independent of the coil length and approximately proportional to $B^{1.5}$ when $R_c{}^2B$ is fixed.

The dot-dashed curves shown in Fig.3 represent the sum of $t_c + t_s$ given by Eq.(11) for $\sigma_1 + \sigma_2 = 4.5$ and 5.0 kg/mm^2 as a function of the magnetic field. The other curves shown will be explained in the following sections.

Conductor dimension and cold mass thickness

The hot spot model gives the following relation among various coil parameters:

$$E_0 J_0{}^2 = \Gamma V_{max} I_0 \qquad (12)$$

where $I_0 = 8000$ A, $V_{max} = 500$ V, J_0 is the current density of the conductor, and the parameter Γ depends upon the maximum temperature T_{max} allowed during a quench and the conductor characteristics, given by $\Gamma \cong 0.9 \times 10^{17}$ A^{2}sm^{-4} for $T_{max} = 100$ K and RRR = 1500. Thus, Eq.(12) yields

$$J_0(A/mm^2) = 600\ E_0{}^{-0.5}\ (MJ). \qquad (13)$$

The axial current density and the conductor width are respectively given by

$$I(kA/mm) = 0.796\ B(Tesla) \qquad (14)$$

$$W_c(mm) = I_0/I - 0.2 = 10.05\ B^{-1}(Tesla) - 0.2 \qquad (15)$$

where the second term in Eq.(15) corresponds to insulation materials. Then, the conductor height can be calculated by using the relation

$$t_c(\mathrm{mm}) = I_0/J_0W_c. \qquad (16)$$

It depends upon the coil length and is approximately proportional to $B^{1.5}$. The dashed curves shown in Fig.3 represent calculated t_c values in units of radiation lengths for the coil lengths of 9 and 15 m.

The thicknesses of the conductor and support cylinder can be optimized by using Eqs.(7), (11), and (16). Eq.(11) must be satisfied for the allowed stress of the conductor. The lower dot-dashed curve shown in Fig.3 for $\sigma_1 + \sigma_2 = 5.0$ kg/mm^2 seems to be a reasonable upper limit. The difference between this curve and the t_c curves can be the thickness of the support cylinder t_s. Calculated t_s values for the two coil lengths satisfy Eqs.(7) and (10). Namely, the requirement for $t_s + t_c$ given by Eq.(11) is which determined from the allowed stress of the conductor is the most stringent and the summed thickness is independent of the conductor length up to 16 m. If a higher stress level can be allowed for the conductor, the other requirements become more important.

The average thickness of NbTi/Cu conductor is proportional to the field strength and estimated to be approximately 0.0698 B(Tesla) in units of radiation lengths.

The schematic diagram of the conductor cross section is shown in Fig.4 as a parameter of the magnetic field. The conductor cross section of the CDF solenoid is also shown for comparison. The aspect ratio is respectively about 8 and 10 for the Type-I and Type-L designs of 2 Tesla in the EoI and it is about 5 for the CDF solenoid. In the Type-I design of the EoI the thickness of the support cylinder must be adjusted to satisfy the requirement of Eq.(11).

Other components

The other components which contribute to the solenoid material thickness are as follows:

1. Honeycomb outer vacuum shell	0.130 X_0
2. Inner vacuum shell	0.079 X_0
3. Radiation shields	0.044 X_0

4. Insulators	0.018 X_0
Sub total	0.271 X_0

The thickness of the honeycomb vacuum shell depends on the coil radius, but in the solenoid designs discussed here its effects are rather small. The other items are nearly independent of the coil radius.

The overall material thickness of the solenoid in the coil radial direction is shown in Fig.3 (partly solid and partly dotted curve) as a function of the magnetic field. We assumed that the sum of the allowed stresses of the superconductor at room and liquid helium temperatures is 5.0 kg/mm^2. In the present optimization the material thickness is independent of the solenoid length. The dotted part corresponding to the field greater than 1.7 Tesla indicates that extensive studies on properties of superconductors are required. A naive extension from the existing aluminum-stabilized superconductors developed for moderate solenoid fields of 1.5 Tesla or less can be very risky. Since pure aluminum used as the stabilizer is mechanically soft, it is not clear that such conductors can stand the magnetic shearing force from NbTi/Cu conductors. In addition, as shown in Fig.3, the aspect ratio of the conductor at higher fields is very large.

IV. Discussion

The conductor parameters discussed in the previous section were determined by the hot spot model which assumes no thermal diffusion of the Joule heat at a normal zone appeared in the superconductor during a quench. When a solenoid with an aluminum outer support cylinder quenches starting from a local spot, the entire solenoid should become normal immediately by quench-back effects and the temperature of the cold mass of the solenoid rises nearly uniformly. No hot spot will appear. The quench-back phenomenon is caused by Joule heating in the support cylinder due to eddy currents by magnetic coupling between the coil and support cylinder.

In the normal operation a quench protection system detects a quench and activates a protection circuit so that the coil excitation current starts flowing through a dump resistor and decreases with a time constant determined by the sum of the dump resistor and the resistance of the normal zone of the solenoid. Immediately after the onset of the quench the induction current in the support cylinder is induced by current flow in the dump resistor. Therefore, the hot spot model can be considered to be extremely conservative as long as the quench protection circuit is operational.

When the quench protection system fails to function properly, quench-back effects take place with some time delay because induction currents in the support cylinder are induced after the resistance of the normal zone in the superconducting coil grows to a certain level. Since it is difficult to obtain delay time accurately, we give a crude estimate below. (For notation see Ref.8.)

The eddy current in the support cylinder I_2 is given by

$$I_2 = I_0 \sqrt{\frac{L_2}{L_1}} \frac{R_1}{R_2} \exp\left(- t/ \left(L_1/R_1 + L_2/R_2\right) \right) \qquad (17)$$

where I_0 is the excitation current, and L_1 (L_2) and R_1 (R_2) are respectively the inductance and resistance of the coil loop (support cylinder). We have I_0 = 8000 A, L_1 = 5.8 H, L_2 = 1.7 μH, and R_2 = 3.9 μΩ. R_1 is the internal resistance of the coil normal zone. Thus we have the following approximate relation soon after t = 0:

$$I_2(\mathrm{A}) = 6.4 \times 10^6 / \tau_1(\mathrm{s}) \qquad (18)$$

where $\tau_1 = L_1/R_1$. Then the corresponding eddy current power is approximately given by

$$P_{eddy}(\mathrm{kW}) = 1.6 \times 10^5 / \tau_1^{\,2}(\mathrm{s}) \qquad (19)$$

For example, for R_1 = 20 mΩ we have τ_1 = 290 s and P_{eddy} = 1.8 kW. This power level is probably sufficiently high to initiate a quench-back.

We made extensive computer simulations for quench

properties of the CDF solenoid. The coil resistance of a normal zone was calculated as a function of the time after the onset of a quench in various cases. (See Fig.13 of Ref.9.) It depends on characteristics of the conductor, particularly propagation velocities of the normal zone in the coil. Since we plan to use a conductor similar to that of the CDF solenoid, the growth rate of the normal zone is expected to be similar [10]. Therefore, we can conclude that it may take only a few seconds before a quench-back begins and that no unusual temperature rise will appear.

It must be noted that a failure mode of the quench protection circuit discussed above is equivalent to the case of R_{ext}(dump resistor) = 0 since a power supply can not add appreciable power to the solenoid for a short period. As shown in Refs.8 and 9, computed maximum voltages to ground and maximum temperature rises have smooth variations as a function of R_{ext}. No unusual behaviours are seen at $R_{ext} = 0$.

The maximum temperature rise of 100 K is determined from the fact that thermal expansion rates of cold mass materials are reasonably small below 100 K and increase rapidly above 100 K. Therefore, thermal cycles which exceed 100 K should be avoided as few as possible. On the other hand, it can be said with confidence that CDF-type solenoids will not be destroyed with thermal damages due to infrequent unusual quenches.

On very rare occasions such as failures of the quench protection circuit, a large fraction of the stored magnetic energy can be absorbed in the cold mass of the solenoid. Thus, the most critical parameter of the solenoid is the entalpy which is defined by the ratio of the stored energy to the cold mass. For example, entalpies of 6.0 and 8.0 J/gm for aluminum correspond to the temperature rises to 70 and 75 K from liquid helium temperature, respectively. The entalpy of the CDF solenoid is 5.4 J/gm. It seems to be very desirable to keep the entalpy below 8 J/gm. In general, solenoids which have lower entalpies can be regarded safer against any modes of quenches.

As discussed in Section III.B, the stored magnetic energy is approximately proportional to the magnetic field when $R_c^2 B$ is fixed. On the other hand, the cold mass is roughly

proportional to the product of the coil radius and the sum of the conductor and support cylinder thicknesses ($t_c + t_s$). Then, if we choose a design in which ($t_c + t_s$) and $R_c^2 B$ are fixed, the entalpy of the solenoid is proportional to B/R_c, namely to $B^{1.5}$. Therefore, a solenoid design with a lower magnetic field is safer with regard to entalpy considerations.

Figure 5 shows a proposed arrangement for a 1.5 Tesla solenoid with a tracking outer radius of 2.20 m. The solenoid inner radius is 2.25 m. In this design the endplug calorimeter can have magnetized iron absorbers and there is no clear distinction between the Type-I and Type-L coil designs. If EM calorimeters with other technologies are desired as in the case of CDF, a solenoid should be designed longer as shown in the figure. Parameters of example designs are given below.

Type	δ(m)	L_c(m)	E_0(MJ)	T(X_0)	C.mass(t)	Ent.(J/gm)
Type-I'	0	9	139	0.86	22	6.4
Type-L'	1.5	12	185	0.86	29	6.4

If we choose a more conservative stress limit of $\sigma_1 + \sigma_2 = 4.5$ kg/mm^2 for the conductor instead of 5.0 kg/mm^2, we have a solenoid thickness of 0.91 X_0 and an entalpy of 6.0 J/gm.

V. Conclusion

Parameter optimization of the Type-L solenoid design was carried out by keeping the momentum analyzing power of the central tracking system constant. Since the inner tracking radius is not well defined, we assume that the product of the magnetic field and the square of the outer tracking radius is constant. This assumption gives conservative results at lower fields twofold. Firstly, if desired, a larger number of measurements is feasible for a longer tracking length. Secondly, since the radial tracking length is always shorter than the outer tracking radius, the fractional change of the tracking length is larger when the inner tracking radius is fixed. The main results obtained under this assumption are as

follows:

1) The stored magnetic energy is approximately proportional to the magnetic field.
2) The sum of the coil and support cylinder thicknesses is determined primarily from the allowed stress of the aluminum-stabilized NbTi/Cu superconductor and approximately proportional to $B^{1.5}$. This implies that the solenoid material thickness is nearly independent of the coil length.
3) The minimum conductor height determined from a quench analysis by the hot spot model is approximately proportional to $B^{1.5}$. It depends upon the coil length.
4) When the thickness of the cold mass cylinder is fixed, the entalpy of the solenoid is roughly proportional to $B^{1.5}$.

Therefore, we conclude that a solenoid with a lower magnetic field has more desirable characteristics in various ways. We note that the cost of a solenoid is expected to be approximately proportional to the three quarter power of the stored energy. On the other hand, since a lower field solenoid has a larger volume, the overall detector volume becomes larger and its cost can be more expensive.

A CDF-type solenoid with an aluminum outer support cylinder seems inconceivable to develop appreciable temperature gradients in the cold mass during a quench. When the quench protection sytem is operational, a quench-back will takes place immediately after the onset of a quench and the entire coil become normal. On very rare occasions such as failures of the quench protection circuit, quench-backs occur with some time delays of a few seconds. Unusual local temperature rises are, however, very unlikely to appear. It is concluded that the CDF-type solenoid can not be destroyed with thermal loads during quenches in any conceivable circumstances.

A reasonable magnetic field seems to be about 1.5 Tesla. Large, thin supercondicting solenoids have been successfully constructed with fields of 1.5 Tesla or less. Fabrication techniques of aluminum-stabilized superconductors using aluminum with RRR greater than 1000 have been well established at these fields. Parameters for a 1.5 Tesla solenoid of 2.25 m

in inner radius and 12 m in length were calculated. The material thickness is about 0.86 X_0 and the entalpy is about 6.4 J/gm. Around 1.5 Tesla the Type-I and Type-L coil designs are almost identical as far as the solenoid construction technique is concerned. Effects of field saturation at the endcap calorimeter are tolerable.

References

1. Expression of Interest by the Solenoidal Detector Collaboration to Construct and Operate a Detector at the Superconducting Super Collider, May 1990.
2. A. Yamamoto, contribution to this Workshop; T. Kondo, "An Air-Core-Solenoidal Detector (ACS) for High p_t Physics at the SSC," Talk presented at the Fermilab Workshop on Solenoidal Detectors for the SSC, Batavia, September 1989.
3. S. Mori, "HCD Hermetic Collider Detector," Institute of Applied Physics, University of Tsukuba, February 1990.
4. R. Kephart, R. Fast, J. Grimson, J. Krebs, and R. Wands, private communication.
5. For a summary report on large superconducting solenoids built recently see, for example, H. Hirabayashi, "Detector Magnets in High Energy Physics," IEEE Trans. on Magnetics 24(1988)1256.
6. Design Report for an Indirectly Cooled 3-m Diameter Superconducting Solenoid for the Fermilab Collider Detector Facility (October 1982), Fermilab, Batavia, IL, unpublished; H. Minemura et al., Nucl. Instr. and Meth. A238(1985)18.
7. R. Wands, J. Grimson, R. Kephart, and D. Theriot, Fermilab Internal Report TM-2750.1113 (May 1982), Fermilab, Batavia, IL, unpublished.
8. S. Mori and M. Noguchi, Jpn. J. Appl. Phys. 22(1983)812.
9. T. Kishimoto, S. Mori, and M. Noguchi, Jpn. J. Appl. Phys. 22(1983)57.
10. H. Hirabayashi et al., Jpn. J. Appl. Phys. 20(1981)2243.

Table I. Main parameters of large superconducting solenoids built recently for colliding beam experiments and the three solenoid designs under consideration for the SDC detector.

Experiment	Central field(T)	Ciol rad.(m)	Length (m)	Stored energy(MJ)	Material thick.(X_0)
CDF	1.5	1.5	5	30	0.86
TOPAZ	1.2	1.5	5.1	20	0.70
VENUS	0.75	1.7	5.6	12	0.52
AMY	3.0	1.2	1.5	40	~6
CLEO-II	1.5	1.5	3.8	25	2.5
ALEPH	1.5	2.7	6.4	130	1.7
DELPHI	1.2	2.8	7.4	109	4.0
H1	1.2	~2.7	~5.8	~76	~1.2
ZEUS	1.8	1.0	2.5	11	0.90
SDC					
Type-S	2.0	2.0	9	205	1.23
Type-I	2.0	2.0	9	190	1.00
Type-L	2.0	2.0	15	317	1.14

Figure Captions

Figure 1. Schematic diagrams of the geometrical relation among the solenoid, calorimeter, and return yoke for the three types of solenoids under consideration for the SDC detector.

Figure 2. Tracking outer radius and the stored magnetic energy as a function of the magenetic field. The product of the field and the square of the tracking radius is kept a constant value of 7.22 Tesla.m^2 as proposed in the EoI. The closed circles correspond to the EoI design field. The ordinate of the top figure is shown for the coil lengths of 9 m (left) and 15 m (right). The triangles indicate the amount corresponding to a radius change of 20 cm, namely one interaction length of a typical calorimeter.

Figure 3. Overall material thickness, the sum of coil and support cylinder thicknesses, and conductor height in units of radiation lengths as a function of the field strength for BR_t^2 = 7.22 Tesla.m^2. σ_1 and σ_2 are the allowed stresses of an aluminum-stabilized superconductor at room and liquid helium temperatures, respectively. The conductor height is given for the coil lengths of 9 and 15 m. The dotted curve for the overall thickness indicates that extensive studies on conductors are needed because most of aluminum-stabilized superconductors have been developed for moderate magnetic fields of about 1.5 Tesla or less.

Figure 4. Aspect ratios of conductors for various magnetic fields for the SDC detector. Also shown is the aspect ratio of the CDF solenoid conductor.

Figure 5. Schematic diagram of the geometrical relation among the solenoid, iron calorimeter, and iron return yoke for a coil design at 1.5 Tesla. The total length of the solenoid depends upon the endplug EM calorimeter design.

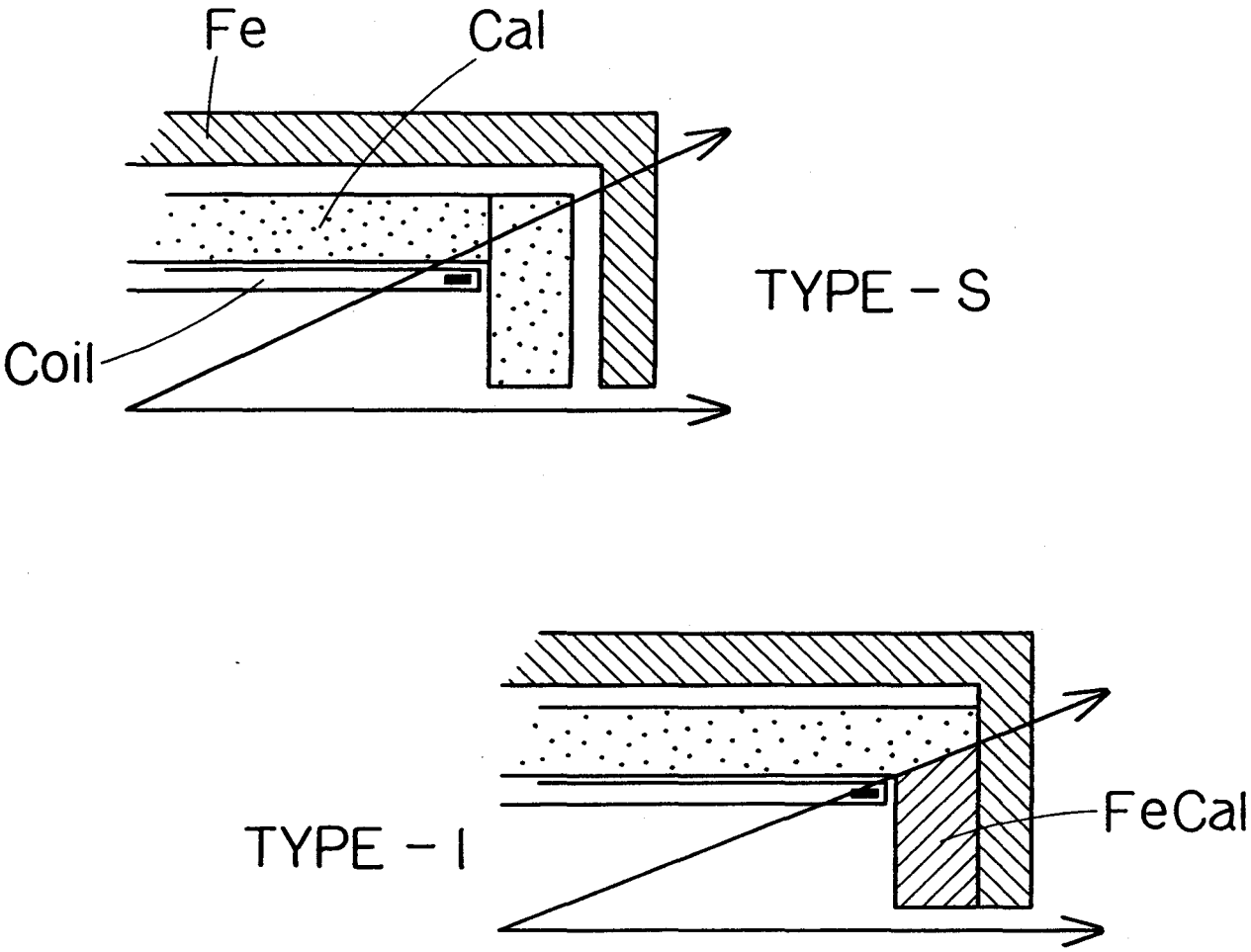

Figure 1.

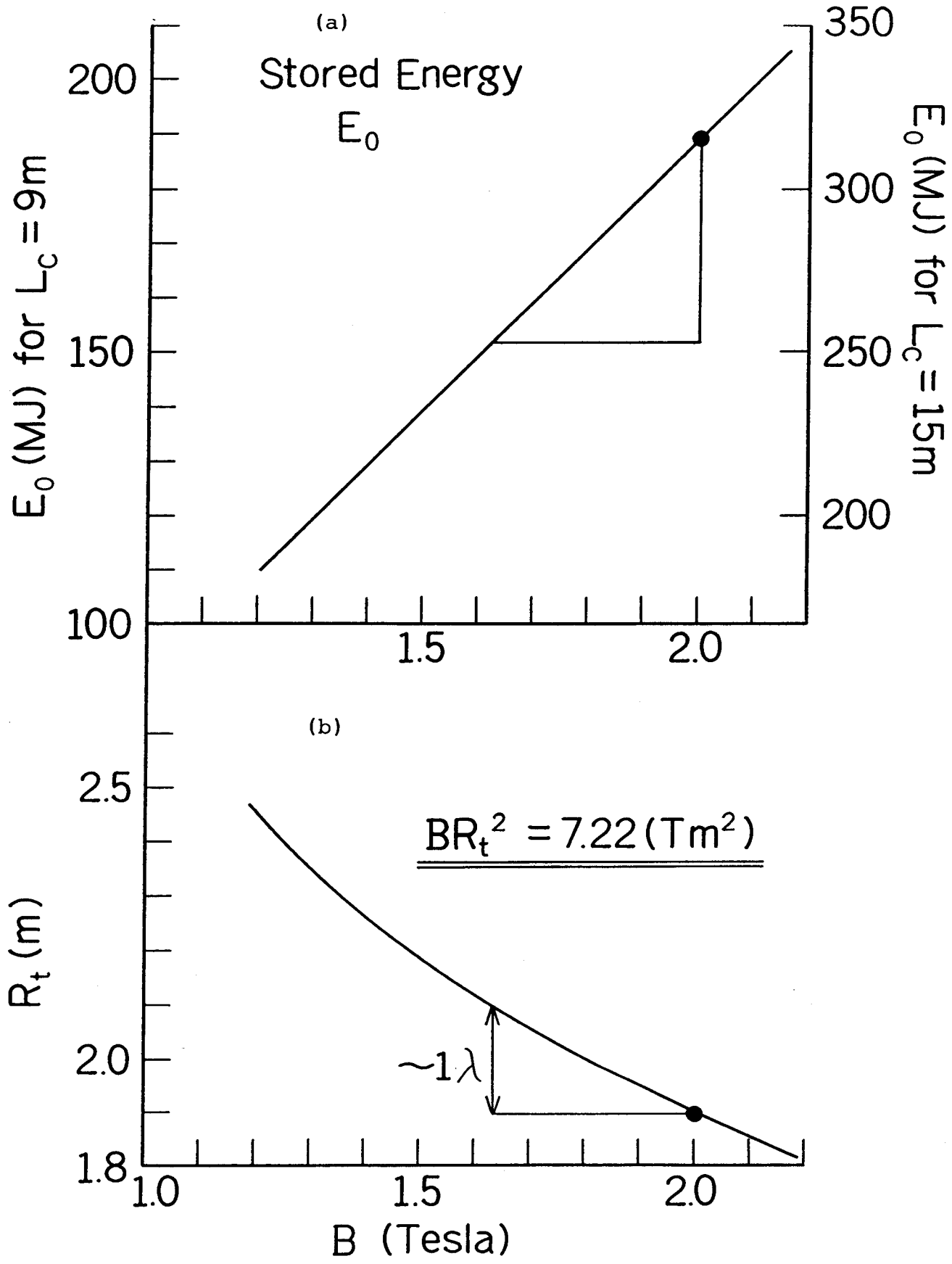
(a)
Stored Energy
E_0
200
150
100
350
300
250
200
E_0 (MJ) for L_c = 9m
E_0 (MJ) for L_c = 15m
1.5
2.0
(b)
$BR_t^2 = 7.22 (Tm^2)$
2.5
2.0
1.8
R_t (m)
~1λ
1.0
1.5
2.0
B (Tesla)

Figure 2.

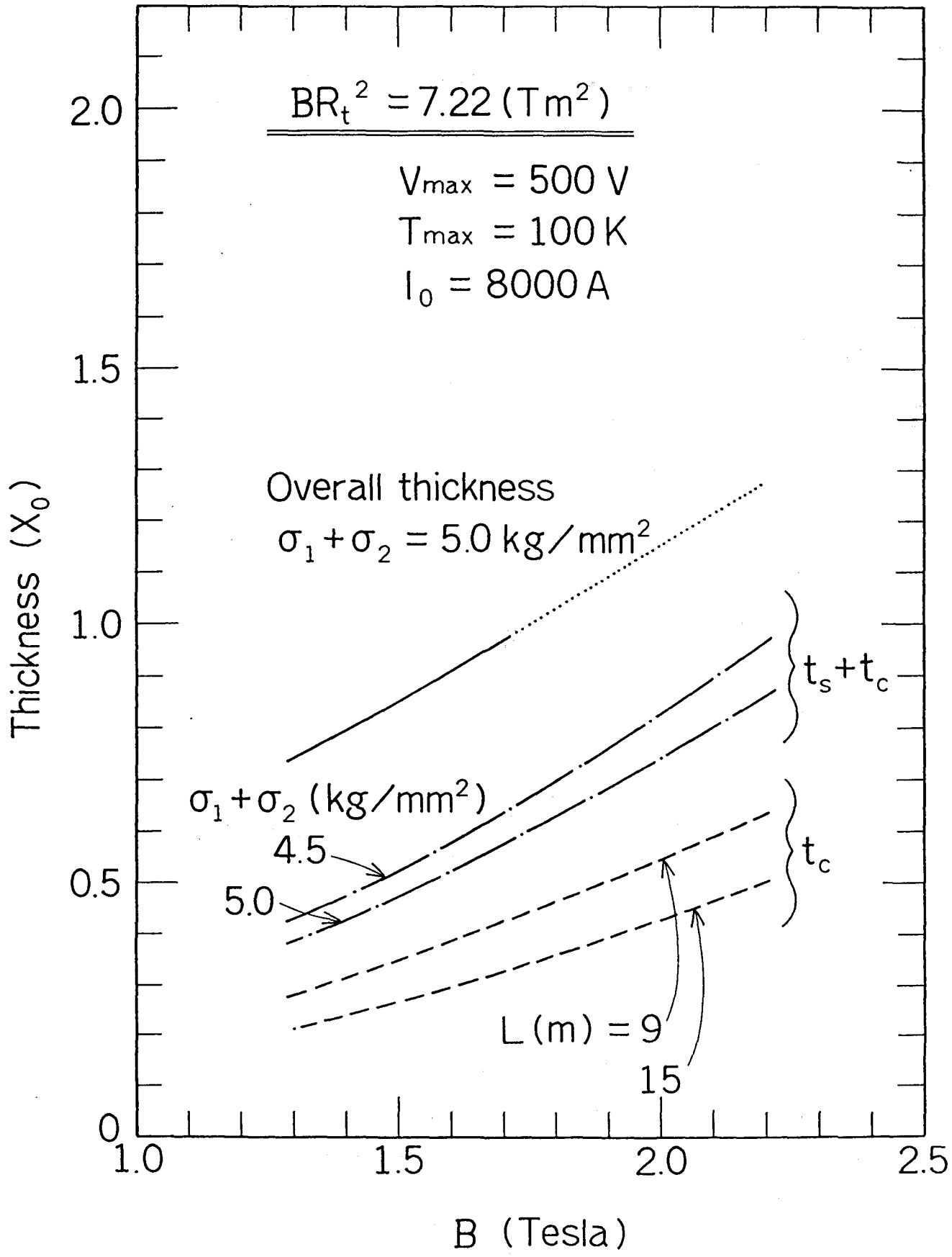
$BR_t^2 = 7.22\,(Tm^2)$
$V_{max} = 500\,V$
$T_{max} = 100\,K$
$I_0 = 8000\,A$
Overall thickness
$\sigma_1 + \sigma_2 = 5.0\,kg/mm^2$
$t_s + t_c$
t_c
$\sigma_1 + \sigma_2\,(kg/mm^2)$
4.5
5.0
L (m) = 9
15
Thickness (X_0)
B (Tesla)
0
0.5
1.0
1.5
2.0
1.0
1.5
2.0
2.5

Figure 3.

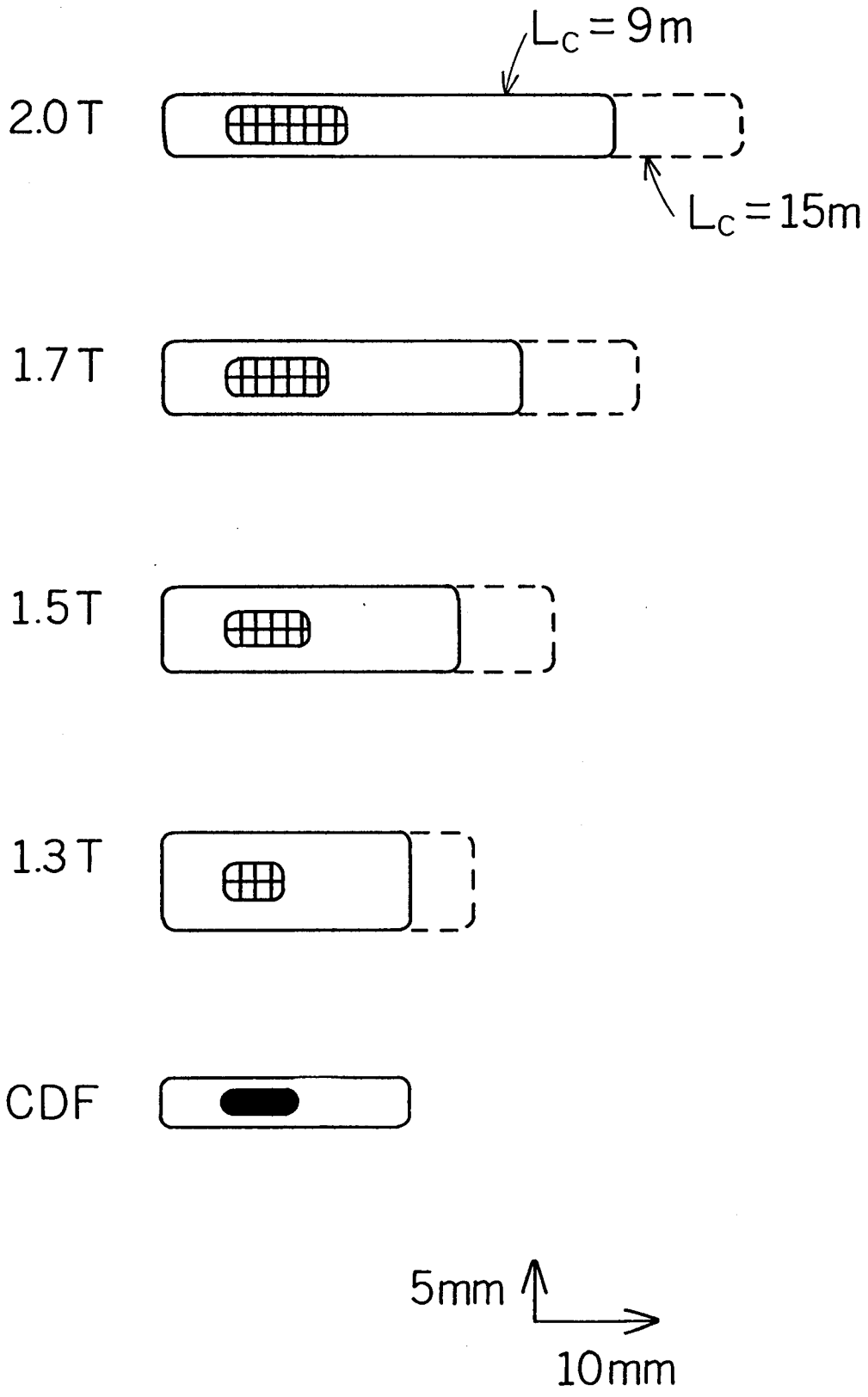

Figure 4.

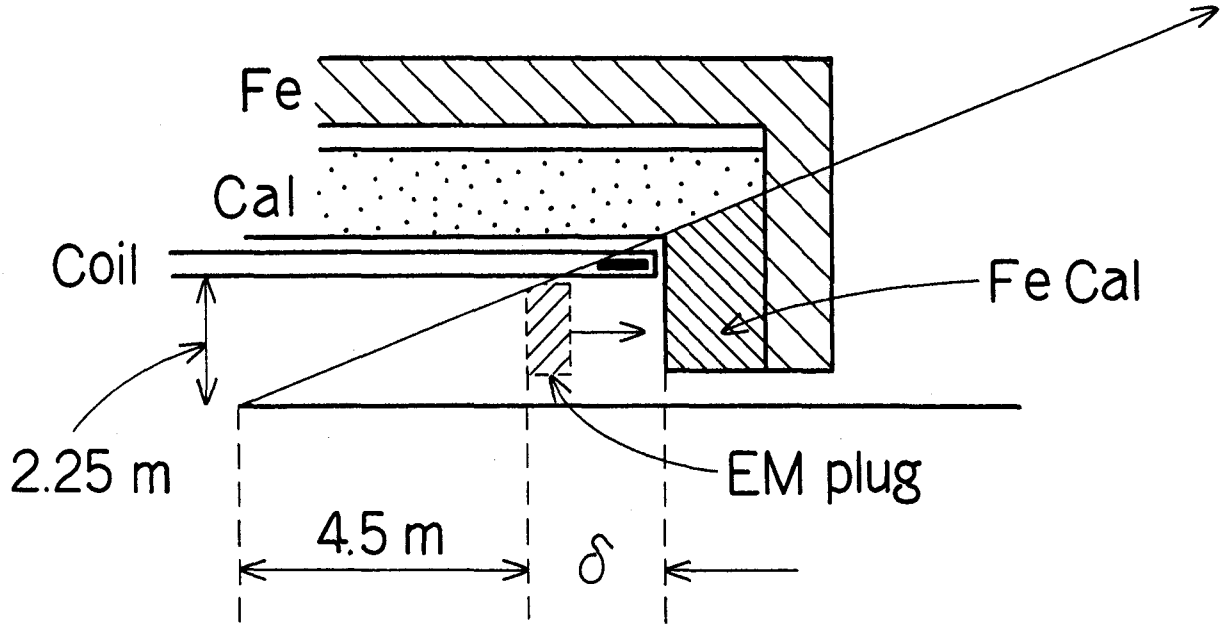

Figure 5.

DESIGN STUDY OF AN

AIR CORE THIN SOLENOID FOR THE SDC DETECTOR

A. Yamamoto, Y. Doi, T. Kondo, Y. Makida and S. Terada

KEK, National Laboratory for High Energy Physics
Tsukuba, Ibaraki, 305, Japan

April 23, 1990

---

*Talk presented at the International Workshop on Solenoidal Detectors for the SSC, held at KEK, Tsukuba, April 23 - 25, 1990.

DESIGN STUDY OF AN

AIR CORE THIN SOLENOID FOR THE SDC DETECTOR

A. Yamamoto, Y. Doi, T. Kondo, Y. Makida and S. Terada

KEK, National Laboratory for High Energy Physics
Tsukuba, Ibaraki, 305, Japan

Design study of an air core thin supercondcuting solenoid for the SDC detector has been made. The solenoid may provide a central magnetic field of 2 T and bending power of 3.6 - 2.7 Tesla meters within a tracking volume of 3.6 m in diameter and 9 m in length. The transparency of 1.16 (Xo) radiation thickness and 0.25 (λo) interaction lengths may be achieved under adequate safety boundary condition. This report describes the design aproach and status of the design study.. The reliability and safety is also discussed.. .

1. INTRODUCTION

An air core thin superconducting solenoid (Type-S) is being discussed as a possible magnet configuration in the central part of the SDC detector [1,2]. It has following advantages in the magnet and detector design:

1) possible more harmetic calorimeter design because of iron-free space available around the end of the coil,
2) negligible axial and radial decentering forces because of the lage distance to the iron returen yoke and
3) possible full excitation test and evaluation before its installation into the detector because of its basic iron free characteristics.

On the other hand, it is enevitable to have the following disadvantages:

1) less uniform magnetic field in the central tracking volume and large fringe fields extending into the volume occupied by calorimetry and other external detectors, and
2) large axial compressibe force on the winding due to radial magnetic field component

around the coil end.

The trade off study is under progress in detail between the air core colsnoid (Type-S) and a solenoid with iron (Type-I, L) [3]. In the following sections, the design process and status will be described and the reliability and saftey will be also discussed.

1. DESIGN CONCEPT

1.1. Requirements

The requirements and boundary conditions on the SDC solenoid magnet design are summarized as follows,

Magnet size:	
Cryostat Inner radius:	1.85 m
Outer radius:	2.2 m
Cryostat half length:	4.5 m
Tracking volume:	
Outer radius:	1.8 m
Half length	4.5 m
Nominal magnetic field:	2 Tesla
Transperency($\eta = 0$):	<1.2 Xo

As shown in Fig. 1, the tracking volume of 1.8 m in radius and 4.5 m in half length is a guide line for the solenoid design in the EoI of the SDC detector [1]. The field of 2 tesla seems to be close to the limit to realize the thin superconducting solenid. The radiation tihckness of the solenoid should be less than 1.2 at $\eta = 0$ in order to keep the transperency of less than 3 Xo ($X = Xo/\sin\theta$) at η ($= -\ln(\tan\theta/2) = 1.5$.

1.2. Design Aproach

To design the air core thin solenoid the following design aproach has been taken:

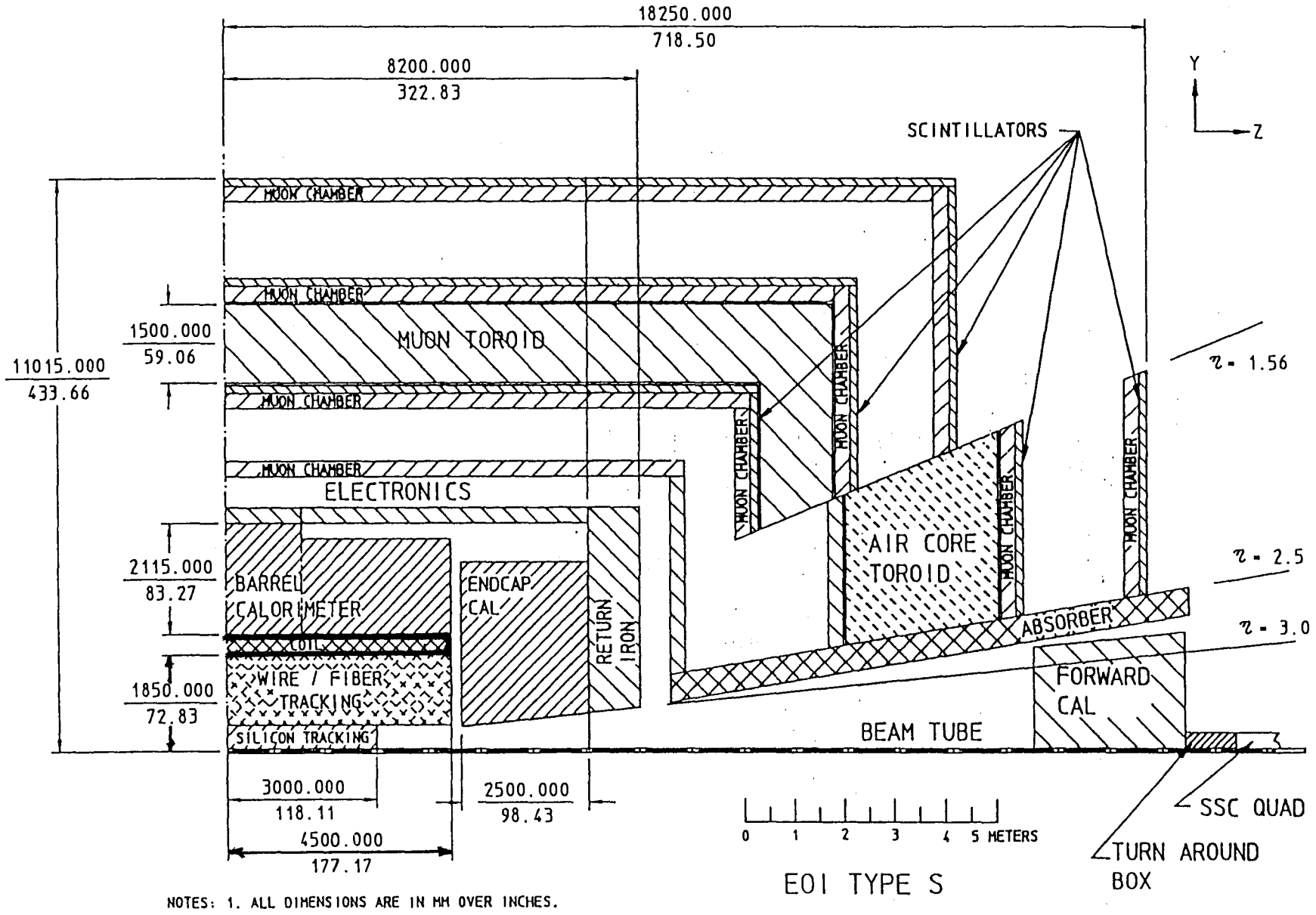

Fig. 1. Cross section of the SDC detector (Type-S).

- As thin as possible and higher E/M required

$1 < X < 1.2 \quad (\text{at } \eta = 0)$

E/M = 7.5 - 10 kJ/kg

- Must stable and safe against quench and full energy dump into the coil

J / Jc = 50 % on the load line.

T max < 100 K (after quench.)

Vmax < 1000 V

Fast Quench propagator with pure Al strip

- Optional current grading (20 %) at the coil end to improve field uniformity in the tracking volume.

Int. **B x dl** = 3.6 - 3.0 T.m (@ $0 < \eta < 1.5$)

The E/M ratio defined by [magnetic stored energy] / [cold mass] of the solenoid has been introduced as a simplified parameter to know the lightness and transparency of the solenid. It enable us to know the averaged temperature rise after quench according to the following relation:

$$R = E/M = H(T1) - H(To)$$

where H = INTEGRAL Cp dT is the enthalpy as a function of the temperature. As shown in Fig. 2, the enthalpy of aluminum of 10 kJ/kg corresponds to T1= 80 K and it is a reasonable value to keep the average temperature rise up to T=80 K and to keep the thermal stress still negligible after a quench and full energy dump in the worst case. Figure 3 shows E/M plots as a function of the stored energy in various magnets being operated in high energy physics experiments. Main parameters of the air core solenoid (Type-S)which we have designed with the above concepts are summarized in Table 1. A schematic cross section of the solenoid at the coil end is shown in Fig. 4.

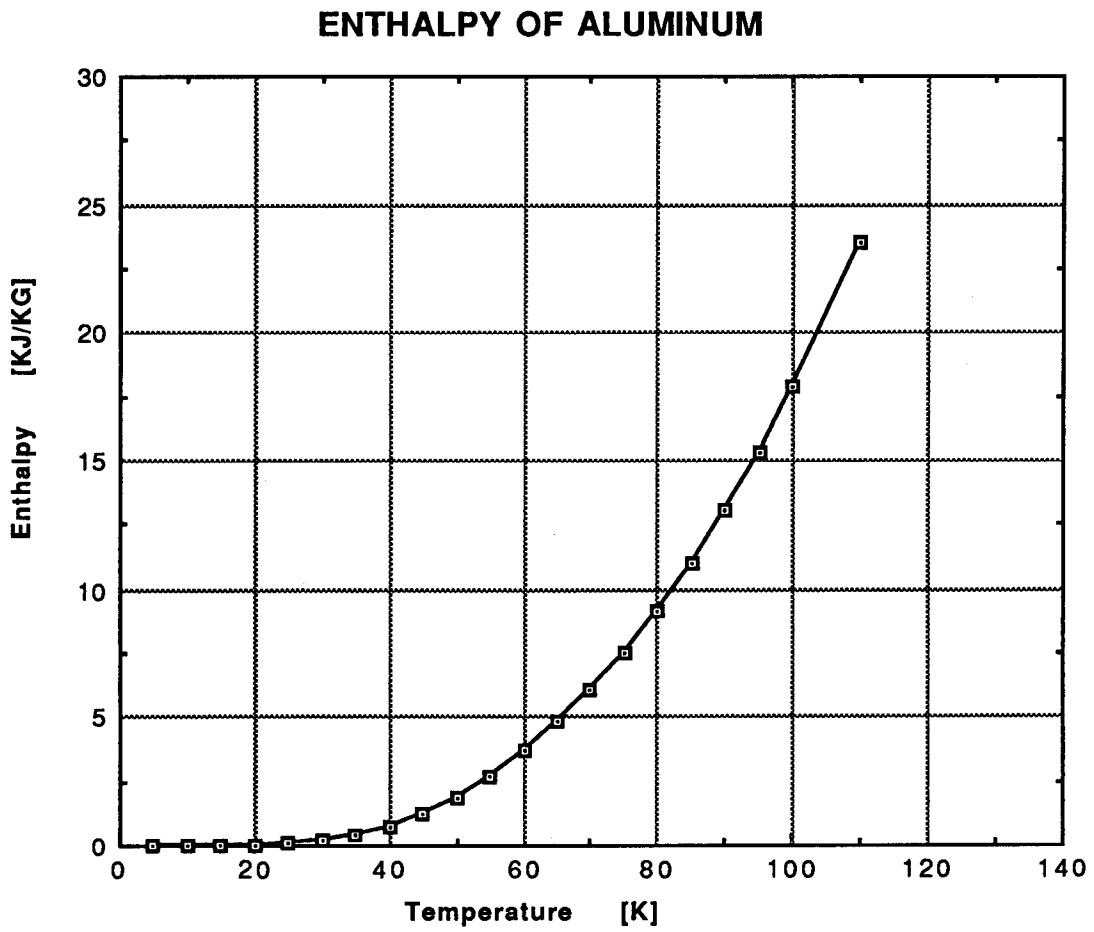

Fig. 2. Enthalpy of aluminum as a function of temperatue.

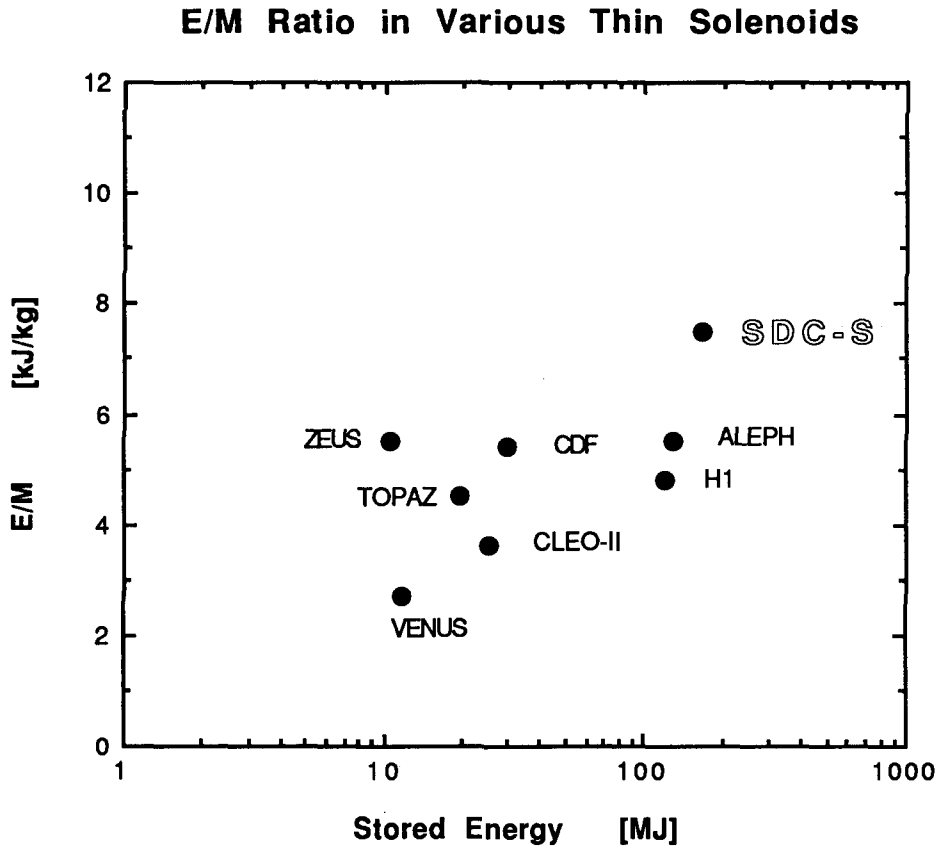

Fig. 3. E/M ratio in thin supercondcuting solenoid used in high energy physics experiments.

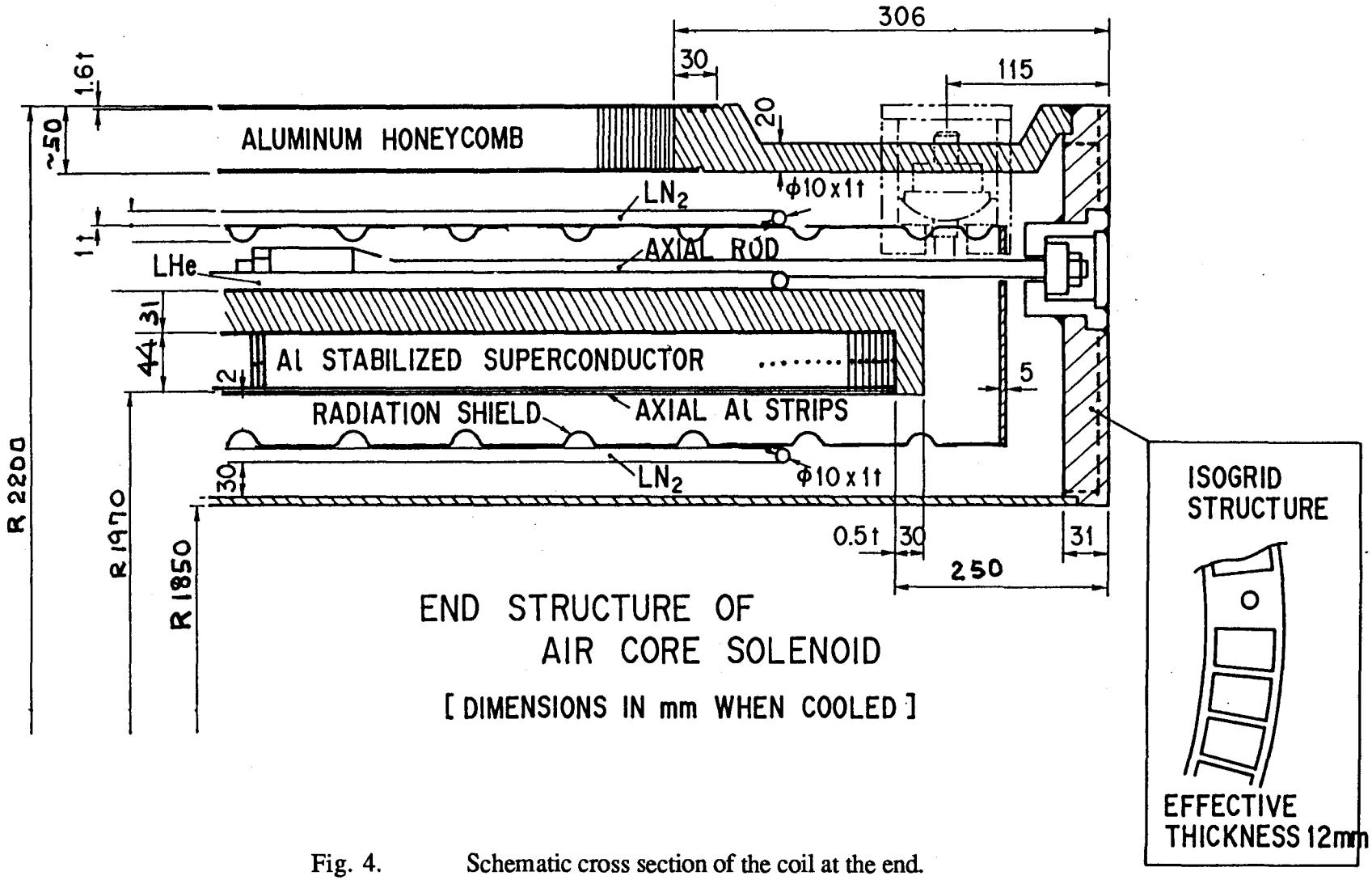

Fig. 4. Schematic cross section of the coil at the end.

Table 1. Design parameters for the SDC solenoid (Type-s)

Design parameters		Ordinal	(Aggressive)
Dimensions:			
Cryostat	Inner radius	1.85 m	
	Outer radius	2.2 m	
	Half length	4.5 m	
Coil	Effect. radius	1.97 m	
	Half length	4.25 m	
	Coil + OSC thick.	44 + 31 mm	
Tracking	Apert. radius	1.8 m	
	Apert Half length	4.5 m	
Transperency	Rad. thickness	1.16 Xo	
	Int. lengths	0.25 λo	
Electrical Parameters			(w/ Grading)
Central Field		2.0 T	
Int. B.dl	(h=0.)	3.6 T.m	(3.6 T.m)
	(h=1.0)	3.4 T.m	(3.6 T.m)
	(h=1.5.)	2.7 T.m	(3.0 T.m)
Nominal Current		10,000 A	
Inductance		3.31 H	(3.64 H)
Stored Energy		166 MJ	(182 MJ)
E/M		7.5 kJ/kg	(8.3 kJ/kg)
Mechanical Parameters			
Effective cold mass		22 tons	(22 tons)
Total weight		32 tons	
Mag. radial pressure(@z=0)		1.6 MN/m^2	
Axial total compressive. force		20 MN	
Superconductor			
Nb.Ti/Cu/Al ratio		0.5/0.5/29	
Overall conductor size		5.5 x 44	(4.6 x 44)
Nb.Ti/Cu cable size		1.6 x 5	
Load line ratio (@2,2 T, 4.2 K)		50 %	
RRR of Pure Al (@B=0 T)		750	
Yield strength of pure Al		>4 kgf/mm^2	

3. FIELD QUALITY

The field distribution of the air core thin solenoid has been evaluated with program ANSYS and an analytical calculation. Figure 5 shows the flux lines and contour plots with ANSYS in cylindrical symmetry coordinates. Figure 6 (a) shows field integral of (Integral **B x dl**) as a function of pseudorapidity, η . The field uniformity is improved by current grading with 20 %

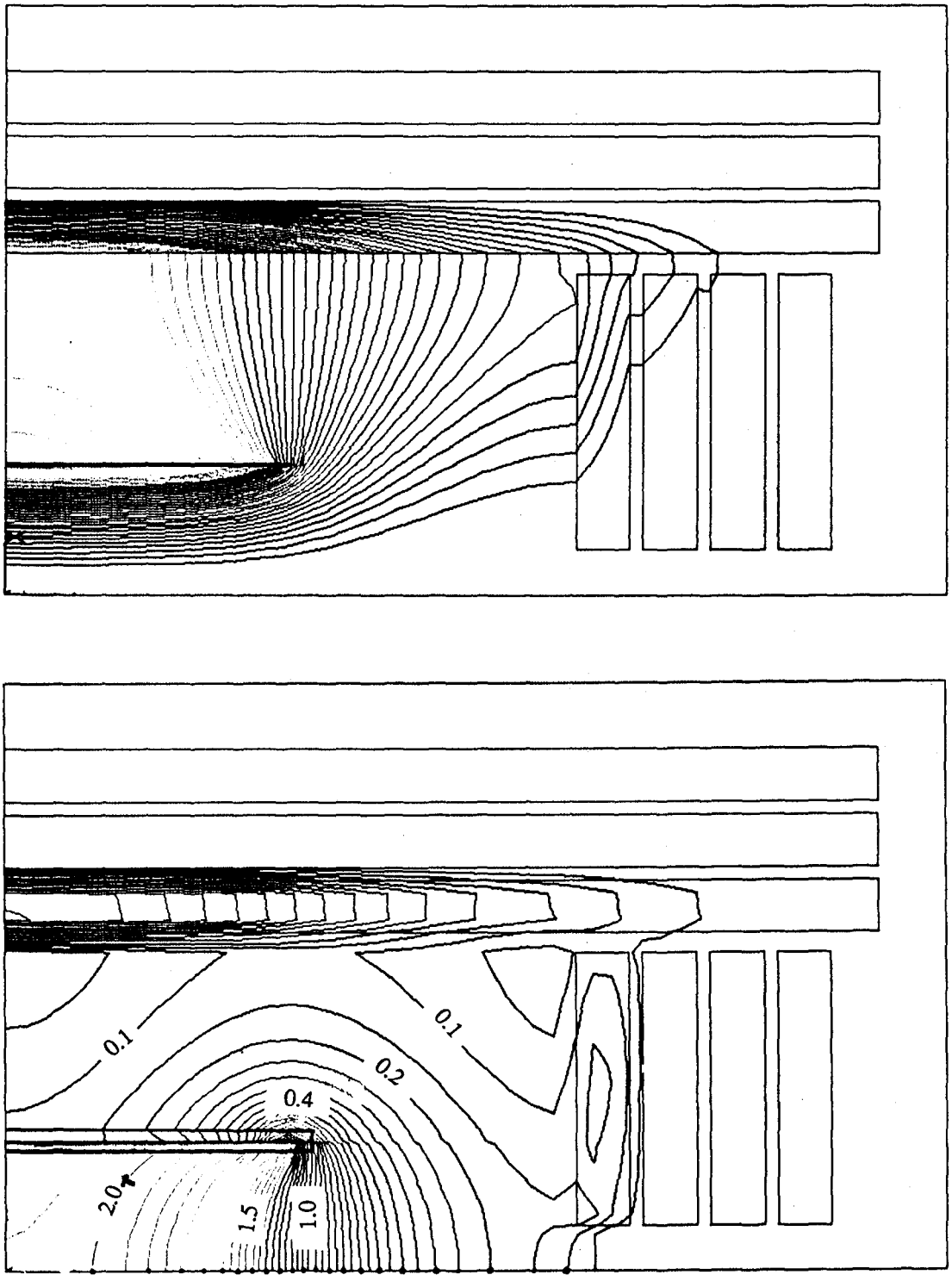

Fig. 5. Magnetic field distribution in the Type-S thin solenoid: flux lines (top) and field contour lines (bottom)

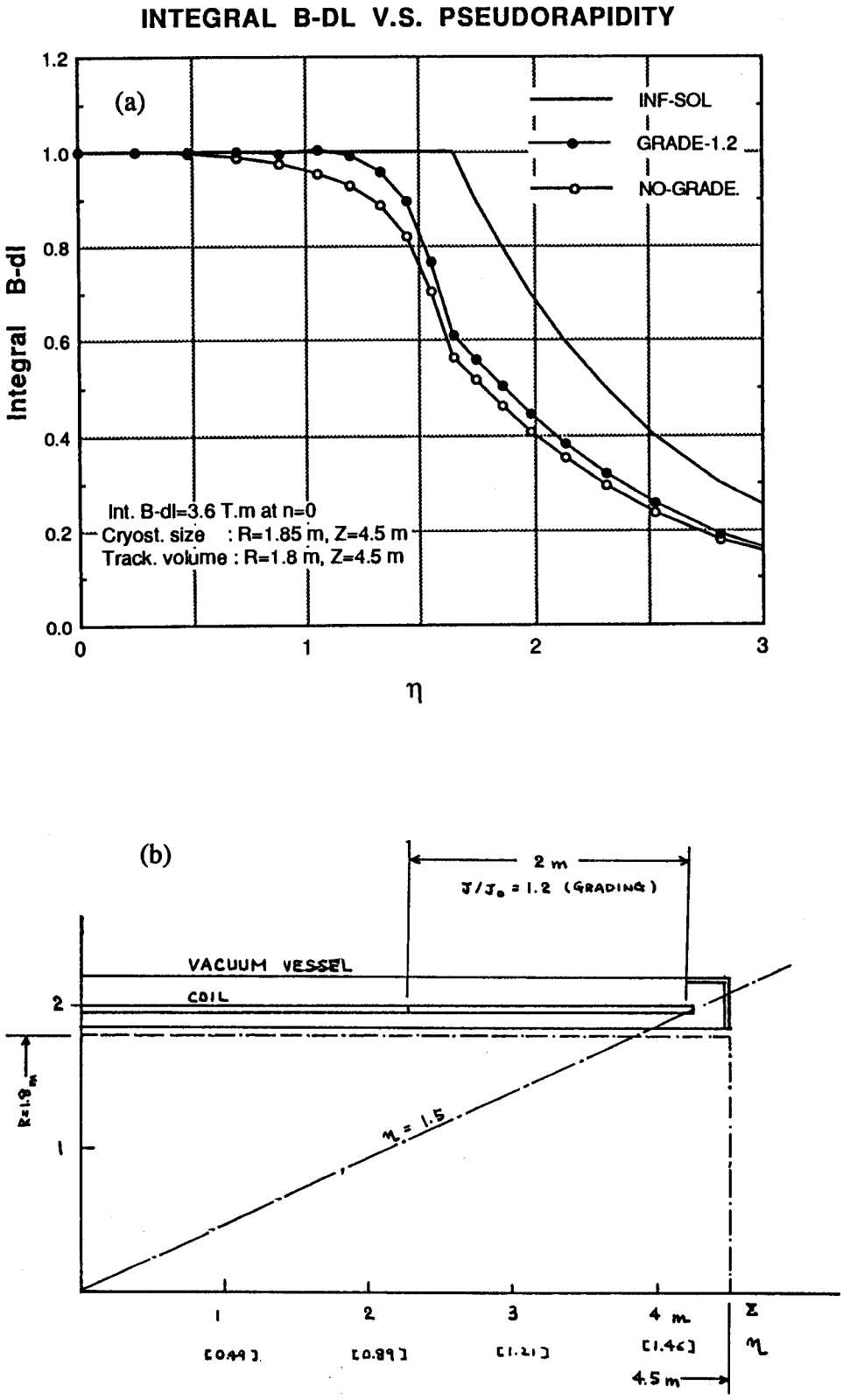

Fig. 6 (a) Field integral (B x dl) as function of pseudorapidity.
(b) Current configuration in the coil and field integrated volume.

higher current density at the coil end of 2 m as indicated in Fig.6 (b). The field integrals in each case are summarized in Table 2.

Table 2. . Integral **B x.dl.** as a function of pseudorapidity.

	Pseudorapidity	no-grading	w/ grading
Int. **B x.dl**	(η=0.)	3.6 T.m	3.6 T.m
	(η=1.0)	3.4 T.m	3.6 T.m
	(η=1.5)	2.7 T.m	3.0 T.m
	(η=2.0)	1.4 T.m	1.6 T.m

*Grading: 20 % high at the coil each end of 2 m in length.

4. TRANSPERENCY

The transparency of the solenoid wall was calculated as summarized in Table 3. The radiation thickness of 1.16 Xo and interaction length of 0.25 λo were obtained in this configuration. We assumed that the E/M ratio is 7.5 kJ/kg with no curent-grading at the coil end. In the case with current grading, the E/M ratio will be increased to 8.3 kJ/kg with the same physical design except for the current density at the coil end.. Figure 7 shows radiation thickness as a function of η.

Table 3. Transperency of the air core thin Solenoid (Type-S).

Element	t-eff	Xo	λo_
Outer vac. Vessel (Al-HNC)	8	0.090	0.0203
Outer rad. shield	2	0.025	0.0051
Outer support cylinder	31	0.348	0.0787
Superconductor			
(Al stab and strip)	42.5	0.478	0.1079
(Nb.Ti/Cu)	1.5	0.094	0.0086
(Ins)	2	0.011	0.0038
Inner radiation shield	2	0.025	0.0051
Inner vac. vessel	7	0.079	0.0178
Super-insulation	2	0.005	0.0023
Total		1.16	0.250

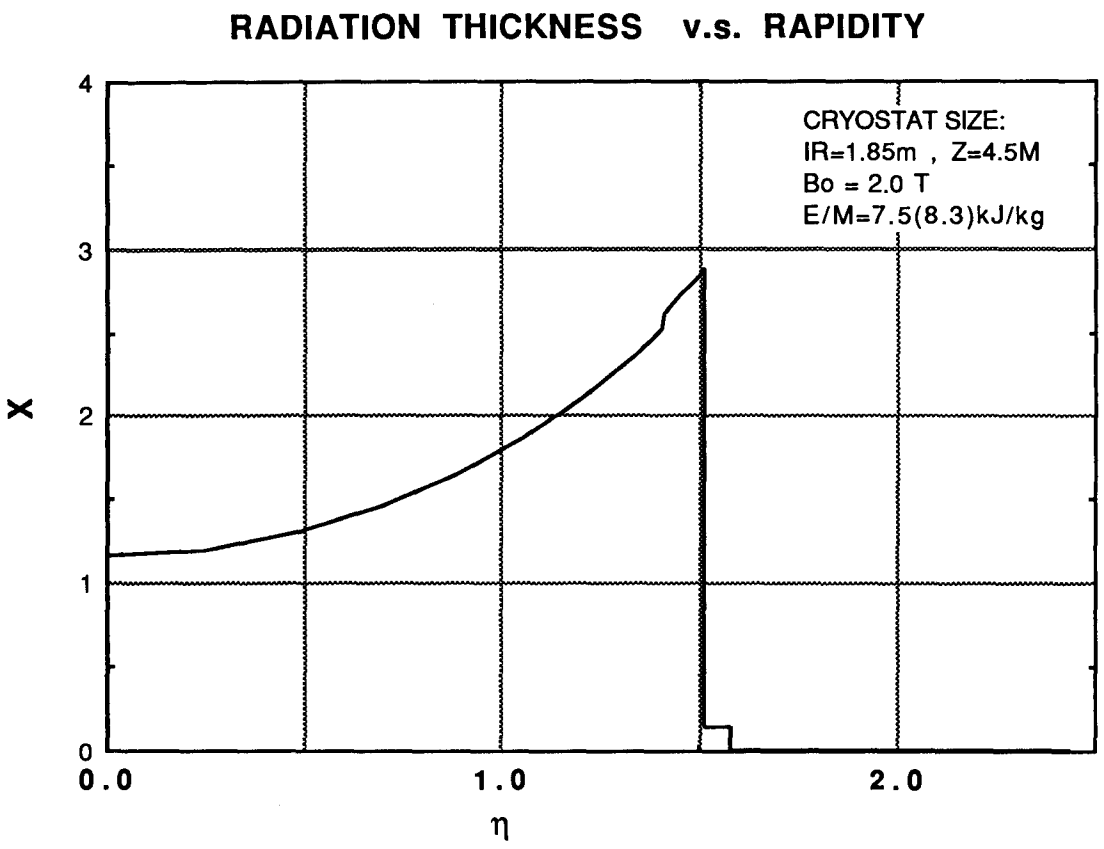

Fig. 7. Radiaton thickness of the coil as a function of pseudorapidity.

In the above table, the following basic parameters are assumed:

Material	Xo	λo
aluminum	89 mm	394 mm
copper	14.3 mm	151 mm
superconductor	16 mm	174 mm
GFRP	190 mm	530 mm
Mylar(SI)	287 mm	857 mm

5. MECHANICAL STABILITY

The mechanical stability in the coil and support structure was evaluated with the finite element analysis [4]. Main results are summarized in Table 4. The mechanical stress in each material is acceptable and the system should be mechanically stable enough.

As described below, it has been recently found that mechanical strength of pure aluminum can be improved by using cold-work technique in addition to control the purity of aluminum and heat treatment [5]. As a result, a yield (0.2 %) strength of 5.7 kgf/mm2 has been obtained at liquid nitrogen temperature, 77 K. This result enables us to consider mechanical design under fully elastic condition as simply described below.:

Radial magnetic pressure in a long solenoid is approximately given by

$$p_r = B_z^2 / 2\mu o = 1.6 \times 10E6 \ N/mm^2 = 0.16 \ kgf/mm^2$$

Therefore, hoop stress in the coil and support cylinder is

$$\sigma_\phi = R/t \times p_r = 2000/75 \times 0.16 = 4.3 \ kgf/mm^2 < 5.7 \ kgf/mm^2$$

On the other hand, the axial force into the coil in the long solenoids is approximately,

$$F_z = dE/dz = B^2 / 2\mu o \times V / z_{coil} = B_z^2 / 2\mu o \times S_{ap} = 2 \times 10^7 \ N = 2{,}000 \ tonf.$$

where E is the stored energy, z is the effective coil length, V is the magnetic volume, and Sap is the area of effective magnetic aperture. Therefore, the averaged axial stress in the coil and support cylinder is

$$\sigma_z = Fz / (2 \pi R t) = 2.1 \text{ kgf/mm}^2 << 5.7 \text{ kgf/mm}^2$$

Then, mechanical strain in the system should be less than 0.1 % as follows:

$$\varepsilon = \sigma / E < 5 / 7{,}000 = 0.07 \%.$$

We have seen, here, it is very helpful to improve the mechanical strength of pure aluminum in order to make sure the mechanical stability and reliability in the SDC thin slenoid, although it is also necessary to make a trade-off study between mechanical stability and quench behaviour.

Table. 4. Computed Mechanical stability of the SDC air core solenoid.

	Cylinder	Stabilizer	Insulator
Material	A5083-O	4N7 Al	GKG/Epoxy
RRR		810	
Young's modulus [kgf/mm2]	7500	7000	3450
Tension. Stress [kgf/mm2]			
Tensile strength (@LN2)	41.5		>20
0.2%Yield st.(@LN2)	16.9	>4	>10
Computed max. stress	9.3	3.8*	<4.2
Shearing Stresss			
Shearing strength(@LN2)			>1.5
Computed max. sh. stress			<0.4
Strain			
Computed max. strain	0.0012	0.0012	0.0012

* Yield strength of 4 kgf/mm^2 assumed

6. QUENCH PROTECTION AND SAFETY

The safety of the solenoid against quench was evaluated with the program "QUENCH". When the protection switch works correctly, the coil must be safe and the peak temperature in the coil is less than 60 K, because the main part of stored energy may be extracted and dumped into the protection resistor of about 0.1 ohms. When the protection switch is failed to work, whole the energy must be dumped into the coil. The peak temperature was computed to be below 100 K with the aid of pure aluminum strip quench propagator [6, 7]. In the worst case with no quench propagator and no quench-back action from the support cylinder, the peak temperature may reach close to 160 K. The calculated results are summarized in Table 5. We conclude this coil will be safe enough against quench.

Table. 5. Quench behaviour and safety condition.

	Switch active	Switch failed
Energy dump in coil / cylinder:	20 MJ	166 MJ
Eneregy dump ratio in coil/cyl.:	12 %	100 %
Averaged temp. rise in coil/cyl:	45 K	75 K
Peak temperature (Tp) in:		
coil with pure Al strips	<60 K	<100 K
coil w/o pure Al strips	<60 K	<160 K

* RRR=750 in Al stablizer and no current grading assumed.

7. STATUS OF R & D FOR THIN SOLENOIDS

7.1. R & D for Al stabilized superconductor

It is one of the most important R & D items to improve (or optimize) mechanical strength of aluminum stabilizer in the superconductor with keeping appropriate residual resistance ratio (RRR). Recently, this effort has been made in the R & D program for superconducting magnets in the particle astrophysics magnet facility project, ASTROMAG [8]. By using the

following process, we could control and improve mechanical strength of pure aluminum stabilizer.

Initial condition:		Purity...4N7 (99.997 %)
Process:	-	Co-Extrusion with Nb.Ti/Cu conductor,
	-	Drawing (Cold-work for Size Reduction),
	-	Heat treatment to simulate curing process of the coil.
Characteristics:		
RRR:		810 (R300 K / R 10 K)
Yield strength:		5.7 kgf/mm**2 (@LN2 temp.)
Ultimate Strength:		14.1 kgf/mm*2 (@LN2 temp.)

The cold work dependence of 4N7 pure aluminum on the mechanical strength is shown in Fig. 8. The above technique can be applied in the SDC solenoid and it may be possible to improve strength up to 6 kgf/mm^2.

The followings are further R and D work suggested to be done for the superconductor in the SDC solenoid.

- Optimization of conductor parameters, especially for RRR and Y.S.
- Co-extrusion with cabled superconductor,
- Large and high aspect ratio (aprox. 10) superconductor,
- Long conductor and superconducting joints,
- Electrical insulation: material, thinness and strength.

7.2 R & D for Honeycomb vaccum vessel

It is obvious that honeycomb structure in the outer vaccuum vessel much help to reduce material in the cryostat wall. The ordinal honeycomb structure, however, is not designed to have harmetic structure to use it in the cryostat. A R & D effort to develop completely harmetic honeycomb structure to guarantee the quality of metal sealing (10^{-9} Torr.l/sec) has been carried out at KEK [9]. A model honeycomb cryostat has been developed with the parameters given in Table 6. Figure 9 shows of pictures of the develped harmetic honeycomb

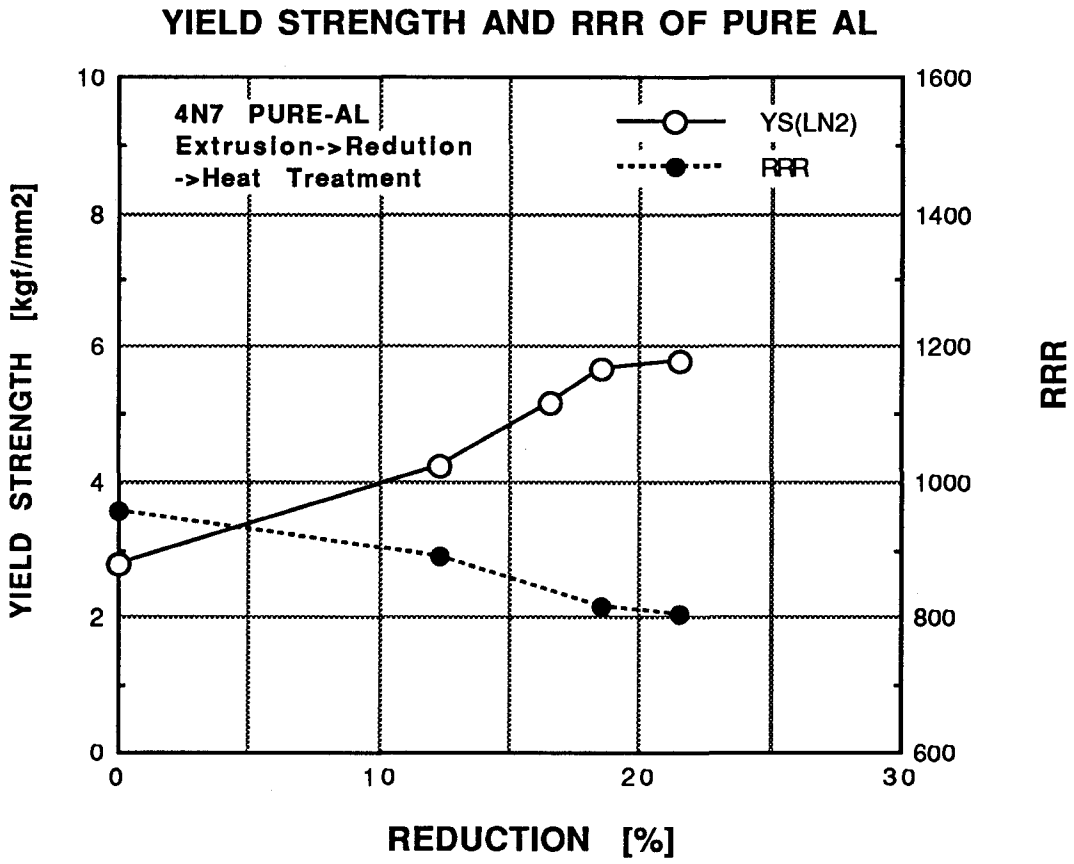

Fig. 8. RRR and yield strength of pure aluminum stabilizer as a function of size reduction ratio during cold work.

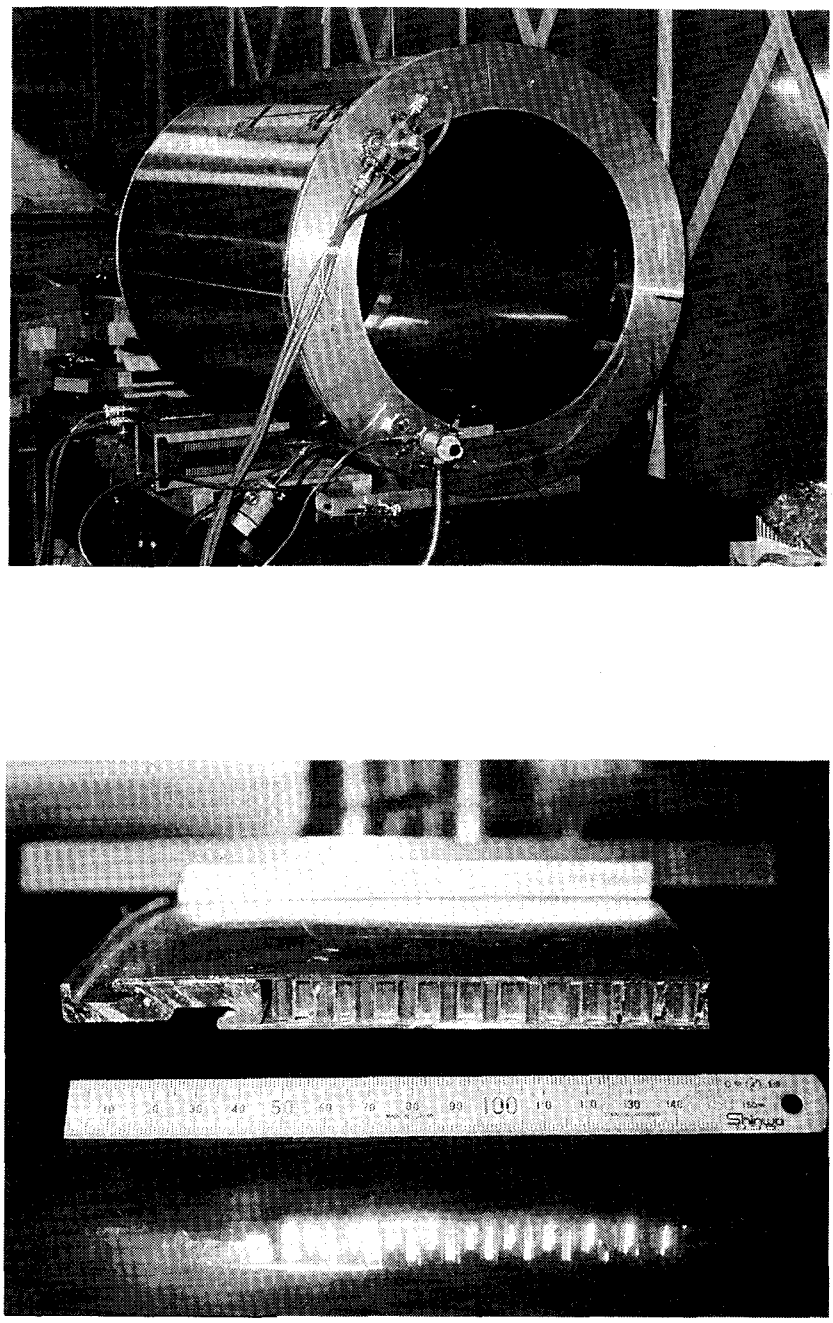

Fig. 9. A test cryostat fabricated with harmetic honeycom structure in outer wall.

Table 6. Main parameters of the model honeycomb vacuum vessel.

Vac. vessel:	1.2 m in diameter,
	1.5 m in length
Wall skin:	1 mm
core:	10 mm
End flange:	Isogrid configuration
	(t-min = 2 mm)
Buck. ext. pressure:	>5 atm (in design)
Weight reduction ratio:	1 / 3.6 (barrel wall)
	1 / 1.7 (end flange)
Performances:	
Pressure	5.4×10^{-6} Torr in 23 h
He Leak rate:	$<1 \times 10^{-9}$ Torr.l/sec
Build-up rate:	3.9×10^{-5} Torr.l/sec
Test pressure: difference	dP = 1 atm. external.

cryostat . A similar R and D work has been done by Toshiba Co. Ltd. to fabricate a super-conducting magnet for cosmic ray balloon experiments, as mentioned below.

7.3. R & D for High E/M magnet.

An air core thin solenoid (PCMAG) has been developed for the balloon borne experiment, BESS, to search for cosmic- ray antimatter with the following parameters [6,7].

size	:	1 m ϕ x 1.3 m
Bo	:	1.2 T
E	:	815 kJ
E/M	:	7 kJ/kg
X	:	0.2 Xo

The development has been successfully carried out and this experience is being very useful to consider the SDC solenoid design with a high E/M ratio of 7.5 kJ/kg or more. The pure

aluminum strip technique [6] to homogenize the coil temperature and to enhace quench propagation velocity will be also applicable in the SDC solenoid.

The following items are suggested for further R & D work to be done for the SDC coil fabrication:

- Full size (4 m diameter) coil winding to establish widing technique and reliable bonding of the coil to the outer support cylinder by using epoxy resin.
- Development of one quater scaled model magnet to investigate the higher E/M ratio (for example, 10 kj/kg) and full energy dump in the coil.

8. SUMMARY AND CONCLUSION

1. The air core thin solenoid is feasible to be built for the SDC detector with the following parameters:

Half aperture size	1.85 m(R) x 4.5 m (Z)	
Central magnetic field	2 Tesla	
		(w/ grading)
Integral B.dl (η =0.0)	3.6 T.m	(3.6 T.m)
(=1.0)	3.4 T.m	(3.6 T.m)
(=1.5)	2.7 T.m	(3.0 T.m)
E/M	7.5 kJ/kg	
Transparency (η =0.0)	1.16 Xo	
	0.25 λo	

2. Basic technologies to realize more tranparent solenoids are being established, i.e.:

   - E/M Ratio of 7 kJ/kg,
   - High strength pure Al stabilizer (Y.S= 5.7kgf/mm^2):
   - Honeycomb structure in outer vacuum wall

3. Further R and D efforts may be suggested to establish the technology to realize large scale air core thin solenoid for the SDC detector as follows:

- Higher mechanical strength in pure aluminum,
- Large and high aspect-ratio superconductor,
- Winding technique of the coil and reliable bonding techniq to the support cylinder

4. The air core solenoid (Type-S) has a disadvantage to support the axial magnetic force by itself due to no iron mirror boundary. On the other hand, it should be a big advantage that full excitation test can be completed without iron structure.

5. It is true that the iron dominated solenoid (Type-I and L) is free from the axial force in normal operation with iron structure. However, it is also true that the magnet must be tested in air before installation into the iron return yoke structure. It means that the iron dominated solenoid also will have to support large axial force in the performance test process in air, even if the full excitation is not intended.

6. We consider that the SDC solenoid magnet should be based on the concept of the air core solenoid design. The additional radiation thickness to take the air core solenoid design should be less than 10 %. Then, the solenoid can be fully tested in air in either case of the Type S or the Type I/L. It may be more conservative way to integrate the detector sytem reliably, and it is also important issue in the large scale detector construction.

ACKNOWLEDGEMENT

We would like to appreciate Toshiba , IHI and Furukawa Electric Companies for their kind co-operation during this work. We would like to thank Professor Hirabayashi, Professor Iwata, Professor Kobayashi and Prof. Takahashi for their continuous encouragement in this project.

REFERENCES:

1. SDC collaboration, Expression of Interest by the Solenoidal Detetor Collaboration (SDC) for the SSC experiment., May, 1990.
2. T. Kondo, "An air-Core Solenoidal Detector (ACS) for High pt Physics at the SSC," Fermilab Workshop on Solenoidal Detector for the SSC, Batavia IL (Sept. 1989)
3. S. Mori, "HCD Hermetic Collider Detector" Institute of Applied Phsics, University of Tsukuba, February, 1990.
4. The analysis done by Toshiba Co. Ltd and IHI Co. Ltd.
5. The conductor developed by The Furukawa Electric. Co.
6. A. Yamamoto et al., IEEE Trans., MAG, 24 (1988) p.1421.
7 Y. Makida et al., Proceeding of the 11th International Conference on Magnet Technology (MT-11), Tsukuba (1989).
8. A; Yamamoto et al,"Al based superconductor and a design for the ASTROMAG test coil," KEK-Astromag-TN-90-1 (Internal) (1990).
9. H. Inoue et al. R and D was done atb Mechanical Engineering Center at KEK.

Short Solenoid *v.s.* Long Solenoid — Effects on Tracking —

Y. Takaiwa,
KEK, Tsukuba, Ibaraki 305, Japan

Abstract

The effects of choice of solenoid design, short or long, on tracking is discussed. In particular, field non-uniformity effect is discussed. The emphasis is on the fact that no serious difference exists except available tracking volume sizes which cannot be decided solely by the tracking and solenoid system designs.

1 Introduction

Solenoidal detectors which will be built for the SSC experiments has to choose a design for the *solenoid.* There may be a few types of them. One extreme among them is a compact solenoid with rather high field to get enough analyzing power for the tracking device inside the solenoid which allows good hermeticity of the calorimeter outside. And the other extreme is a large solenoid to get good analyzing power of inner tracker with moderate field strength [1,2]. Before getting into dicussions of dependence on the solenoid types, the requirements to the inner part from the outer parts of the detector can be discussed as general comments. For example, calorimeter system, which is usually located after the inner tracker and the solenoid, does not like any thick material in front which causes premature shower development and dissipation of shower energy before the calorimeter. Also it does not like any structure giving dead or insensitive areas of the calorimters such as vessel walls and supports, cable paths, chimneys and even beam holes; they are causing bad hermeticity of the calorimeter system. Another fact to consider is that bigger size of the inner part requires bigger size and more material of the detector, which directly effects on its cost as a consequence.

Possible choices of the solenoid design are listed below and also requirements from the tracking system which might be relevant to the solenoid designs are also listed.

A)	Long	or Short
B)	Large	or Compact
C)	High Field	or Low Field
D)	Floating	or Close Return Yoke
E)	Thick	or Thin

wider η (pseudo rapidity) coverage	length	A) D)
long lever arm, large $Bd\ell$	radius, field strength	B) C)
simple in tracking analysis	field quality	D)
less problems due to background events (hit rate, radiation level, electric noises, etc.)	radius, field strength	B) C)
trigger efficiency for high p_T tracks	field quality	D)

Looking at these tables, the issues are categorized into two types; one is closely related to designing and engineering issues such as the size of the tracking volume and the other is relevant to capability of data processing mechanisms. The issues of the former type need to be discussed among the collaboration and the discussion will last until finallize the detector design, therefore I leave them to the discussion of the later time. In this note, the issue which is thought as a major problem related to the choice of the solenoid is discussed. That is the effect of non-uniform magnetic field which obviously classified into the second type mentioned above.

2 Magnetic Field Uniformity

It seems that two types of solenoid designs are seriously proposed for the general purpose detectors at the SSC which make significant difference in uniformity of the field; one is long solenoid and return yoke is closely attached to it, and the other is the air core type solenoid (ACS) which allows calorimeter system to surround tracking system with less inside structure putting return yoke at rather distant location. For the long type solenoid uniform field can be achieved well enough, however, it puts some structure of material

in front and within the calorimeter region. On the other hand, ACS type solenoid gives non-uniform field within the tracking volume, whose effects are the main subjects of this note. The analysis of tracking is simple when the field is uniform and it is probably easier and for triggering and event pre-selection. However, we would like to see the effect in detail to make final decision of the whole detector design; which difficulty is the more serious one, field non-uniformity to the tracking analysis or non-uniform structure of the calorimetry system. In order to start such studies the non-uniformity character of the ACS type solenoid is reviewed in this section. In the next section, the effect of it on the tracking is discussed.

In the ACS design used for this memo, a solenoid magnet has dimension of 1.8 m for inner radius and 2.0 m for outer radius of cryostat with 1.9 m of coil conductor radius and length is about 8 m for the cryostat and 7.7 m for the coil and it gives the field strength of 2.0 Tesla at the center. The liquid Ar calorimeter system covers it upto $\eta = 3$ and then muon toroid system which is also used as the flux return for the solenoid is put at the back of it. Because of this geometry magnetic flux generated by the solenoid is diffusing at the edge of the solenoid. The resulting magnetic field gives not only stray field in the calorimters but also non-uniformity inside the tracking volume.

A field map of the ACS is calculated by POISSON code and the contour maps of B_z and B_r for typical ACS solenoid is shown by Yamamoto in a previous talk. According to this it is seen that, although the central value of the longitudinal component of the field, B_z, is 2.0 Tesla, B_z at the edge of the solenoid is about 1.1 Tesla which is about 50% of deviation from the uniformity. Also the field has a radial component, B_r, which increases with increasing z and r, and it amounts to about 20% or 30% of central B_z value around the same region. To see the effect of this, it is useful to see the "analyzing power" of the solenoid, which is defined as an integral of the field strength that is felt by a moving charged particle, so called $Bd\ell$. In the case of solenoidal geometry, $Bd\ell$ is calculated as $\int B_z d\ell_T$, for longitudinal component only where the integral is made along the particle path. If, however, the radial component exists this should be modified to the form of $\int |\vec{B} \times d\vec{\ell}|$. The plots for them are shown in Figure 1. In this figure, integrals of $B_z d\ell_T$ and $|\vec{B} \times d\vec{\ell}|$ together with the case of uniform field are plotted against pseudo rapidity, η. In long solenoid design the field uniformity within the same tracking volume is so good that a curve for uniform field can represent as the long solenoid case.

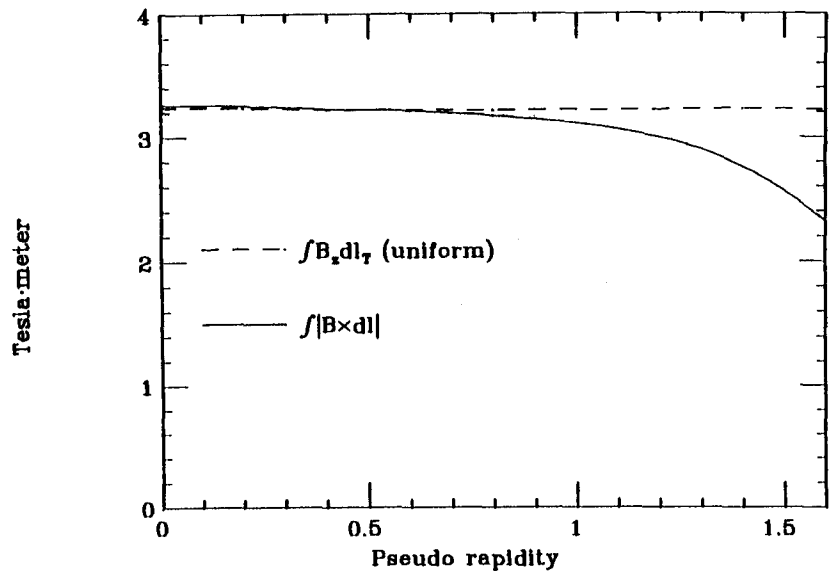

Figure 1: $Bd\ell$ in non-uniform Field

3 Tracking in non-uniform field

It is possible to perform track fitting no matter how the magnetic field is inhomogeneous if we know precise field map information in such field as we know from the experiences of bubble chamber and fixed target experiment data analysis. The procedure may be complicated and time consuming for really general cases, however, it can be simple and fast when the configuration of field is restricted to a certain type. As an example for this kind of situation is, in fact, a solenoid type magnetic field, as demonstrated by AMY experiment at TRISTAN.

The AMY is an existing detector that has similar non-uniform magnetic field of the solenoid [4], not because of the location of the return yoke but by the reason of strong field in a compact tracking volume, about 1.6 m in both diameter and length with 3 Tesla magnetic field at the center and field line generated by the solenoid is shown in Figure 2. The deviation from the uniformity in AMY is about 30% at the region of the edge of the solenoid, which is comparable to the ACS solenoid design. and the method of AMY to treat such field non-uniformity may be applicable to the ACS type solenoidal detector for the SSC experiments.

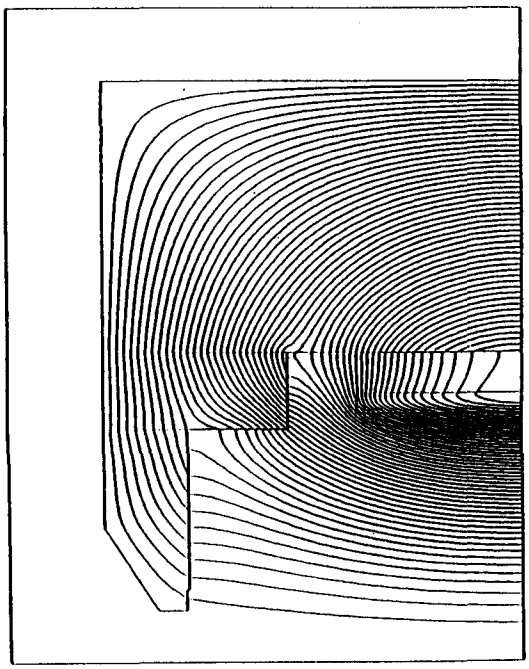

Figure 2: AMY solenoid field lines

The method of AMY called *"IMFIT"* [6] is summarized in the following. Starting from track parameters assuming uniform field, the track is re-fitted with the trajectory function of the particle in the inhomogeneous field. The trajectory function can be written down with a certain approximation for the field which is good enough for high p_T tracks within a reasonable range of η. Then, if necessary, the re-fitting is iterated to get better χ^2 using better approximation for the field.

The approximation to the field is made as the form of truncated power series in r and z assuming that it satisfies Maxwell equation and it can be expressed as

$$B_z(r,z) = B_0\{1 + \alpha(r^2 - 2z^2) + \beta(r^4 + \frac{8}{3}z^4 - 8r^2z^2)\}$$

$$B_r(r,z) = B_0\{2rz\alpha + \beta(-\frac{16}{3}z^3r + 4zr^3)\}$$

$$B_\phi(r,z) = 0$$

where B_0 is the central value of the magnetic field and α and β are the expansion coefficients. When β is small enough, it is not necessary to keep terms of fourth power of r and z and for this approximation ($\beta = 0$), trajectory function,

$$\phi = \phi(r; p_T, d_0, \phi_0, z_0, \cot\theta_0) = \arcsin\{\frac{r^2 - 2\rho d + d^2}{2(\rho - d)r}\} + \Delta\phi$$

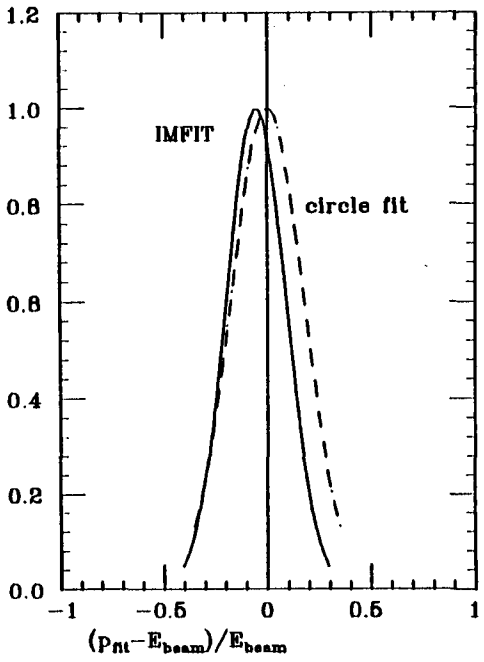

Figure 3: $(p_{fit} - E_{beam})/E_{beam}$ for intermediate angle Bhabha scattering of AMY

can be written down, again using expansion in r and z, where a term expressed by arcsin is the formula for uniform field and $\Delta\phi$ is the correction term. Further approximation that z trajectory function is not affected by the field non-uniformity is made here but it can be improved if necessary. The advantage of this IMFIT is that the trajectory function can be wriiten down analytically and minimization procedure requires no tracing of particles in the field but only calculation of polynomials and trigonometric functions.

Power of this method is demonstrated in analysis of intermediate angle Bhabha scattering of AMY experiment. In Figure 3 the distribution of $(p_{fit} - E_{beam})/E_{beam}$ of $e^{\pm}$ for intermediate angle Bhabha scattering ($\theta < 60°$) is shown. The solid curve is the result of IMFIT and the dashed curve shows the result without IMFIT. The picture shows the shift of the peak due to non-uniformity correction and deviation from the nominal value E_{beam} of IMFIT result is consistent with radiative correction.

For the purpose of illustration a following toy model is considered as a tracking system in the ACS solenoidal field. The ACS magnetic field is well approximated by the form of power series of r and z described above with the values of $\alpha = 0.00876m^{-2}$ and $\beta = -0.000463m^{-4}$. The value of β is small enough to be neglected in application of IMFIT; it is even better than AMY detector.

Tracking device with cylindrical (layer) geometry without specifying the technique is

Table 1: layer radius of tracking device

	radii of layers in cm			
super layer 0	$r_1 = 10.0$	$r_2 = 10.4$	$r_3 = 10.8$	$r_4 = 11.2$
	$r_5 = 12.0$	$r_6 = 12.4$	$r_7 = 12.8$	$r_8 = 13.2$
super layer 1	$r_1 = 50.0$	$r_2 = 50.8$	$r_3 = 51.6$	$r_4 = 52.4$
	$r_5 = 53.2$	$r_6 = 54.0$	$r_7 = 54.8$	$r_8 = 55.6$
super layer 2	$r_1 = 70.0$	$r_2 = 70.8$	$r_3 = 71.6$	$r_4 = 72.4$
	$r_5 = 73.2$	$r_6 = 74.0$	$r_7 = 74.8$	$r_8 = 75.6$
super layer 3	$r_1 = 90.0$	$r_2 = 90.8$	$r_3 = 91.6$	$r_4 = 92.4$
	$r_5 = 93.2$	$r_6 = 94.0$	$r_7 = 94.8$	$r_8 = 95.6$
super layer 4	$r_1 = 110.0$	$r_2 = 110.8$	$r_3 = 111.6$	$r_4 = 112.4$
	$r_5 = 113.2$	$r_6 = 114.0$	$r_7 = 114.8$	$r_8 = 115.6$
super layer 5	$r_1 = 130.0$	$r_2 = 130.8$	$r_3 = 131.6$	$r_4 = 132.4$
	$r_5 = 133.2$	$r_6 = 134.0$	$r_7 = 134.8$	$r_8 = 135.6$
super layer 6	$r_1 = 150.0$	$r_2 = 150.8$	$r_3 = 151.6$	$r_4 = 152.4$
	$r_5 = 153.2$	$r_6 = 154.0$	$r_7 = 154.8$	$r_8 = 155.6$

to give hit points of a charged particle on the cylinder surface with specified position resolution. And the system consists of one inner superlayer and six ordinary super layers each of which in turn consists of eight layers of such cylinders and inner super layer has better spatial resolution than the ordinary ones. The radii of these layers are shown in Table 1. A particle starts from the origin with given momentum in this tracking system which is located in the non-uniform field of the ACS solenoid, and the particle trajectory is traced in this volume using usual swimming routine in the magnet field, giving hit points on layers of the tracking devices with spatial resolution of 50 μm for the inner super layer and 200 μm for the ordinary super layers. Those hit points are subject to circle (helix) fit, and the curvature is translated into the p_T using typical B_z, say 2.0 Tesla, in the ACS field. Then the IMFIT is appllied to this model tracker and results are compared with the results without IMFIT.

The result of the game is shown in the Figure 4. for particles with 100 GeV/c of p_T at various η. In this Figure mean of the the fitted values for transverse momentum p_T^{fit} and $\Delta p_T/p_T^{fit}$ are plotted where Δp_T is the *r.m.s.* of the fitted p_T. The pictures clearly show that when no correction is made the effect of non-uniformity is seen as a shift of mean value of the fitted p_T upwards from the original p_T which is consistent with the fact that the analyzing power of the ACS solenoidal field decreases as η increases towards the

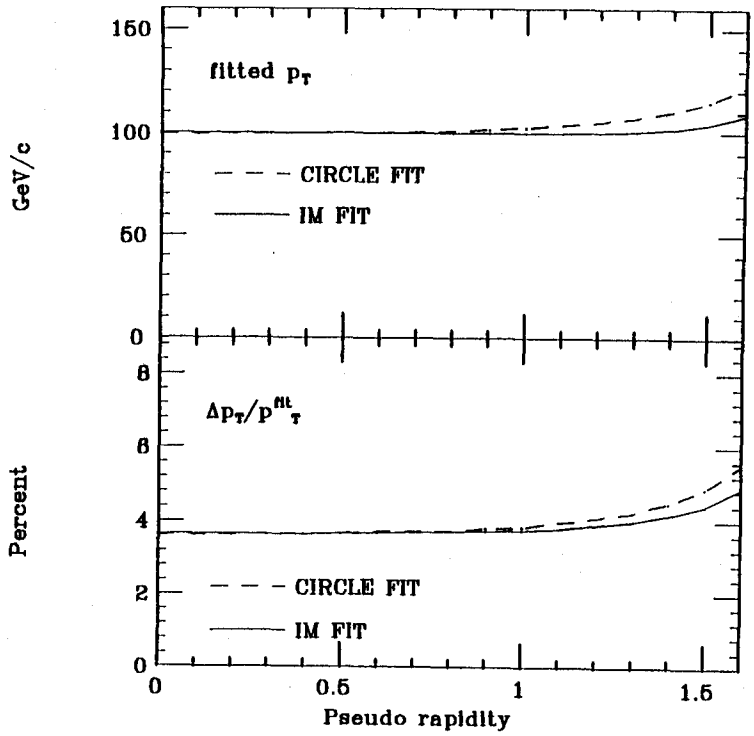

Figure 4: IMFIT for p_T

edge of the solenoid. They also show that $\Delta p_T/p_T^{fit}$ is increasing with increasing η which is also consistent with decreasing $Bd\ell$.

When the IMFIT is appllied the result indicates that the fitted p_T reduces to the true value for more extended region of η although it is still slightly higher than the actual p_T in the higher region of η. The resolution of the fitted p_T represented by the r.m.s. is also decreased from the values with uncorrected fitting result. Now we may hope that the air core solenoid type detector such as the ACS is not so terrible as is thought first, however, it is also true that situation is much simpler if we can achieve uniform field for the tracking volume.

4 Discussions

Observing that non-uniform magnetic field can be managed in the case of ACS solenoid, some discussions on the tracking are given below.

- Effects on Trigger and Fast Filter?

Naive estimate of p_T assuming uniform field is overestimation and more events than required will be selected, however, we won't miss good events. The question is whether we can achieve such accurate resolution that unwanted events are cut sharply at the threshold in any case by the algorithms used in these stages. Even so the effect of non-uniformity, if known in advance, can be managed somehow but the effect of this should not be significant.

- Pattern Recognition?

  Usually pattern recognition is performed by conneting locally constructed track segments (vectors) with adjacent segments, so that there will be no serious differences between uniform and non-uniform field because non-uniformity in such a local area is small. However, whether pattern recognition is possible or not is not a trivial question but requires substantial amount of efforts in both situations. At this stage most of computing power will be consumed in event analysis if general purpose pattern recognition is assumed. It may be better to think of simpler algorithms for certain classes of physics and events which can be used, in particular, for fast event selections.

- Efficient Track Fitting?

  Once pattern recognition is done well enough, then the track fitting is only a matter of computing power and usually it is only a fraction of pattern recognition stage. Addtion due to non-uniform field is not significant compared with the pattern recognition as is discussed above.

- Computing Power?

  It is obvious as dicussed above the pattern recognition will be a dominant part of data analysis for SSC experiments and it should be performed anyway. The question is whether existing algorithms for pattern recognition and track fitting are the realistic ones considering available computing power by the time of experiments. This depends on progress in technology of computing facilities and software which is very hard to predict for more than five years from now. The answer is not trivial and we may have to work until then, although there exists some projects and hope for them.

5 Conclusions

Finally I would like to list up conclusions of my talk.

- Almost of issues of tracking system are independent of the choice of solenoid types.
- The effect of non-uniform field is not a real issue but manageable reasonably well.
- The issues of tracking system are (1) size of $Bd\ell$ (high B field and long lever arm or large radius of the tracking volume), (2) enough η coverage (length of the tracking volume), and (3) the good performance of the tracking devices of the system.
- The size of tracking volume directly effects on the designs of the other parts of the detector system and its cost estimation which should be discussed based upon physics purposes and its cost effectiveness.

Obviously they do not cover all the possible questions, however, it may be said that the choice of the solenoid does not solve all such problems of tracking of SSC experiments. The tracking in SSC environment is really tough and we need to do lots of work in various aspects before final design and realization of the experiments.

References

[1] G. G. Hanson et al., *Proceedings of the workshop on Experiments, Detectors, and Experimental Areas for the Supercollider*, Berkeley 1987, p.340.

[2] J. Kirkby et al., *ibid.*, p.388.

[3] T. Kondo, KEK preprint 89-191, *Talk given at the Fermilab Workshop on Solenoidal Detector for the SSC*, September 25-26, 1989.

[4] K. Tsuchiya, S. Terada, A. Maki et al., *IEEE Trans. Magn. MAG-22 (1987)*

[5] A. Yamamoto, *private communication.*

[6] K. Ueno, *private communication.*

Coil Effects on the Calorimeter

J.M. Hauptman
Physics Department, Iowa State University
Ames IA 50011 USA

May 1990

Abstract

The long coil (CDF-like design) and the short coil (air-core design) are compared from the perspective of the calorimeter performance. We calculate and compare (i) degradation of jet energy resolution, (ii) fake missing E_T trigger rate, (iii) edge leakage in the bevel of the long coil, and (iv) readout problems for liquid ionization and scintillation technologies in the end caps. From the perspective of the calorimeter *alone*, that is, without consideration for tracking or triggering, the short coil geometry is preferable to the long coil geometry.

1. Energy Resolution Degradation

The geometry of the long and short coils for the present calculations are displayed in Figures 1(a,b), and the relevant dimensions are given in Table 1.

Table 1. Calorimeter, Coil, and Tracking parameters used in this study.

Parameter	Short Coil	Long Coil
$R_{calorimeter}$	200 cm	235 cm
$Z_{tracking}$	400 cm	500 cm
X_0^{coil}	1.0–1.2 X_0	1.0–1.2 X_0
λ_{coil}	0.25 λ_p	0.25 λ_p

The effect of dead regions, both in front of and also embedded within the calorimeter mass, on the energy resolution of the calorimeter have been parameterized using CCFR data.[1] Dead space in a calorimeter is characterized by its beginning point (λ_0) and its depth (λ), both in units of proton absorptions lengths. Thus, in the central region of the calorimeter, up to the transition between barrel and end cap calorimeters, both the long and short coils are characterized by

$$\lambda_0 = 0 \quad \text{and} \quad \lambda = \lambda_{coil}/\sin\theta, \tag{1.1}$$

where θ is the polar angle. For jets impinging on the end cap of the long coil geometry, the dead material of the coil is embedded within the calorimeter mass, and is characterized by

$$\lambda_0 = (R_{calor}/\sin\theta - Z_{tracking}/\cos\theta) \times (\lambda_{proton}/\text{cm}) \tag{1.2}$$

[1] M. Pang, J. Hauptman, "Hermeticity Study using the CCFR data", SSC-SDC-11 note, 15 Sept 1989.

and, of course, with the same projected depth for the coil,

$$\lambda = \lambda_{\rm coil}/\sin\theta. \tag{1.3}$$

The resolution degradation is expressed as a multiplicative factor of the form

$$1 + b_1\lambda + b_2\lambda^2 + b_3\lambda^3, \tag{1.4}$$

where the coefficients b_k are smooth functions of λ_0, and are parameterized from data by selectively removing measurement gaps from the CCFR calorimeter for many sets of (λ_0,λ) values, and fitting the resulting energy resolution. Thus, the energy resolution of a jet impinging on a calorimeter with dead material (λ_0,λ) is

$$\sigma/E = k/\sqrt{E} \times (1 + b_1\lambda + b_2\lambda^2 + b_3\lambda^3). \tag{1.5}$$

The degradation of the energy resolution on a jet energy measurement is then calculated by evaluating this function over the rapidity range $0< \eta <3$, and convoluting this with the transverse energy profile of a jet. This is shown in Figure 2(a) for the long coil with a bevelled edge, and in Figure 2(b) for the short coil. The differences are not large, although the long coil is slightly worse due to a deeped projected coil at larger z.

2. Fake Missing E_T Trigger Rate

One potential concern for an imperfect calorimeter is the trigger rate induced by simply mismeasuring the energy of a jet due to dead volumes in the calorimeter, and thereby satisfying a missing E_T trigger threshold. The production rate of QCD jets is about 10^4 Hz for several hundred GeV jets, and so even a small fraction of mismeasured QCD jets can be troublesome. I maintain the prejudice that the SSC will be an unforgiving machine, and that we will not have the luxury of making detailed and complicated corrections off-line (the corrections themselves will be arduous to calculate), with multiple off-line passes over the data as is sometimes done in the essentially zero-rate, zero-background environment of an e^+e^- machine. Therefore, we have calculated the absolute missing E_T trigger rate at $\mathcal{L}$=10^{33} $cm^{-2}sec^{-1}$ for the EHLQ single-jet cross section as a function of dead material (λ_0,λ) in a calorimeter, and as a function of the triggering threshold.[2] The fraction of QCD jets mismeasured by more than a specified triggering threshold E_{thr} is again parameterized from CCFR data. The resulting fake missing E_T trigger rate is calculated as

$$\text{Fake } \not{E}_T \text{ Rate} = \int_{-3}^{+3} dy \int_{E_{thr}}^{\infty} dp_T \frac{d\sigma}{dp_T dy} \times \mathcal{L} \times f. \tag{2.6}$$

where $\mathcal{L} = 10^{33}$ $cm^{-2}s^{-1}$ = 1 event/nanobarn/second is the luminosity, $d\sigma/dp_T dy$ is the differential cross section for jet+X from EHLQ, and f is the fraction of jets at momentum p_T which loose more than E_{thr} of energy due to dead spaces.

Evaluating this rate for the geometry of the long and short coils yields the differential trigger rates in rapidity shown in Figures 3(a-b), as functions of the

[2] M.Pang, J.Hauptman, "Fake Missing E_T Trigger Rates Due to Non-Hermeticity, Finite Energy Resolution, and Finite Depth (using CCFR data)", December 1989.

triggering threshold. Figure 3(a) is for the long coil with a bevelled edge, Figure 3(b) is for the long coil without a bevel, and Figure 3(c) is for the short coil. The total trigger rates integrated over rapidity are also shown on the plot, and are in the neighborhood of 20-30 Hz at a triggering threshold of 50 GeV for both coil geometries, although the long coil is slightly worse.

3. Side Leakage in the Bevel of the Long Coil

The long coil geometry may have a bevelled edge as in Figure 1(a), or have no bevel (strictly CDF-like) with a right angle corner on the end cap. Clearly the bevelled geometry is better, since in the strictly-CDF geometry incident hadrons may interact and begin to shower in the corner, whereupon the calorimeter mass ends and the shower particles are presented with 2.6 radiation lengths of dead material in the coil. If the shower development is such that the dead material is near shower maximum, then a large population of particles are at lower energies and may be absorbed in the coil. In CDF, a rapidity bite of about $\Delta\eta$=0.3 is lost for reconstruction purposes due to this corner.

Since the Workshop, I have run GEANT on a bevelled edge geometry, such as shown in Figure 1(a), including a three-part aluminum coil of about 1.1 X_0 total, and a 1.8 T field. Incident 100 GeV π^+ from the interaction region were aimed at the bevel with several impact parameters, δ, with respect to the edge. A few events are shown in Figures 4(a-d) for impact parameters of δ=1, 2, 5, and 10 cms. The same plots for an incident 300 GeV π^+ are shown in Figures 5(a-d).

There are three remarks to make here:

1. There can be substantial leakage out the side of the bevel, mostly in the form of low energy shower particles. The higher momentum particles of the shower maintain the incident particle direction, and stay within the calorimeter mass.

2. The tracking volume can be flooded with particles. Since the particles at shower maximum are low energy and nearly isotropic, many shower particles exit backwards into the tracking volume, and spiral through the outer layers of the straw tubes. This could disrupt the triggering layers, and augment the straw occupancy.

3. Some of the shower energy is transported to the "wrong" place in the calorimeter, e.g. from the plug region into the barrel, thereby leading to a mismeasurement of the p_T of the particle. This mismeasurement yields a larger p_T, and is therefore a concern for the trigger. However, this is ameliorated by the circumstance that the leaking particles are lower energy, and they are preferentially absorbed in the coil, leading in many cases just to missing energy, rather than misplaced energy.

A more detailed study with GEANT of jet mismeasurement is now in progress, however it will take some time for me to accumulate sufficient CPU.

Nevertheless, it seems clear that a geometric discontinuity of the magnitude of the bevel for the long coil is quite deleterious. Since jets from SUSY, the Higgs, or

other high-mass processes will have several hundreds of GeV and be isotropically distributed in the detector, a substantial fraction of all such interesting events will put a jet into this bevel region, so this becomes also an acceptance issue.

Item 2. above may prove to be the most serious: in effect, the single-track sensitive inner cavity of the detector is being exposed to the inside of a calorimeter, which has a very large particle population.

4. Transformer and Photomultiplier Readout

Recent measurements[3] have shown that the transformer coupling for a liquid argon calorimeter is reduced in a magnetic field, but that these tranformers can be effectively shielded up to about 0.5 T, but at present not beyond 0.5 T. This work is in progress. For photomultiplier readout of scintillator, the photomultiplier tubes can also be shielded up to about 0.5 T, but not beyond. The long coil maintains a full field of 1.8T throughout the end cap volume, with negligible field in the barrel region. The short coil design maintains field strengths as high as 0.6T in both end cap and barrel near the coil end, but lower fields elsewhere. The short coil might allow liquid argon or photomultiplier readout in the end cap. However, this issue may have a solution in either of these two cases: an electrostatic transformer for liquid ionization and fiber piping to the zero-field region for scintillator calorimetry. Therefore, the long coil may not be a problem for calorimeter readout.

Conclusions

We list the four criteria we have used to conpare the long and short coils in the table below. On all accounts, we find the short coil preferable to the long coil.

Criterion	Short Coil	Long Coil
Energy Resolution	Better	Worse
Missing E_T	Better	Worse
Geometric Discontinuity	Small	Large
Readout Restrictions	Weak	-

For the point of view of calorimeter performance *alone*, that is, without regard for the problems of tracking and triggering, we find that the short coil is a preferable geometry. Although some criteria offer only small (10-30%) quantitative differences between the long and short coil geometries, the leakage of low energy shower particles out the edge of the bevel into the tracking volume in the long coil design is a serious problem.

Acknowledgements

This work was supported mainly by DOE contract DE–AC02–85ER40193, and partially by the Associate Director for Planning and Technology Application, Ames Laboratory.

[3] F. Lobkowicz, presented at the SDC Calorimeter workshop at LBL, January 19-21, 1990; and also at the Liquid Argon Subsystem meeting, BNL, February 2-3, 1990.

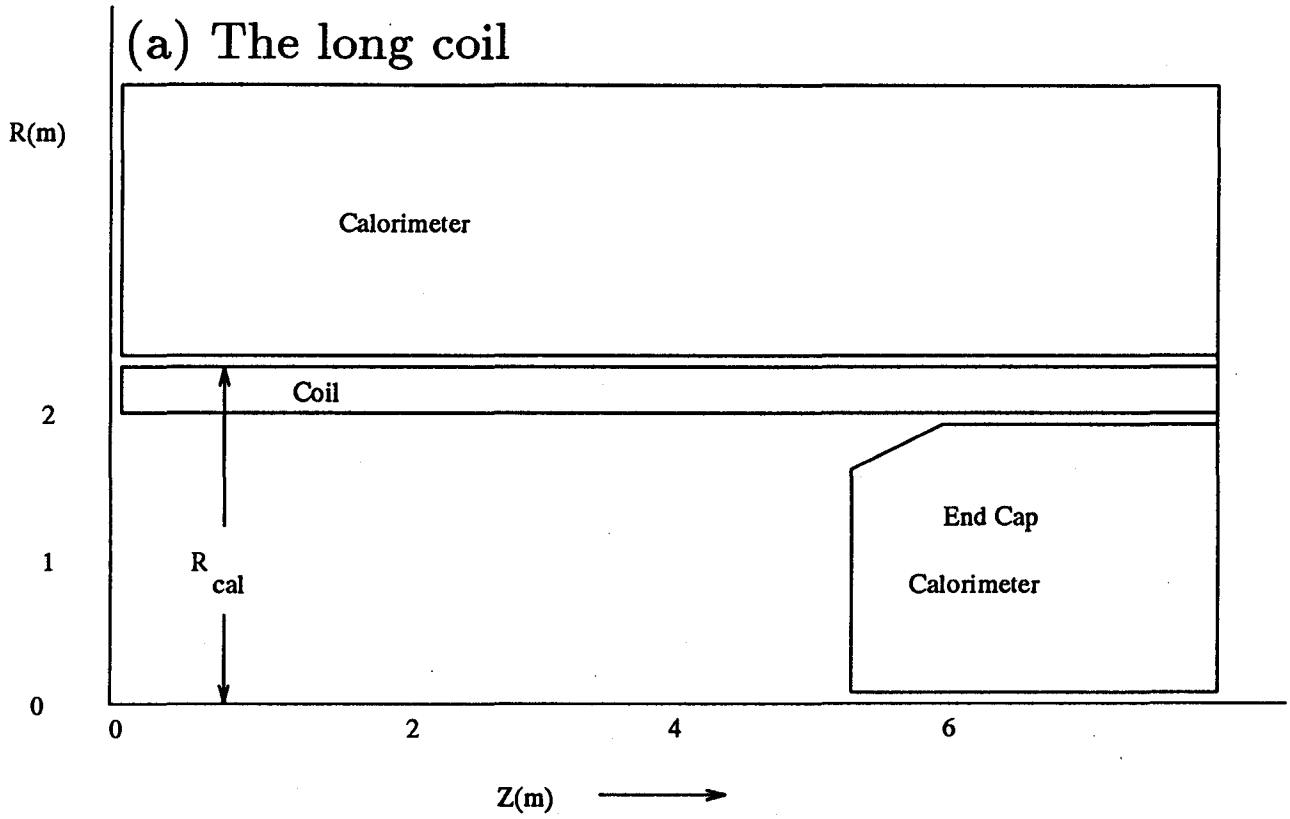

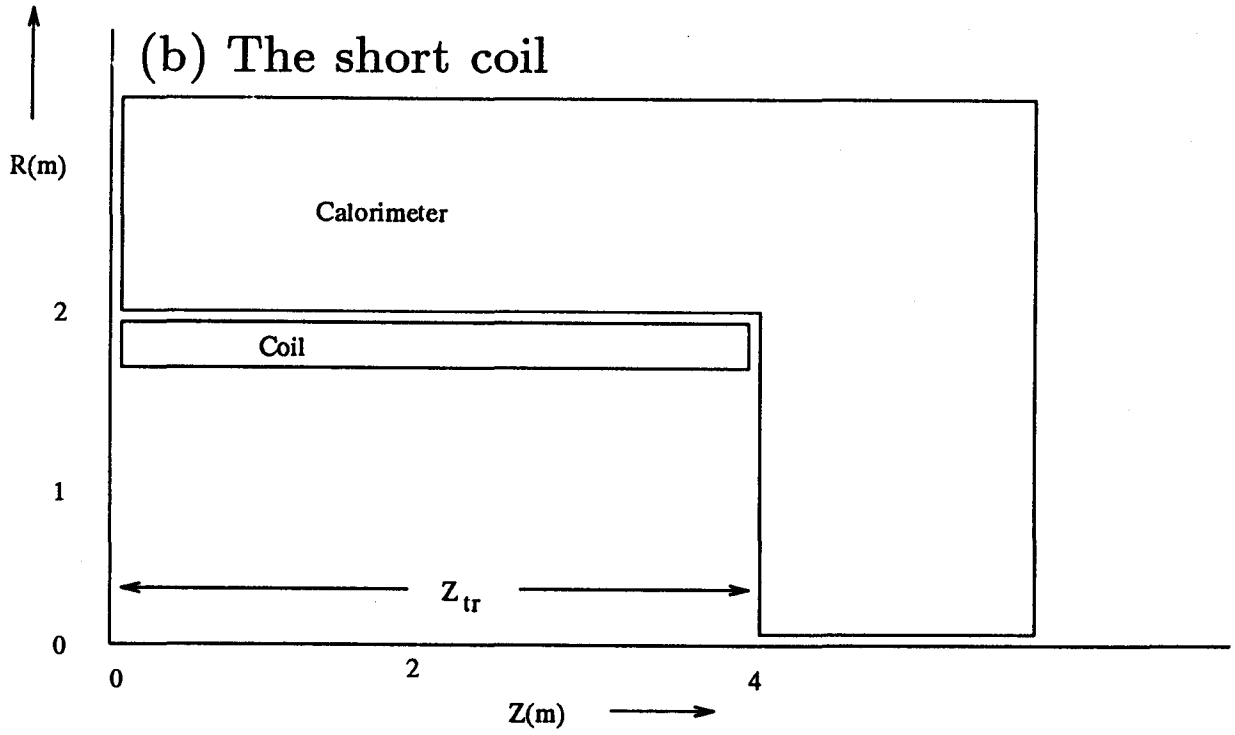

Figure 1. (a) The long coil (CDF-like) geometry, with a bevel. (b) The short coil (air-core-like) geometry. Dimensions are given in

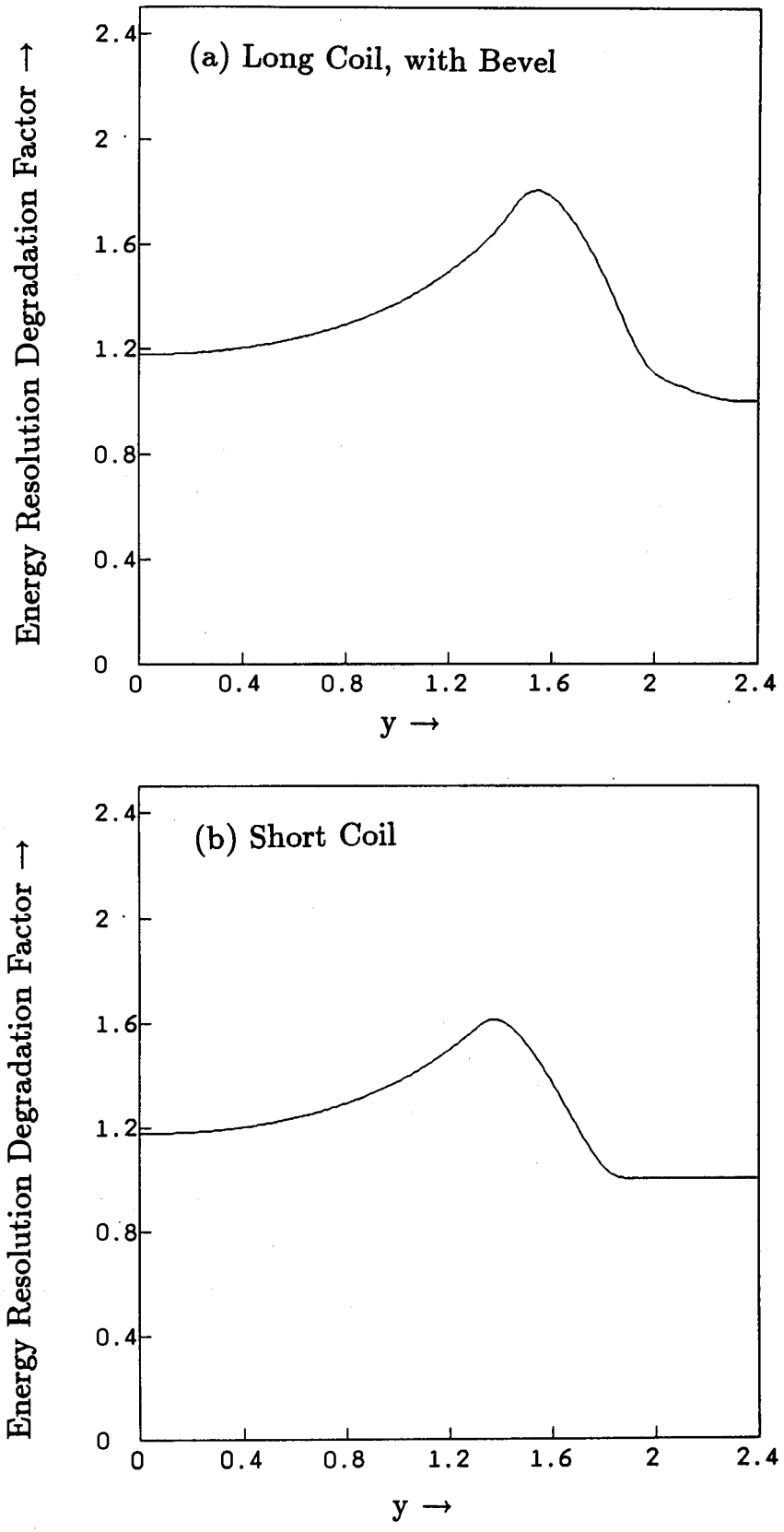

Figure 2. Energy resolution degradation due to the dead space of the coil for (a) the long coil with bevel, and (b) the short coil.

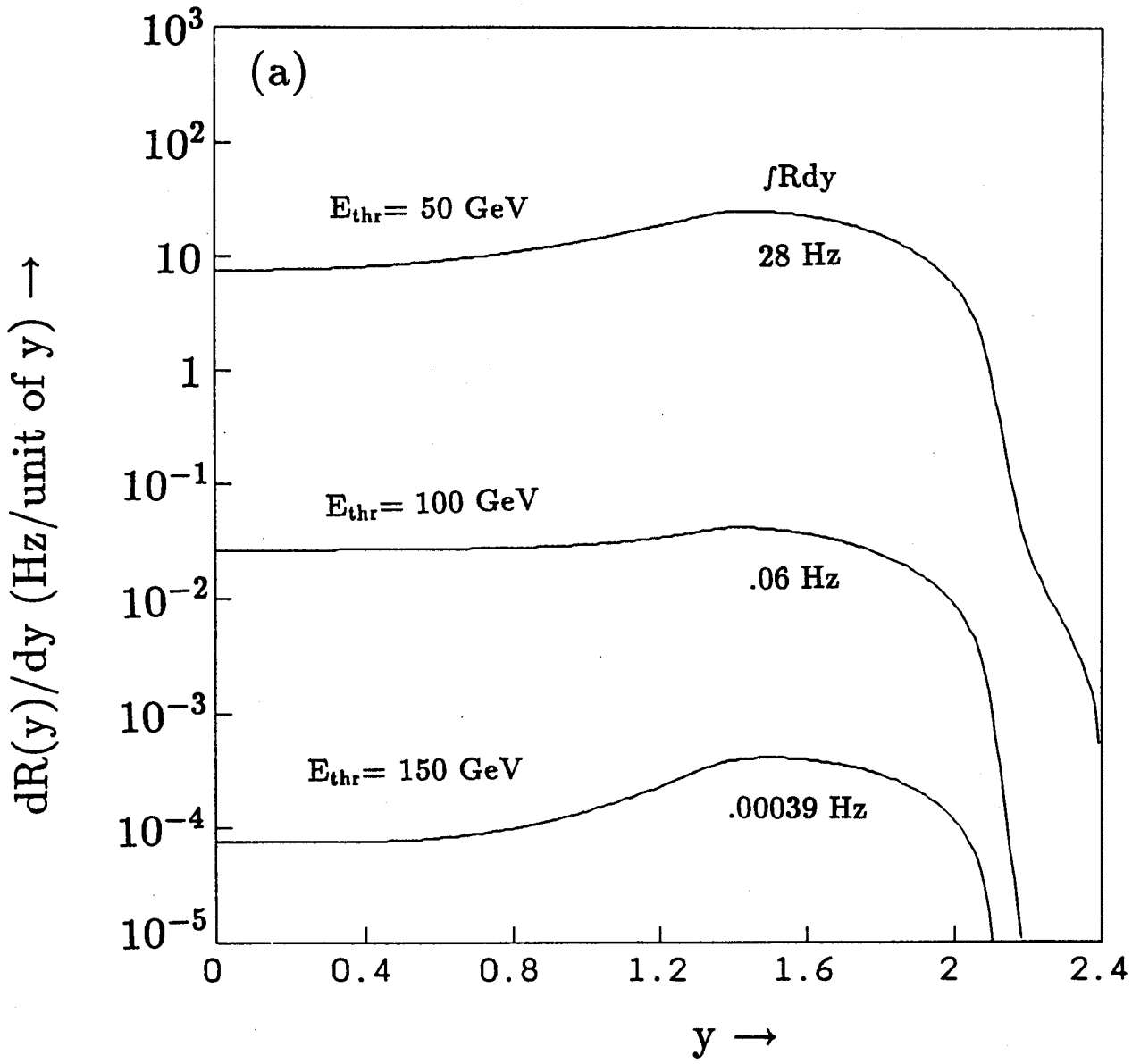

Figure 3. The trigger rate per unit of radidity due to fake missing E_T exceeding a specific triggering threshold, due to the dead space of (a) the long coil with bevel, (b) long coil without bevel, and (c) the short coil.

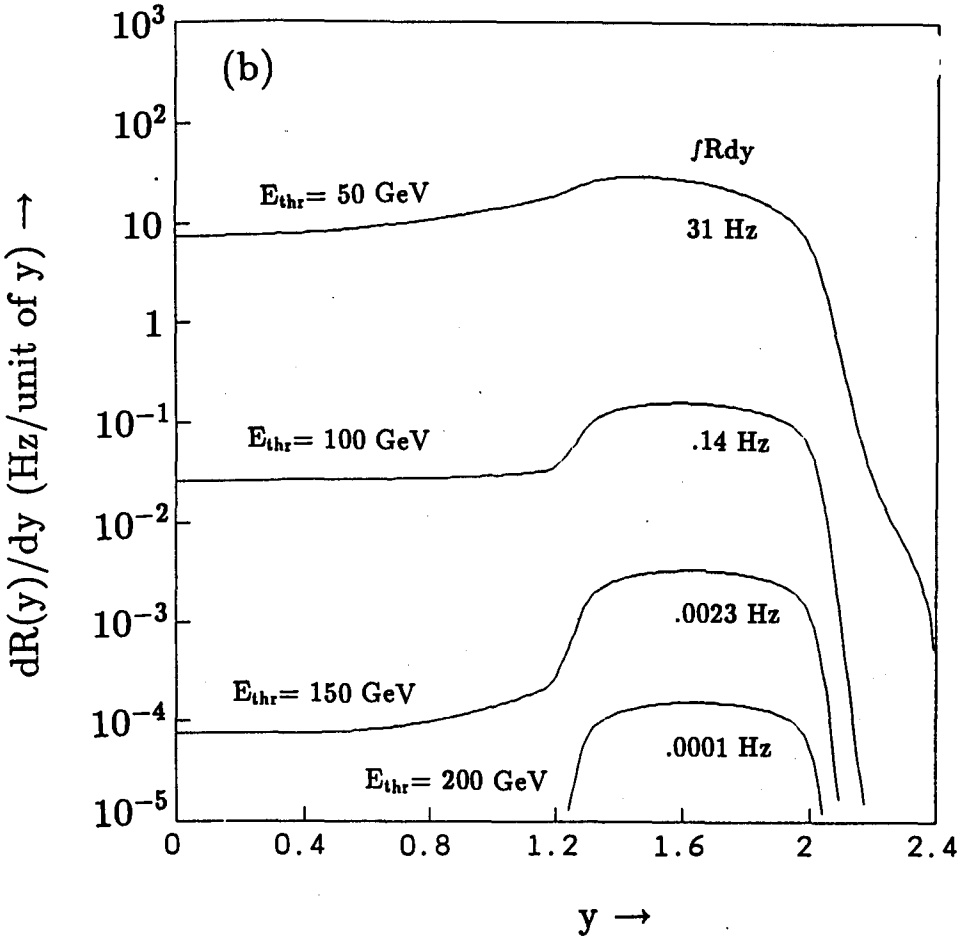
(b)
∫Rdy
E_{thr}= 50 GeV
31 Hz
E_{thr}= 100 GeV
.14 Hz
.0023 Hz
E_{thr}= 150 GeV
.0001 Hz
E_{thr}= 200 GeV
dR(y)/dy (Hz/unit of y) →
y →

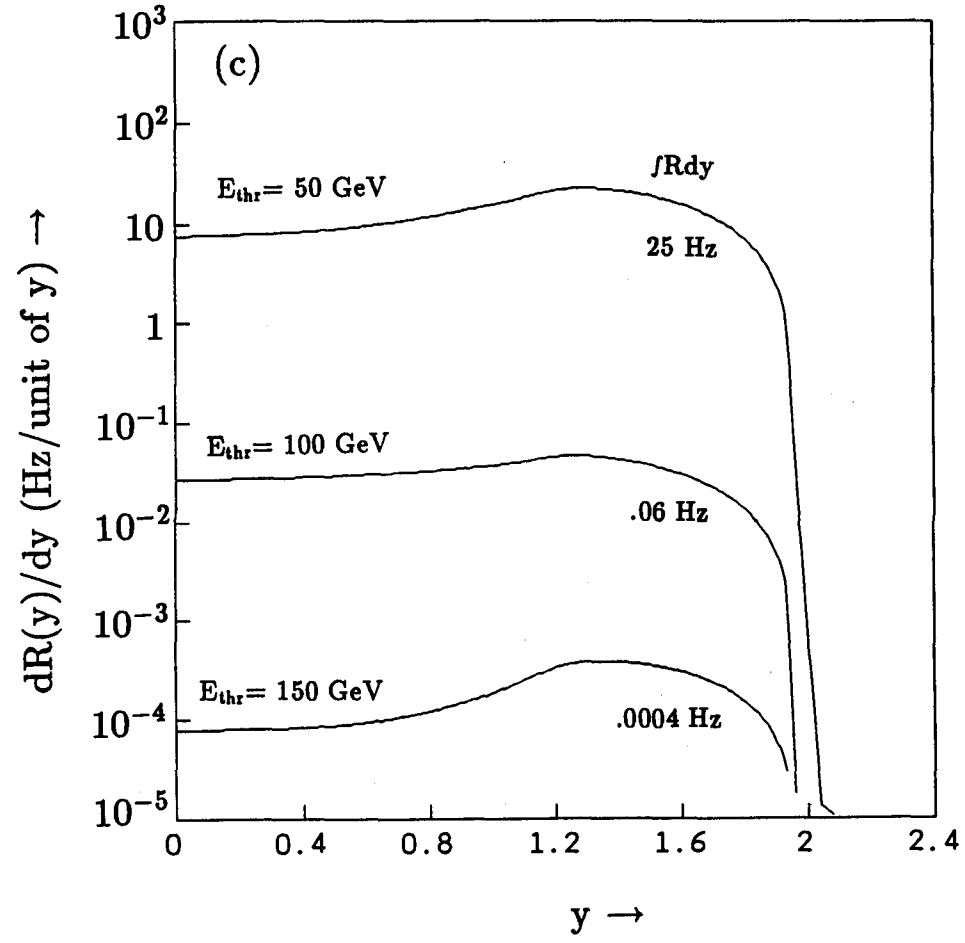
(c)
∫Rdy
E_{thr}= 50 GeV
25 Hz
E_{thr}= 100 GeV
.06 Hz
E_{thr}= 150 GeV
.0004 Hz
dR(y)/dy (Hz/unit of y) →
y →

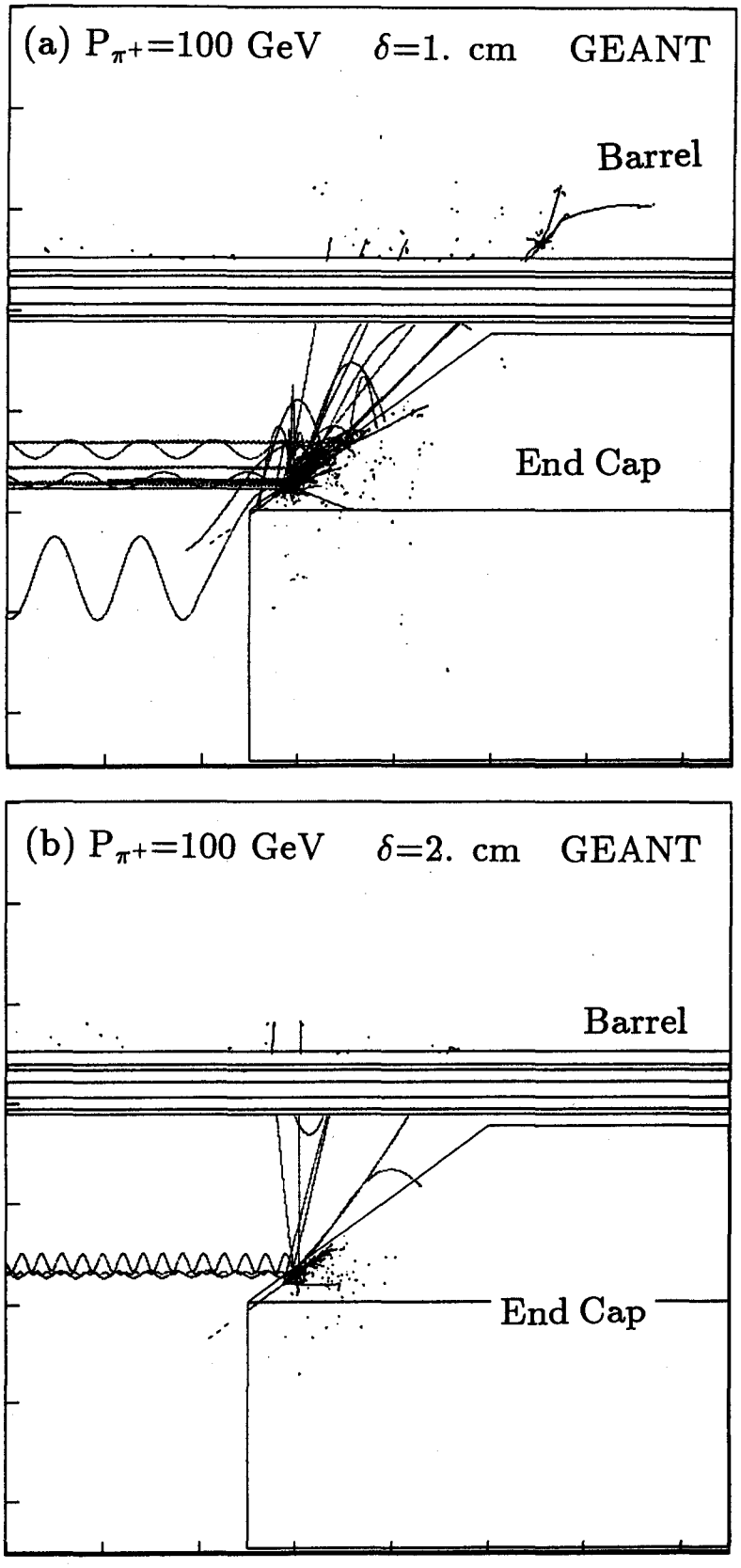

Figure 4. Several GEANT events with 100 GeV incident π^+ mesons striking near the bevel. The perpendicular distance of the π^+ from the projective bevel edge (δ) is (a) 1.0 cm, (b) 2.0 cm, (c) 5.0 cm, and (d) 10. cm. The field of view is 3m by 3m, centered on the bevelled edge.

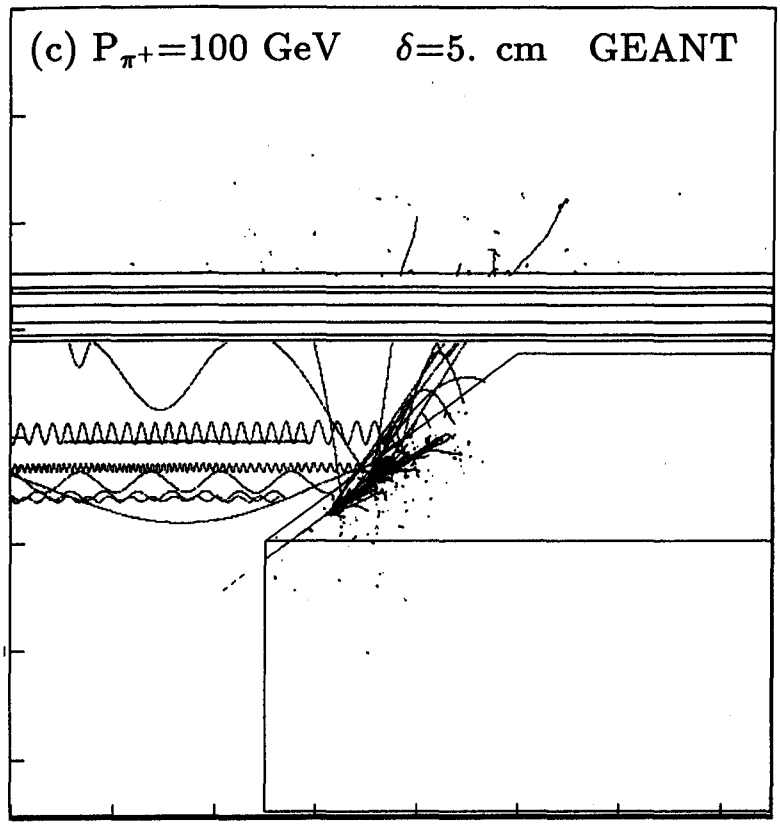
(c) P_{π^+}=100 GeV δ=5. cm GEANT

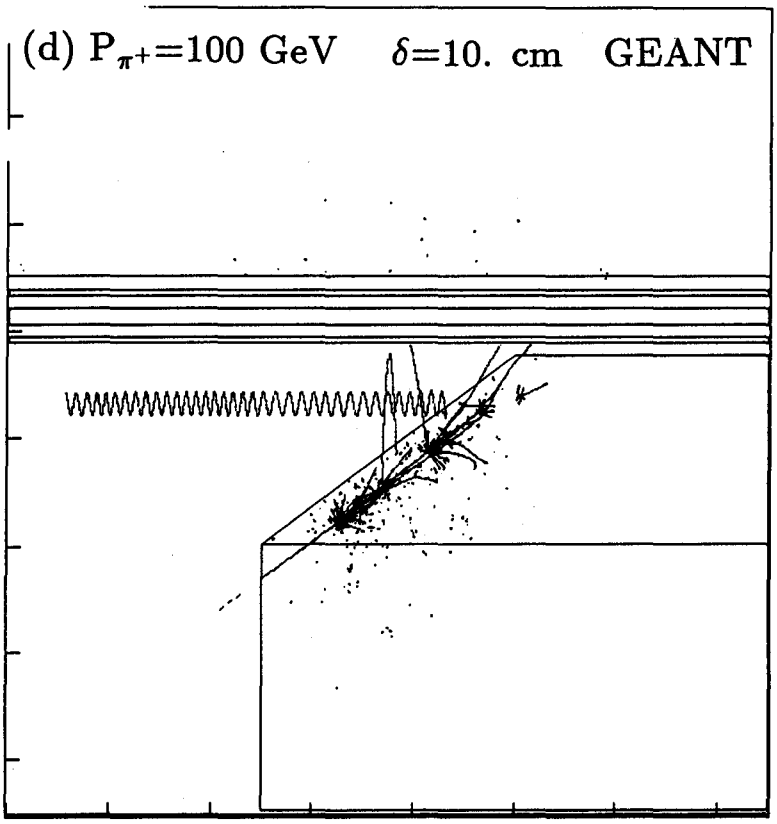
(d) P_{π^+}=100 GeV δ=10. cm GEANT

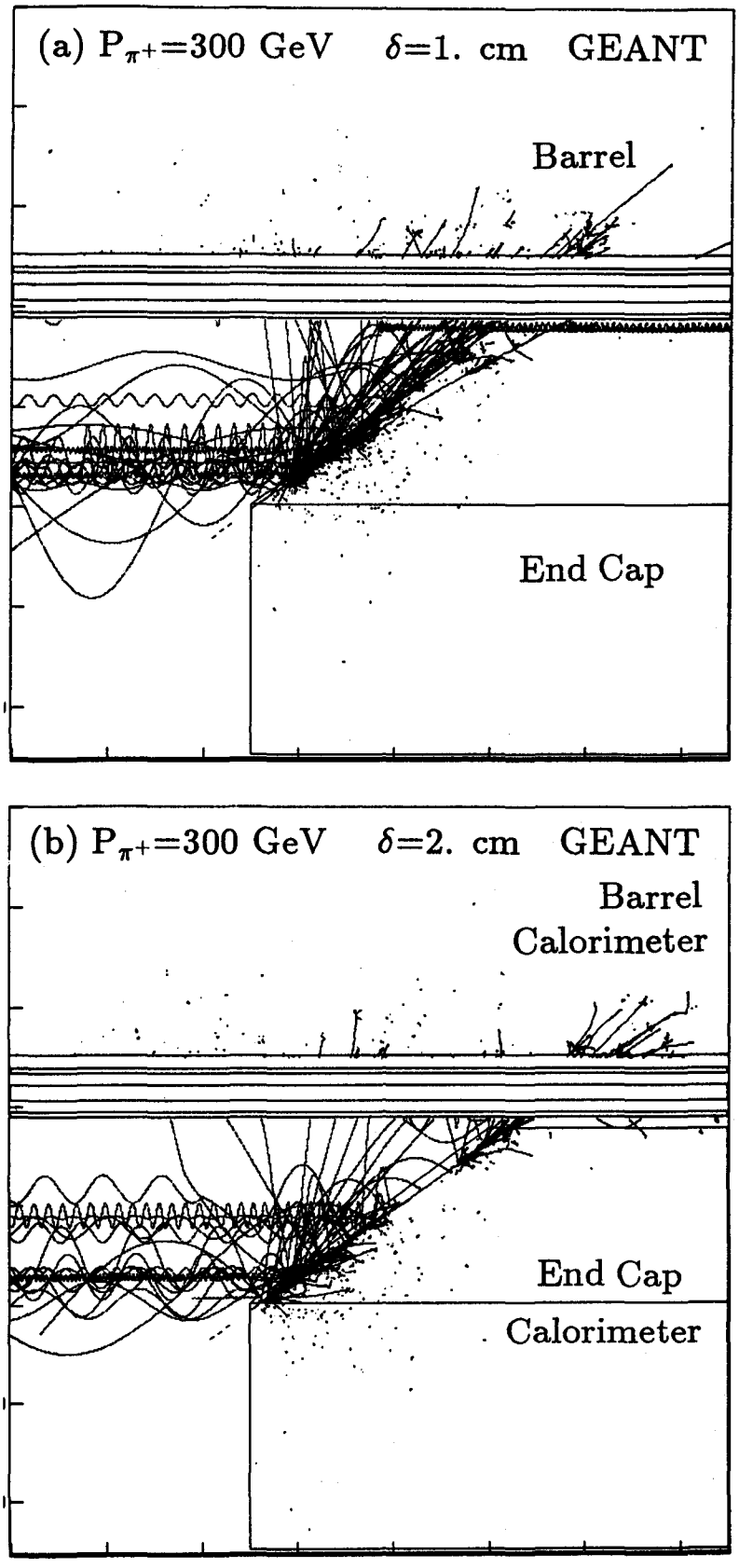

Figure 5. Several GEANT events with 300 GeV incident π^+ mesons striking near the bevel. The perpendicular distance of the π^+ from the projective bevel edge (δ) is (a) 1.0 cm, (b) 2.0 cm, (c) 5.0 cm, and (d) 10. cm. The field of view is 3m by 3m, centered on the bevelled edge.

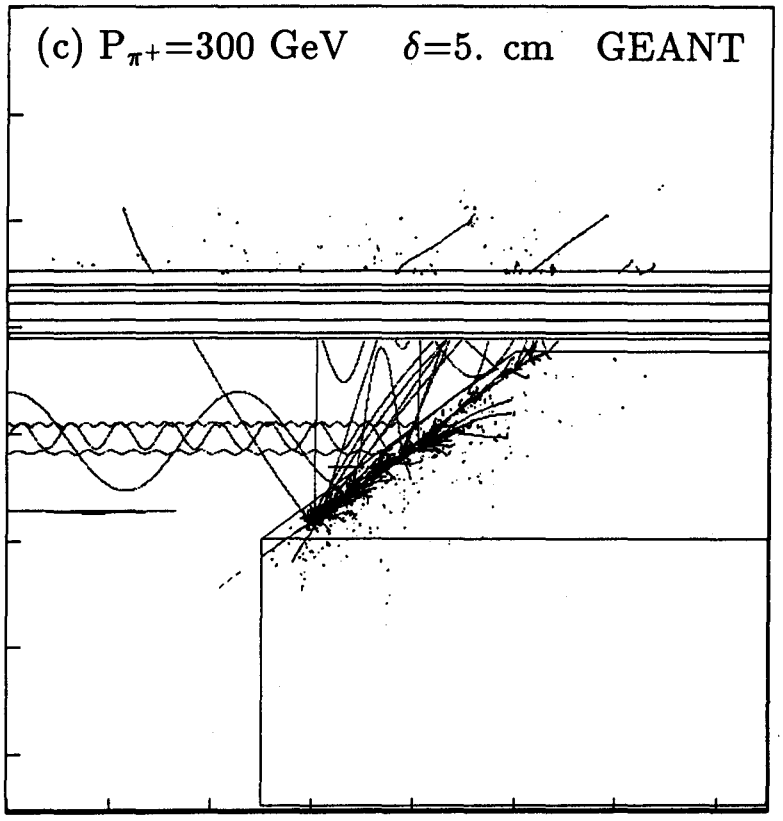
(c) P_{π^+}=300 GeV δ=5. cm GEANT

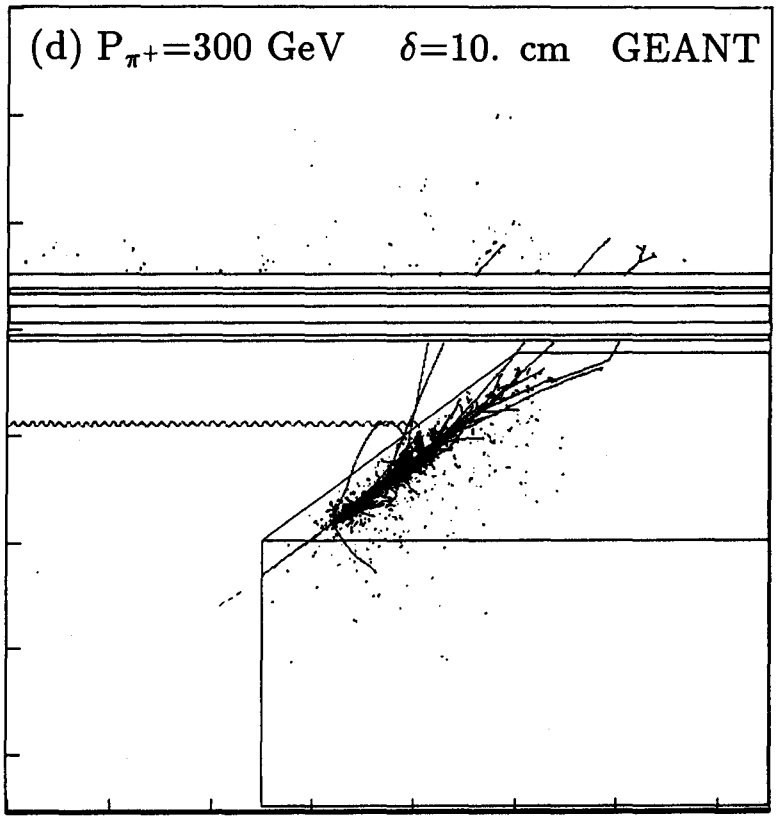
(d) P_{π^+}=300 GeV δ=10. cm GEANT

Electron ID

April 24, 9:00-10:55

Electron Identification at CDF

Shinhong Kim
The CDF collaboration*
Institutes of Physics, University of Tsukuba
Tsukuba, Ibaraki, Japan

Abstract

Electron identification at CDF is performed using the information of lateral and longitudinal shower spread, the track-cluster position match and the energy-momentum match. The tracking chamber with a solenoidal magnetic field at CDF is useful for rejecting the backgrounds such as the $\pi^{\pm}$-π^0 overlaps, the π^0 /γ conversions and interactive $\pi^{\pm}$ in electromagnetic calorimeter: The energy-momentum match cut can decrease the background due to the $\pi^{\pm}$-π^0 overlaps for non-isolated electrons with Et above 10 GeV by a factor of 20. The conversion electrons are identified using track information with an efficiency of 80 ± 3 %. The charge of electrons from W decay can be determined in the pseudorapidity range of $|\eta| < 1.7$ at CDF. The charge determination is important for background estimation of Drell-Yan physics and heavy flavour physics.

* The CDF collaboration
Argonne National Laboratory - Brandeis University -
University of Chicago - Fermi National Accelerator Laboratory -
Laboratori Nazionali di Frascati, Instituto Nationale di Fisica - Harvard University -
University of Illinois, Urbana - National Laboratory for High Energy Physics (KEK) -
Lawrence Berkeley Laboratory - University of Pennsylvania -
Instituto Nationale di Fisica Nucleare, University and Scuola Normale Superiore of Pisa -
Purdue University - Rockefeller University -
Rutgers University - Texas A&M University -
University of Tsukuba - University of Wisconsin

1. Introduction

The CDF proton-antiproton collision experiment logged data on tape corresponding to an integrated luminosity of 4.4 pb^{-1} between September 1988 and May 1989. The electron identification algorithm at CDF has been studied using this data sample. The CDF detector is a 4π general purpose detector with a solenoidal magnet. The electromagnetic calorimeter is divided into the central ($|\eta| < 1.1$), plug ($1.1 < |\eta| < 2.4$) and forward ($2.2 < |\eta| < 4.2$) regions. The electron identification in the central and plug region will be discussed.

In section 2, we describe briefly the CDF detector relating to the electron identification in the central and plug region. Further details of the CDF detector is obtained elsewhere[1]. The electron identification is described with a stress on the energy-momentum match in the central and plug region in section 3. The rejection of conversion electrons and the charge determination of electrons are discussed in sections 4 and 5, respectively.

2. The CDF Detector

The central tracking chamber (CTC) inside of a 1.5 Tesla solenoidal magnet provides charged particle tracking and momentum reconstruction. The chamber has 84 sense layers grouped into 9 superlayers with radii between 31 and 132cm. Five of superlayers consist of 12 axial wires and four stereo superlayers consist of 6 sense wires tilted by $\pm 3°$ to the beam direction which gives the z hit position. The CTC gives the momentum resolution of $\delta P_T/P_T^2 = 0.0011$ (GeV/c^{-1}) in the pseudorapidity region of $|\eta| < 1.0$ for vertex constraint tracks.

The innermost detector required in electron identification is the Vertex Time Projection Chamber (VTPC) with an active area of radii between 6.8 and 21 cm. The VTPC provides good r-z reconstruction in the pseudorapidity range of $|\eta| < 3.5$ and is used to determine the z position of the primary event vertex with an accuracy of ~3mm rms. It is also used for the rejection of conversion electrons at its outside wall, and the track-cluster position match in the plug region.

The electromagnetic (hadron) calorimeter uses lead sheets (iron plates) alternated with scintillator as the active medium in the central region, and with propotional chamber with cathod pad readout in the plug and forward region. All calorimeters have a tower geometry where each tower is projective, i.e., points at the interaction region. The size of tower was optimized to give the lateral spread information of jets and electrons, and is 0.1 in eta and 15° (central region) or 5° (plug and forward regions) in azimuthal angle. Since

the central electromagnetic calorimeter (CEM) has coarser lateral segmentation than the plug and forward electromagnetic calorimeters (PEM and FEM), it has a layer of proportional chamber (CES) placed approximately at a shower maximum (6 radiation length) to obtain accurate shower centroid and lateral shower profile. The electromagnetic calorimeters have a spatial resolution of ~ 2 mm over the full solid angle. In the PEM, there are three samples in depth to provide the longitudinal shower shape information.

3. Electron Identification

Electron identification at CDF is performed using the information of lateral and longitudinal shower shape, the track-cluster position match and the energy-momentum match. The above information is given by the following quantities in the central and plug region:

Table 1. Measured Quantities for Electron Identification

information	central region	plug region
longitudinal shower shape	HAD/EM	HAD/EM $\chi^2_{longitudinal}$
lateral shower shape	χ^2_{strip} χ^2_{wire} LSHR	$\chi^2_{lateral\ 5x5}$ $\chi^2_{lateral\ 3x3}$
track-cluster position match	ΔZ, $\Delta r\phi$	$\Delta\eta$, $\Delta\phi$
momentum-energy match	E/P	E/P (restricted region $\lvert\eta\rvert < 1.7$)
Isolation	ISOL(R < 0.4) Border	ISOL(R < 0.4)

Here,

(a) Had/EM is the ratio of hadronic to electromagnetic energy deposition.

(b) $\chi^2_{longitudinal}$ is the deviation of the measured longitudinal shower shape from testbeam electron shower in the PEM.

(c) χ^2_{strip}, χ^2_{wire} and LSHR are the deviation of the measured lateral shower shape from testbeam electron shower with CES strips, CES wires and CEM three towers, respectively.

(d) $\chi^2_{lateral\ 3x3}$ and $\chi^2_{lateral\ 5x5}$ are the deviation of the measured lateral shower shape from testbeam electron shower with PEM 3x3 towers and PEM 5x5 towers in $\eta x \phi$, respectively.

(e) ΔZ and $\Delta r\phi$ are the geometrical matching of the shower centroid measured in CES with a track reconstructed in CTC in the z and ϕ directions, respectively.

(f) $\Delta\eta$ and $\Delta\phi$ are the geometrical matching of the shower centroid measured in PEM towers with a track reconstructed in CTC or VTPC in the η and ϕ directions, respectively.

(g) E/P is the ratio of the EM cluster energy to the momentum of an associated track.

(h) ISOL(R<0.4) is the energy around the electron within a cone with a radius of 0.4 in η - ϕ coordinates, divided by the electron energy.

(i) Border Tower Energy is the sum of the energy deposit in CEM towers adjacent to the electron cluster.

Identifying electrons with the above quantities, the CDF obtained results on W/Z physics and heavy flavour physics as described elsewhere[2]-[5]. The efficiencies for electron identification were 86±3% and 96±2% for tight and loose cuts, respectively[5].

How Effective is the E/P cut ?

To see how effective the E/P cut is, we used an event sample triggered by requiring two or more EM clusters with Et > 10 GeV (Diphoton_10 trigger). From this event sample, we selected central electrons and π^0 /γ 's with Et >10 GeV using the information of longitudinal and lateral shower shape, i.e., Had/EM < 0.055 + 0.045 x E (GeV)/100 and LSHR < 0.2. 14,278 clusters passed these cuts.

Out of 14,278 clusters, there were 7,639 (54%) clusters without any associated tracks, 4,674 (33%) clusters with one track and 1,872 (13%) clusters with two or more tracks. The E/P distribution is shown for the EM clusters with one track in Fig.1. Applying the E/P cut of $0.6 < E/P < 1.4$, we could reduce the 4,674 clusters to 767 (16%) clusters. In Figs. 2a - 2d, ΔZ and $\Delta\phi$ are shown before and after the E/P cut of $0.6 < E/P < 1.4$. It shows that the E/P cut decreased the background contamination from ~45% to ~3% in the window of track-cluster postion match of $|\Delta Z| < 3$ cm and $|\Delta\phi| < 0.02$ radians. In this event sample, the number of non-isolated prompt electrons is estimated to be 580. Thus the E/P cut decreases the background for non-isolated electrons with Et > 10 GeV by a factor of 20. This background is mainly due to the $\pi^{\pm}$-π^0 overlapping.

4. Rejection of Conversion Electron

The conversion of π^0 /γ at the material inside of the CTC and the π^0 Dalitz decays give rise to backgrounds of non-prompt electrons. Such electron pairs are rejected using tracking information at CDF. The conversion electrons were identified by requiring that

(a) there is no track in VTPC (# hits found/ # hits expected < 0.2) or

(b) $|S| < 2$cm and $\Delta\theta < 5°$ or $M_{2tracks} < 0.5$ GeV , where $\Delta\theta$ is the minimum difference in polar angle between two tracks, S is the separation of two track circles in the x-y plane, $S = D - |\rho_1| - |\rho_2|$ (D is the distance between circle centers and ρ's are the circle radii.) and $M_{2tracks}$ is mass reconstructed with two track momenta.

To estimate the efficiency and over-efficiency for conversion electron identification, the inclusive central electrons were selected requiring Et >12GeV, Had/EM < 0.05, $\chi^2_{strip}<10$, $\chi^2_{wire}<10$, LSHR < 0.2, $\Delta Z < 3.0$ cm, $\Delta r\phi < 1.5$ cm, E/P < 1.5 and Border Tower Et < 1.5 GeV. Out of these electrons, conversion electrons were identified by the above algorithm (a) or (b). The over-efficiency of conversion electron identification, i.e., the inefficiency of prompt electron detection is given by n_B/n , where n_B is the number of electron pairs with the same charge and n is the number of all electrons with tracks in VTPC. The efficiency ε of conversion electron identification is calculated using the ratio of the number of electrons satisfying both (a) and (b) to the number of electrons satisfying (a), $\varepsilon_1 = N_F/N$ as follows:

$$\varepsilon = (N + n_F - n_B)/ (N + (n_F - n_B)/\varepsilon_1),$$

where n_F is the number of electrons satisfying (b) with tracks in VTPC. The over-efficiency and the efficiency of conversion pair identification are 5.0 ± 0.3 % and 80 ± 3 %, respectively.

In this inclusive electron event sample, ~ 30% was found to be conversions.

5. The charge measurement of electrons and the background estimate with same-sign lepton pairs

The E/P distributions of electrons from W decay are shown in the central ($|\eta| < 1.1$) and plug ($1.3 < |\eta| < 1.7$) regions in Figs. 3a and 3b, respectively. The E/P distribution of central electrons are consistent with $W \rightarrow e\nu$ simulation including radiative correction as shown in Fig.3a. The E/P distribution of the plug electrons is broader than that of the central electrons by a factor of 3. It can be explained by the worse momentum resolution due to the shorter magnetic field length in $1.3 < |\eta| < 1.7$. The charge asymmetry in W decay electron was measured as shown in Fig.4. The charge of electrons from W decay can be determined in the pseudorapidity range $|\eta| < 1.7$.

The charge determination is important for background estimation in Drell-Yan physics and heavy flavour physics. In Drell-Yan physics, background sources are the $\pi^{\pm}$-π^0 overlaps, the π^0/γ conversions, interactive $\pi^{\pm}$ in CEM or PEM and prompt electrons from b or c semileptonic decay. Out of these backgrounds, we can suppress and estimate the contamination of the $\pi^{\pm}$-π^0 overlaps using the quantities, E/P, ΔZ and $\Delta\phi$, and the contamination of the π^0/γ conversions using the method described in previous section. About the interactive $\pi^{\pm}$ in CEM or PEM, and prompt electrons from b or c semileptonic decay, we use ISOL(R<0.4) distribution to suppress and estimate their contaminations. We selected a dielectron event sample requiring two electrons with Pt > 6GeV/c, Had/EM < 0.055 + 0.045 x E (GeV)/100, χ^2_{strip}<15, LSHR < 0.2, ΔZ < 3.0 cm, $\Delta r\phi$ < 1.5 cm, E/P < 1.5 and an associated VTPC track, and $M_{ee} > 15$ GeV/c^2. The ISOL distributions are shown in Fig.5 for the opposite sign pairs by a solid line, and for the same sign pairs by a dashed line. We can see the ISOL distribution of backgrounds (mainly electrons from b or c semileptonic decay) from the same sign pairs, and can estimate the background contamination after the ISOL cut.

In the same way, we can study the background of top quark search in dilepton channel using the same sign pairs. We looked at scatter plots of electron Et versus muon Pt for the same sign e-μ pairs and the opposite sign e-μ pairs, and found that they showed very similar distributions to each other.

6. Summary

Electron identification at CDF is good enough for W/Z physics and heavy flavour physics. The tracking chamber with a solenoidal magnetic field at CDF is useful for

rejectiing the backgrounds such as the $\pi^{\pm}$-π^0 overlaps, the π^0 /γ conversions and interactive $\pi^{\pm}$ in electromagnetic calorimeter, for prompt electrons: The E/P cut reject backgrounds for non-isolated electron sample (Et >10 GeV) by a factor of 20 at CDF. Requiring a tight track-cluster position match together with the E/P cut, we decrease the background contamination down to 3%. Tracking with magnetic field is powerful for rejection of conversion electrons. Charge of W electron can be measured in the range $|\eta| <$ 1.7 at CDF. Charge measurement of lepton is very effective for the background estimation in Drell-Yan physics and Heavy flavor physics.

From the above points, large coverage of solenoid in η is favourable for good identification of electron.

References

1) F. Abe et al., Nucl. Instrum. Methods Phys. Res., Sect. A **271**, 387 (1988).
2) F. Abe et al., Phys. Rev. Lett. **63**, 720 (1989)
3) F. Abe et al., Phys. Rev. Lett. **64**, 142 (1990)
4) F. Abe et al., Phys. Rev. Lett. **64**, 147 (1990)
5) F. Abe et al., Phys. Rev. Lett. **64**, 152 (1990)

Figure Caption

Fig.1. The E/P distribution for the central electromagnetic clusters with a track together with a histogram of multiplicity of associated tracks with the central electromagnetic clusters in the up-right side.

Fig.2. The distributions of the deviation of cluster centroid from associated tracks (a) in z direction without the E/P cut, (b) in ϕ direction without the E/P cut, (c) in z direction after the E/P cut and (d) in ϕ direction after the E/P cut, for the central electromagnetic clusters with a track.

Fig.3. The E/P distributions of electrons from W decay in (a) the central and (b) the plug regions together with the E/P for $W \rightarrow e\nu$ simulation including radiative correction.

Fig.4. A plot of the charge asymmetry in electrons from W decay versus electron pseudorapidity together with theoretical predictions with several structure functions.

Fig.5. The ISOL(R<0.4) distribution for electron pairs with the opposite charge (solid line) and the same charge (dashed line) in Drell-Yan event sample with Pt (e) > 6 GeV/c and $M_{ee} > 15 GeV/c^2$.

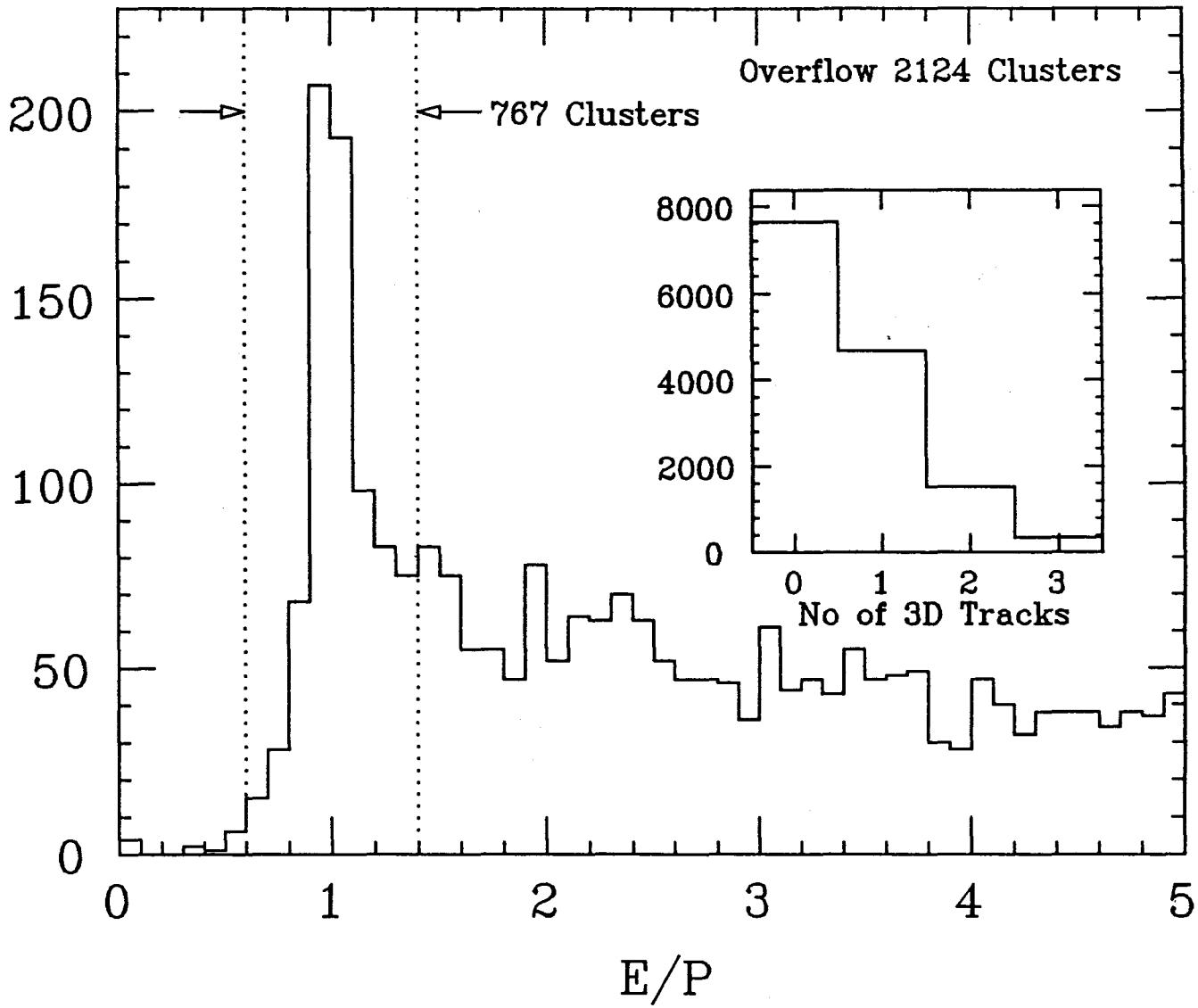
Overflow 2124 Clusters
767 Clusters
200
150
100
50
0
0
1
2
3
4
5
E/P
8000
6000
4000
2000
0
0
1
2
3
No of 3D Tracks

Fig.1

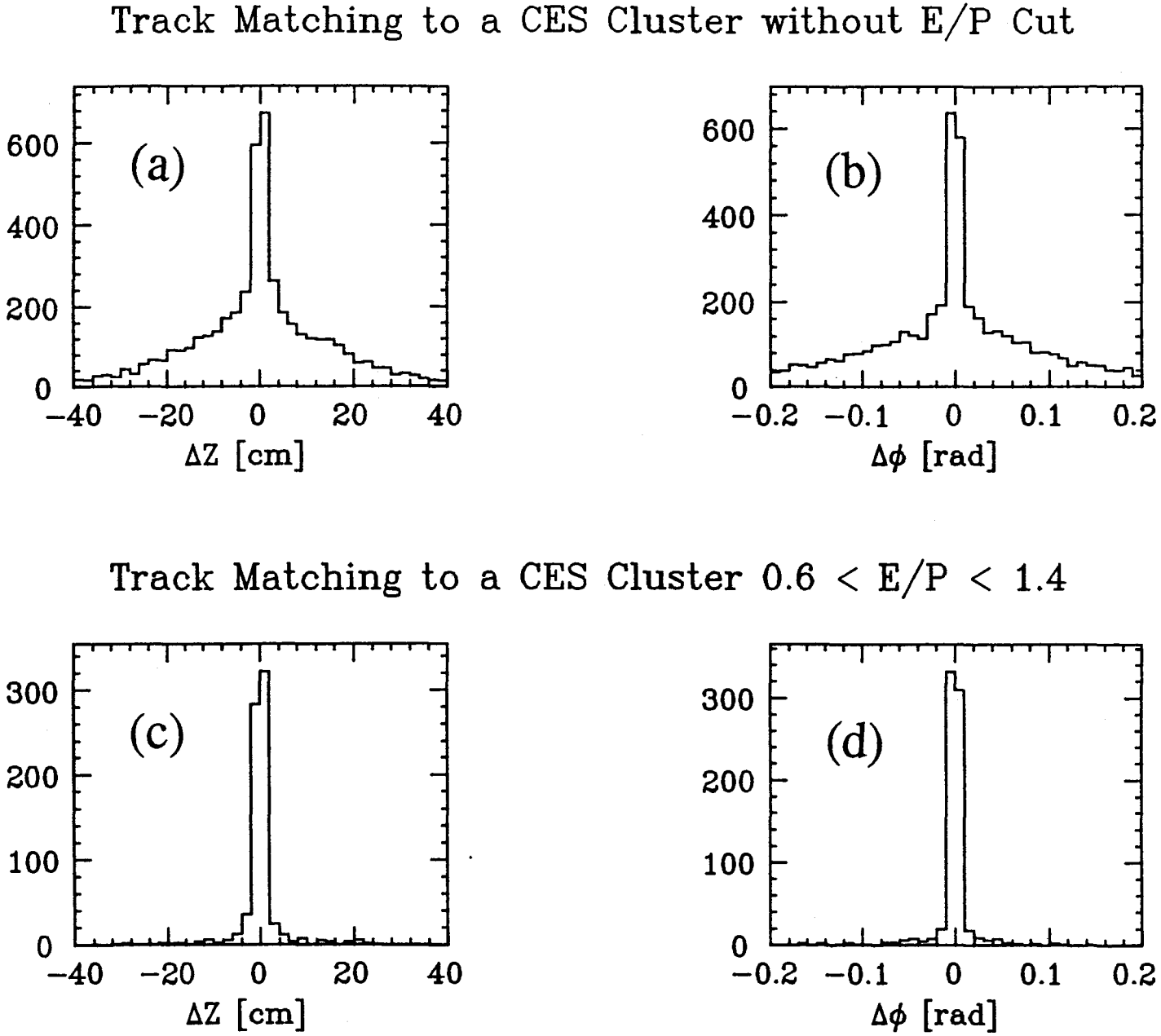
Track Matching to a CES Cluster without E/P Cut
(a)
600
400
200
0
−40
−20
0
20
40
ΔZ [cm]
(b)
600
400
200
0
−0.2
−0.1
0
0.1
0.2
Δφ [rad]
Track Matching to a CES Cluster 0.6 < E/P < 1.4
(c)
300
200
100
0
−40
−20
0
20
40
ΔZ [cm]
(d)
300
200
100
0
−0.2
−0.1
0
0.1
0.2
Δφ [rad]

Fig.2

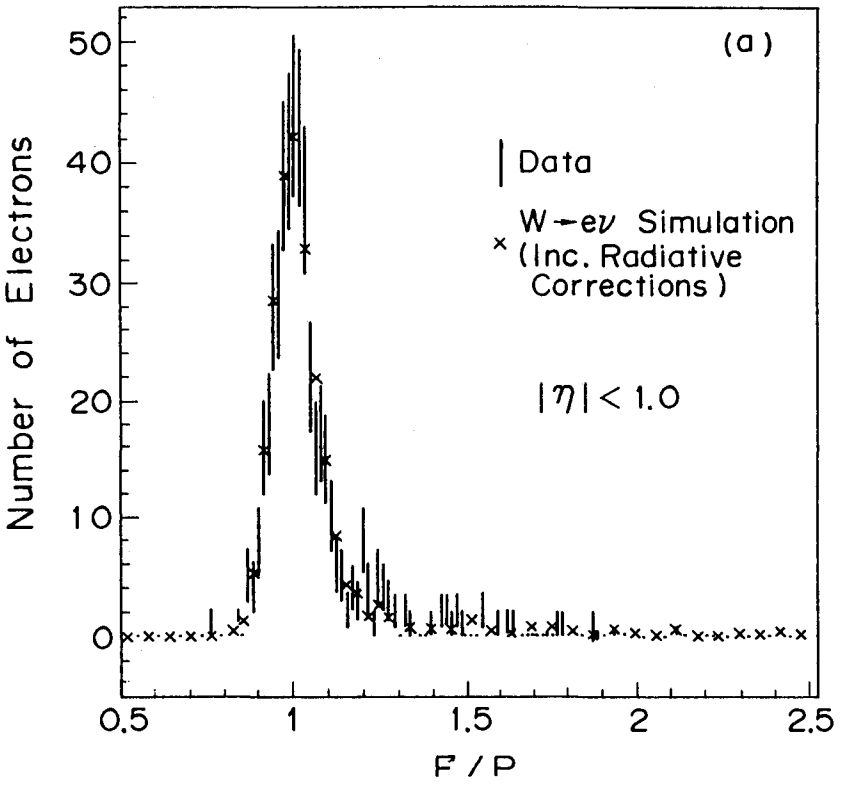
(a)
Data
W→eν Simulation
(Inc. Radiative
Corrections)
|η| < 1.0
Number of Electrons
E / P
0
10
20
30
40
50
0.5
1
1.5
2
2.5

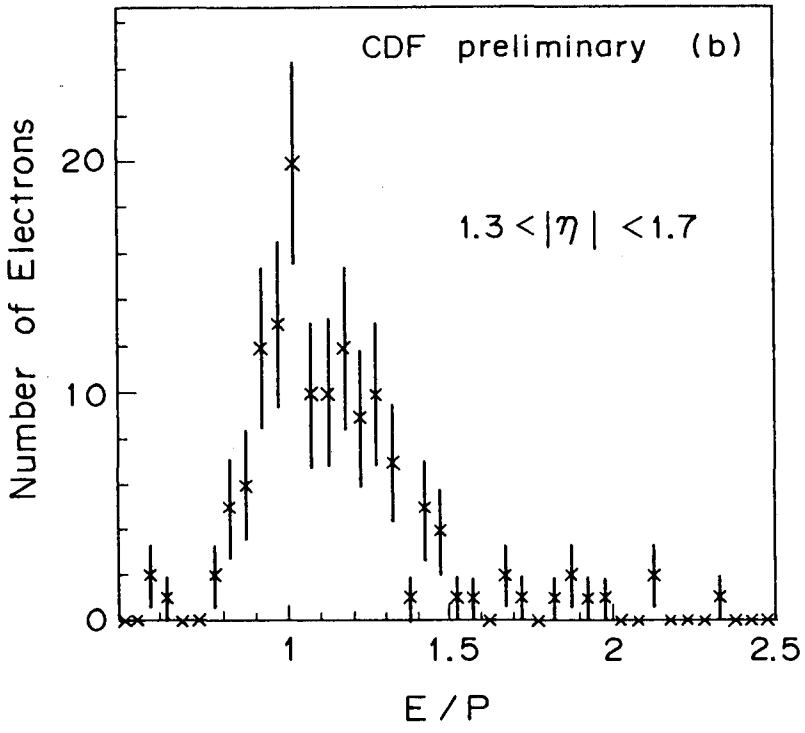
CDF preliminary (b)
1.3 < |η| < 1.7
Number of Electrons
E / P
0
10
20
1
1.5
2
2.5

Fig.3

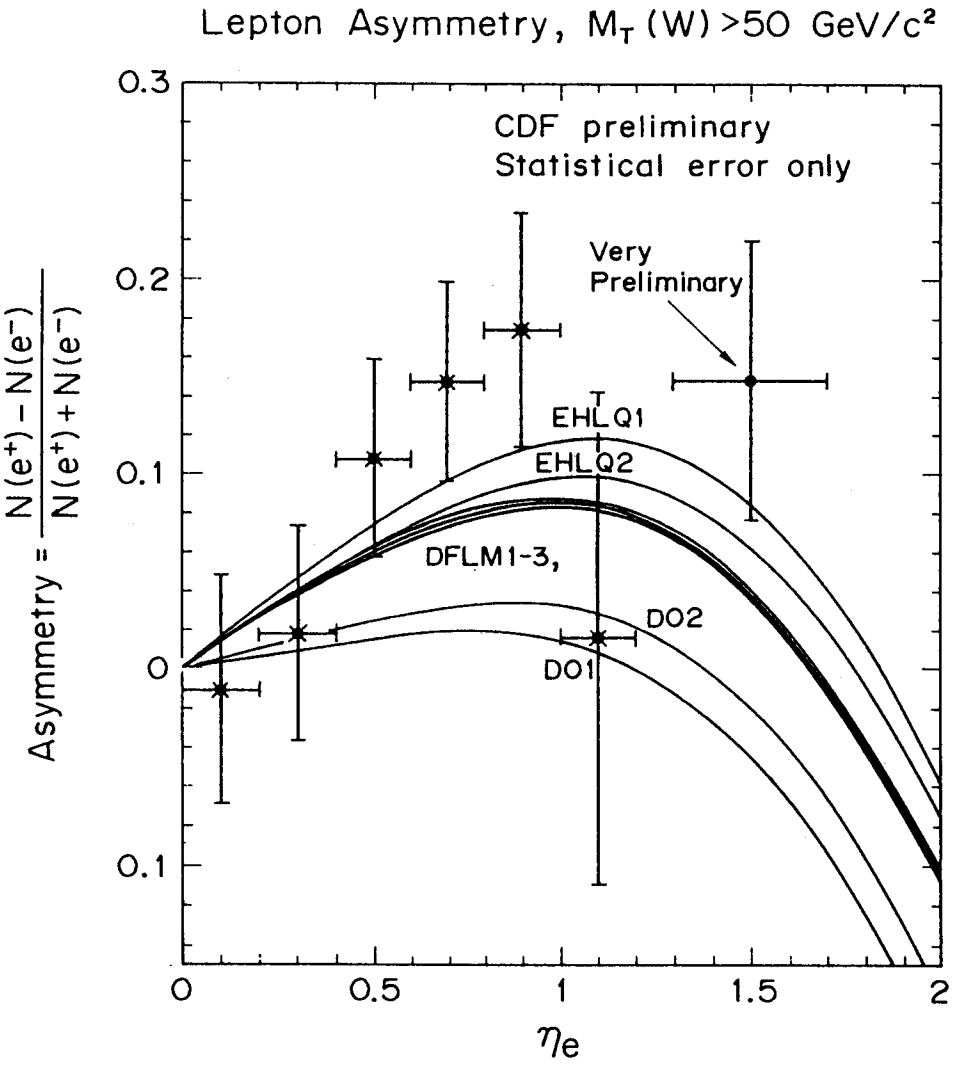
Lepton Asymmetry, M_T (W) >50 GeV/c^2
CDF preliminary
Statistical error only
Very
Preliminary
EHLQ1
EHLQ2
DFLM1-3,
DO2
DO1
Asymmetry = $\frac{N(e^+) - N(e^-)}{N(e^+) + N(e^-)}$
0.3
0.2
0.1
0
0.1
0
0.5
1
1.5
2
η_e

Fig.4

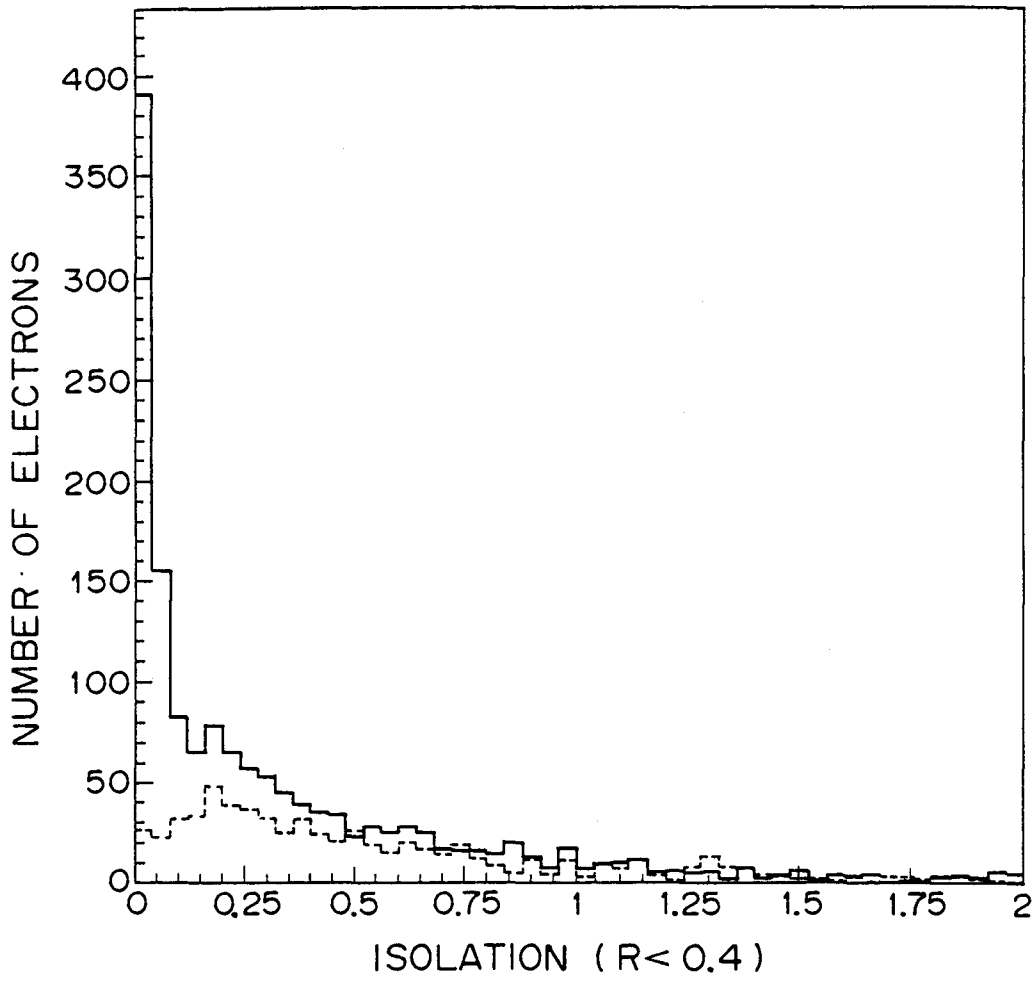
NUMBER OF ELECTRONS
400
350
300
250
200
150
100
50
0
0
0.25
0.5
0.75
1
1.25
1.5
1.75
2
ISOLATION (R< 0.4)

Fig.5

Detection of Isolated Electrons in Heavy Higgs Search

Hiroyuki Iwasaki
KEK, *Tsukuba, Ibaraki, JAPAN*

Abstract

We studied the process $pp \to H^0 \to Z^0Z^0 \to 4e$ for very heavy Higgs mass, $M_H = 800$ GeV, at $\sqrt{s} = 40$ TeV with using PYTHIA5.3. The analysis is based entirely on a calorimetry detector. We investigated a validity of requiring just an isolated electromagnetic activity rather than positively identifying an electron. We found that such "EM-ID" is useful for this particular physics process. Also, we examined effects of "bad" regions in the calorimeter to the geometrical acceptance and the mass resolution of Z^0. The "bad" regions do not cause obvious deterioration on the mass resolution, and improve about factor two in geometrical acceptance.

1 Introduction

To uncover the mechanism of the spontaneous symmetry braking in the electroweak theory is one of the most important physics for SSC. According to the model of the minimal Higgs doublet, a physical Higgs scalar exists. Experimentally, the mass range between 32 MeV and 24 GeV is excluded recently by the ALEPH collaboration[1]. We do not know theoretically about its mass scale, except that it is less than ~ 1 TeV for the perturbative approach to be valid[2]. For this purpose, we must be capable of detecting the Higgs boson up to this region.

A heavy Higgs($M_H > 2M_{W/Z}$) predominantly decay into W^+W^- or Z^0Z^0 pair. However, it is now turned out that the top-quark is expected to be heavier than the $W^\pm/Z^0$ mass[3]. Then the W^+W^- pairs can be produced copiously via $t\bar{t}$ production. Reconstruction of Z^0 through the hadronic decay mode is confronted with difficulties due to the large QCD background. The practical signal modes are therefore $H^0 \to Z^0Z^0 \to l\bar{l}\, l'\bar{l}'$, where l (l') stands for e or μ (e, μ or ν's). In this report, we will concentrate on the decay mode, $H^0 \to 4e$, and study requirements related to electron identification(e-ID).

Suppose that $\epsilon(1e)$ is the efficiency of e-ID for an electron, the detection efficiency for four electrons is $\epsilon(1e)^4$. Even the e-ID efficiency for an electron is 90%, it becomes 66% for four electrons. In fact, the CDF group reports $\sim$ 86% for $\epsilon(1e)$[4], and we do not know its value under the SSC environment with a realistic detector system. Moreover, if the Higgs mass is as heavy as 800 GeV, we need higher luminosity than $10^{33}\ cm^{-2}s^{-1}$. Even with the 16 times higher luminosity, we do not gain at all if $\epsilon(1e)$ becomes factor two worse. On the other hand, the process $H^0 \rightarrow Z^0Z^0 \rightarrow 4e$ has a clean topology with the strict kinematical constraints. Therefore, we may not have to identify electrons positively, but an isolation requirement for electromagnetic activity("EM-ID") might be enough to suppress backgrounds. If it is possible, the better detection efficiency is expected, and especially so under the higher luminosity. One of the topics in this report is to investigate the capability of the "EM-ID" for this particular physics process.

The second topic is about the geometrical acceptance. A study on the requirements to e-ID for the process $H \rightarrow Z^0Z^0 \rightarrow l\bar{l}\,l'\bar{l}'$ has been done by Yamamoto *et al.*[5]. They studied the detection efficiencies of the heavy Higgs bosons by taking account of the realistic calorimeter geometry. According to the Martin-Marietta design of the liquid argon calorimeter, there are nonnegligible materials in front of the electromagnetic calorimeter at around $|\eta| \simeq 0.73$ (η is the pseudorapidity, $\eta = -\ln(\tan\theta/2)$) corresponding to the support structures and $|\eta| \simeq 1.5$ corresponding to the barrel-endcap boundaries. They abandoned to use these regions as well as the boundaries of modules in ϕ for the electron detection. If four electrons are required in the final state, the geometrical acceptance becomes less than 40%(the η-coverage of 3 is assumed). Motivated with the result, we examined effects on the geometrical acceptance and the Z^0-mass resolution when one electron was allowed to enter those kind of "bad" regions.

2 Methodology

2.1 Event generation

The process which we consider is $H^0 \rightarrow Z^0Z^0 \rightarrow 4e$, where the Higgs is produced via pp-collision at $\sqrt{s}$ = 40 TeV. The top-quark mass is assumed to be 150 GeV. As we stated before, we will concentrate our study on the very heavy Higgs, M_H = 800 GeV. We used the PYTHIA version 5.3[6] for the event generation.

The production cross section of Higgs versus its mass is plotted in Fig.1. Indeed its production rate is not necessarily small, but the branching ratio to the 4e-mode is too small($\sim 3 \times 10^{-4}$). The resulting event rate of the 4e-mode for $M_H = 800$ GeV is only 11.8 events with the integrated luminosity of $10^{40}\, cm^{-2}$. The mass distribution, the rapidity (y_H) distribution, and the the transverse momentum (p_T) distribution are shown in Fig.2a, Fig.2b and Fig.2c, respectively. We generated 1000 events for this process. Since the decay width of the Higgs boson is proportional to M_H^3, it becomes about 300 GeV for $M_H = 800$ GeV (Fig.2a). Since it is heavy, it is produced in the central region, $|y_H| < 2$ (Fig.2b). As for the transverse momentum, it has the large tail (Fig.2c). As the result, the Z^0 bosons are not necessarily produced in the back-to-back configuration. In Fig.2d, the acoplanarity angle between the two Z^0 bosons is shown. We should note that the jet activity is not small even in this type of "clean" physics process.

2.2 Detector

The detector used in this analysis is a calorimeter system only. It covers up to $|\eta| = 3$ and has the tower geometry with the tower size $\Delta\eta \times \Delta\phi = 0.05 \times 0.05$. Each tower is longitudinally segmented into two parts, an electromagnetic section(EM) and a hadronic one(HAD). The energy resolutions of the electromagnetic and hadronic sections are $\sigma_E/E = 0.2/\sqrt{E} + 0.02$ and $0.5/\sqrt{E} + 0.02$, respectively, where E is the deposited energy in the tower in GeV. The angular resolutions are $\sigma_\eta = \sigma_\phi = 2.5 \times 10^{-3}$, which corresponds to the position resolution of $\sigma_x = 5mm$ at $2m$ away from the interaction point at $\eta = 0$. Worse energy and angular resolutions are used in some "bad" regions as explained in the followings.

Fig.3a shows a quadrant side view of a liquid argon calorimeter with a coil inside designed by the KEK group[7,8]. In Fig.3b, the materials in front of the EM section in radiation length(X_0) is plotted as a function of pseudorapidity[1][9]. The blank area is due to the magnet, and the shaded area is due to the vessel walls of the calorimeter. The thickness is about $2\,X_0$ at $\eta = 0$, and gradually increases up to $4\,X_0$ at $\eta \simeq 1.4$. At $\eta \simeq 1.5$, the thickness becomes $\sim 6\ X_0$. In Fig.4, we plot the energy resolution versus the material thickness in front of the calorimeter calculated by using the EGS simulation[10]. Without any correction(filled circle), the resolution becomes considerably worse beyond $X_0 > 2$. However, by using the "massless-gap method"(open circle), where some absorber plates are removed

[1]Since the calorimeter design is revised frequently, the figure should be taken so.

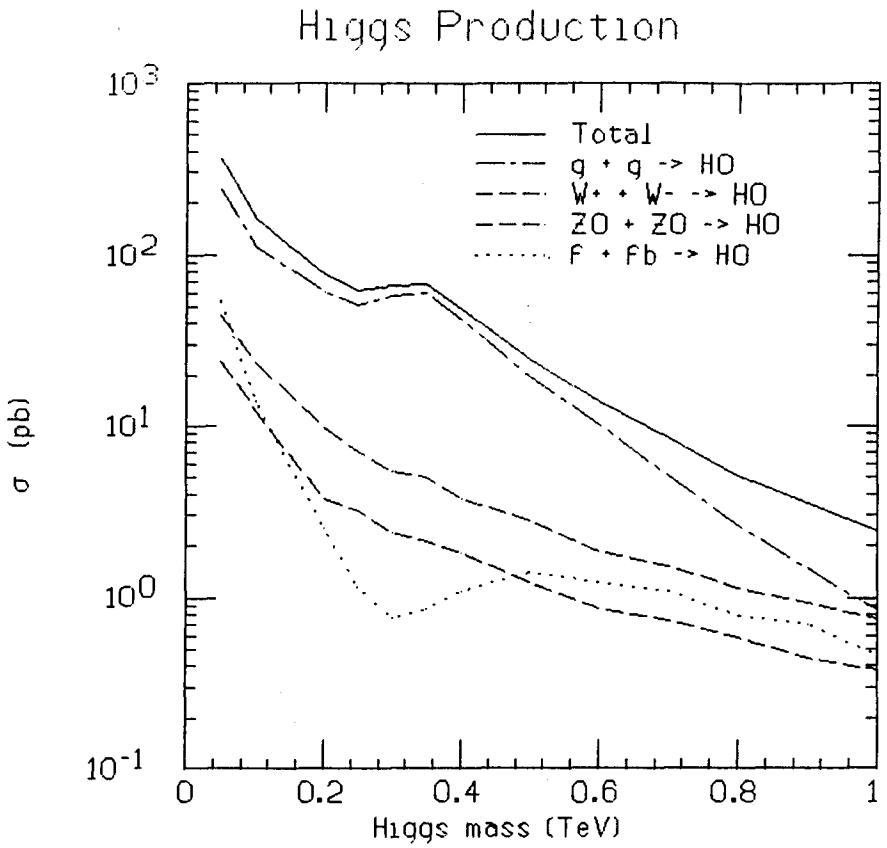

Fig.1. The Higgs production cross section versus its mass via pp-collision at $\sqrt{s}$ = 40 TeV calculated by using PYTHIA version 5.3[6]. The top-quark mass is assumed to be 150 GeV.

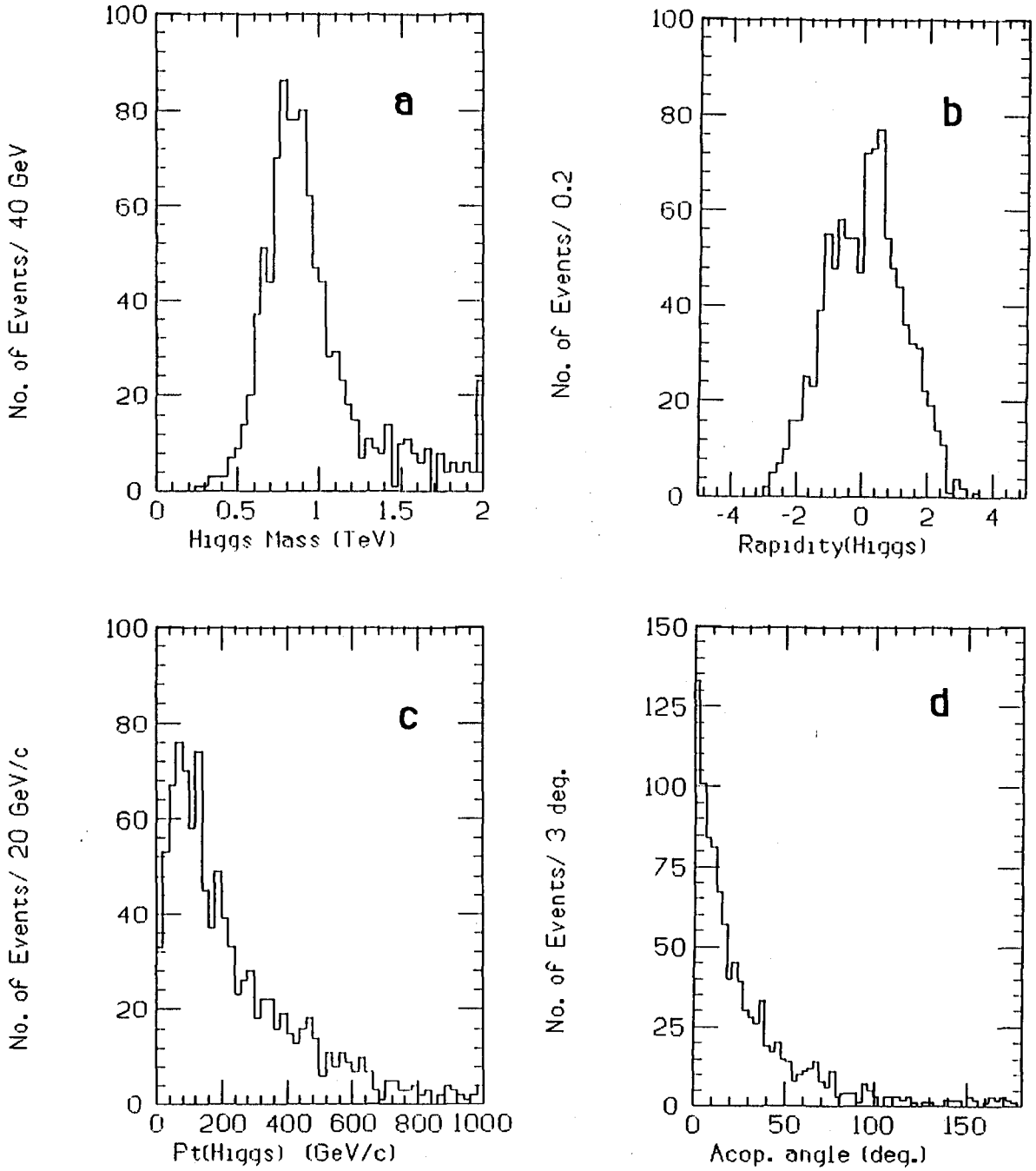

Fig.2. (a) The mass distribution of the Higgs boson at $M_{II} = 0.8$ TeV. (b) Its rapidity distribution. (c) Its transverse momentum(P_T) distribution. (d) The acoplanarity angle between the two Z^0 bosons which are the decay products of the Higgs boson.

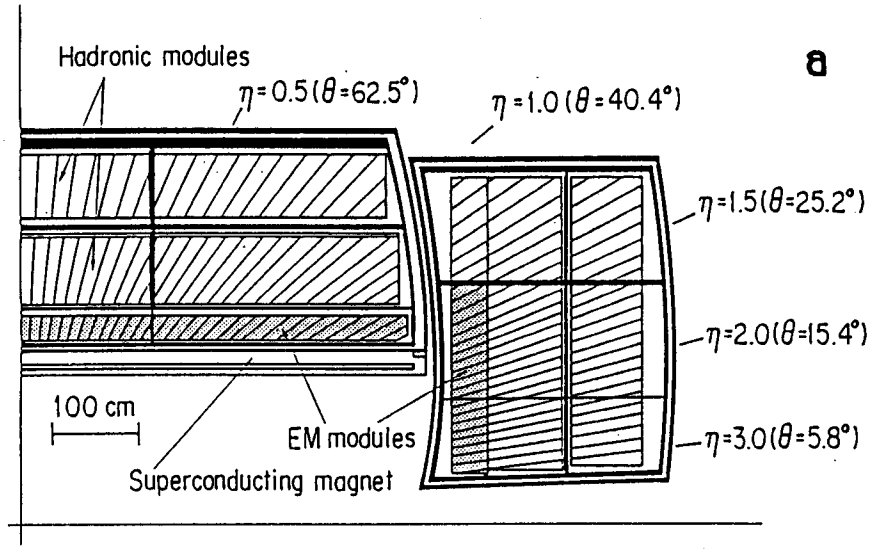

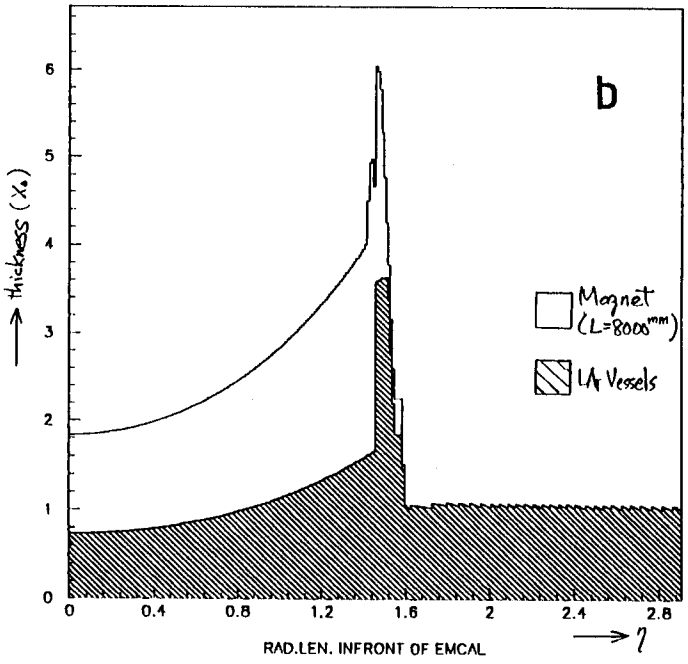

Fig.3. (a) A quadrant side view of a liquid argon calorimeter with a coil inside[7,8]. (b) The materials in front of the electromagnetic section in radiation length(X_0) versus pseudorapidity[9]. The blank area is due to the coil, and the shaded area is due to the vessel walls of the calorimeter.

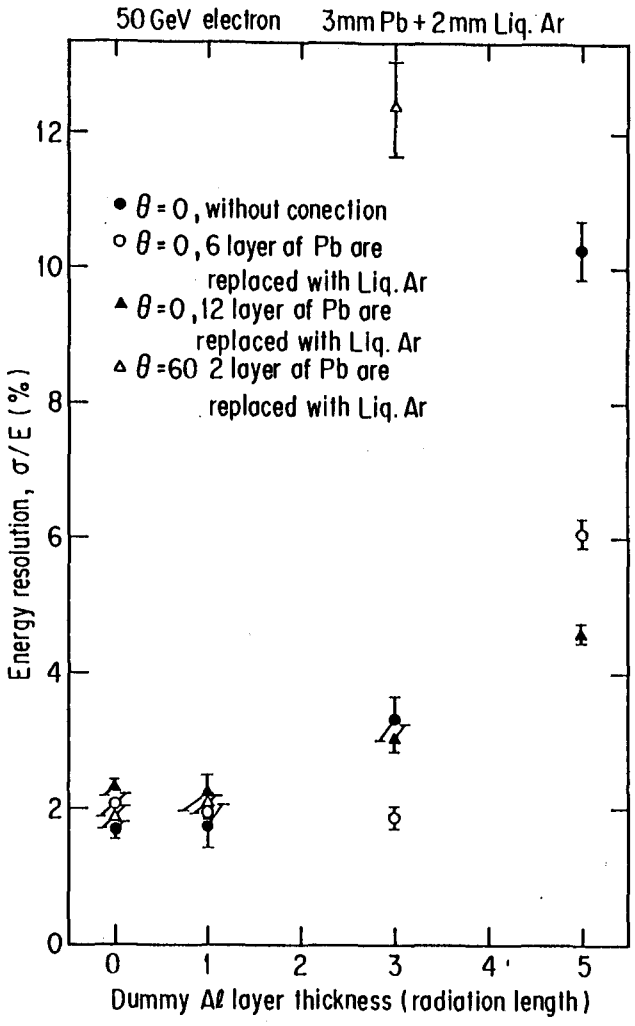

Fig.4. The energy resolution versus the material thickness in front of the electromagnetic calorimeter calculated by using the EGS simulation[10].

Table 1. Resolution parameters of the EM calorimeter

η	A ($\sigma_E/E = \mathrm{A}/\sqrt{E} + 0.02$) "good" in ϕ	"bad" in ϕ	$\sigma_\eta = \sigma_\phi$
"good" in η	0.2	0.4	2.5×10^{-3}
$1.1 < \lvert\eta\rvert < 1.4$	0.3	0.5	5.0×10^{-3}
$1.4 < \lvert\eta\rvert < 1.55$	0.6	0.8	1.0×10^{-2}

but the shower sampling is kept working, the resolution becomes the same level up to $X_0 \simeq 3$ as that at $X_0 = 0$. Thus, we define the "bad" region in η where the thickness is larger than $3\,X_0$, namely $1.1 < \eta < 1.55$.

We assume "bad" tower-rows every 16 tower-rows in ϕ, which corresponds to about $6mm$ "bad" boundary region between the two adjacent towers if the EM section is placed at $2m$ away from the beam line. The energy resolutions and the angular resolutions in the "bad" regions are summarized in Table1. Since the position resolution is better for an electron hitting the tower boundary, we assume the angular resolutions are independent of ϕ.

2.3 Event analysis

In the energy deposition in a tower, we assume that all the electromagnetic(hadronic) energy is deposited only in the electromagnetic(hadronic) section, and that there is no correlation between the two sections. Deposited energy in a tower is smeared independently for electromagnetic activity and hadronic one. The transverse sharing of shower energy between towers is also neglected.

For each electron, which are decay product of a Higgs boson, its hit position is smeared. The electromagnetic energies in all the towers inside the window of ± 1 in η and ϕ (3×3 towers) around the tower where the electron hits are merged($\equiv E^{EM}(3\times 3)$). For the hadronic activity with respect to the electron, it is defined as an energy sum inside the window of ± 3 in η and ϕ (7×7 towers) for all the particles except $e^{\pm}$, $\mu^{\pm}$, and ν's ($\equiv E^{HAD}(7 \times 7)$). The same merging procedure is also applied to γ or $e^{\pm}$, which is not the decay product of the Higgs boson, if its E_T in a seed tower is larger than 5 GeV. These clusters are referred to as fake clusters.

Selection requirements

Event selection criteria are the followings.

1. $|\eta|$ is less than 2.8 for all the four electrons.

2. Number of electrons which enter the good regions, N_{good}, is 3 or 4.

3. Transverse energy, $E_T^{EM}(3 \times 3)$, is larger than 20 GeV for all the four electrons.

4. For each electron, the ratio of hadronic activity to that of the electron, HAD/EM, is less than 0.1:

$$HAD/EM \equiv \frac{E_T^{HAD}(7\times 7)}{E_T^{EM}(3\times 3)} < 0.1.$$

5. We select a combination of electron pairs in such a way to minimize the quantity,

$$(M(e_1e_2) - M_Z)^2 + (M(e_3e_4) - M_Z)^2.$$

6. The mass difference, $|M(e_ie_j) - M_Z|$, is less than 10 GeV for both the Z^0 candidates.

3 Results

3.1 Detection efficiency and mass resolution

3.1.1 Geometrical cuts

Fig.5a shows the pseudorapidity distribution of electrons which are the decay products of the Higgs boson. More than 80% of the electrons enter within $|\eta| = 2$. However, if all the four electrons are to be detected, the detector coverage should be up to $|\eta| \simeq 3$. Fig.5b shows the distribution of the maximum pseudorapidity out of the four electrons in an event, $|\eta|_{max}$. If we require $|\eta|_{max} < 2.8$, 86% of the events survive.

N_{good} (defined in section 2.3) distribution for those events which satisfy $|\eta|_{max} < 2.8$ is shown in Fig.6. If we require all the electrons to enter the "good" regions, only about 40% of the events remain. However, if we can allow one electron to enter the "bad" regions, we gain other 40% of the events. As we will see later, it is really the case. The resulting detection efficiency due to the geometrical cuts becomes 77%.

3.1.2 Physics cuts and mass resolutions

Fig.7 shows the minimum transverse energy of the electrons in an event , $E_T^{EM}(3\times 3)_{min}$, after the geometrical cuts. If we require $E_T^{EM}(3\times 3)_{min}$ to be larger than 20 GeV, 96% of the events survive. The measure of the isolation, HAD/EM, is plotted in Fig.8a for the signal electrons which satisfy $E_T^{EM}(3\times 3) > 20$ GeV. It has

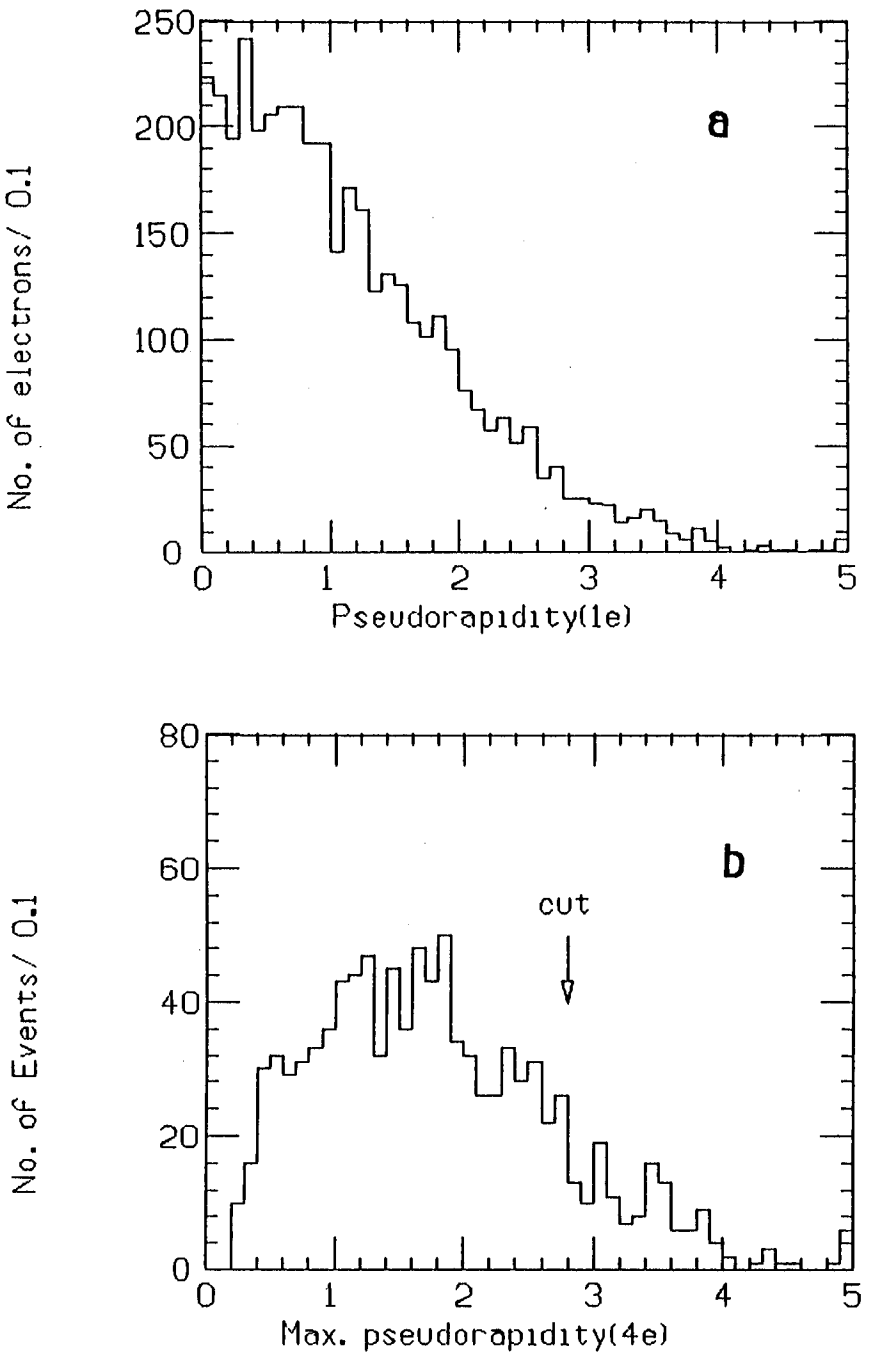

Fig.5. (a) The pseudorapidity distribution of each electron which is a decay product of the Higgs boson. (b) The distribution of the maximum pseudorapidity out of the four electrons in an event.

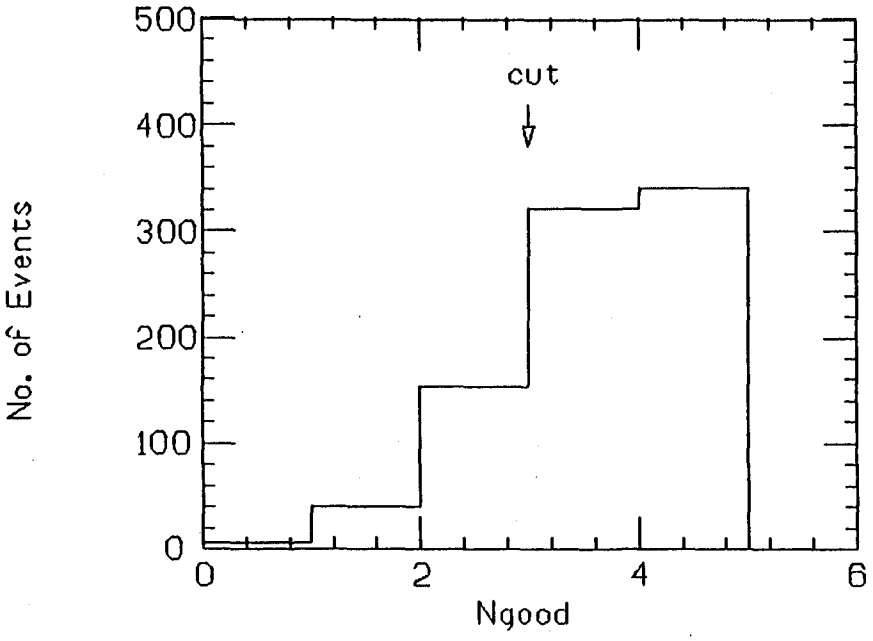

Fig.6. N_{good} (defined in section 2.3) distribution for those events where $|\eta|_{max} < 2.8$ is satisfied.

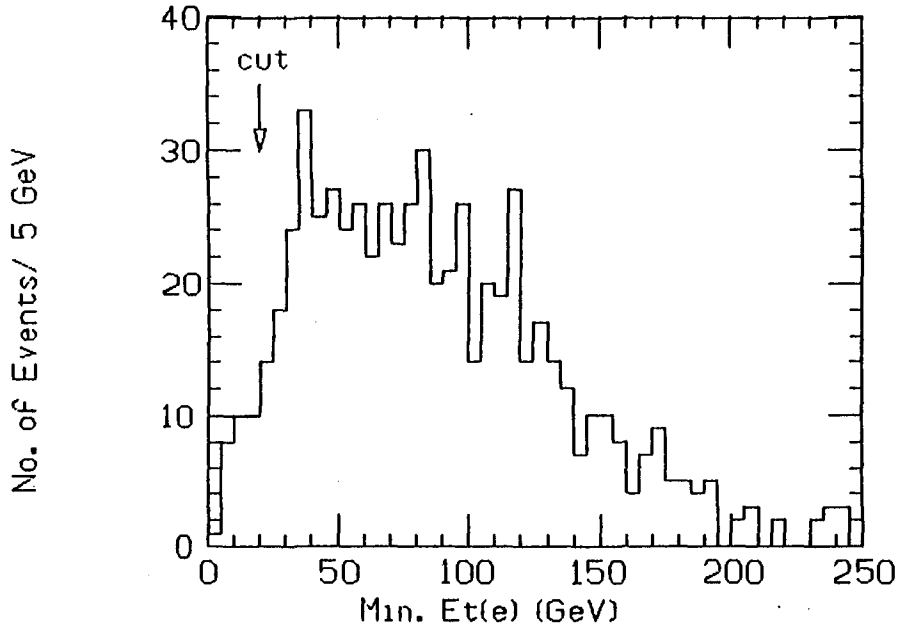

Fig.7. The minimum transverse energy of the electrons in an event after the geometrical cuts.

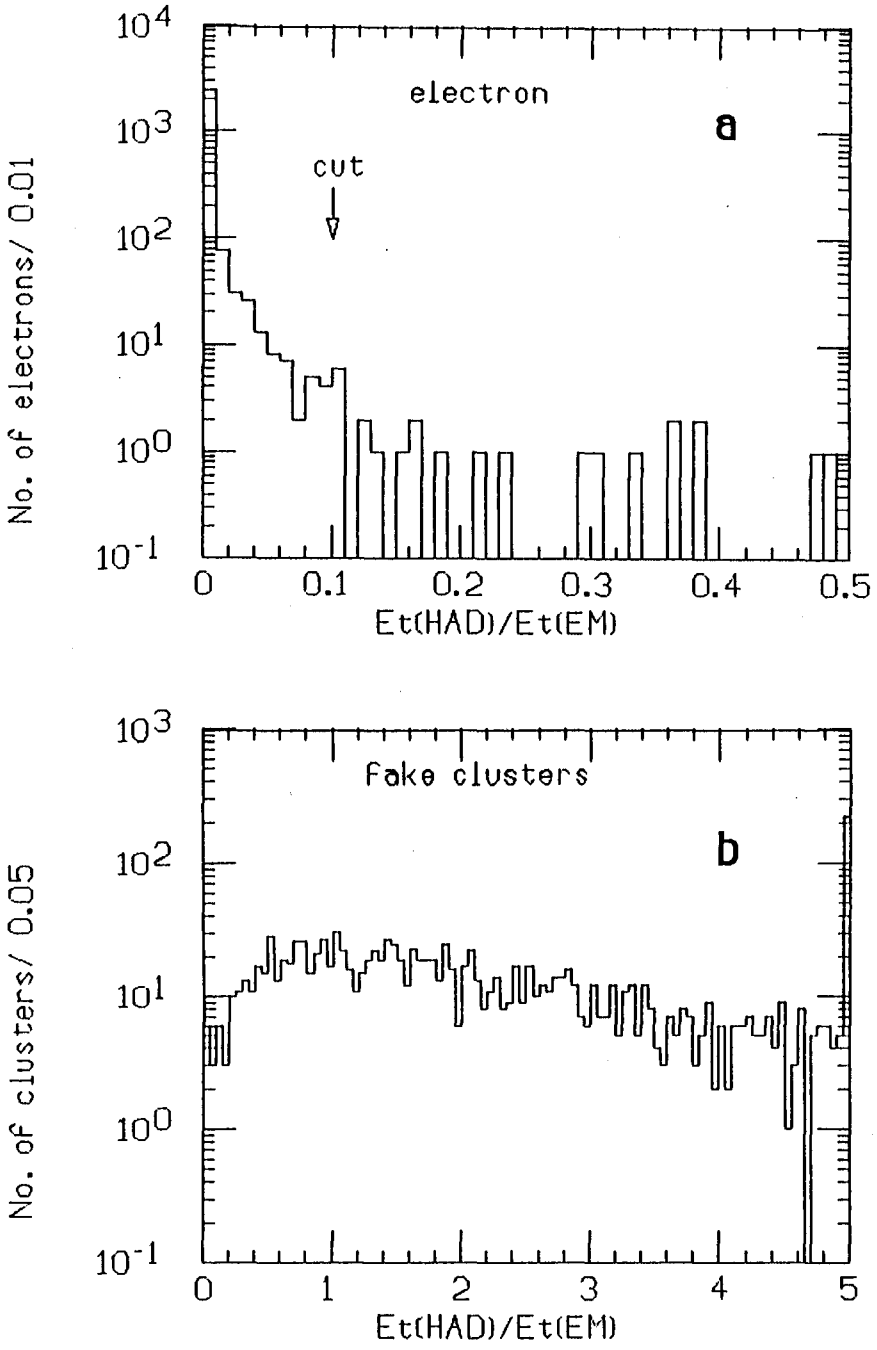

Fig.8. (a) The measure of the isolation, HAD/EM, for the signal electrons which satisfy $E_T^{EM}(3\times3) > 20$ GeV/c. (b) The distribution for fake clusters which satisfy $E_T^{EM}(3 \times 3) > 20$ GeV/c in the same process, $pp \rightarrow H^0 \rightarrow 4e$.

a sharp peak at $HAD/EM \simeq 0$, and 99% of the electrons satisfy the requirement, $HAD/EM < 0.1$. Being required for all the four electrons in an event to satisfy the isolation condition, 96% of the events remain.

After the geometrical cuts and the isolation cut, we select a combination of electron pairs, for which the quantity, $(M(e_1e_2) - M_Z)^2 + (M(e_3e_4) - M_Z)^2$, is the smallest. There is no wrong combination out of 610 events. Fig.9a shows the invariant mass distribution of the electron pair where both of them enter the "good" regions after the $E_T^{EM}(3 \times 3)_{min}$ and the HAD/EM cuts. Fig.9b shows the similar distribution, but one of the electrons enters the "bad" regions. There is no obvious difference between the two distributions [2]. If we require both the Z^0 candidates to satisfy the condition, $|M(ee) - M_Z| < 10$ GeV, 92% of the events survive.

Invariant mass distribution of four electrons, $M(ZZ)$, after all the physics cuts is plotted in Fig.10. The broad peak is simply due to its natural width(see Fig.2a) Contribution from the detector resolution is negligible. If we select the region, 600 GeV $< M(ZZ) <$ 1200 GeV, 78% of the events survive. In Table 2, we summarize the requirements, the efficiencies, and the number of events after the each requirement step with the nominal integrated luminosity for one experimental year, $10^4\,\mathrm{pb}^{-1}$.

3.2 Answers to the questions

3.2.1 Do we really need e-ID?

The HAD/EM distribution for the fake clusters in the same process, $pp \rightarrow H^0 \rightarrow 4e$, is shown in Fig.8b. Note that the horizontal scale is different from Fig.8a. After the isolation cut, 0.9×10^{-2} clusters per event remain. Since we apply only "EM-ID", these fake clusters are considered as electrons. Taking account of this rate and the probability to choose a wrong combination of electron pairs($< 2 \times 10^{-3}$), we do not have to identify electrons positively, but just to require isolated EM-clusters as long as the signal events are concerned. As we will see in the next section, the "EM-ID" is enough to suppress the backgrounds to negligible level. The only exception is the continuum Z^0Z^0 production, where application of the positive e-ID dose not help further than the "EM-ID". Thus, we may conclude

[2] As a check, we plot the $M(ee)$-distribution in Fig.9c similar to Fig.9b, but with the twice worse resolution in the "bad" regions for both energy and angular measurements. In this case the difference from Fig.9a is obvious

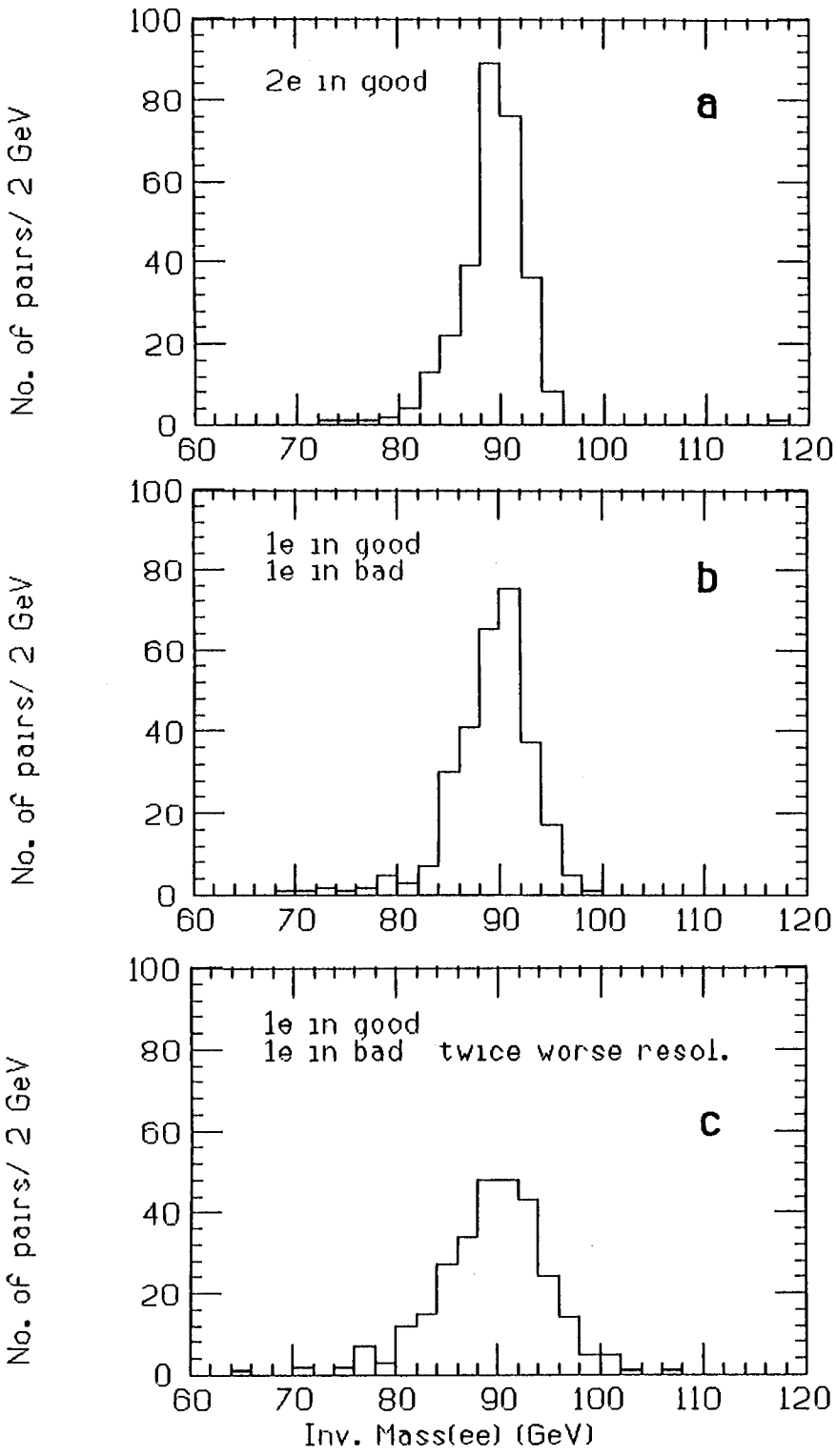

Fig.9. (a) The invariant mass distribution of the electron pair where both of them enter the "good" regions after the E_T^{EM}(3×3) and the HAD/EM cuts. (b) Similar distribution as (a), but one of the electrons enter the "bad" regions. (c) Similar distribution as (b), but with the twice worse resolution in the "bad" regions for both energy and angular measurements.

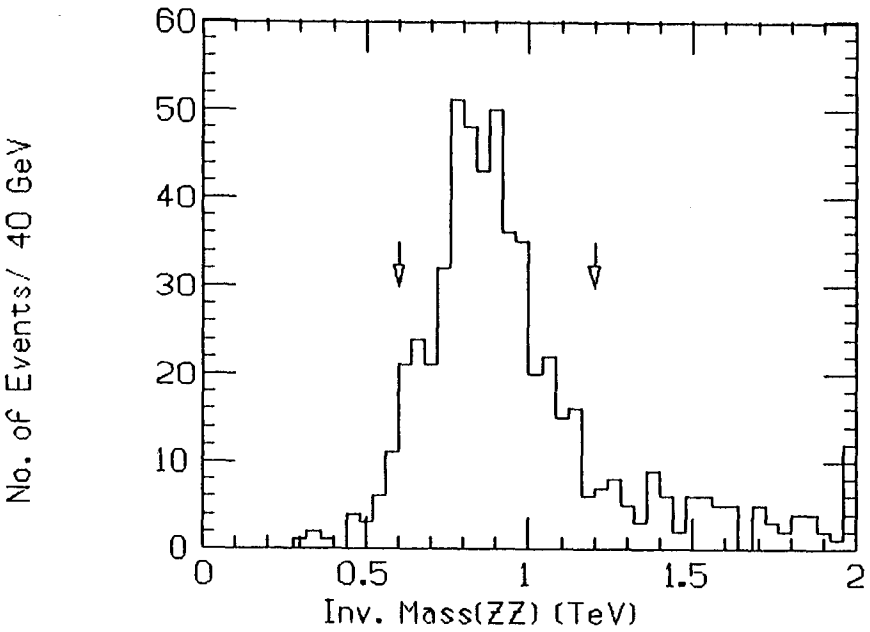

Fig.10. The invariant mass distribution of the four electrons, $M(ZZ)$, after the physics cuts.

Table 2. Efficiencies and the number of events per year

	$H^0 \to 4e$		$Z^0Z^0 \to 4e$ (continuum)	
Cross section	1.18×10^{-3} pb		3.49×10^{-3} pb	
selection	effic.	Evts/ yr.	effic.	Evts/ yr.
without cuts		11.8		34.9
$\|\eta\|_{max} < 2.8$	0.86	10.2	0.41	14.5
$N_{good} = 3, 4$	0.77	7.8	0.79	11.5
$E_T^{EM} > 20$ GeV	0.96	7.5	0.65	7.5
HAD/EM	0.96	7.2	0.98	7.3
$\|\Delta M_Z\| < 10$ GeV	0.92	6.6	1.00	7.3
$0.6 < M_{ll} < 1.2$ TeV	0.78	5.2	0.24	1.8
overall	0.44	5.2	0.05	1.8

One experimental year corresponds to $10^4 pb^{-1}$

that the requirement of isolated electromagnetic activity is enough for the heavy Higgs search in the process, $pp \to H^0 \to 4e$.

3.2.2 De we have to abandon the "bad" regions?

As we see in the previous subsection, the mass resolution of Z^0 with one "bad" electron is almost the same as that with two "good" electrons. If the assumption for the energy resolutions and the angular resolutions is not so far away from the reality, we can use the "bad" regions with keeping good quality in mass resolution. By just allowing one electron may enter the "bad" regions, the geometrical acceptance becomes about twice larger.

4 Background study

4.1 $q\bar{q} \to Z^0Z^0 \to 4e$ (continuum)

The cross section is 3.5×10^{-3} pb for $\sqrt{\hat{s}} > 400$ GeV, where $\sqrt{\hat{s}}$ is the cm energy in the $q\bar{q}$ system. It is about three times larger than that of the Higgs production, $H^0 \to 4e$, at $M_H = 800$ GeV. We generated 3000 events for this process. The $|\eta|_{max}$ distribution, the $E_T(3\times3)_{min}$ distribution, and the $M(ZZ)$ distribution are plotted in Fig.11, Fig.12, and Fig.13, respectively. Other distributions are similar to those for signal events. About 41% of the events enter the region, $|\eta|_{max} < 2.8$. The requirement of $E_T(3 \times 3)_{min} > 20$ GeV rejects 35% of the events after the geometrical cut. As for the $M(ZZ)$ distribution, 24% of events enter the signal region, 600 GeV $< M(ZZ) <$ 1200 GeV. The resulting overall detection efficiency is 5%, which is to be compared with 44% for the signal. The detection efficiencies and the number of events at each step are also summarized in Table 2

4.2 $pp \to Z^0 + jet \to 2e + jet$

The cross section is 30.7 pb for $\sqrt{\hat{s}} > 400$ GeV and $p_T > 100$ GeV. It is 2.6×10^4 times larger than the signal process, $H^0 \to 4e$. We generated 10000 events for this process. In Fig.14, we show the HAD/EM distribution for those clusters (except the electrons from Z^0) which satisfy $|\eta| < 2.8$ for the seed tower, and $E_T^{EM}(3\times3) >$ 20 GeV. Since our requirement for an electron is just the HAD/EM value should be less than 0.1, the rate to misidentify the fake cluster as an electron is 0.7×10^{-2}

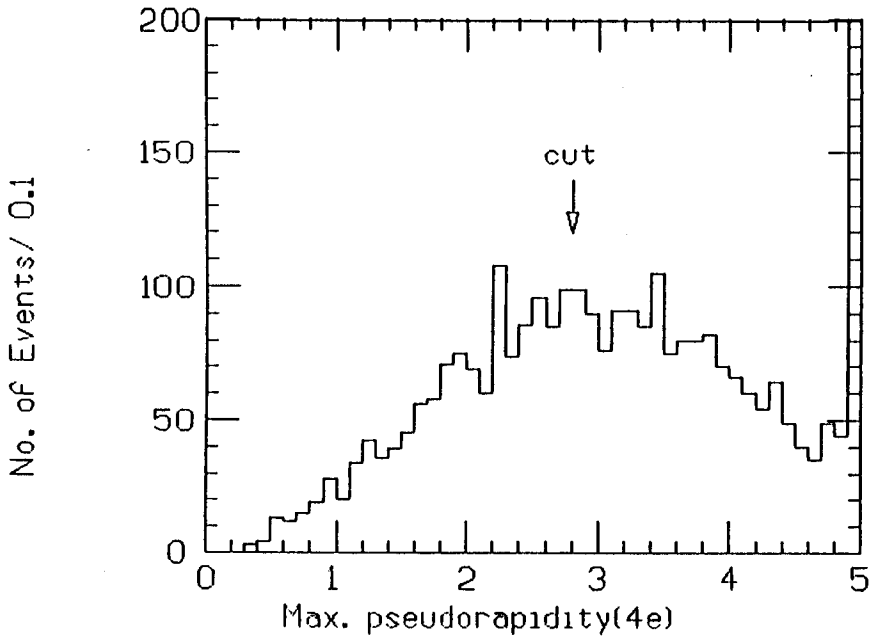

Fig.11. The $|\eta|_{max}$ distribution for the continuum process, $q\bar{q} \rightarrow Z^0 Z^0 \rightarrow 4e$.

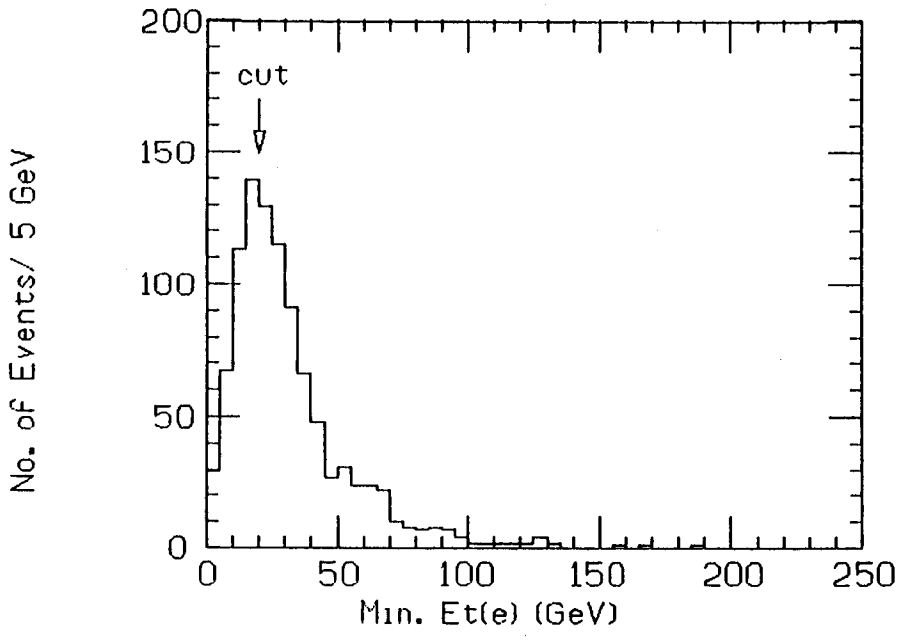

Fig.12. The $E_T^{EM}(3 \times 3)_{min}$ distribution for the continuum process, $q\bar{q} \rightarrow Z^0 Z^0 \rightarrow 4e$.

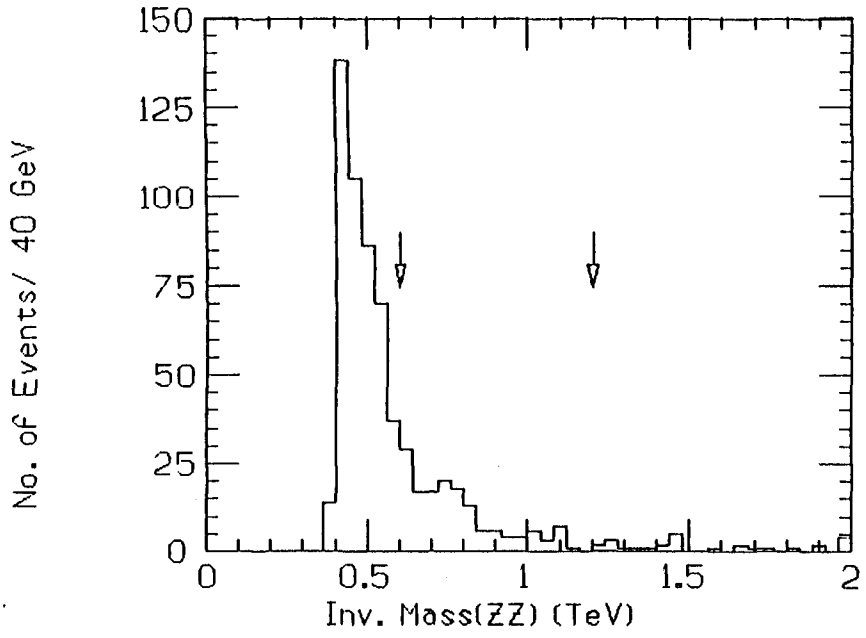

Fig.13. The invariant mass distribution of the four electrons for the continuum process, $q\bar{q} \rightarrow Z^0 Z^0 \rightarrow 4e$.

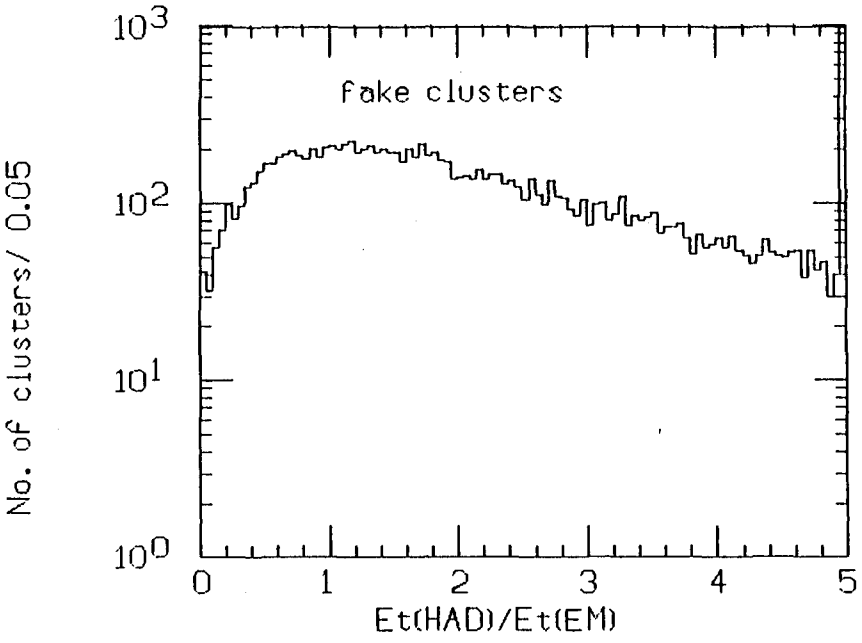

Fig.14. The HAD/EM distribution for those clusters which satisfy $|\eta| < 2.8$ for the seed tower, and $E_T^{EM}(3 \times 3) > 20$ GeV for the process, $pp \rightarrow Z^0 + jet \rightarrow 2e + jet$.

clusters per event. Therefore, the probability to find two such fake clusters in an event is about 5×10^{-5}. We need millions of events, if we straightforwardly estimate the probability to misidentify the "electron" pair as Z^0. Instead, we could estimate the probability using the same cluster sample without imposing the isolation requirement, $HAD/EM < 0.1$. In Fig.15, we plot the invariant mass distribution of the cluster pair for which the distance between the two clusters, $\Delta R(= \sqrt{(\Delta\eta)^2 + (\Delta\phi)^2})$, is larger than 0.2. From the figure, we estimate the probability that the pair is consistent with Z^0 to be about 10%. The invariant mass distribution of the real Z^0 and the fake Z^0, $M(Z\text{"}Z\text{"})$, is plotted in Fig.16. The probability to fake the Higgs boson, 600 GeV $< M(Z\text{"}Z\text{"}) <$ 1200 GeV, is less than 2×10^{-3}. The resulting overall probability to fake Higgs signal for the current process is estimated to be less than $\sim 1 \times 10^{-8}$. It corresponds to the cross section of 3.1×10^{-7} pb, which should be compared to 5.2×10^{-4} pb $(= \sigma(H^0 \rightarrow 4e) \times 44\%)$ for signal. Although the estimation is rather crude, this background would be negligible.

4.3 Other backgrounds

4.3.1 $q\bar{q} \rightarrow Z^0\gamma g$ / $gq(/\bar{q}) \rightarrow Z^0\gamma q(/\bar{q})$

The cross sections for these processes would be roughly about order $O(\alpha)$ smaller than that of $pp \rightarrow Z^0 jet$, where α is the fine structure constant. Since we do not positively require the electron identification in the present study, we inevitably consider the photon as an electron. The probability to find a fake cluster in an jet (or jets) per event, $\varepsilon(j \rightarrow \text{"}e\text{"})$, is order of $\sim 1 \times 10^{-2}$, which is the same order of α. Therefore, the overall background level of these processes are estimated to be the same order as that of $pp \rightarrow Z^0 jet$, and are therefore negligible.

$$Bkgd(Z^0\gamma j) \simeq Bkgd(Z^0 j)\frac{O(\alpha)}{\varepsilon(j \rightarrow \text{"}e\text{"})} \simeq Bkgd(Z^0 j)$$

4.3.2 $q\bar{q} \rightarrow Z^0\gamma\gamma$

Since the cross section for $pp \rightarrow Z^0\gamma$ is almost the same for $pp \rightarrow Z^0Z^0$ at $\sqrt{s} =$ 40 TeV[11], we could estimate the cross section for $pp \rightarrow Z^0 2\gamma \rightarrow 2e2\gamma$ as

$$\frac{\sigma(pp \rightarrow Z2\gamma \rightarrow 2e2\gamma)}{\sigma(pp \rightarrow ZZ \rightarrow 4e)} \simeq \frac{\sigma(pp \rightarrow Z\gamma)\, O(\alpha)}{\sigma(pp \rightarrow ZZ)\, Br(Z \rightarrow 2e)} \simeq \frac{1}{4},$$

where $Br(Z^0 \rightarrow 2e)$ is the branching ratio of the decay mode $Z^0 \rightarrow e^-e^+$. Moreover, the probability for the γ pair to be consistent with the Z^0 mass, $\varepsilon(2\gamma \rightarrow \text{"}Z\text{"})$,

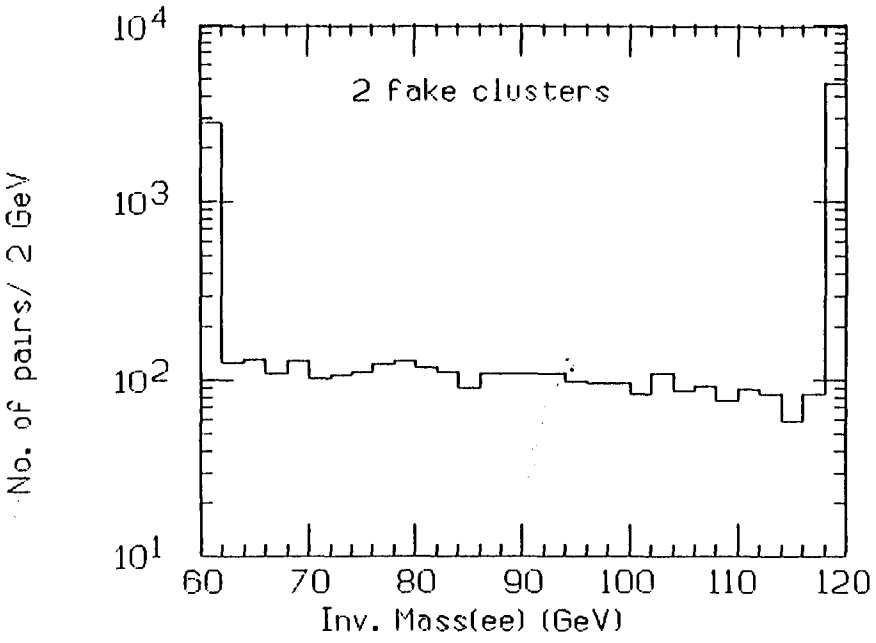

Fig.15. The invariant mass distribution of the fake cluster pair, $M(\text{“}e\text{”}\text{“}e\text{”})$, for which the distance between the two cluster, ΔR, is larger than 0.2 for the process, $pp \to Z^0 + jet \to 2e + jet$.

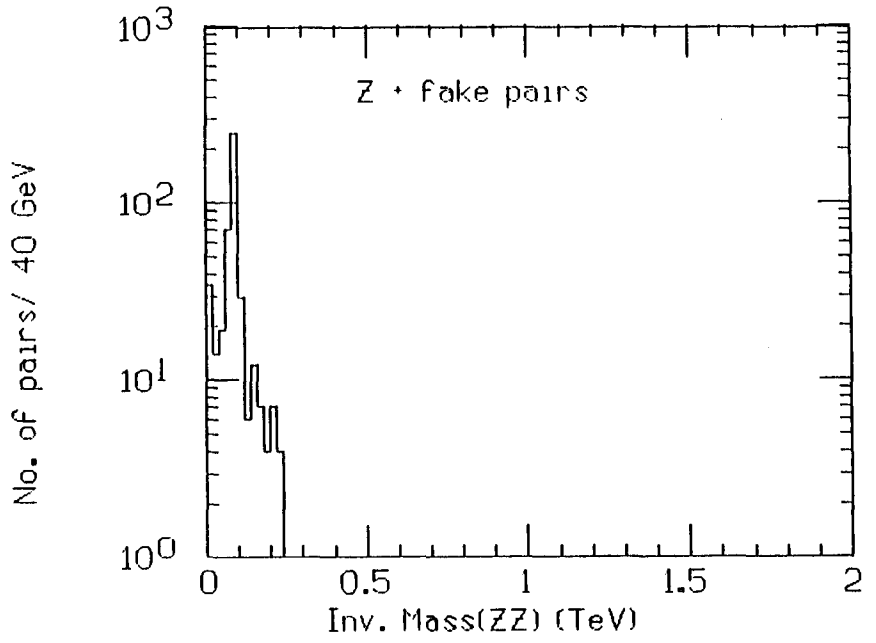

Fig.16. The invariant mass distribution of the real Z^0 and the fake Z^0, $M(Z\text{“}Z\text{”})$, for the process, $pp \to Z^0 + jet \to 2e + jet$.

is expected to be at most oder of $\sim$ 10%. Thus this process would be negligible compared to the continuum process, $pp \rightarrow ZZ \rightarrow 4e$.

$$Bkgd(Z^0\gamma\gamma) \simeq Bkgd(Z^0Z^0)\frac{1}{4}\varepsilon(2\gamma \rightarrow \text{“}Z\text{”}) \ll Bkgd(Z^0Z^0)$$

4.3.3 $qq \rightarrow \gamma\gamma\gamma\gamma$

With the similar argument as in the previous section, this background level is estimated as

$$Bkgd(\gamma\gamma\gamma\gamma) \simeq Bkgd(Z^0\gamma\gamma)\frac{O(\alpha)\,\varepsilon(2\gamma \rightarrow \text{“}Z\text{”})}{Br(Z \rightarrow 2e)} \ll Bkgd(Z^0\gamma\gamma)$$

Thus, this process is further smaller than the process $q\bar{q} \rightarrow Z^0\gamma\gamma$, and is negligible.

4.3.4 $q\bar{q} \rightarrow \gamma\gamma\gamma g$ / $gq(/\bar{q}) \rightarrow \gamma\gamma\gamma q(/\bar{q})$

With the similar argument as in section 4.3.1, this background level is estimated as

$$Bkgd(\gamma\gamma\gamma g) \simeq Bkgd(\gamma\gamma\gamma\gamma)\frac{O(\alpha_s)}{O(\alpha)}\varepsilon(j \rightarrow \text{“}e\text{”}) < Bkgd(\gamma\gamma\gamma\gamma),$$

where α_s is the strong coupling constant. Therefore, this process is also negligible.

5 Summary

We studied the process $pp \rightarrow H^0 \rightarrow Z^0Z^0 \rightarrow 4e$ for very heavy Higgs mass, $M_H = 800$ GeV, at $\sqrt{s} = 40$ TeV with using PYTHIA5.3. The analysis was based entirely on the calorimetry detector. We took account of the “bad” regions in the calorimeter system at the barrel-endcap boundaries and the module boundaries.

If we use only the “good” regions and apply positive e-ID, the efficiency becomes only about 15 %. Since the cross section itself is small, we have to save signal events as much as possible with keeping good signal-to-background ratio. For this purpose, we investigated the validity of “EM-ID” instead of e-ID and examined effects of the “bad” regions to the acceptance and the mass resolution of Z^0.

As for the first subject, the isolation requirement on electromagnetic activities is enough for this particular physics process. The main background is the continuum Z^0Z^0 production, where the positive e-ID does not help to suppress further. The signal-to-background ratio is about 3. Other backgrounds such as

$Z^0 + jet$, $Z^0 + jet + \gamma$, and $Z^0 + \gamma + \gamma$, are estimated to be negligible. As for the second subject, the "bad" regions do not cause obvious deterioration on the mass resolution of Z^0, and improve about factor two in geometrical acceptance.

Even with the contrivances to loosen the e-ID and to use the "bad" regions, the overall detection efficiency is about 45 %. Since the cross section is too small for the very heavy Higgs boson, we need much higher luminosity than $10^{33}\, cm^{-2}s^{-1}$. Under such environment, the "EM-ID" would be much effective in the detection efficiency than the positive e-ID.

References

[1] ALEPH Collab., D. Decamp et al., Phys. Lett. **B 236** (1990) 233; Phys. Lett. **B 241** (1990) 141.

[2] B. W. Lee, C. Quigg, and H. B. Thacker, Phys. Rev. Lett. **38** (1977) 883; Phys. Rev. **D 16** (1977) 1519.

[3] CDF Collab., F. Abe et al., Phys. Rev. Lett **64** (1990) 142. P. J. Franzini, Phys. Rep. **173** (1989) 1.

[4] S. Kim, talk in this Workshop.

[5] H. Yamamoto, Solenoidal Detector Notes, SSC-SDE-9 (Aug. 1989); J. Bensinger, H. Yamamoto, and E. M. Wang, talk presented at ANL Workshop (Nov. 16-18, 1989).

[6] H. -U. Bengtsson and T. Sjöstrand, "PYTHIA: The Lund Monte Carlo for Hadronic Processes",*Proc. of the 1986 Summer Study on the Physics of the Superconducting Supercollider*, ed. R. Donaldson and J. Marx, Snowmass, Colorado, 1986, p. 311.

[7] Y. Unno, talk in the calorimeter session of this Workshop.

[8] A. Yamamoto, talk in this Workshop.

[9] M. Asai, talk in the calorimeter session of this Workshop.

[10] H. Hirayama, talk in the calorimeter session of this Workshop.

[11] E. Eichten, I. Hinchliffe, K. Lane, and C. Quigg, Rev. Mod. Phys. **56** (1984) 579.

Electrons Identification for Top Quarks at SSC

H. H. Williams
University of Pennsylvania

******** This summary is written by the proceeding **********
******** editor based on the transparencies presented. ********

Part of overall study of $t\bar{t}$ reconstruction

Mt=150GeV, ISAJET, B=15kG, Tracking volume r=1.7m, 3.4m long,
Spherical calorimeter $\Delta\eta$ x $\Delta\phi$ = 0.05 x 0.063,
QFL simulation with $0.15/\sqrt{E_{em}} + 0.01$ and $0.50/\sqrt{E_{had}} + 0.03$

Conclusion on H/EM cut and isolation

- Appears to be no problem for liquid inonization calorimeters for luminosities of several x 10^{33} $cm^{-2}s^{-1}$.
- Scintillator calorimeter OK to still higher luminosity.
- Use E_t^{bord} rather than E_t^{cone}

Comments on conversions

- Conversions are dominant background until they are removed.
- CDF algorithm works very well but relies on detailed tracking may not be very robust at SSC.
- Measurement of pulse height in 1st layer of silicon likely to be better, more robust.
- Still need to extrapolate stiff electron track to silicon.
- Does this work at very high luminosity? If not, whatelse?

Pileup Issues on the Electron Identification

Yoshihide Sakai

KEK, National Laboratory for High Energy Physics

Tsukuba, Ibaraki, Japan 305

ABSTRACT

The effect of pileup on the electron identification has been studied taking into account the time evolution of the realistic detector signal. The emphasis is placed on the effect to the electron isolation requirement. The study shows effect due to the pulse length can be greatly reduced by the wave form measurement using neighboring two bunches.

INTRODUCTION

At the SSC, the interaction rate of 10^8 Hz is expected from the total p-p cross section of about 100 mb at $\sqrt{s} = 40$ TeV and designed luminosity of $L = 10^{33}cm^{-2}sec^{-1}$. Therefore, it is generally thought that the pileup effect is important at the SSC. There are two different sources for so called 'pileup', which are sometimes mixed and treated together.

1) Due to multi-interactions at single beam crossing: Since the rate of beam crossing of SSC accelerator is 60 MHz, an average of 1.6 interactions is expected for interaction rate of 10^8 Hz. This indicates that a considerable fraction of beam crossing have 2 or more interactions overlapped together.

2) Due to detector signal time response: If detector signal is much longer than a beam crossing interval (16 nsec), a signal contributes to several beam crossings. For example, effectively events from 6 beam crossings would contribute in case of 100 nsec wide signal. This effect would be important for calorimeter.

Generally, the detector with faster signal is preferred considering item 2). If signal width is less than 16 nsec, then the detector is free from the effect of the

item 2), but still the effect from item 1) can not be avoided.

The effect of pileup will show up in various aspects, such as trigger rates, jet reconstruction, track pattern recognition etc. Here, the effect on electron analysis is considered. An electron in most of the interesting physics is an 'isolated electron'. An isolation requirement usually imposes a small energy around an electron and would be affected by pileup. Also, electron identification itself would be affected by pileup. In the following, the effect of pile up on above two aspects is discussed.

EFFECT ON ELECTRON ISOLATION

Recently, a study of effect of pileup on electron isolation for top event selection was done by F.Page.[1] He studied isolation of electron originated from top with mass of 140 GeV by looking a sum of E_T of particles within cone of $\Delta R = \sqrt{\Delta y^2 + \Delta\phi^2} < 0.2$ or 0.4 around an electron. He superimposed 10 minimum bias events (1.6 interactions $\times$ 6 crossings) onto top events and compared E_T sum distributions for pileup and no pileup cases. He found the contribution from superimposed events to E_T within cone is considerably large and concluded that the pileup was serious problem. (He used minimum bias events only, but it is considered that the two jet events with low P_t are also taken into account as 'pileup' events.[2] In this case, the pileup effect would be even larger.) However, in reality some events are coming from different crossings and contribution would be different. This effect is not taken into account in above study. In order to take this into account, one needs to study a time evolution of signal and interactions at each beam crossing.

Simulation of Time Evolution of Signal with Pileup

Here, Liq. Ar calorimeter is considered, since wave form of the Liq. Ar detector signal can be analytically calculated and Liq. Ar has slower signal than other detectors. However, the discussion holds for any type of detectors in principle. The wave form of shaper amplifier for impulse signal can be written with parameters of peaking time (τ_p), number of differentiation (n), and number

of integration (m). A parameter n = 1, 2, 3 gives Poisson, bipolar, and three lobe shaping, respectively. The wave form for Liq. Ar detector signal can be obtained by convoluting an impulse wave form with Liq. Ar signal $A \cdot (T_d - t)$, where T_d is a maximum drift time of electron between Liq. Ar gap. Fig. 1 shows some examples of wave form. Note that the peak position of convoluted signal with $T_d = 400$ nsec is about twice of τ_p.

The pileup effect on the wave form of signal has been studied by several people.[3,4] They generated the minimum bias/Low P_t tow-jet events at each crossing according to Poisson distribution of average 1.6 events and superimposed wave forms for calorimeter cell which has actual signal. An example of wave form superimposed with pileup signals studied by T.Kondo[4] is shown in Fig. 2.

Effect of Pileup on Electron Isolation with Wave Form Simulation

The effect of pileup to electron isolation has been studied incorporating Liq. Ar calorimeter wave form analysis mentioned above. Higgs events with decay channel of Higgs $\rightarrow W^+W^- \rightarrow e\nu +$ jets are used for study. Events are generated using ISAJET[5] program and Higgs mass is chosen at 400 GeV. For pileup events, TWOJET events with $3 < P_t < 200$ GeV are generated using ISAJET program. Calorimeter segmentation is assumed to be $\Delta y \times \Delta\phi = 0.05 \times 0.05$ and all particles are assumed to deposit all energy into one calorimeter tower which they hit. Electrons, photons, π^0's, and η^0's deposit all energy into EM part with energy resolution of $\sigma_E/E = 15\%/\sqrt{E}$, while hadrons deposit all energy into hadron part with $\sigma_E/E = 50\%/\sqrt{E}$. Muons are assumed to deposit 3 GeV in hadron part.

For wave form analysis, bipolar shaping with 3 integration (n=2 and m=3), $\tau_p = 50$ nsec, and $T_d = 400$ nsec are chosen here. This gives peak position of output signal around 100 nsec. The calorimeter signal is assumed to be sampled at every beam crossing (via either analog memory or FADC). The beam crossing for Higgs event is assumed to be (at least roughly) determined at the trigger stage and the data for several beam crossings around Higgs event are read out.

Electron isolation is studied in the same way as done by F.Page: Distributions are compared for a sum of E_T of calorimeter towers within cone of $\Delta R =$

$\sqrt{\Delta y^2 + \Delta\phi^2} < 0.2$ or 0.4 around the tower which an electron from W hits. For wave form simulation case, energy deposit of calorimeter is calculated with two different ways:

A) Use sampled pulse hight for beam crossing of Higgs event. Towers with negative energy are not used for sum assuming the data below pedestals are suppressed in the readout.

B) Use sampled pulse hight for three beam crossings (± 1 around Higgs event crossing) and fit them with parabola to get peak pulse hight and timing as done by T.Kondo's study. Towers with peak timing inconsistent with Higgs event crossing ($|\Delta T| > 10$ nsec) are rejected from sum.

Fig. 3 shows distribution of fitted peak time for towers within cone of $\Delta R < 0.4$. Clear peaks corresponding beam crossings can be seen. The intervals of peaks different from beam crossing interval reflects the fact that the pulse shape is not parabola. Most of signal from different crossings can be rejected by a requirement of $|\Delta T| < 10$ nsec. Fig. 4 (a) shows E_T sum distributions within $\Delta R < 0.4$ for cases of no pileup, average 1.6 events superimposed, and average 10 events superimposed. In this case, TWOJET events are just superimposed according to Poisson distribution and no wave form simulation is done. Fig. 4 (b) shows corresponding distribution with wave form simulation for calorimeter energy calculated by methods A and B, respectively. Superimposing average 1.6 events has only small effect but superimposing average 10 events gives quite large effect and the isolation requirement will be seriously damaged as pointed out previously. With wave form simulation, energy calculation by method A gives similar result as superimposition of average 10 events and superimposition method seems good approximation for this case. However, energy calculation by method B eliminates most of the effects by signals from different beam crossing and the distribution is almost same as one with average 1.6 events superimposed, which can not be avoid in any case. Fig. 5 (a) and (b) show corresponding distributions for $\Delta R < 0.2$ case and show same effect as $\Delta R < 0.4$ case.

Therefore, it is essential to record the wave form information of the calorimeter signal in order to avoid the pileup effect on isolation for slow signal detector

such as Liq. Ar. However, sampling 3 beam crossings and simple parabola fitting is good enough to eliminate the pileup effect from different crossings.

Effect of Pileup to Efficiency and Background Rejection

With presence of pileup effect, one has to increase a threshold of E_T sum cut for isolation in order to keep the efficiency for signal events. Increasing threshold usually decreases the rejection power for background. However, the background events also suffers the pileup effect with same way as signal events. Therefore, the above effects tend to cancel each other.

The effect of pileup to the efficiency and background rejection has been studied by H.Yamamoto.[6] He used Higgs $\rightarrow$ ZZ $\rightarrow$ 4e events for signal and $t\bar{t} \rightarrow$ 4e + jets events as background. He studied the efficiency for Higgs and background rejection as a function of E_T sum cut value with no pileup and with pileup case. His result shows some tendency of cancellation when the background rejection is fixed.

EFFECT ON ELECTRON IDENTIFICATION

Pileup may also cause an effect on the electron identification itself. Here, the effect of pileup for electron identification has been studied in two cases:

1) One of the most effective electron identification is matching of energy deposit in EM calorimeter and momentum measured by tracking system. Fig. 6 shows distribution of $(E_{EM} - p)/\sqrt{p}$ for no pileup and average 10 events superimposed case. (a factor $1/\sqrt{p}$ is to cancel the energy dependence of resolution.) Here, E_{EM} is a sum of energy in 3 $\times$ 3 EM towers ($\Delta\eta \times \Delta y = 0.15 \times 0.15$) around the electron decayed from W in Higgs events studied above. p is momentum of electron which is supposed to be measured by tracking system, but here generated momentum was taken for simplicity. The effect of pileup is small even with average 10 events superimposed case (no wave form simulation).

2) Another way of identifying electron is to require the most energy being deposited in EM part of the calorimeter and only small energy deposit in hadronic

part. Fig. 7 shows distribution of $E_T(HAD)/E_T(EM)$ for 3×3 calorimeter towers around the electron decayed from W. Again, the effect of pileup is small enough even with average 10 events superimposed case.

Therefore, the effect of pileup to the electron identification is small enough with studied calorimeter segmentation even with higher luminosity ($L \sim 10^{34}$ $cm^{-2}sec^{-1}$).

SUMMARY

The effect of pileup to electron identification is studied in the following aspects:

The effect on electron isolation has been studied with realistic detector signal wave form simulation. The effect due to slow time response of signal can be reduced to insignificant level if the wave form of the signal is recorded (three beam crossing samples are enough). The effect of multi-interactions in same beam crossing can not be avoided. This effect is not serious at luminosity of 10^{33} $cm^{-2}sec^{-1}$. At high luminosity ($L = 10^{34}$ $cm^{-2}sec^{-1}$), this effect will be quite serious. One hope is that we may be able to find the isolation requirement which is insensitive to pileup effect. For example, in summing E_T within cone, one may sum up towers inly with $E_T > 1$ GeV. This reduces the pileup effect considerably as shown in Fig. 8, but need more study including background rejection. Another hope is that pileup effect cancels in some extent considering the efficiency vs background rejection. We need further study for these aspects.

On the other hand, pileup effect on electron ID itself seems to be small even for high luminosity.

The author wishes to thank Prof. T.Kondo and Dr. H.Iwasaki for providing a information of their study and their programs.

REFERENCES

1) F.Page, talk given at Workshop on Simulation for SSC, Jan 1990, Dallas.

2) A.Bay *et al.*, in proceedings of Snowmass '88, p882; J.Freeman and C.Newman-Holmes, in proceedings of Workshop on Experiments, Detectors, and Experimental areas for the Supercollider, Berkeley, 1987.

3) E.Stern, talk given at Workshop on Simulation for SSC, Jan 1990, Dallas.

4) Study done by T.Kondo and H.Iwasaki, mentioned in T.Kondo, "ACS Detector", KEK Preprint 89-191, JSD-NOTE-1990-005.

5) F.E.Paige and S.D.Protopopescu, BNL-37066 (1985).

6) H.Yamamoto, talk given at Workshop on Simulation for SSC, Jan 1990, Dallas.

FIGURE CAPTIONS

Fig. 1. Wave forms for different parameters for shaping. Solid, dashed, and dot-dashed lines shows Poisson, bipolar, and three-lobe shaping.

Fig. 2. Time evolution of simulated Liq. Ar signals with pileup events.

Fig. 3. Time distribution of fitted peak for calorimeter towers within cone of ΔR of 0.4 around electron.

Fig. 4. E_T sum distribution for $\Delta R < 0.4$ case: (a) no wave form analysis. Solid line shows no pileup case, dashed line shows average 1.6 events superimposed, and dot-dashed line shows average 10 events superimposed. (b) with wave form simulation. Dashed line shows energy calculated by method A and dotted line shows energy calculated by method B (see text).

Fig. 5. E_T sum distribution for $\Delta R < 0.2$ case: (a) no wave form analysis. Solid line shows no pileup case, dashed line shows average 1.6 events superimposed, and dot-dashed line shows average 10 events superimposed. (b) with wave form simulation. Dashed line shows energy calculated by method A and dotted line shows energy calculated by method B (see text).

Fig. 6. $(E_{EM} - p)/\sqrt{p}$ distribution for no pileup case (solid line) and for average 10 events superimposed case.

Fig. 7. $(E_T(HAD)/E_T(EM)$ distribution for no pileup case (solid line) and for average 10 events superimposed case.

Fig. 8. E_T sum distribution for $\Delta R < 0.4$ case: Towers only with $E_T > 1$ GeV are used in sum. Solid line shows no pileup case, dashed line shows average 1.6 events superimposed, and dot-dashed line shows average 10 events superimposed.

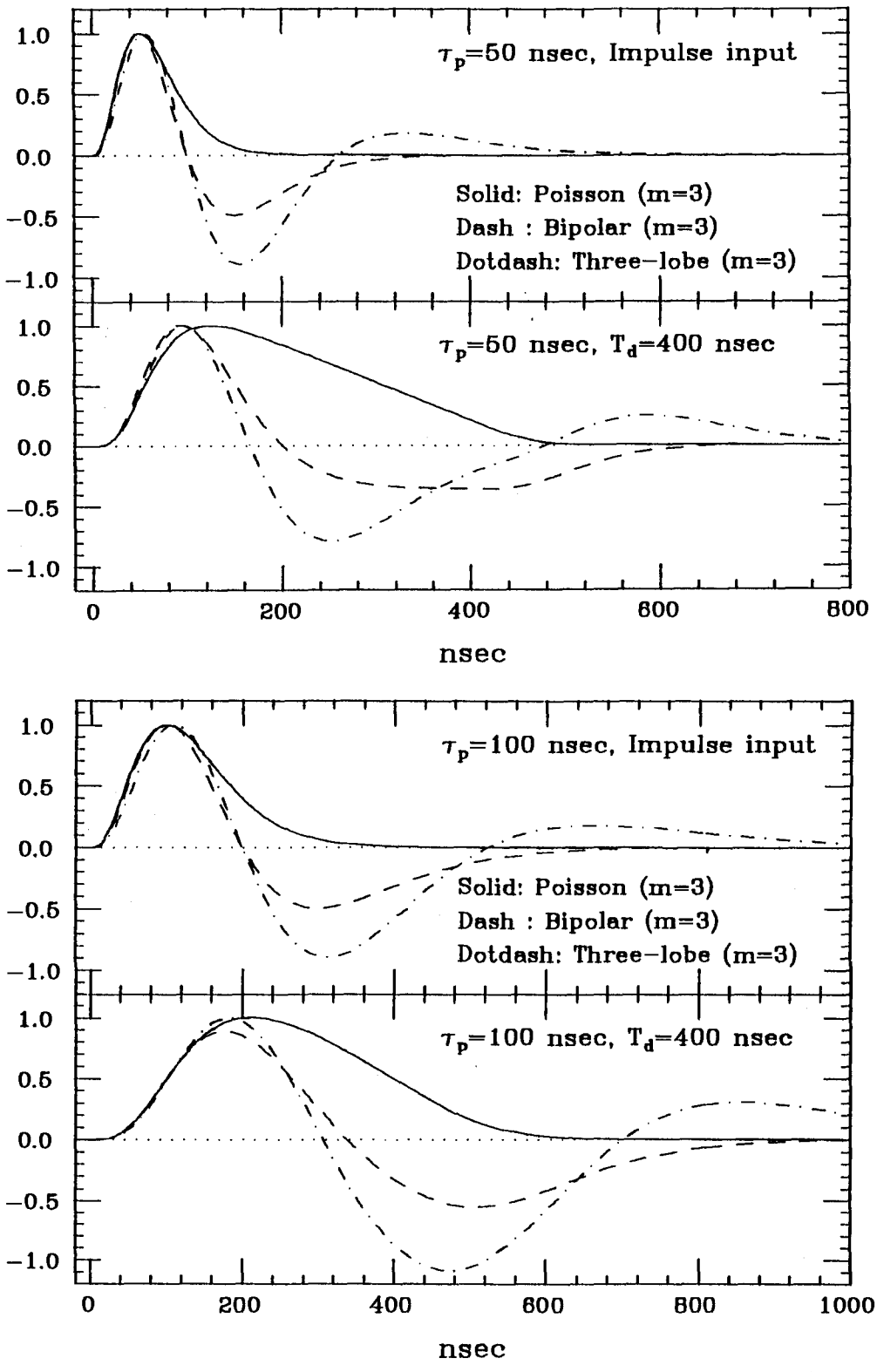
1.0
0.5
0.0
−0.5
−1.0
τp=50 nsec, Impulse input
Solid: Poisson (m=3)
Dash : Bipolar (m=3)
Dotdash: Three−lobe (m=3)
τp=50 nsec, Td=400 nsec
0
200
400
600
800
nsec
τp=100 nsec, Impulse input
τp=100 nsec, Td=400 nsec
1000

Fig. 1

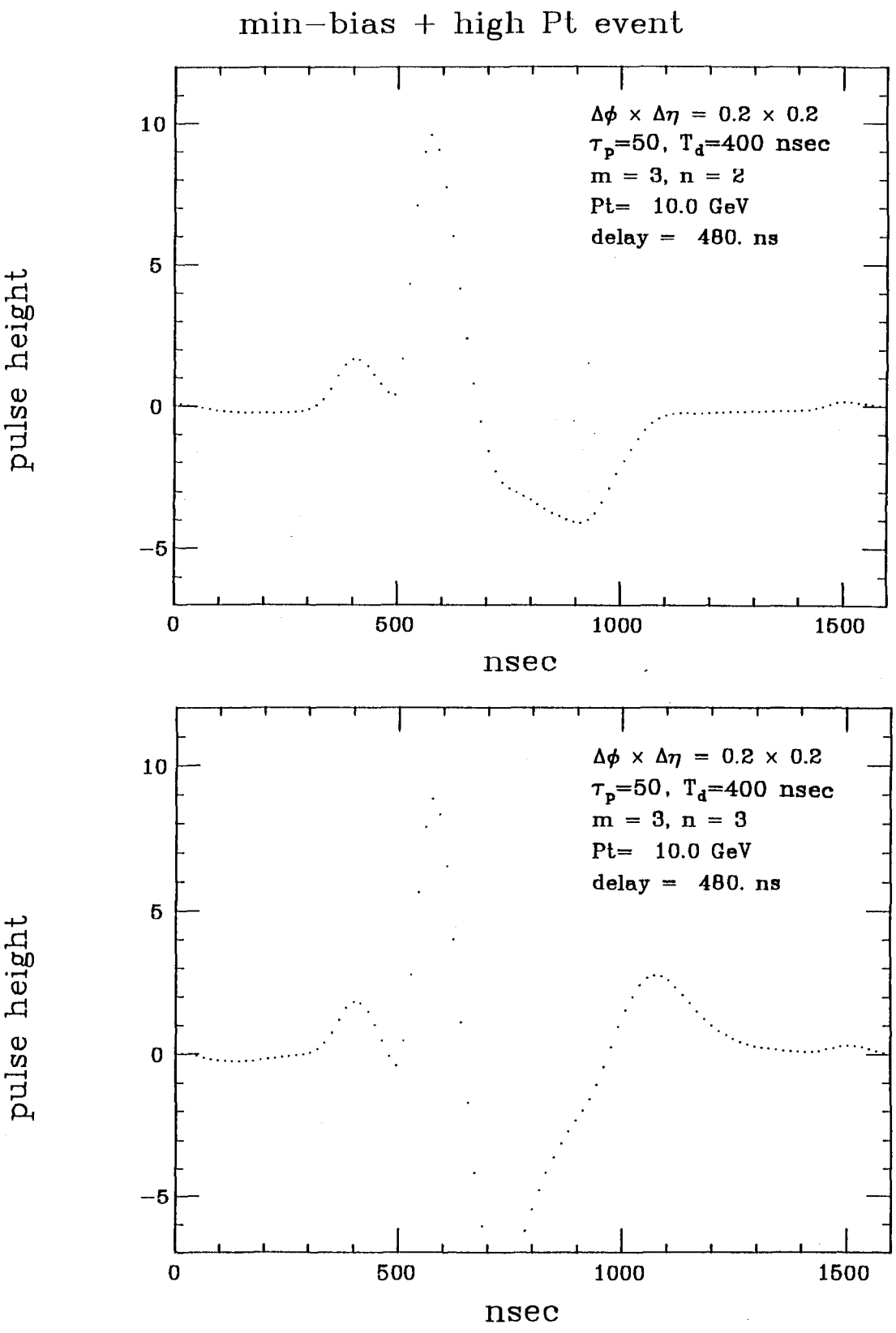
min−bias + high Pt event
pulse height
10
5
0
−5
0
500
1000
1500
nsec
Δφ × Δη = 0.2 × 0.2
τp=50, Td=400 nsec
m = 3, n = 2
Pt= 10.0 GeV
delay = 480. ns
pulse height
10
5
0
−5
0
500
1000
1500
nsec
Δφ × Δη = 0.2 × 0.2
τp=50, Td=400 nsec
m = 3, n = 3
Pt= 10.0 GeV
delay = 480. ns

Fig. 2

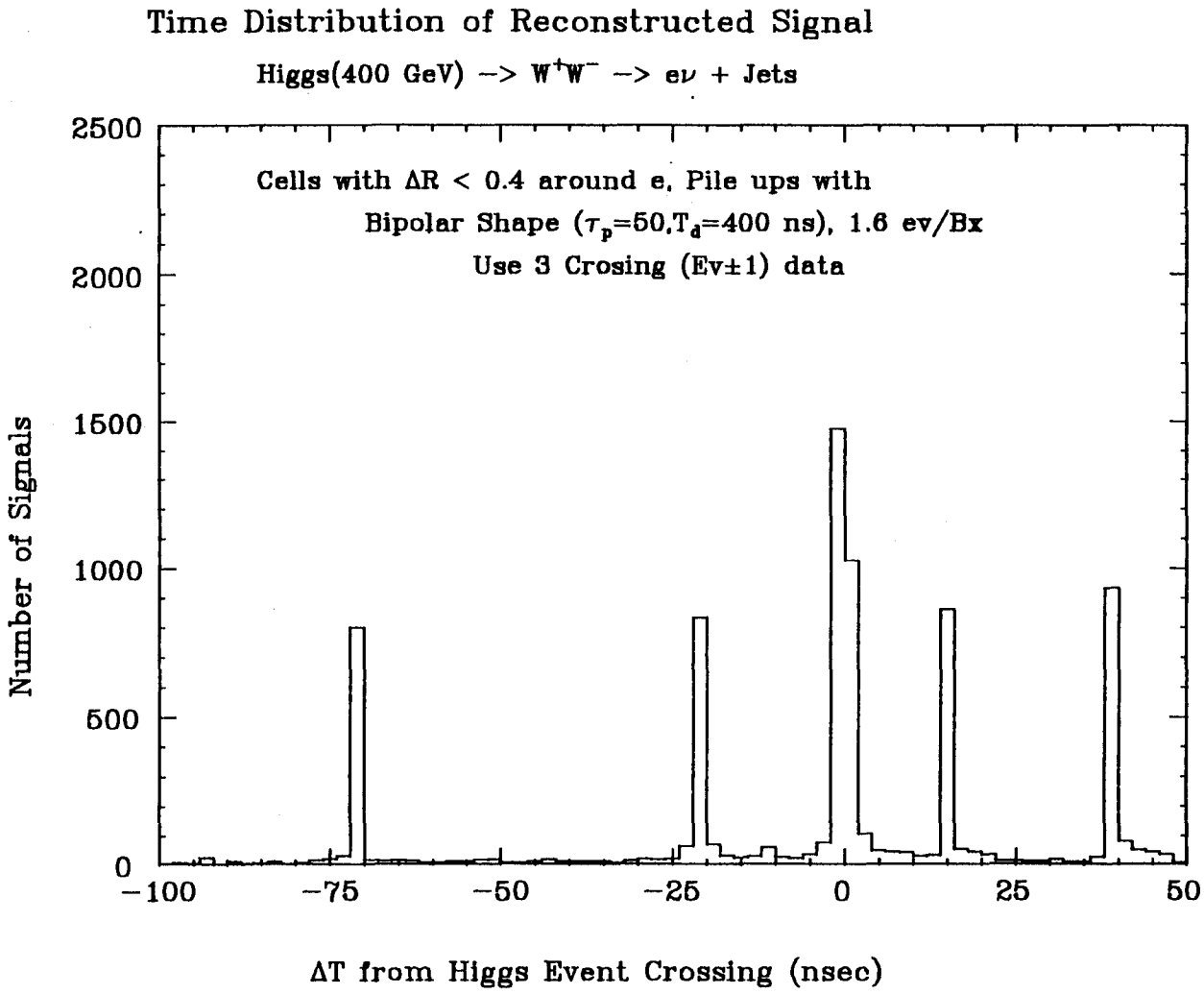
Time Distribution of Reconstructed Signal
Higgs(400 GeV) -> W+W- -> eν + Jets
Cells with ΔR < 0.4 around e, Pile ups with
Bipolar Shape (τp=50,Td=400 ns), 1.6 ev/Bx
Use 3 Crosing (Ev±1) data
Number of Signals
2500
2000
1500
1000
500
0
−100
−75
−50
−25
0
25
50
ΔT from Higgs Event Crossing (nsec)

Fig. 3

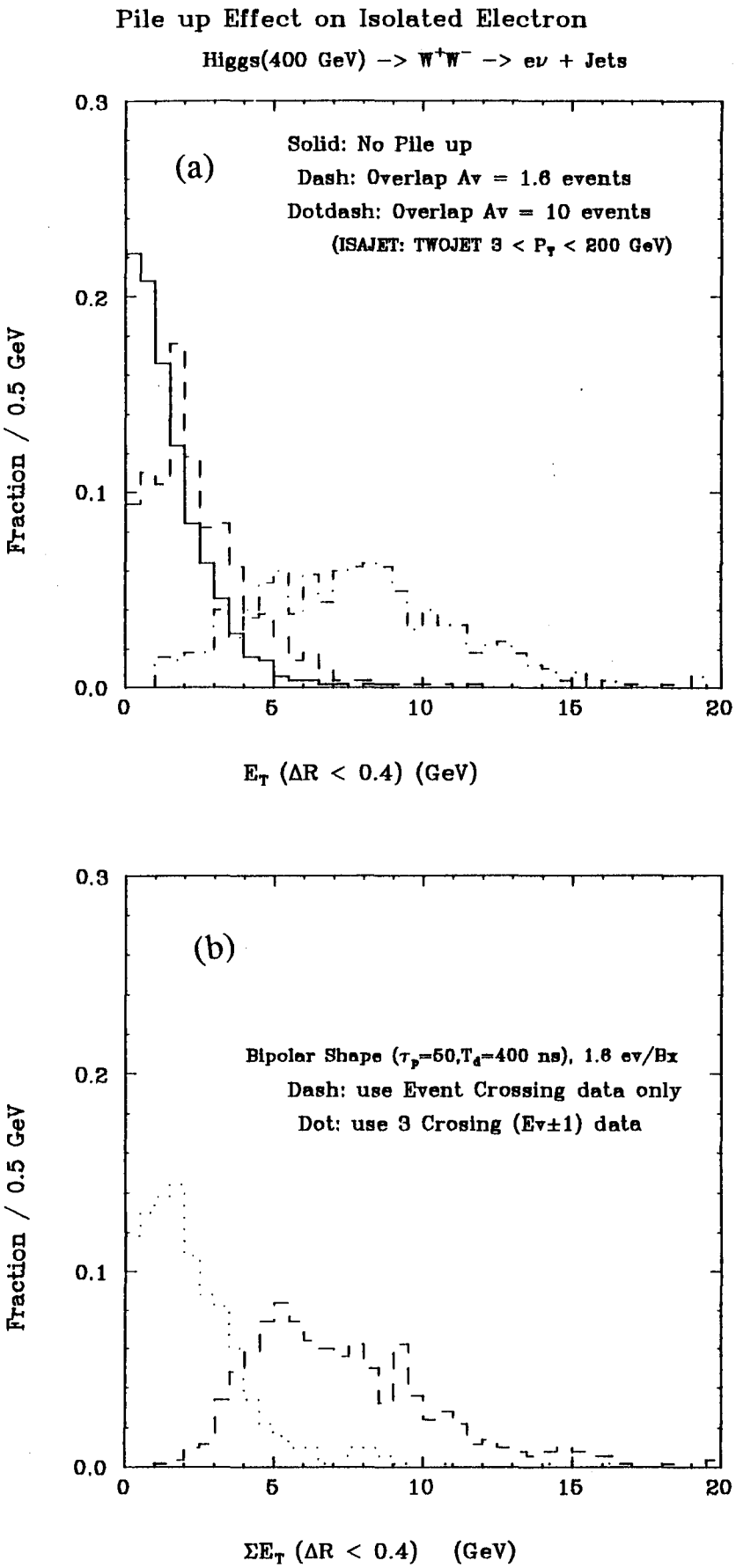
Pile up Effect on Isolated Electron
Higgs(400 GeV) -> W+W- -> eν + Jets
(a)
Solid: No Pile up
Dash: Overlap Av = 1.6 events
Dotdash: Overlap Av = 10 events
(ISAJET: TWOJET 3 < P_T < 200 GeV)
Fraction / 0.5 GeV
E_T (ΔR < 0.4) (GeV)
(b)
Bipolar Shape (τ_p=50,T_d=400 ns), 1.6 ev/Bx
Dash: use Event Crossing data only
Dot: use 3 Crosing (Ev±1) data
Fraction / 0.5 GeV
ΣE_T (ΔR < 0.4) (GeV)

Fig. 4

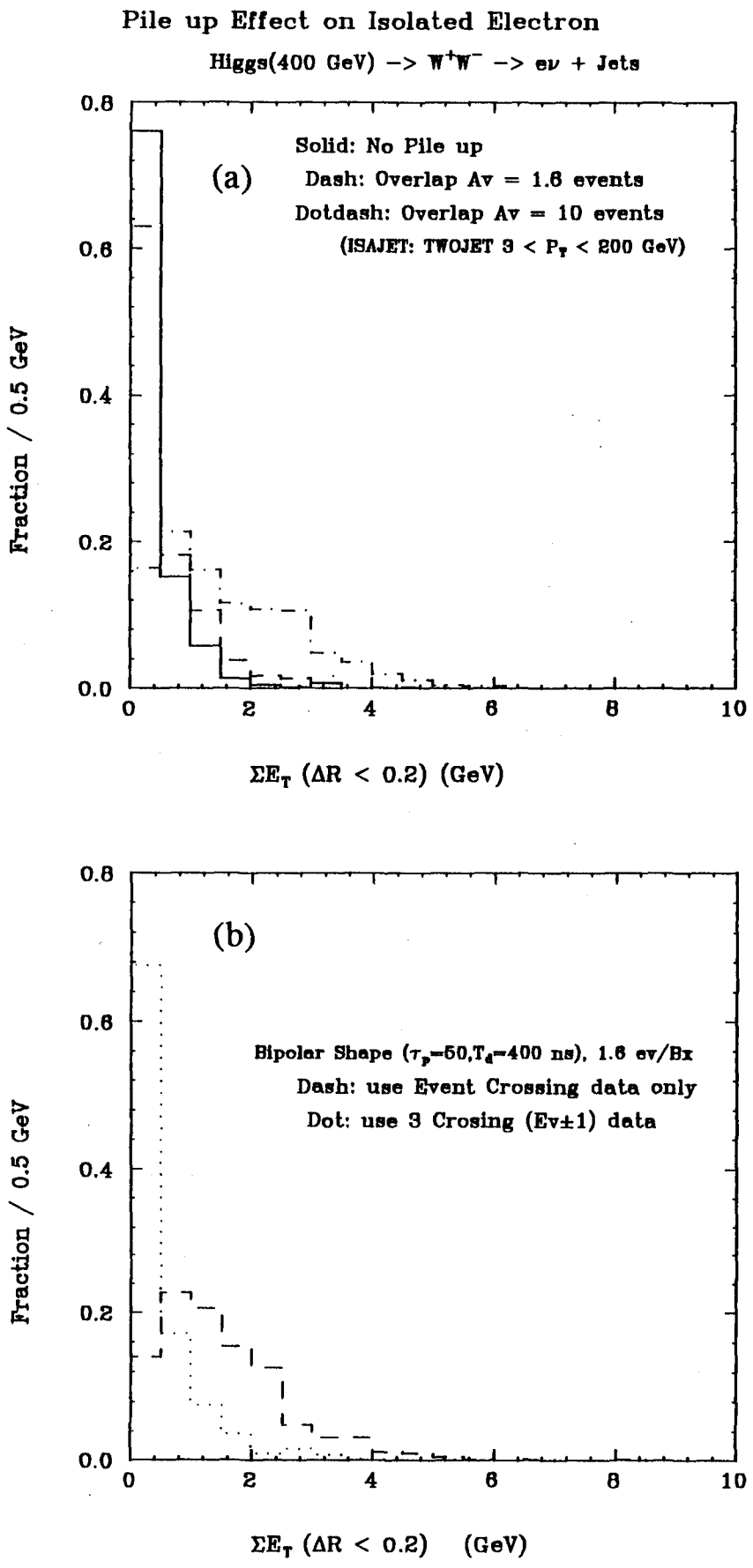
Pile up Effect on Isolated Electron
Higgs(400 GeV) -> W+W- -> eν + Jets
(a)
Solid: No Pile up
Dash: Overlap Av = 1.6 events
Dotdash: Overlap Av = 10 events
(ISAJET: TWOJET 3 < PT < 200 GeV)
Fraction / 0.5 GeV
ΣET (ΔR < 0.2) (GeV)
(b)
Bipolar Shape (τp=50,Td=400 ns), 1.6 ev/Bx
Dash: use Event Crossing data only
Dot: use 3 Crosing (Ev±1) data
Fraction / 0.5 GeV
ΣET (ΔR < 0.2) (GeV)

Fig. 5

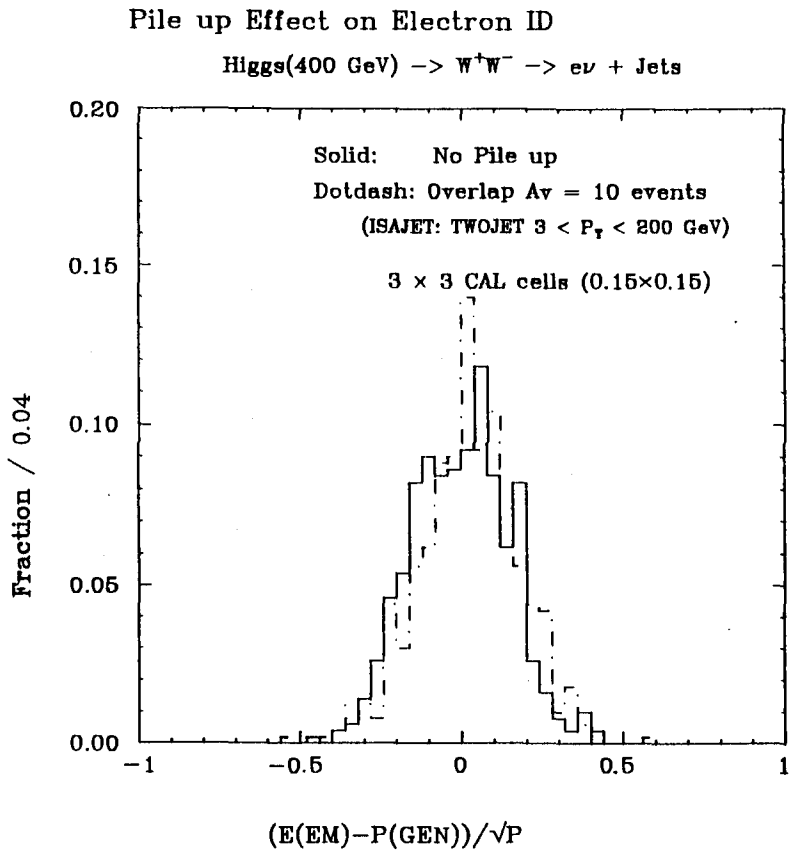
Pile up Effect on Electron ID
Higgs(400 GeV) -> W+W- -> eν + Jets
Solid: No Pile up
Dotdash: Overlap Av = 10 events
(ISAJET: TWOJET 3 < P_T < 200 GeV)
3 x 3 CAL cells (0.15×0.15)
Fraction / 0.04
0.20
0.15
0.10
0.05
0.00
−1
−0.5
0
0.5
1
(E(EM)−P(GEN))/√P

Fig. 6

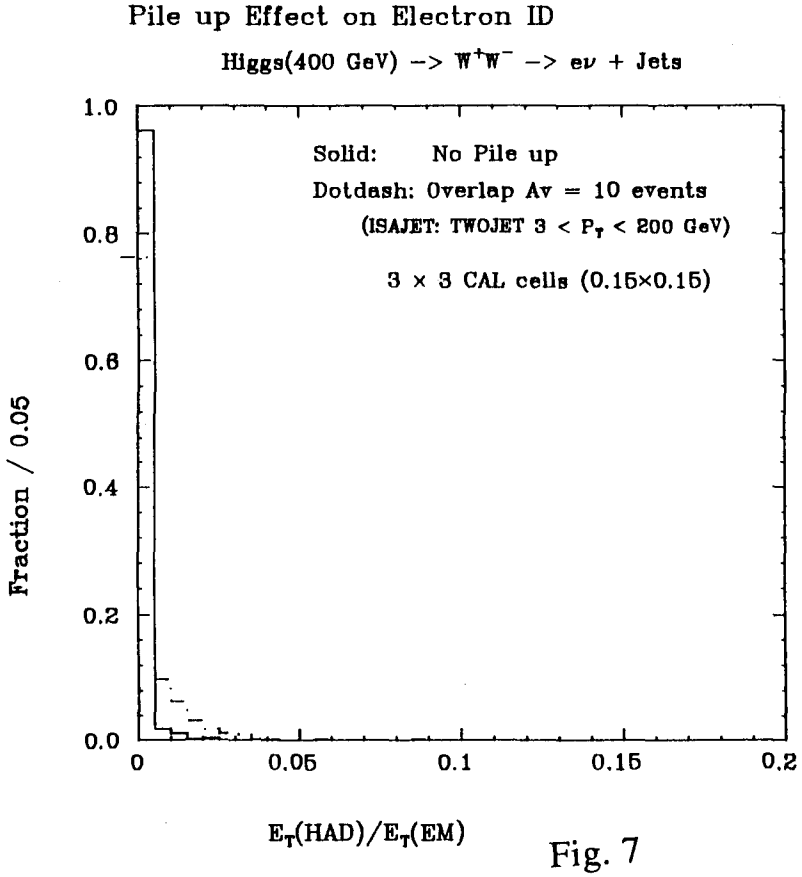
Pile up Effect on Electron ID
Higgs(400 GeV) -> W+W- -> eν + Jets
Solid: No Pile up
Dotdash: Overlap Av = 10 events
(ISAJET: TWOJET 3 < P_T < 200 GeV)
3 x 3 CAL cells (0.15×0.15)
Fraction / 0.05
1.0
0.8
0.6
0.4
0.2
0.0
0
0.05
0.1
0.15
0.2
E_T(HAD)/E_T(EM)

Fig. 7

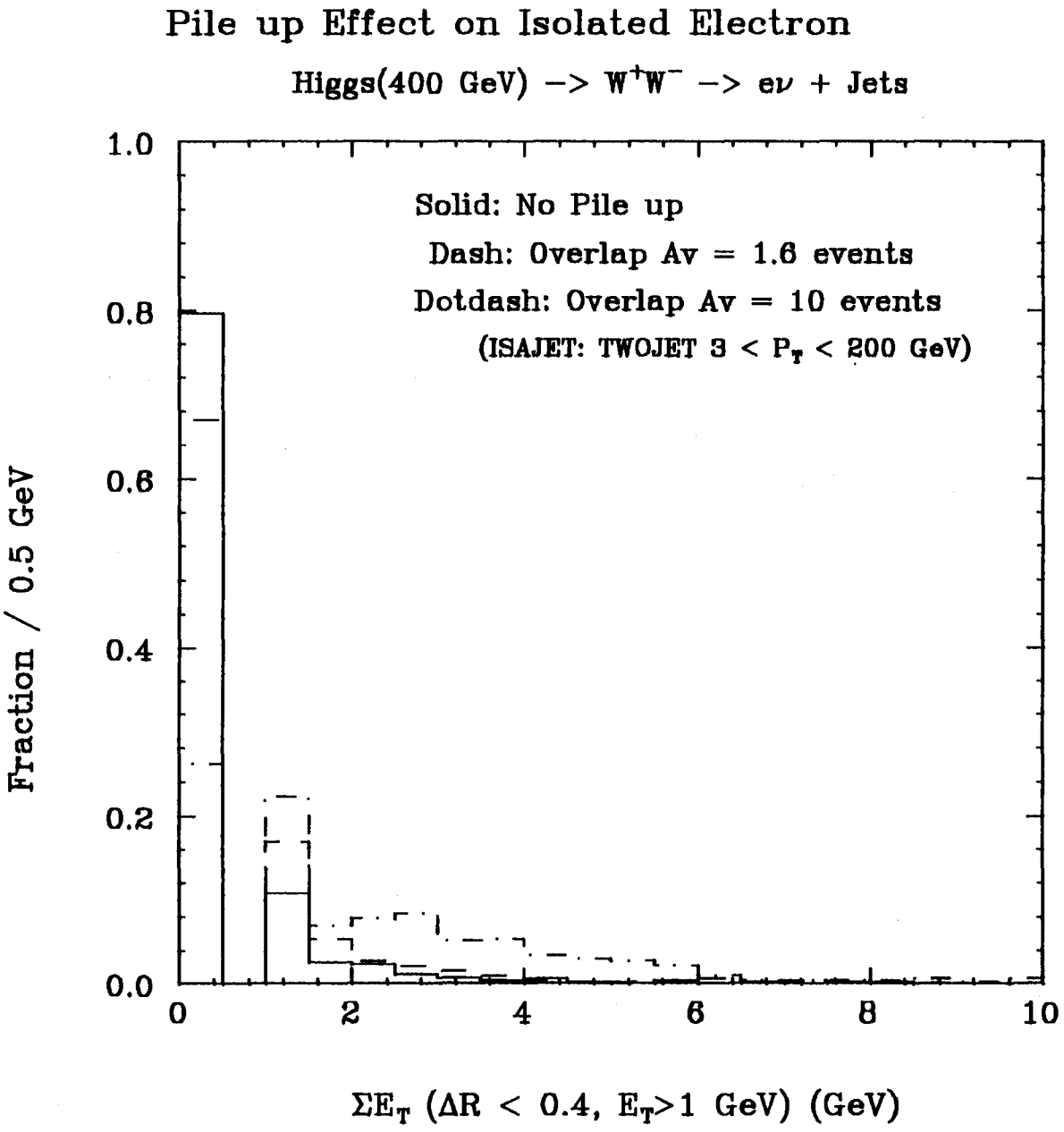
Pile up Effect on Isolated Electron
Higgs(400 GeV) -> W+W- -> eν + Jets
Solid: No Pile up
Dash: Overlap Av = 1.6 events
Dotdash: Overlap Av = 10 events
(ISAJET: TWOJET 3 < P_T < 200 GeV)
Fraction / 0.5 GeV
1.0
0.8
0.6
0.4
0.2
0.0
0
2
4
6
8
10
ΣE_T (ΔR < 0.4, E_T>1 GeV) (GeV)

Fig. 8

Integrated Tracking System

April 25, 9:00-10:40

Tracking Volume for Solenoidal Detector at the SSC

A. SEIDEN
Santa Cruz Institute for Particle Physics
University of California, Santa Cruz, CA 95064

Abstract

We present some of the considerations related to choosing the optimum tracking volume for a solenoidal detector at the SSC. Substantial further work is needed to achieve an optimum design.

1. Introduction

The choice of the tracking volume for a solenoidal SSC detector has many effects on the overall detector. First of all, the tracking performance is affected in the areas of

(a) Acceptance,

(b) Momentum resolution,

(c) Occupancy and its effect on pattern recognition, and

(d) Triggering schemes using the tracking information.

More generally,

(e) The calorimeter dimensions affect jet mass reconstruction because of shower spreading.

(f) The shapes of the calorimeter towers are affected by the volume, particularly the ratio of the half-length to the radius, if we wish to maintain projective geometry.

(g) The number of radiation lengths of coil traversed depends on the geometry. The maximum is in the corners, which again depends on the ratio of the half-length to the radius.

(h) The overall detector cost grows as the tracking volume increases, since the outer detectors generally require fixed depths for calorimetry or muon detection and tracking.

Note: Items (b), (c) and (e) argue for a large radius and half-length. Items (f) and (g) argue for a small half-length, while (h) would argue for a small radius and half-length.

The issue of mass reconstruction for calorimeters of varying dimension is discussed in reference 1. We discuss here mostly the tracking issues. For the discussion, we will assume a B field of about 2 Tesla, which is a practical maximum for coils of large radius $\gtrsim 1.5$ m. Small changes in dimensions will generally have small effects on the tracking performance. This makes the final decision somewhat qualitative.

2. Resolution Requirements for the Higgs Boson

The Standard Model with a single Higgs boson provides an important benchmark for SSC physics. The Higgs will show up in the final states of two gauge bosons as must any other source of electroweak symmetry breaking. An SSC experiment should do as well as possible (acceptance and resolution) on this channel in order to allow some room for surprises, such as multiple Higgs bosons. We discuss below the resolution requirements in a general way. In the next section we look at the implications for the tracking volume.

We look specifically at the Higgs decay into Z^0Z^0 which subsequently decay to electrons or muons.[2] This provides the cleanest final state for Higgs detection. Four values for the Higgs mass were studies: 200, 400, 600, or 800 GeV. Events were generated at each of the above masses using PYTHIA 4.8. Leptons were accepted provided they had $P_\perp > 10$ GeV and rapidity $|Y| \leq 2.5$. Figure 1 shows the fraction of Higgs events accepted from all events as a function of the above kinematic cuts. For the values chosen 54% of all Higgs events were accepted for a Higgs mass of 200 GeV, increasing to 80% at 800 GeV. To simulate the detector response, the lepton momenta were folded with gaussian resolution functions with standard deviations parametrized as

$$\frac{\sigma_{P_\perp}}{P_\perp} = \sqrt{(0.008)^2 + (\alpha P_\perp)^2}, \quad P_\perp \text{ in TeV}.$$

The parameter α was varied from 0.05–0.5. The multiple scattering contribution to the resolution has been taken to be 0.008.

The Higgs decay has two natural resolution parameters associated with event reconstruction. These are the natural width of the Z^0 and the natural width of the H^0. A detector which allows mass reconstruction with a mass resolution comparable to the Z^0 width will do the best job in background rejection, and will not require many additional cuts (for example, on the Z^0 transverse momentum, which loses large numbers of events, especially for lower Higgs masses). The Higgs width compared to its mass is similar or smaller than that of the Z^0 for masses below about 300 GeV. Above this mass, the ratio grows rapidly.

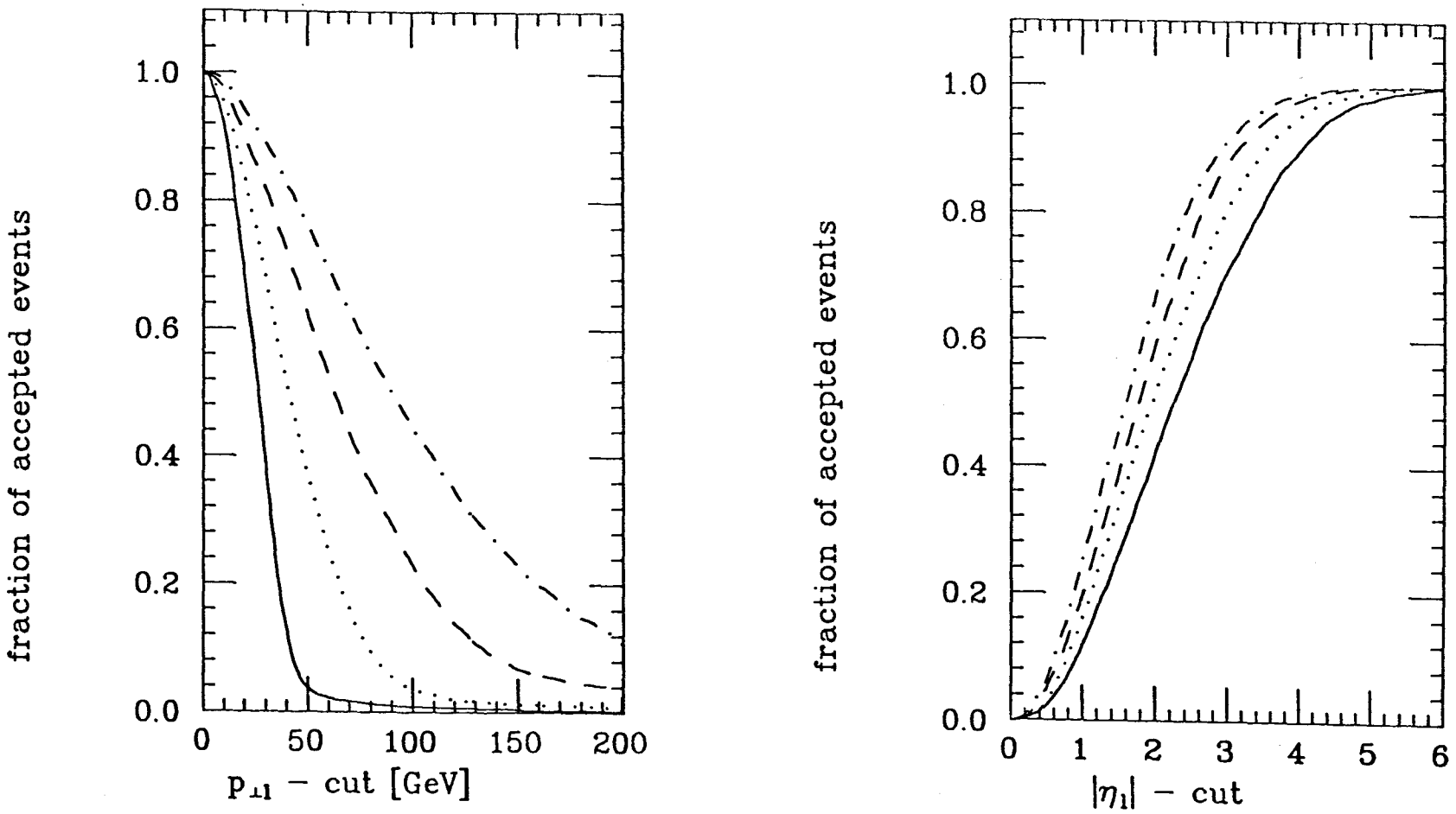

solid: M_H = 200 GeV, dotted: M_H = 400 GeV
dashed: M_H = 600 GeV, dashed-dotted: M_H = 800 GeV

Fig. 1

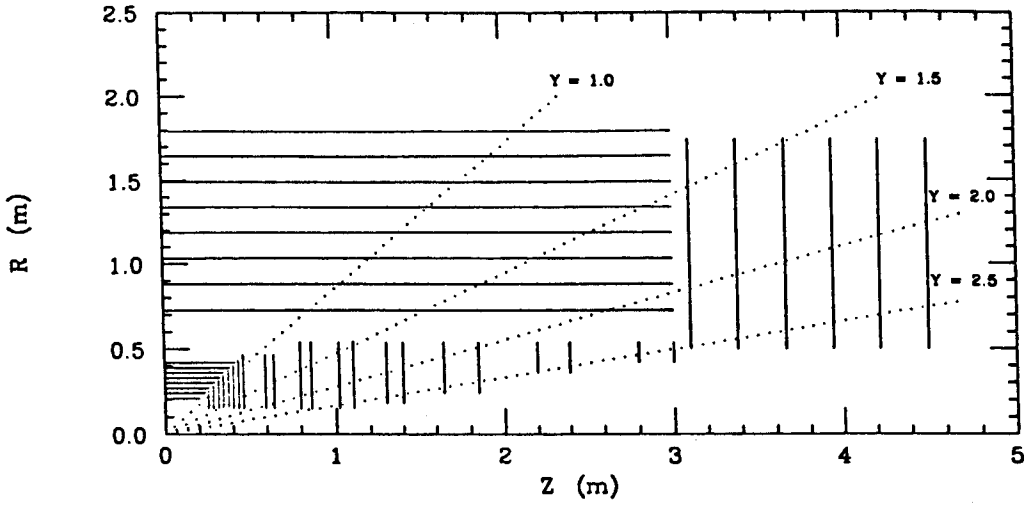

Fig. 4 Model tracking detector consisting of 8 layers axial silicon, 22 layers radial silicon, 8 superlayers straw tube drift chambers and 6 superlayers of radial drift chambers.

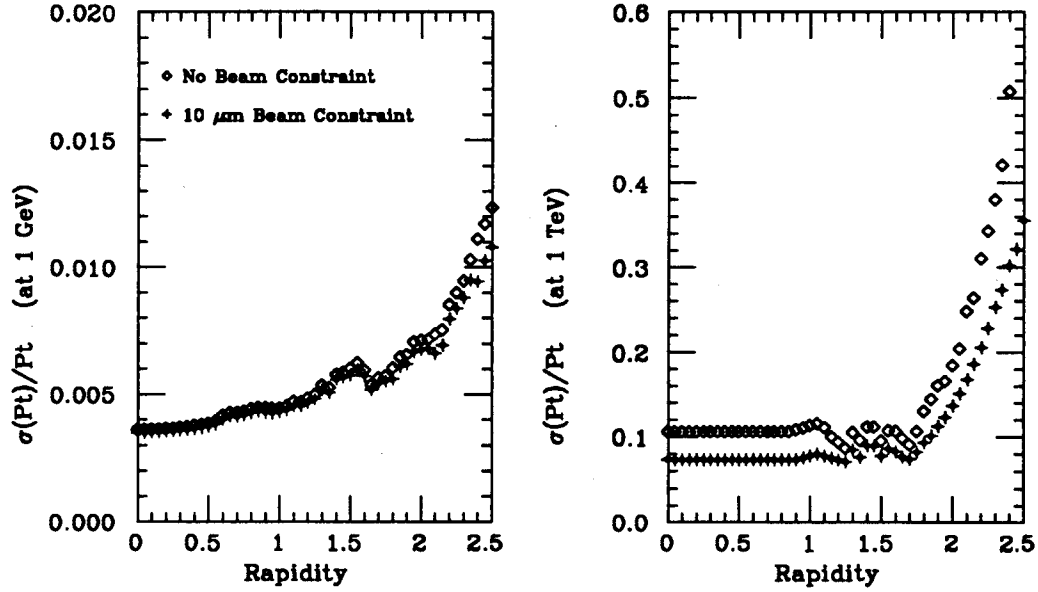

Fig. 5 Momentum resolution of system with outer tracker and silicon strips.

The trajectory for a high momentum track coming from the origin in r, ϕ, is

$$\phi = \phi_0 + Kr, \quad z = r \tan \lambda + z_0$$

where $\phi_0, K, \tan \lambda, z_0$ are constants describing the trajectory,

$$K = \frac{1}{2 \times \text{Radius of Curvature}}.$$

Thus a local tracking section in the barrel measures $\frac{d\phi}{dr} = K$, while in the endcaps we measure $\frac{d\phi}{dz} = \frac{K}{\tan(\lambda)}$.

For a fixed ϕ measurement accuracy, the length of the tracking section in z must scale like $\tan\lambda$ to locally determine K with a fixed accuracy for a trigger. For the barrel a tracking section of length $\Delta r \simeq$ 3–5 cm is adequate. This implies a tracking section of length $\Delta z \simeq$ 18–30 cm is needed at $Y = 2.5$ if ϕ is directly measured.

In reality, if we use a radial drift chamber we measure $d = r\phi$ rather than ϕ directly. We can use d/z as the quantity which exhibits bending. This gives expressions

$$\delta K_{\text{barrel}} \propto \frac{1}{r_{\text{barrel}}} \left[\frac{\sigma_{\text{position}}}{\Delta r}\right]$$

where Δr is the tracking segment length in the barrel, and

$$\delta K_{\text{forward}} \propto \frac{1}{r_{\text{forward}}} \tan(\lambda) \left[\frac{\sigma_{\text{position}}}{\Delta z}\right]$$

where Δz is the tracking segment length in the endcap region.

Taking into account the $\tan(\lambda)$ factor and the lever arm reduction when comparing r_{barrel} and r_{forward}, we conclude that a tracking length $\sim$ 60 cm to 1 m is needed for a wire chamber trigger. This assumes that the tracking has no confusion problems over such large lengths which needs to be verified with a careful study.

In conclusion we see that a radius $\sim$ 1.8 m is well matched to the resolution needed at the SSC. A half-length $\sim$3.5–4.0 m is likely adequate for triggered, with poorer momentum resolution achieved at very forward rapidities. To achieve equally good resolution at $Y = 2.5$ as at $Y = 0$ with wire chamber tracking would require an impractically long detector. Extending high resolution silicon out to larger half-lengths would improve the momentum resolution but at some point becomes prohibitively expensive.

REFERENCES

1. A. Bay *et al.*, *Proceedings of the Summer Study on High Energy Physics in the 1990s,* Snowmass, Colorado, 1988, edited by S. Jensen (World Scientific, Singapore, 1989), p. 882.
2. For a more detailed discussion see D. Pitzl, SCIPP Preprint 90/07 (1990).
3. The author thanks Jim Hylen for the resolution calculations.

Effects of radiation thickness

T. Ohsugi
Hiroshima University

******** This summary is written by the proceeding **********
******** editor based on the transparencies presented. ********

1) For the electron ID, asymmetric conversion is a problem. Cross section of isolated γ production is much larger that that of interesting isolated electron event. Even material of 1% X_0 is of problem.

2) For the detection of isolated γ, there is no qualitative difference between thickness of 10% and 30% X_0.

3) Hit-rate around r=80 cm decreases by 20%, if material thickness cut down a half.

4) Hit-rate of straws inside 1m radius is too high. I have concern about performance of the straw inside 1m.

INTEGRATED TRACKING CONFIGURATION I: SILICON AND WIRE CHAMBERS*

GAIL G. HANSON
Indiana University, Bloomington, Indiana 47405 USA

ABSTRACT

A conceptual design of a tracking system for a solenoidal detector is presented. The tracking system consists of silicon pixels and microstrip detectors at small radius and wire chambers at larger radius. The goals for the tracking system design are to provide momentum measurements of all charged particles with p_T above a few GeV/c for $|\eta| \lesssim 2.5$ and to provide a fast trigger for such particles.

1. TRACKING SYSTEM DESIGN

The conceptual design for the tracking system is shown in Fig. 1. It consists of:

- A high-resolution two-dimensional pixel detector to aid in pattern recognition and detect separated vertices from long-lived particles and multiple p-p interactions;
- An array of segmented silicon microstrip detectors to provide a powerful pattern recognition tool even in the cores of jets;
- A wire chamber system to provide the high-precision momentum measurements and trigger information for high-p_T tracks.

* Work supported by the Department of Energy, contract DE–AC02–84ER40125.

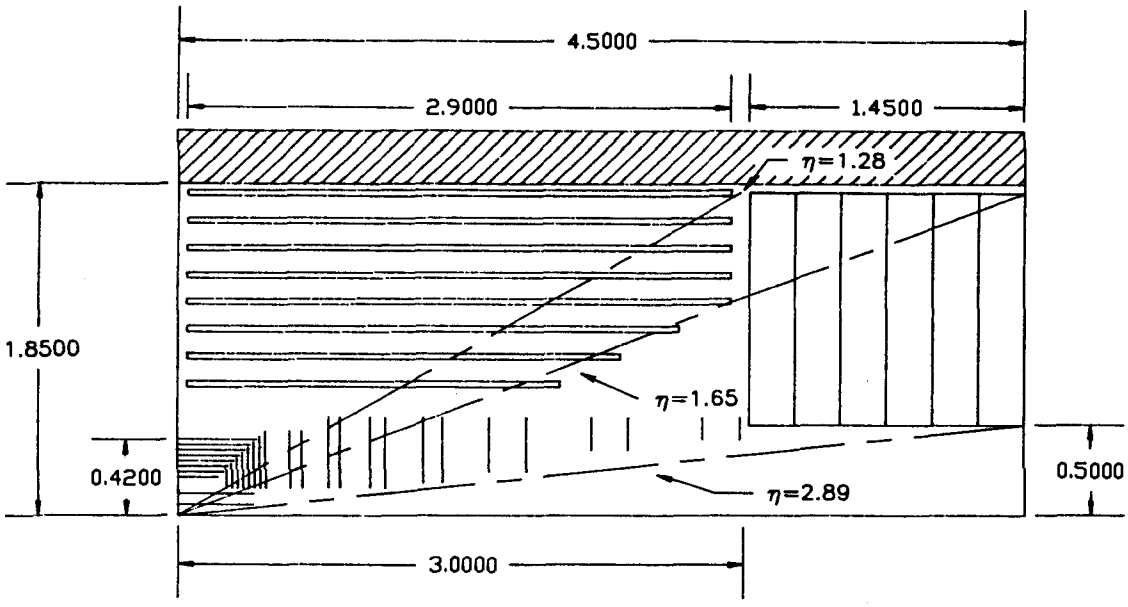

Fig. 1. Conceptual design for a pixel, silicon strip, and wire chamber tracking system for a solenoidal detector.

1.1. Pixel Vertex Detector

The pixel vertex detector[1] provides three-dimensional position measurements. It consists of two concentric cylindrical layers of pixel arrays within a radius of 10 cm from the interaction point and covers a pseudorapidity range $|\eta| \lesssim 2.5$, extending to $|z| = 40$ cm, where z is the distance along the beam line. The pixel sizes are expected to be 30 μm $\times$ 300 μm in the ϕ and z directions, respectively. The position resolutions should be better than 10 μm in ϕ and 100 μm in z. The pixel arrays are shingled in both ϕ and z to provide complete coverage. The detectors will be about 300 μm thick, and a particle at normal incidence will traverse about 2% of a radiation length of material.

Because of the high particle rate, a "smart pixel" electronic system architecture is being developed to buffer information and read out events efficiently. A smart pixel signals when it is struck, stores the analog signal, and is read out only if it is associated with a valid trigger event. All circuit functions prior to readout are on the chip. The electronics will either be fabricated directly on the detector silicon or be part of a hybrid detector/readout system using indium bump-bonding technology.

1.2. Silicon Microstrip Detector

The silicon microstrip detector[2] covers the radial region from about 15 cm to 60 cm. The system consists of either double-sided detectors with axial strips on one side and stereo on the other or of many short strips aligned on a common sub-

strate. The detectors are arranged in superlayers, each with four measurements, in a cylindrical barrel region and also in planar endcaps. The intermediate angle detectors are spaced along the beam to a distance of nearly 3 m from the interaction point to allow good momentum measurement to large rapidities. About 32 m^2 of silicon are needed. The supports must withstand both thermal and radiation effects and are expected to be made of either a graphite-based composite or beryllium. The goal is to have less than 5% of a radiation length of material at normal incidence.

Double-sided detectors with sizes up to 3 cm × 8 cm may be wire-bonded together to make larger units for electronic readout. The pitch in the barrel modules is 50 μm, whereas in the intermediate angle detectors the pitch varies with distance from the beam line. The heat load is about 1 mW/channel. Heat load is a major concern, and cooling by an evaporation-wick technique is being studied.

The spatial resolution is expected to be 15 μm, and the double-hit resolution is expected to be 150 μm. With such excellent position determination, the silicon microstrip system is expected to provide superior pattern recognition even in the cores of jets with p_T up to about 1 TeV/c. There are about 10 million channels in the system.

The pixel detector and silicon microstrip detector will have a common support system and will form an integrated high-resolution tracking device.

1.3. Straw Tube Central Tracking

Wire chambers are used for tracking for radii between 60 cm and 180 cm. They are suitable for spanning the tracking length needed for precise momentum measurement inside the large magnetic volume. They can also provide a fast trigger for tracks with p_T larger than some minimum value by the requirement that track segments in outer layers point back to the interaction point.

To meet the constraints imposed by radiation damage, current draw, chamber lifetime, gain reduction from large particle flux, hit rate, loss of data because of high occupancy, and pattern recognition in the complex environment, drift cells must be made as small as practical.[3] Acceptable current draw and lifetime can be obtained with a 4 mm diameter straw tube chamber about 50 cm from the beam line; the other operating limits are somewhat less restrictive. This is also the practical lower limit on the diameter from considerations of track ionization length and electrostatic stability. Occupancy is minimized by use of a fast gas, such as a mixture containing CF_4.

Straw tube chambers are used in the central tracking region, $|\eta| \lesssim 1.5$. Eight layers of straw tubes are close-packed to form superlayers, as shown in Fig. 2. A

half-cell stagger between layers permits resolution of left-right and crossing-time ambiguities. Local track segments found in each superlayer are linked to form tracks.

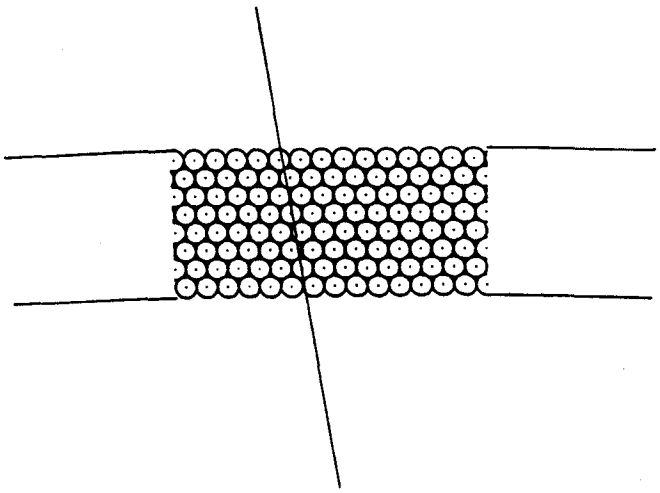

Fig. 2. Cross sectional view of the eight layers of a superlayer of straw tubes.

The coordinate along the wire is measured by means of small-angle stereo. With a spatial resolution of 100-150 μm per wire in the r-ϕ projection, the expected resolution in z is 2–3 mm. The superlayers are ordered axial, $\sim$ +3°, axial, $\sim$ -3°, etc., for a total of eight equally-spaced superlayers spanning $70 < r < 180$ cm, as shown in Fig. 1. The double-hit resolution is 2 mm. The maximum straw length is limited by signal attenuation to about 3 m. Straws up to 3.5 m long with wire supports inside the straws every 80 cm for electrostatic stability have been operated at the required voltage.[4] The central tracking system design therefore contains an electrical break near the middle. The current draw per wire at the operating gas gain of 2×10^4 is shown as a function of radius in Fig. 3(a); it is less than 0.35 μA/wire over the entire system and less than 0.15 μA/wire for radii beyond 150 cm at the SSC design luminosity of 10^{33} cm^{-2} s^{-1}. The occupancy as a function of radius is shown in Fig. 3(b); it is less than 5% over the entire system and less than 2% at large radii at the SSC design luminosity. These values should be multiplied by about a factor of two for curling tracks in a 2 Tesla magnetic field.

Two methods of support are being investigated. One method involves carbon-composite cylinders supporting each superlayer of straws. The other is based on a

(a)

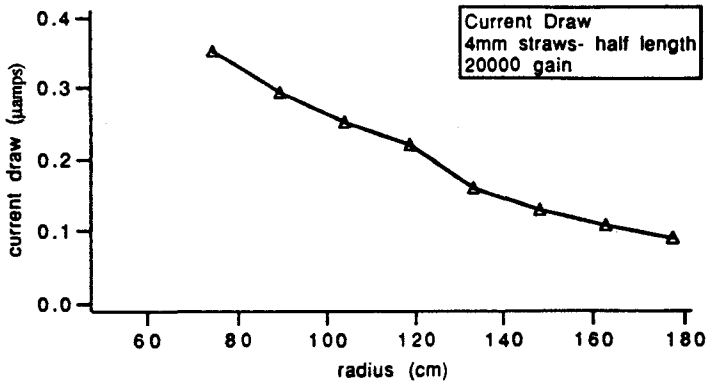

(b)

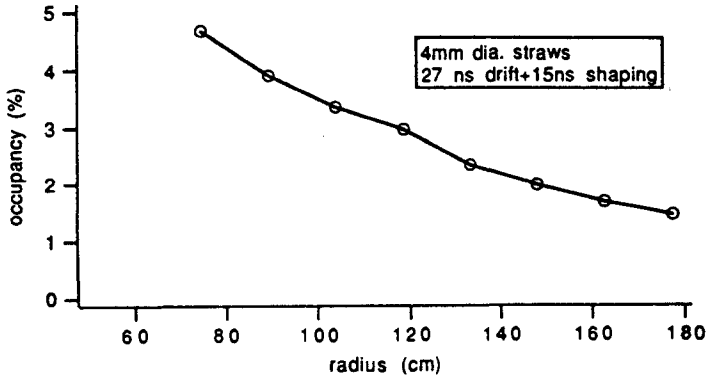

Fig. 3. (a) Current draw per wire *vs.* radius in the straw tube central tracking system for a gas gain of 2×10^4 at the SSC design luminosity. (b) Occupancy *vs.* radius in the straw tube central tracking system at the SSC design luminosity.

carbon-composite framework supporting replaceable modules of straws, as shown in Fig. 4.

There are 2.5×10^5 channels in the central tracking system. The amount of material traversed by a particle at normal incidence is 6%. There is additional material at the ends due to endplate wire supports and electronics, gas manifolds, high-voltage capacitors, and optical-fiber cabling.

1.4. Wire Chamber Intermediate Angle Tracking

For the intermediate angle tracking region ($1.3 \leq |\eta| \leq 2.5$) two approaches involving wires perpendicular to the beam direction are being considered. The

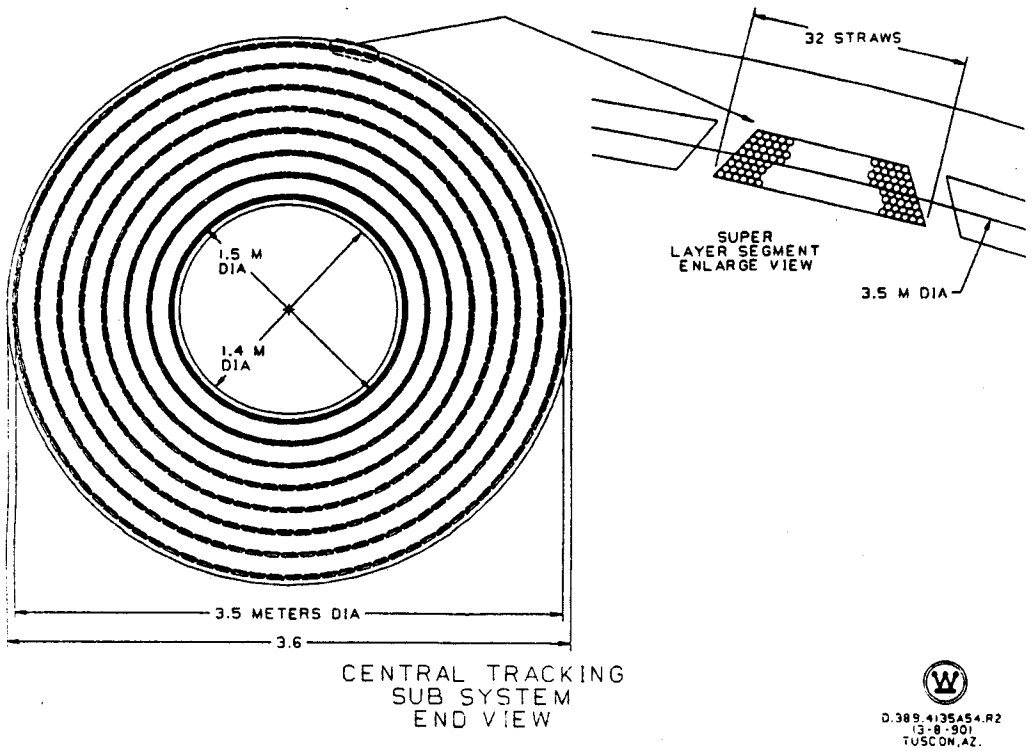

Fig. 4. Support system for replaceable modules of straws.

first employs crossed planar superlayers of straw tubes. The second involves the use of arrays of transverse drift cells which are optimized for fast track finding and reconstruction in a uniform axial magnetic field, much like the intermediate angle track detector in the H1 experiment at HERA[5], shown in Fig. 5(a). In the latter this is efficiently achieved by means of radial sense wires, but the requirements both of a fast gas with large Lorentz angle and of high rate capability at the SSC mean that further consideration of the wire orientation is necessary; work is underway. Such a detector would contain about 300 azimuthal wedges to meet the constraints on current draw and occupancy over the full radial range. The coordinate along the wire will be measured with planes of wires tilted at small angles to the nominal wire direction, as shown in Fig. 5(b). The total number of channels for the intermediate angle tracking system is about 6×10^4. An estimate of the percentage of a radiation length as a function of $|\eta|$ for the wire chamber central and intermediate angle tracking systems is shown in Fig. 6.

We anticipate readout of the pulse integral as well as timing from as many wires in the system as practical. This will extend the capability of the central and intermediate angle track detection to searches for particles with anomalous charge. Furthermore, if suitable radiator material is distributed throughout the wire chamber tracking volume between modules of either straw or other wire con-

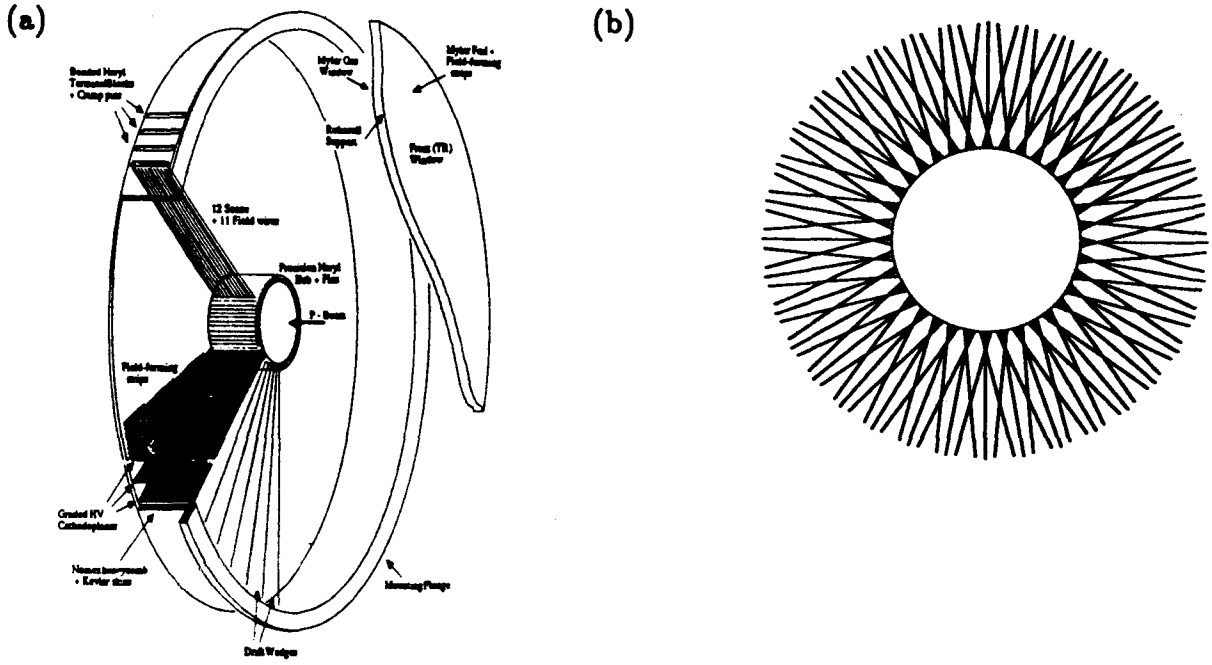

Fig. 5. (a) Schematic view of a radial wire drift chamber, as in the H1 forward tracking system, indicating the principles of construction and function. (b) Schematic view of wires tilted at a small angle to the radial direction in order to measure the coordinate along the radial wires.

figurations, pulse integral readout opens up the possibility of enhancing electron identification by detecting transition radiation X-rays.[6]

1.5. Tracking System Performance

The expected performance of the tracking system is shown in Fig. 7. Figure 7(a) shows the momentum resolution in a 2 Tesla magnetic field as a function of $|\eta|$ for the cases of no beam constraint and no pixels, 20 μm beam constraint and no pixels, and two layers of pixels without a beam constraint. Our goal is to achieve a momentum resolution of $\sigma_{p_T}/p_T \lesssim 0.2 p_T$ (TeV/c) in the central region and $\lesssim 1.0 p_T$ (TeV/c) over $|\eta| \lesssim 2.5$. The predicted resolution is better than this, but there may be some degradation in the real system due to systematic effects. Figure 7(b) shows the impact parameter resolution as a function of momentum including the silicon microstrip detector with and without the pixels. These resolutions are comfortably below the impact parameters expected from B meson decays.

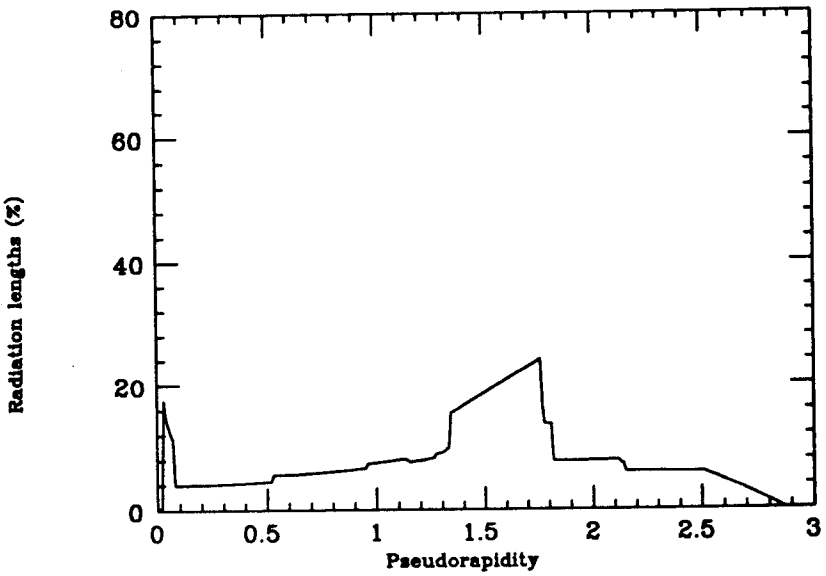

Fig. 6. Estimated percentage of a radiation length of material *vs.* $|\eta|$ for the straw tube central tracking system and the wire chamber intermediate angle tracking system.

2. WIRE CHAMBER ELECTRONICS

2.1. Front End Electronics

The wire chamber front end electronics will use radiation-hardened bipolar and/or CMOS technology. The drift time measurement resolution must be < 0.5 ns. The front end electronics consists of the following components:

- Preamplifier/shaper with signal tail cancellation
- Low power differential discriminator
- Time-to-voltage converter (TMC) and Analog Memory Unit with some trigger control[7]

or

- Time Memory Cell (TMC) digital time measurement[8]
- Data collection chip

Figure 8 shows block diagrams for both the TMC and TVC designs, for both of which prototyping is well underway. Similar electronics can be used for radial wire chambers, for which there would be a 16 ns double-pulse resolution. Pulse integral measurements for transition radiation detection can also be incorporated.

One issue that is beginning to be addressed is the cost of the electronics for wire chambers. The electronics being designed, including time measurement and trigger, is located entirely on the chamber endplate, attached directly to the wires. Thus there isn't a cable for every channel going from the detector to crates of FASTBUS electronics. The data is buffered and read out over a small number

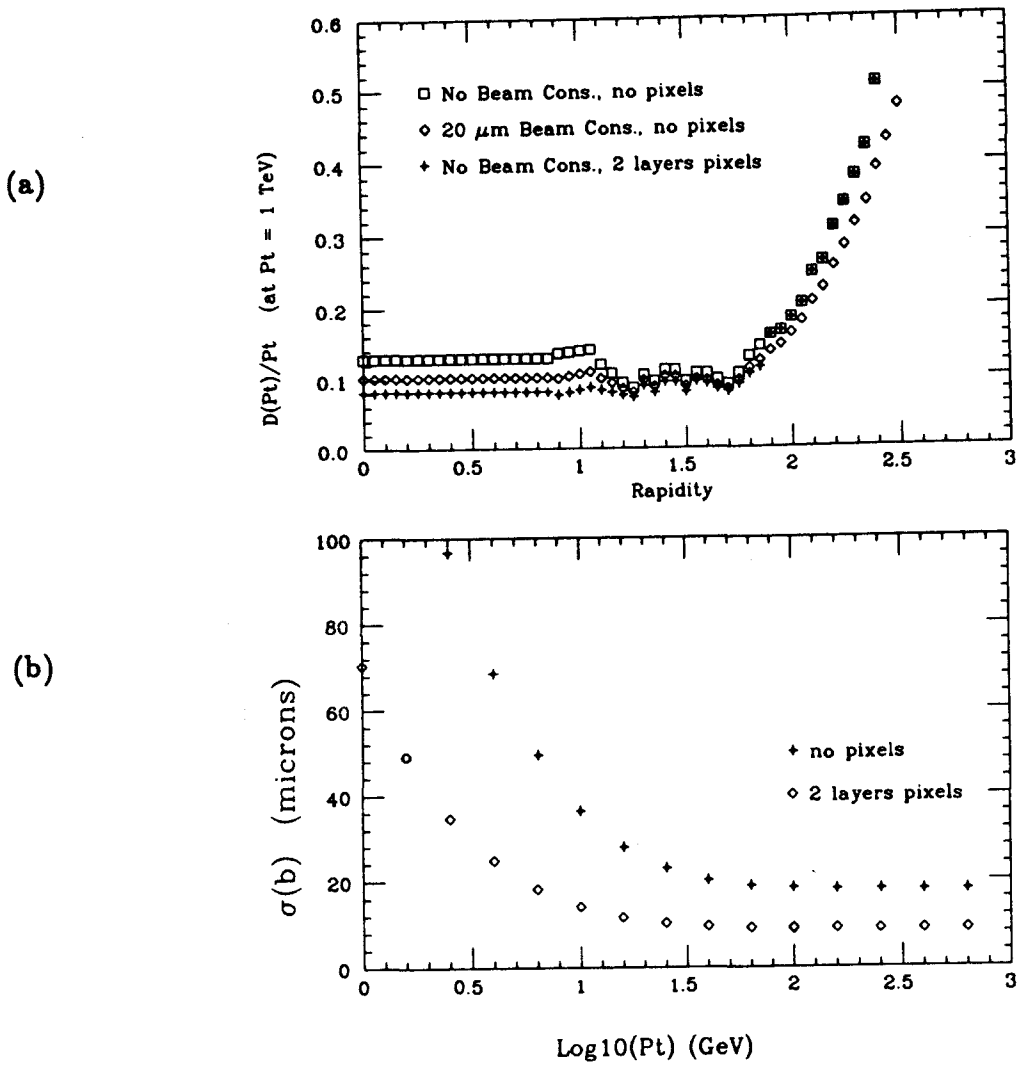

Fig. 7. (a) Momentum resolution in a 2 Tesla magnetic field as a function of $|\eta|$ for the proposed tracking system. (b) Impact parameter resolution as a function of momentum for the proposed tracking system.

of optical fibers. A preliminary cost estimate (not including the trigger) indicates a cost of less than \$35 per channel for TVC-based straw tube electronics.[9]

2.2. Track Segment Finding and Triggering

Track segments can be found locally in the superlayers. They can be characterized as local straight line segments since the sagitta over a superlayer is too small to measure for a relatively high p_T track. The two parameters characterizing a line segment could be the slope relative to a radial line at the track segment and the position given by the azimuthal angle. The slope is then a measurement of the p_T of the track. Since the radial extent of a superlayer of straw tubes is only about 3 cm, the displacement from a radial line is less than the cell width for a track with $p_T \gtrsim 10$ GeV/c in a 2 Tesla magnetic field. Thus drift times are

(a)

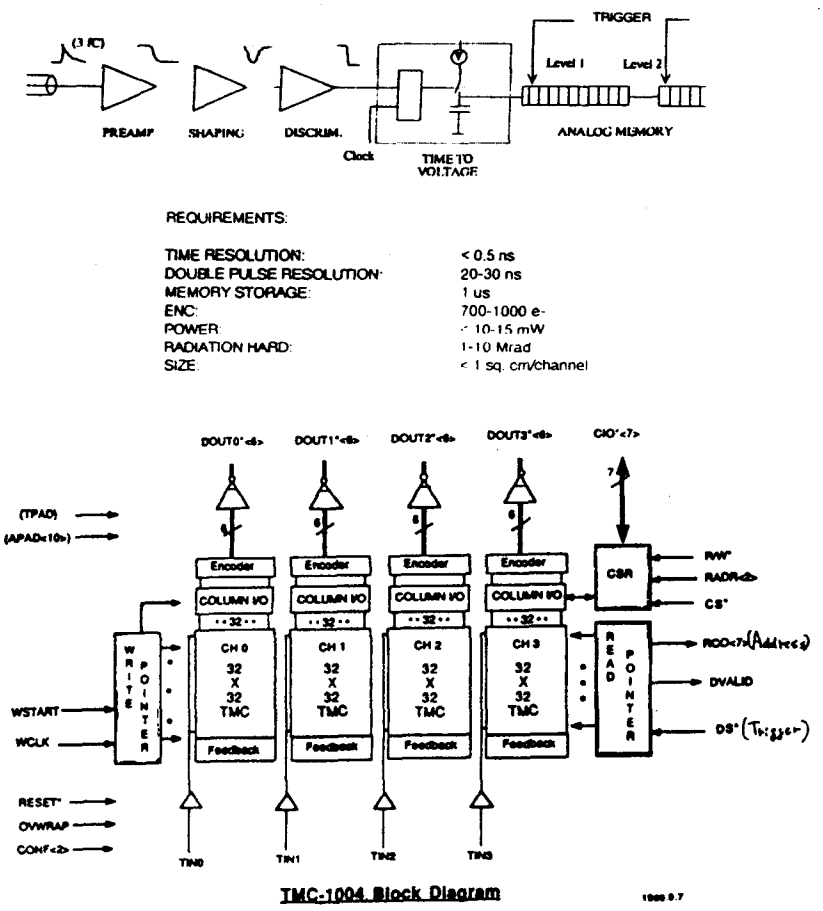

(b)

Fig. 8. (a) Block diagram for TMC-1004. (b) Block diagram for TVC-based front end electronics.

needed in the segment finding. An added complication is the need to have an estimate of the position of the track along the length of the wire since the propagation time is about 10 ns. Once track segments are found, they can be matched to clusters in the calorimeter, for example. Electronics is being developed to find the track segments with p_T larger than some cutoff value, for example, the synchronizer design of J. Chapman.[10] Similar efforts are taking place in Japan. These track segments can then be used in the trigger, possibly even at the first level.

The coordinate (z-coordinate) of a track along a superlayer parallel to the beam direction may be found by measuring the displacement of the track seg-

ments between the axial and stereo superlayers (provided the linking can be accomplished). For this purpose one would not even have to use the drift times, although if the track is subject to a high-p_T cut this would probably be done using the track segments found in the trigger electronics. With 3° stereo, the displacement for a 3-m-long wire would be within ± 7.9 cm. Since the radius of the cell is 2 mm, this technique gives a resolution in z of 3.8 cm, which corresponds to $\sim$ 0.1 ns propagation time.

3. RESEARCH AND DEVELOPMENT ISSUES

The are many questions that must be answered before we can arrive at a final design for an integrated silicon and wire chamber tracking system. Much of the R&D is being carried out in several SSC subsystem and generic programs.[1,2,11,12,13] Some of the relevant research is summarized below.

The viability of the pixel and silicon strip system that occupies the inner part of the tracking volume depends on the resolution of such issues as fabrication technology, circuit design, radiation hardness, mechanical and thermal stability, precision alignment, adequate heat removal and ease of assembly.

For the outer part of the tracking volume, wire chamber technology is mature, although its application in the SSC environment poses unprecedented challenges. Research and development areas include minimizing material in the supports and end regions, incorporation of electronics, gas manifolds and high voltage distribution, precision alignment, and thermal management. Also included are the investigation of a hexagonal cell option, which might decrease the amount of material and improve the assembly procedure, and the R&D specific to the intermediate angle tracking system.

Research and development in the areas of front end, data acquisition and triggering electronics for the various components of the tracking system is advancing.

Engineering design leading to an integrated low-mass support system incorporating the necessary precise alignment is beginning. In addition, engineering design leading to the integration and assembly of the tracking system into the overall detector is being proposed. This includes evaluation of the mechanical support structures, integration of the tracking system components, cabling and power distribution, and development of the assembly, maintenance, and repair procedures.

4. POSSIBILITIES FOR HIGH-LUMINOSITY PERFORMANCE

Computer simulation studies of track segment finding have been carried out for the tracking system design for the "Large Solenoid Detector"[14] at the SSC design luminosity of 10^{33} cm^{-2} s^{-1}. These simulations[15] included background from minimum bias events within the resolving times of the cells, interactions of the particles with the material in the tracking system, curling tracks in a 2 Tesla magnetic field, and loss of hits due to the double-hit resolution. Over 80% of the track segments in the outer superlayers were found for high-p_T e's and μ's from Higgs boson decays with a crude segment-finding algorithm. Since that tracking system was designed, improvements have been made because of detector R&D efforts. These new developments have been incorporated in the design of the tracking system described here:

- The outer radius of the tracking system has increased from 1.5 to 1.8 m.
- Since there is a break in the wires in the middle due to signal attenuation, the rapidity range covered by a wire has decreased by about a factor of two.
- In the previous design, the cell width for the outer superlayers was nearly 7 mm. In the present design 4 mm diameter cells are used throughout.
- The old simulation used a drift velocity of 50 μm/ns. Since that time fast gases with drift velocities $\sim$ 100 μm/ns have been shown to work.[4]

The relevant proportionality factors are given by

$$Occupancy \propto \frac{\eta_{max}\, n_B\, w}{r},$$

where η_{max} is the rapidity coverage of the wire, n_B is the number of bunch crossings during the resolving time of the cell, w is the width of the cell, and r is the radius. For the outer superlayers the largest improvement has occurred in the factor n_B because of both the decrease in the cell diameter and the increase in the drift velocity. A comparison between the old design and the present one shows that n_B has decreased from 4.3 to 1.4. Including the other improvements (two factors of two), we find that the occupancy for the present design is only 8% that of the previous design! This means that track segment finding in the outer superlayers of the design described here should work as well at a luminosity of 10^{34} cm^{-2} s^{-1} as the old simulation for 10^{33} cm^{-2} s^{-1}. Of course, this will have to be checked with simulations. There are other factors involved in running such a straw tube system as described here at 10^{34} cm^{-2} s^{-1}, such as the current draw per wire. Based on the scaling factors described above, the current draw for the present design is 18% that of the old design. Much more work is needed, but

there is reason to hope that at a luminosity of 10^{34} cm^{-2} s^{-1} the outer superlayers of the straw tube tracking system will not only survive but also still be usable for finding track segments and providing a trigger.

ACKNOWLEDGMENTS

We would like to thank the organizers of the Workshop, particularly T. Kondo, for providing such a well-organized and congenial environment and for the opportunity to meet and work with so many of our colleagues in Japan. We gratefully acknowledge the support of the Department of Energy for SSC detector research and development.

REFERENCES

1. "SSC Detector R&D Proposal: Development of Technology for Pixel Vertex Detector," D. Nygren, contact person (1989).
2. "Subsystem R&D Proposal to Develop a Silicon Tracking System," A. Seiden, contact person (1989).
3. D. G. Cassel, G. G. Hanson *et al.*, "Report of the Central Tracking Group," *Proceedings of the 1986 Summer Study on the Physics of the Superconducting Supercollider, edited by R. Donaldson and J. Marx, Snowmass, CO, 1986*, p. 377.
4. H. Ogren, "Progress Report from Straw Chamber Subgroup," in these Proceedings.
5. G. A. Beck *et al.*, "Radial Wire Drift Chambers for the H1 Forward Track Detector at HERA: Design, Construction and Performance," *Proceedings of the Wire Chamber Conference, Vienna, Austria, 1989*, Nucl. Instr. and Meth. **A283**, 471 (1989).
6. H. Grässler *et al.*, "Simultaneous Track Reconstruction and Electron Identification in the H1 Radial Wire Drift Chambers," *Proceedings of the Wire Chamber Conference, Vienna, Austria, 1989*, Nucl. Instr. and Meth. **A283**, 622 (1989); S. Ahlen *et al.*, "Proposal to Develop An Integrated High Rate Transition Radiation Detector for the SSC," SSC PC-011, October, 1989; B. Dolgoshein, "The Transition Radiation Detector for High-Lorentz-Factor Particle Identification at High-Luminosity Hadron Colliders," *Proceedings of the ECFA Study Week on Instrumentation Technology for High-Luminosity Hadron Colliders, Barcelona, Spain, 1989*, p. 650.
7. F. M. Newcomer *et al.*, "High-speed Bipolar Integrated Circuits for SSC Applications," *Proceedings of the Wire Chamber Conference, Vienna, Austria, 1989*, Nucl. Instr. and Meth. **A283**, 806 (1989).

8. Y. Arai, "Development of TMC Chip and Track Trigger," in these Proceedings; Y. Arai and T. Ohsugi, "TMC – A CMOS Time to Digital Converter VLSI," IEEE Trans. Nucl. Sci. **NS-36**, 528 (1989); Y. Arai, "A Time Measurement System at the SSC," *Proceedings of the Workshop on Triggering and Data Acquisition for Experiments at the Supercollider, Toronto, Canada, 1989*, SSC-SR-1039, p. 125.
9. F. M. Newcomer and R. Van Berg, "Straw Electronics Cost Summary," unpublished (1990).
10. J. Chapman, "Tracking Trigger," in these Proceedings; S. Kim, "Tracking Trigger Study," in these Proceedings.
11. "SSC Detector Subsystem Proposal: Central and Forward Tracking with Wire Chambers," G. Hanson, contact person (1989).
12. "SSC Detector Subsystem Proposal: A Hybrid Straw Tube/Scintillating Fiber Tracking System," A. Goshaw, contact person (1989).
13. S. Parker, "A Proposal to Develop a VLSI Pixel Device for Particle Detection," (1987).
14. G. G. Hanson, S. Mori, L. G. Pondrom, H. H. Williams *et al.*, "Report of the Large Solenoid Detector Group," *Proceedings of the Workshop on Experiments, Detectors, and Experimental Areas for the Supercollider*, edited by R. Donaldson and M.G.D. Gilchriese, Berkeley, CA, 1987, p. 340.
15. G. G. Hanson, B. B. Niczyporuk and A. P. T. Palounek, "Wire Chamber Requirements and Tracking Simulation Studies for Tracking Systems at the Superconducting Super Collider," *Proceedings of the Wire Chamber Conference, Vienna, Austria, 1989*, Nucl. Instr. and Meth. **A283**, 735 (1989).

INTEGRATED TRACKING SYSTEM
CONFIGURATION II

John E. Elias

Fermilab

ABSTRACT

A conceptual design for an integrated central tracking system based on silicon pixel, silicon strip, and scintillating fiber technologies is described. Issues of occupancy and material in the tracking volume are discussed. A technique for providing a powerful real-time first level trigger with sagitta resolution of 0.5 to 1 mm is presented. The design is characterized by very low occupancies, single crossing time resolution, simple binary electronics, and some degree of $L = 10^{34}$ potential.

I. INTRODUCTION

In a solenoidal magnetic detector for the SSC, tracking is involved in a crucial way in four areas:

1) Lepton Identification. The tracking system is integral to both identifying and measuring isolated leptons.
2) Event Reconstruction. Pattern recognition capability is the basis for identifying conversions, tagging heavy flavor jets, and reconstruction of part or all of an event.
3) Triggering. Many trigger algorithms rely on matching calorimeter and muon spectrometer information to prompt tracking momentum information especially for electron, muon, and photon triggers. Vector information, $P_t(\varphi)$, is required.
4) Multiple Vertices. Both multiple primary and secondary verticies must be disentangled to properly reconstruct multi-lepton data.

These four simplified criteria form the basis for the conceptual design of a tracking system. "Integrated Tracking" is an admission that no one technology can address the requirements adequately. In fact, a mix of technologies is proposed with each being deployed to maximum advantage. Resolution is not stressed as $BL^2 = 2T * (1.8m)^2$ makes it almost easy. Figure 1 shows a schematic layout for the proposed design.

CONFIGURATION II

RADIUS	TECHNOLOGY	ADVANTAGE AREA
5 - 10 cm	silicon pixels	multiple and secondary vertex reconstruction
15 - 50 cm	silicon strips	pattern recognition
70 - 180 cm	scintillating fibers	triggering

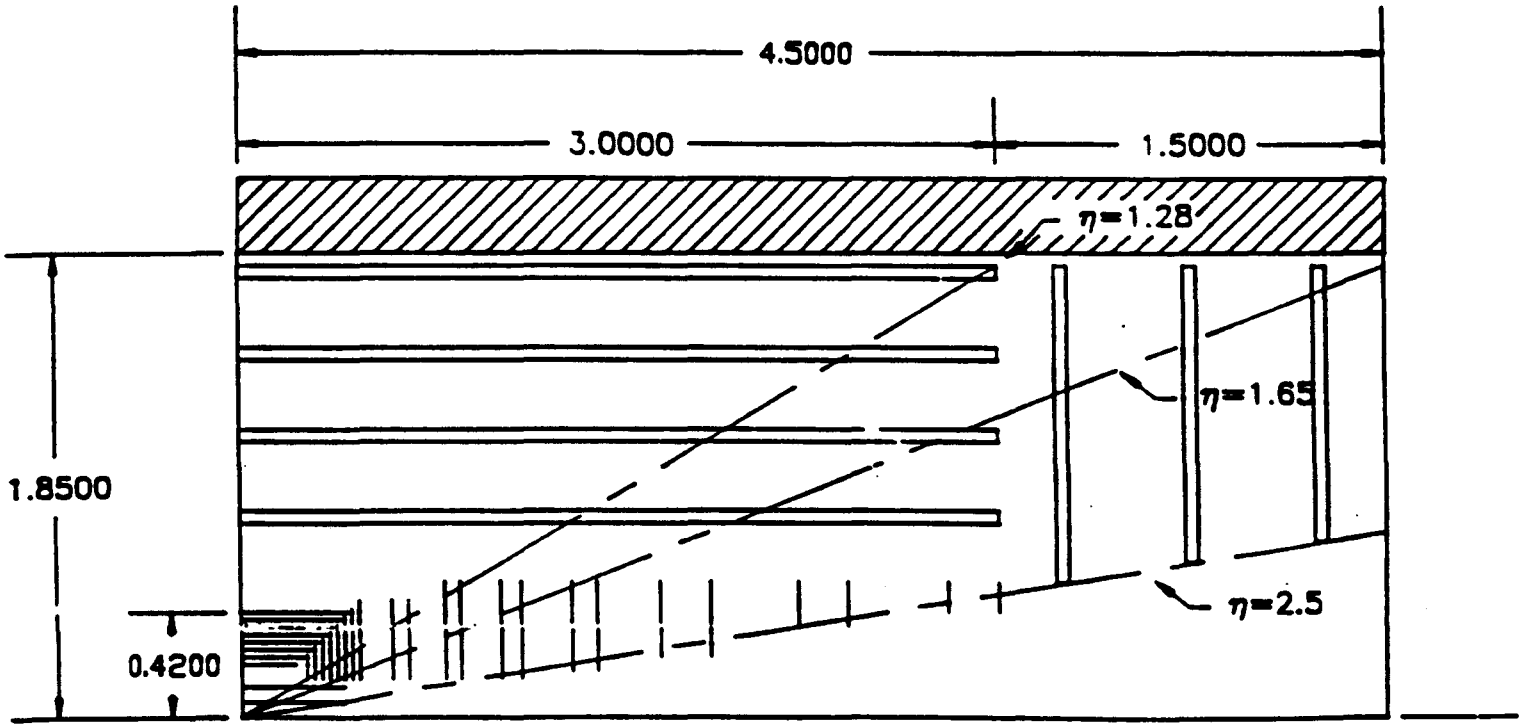

A pixel, silicon strip, and scintillating fiber tracking system for the SDC detector.

Figure 1.

The general characteristics and strategy for the design of Configuration II as listed below also come with some admitted problems and engineering challenges. Of these, the most significant are the high channel count ($> 10^7$), the amount of material inside of the trigger superlayers, triggering in the intermediate region $1.5 < \eta < 2.5$, linking between layers and technologies, and alignment tolerances.

GENERAL CHARACTERISTICS FOR CONFIGURATION II

- LOW OCCUPANCY The individual tracking elements are sized and placed to achieve low occupancies ranging from 10^{-4} to 5×10^{-2}.
- BINARY ELECTRONICS All elements use simple "yes-no" hit-bit electronics for readout. Non-trigger elements have sparsification done locally to minimize interconnects and inert material.
- 16 NSEC TIME RESOLUTION All elements have the capability to resolve and measure individual crossings without pileup from preceding crossings.
- POWERFUL TRIGGER For each crossing, $P_t(\varphi)$ measurements are provided for all stiff tracks with a resolution of 0.5 to 1 mm in the sagitta.
- $L = 10^{34}$ CAPABILITIES Stereo fiber layers are included in the outer two superlayers; refer to the high luminosity discussion by D. Green herein.

II. ASPECTS OF TRACKING AT THE SSC - A REMINDER

As mentioned numerous times at this meeting, the Q-value for reactions like $pp \rightarrow H \rightarrow ZZ$ where the Z's decay to four leptons are so large that there is significant useful rate out to $\eta = 2.5$ to 3. Such large rapidity coverage poses occupancy and pattern recognition problems for long axial elements at intermediate radii. The choice of where to place the transition from axial to radial deployment has been made for the silicon strips, but is only provisional for the fibers.

The flux of neutrons in the tracking volume is determined by the choice of calorimeter material and the high η region configuration. There can be more than two orders of magnitude difference between uranium calorimetry closed tightly around the beam pipe and iron/lead calorimetry with a separate forward calorimeter removed by a few meters. For this latter case, hit rates of a few kilohertz have been estimated.

Captured particles, or loopers, have a very different appearance due to the SSC time structure. The capture momentum is ~550 MeV/c inside the solenoid, and the time for one orbit is about 30 nsec or nearly three crossings. The diameter of this loop, 1.8m, is large enough to drive a Honda through. Loopers will stay in the tracking volume for 5 to 10 crossings and appear as a steady state background, much like neutrons. Further more, only a portion of the orbit will be visible in the data, approximately 10 to 15 nsec worth of travel along the helix.

Particle densities can be expected to increase by a factor of 10 over what has been experienced at the TeVatron with CDF. The log(s) increase is a factor of 2, the most probable number of interactions per crossing at $L = 10^{33}$ is 1.9, and the traffic from neutrons, persistent loopers, and increased conversions (more than 4 times the material) contributes a factor of 2.5.

Occupancy in the SSC configuration is markedly different from that in conventional drift chamber configurations. The material is spread over $0 < R < 180$cm, approximately uniformly in the silicon and fiber layers. This is in contrast to material concentrated over $0 < R < 25$ cm followed by a more or less massless open drift chamber from 25 cm $< R < 150$ cm. There are two important consequences for conversions and occupancy that follow from the uniform material distribution. Conversions become much easier to identify; a track simply starts in layer N with no track inside. Only the material inside the first sensitive layer is akin to the open drift chamber problem where a search for possible soft opposite sign partners must be done. Occupancy becomes nearly independent of the amount of material. As the layers become thinner, the probability for conversions,

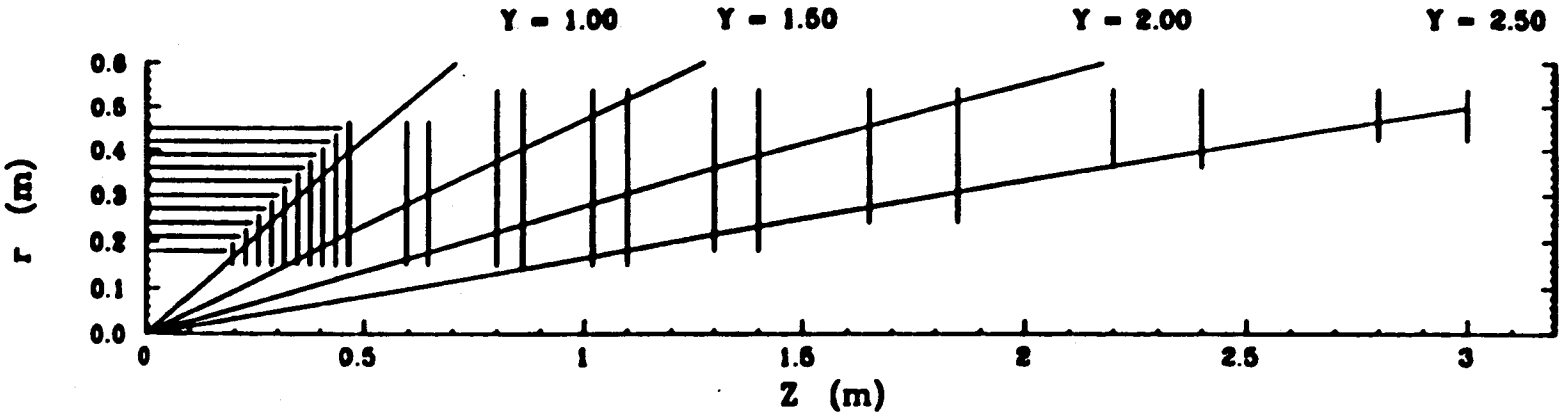

SSC Silicon Microstrip Tracker

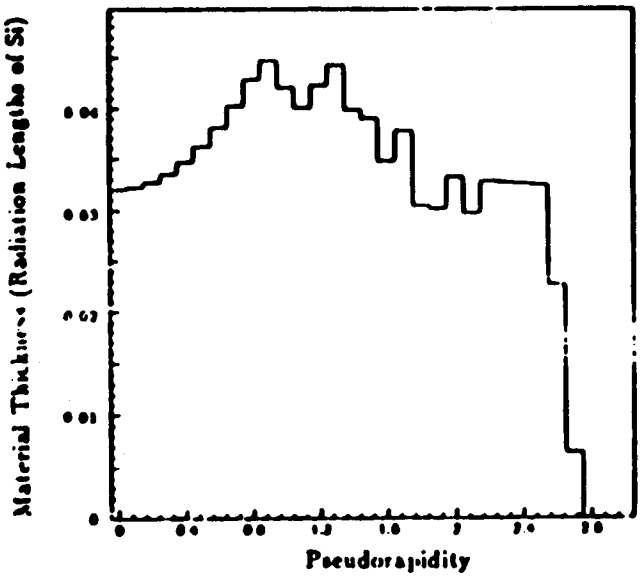

Material for silicon alone

Figure 2.

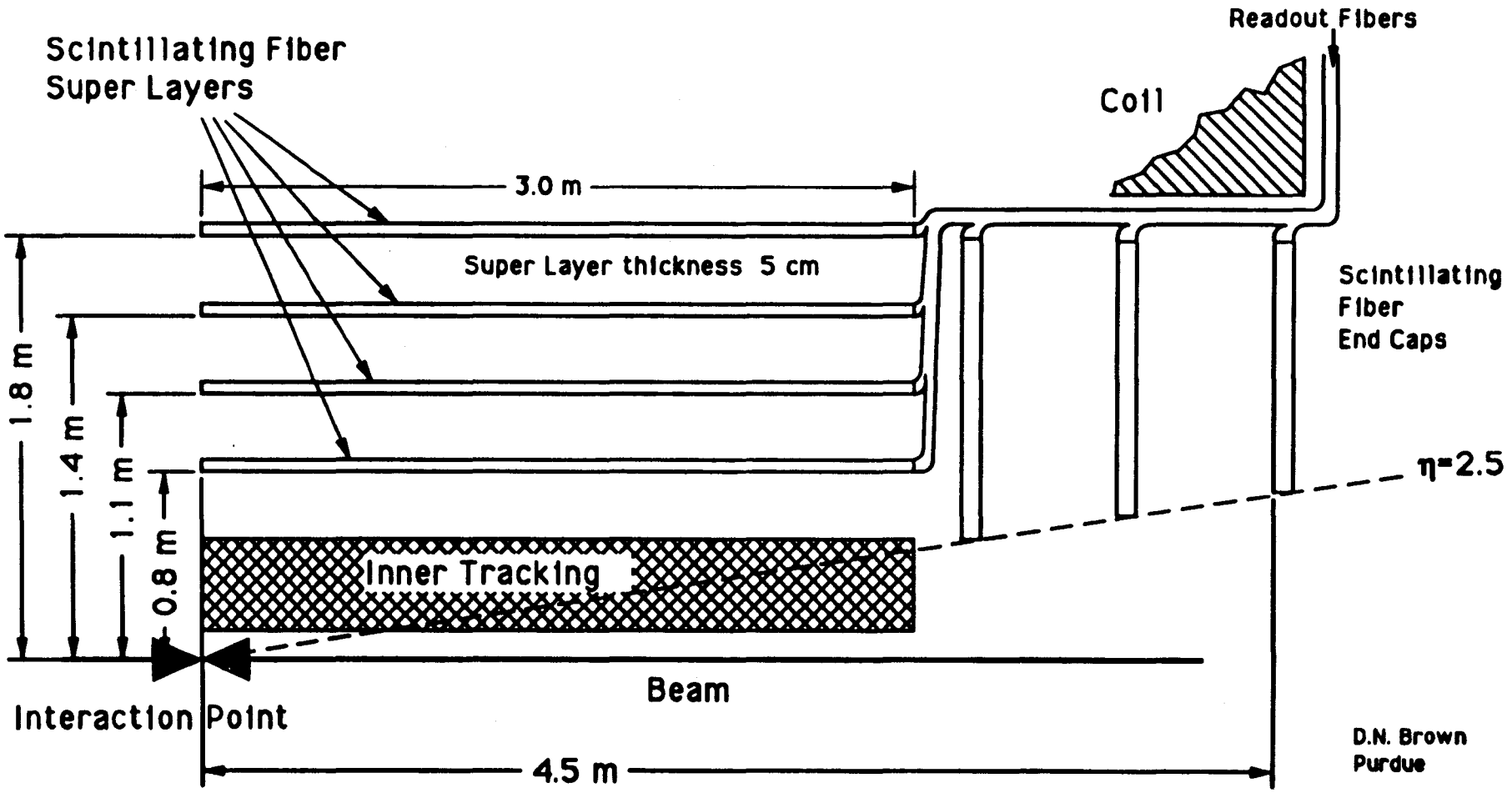

Figure 3. Fiber layout including readout.

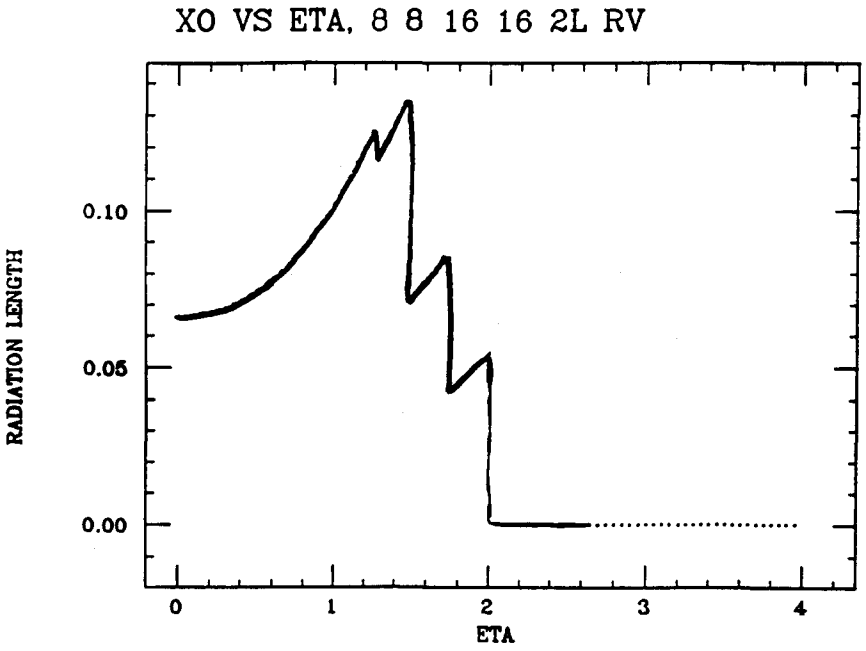

Figure 4. Material for fibers, readouts, and support.

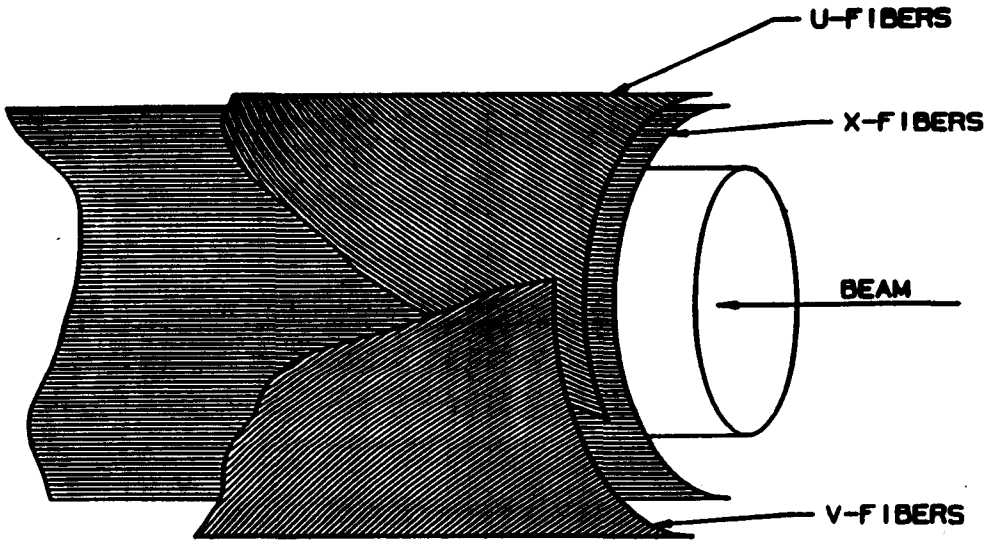

Figure 5. Deployment of stereo layers.

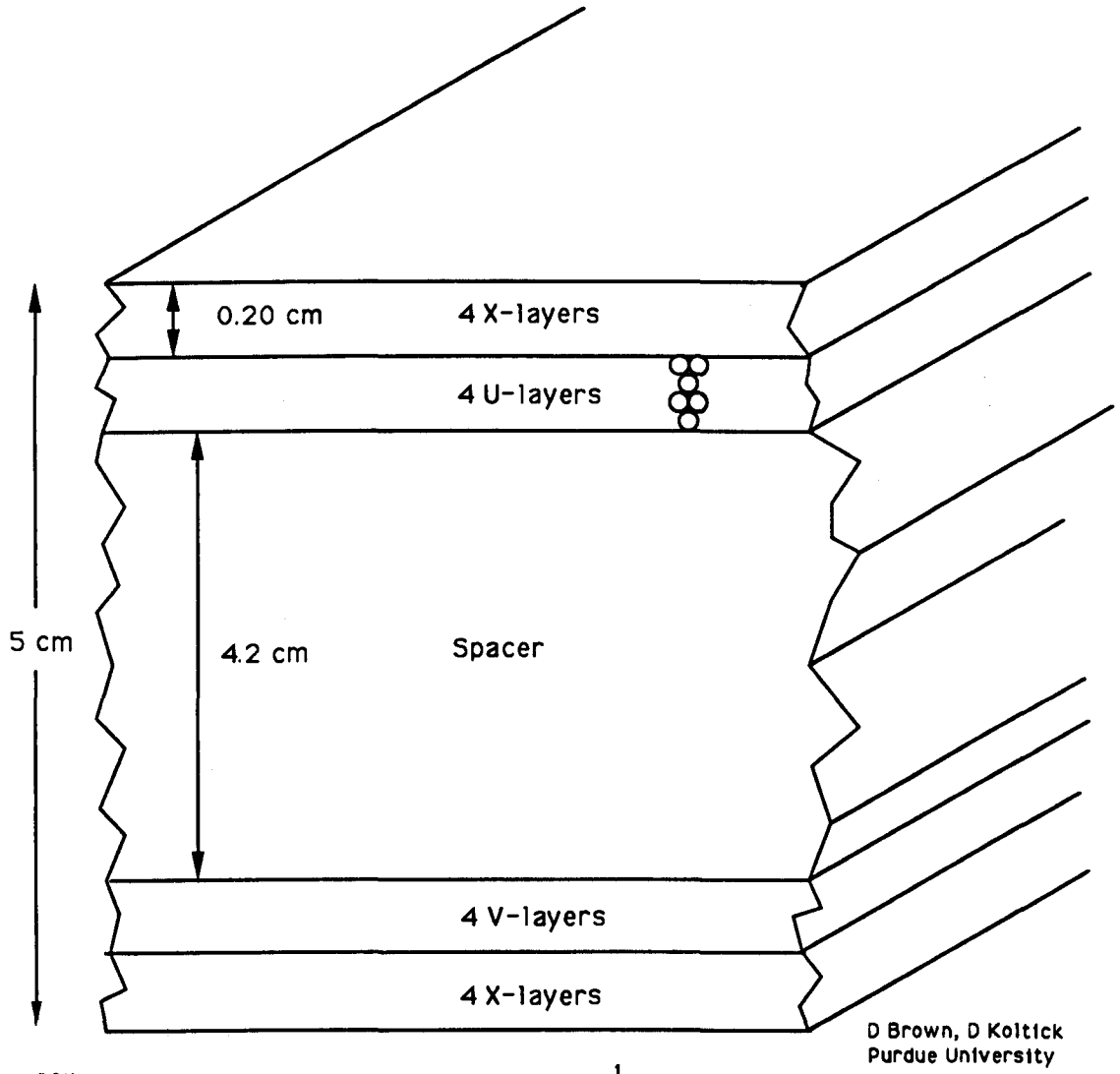

$$\frac{\#\text{fibers}}{\text{super layer}} = \#\text{ layers} \times 2\pi R_{\text{average}} \frac{1}{d_{\text{fiber}}}$$

Superlayer	ave. Radius (cm)	# of Layers	No. of fibers
1	80.0	8	80,400
2	112.5	8	113,100
3	145.0	16	291,500
4	177.5	16	356,900
			841,900

Total no. of fibers = 2 halves x 841,900 = 1,684,000

Figure 6.

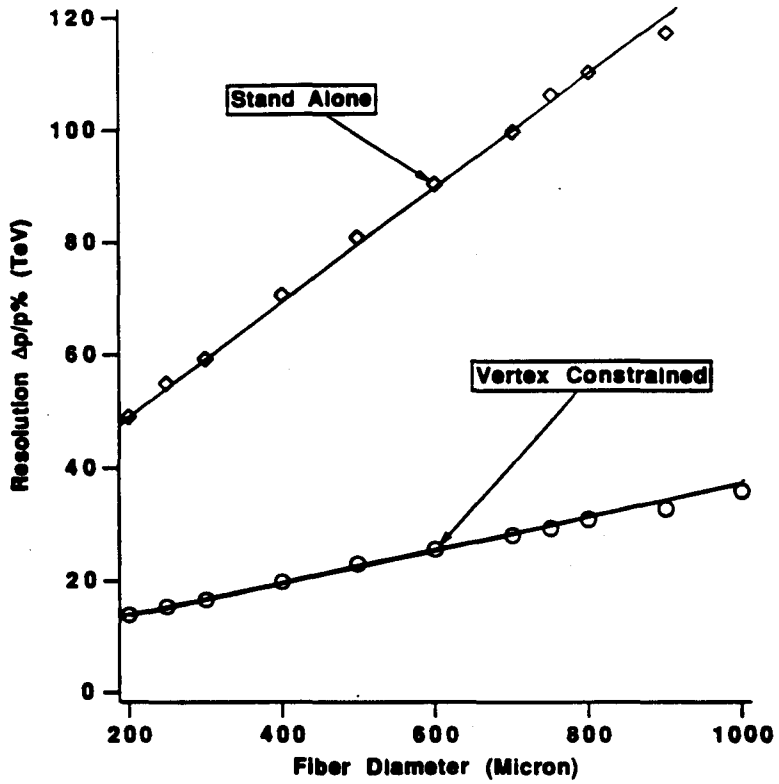

Figure 7. Fiber tracking resolution versus fiber diameter.

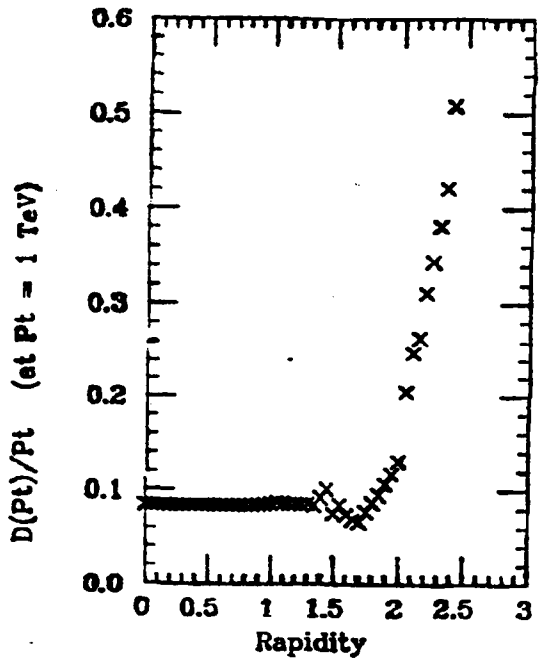

Figure 8. Tracking system resolution as a function of rapidity.

delta rays, and Comptons drops, but the loopers survive longer and compensate. As the layers become thicker, the loopers are quenched more quickly, but the soft processes increase and compensate.

The charged particle occupancies can be naively estimated using 8 particles per unit of rapidity, 8 photons per unit of rapidity with 10% of a radiation length, and 2 interactions per crossing. For a 500 micron fiber layer at R = 100cm, the occupancy then is 0.25% corresponding to a 150 KHz counting rate per fiber. Using a Kadel factor* of 2.5 as described above yields 0.6% as the occupancy estimate and 375 KHz as the average rate..

III SYSTEM PARAMETERS

Fortunately, the previous speaker presented most of the details concerning the silicon pixel and strip designs making my task easier. Figure 2 shows the layout of the planes in more detail and includes the amount of material versus rapidity plot - excluding the structural support which approximately doubles it. Figure 3 is a layout of the fibers including the clear readout fibers. A plot of material versus rapidity is shown as Figure 4 where each fiber is counted at least twice because of the readout.

Fiber superlayers are built up from nested doublets. A view, whether axial or stereo, is two such doublets or four closely packed layers of fibers. Stereo takes no more space than does axial as illustrated in Figure 5. The minimum superlayer is composed of two identical axial views separated by 4 to 5 cm so that local track vectors are produced by the 8 individual fiber layers involved. Figure 6 shows the cross section of a stereo and axial superlayer and includes a table listing the parameters of all four superlayers.

The resolution curves shown in Figure 7 for the fiber layers in stand-alone mode show that 500 micron fiber diameter as needed for occupancy at L = 10^{34} provides

---

* Kadel factor = (observed wire current)/(predicted wire current) is applicable to silicon and fiber situation as well.

excellent resolution. Overall system resolution is shown in Figure 8 with all elements included.

Readout of fibers can be done either from the 90-degree (or $\eta = 0$) end or from the large η end. The first case is preferred for pulse height or signal size reasons as the extra path length in the scintillator as η increases can compensate for attenuation in the fiber. However, time dispersion is maximized and limits the length of a fiber to 2 meters to avoid pileup from the previous crossing. With readout on the large η end, the time dispersion is minimized; fibers as long as 5 meters are allowed by the 16 nsec crossing interval. The pulse height variation, however, is now maximal and can reach 20 to 1 when photostatistics are taken into account.

Work is only beginning on possibilities for the intermediate region outside of the silicon strips. Figure 9 shows two potential configurations capable of "stereo" measurements of $d\varphi/dz$ that are made possible by the flexibility of scintillating fibers.

IV. TRIGGER

Triggering information available from the scintillating fiber axial layers is very precise due to the 500 micron granularity. The hit bits comprise the full measurement rather than a rough approximation as in drift chambers. Thus, the fibers enable P/E trigger cuts for electrons and P (tracking) to P (muon spectrometer) matching trigger cuts for muons to be made at the first level of the trigger hierarchy. In addition, a reliable stand-alone stiff track trigger is available for monitoring and efficiency cross-check purposes.

The trigger information is obtained by pipeline processing the axial hit bits in each superlayer to form local track segments and then linking those track stubs through the four superlayers to form stiff tracks. In more detail, the trigger logic flow has four steps.

- CLUSTERING In each axial view, the patterns corresponding to radial tracks are recognized and encoded. Figure 10 shows examples of these clusters.

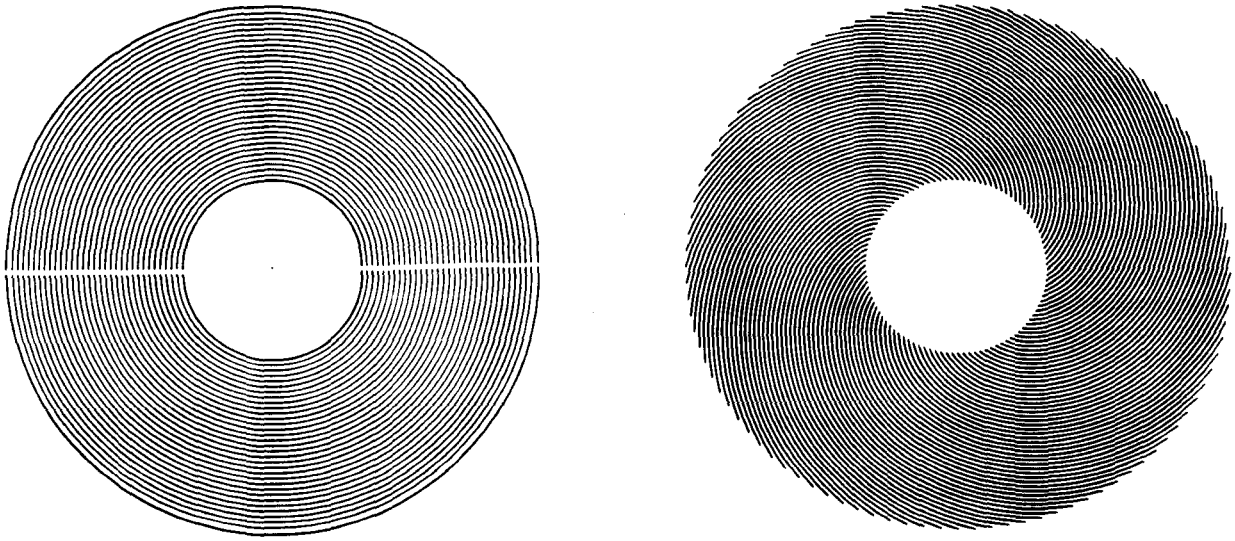

Figure 9. Intermediate region possible configurations.

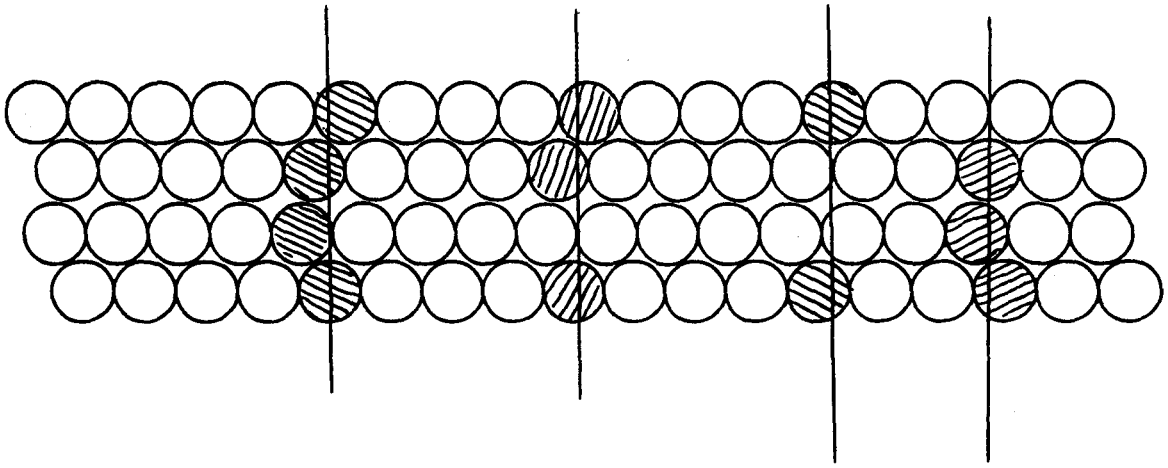

Figure 10. Examples of clustering with offset doublets of fibers.

- CONNECTING In each superlayer, the clusters are connected across the 4 cm gap separating inner and outer fiber layers to form track stubs and encoded. Figure 11 shows an example of track stubs.
- LINKING Track stubs from each superlayer are linked using a programmable momentum threshold to form stiff tracks.
- ENCODING The found tracks are encoded in units of the sagitta with 0.5 mm granularity.

Since the processing is pipelined, the stiff track information is produced at 60 MHz rate after the pipeline delay of about 30 crossings. For all tracks in each crossing, $P_t(\varphi)$ is determined and sent to the trigger where φ is encoded as the sagitta in 0.5mm units.

The first two steps, clustering and connecting, which process φ slices of a superlayer, are envisioned as hard-wired logic arrays. Since a digital data pipeline is required for creating the first level trigger time window, this logic array can be incorporated on the same custom silicon chip as the pipeline. A functional block diagram for such an ASIC is shown in Figure 12. At this time, an electronics group at Fermilab led by G.W. Foster has MOSIS designs out for fabrication for the digital pipeline and the track stub logic pipeline in order to demonstrate viability and test trigger efficiency. First chips are due in about four weeks.

Linking is of necessity a programmable process rather than hardwired. Not only is the minimum momentum threshold a variable, but changes are also possible in relative alignment of superlayers and in the beam position that affect linking in a fundamental way. The complexity of the linker depends on the minimum momentum selected. For 20 GeV/c, the search region at the innermost superlayer is about 20 fibers wide, but for 5 GeV/c this increases to 80 fibers. Monte Carlo studies are being prepared to quantify this aspect of the trigger.

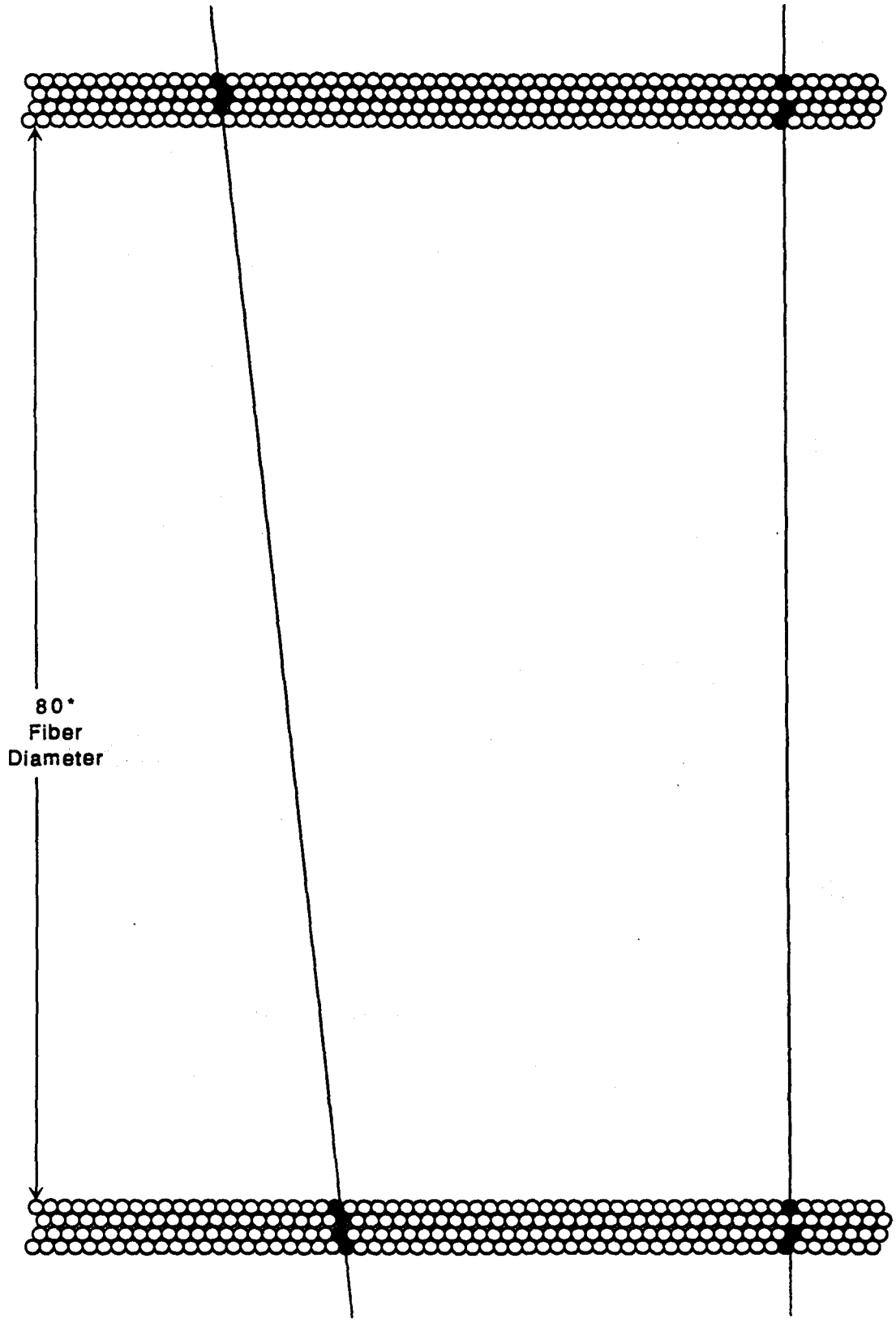

Figure 11. Superlayer track stub examples.

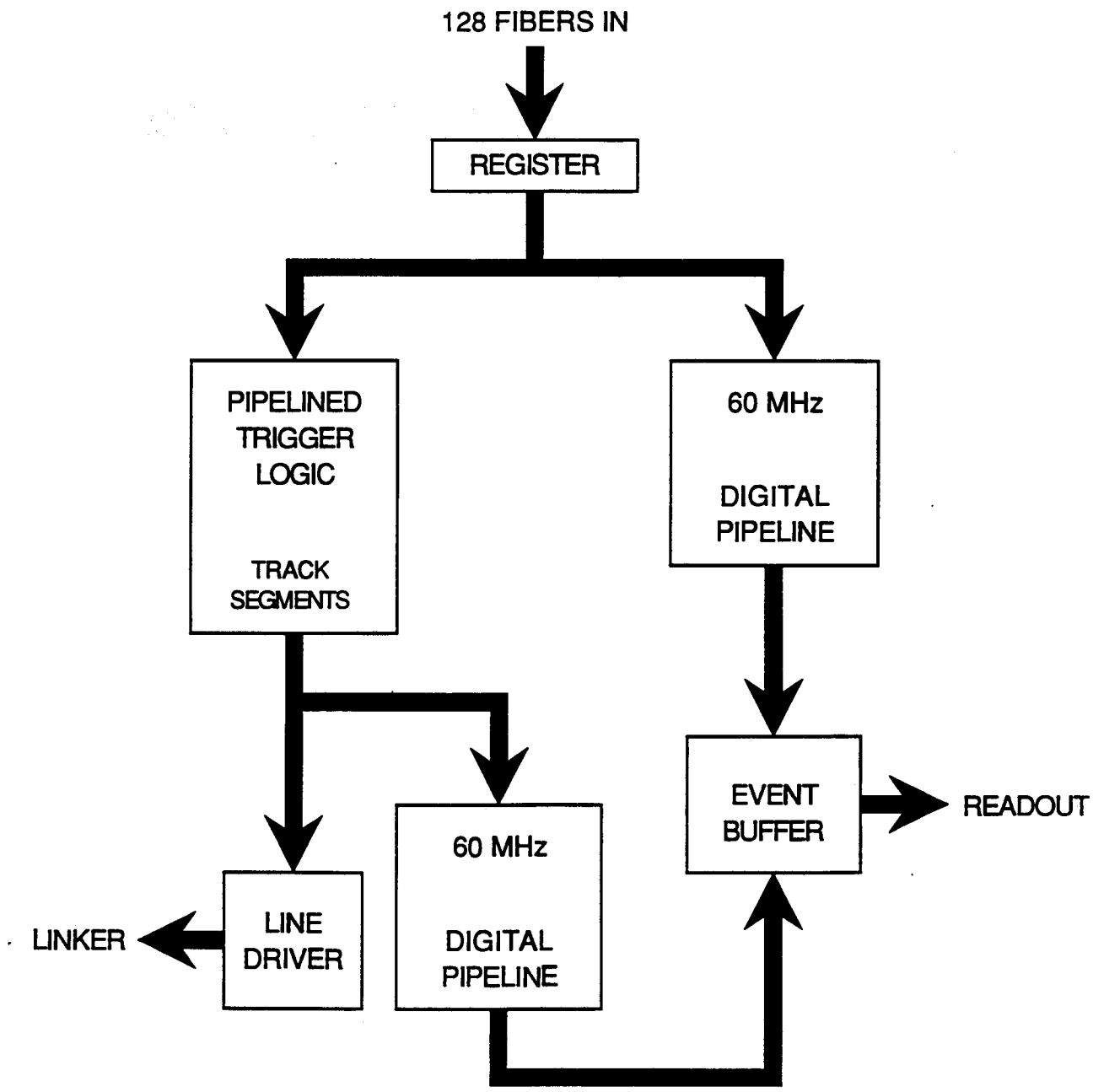

Fiber Superlayer Pipeline ASIC Chip

Functional Block Diagram

Figure 12.

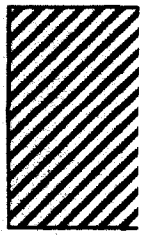

Parallel Session: Tracking

April 24, 13:30-17:00

Pattern recognition study for the ACS detector

F. Abe
KEK

(Equivalent talk presented at Physics, computing, and simulation session)

Progress Report on the Design of the Hybrid Central Tracking Chamber

S. H. Oh, A. T. Goshaw, W. J. Robertson
Department of Physics
Duke University
Durham, N.C. 27706

May 30, 1990

I. Hybrid Central Tracking Chamber.

There are several proposals to construct the outer tracking chamber for the Solenoid Detector Collaboration (SDC). One design depends entirely on the straw tube wire chamber. Another design uses only scintillating fibers. In the first design, there are superlayers of longitudinal straw (along the beam axis; z axis) to measure the r-ϕ location. The z measurement is accomplished by using superlayers with slanted straws (u-v layers at about 3-4 degrees with respect to the longitudinal straws). Each superlayer consists of 8-10 straw tube layers. The diameter of the straw tubes is 4 mm. The slanted superlayers tend to complicate the construction of the chamber because the straw tubes can not be laid on a cylindrical surface. The second design is similar to the first except that scintillating fibers are used instead of straws. In this design there is no complication with u-v layers because the fibers are flexible and can be wound onto a cylindrical surface. However the number of channels for this design becomes prohibitively large for reasonable pattern recognition.

Our hybrid design employs both techniques. It measures the r-ϕ coordinates using longitudinal straws and measures the z position using u-v fibers. Figure 1 shows a conceptual design of the Hybrid Central Tracking Chamber (HCTC). It consists of several superlayers. Each superlayer consists of a cylindrical shell and 8 layers of straw tubes mounted on the inner and outer surfaces of the cylindrical shell as shown in Figure 2. In some superlayers, one of the 8 straw tube layers is replaced by the u-v scintillating fibers to measure the z coordinates of tracks as shown in Figure 3.

There are several advantages to the HCTC design. First the number of channels are much reduced compared to a design with all scintillating fibers. Second, since the u-v straws are replaced by u-v fibers, and fibers can be wound onto a cylindrical surface, there is less complexity in the construction. Third, the u-v fibers and longitudinal straws form a "triplet" such that 3 dimensional space points can be obtained from hits. This is not possible with u-v straws. It may also be useful to have a couple of layers of z fibers for calibration and monitoring purposes. Using accurately positioned z fibers, the wire position and electron drift velocity can be determined.

II. Conceptual Design.

In this section we describe the conceptual design of the Central Tracking Chamber (CTC) using the hybrid concept. As shown in Figure 1, the CTC consists of several superlayers. Each superlayer is based on a cylindrical structure which can be made of, for example, two thin carbon fiber skins which sandwich light material to provide rigidity. Our present design calls for a 6 meter long cylindrical structure. Tubes will be placed on the structure layer by layer. As shown in Figure 4 , we have already demonstrated a technique which enable us to place straw tubes straight within 100 μm over a length of several meters. In Figure 4, the position of straw tubes is plotted as a function of distance along the tube length. As seen in the figure, tubes are straight within 100 μm. The line in the figure is the expected distance from a reference line.

The proper end-plate design is very important since straw tube, electronic, gas and high voltage connections and cooling are done through end-plates. Our end-plate consists of two plates with space between them (Figure 5). Tubes are fitted to the inner plate, and feed-throughs are inserted from the outer plate for sense wire, high voltage and amplifier connection. The wire position is determined by the location of the feed-throughs independent of the tube. The space between the plates serves as a plenum to provide gas flow to straw tubes. The gas may be cooled to offset the heat generated from

tubes due to gas heating.

Each superlayer is expected to be assembled separately in order to save construction time. After all superlayers are constructed, they will be put together to make the final Central Tracking Chamber. The detailed construction scheme has not been worked out at the present time.

III. Search for a Gas mixture.

Due to the short bunch crossing time (16ns) of the SSC machine, it is important to use a gas (or a gas mixture) with fast electron drift velocity. It has been shown that CF_4 produces drift velocities larger than 100 μm/ns for the electric field inside tubes. However CF_4 alone does not produce good spatial resolution, so it is commonly mixed with hydrocarbon gases, such as methane, ethane or isobutane to obtain a satisfactory resolution ($\sim$ 100 μm of intrinsic resolution.). For these gas mixtures, in order to obtain an adequate gain ($\sim$ 20000), the operating voltage has to be greater than 2000 volts. Since the wire instability grows as a function of the voltage squared as shown in Section IV, it is desirable to lower the operating voltage as much as possible.

We have discovered that we can lower the operating voltage by $\sim$ 20% without affecting the drift velocity and resolution by adding argon to the gas mixtures of CF_4 and hydrocarbon gases. In Figure 6, the time distribution from a 4 mm diameter straw tube chamber using a mixture of CF_4-Ethane (50-50) is plotted. The voltage used for this gas is 2200 Volts. The width of the distribution is about 20 ns, which corresponds to a drift velocity of 100 μm/ns. In Figure 7, the same is plotted for CF_4-Ethane-Ar (33-33-33) mixture. The operating voltage for this gas mixture is 1850 volts for the same gain. The width is still about 20 ns.

We also measured the resolution by using a 4 straw tube (4 mm diameter) chamber and cosmic rays. In Figure 8 the residual of reconstructed cosmic ray tracks is plotted for the gas mixture containing argon, and we obtain a sigma of about 100 μm , comparable to other gas mixtures tested. The result in Figure 8 is preliminary since no effort was made to correct for the wire position and drift velocity as a function of distance from the sense wire (constant velocity is assumed here). At the present time, we are varying the fraction of argon to obtain the best gas mixture.

IV. Electrostatic Stability of Straw Tubes.

The straw tube design for the central tracking chamber in a solenoidal detector at the SSC calls for 4 mm diameter detector elements. The sense wire would be operated around 2000 volts to achieve gas gains which give suitable signal pulses. The ideal case in which the sense wire is exactly centered within a perfectly cylindrical cathode is electrostatically stable. Practically, however, the sense wire will not be exactly centered due to positioning error and gravitational sag and the straw tube cathode will be neither perfectly cylindrical nor perfectly straight. Therefore it is important to determine the conditions under which an operational straw tube detector element will perform satisfactorily. The electrostatic force due to offset of the sense wire in the straw tube is given by:

$$F_E = \frac{2\pi\epsilon_0 V^2 \delta}{R^2 (ln(R/r))^2}$$

where V is the sense wire potential, δ is the offset of the sense wire from the center of the straw tube, R is the radius of the straw tube cathode and r is the radius of the sense wire.

We have constructed a straw tube model of stainless steel tubing which is held in alignment by a 3/4 inch square steel "backbone" and machined mounting brackets. The tubing has an inner diameter of 3.9 mm. The steel tube is placed in a horizontal orientation. A manifold on one end allows gas flow to purge air from the tube to eliminate molecular ionization currents which occur with oxygen and nitrogen at high electric field. We have used CH_4, CO_2 and CF_4 as stable gases.

We find that the longest cell that is stable above 2.5 kV with a 25 μm sense wire centered in the tube under 50 grams tension is one meter. The tensile strength of 25 μm diameter tungsten wire is 150 - 200 grams so the applied tension to the wire should be kept below 100 grams. Keeping the wire tension to a minimum will also reduce the mechanical load on the detector assembly.

Using a one meter long tube, we have conducted a series of tests to determine the effect of a position offset of the wire in the tube on the maximum voltage the cell can sustain before breakdown. A sense wire is positioned in the tube so as to be centered vertically. The horizontal position of the sense

wire with respect to the center of the tube is adjustable. The distance from the center of the tube to the position of the sense wire is measured by means of a travelling microscope to an accuracy of better than 20 μm. The wire position was adjusted relative to the center of the tube and the potential on the wire was then increased until breakdown occurred in the cell.

Figure 9 shows the maximum stable operating voltage that a one meter long cell filled with CH_4 can sustain when the sense wire is displaced from the center of the cathode for two different wire tensions of 50 and 100 grams. These tests show that wire offsets of up to a few hundred μm will not compromise cell operation.

One can predict the motion of the sense wire under increasing electric potential. This has been studied by drilling a hole in the middle of the steel tube to observe the position of the sense wire with a travelling microscope as the wire potential is raised.

The sense wire was positioned off center by a known amount (δ). The sense wire potential was increased and the deflection of the midpoint of the wire (d) from its initial position was measured. This deflection can be calculated and is related to the potential on the wire to good approximation by the expressions

$$d = \frac{L^2 F_E}{8T}$$

$$d = \frac{2\pi\epsilon_o V^2 L^2 (\delta + d/2)}{R^2 (ln(R/r))^2}$$

For a one meter long wire the displacement is given by

$$d = \frac{\delta(\frac{V}{V_o})^2}{(1-\frac{1}{2}(\frac{V}{V_o})^2)}$$

where $V_o = 2700\sqrt{\frac{T}{50}}$

with T the wire tension in grams and
V the applied potential in volts.

Figure 10 shows measurements of the wire deflection versus sense wire potential for tensions of 50 and 100 grams. The lower set of data in each case is with an initial offset of 100 μm and the upper set of data is for an initial offset of 200 μm. The solid curves are predictions from the formula for the wire deflection. The open circle data points are for initial offset in one direction while the closed circle data points are for initial offset in the opposite direction. The discrepancies between the data are indicative of some nonlinearity of the tube. The measurements agree quite well with the predictions of the above calculations.

With 50 grams wire tension the amount of deflection of the wire from its initial position is about 100 μm at potentials at which the straw tubes are expected to be operated. In order to optimize spatial measurement resolution such wire deflection must be minimized. Therefore, 50 grams of tension is probably acceptable with wire supports at distance intervals of one meter.

V. Sense Wire Support.

To achieve adequate geometric acceptance for charged tracks the SSC central tracking chamber will have to be six meters long at an outer radius of 1.7 meters. Some designs call for a gap in the middle of the chamber in which case straw tube cells may be about three meters long. In either case it will be necessary to provide centering support for the sense wires in the straw tubes at about one meter intervals to ensure electrostatic stability.

The wire supports must center the wire in the straw tube while at the same time not restricting gas flow through the tube. Our design for the wire support consists of a plastic cylinder with a helical groove which is a cylinder radius deep and makes at least one complete revolution around the cylinder in a length of 1-2 cm. Such a device will provide gravitational support regardless of the orientation of the tube. A schematic drawing of the wire support design with cross section views is shown in Figure 11. Enlargement of a prototype wire support fixture is shown in Figure 12. Production of an injection molding form is in progress and the first molded fixtures should be available for testing within a month.

The wire supports will be attached to the straw tube. The wire will then be threaded through the tube. This has the advantage that if a wire should break during installation in a straw tube it will be easy to remove the broken

wire and restring the tube. We have used air flow through the tube to draw and guide the sense wire. We believe that this procedure will also work with the wire support pieces in place.

We have assembled several layers of 2 meter long straw tubes on a machined base plate which has been aligned to be flat to better than 100 μm . The tubes are made up of two 1 meter long straws with a short piece of transparent (unaluminized) straw spliced between the 1 meter straws. The splice straw contains two temporary wire support pieces shaped as shown below, which have been oriented so that the wedges are opposed to one another to provide wire support in all directions. The two pieces are separated by 1 cm. The temporary wire supports were not precision machined and the wire position in the straw tubes is off center by as much as 100 - 150 μm at the wire support. It is possible, however, to apply up to 2700 volts to the wire. At higher potentials breakdown occurs at the end of the straw tube where an aluminum insert aligns the straw with the end plate.

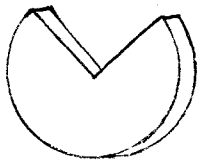

VI. Termination.

The present design of the outer CTC of SDC is 6 meters in length. One proposed design is to construct two 3 meter long chambers. At one end of each chamber, readout electronics are mounted, and some kind of terminations is mounted at the other end in order to reduce reflection and noise. This concept is not very attractive because of the amount of material at 90 degrees with respect the beam axis. In this section we present a design without such a drawback.

Our design uses continuous 6 meter long straw tubes placed on the supporting cylindrical structure. Inside tubes, wire supports described in Section V are positioned about every 1 meter. At the middle of the tube, the sense wire is terminated using the scheme shown in Figures 13 and 14. Figure 13 illustrates the case in which the sense wire is at positive high voltage and the inner tube surface (cathode) is at ground. In Figure 14 the sense wire is at ground and the cathode surface is at negative high voltage. The latter scheme is attractive because it does not require decoupling capacitors for readout electronics.

In both designs, the sense wire is cut at the middle and joined together using an insulating wire to make two independent 3 meter chambers. At the middle, each section of wire is terminated through a resistor and a capacitor. The resistor is made of a thin half cylinder on which the sense wire rests. The required capacitance to ground is provided by inserting a short tube which fits tightly inside the 4 mm diameter tube. We note that the capacitance of a straw tube with 4 mm diameter and wall thickness of 50 μm is about 100 pf/cm, when the tube has a conductive surface inside and outside of the tube. 50 μm of mylar has a dielectric strength of 9000 volts.

Figure Captions.

Figure 1. A conceptual design of the HCTC consisting of several cylindrical superlayers.

Figure 2. Cross section of a superlayer consisting of a cylindrical supporting structure and two layers 8 tubes deep.

Figure 3. Same as Figure 2, except one of the tube layers is replaced by u-v scintillating fibers for z measurement.

Figure 4. Measured tube position as a function of tube length. The solid line is the expected tube position from a reference line.

Figure 5. End plate design consisting of two plates.

Figure 6. Time distribution using CF_4-Ethane (50-50) mixture. The operating voltage is 2200 Volts.

Figure 7. Time distribution using CF_4-Ethane-Ar (33-33-33). The operating voltage is 1850 Volts.

Figure 8. Residual of reconstructed cosmic ray tracks. CF_4-Ethane-Ar (33-33-33) mixture is used.

Figure 9. Maximum stable operating voltage for two different wire tensions of 50 and 100 grams as a function of initial wire offset.

Figure 10. Wire deflection as a function of voltage for two different initial displacement, 100 (lower set) and 200 (upper set)μm.

Figure on left is for 50 gram tension, and the figure on right is for 100 gram tension.The solid curves are the prediction from the formula in text.

Figure 11, 12. Duke wire support design.

Figure 13. A design which eliminates the end plates in the middle of CTC by terminating wire inside the tube. This design illustrates the operational mode in which the sense wire is at positive high voltage and the cathode is at ground

Figure 14. Same as Figure 13 but for grounded sense wire and the cathode at negative high voltage.

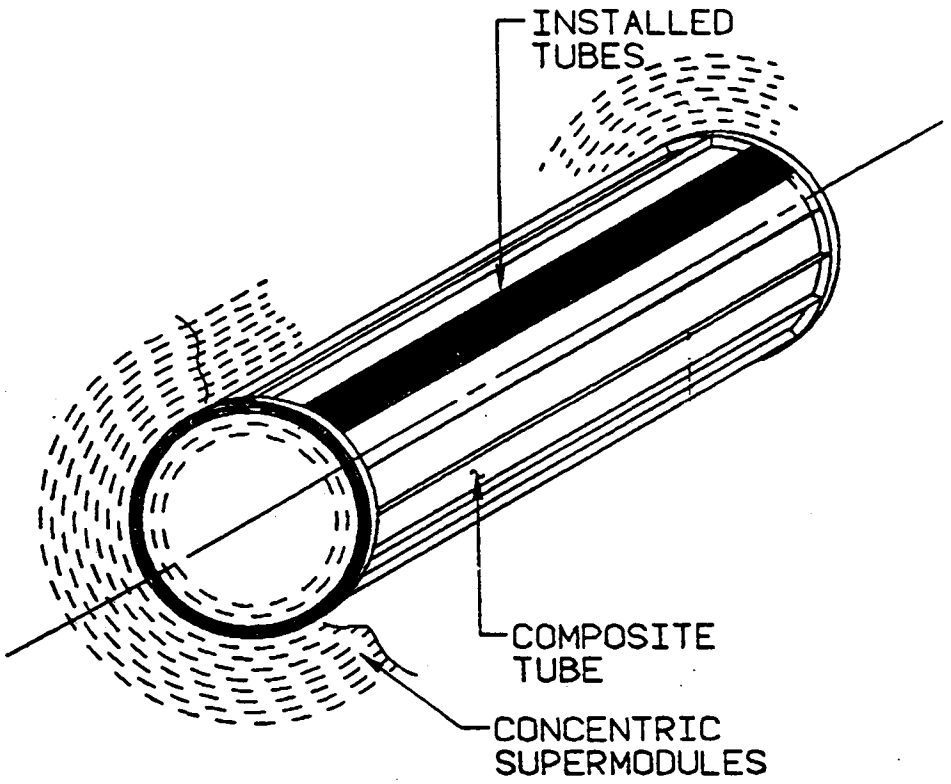

FIGURE 1

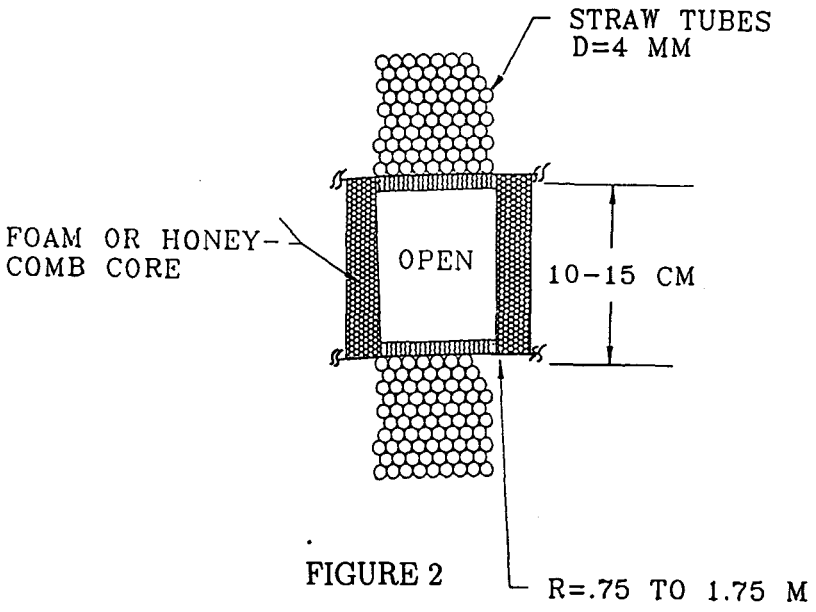

FIGURE 2

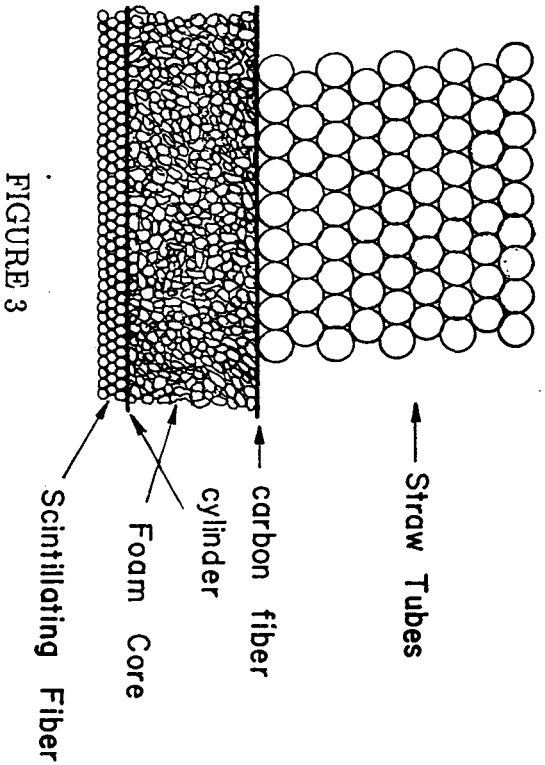

FIGURE 3

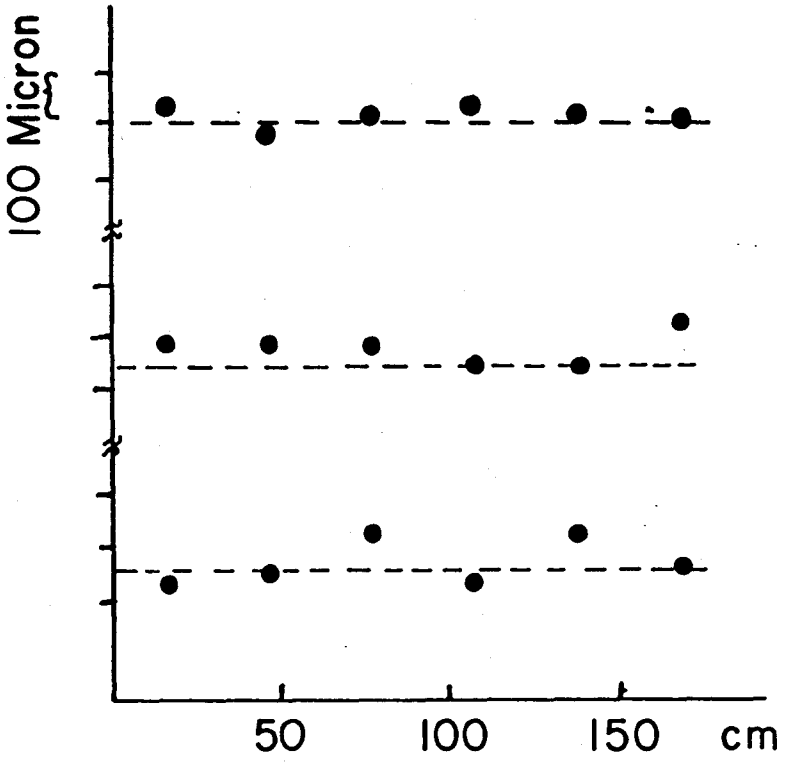

FIGURE 4

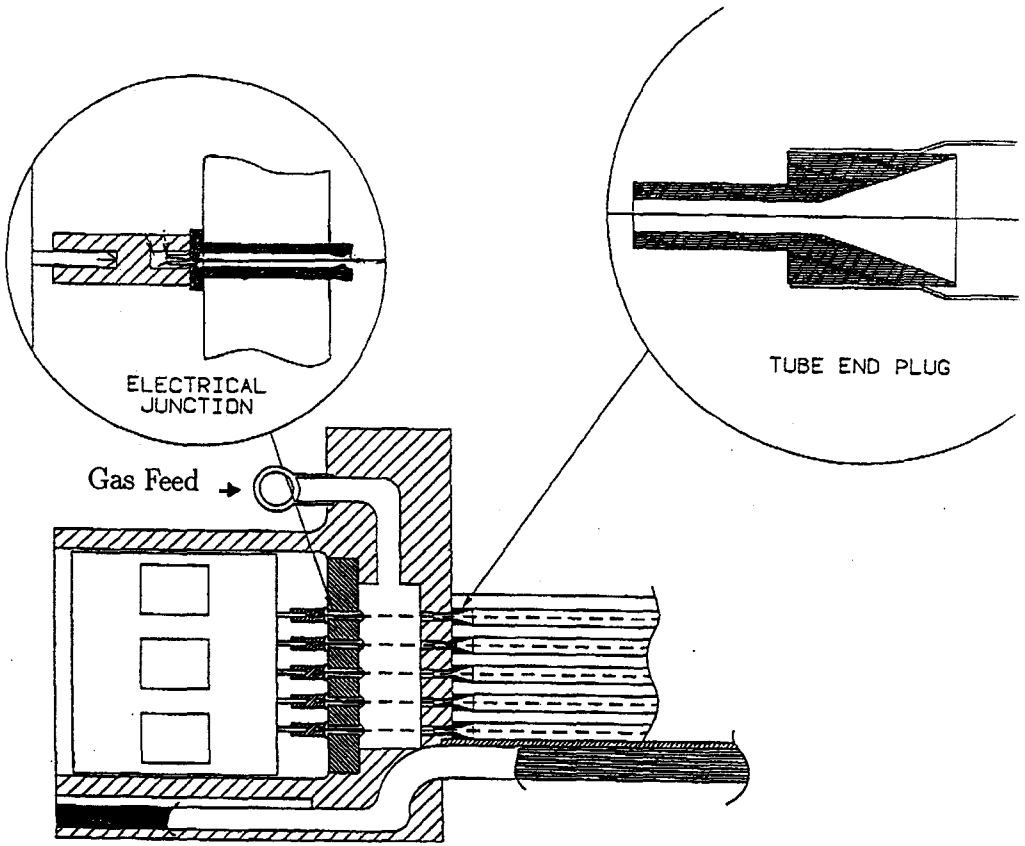

FIGURE 5

CF_4-Ethane (50-50), HV = 2200 Volts.

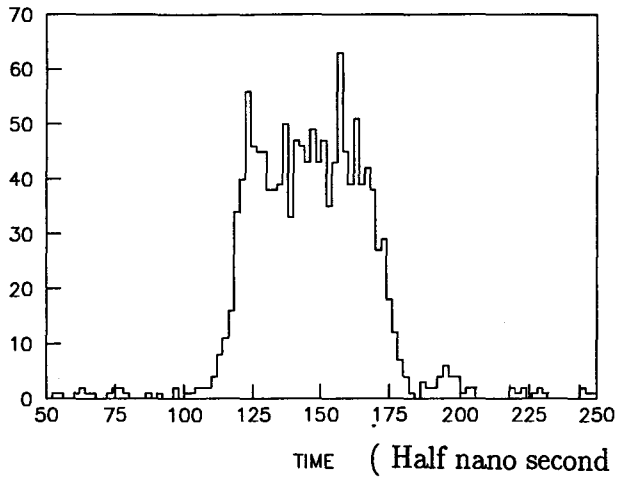

FIGURE 6

Ar-Ethane- CF_4 (33-33-33), HV=1850 Volts.

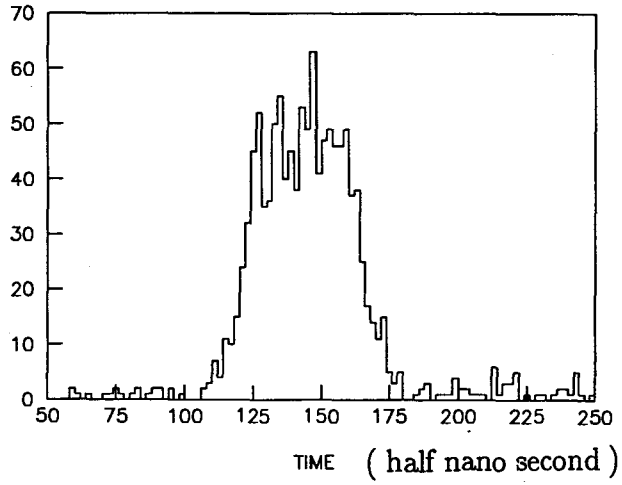

FIGURE 7

Ar-Ethane- CF_4 (33-33-33), HV=1850 Volts.

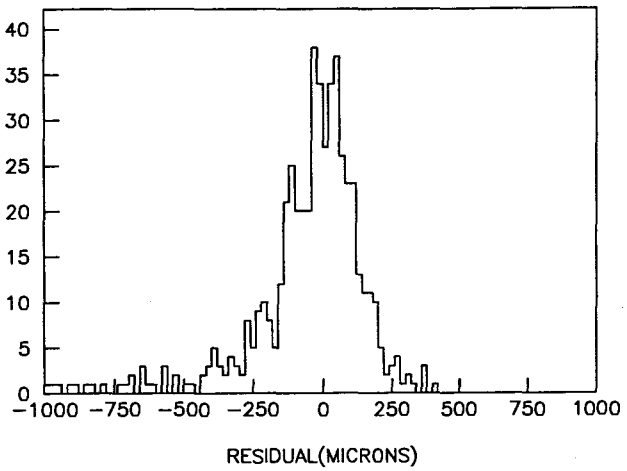

FIGURE 8

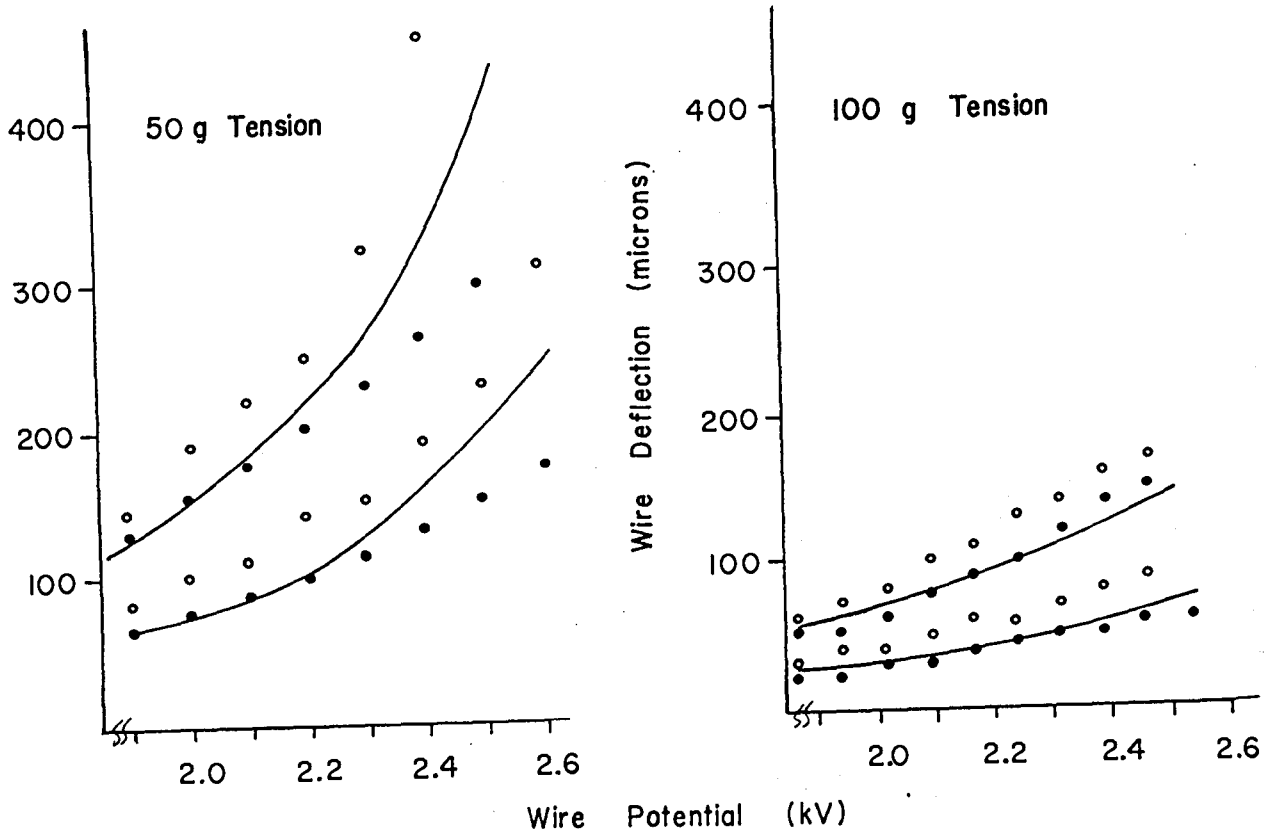

FIGURE 10

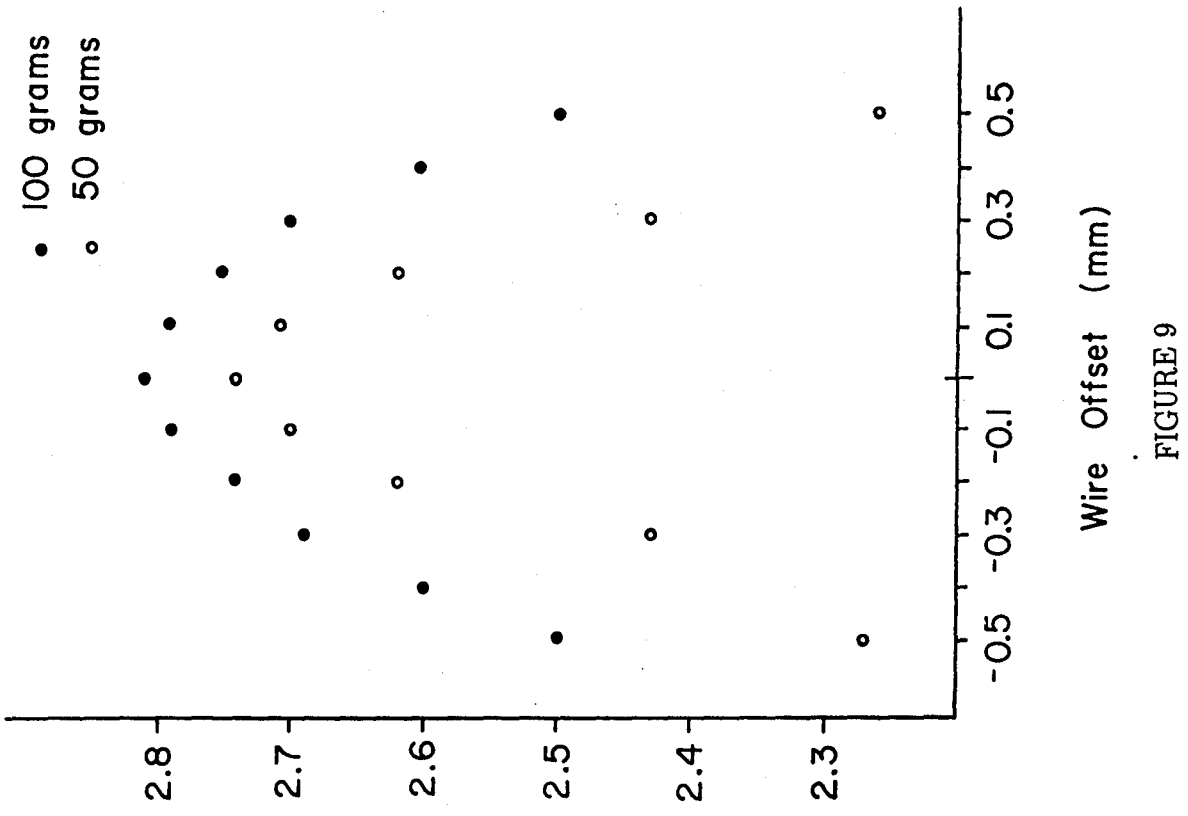

FIGURE 9

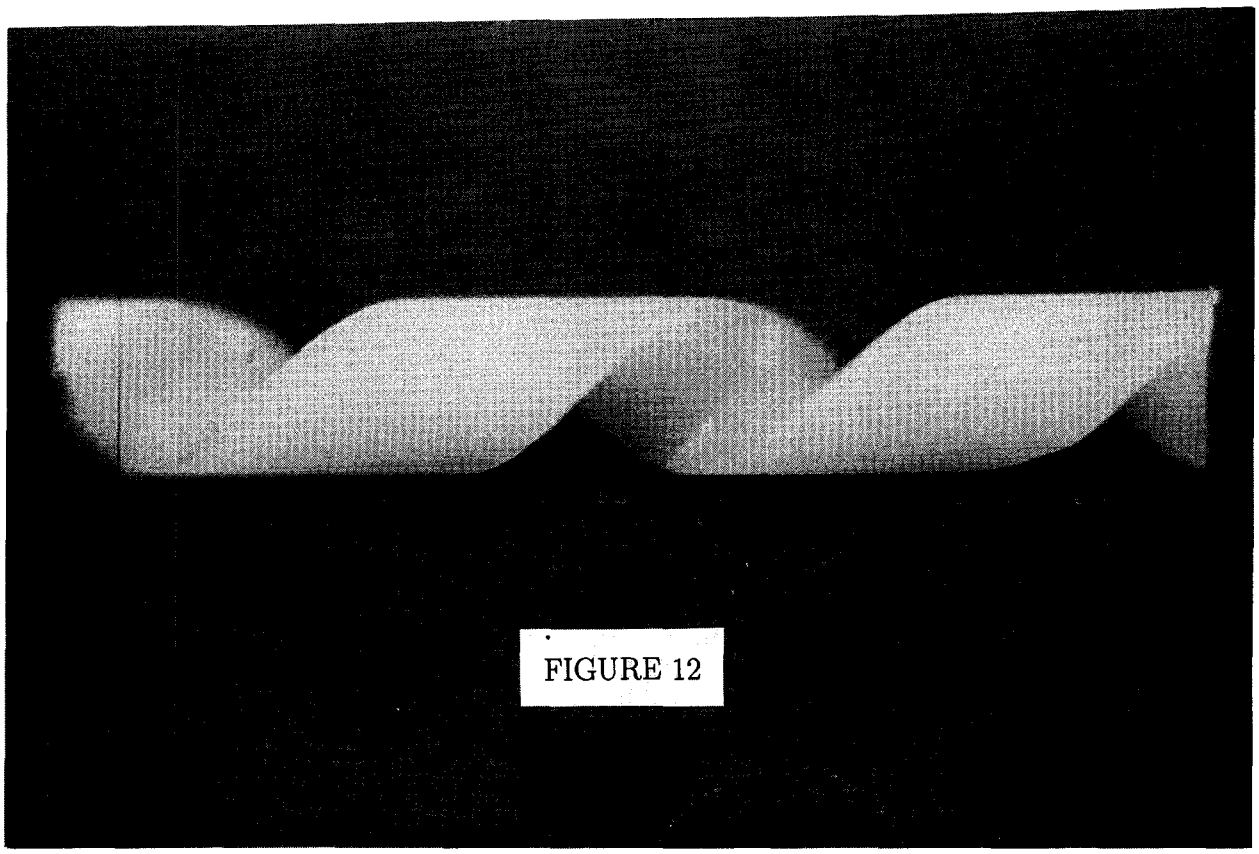

FIGURE 12

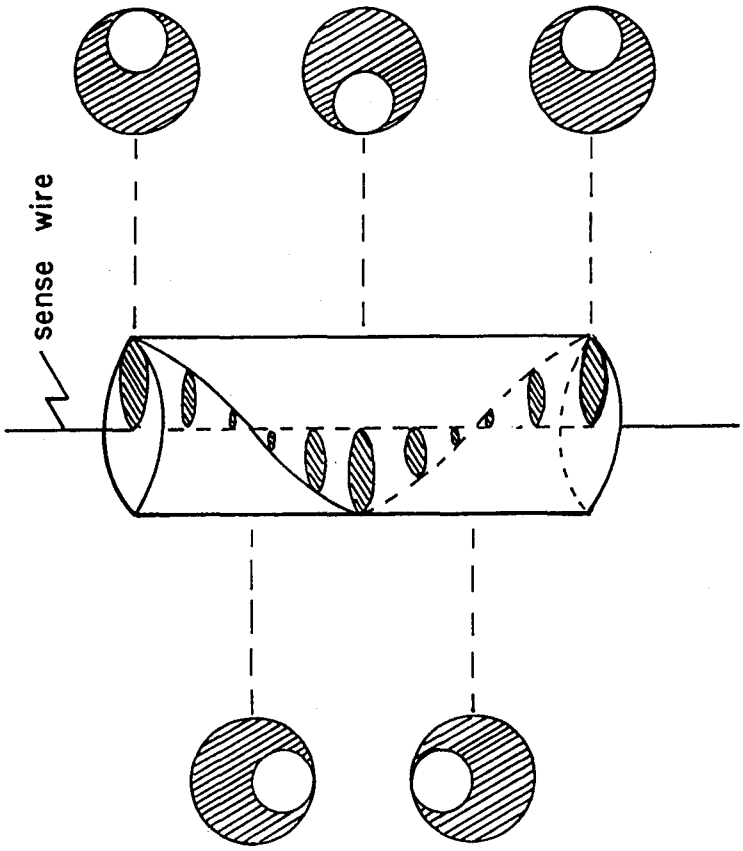

FIGURE 11

FIGURE 13

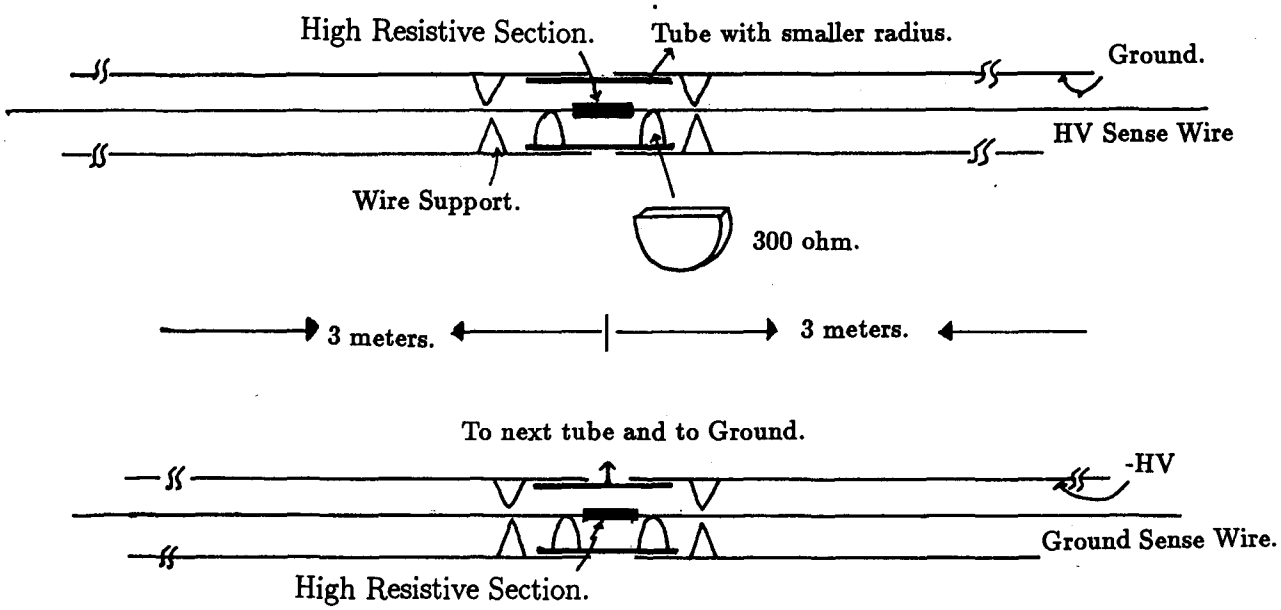

FIGURE 14

Hit Rate Studies of the Straw Chambers in the Hybrid Tracker

Makoto Asai
Hiroshima Institute of Technology
2-1-1 Miyake, Saeki-ku, Hiroshima 731-51, Japan

We estimated the hit rates of the straw chambers in the hybrid tracker by using the ISAJET event generator and the GEANT detector simulator. Radius dependences of the hit rates are obtained for three models, the "EoI full design" model and 1/2 and 1/3 reduced of the full design. For the innermost layer, the hit rate of a 4 $mm\phi$ straw becomes more than 4 MHz for all of the three models at $\mathcal{L} = 10^{33} cm^{-2} s^{-1}$. Hit rates are not sensitive to the thickness of the tracker.

1 Introduction

Straw chamber tracker is one of the most promising tracker for the central tracking system of the SSC experiments. But for the SSC environments, straw chamber may have a severe difficulty of the high hit rate.

Event rate of the minimum bias event is expected to be 100 MHz at $\mathcal{L} = 10^{33} cm^{-2} s^{-1}$ and the charged multiplicity per unit pseudo-rapidity is about seven. Not only the primary particles but the secondary products such as delta-rays and positron-electron pairs from gamma conversions should be taken into account to estimate the hit rate. Curling tracks inside the tracking volume by the solenoidal field are also expected to increase the hit rate significantly. To estimate effects of these secondary products and curling-ups, we employed GEANT.

In this study, we used the event-generator code ISAJET version 6.21 and selected low-Pt twojet event to generate minimum bias events.

2 Models of the straw chamber tracker

The model straw chamber we used in this study was based on the hybrid tracker system described in the Expression of Interest by the Solenoidal Detector Collaboration. This model (Model#1) has 10 layers of silicon microstrip detector and 13 superlayers of straw chamber tracker. Fig.1 is a schematic view of Model#1. Each superlayer has 10 layers of 4 $mm\phi$ straws and the thickness of a superlayer is 0.8 $\%X_0$. Each straw chamber is divided into two for the Z-segmentation.

We also used two other models to estimate the effect of the tracker thickness. One is the 1/2 reduced of the EoI model (Model#2) and the other is the 1/3 reduced of the EoI model (Model#3). Fig.2 and Fig.3 are the schematic views of these two models. For

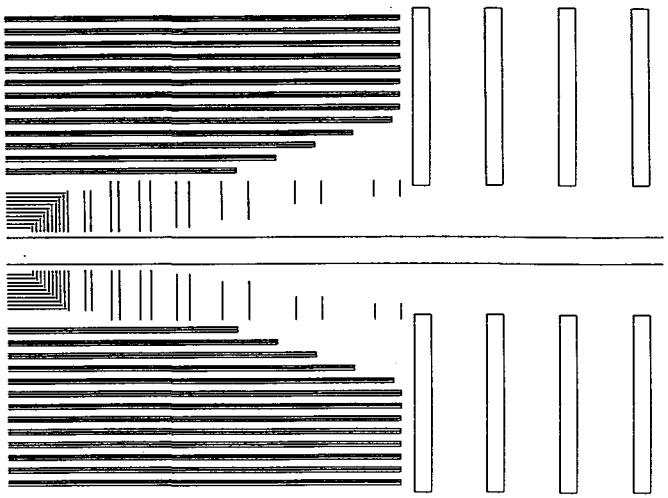

Figure 1: Schematic view of Model#1 (EoI full model)

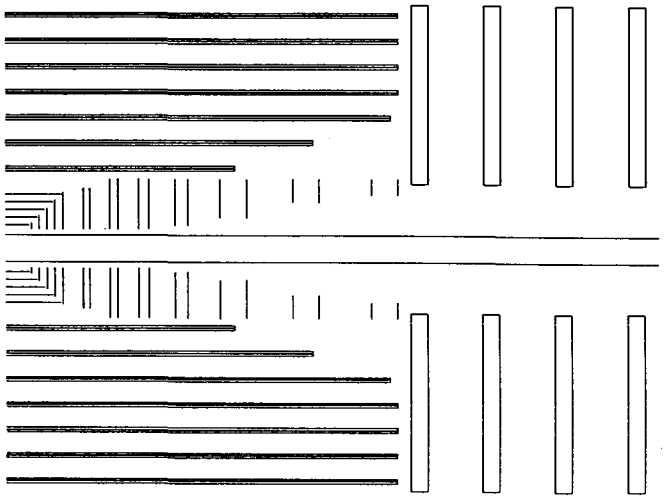

Figure 2: Schematic view of Model#2 (1/2 reduced model)

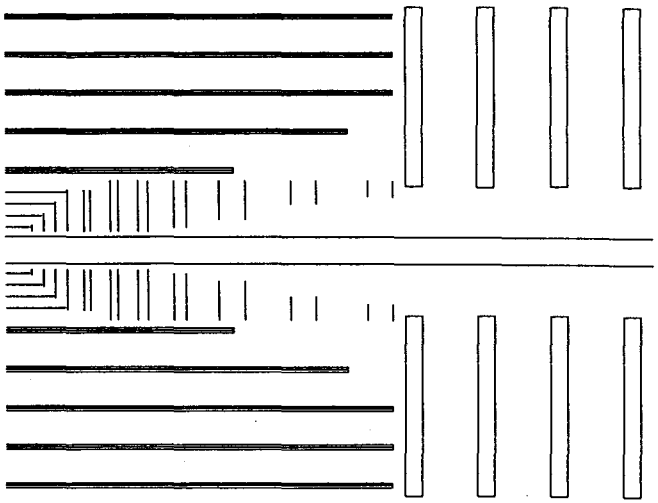

Figure 3: Schematic view of Model#3 (1/3 reduced model)

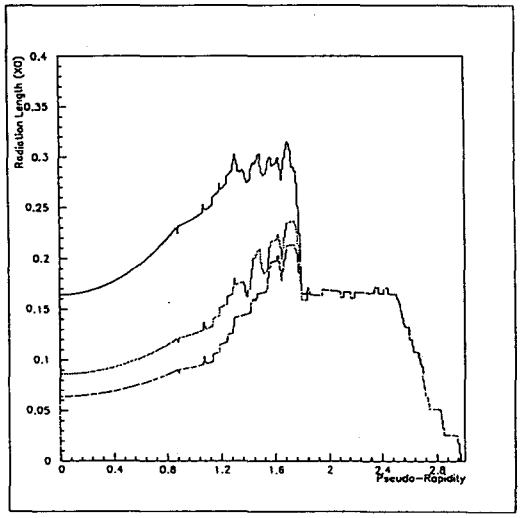

Figure 4: Total thickness of three models with respect to pseudo-rapidity

these reduced models, the thickness of each superlayer is not changed but the numbers of the superlayers are reduced.

Fig.4 shows the total thickness of these three models against the pseudo-rapidity. At $\eta = 0$, thickness of three models are 16.5 $\%X_0$, 8.5 $\%X_0$, and 6.5 $\%X_0$, respectively, while at $\eta = 1.6$, where the thickness become the maximum, thickness of the models are 33 $\%X_0$, 23 $\%X_0$, and 21 $\%X_0$, respectively.

3 Estimation of the hit rates

Secondary interactions such as pair production, decay in flight, hadronic interaction, delta-ray, multiple scattering, ionization loss, etc., were taken into account by using GEANT. All the cut-off energies used in this study were set to 1 MeV. No backward scattering from the calorimeter or the solenoid magnet is considered. The solenoidal field was set to 2 Tesla.

We put 32 test straw tubes into the each superlayer to estimate the hit rate. These tubes were divided into two, the number of Z-segmentation. The probability that a test tube in a superlayer was hitted by at least one charged track was obtained by the average over the 32 test tubes and over two segmentations. Hit rate was estimated by the product of this probability and the minimum bias event rate.

The radius dependences of the hit rate with respect to three models are shown in Fig.5. 200 minimum bias events were used and the statistical error is arround 10 % at 1 MHz point. So, the detail structures in the figure indicate statistical fluctuation. Table 1 shows the summary of the hit rate.

4 Discussions

As shown in Fig.5, while the thickness is reduced to 1/3, the hit rate of Model#3 is almost the same as the hit rate of Model#1. This means that hit rate is not sensitive to the thickness of the tracker. The less the tracker material is, the less secondary interactions occur, but the longer the loopers live. If one consider about the maximum drift time of liberated electron and event pile-up, one had better uses a straw chamber at less than 1 MHz. So, if the segmentation in Z-direction is kept to two, the available

Table 1: Summary of the hit rate

Radius (cm)	Model#1 (MHz)	Model#2 (MHz)	Model#3 (MHz)
60	4.2	4.2	3.7
120	1.5	1.4	1.3
180	0.3	0.3	0.3

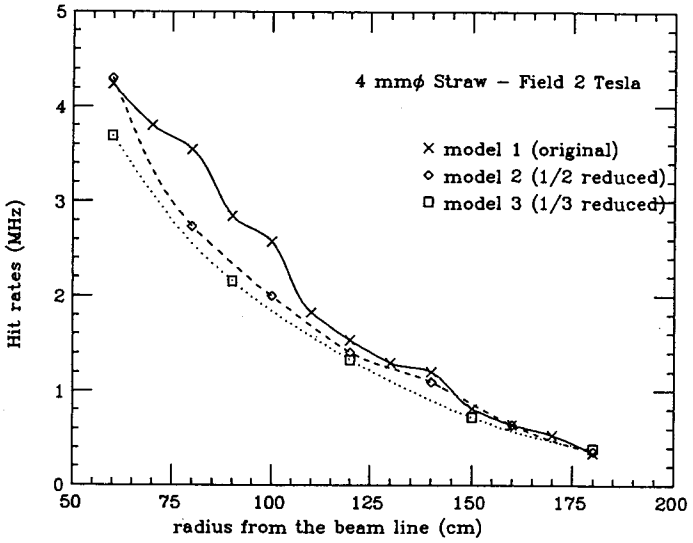

Figure 5: The radius dependences of the hit rate

region for straw chamber tracker is limited to regions whose radii are outer than about 140 *cm*.

If the number of Z-segmentation can be increased from 2 to 6, hit rate will reduced to almost 1/3. The cost of the tracker system is linearly proportional to the number of the channels. So, increasing the Z-segmentation and reducing the number of the superlayers is the right way to realize the straw chamber tracking system.

A Scintillating Fiber Tracker for the SSC

D. Adams[i], M. Atac[a,b], C. Anway[a], T. Armstrong[g], B. Baumbaugh[d], P. Berge[b], M. Binkley[b], J. Bishop[d], N. Biswas[d], H. Brasheare[e], A. Bross[b], C. Buchanan[a], N. Cason[d], R. Chaney[i], D. Chrisman[a], A. Clark[b], D. Cline[a], H. Cohn[e], M. Corcoran[l], J. Elias[b], M. Emery[e], E. Fenyvesi, G. Foster[b], J.M. Gaillard[b], J. Godfrey[d], H. Goldberg[c], H. Hammack[j], A. Hasan[g], S. Heppelmann[g], V. Kenney[d], R. Kephart[b], D. Koltick[h], J. Kolonko[a], K. Kondo[k], R. Lewis[g], R. McIlwain[h], S. Margulies[c], H. Miettenen[i], B. Oh[g], T. Okusawa[f], J. Passaneau[g], J. Piekarz[d], M. Rennich[e], R. Ruchti[d], W. Shephard[d], E. Shibata[h], G. Smith[g], J. Solomon[c], K. Takikawa[k], S. Tkaczyk[b], R. Todd[e], W. Toothacker[g], R. Wagner[b], J. Whitmore[g], W. Zebrisie[e].

University of California at Los Angeles[a]
Fermi National Accelerator Laboratory[b]
University of Illinois at Chicago[c]
University of Notre Dame[d]
Oak Ridge National Laboratory[e]
Osaka City University[f]
Pennsylvania State University[g]
Purdue University[h]
Rice University[i]
University of Texas at Dallas[j]
Tsukuba University[k]

Presented by

D. Koltick
Physics Department
Purdue University
West Lafayette, Indiana 47907

Introduction

The SSC has great potential to explore very high center of mass energies however this is achievable largely by operating at the planned luminosity of $L=10^{33}$ cm^{-2} sec^{-1} and in the case of searching for a high mass Higgs boson is achievable only at luminosities, approaching $L=10^{34}$ cm^{-2} sec^{-1}. As is well known at such luminosities more than one inelastic collision takes place per beam crossing. At 10^{33} the most likely number of events per crossing is 2. At 10^{34} the number is 20 (see Fig. 1). Applying present technology to the detection of the collision products from a single crossing of these 20 TeV beams would undoubtedly work and be the most logical approach to a "tried and true" detector, if it were not for the fact that a beam crossing occurs every $16 \cdot 10^{-9}$ sec or at a rate of 62.5 Megahertz. Such extreme rates call for detectors with a high degree of segmentation, capable of very fast response or burst rates, and because of the inherent need to employ large numbers of the basic detecting element, they must also be simple in order to have a chance of being reliable over a long term and they must be low cost. And finally they must be capable of withstanding the radiation environment of the SSC. With these considerations it is the belief of the SDC scintillating fiber tracking group that older technologies are not capable of withstanding the environment at 10^{34} and that scintillating fibers can be shown to be the correct choice for a central tracker at the SSC. Our goal is to develop a high rate tracking system appropriate for the SSC, based on the scintillating fiber technology. Such technology makes affordable the prospect of tracking particles with high spatial and temporal resolution, low occupancy and good efficiency. The tracker we envision will be built in such a way to maximize the physics obtainable through the study of charged particles in the SSC energy range.

Scintillating Fiber Tracker

The basic element of a Scintillating Fiber Tracker (SFT) we envision is shown in Fig. 2. It consists of a scintillating fiber, spliced to a clear optical fiber wave guide. The wave guide will be made of the same material as the scintillating fiber, except the scintillating dye will be left out. The scintillating fiber typically contains about 1% of a dopant by weight, which does not alter the

fibers mechanical properties significantly from that of the undoped fiber. The wave guide will transmit the scintillation light out of the tracking volume and into a liquid helium cryostat containing a solid state photomultiplier sensitive to and optimized for visible light detection called a Visual Light Photon Counter or a VLPC. The VLPC will be electrically connected to a nitrogen temperature amplifier which will deliver the single bit of digital information, that the fiber was hit, to the data taking and trigger electronics. Each of the individual elements described above will in turn be discussed in detail.

Fibers

Presently we intend to use fibers of 500 μm diameter. When correlated with other fibers in a tracker, they are capable of yielding resolutions of 100 μm or better depending on construction accuracy, as shown in Fig. 3. Fibers of this diameter also yield a reasonable number of total channels capable of accomplishing the physics goals of a central tracker at a reasonable cost. The light output of such a fiber is dependent on a number of variables, but a reasonable amount of light can be expected as can be seen from the following argument; At a density of 1 g/cm^3, a single fiber will absorb approximately 100 keV from the passage of a minimum ionizing charged particle. Typical organic scintillators are capable of converting ~3% of this energy into visible photons. Being conservative, we can expect over 1000 visible photons to be created by the passage of the particle. Of these photons, about 4% are trapped by total internal reflection within a given direction, to be transmitted. The fraction of photons captured by the fiber in a single direction is given by the indices of refraction of the core and cladding material. We are presently working with core made of polystyrene with n_{core}= 1.59 and 15 μm thick acrylic (PPMA) claddings with n_{clad}=1.49 (good claddings with n_{clad} as low as 1.41 are available). The trapping efficiency in one direction is approximately given by:

$$T_{efficency} = \frac{1}{2}(1 - \frac{n_{cladding}}{n_{core}})$$

Conservatively we can expect 30 to 40 photons to be traveling down the fiber in each direction after the passage of a charged particle. Furthermore we can expect the emission of these photons to occur promptly because, in general, scintillators have decay time constants in the range of 10^{-9} to 10^{-8} sec, quite adequate for operation at the SSC.

As is shown in Fig. 4, fibers are flexible and because they operate in an inherently passive manner they can be formed into any shape without penalty. This makes construction of stereo layers particularly simple, especially when compared to other technologies. This also means that the fibers will be forgiving during construction and operation. If a fiber or section of fibers is misplaced, shifted due to structural settling or slightly out of alignment for any reason they will continue to operate. Corrections for such problems would simply be made in the software. Problems of this nature would not become a major mechanical undertaking as may well be the case with wire based technologies.

Visible Light Photon Counter (VLPC)

The most promising readout device for the fiber tracker is the Visible Light Photon Counter or VLPC. This is a device now underdevelopment at Rockwell International and whose operation has been reported in the literature[1,2] since 1987. Our group is presently working with a variant of the VLPC, the SSPM (Solid State PhotoMultiplier) which is already quite capable of handling the SSC environment. A comparison between the presently available device and the VLPC is shown in Table 1. As can be seen, each of these devices has high quantum efficiency (Q.E. > 60%) and high gain (G > $5{\cdot}10^4$). A schematic of the device is shown in Fig. 5. The device structure and appropriate bias conditions make possible the creation of a localized avalanches in a thin, ~4 μm, high electric field region, of electric field strength, E~7kV/cm, in response to the absorption of a photon. Because of the thinness of the device the electron collection occurs on the time scale of a nanosecond. The positive charge on the other hand takes a few microseconds to be collected because of the low electric field strength, E~1keV, in the IRL region. While the long collection time of the positive charge does limit the ultimate rate that the device can handle, the dead region due to a single avalanche is localized and limited to an area with a radius of ~8 μm or ~$2{\cdot}10^{-6}$ cm^2. The device then is capable of very high rates because the photon flux occurs randomly over the entire surface of the device. The main improvement of the VLPC over the SSPM is to thin the (IRL) region of the device from its present ~25μm to about ~6μm. This will reduce the device's

sensitivity to wave lengths above 1μm while simultaneously improving its rate capability and noise.

The only drawback of such devices is that they must operate at 7° K. However with present technology low temperature operation of equipment has become commonplace, with almost all modern detectors using superconducting magnets. As is well known the SSC itself is based on superconducting technology. We see no major problems in this area. The total heat load produced at liquid helium temperatures will be ~50 watts including a safety factor of 5. We expect a heat load of ~10 kwatts at liquid nitrogen temperatures.

Our group is presently operating SSPM devices and is preparing a prototype fiber system comprised of ~100 fibers individually coupled to SSPM channels for a beam test later this year, 1990. A sample output from a single SSPM is shown in Fig. 6.

Radiation Damage

The VLPC - scintillating fiber combination can also form a robust detector from a radiation damage point of view. Fig. 7 shows the amount of attenuation per meter in unirradiated polystyrene as a function of wavelength[3]. The relative effect of radiation exposure as a function of wavelength[3] is shown in Fig. 8. These data show that the transmission of short wavelengths is most effected by the damage while at longer wavelengths there is very little effect even after very large doses. These data suggest that a scintillating fiber that fluoresces near 550 nm should have excellent long term transmission properties even after the high radiation doses expected at the SSC. At this same wavelength then, 550 nm, where the radiation damage is small, the attenuation is a minimum. As a further advantage, the quantum efficiency of the VLPC is expected to be 80% in this same wavelength region (presently we are obtaining 60% quantum efficiency with the SSPMs). This combination of properties means that fibers and the VLPC are already naturally optimized for operation in a high radiation environment like the SSC, being much less sensitive to radiation than a system optimized for bialkali type photocathodes, λ~420 nm.

The radiation dose expected[4] for the fiber central tracker is calculated to be less than 5 megarad, assuming 10 years of operation with the detector, a safety factor of 5 and a luminosity $L=10^{34}$ cm^{-2} sec^{-1}. At the SSC, the luminosity is so large that the main source of radiation is the interaction point. By comparison beam-gas collisions and expected particle loss contributions are small. The SSC is unlike presently operating hadron colliders, because it will have luminosities thousands of time larger.

SCINTILLATORS

To satisfy simultaneously the demands of high photon yield, the need for yellow-green fluorescence (550 nm), minimal self absorption within the fiber and good radiation resistance, requires the development of new scintillation materials. Several candidate materials are under study including single-dye and multi-dye polystyrene scintillators. Of the former type are scintillators containing large Stokes' Shift dyes such as 3HF; of the latter type are several combinations including primaries such as MOPOM and pTerphenyl and secondaries such as K27 and BBQ. Several of these scintillators have fluorescence efficiency comparable to NE110, but have long wavelength emission (>500nm) and the prospects for low self absorption and excellent radiation resistance properties. Our group has a major developmental effort underway is this area.

Tracker for the SSC

All of the properties of the fibers and readout that we have discussed readily lend themselves to the construction of a scintillating fiber tracker for the SSC. The fibers would be formed into superlayers as is shown in Fig. 9. The radial width of a superlayer is 4 to 5 cm. We are investigating the best manner in which to stack the component fiber layers for optimal efficiency and tracking resolution. A simple solution of just staggering fiber layers yields $\sigma_0 = 80\mu m$. In almost all designs the fibers are first drawn to a precision of 1% in the diameter. The fibers are then accurately formed into ribbons allowing a small space, ~1%, between fibers, in order to take into account the diameter variations from fiber to fiber. These precision ribbons are then placed onto a carbon-fiber epoxy structure to form a superlayer. The superlayers are then placed within the central tracking volume as shown in Fig. 10. This arrangement is based on the following pattern recognition strategy, based on forming track vector segments. The angular resolution of a track recorded in the axial fiber layer in one half of a superlayer is just sufficient to be pointed across the 4 to 5 cm gap and into the other axial layer, within that superlayer. This selects the appropriate hits with that single superlayer. The separation of superlayers is such that the vectors formed by combining the information from the two axial layers with a single superlayer,

point selectively to a small region within the next superlayer to locate matching vectors in this superlayer for a multilayer pattern analysis. We are undertaking simulations to check that 4 superlayers is enough to achieve high efficiency tracking at the SSC for luminosity as high as 10^{34}. Our present design contains a total of $1{\cdot}8.10^6$ scintillating fibers in the central tracking region. Even at the highest SSC luminosity we expect an occupancy rate of less than 10%, including the effect of loopers from previous beam crossings. For the candidate tracking system, Fig. 11 shows the momentum resolution as a function of fiber diameter. For a system of 500 μm diameter fibers, $\delta p/p \sim 23\% p(TeV)$ is obtainable if the location of the vertex is known. This value includes fiber to fiber inaccuracies as large as 25μm and a system efficiency of 90%.

References

1. M.D. Petroff and M.G.Stapelbroek ;IEEE Trans. on Nucl.Sci.,Vol.36,No.1,Feb.1989,158.

2. M.D.Petroff and M.Atac ;IEEE Trans. on Nucl. Sci.,Vol.36,No.1, (Feb. 1989)163.

3. A. Bross, Proceedings of the Workshop on Scintillating Fiber Detector Development for the SSC, 1988, Fermilab.

4. D.E. Groom, Snowmass 1988,World Scientific, Editor S. Jensen page 711.

	VLPC IMPROVED	SSPM PRESENT VERSION
GAIN	$5{\cdot}10^4$	$5{\cdot}10^4$
SINGLE PHOTON SENSITIVITY	0.4 μm to 1 μm	0.4 μm to 28 μm
Quantum Efficiency	80%	60%
Rate Capability 500μm x 500μm Device	10^7 photo-electrons per second	$3{\cdot}10^6$ photo-electrons per second
Magnetic Field	No Effect	No Effect
Total thickness of Active Device	~10 μm	~30 μm
Temperature of Operation	7^0 K	7^0 K
Radiation Environment	No Effect due to Thinness of Device	No Effect due to Thinness of Device
Estimated Cost In Large Quantities	$2-3	Not Available Commercially

Table 1

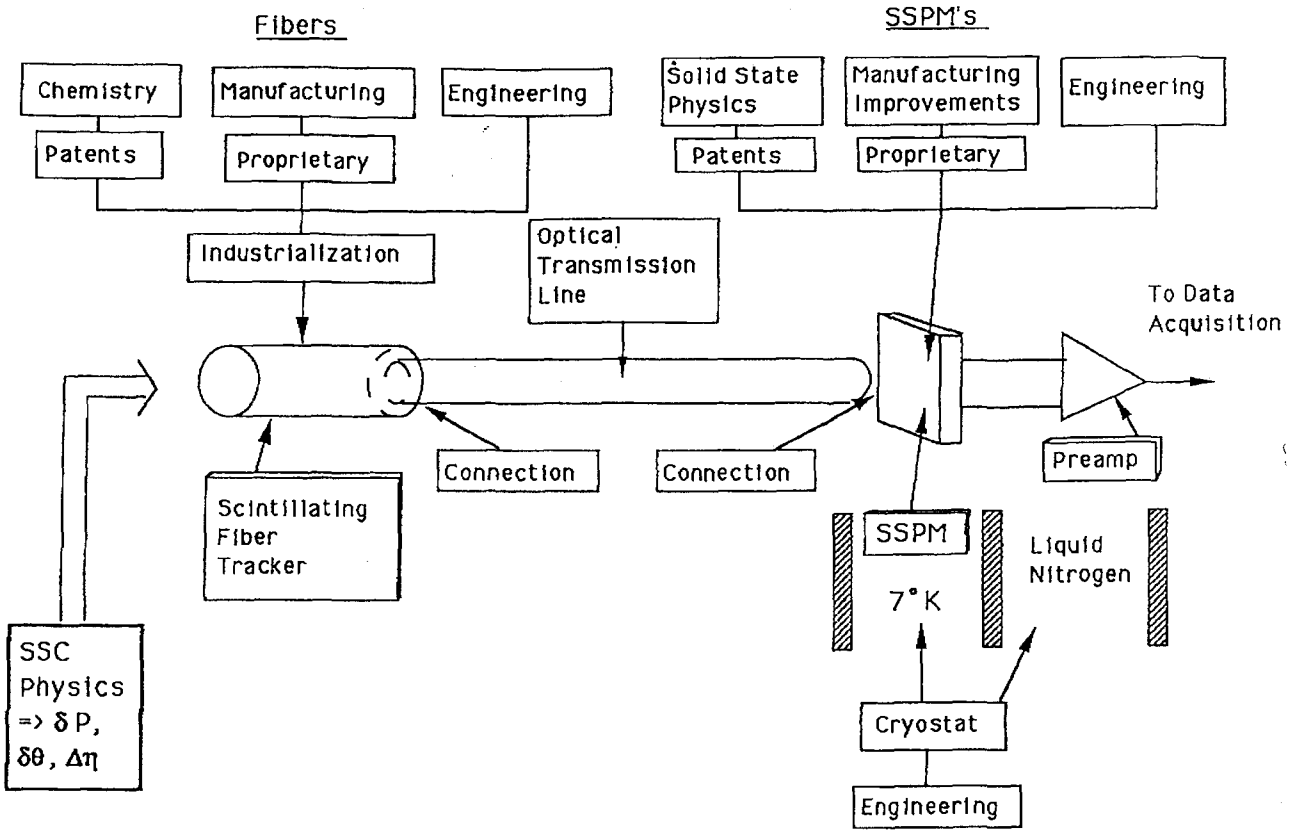

Figure 2

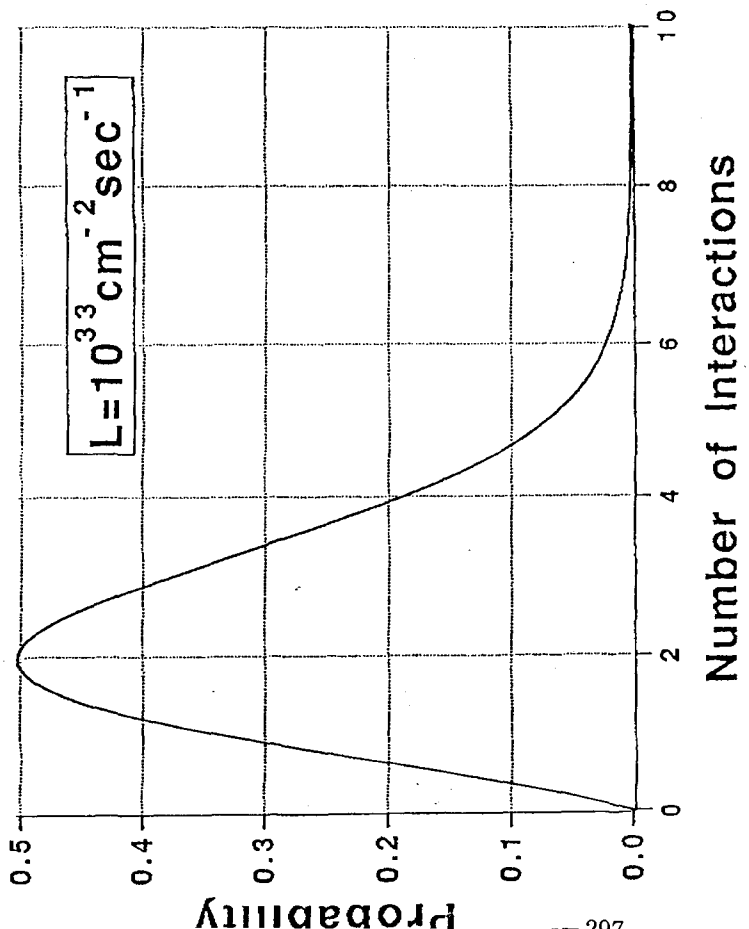

Figure 1. The estimated cross section for p-p collisions is 100mb at 40 TeV yielding the above poisson distribution for the number of interaction per crossing.

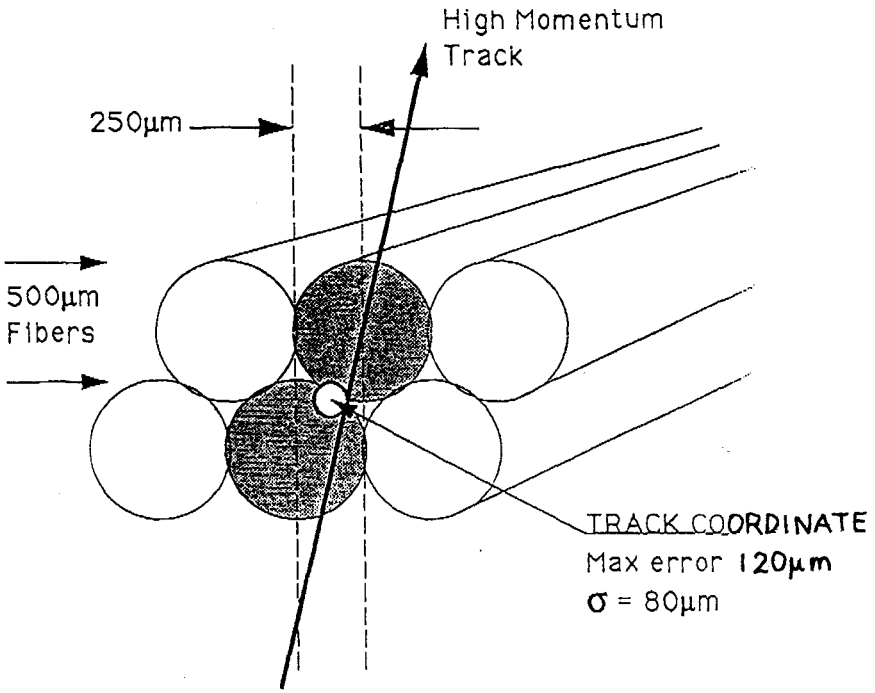

Figure 3. Schematically shown the resolution obtainable using 500μm Fibers. By staggering the fiber layers a passing track can be localized to a strip only 250 μm wide. By taking the coordinate at the center of the strip the maximum error reduces to 125 μm. The yields a measuring resolution of 80 μm.

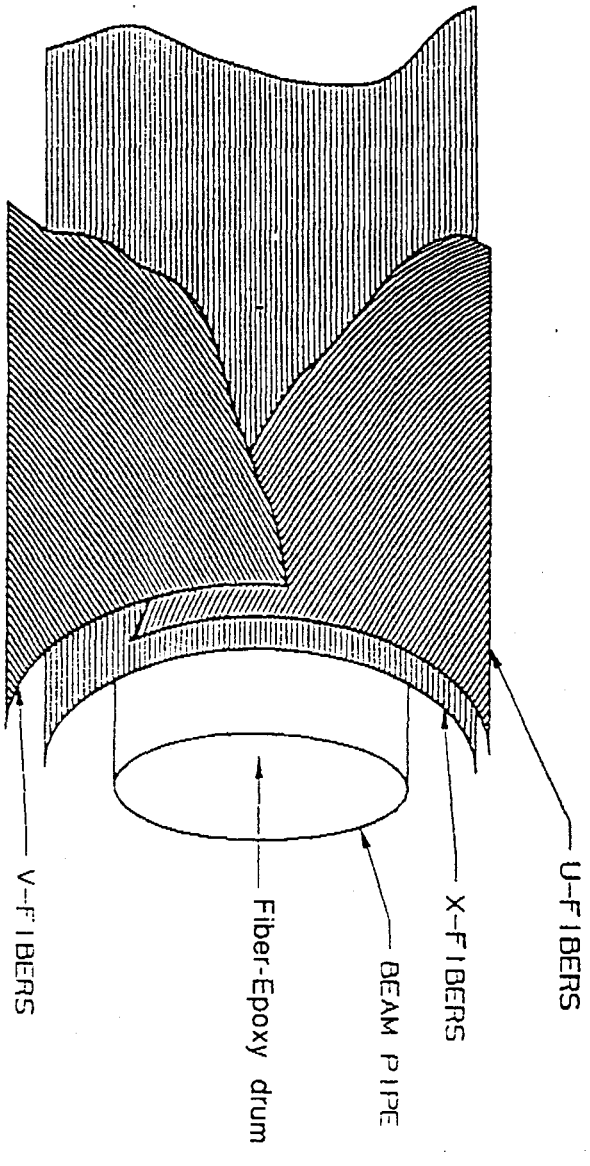

Figure 4. Schematic showing the ease of constructing the scintillating Fiber tracker.

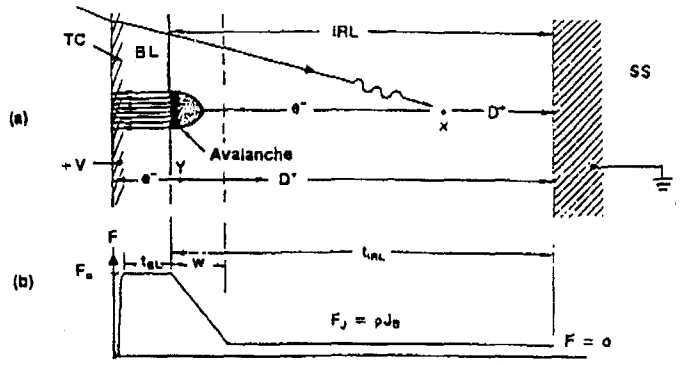

Figure 5

a) SSPM layer configuration with schematic representation of the gerneration of bias current and the effects following the absorption of a photon. b)Electric field profile.

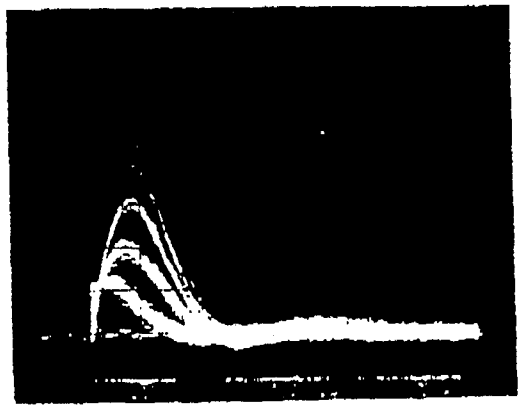

Figure 6. SSPM output signal showing the detection of 1,2,3 and 4 photon-electrons.

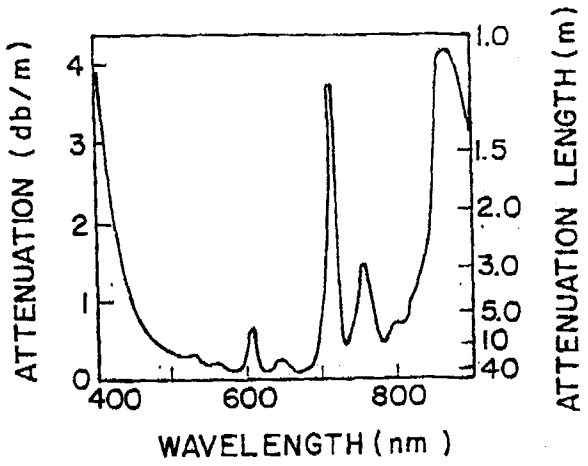

Figure 7. Optical transmission in polystyrene as a function of wavelenght.

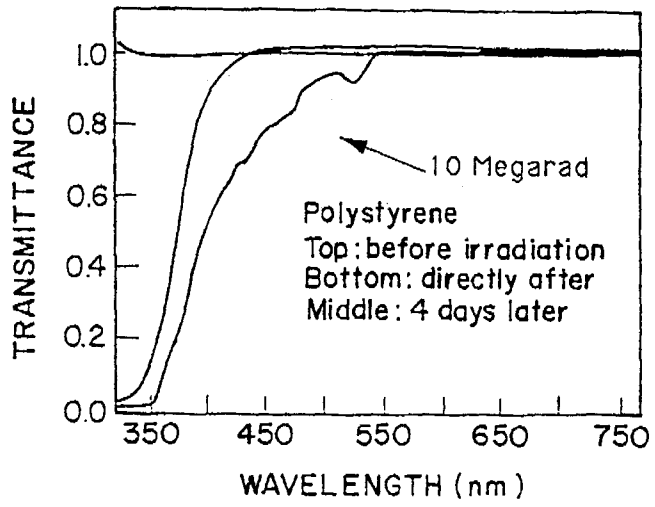

Figure 8. Optical transmission in polystyrene as a function of *radiation* dose using a cobalt 60 gamma source.

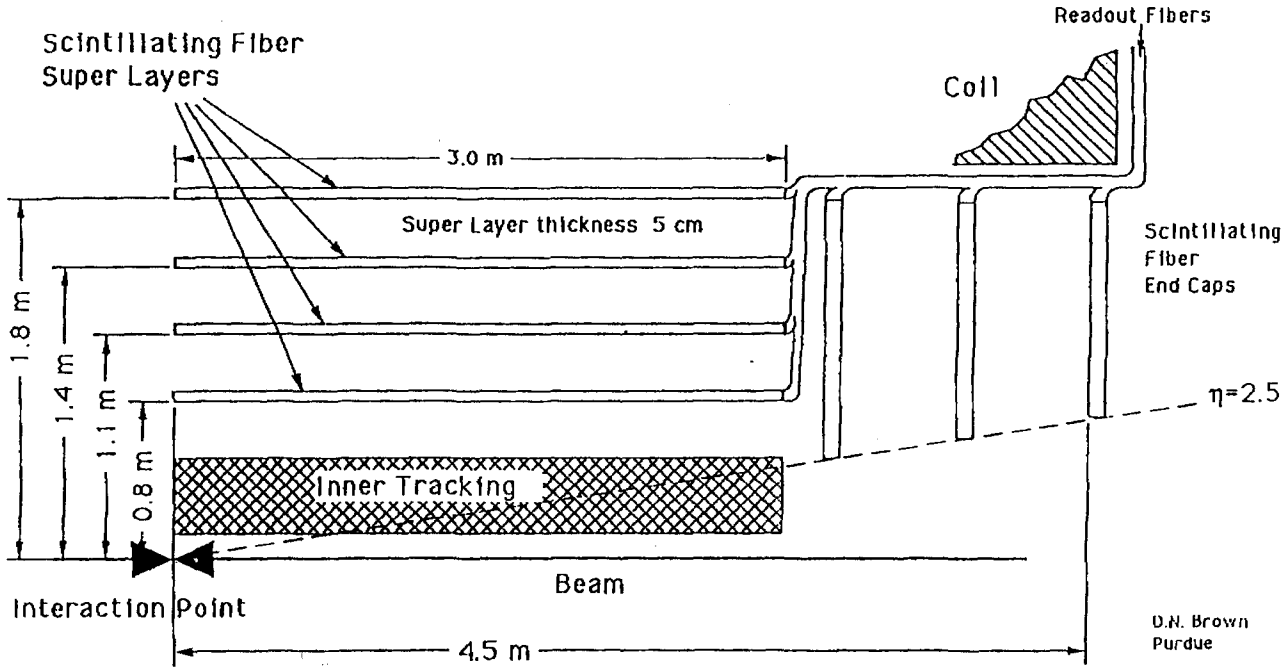

Figure 10. Cross sectional view of the scintillating Fiber tracking system. The break in the tracker at the interaction point is done so that the Fibers responds to only one beam crossing.

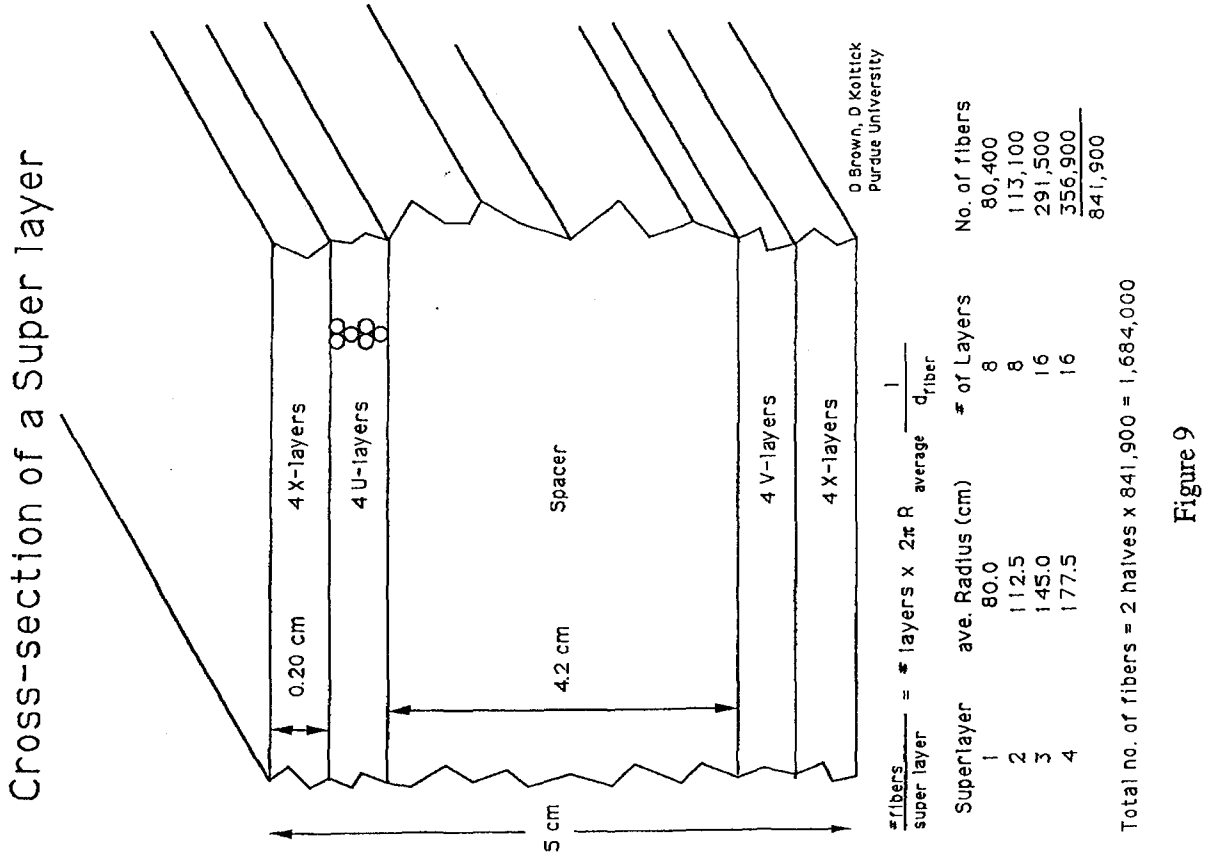

Figure 9

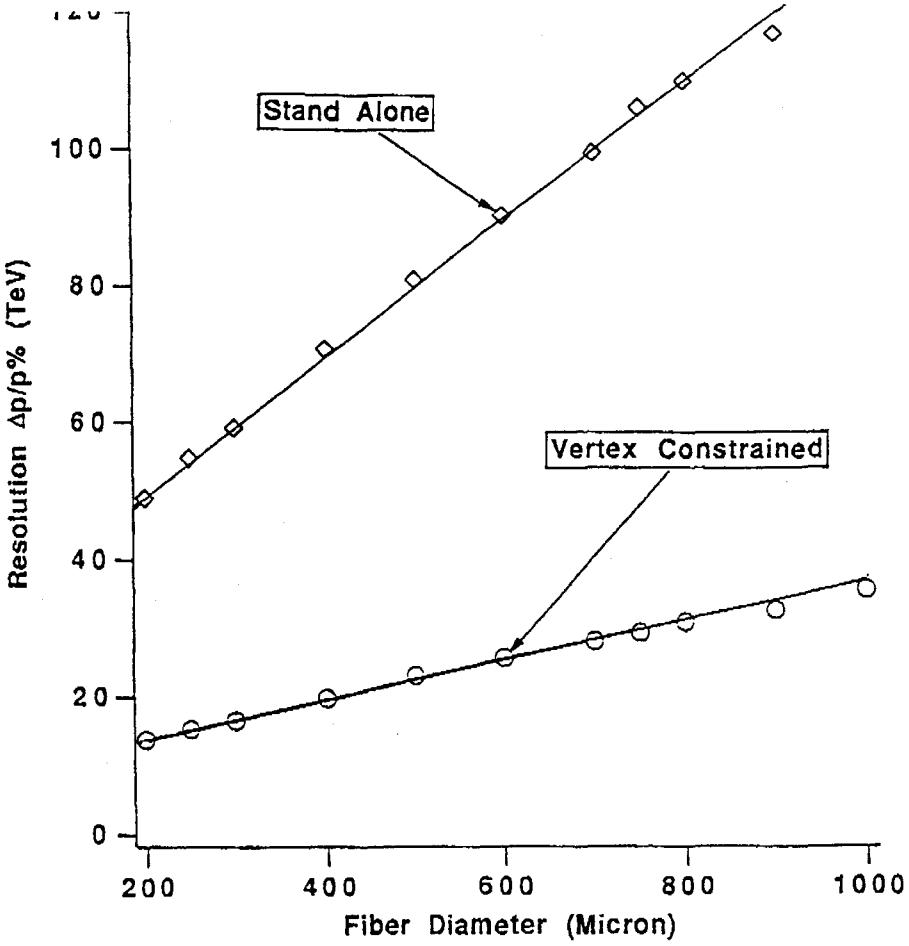

Figure 11. Momentum resolution for high momentum tracks as a function of fiber diameter for the tracking system discussed. An error of 25mm in fiber to fiber place is assumed for construction and the fiber efficiency is assumed to be 90%.

May 29, 1990
IUHEP-90-9

Progress Report on 4 mm Straw Chambers

Harold Ogren
Indiana University
Bloomington , IN 47405

Introduction

Cylindrical drift chambers made with wound mylar cathodes (Straw Chambers) were developed almost a decade ago. I am going to report on recent developments i in the design of these chambers for an SSC detector. This work was carried out at Indiana University under an SSC R&D grant and as part of the Central and Forward Tracking with Wire Chambers Subsystem group [1]

The central tracking system for SDC

The central wire tracking chamber for the SDC will consist of 8 superlayers. Each superlayer consists of two cylindrical sections 3 meters in length. Each superlayer contains 8 layers of straws. The inner radius is 0.7 meters, the outer is 1.8 meters. One quarter of the tracking system is shown in Fig. 1.

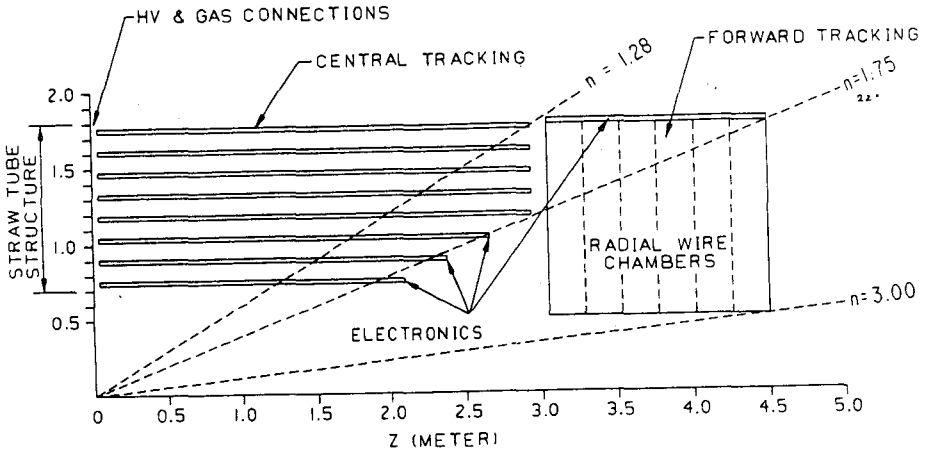

Fig. 1. Possible layout of SDC central wire tracking system

In Fig. 2 we see the end view of the central wire tracking chamber and the the eight super layers. The superlayers are constructed from a ring of identical modules, holding up to 256 straws. Four of the superlayers are stereo and four are axial. The stereo layers are formed by orienting a module of straws at a 3 degree angle. (The modules (and straws) are kept straight).
The total number of module will be about 544*2.
Since straws type detectors have been used in a number of experiments in the past ten years, the primary task is to define the mechanical specification for the superlayers, modules, and straws, and to integrate the system with the silicon tracker.

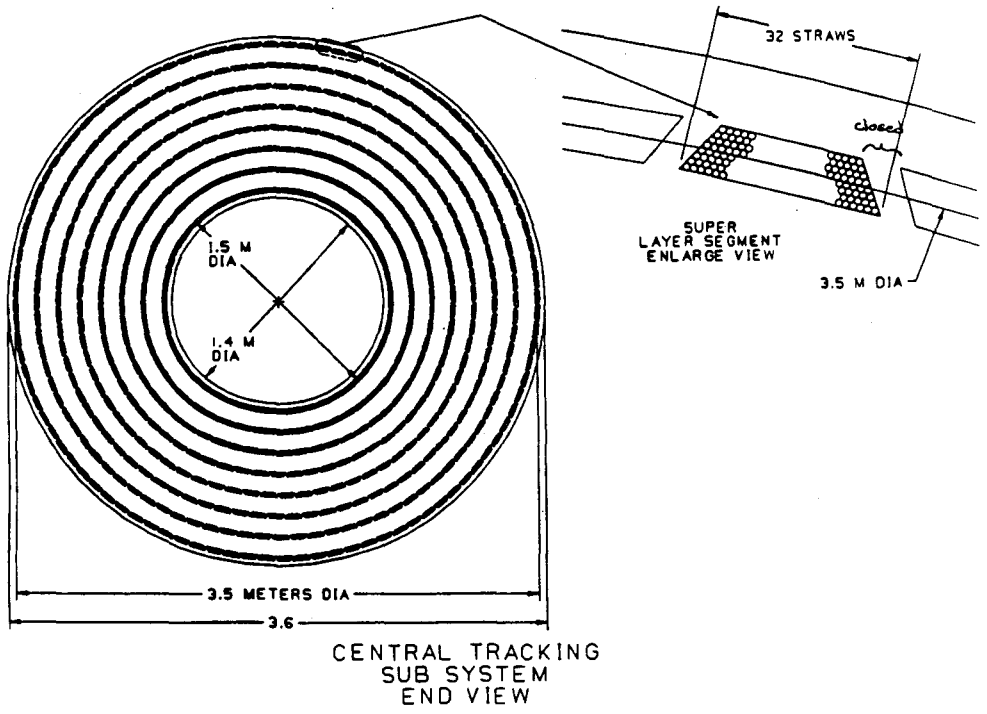

Fig. 2. End View of central wire tracker with detail of a module

The SSC Environment

The hit rate, current draw, occupancy, and charge/unit length were calculated using the rates predicted by D. Groom at a nominal luminosity of 10^{33} cm $^{-2}$ sec $^{-1}$. They are shown in Fig. 3 a,b and Fig. 4 a,b. The effects of the magnetic field (loopers) will increase these predictions at intermediate radii and decease them for the larger radii, however these the general dependance and are a valuable guide for chamber construction. The current draw for each straw may be the limiting feature for the operation at SSC. It s principally for this reason that the straws are split into two sections axially.

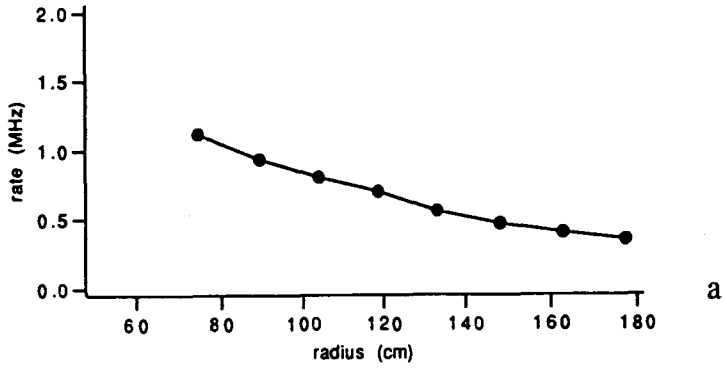

a

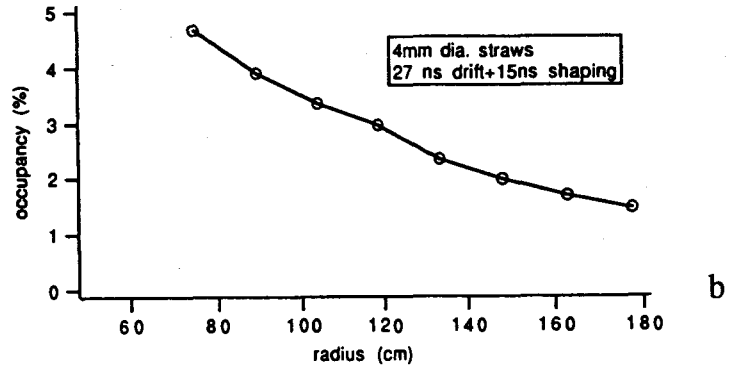

b

Fig. 3. a)The hit rate per wire and b) occupancy versus superlayer radius

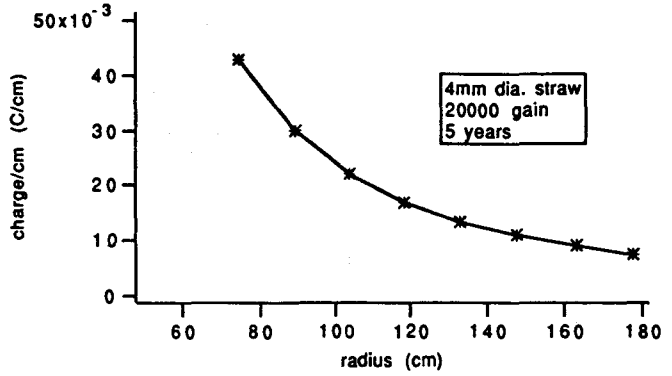

a

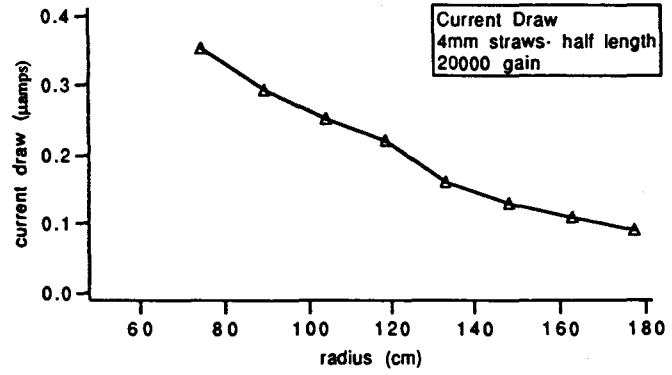

b

Fig. 4. a) The charge per centimeter and b) current draw versus radius

Modular Design Aspects
We are interested in the design of modular systems for the SSC. We believe that there are several compelling reasons for this:

1) Alignment
- The module's cross section stability aligns the straws internally
- The support structure maintains the modules in position.

2) Compressional Loading
- The compressional loading due to the wire tension (12 Kg for 256 wires) is taken up entirely by the external module.
- Since the module takes up the compression, the end support structure can be very light.

3) Mass Production
- The 240,000 channels of drift tubes is much larger number of wires than past detectors. With a modular approach the 1088 identical modules can be built by industry.
- Endplate design is simplified, HV, gas, electronics card are all identical.

4) Testing
- Each module can be tested, calibrated, and measure before assembly.
- HV and gas tests can be completed before assembly.
- The completed electronics and trigger can be tested before assembly.

5) Repair
- Modules can be repaired both before and after assembly.
- Modules can be replaced during major shutdown periods.

Module construction

As part of our SSC Tracking Subsystem development, we are planning on constructing several smaller modules this summer. The purpose of these smaller test modules is to determine the multi-straw alignment, to workout an endplate design, to begin to understand construction techniques with carbon fiber composites, and to investigate integration of the electronics in the modular design. The first modules will be about 1 meter in length. Fig. 5 shows a endview of a 64 straw prototype chamber.

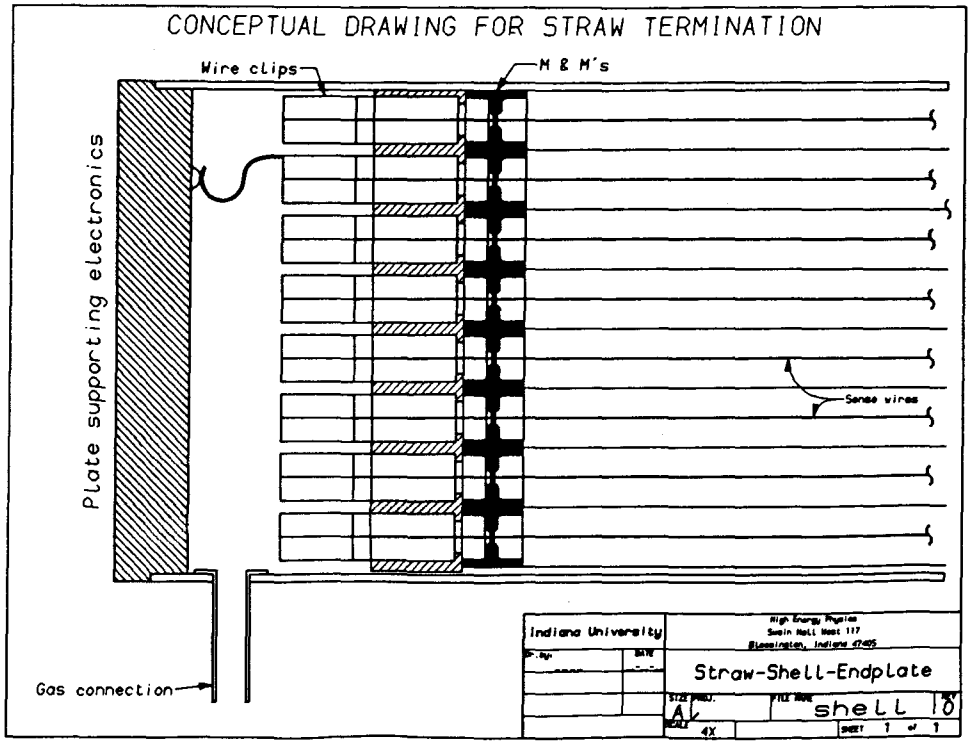

Fig. 5. Side view of a possible small straw test module

We are trying to workout a minimal mass design for the modules . One possibility is to slightly compress the wire supports with the outer shell in order to set the straw spacings. In this case the endplate provides the wire tension, but does not have to position the wire accurately. We have several preliminary designs that utilize this idea. The sideview, showing the end cap and wire attachment pin are shown in Fig. 6. Details of the endplate and the wire connection pin are shown in Fig. 7, and Fig. 8.

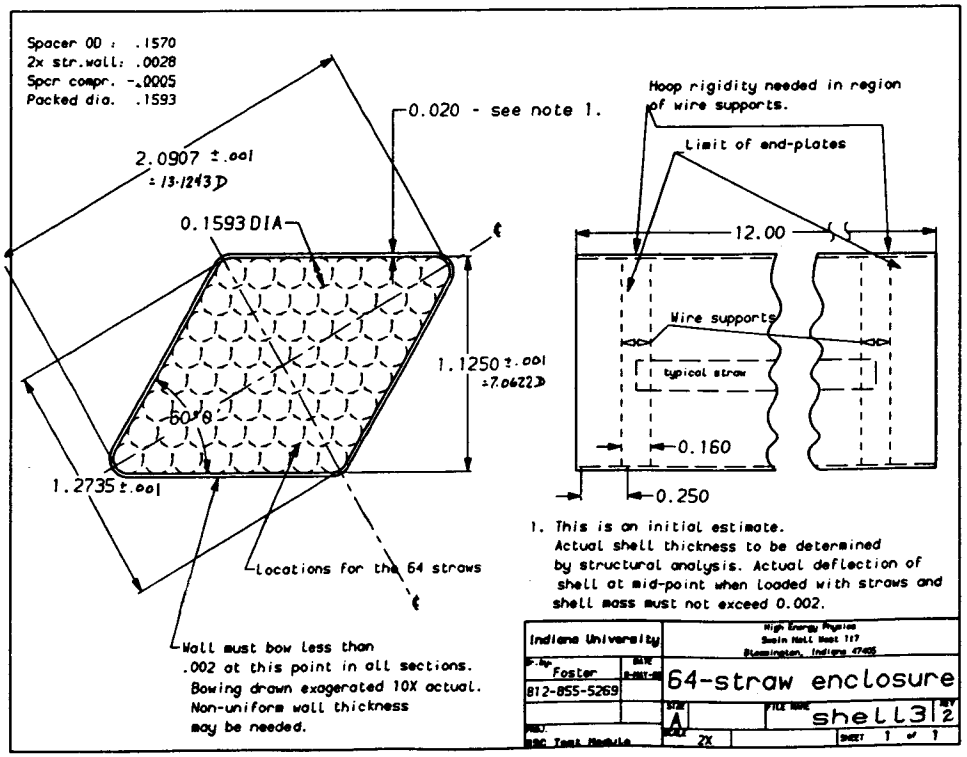

Fig. 6. End view of a possible 64 straw test module

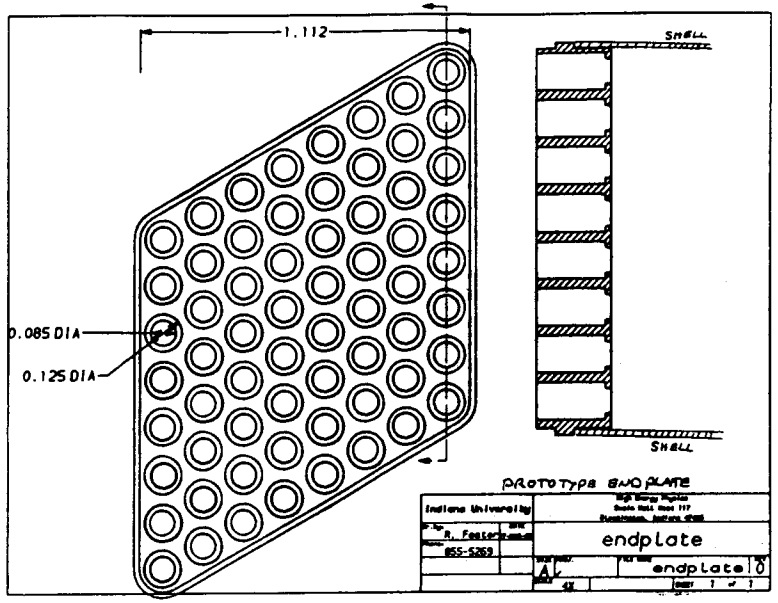

Fig. 7. End view of an endplate for a 64 straw module

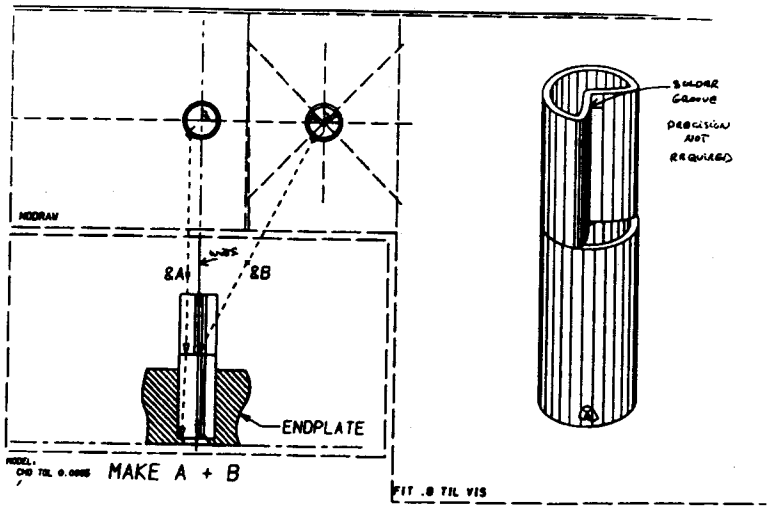

Fig. 8. A possible wire fastener for the 64 straw endplate

Basic straw cell, design

The straws we are presently using are 2 meters long.[2] Construction of 3 meter straws is not thought to be a problem. The general method is shown in Fig. 9. Two thin films are wound on a precision mandrel. The straws we are using are made with an aluminized (1000A) polycarbonate layer and an outer wrap of mylar. Both films are 12 microns thick.

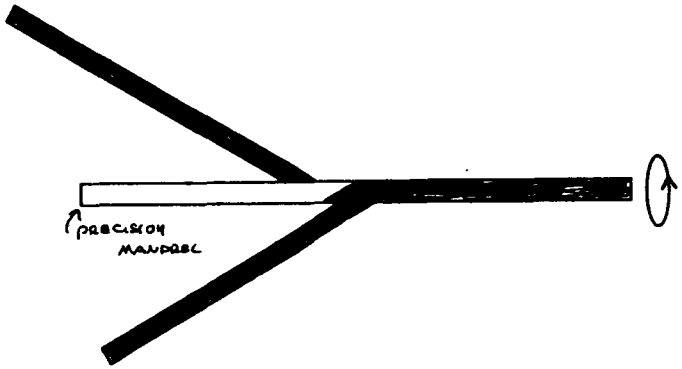

Fig. 9. Schematic of straw construction

Some of the R&D areas we are working on are fabrication of thinner straws, investigating other materials such as Kapton, and increasing the metallic coating to reduce the cathode resistance.

Electrostatic stability

One of the original uncertainties for straw construction was electrostatic stability. This is now well understood.[3] We, and others, have calculated the wire displacement as a function of offset as shown in the figure. Our conclusion is that for 4 mm diameter straws with 25 micron wire and 50 micron construction and alignment accuracy, we will need wire supports about every 80 cm at 2000 volts. The stability plot is shown in Fig. 10. This shows the electrostatic deflection amplitude as a function of the centering offset and the applied voltage.

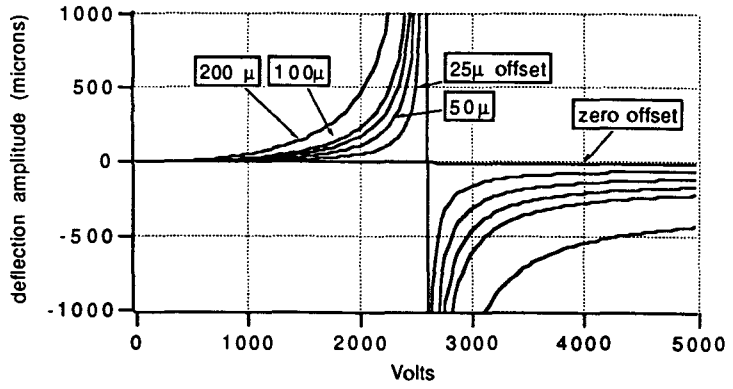

Fig. 10. The wire deflection amplitude versus voltage for several offsets

Requirements for the wire support

The design criteria for the wire supports are:

- •Center the sense wire within 25 microns
- •Allow free gas flow, restrict no more than 50%
- •Insulate the HV at 2 to 2.5 KV
- •Minimize multiple scattering
- •Minimize detector dead space
- •Allow rapid, low cost, and automated construction
- •Have long term dimension stability, radiation resistant
- •Allow accurate positioning along the wire

Several designs are shown in the next figures. Fig. 11 shows the "M&M" design which has been manufactured by Sabin Co., Bloomington, In. The unique feature of this design is that the wire is melted into position with small precision fixture shown in the same figure. A short pulse of current into a 1 inch section of the wire heats it sufficiently to melt the Delrin and allow the tensioned wire to move to the center. This support has been used in a 3.5 meter straw cell. Two other support designs are shown in Fig. 12 and 13. The " double V" design is being presently

manufactured for use in the prototype modules we are building this summer. It has the advantage over the "M&M" of allowing restringing.

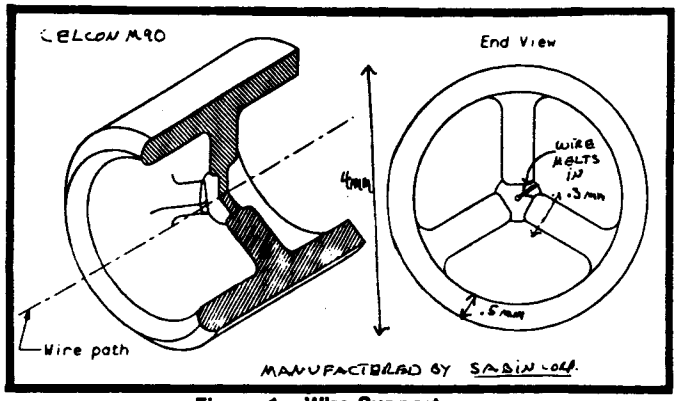

Figure 1 Wire Support

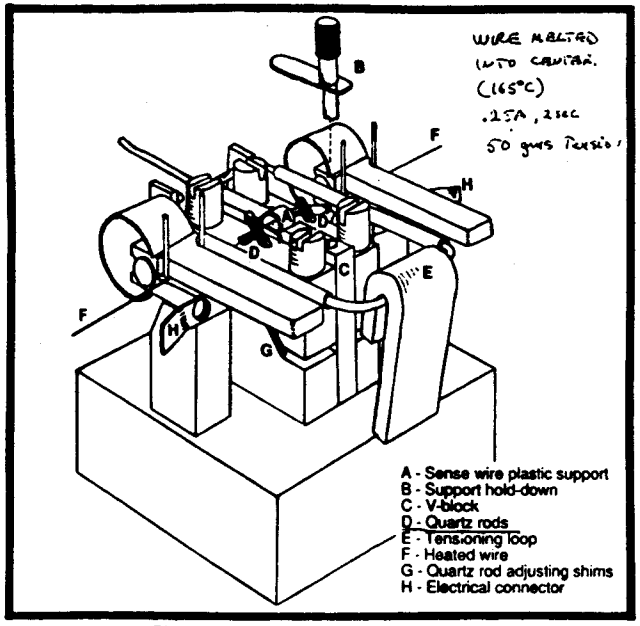

Fig. 11. Two views of an "M&M" wire spacer and the alignment jig for melting wire in.

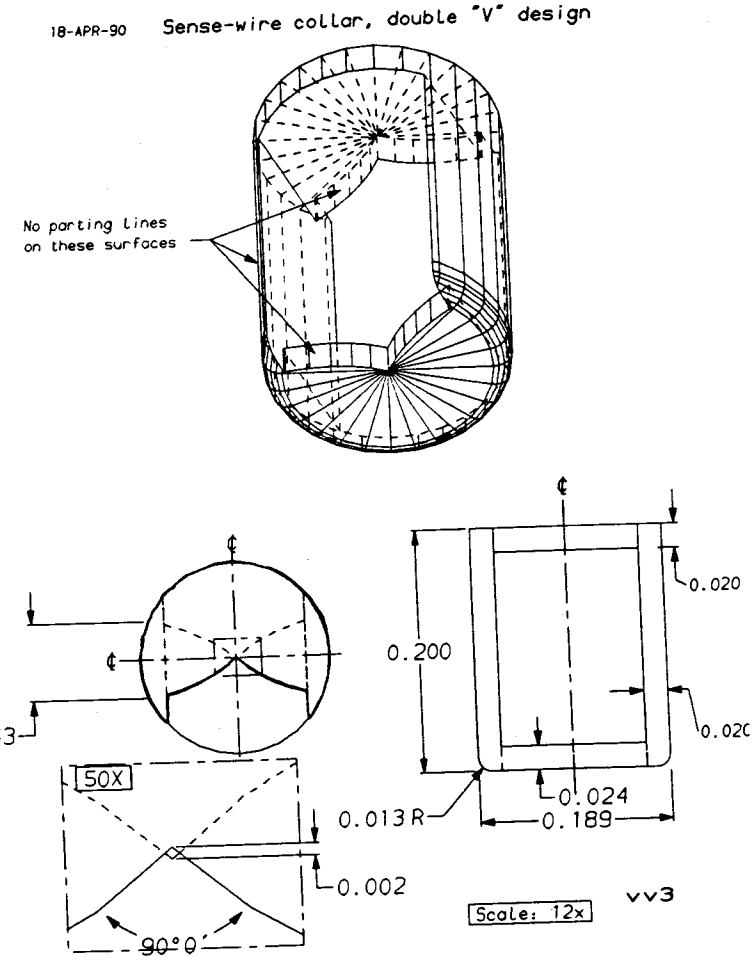

Fig. 12. A possible wire support of the "double V" variety

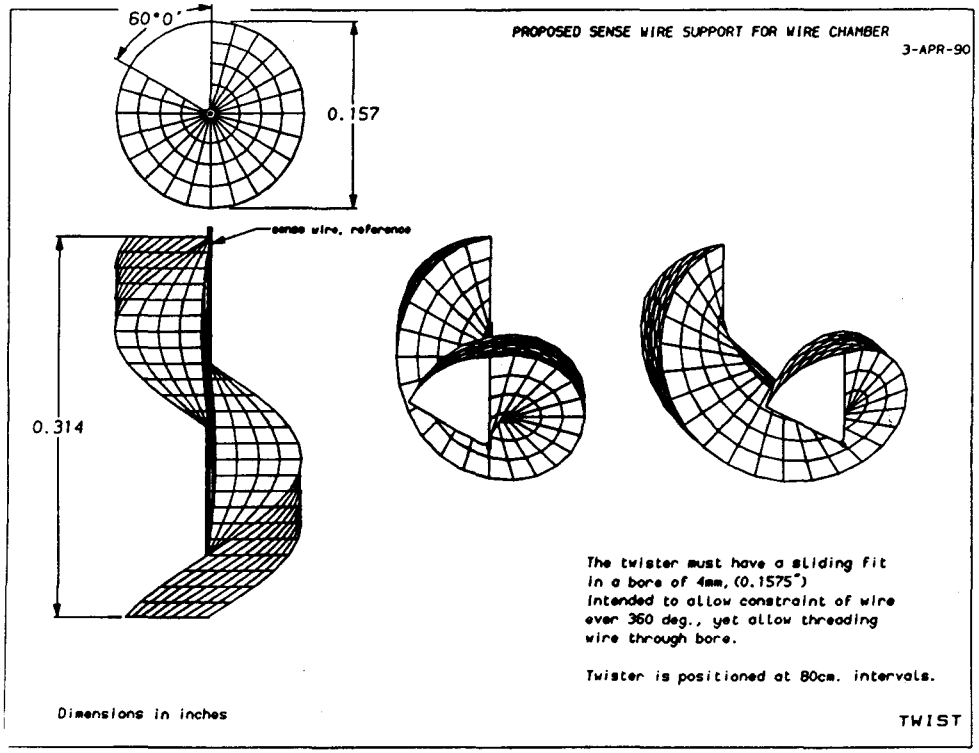

Fig. 13. A possible wire support of the "twister" variety

Drift Chamber tests

A number of studies have been done on drift chamber gases. These have been reported[4] previously , so I will mention only a few of the results to show that we have an example of a gas that will work at the SSC. The speeds of various gasses are shown in Fig. 14 a,b,c,d. The fastest gas we have studied is CF_4. with 20% isobutane, shown in 14 d. The drift time with no magnetic field is 19 ns for 2 mm drift.

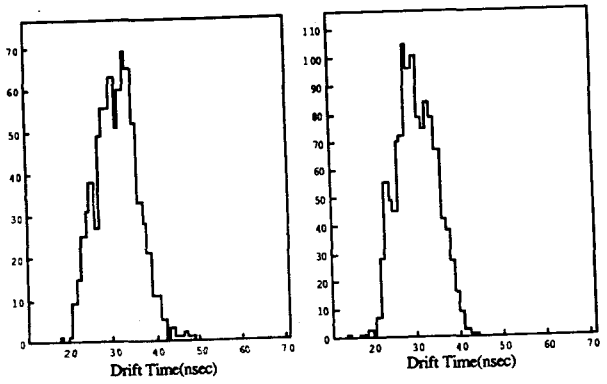

Fig. 14 . a) TDC distribution for Ar-Ethane(50%) b) TDC distribution for HRS gas

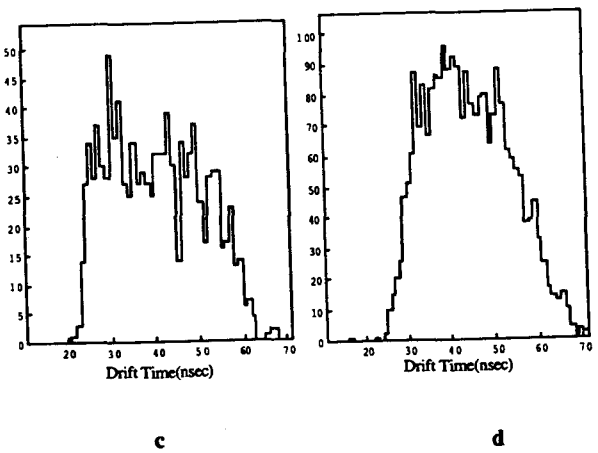

Fig.14. c) TDC distribution for CF_4 d) TDC distribution for CF_4 -Isobutane(20%)

The resolution of this gas, for various isobutane concentrations is shown in Fig. 15
This gas gives us a resolution of about 100 microns and full efficiency at about 2000 Volts. Other gases are still under study.

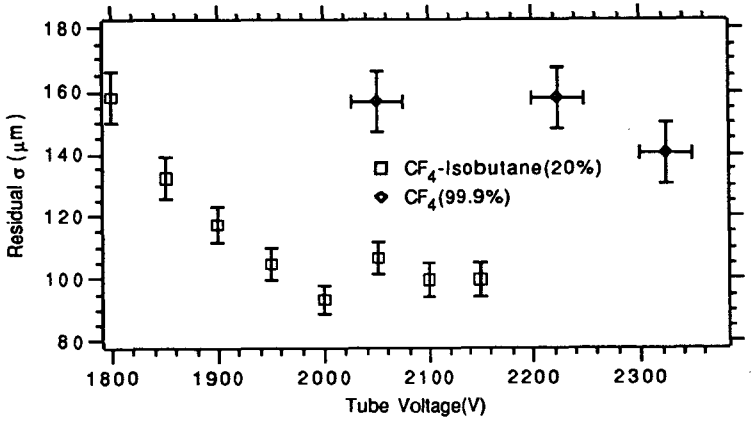

Fig. 15. Wire resolution for CF4 gas mixtures

We have also measure the efficiency of these gas mixtures as a function of voltage. These measurements, shown in Fig. 16, will depend rather importantly on the noise immunity of the electronics and the resulting threshold level, so they should only be taken as an indication of the signal size for this particular gas.

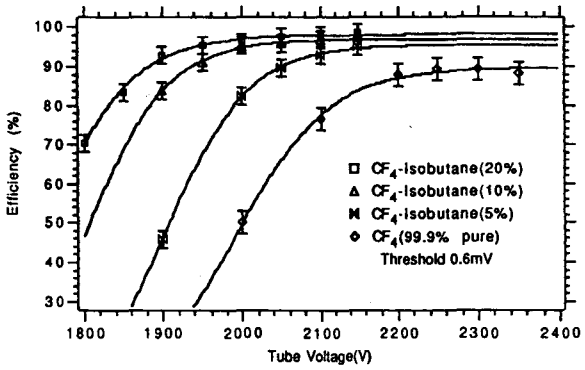

Fig. 16. Cosmic ray efficiencies for CF_4 mixtures

Long straw tests at Indiana University
In addition to the basic chamber operation studies that I reported above, we have begun a program for directly measuring the properties of long straw systems- chambers as long as those required for SSC. The goals of this program are:

- Establish construction techniques
- study signal attenuation
- Study termination
- Verify short straw performance
- verify support-stability calculations

As part of this program we have constructed a 2 meter, six straw array and completed a 3.5 meter, six straw array. The six straws are held in a precision machined V groove 3.6 meters in length. The basic test system for cosmic rays in shown in Fig. 17.

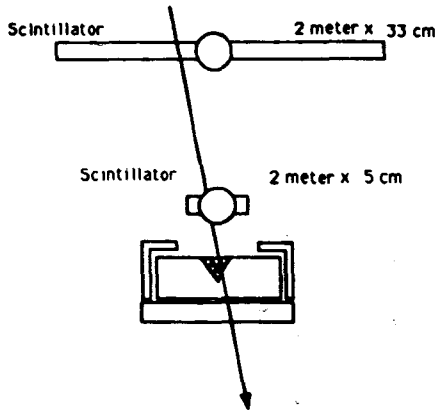

Fig. 17. Layout for 6 straw chamber cosmic ray tests

In the case of the 3.5 meter straw array, two straws were spliced together to give the full length. Wire spacers of the "M&M" design were positioned every 60 cm. Our initial tests satisfy us that the system is electostatically stable and that the performance is very similar to the short straw system. In Fig. 18 we show the measure pulse height from a Fe^{55} source for a 3.5 meter straw tube operating at 2300 V. Both the direct and the reflected pulse can be seen. The pulse is extremely short.

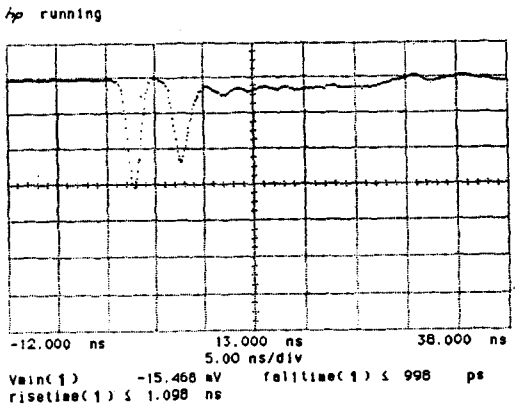

Fig. 18. Direct signal from Fe^{55} source with reflection pulse

The far end of the straw was satisfactorily terminated with 223 ohms through 34 Pf. This is consistent with the calculated value of 310 ohms for the impedance of the straw transmission line. The terminated pulse is shown in Fig. 19.

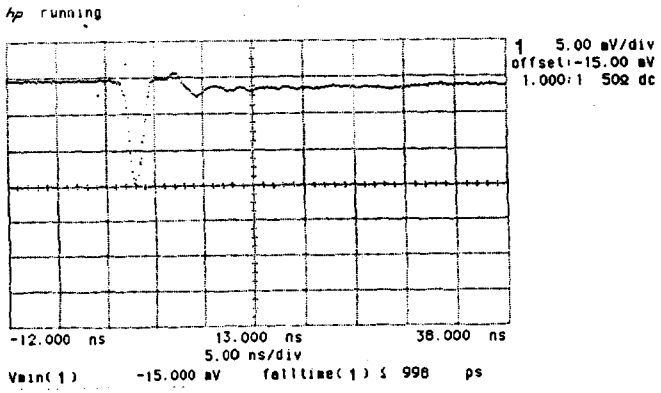

Fig. 19. Signal after termination at far end.

Using the terminated pulse we were able to measure the attenuation of the Fe^{55} signal in the straw chamber. This is shown in Fig. 20. We find an attenuation length of somewhat over 4 meters. This would be satisfactory for the 3 meter length chambers foreseen at SSC, but is somewhat shorter than a simple calculation would predict. We are investigating the effects of the splice resistance and the total cathode resistance.

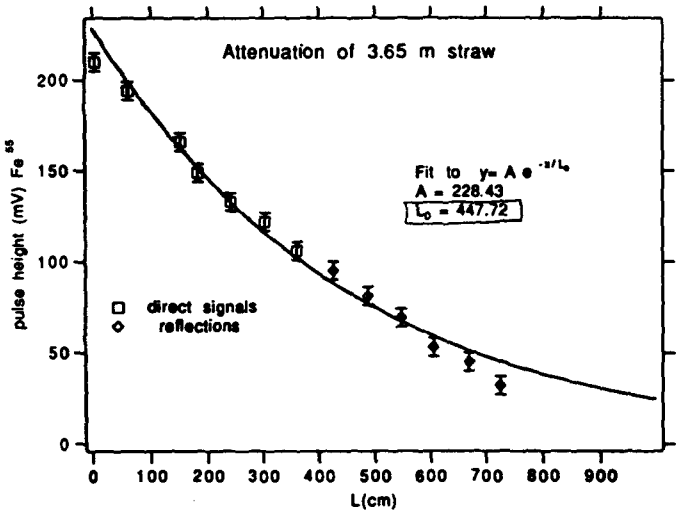

Fig. 20. A measure of the signal attenuation in a 3.5 meter straw

We were also able to make a series of measurements on the 2 meter six straw system using the University of Pennsylvania electronics. The signal from a cosmic ray in the 2 meter straw. is shown in Fig. 21. The signal shown is the output of the University of Pennsylvania preamplifier with tail cancelation circuitry . Note the very short recovery time of the signal to the base line.

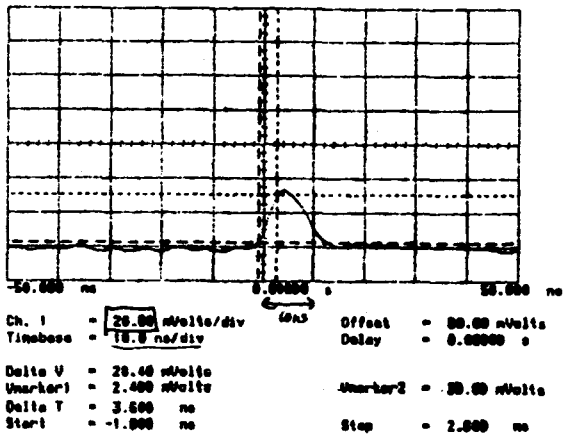

Fig. 21. A "typical" cosmic ray signal after amplification and tail cancelation

Signal Calculations

We have calculated the signal characteristics of the 4 mm straws based on the work done by Iwasaki.[5] We note that there is an impressive gain in signal size going to a fast gas at higher voltage. Figure 22 shows the calculated signal from a 3 meter straw for both 7 mm and 4 mm diameters. The 4 mm straw gives almost twice the signal, and has a much faster rise time. We feel that both jitter and walk errors will be tolerable in 4 mm straws. of 3 meter length.

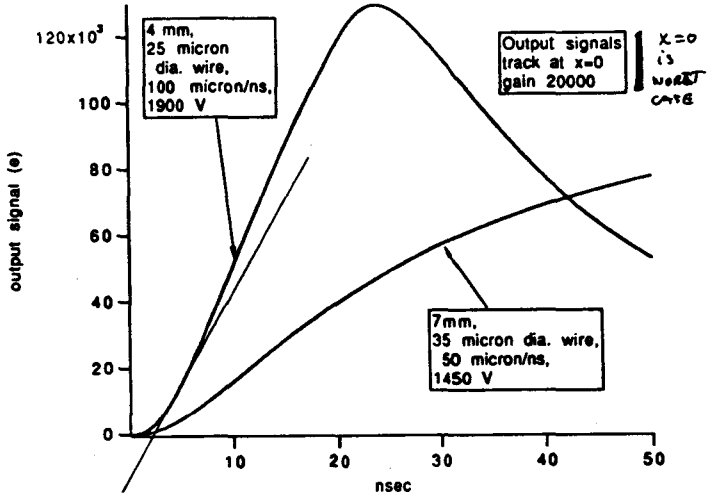

Fig.22. A calculation of the signal size from two different gases and straw diameters

Summary

Large scale mechanical design of a modular straw system is underway by Westinghouse. This design will include the integration with Si system , the module support , and a study of the alignment and stability of the system.

The modular approach to constructing a tracking system will be studied this summer with the construction of several 64 straw modules. These will be available for testing by collaboration. Tests might include :

- •electronics evaluation
- •High rate beam studies
- • Trigger electronics
- • Gas flow and heating studies
- • Radiation testing
- • precision track linking and resolution

We would like to stress that basic R&D still very useful by any group. We would like to help you get started if you are interested. Some areas of useful activity might be:

- •Straw tube materials
- •wire studies
- •spacer designs
- •fast gases- response in B fields
- •endplate design- signal coupling
- •termination- capacitors

References

1. Central and Forward Tracking with wire chambers, SSC Detector subsystem,
   Indiana University
      D. Blockus, R. Crittenden, A. Dzierba, R. Foster,G. Hanson, C. Neyman, H. Ogren, D. Rust
   University of Colorado
      G. Baranko, H. Cheung, J. Carr, J. Cumalat, E. Erdos, W.T. Ford, J. Ginkel, U. Nauenberg, P. Rankin, G. Schultz, J. G. Smith
   University of Pennsylvania
      F. Newcomer, R. Van Berg, H.H. Williams
   KEK National Laboratory
      Y. Arai
   Lawrence Berkeley Laboratory
      A. Palounek
   University of Michigan
      J. Chapman
   University of California, Davis
      R. Breedon, W. Ko, R. Lander, K. Maeshima, J. Smith
   Rutherford Appleton Laboratory
      J.C. Hart, N. McCubbin, D. Saxon, P. Sharp
   University of Liverpool
      P. Booth, J. Dainton, E. Gabathuler
   Westinghouse Science and Technology Center
      D.Hackworth, J. Hendrickson, J. Barkel, R. Svendrud
   Oak Ridge National Laboratory
      T. Shannon

2) The 4 mm straws we used were made by Precision Paper Tubes, Wheeling Ill.

3) Wire Stability tests on 4 mm straw chambers, H. Ogren, et. al., IUHEE 90-2

4) Gas Studies on 4 mm diameter straw drift chambers, C. Neyman, IUHEE 90-1

5) A study of Time resolution for a Straw Chamber, H. Iwasaki KEK 89-158

A Large Scale Knife-Edge Chamber

Akihiro Maki
KEK

There has been enormous efforts to develop various kinds of new detectors which were intended to be used in the experiments at the Superconducting Super Collider (SSC). However, still more efforts are required in some subsystems. In my personal view, we do not yet have any promising solution for the tracking detector in the SSC experiments, specially in the high luminosity option of $10^{34}/\mathrm{sec}/\mathrm{cm}^2$. In that sense, still more R&D efforts with new idea should be encouraged.

To date three different tracking detectors, Straw Tube Chamber, Silicon Strip Detector and Scintillation Fiber Detector, and their combinations have been proposed for the SSC experiments. However all of them have their own problems as the tracking detectors in the very high luminosity experiment at the SSC. Silicon strip detectors are practically considered to be used only in small radius around the beam pipe. Most questionable issue is the radiation hardness of this detector, while it has excellent spatial resolution and low occupancy. Also this detector is not the best in its response speed.

Straw tube chamber would have problems in its radiation hardness, occupancy and chamber construction with 2 to 3 meters long wire. The spatial resolution is not superior to other detectors. This, together with the radiation problem, requires that this chamber must locate further away from the beam line, equivalently requires long chambers.

Scintillation fiber detector is excellent in its speed, spatial resolution and low occupancy. However the fatal problem is the readout devices which have not developed yet. Question on its radiation hardness has not yet been totally solved.

As one of the solution to this challenge, a knife-edge chamber was proposed by Texas A&M group [1]. The knife-edge chamber is essentially a multi-wire proportional chamber (MWPC) which has been used in high energy physics experiments for long time. Traditional MWPC has parallel anode wires which are strung at distance of 1mm from each other at the minimum. It was very difficult to string wires at smaller distance. The idea of the Texas people is to make sharp edges, instead of wires, on the surface of the silicon wafer by the orientation dependent etching technique. In this way, small pitch of the anode could be achieved. This chamber has, however, a drawback which is shared with the silicon strip detector, i.e., the size of a single chamber is limited by that of silicon wafer. That means larger number of channels if you want install them at large radius.

Recently at KEK, a program has been started to overcome this problem. These days people are so much impressed by the rapid progress of the integrated circuit fabrication technology and mostly see the one side of the whole technology involved in this field, i.e., photofabrication technology. However, the today's IC technology is supported not only by the photofabrication technology but also by the precision machining technology of the same precision. Without the machining of the same precision, people can not align the photomask with the required precision.

KEK method is to make v-shape grooves on a metal plate, like a nickel-plated steel, and to use the metal plate as a negative to make sharp-edged electrodes. After this process, there are two possibilities are under consideration at the moment. The first possibility is to use the elecroforming technique (Fig.1). With a proper photomask on the surface of the metal plate with v-shape grooves, the electrode can be formed by the electro-plating with the metal plate as the cathode. Then transfer the electrodes onto a surface of a non-conductive sheet, like a polyimid resin sheet or a CFRP plate. For the far end cathode, a sheet of aluminized polyester resin or polyimid resin is stretched with an insulating frame between the two plastic sheets.

The second possibility is to use the plastic molding technique by using the machined metal plate as a negative (Fig.2). Once a plastic resin sheet is formed with sharp edges on one side of the sheet, electrodes can be printed on the resin surface by vapor deposition or ion sputtering by using the same photomask as that of the electroforming case. These chambers are arranged as shown in Fig.3 in a real experiment. Four planes of the chamber can be supported by a single substrate of CFRP or carbon graphite of 200 or 300 μm thick.

In order to maintain a good spatial resolution, the chamber thickness must be kept as thin as possible, while the efficiency is severely limited by the chamber thickness. To solve this problem, the use of heavy gas, like xenon, and pressurized gas must be considered. Multiple layer unit can help solving this problem.

Recently KEK machine shop has built a high precision shaper machine to produce gratings for the synchrotron radiation research. The specification of this machine is given in table 1. Using this machine, we made the first trial to make v-shape grooves with 50 μm pitch. Length of the grooves are 8cm. In Fig.4 to Fig.7, we show several pictures of the machine and the product. Fig.4 is the shaping machine. The transverse (X) position is determined with a precision micrometer set by a computer-controled pulse moter to the precision of 0.1 μm. The vertical (Y) position is determined with a combination of a piezo and a micrometer which is the same as that for X-position, to the precision of 0.1 μm. The whole head is pulled back and forth with a steel wire on an air baring (Z direction). Fig.5 is the diamond bit actually used for the first trial. There is no defect seen on the bit to less than a micron. Fig.6 is a microscopic picture of the grooves. The distance between the two grooves is 50 μm. The edge of the grooves were made quite clean. Fig.7 is the same groove further magnified with an electron microscope and the groove was lighted from one side to see the bottom of the groove. The structure of the bottom which becomes top edge of the anode is seen. That is smooth to about 0.1 μm. The shape of the machined metal surface was measured with a surface

shape measuring machine (Fig.8). It is confirmed again that the shape was made good to 0.1 μm precision.

Next step we are going to push forward is to make knife-edges on the surface of a plastic resin which exactly follow the grooves, or to make electroformed knif-edge and transfer them onto a plastic sheet. We are expecting to have the first chamber tested in a few months time.

Table 1. Specification of the KEK precision shaper machine

KEK Precision Shaper Machine

X-axis	stroke	100 mm
	min. setting	1 μm
	precision	0.1 μm
Y-axis	stroke	100 mm
	speed	10 $\sim$ 50 cm/sec
Z-axis	micrometer stroke	25 mm
	piezo stroke	1000 V - 40 μm
	precision	0.1 μm

Fig 1

Reference

[1] S.M.Elliott, P.M.McIntyre, and M.Popovic;
"The knife-edge chamber, A track chamber for SSC detectors",
Texas A&M preprint, submitted to NIM, August 1,1989.

Figure Captions

Fig.1. Fabrication procedure of the knife-edge chamber by the electroforming technology.
Fig.2. Fabrication procedure of the knife-edge chamber by the molding technology.
Fig.3. A four layer unit of the knife-edge chambers which is supported by a sigle layer of CFRP or carbon graphite of 200 or 300 μm thick.
Fig.4. The precision shaper machine built at the KEK machine shop.
Fig.5. The diamond bit used for the v-shape grooves.
Fig.6. The microscopic picture of the grooves.
Fig.7. The magnified view of the groove which shows detailed stracture of the bottom of the groove.
Fig.8. The shape of the machined plate measured with a surface shape measuring machine.

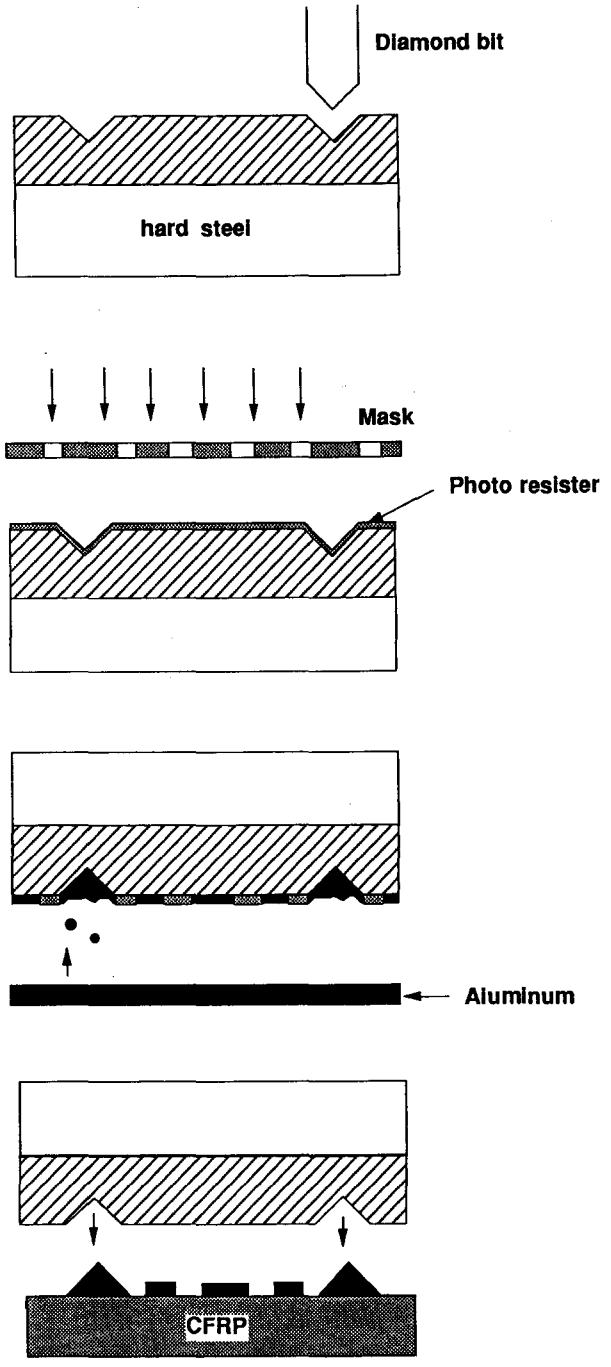

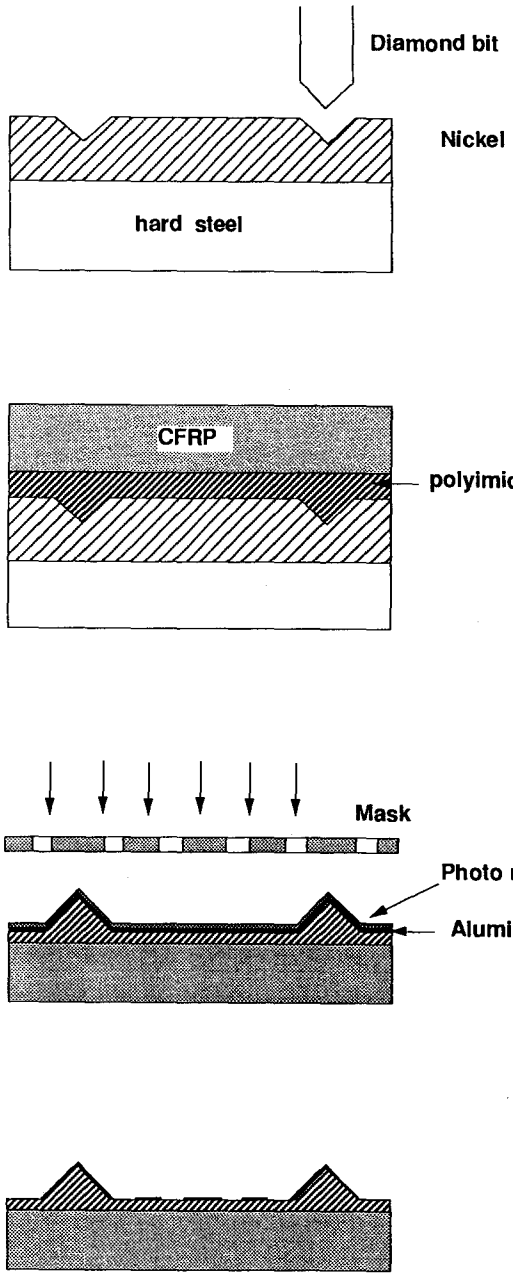
Diamond bit
Nickel
hard steel
CFRP
polyimid
(by Molding
or C.V.D.)
Mask
Photo resister
Aluminum

Fig 2

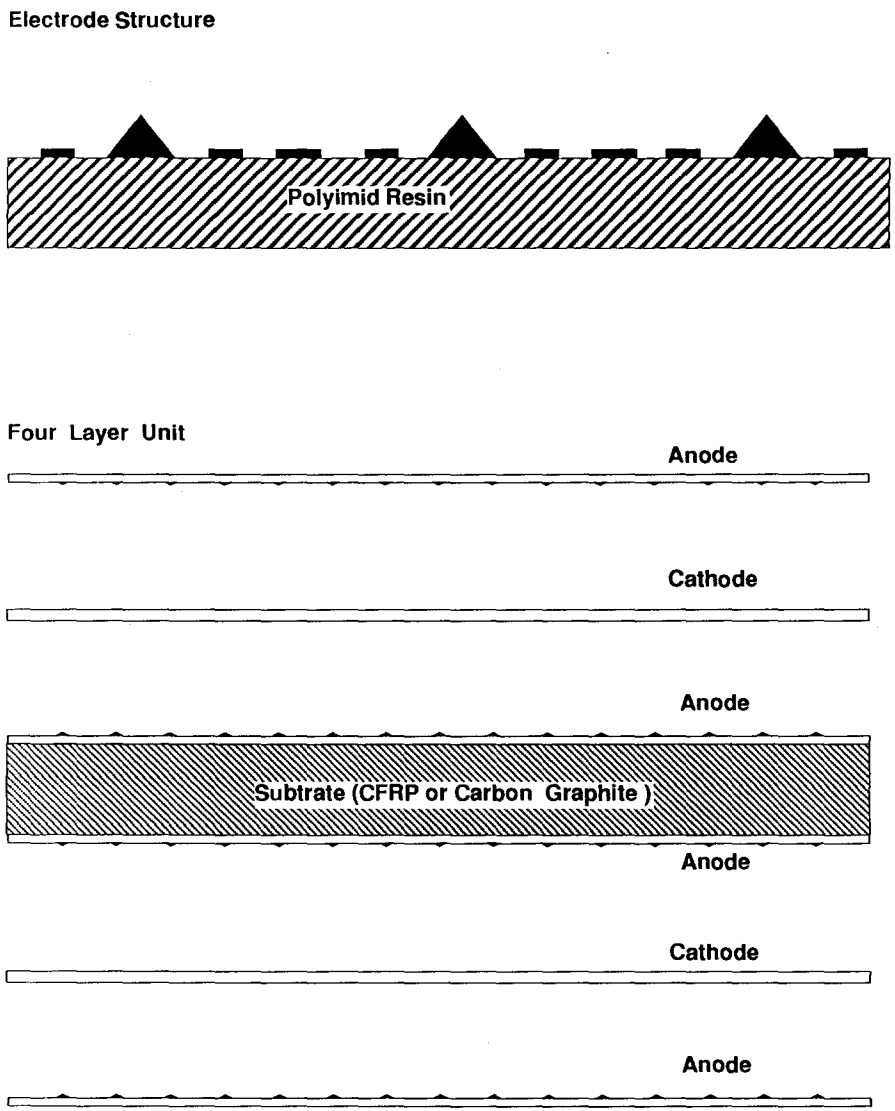
Electrode Structure
Polyimid Resin
Four Layer Unit
Anode
Cathode
Anode
Subtrate (CFRP or Carbon Graphite)
Anode
Cathode
Anode

Fig 3

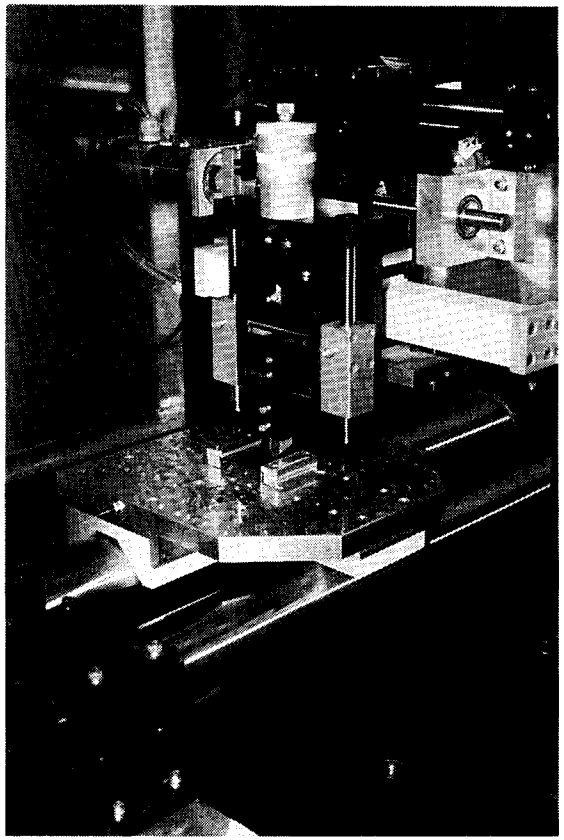

Fig. 4

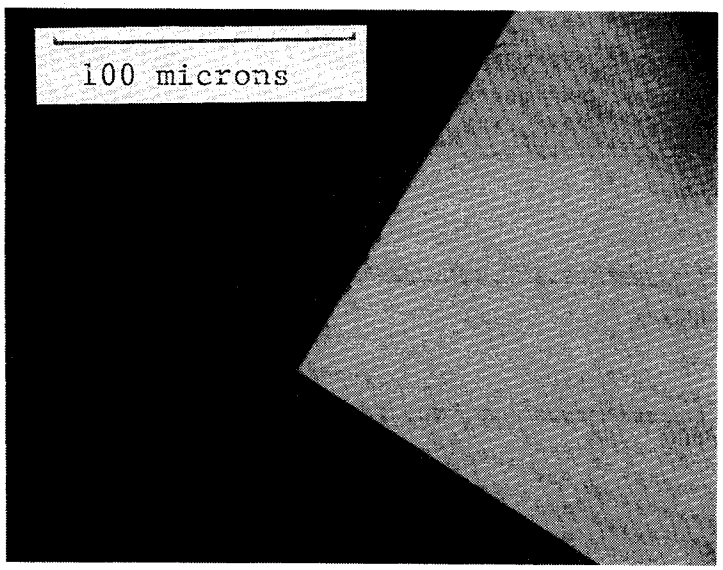

Fig. 5

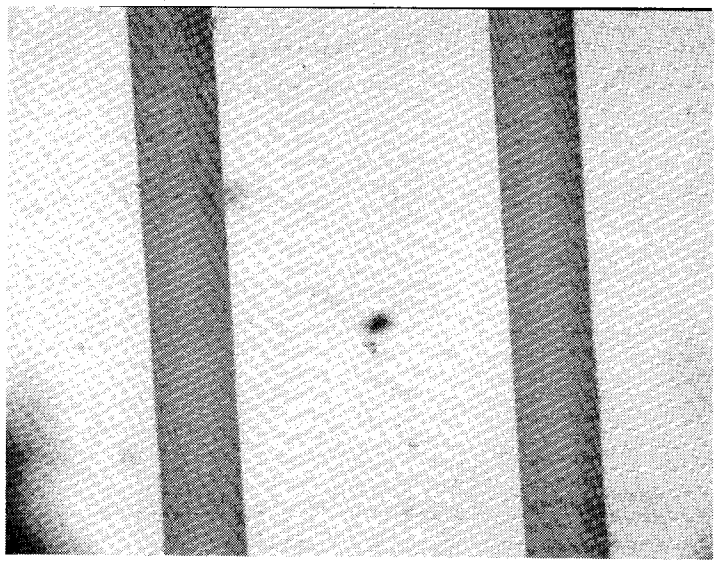

Fig. 6

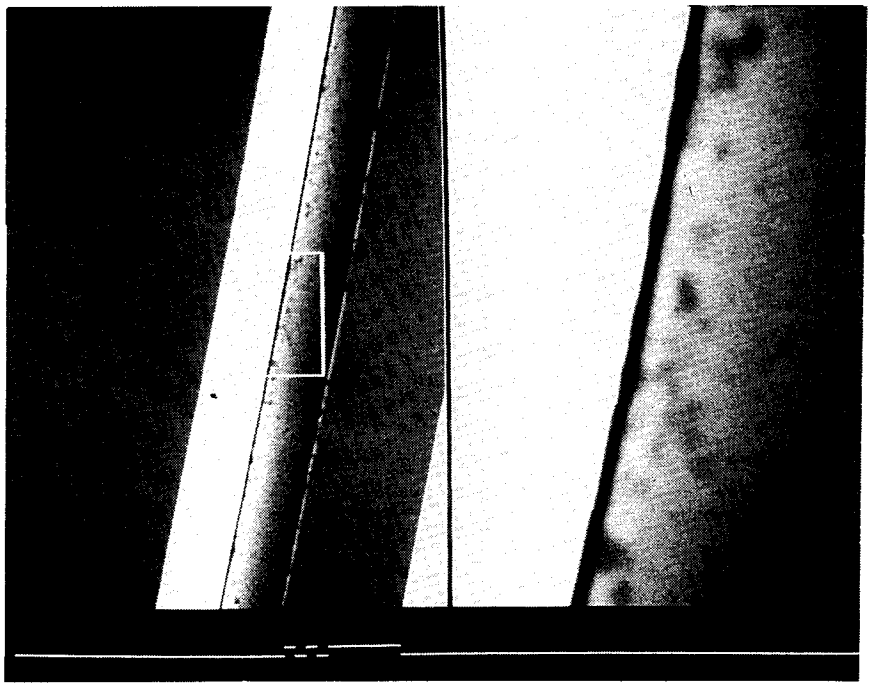

Fig. 7

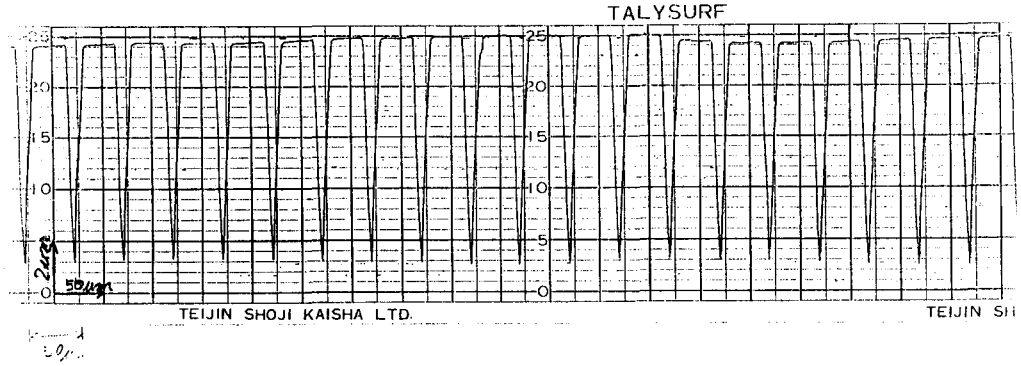
TALYSURF
TEIJIN SHOJI KAISHA LTD.
TEIJIN SH

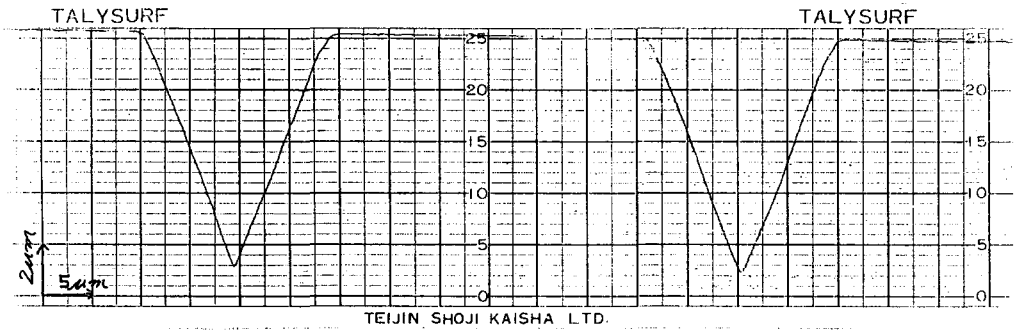
TALYSURF
TALYSURF
TEIJIN SHOJI KAISHA LTD.

Fig. 8

THE PERFORMANCE OF SILICON STRIP DETECTOR FOR ANGLED TRACKS

Tajima H., Nakamura M., Saito K. and. Niwa K.

Depertment of Physics, Nagoya University, 464-01, Japan

presented by Tajima H.

Abstract : The performance of Silicon strip detector for angled tracks is discussed. The results of a Monte Carlo simulation and a beam test are presented.

Introduction

In colliding beam experiments, tracking detectors should work over a large anguler range. But in a thick detector, an angled track generates electron-hole pairs for a long region. Fig.1 shows a schematic view in the case of a 300 μm thick Silicon strip detector (SSD). Fluctuations of the energy loss and electronics noise could cause a serious degradation of the position resolution, thus a Monte Carlo simulation and a beam test were performed to study and understand the performance of SSD for angled tracks. The details of the simulation are described in the next section and the results of the beam test are discussed in Section 2.

1. Monte Carlo simulation

The Monte Carlo simulation was performed in the following way.

1) Signal is generated in each strip with Landau distribution according to the track length of a charged particle passed through.

2) Noise is added to the signal of each strip with Gaussian distribution of 5 KeV σ. This value corresponds to the noise of VLSI readout circuits[1] currentry available. Fig.2 shows some examples of the simulated events.

3) Assuming that the incident angle of the particle is known with the anguler resolution of 2 mrad, the size of the hit cluster is determined by this incident angle.

4) The hit cluster which gives the sum of the signals maximum is searched.

5) At the both end-strips of the selected cluster, the track lengths of the particle are calculated by using the correlation between the track length and the energy loss in Silicon (signal of each strip). Fig.3 shows this correlation and the result of the parabolic fitting is presented by the solid curve. The track lengths and the incident angle give the both end-positions (the entrance position and the exit position of the particle).

6) The particle position in the mid-plane of the detector is obtained as the center of the both end-positions.

The anguler dependence of the position resolution of SSD are shown in fig.4. Fig.4a indicates that the resolution is better than 30 μm for strip pitch of 100 μm as well as 50 μm. The noise of readout electronics is dominated to the position resolution as seen in fig.4b. Fig.4c shows the effect of the anguler resolution of the tracking system, which is negligible if the incident angle is greater than 20 deg. Fig.4d shows that the position resolution is very sensitive to the flatness of SSD.

It should be noted that all the analog data of SSD are used to obtain the above position resolutions.

2. Beam test

Fig.5 shows the setup of the beam test. The incident position of a particle on the tested detector was measured by two 25 μm pitch SSD which sandwitched the tested detector. The p-strip side of a double sided SSD[2] with strip pitch of 100 μm is used for this test. Signals of the tested detector were readout by the Hybrid circuits (LeCroy,HQV810) whose noise σ is about 3.3 KeV. In this test the position resolution of SSD is measured with the incident angle of 30 and 60 deg.

Fig.6 shows the distribution of the difference between the position measured by the reference detectors and the position calculated by using the signals of the tested detector in the case of the incident angle of 30 deg. In this figure the measured distribution is shown by a solid line and the simulated distribution is shown by a dotted line. A Gaussian fitting, which is shown by a solid curve, was performed in the central region of the measured distribution and the standard deviation was 22.3 μm.

Because this standard deviation includes also the systematic error of 14.8 μm, which is estimated from multiple Coulomb scattering and from the position resolution of the reference detectors as shown in fig.7, the position resolution of SSD is obtained by de-convoluting the systematic error (i.e. 14.8 μm from 22.3 μm). Consequently, the position resolution was estimated to be 17 μm in the case of the incident angle of 30 deg. Fig.8 shows the same distribution as fig.6 but in the case of the incident angle of 60 deg. Because the systematic error in this case is 6.5 μm, the position resolution was estimated to be 14 μm.

The measured anguler depedence of the resolution is compared with the simulated one in fig.9. The difference between the measured and the simulated resolution is mainly due to the fact that, in de-convoluting the systematic error of the reference, the distributions of the deviation are treated as Gaussian, which are not really as shown in figs.6,7,8.

As the results, we can say the paremeters used in the simulation are almost reasonable and the results of the simulation agree with the experimental results well.

Conclusions

From the results of the Monte Carlo simulation and the beam test, the performance of Silicon strip detector for angled tracks is evaluated to be fairly well. For a further study, the next beam test in the anguler range of 10-80 deg with 10 deg step is being planned.

References

[1] J.C.Stanton, I.E.E.E. NS**36**, No.1 (1989) 532.

[2] Nakamura M., these proceedings.

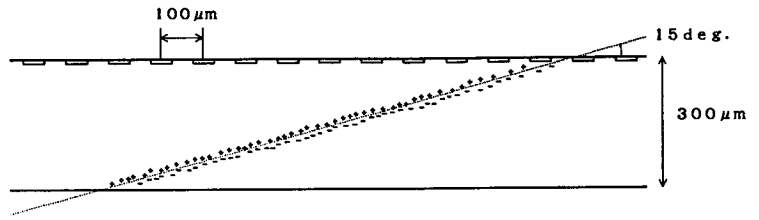

Fig. 1 an angled track gererates e-h pairs in a long region

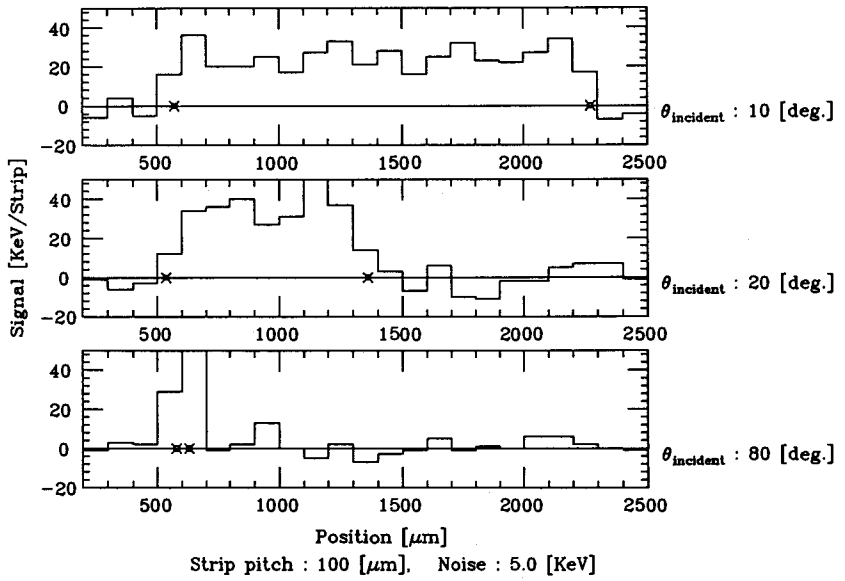

Fig.2 Some examples of simulated events.

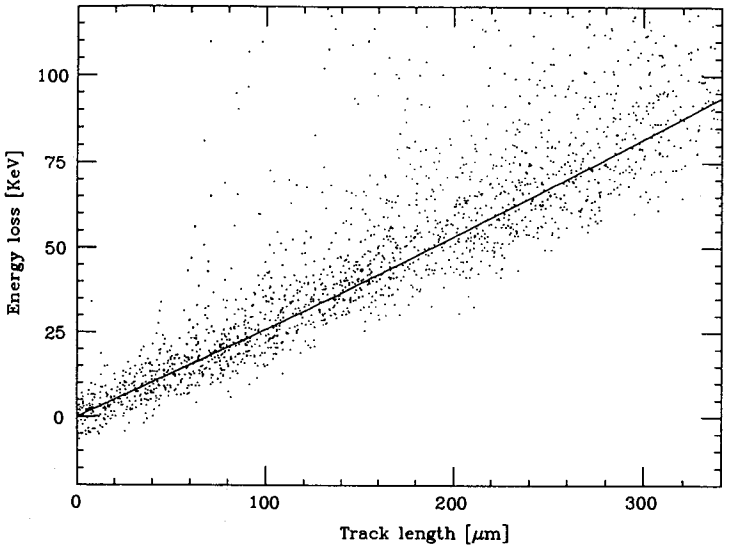

Fig.3 Correlation between the track length and the energy loss in Si.

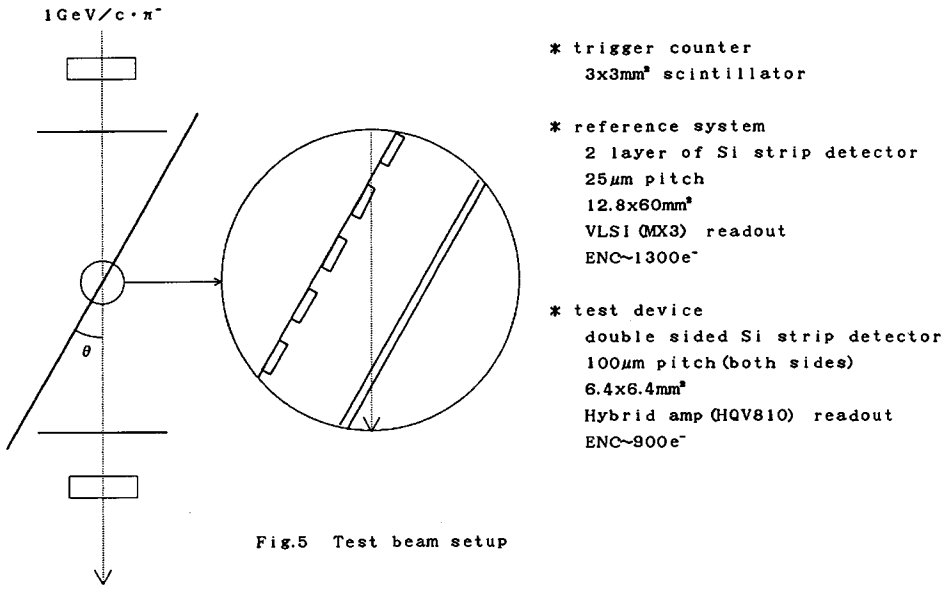

Fig.5 Test beam setup

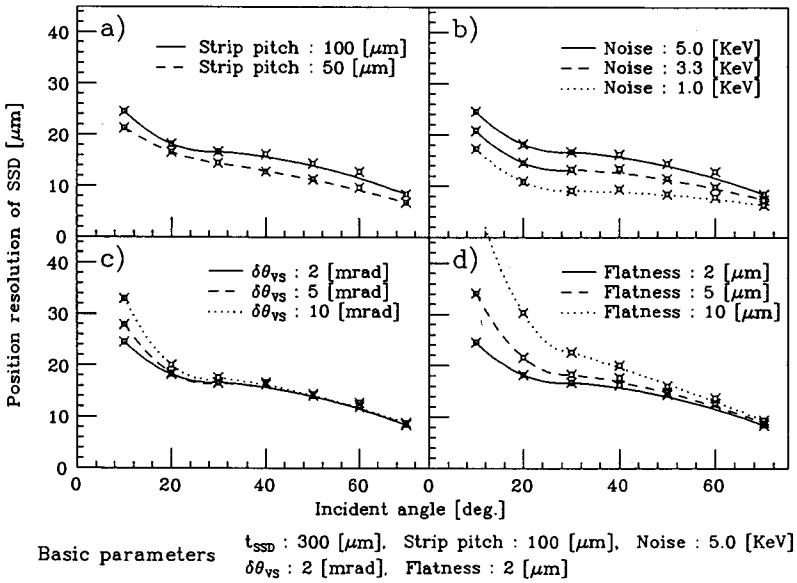

Fig.4 The anguler dependence of the position resolution of SSD.

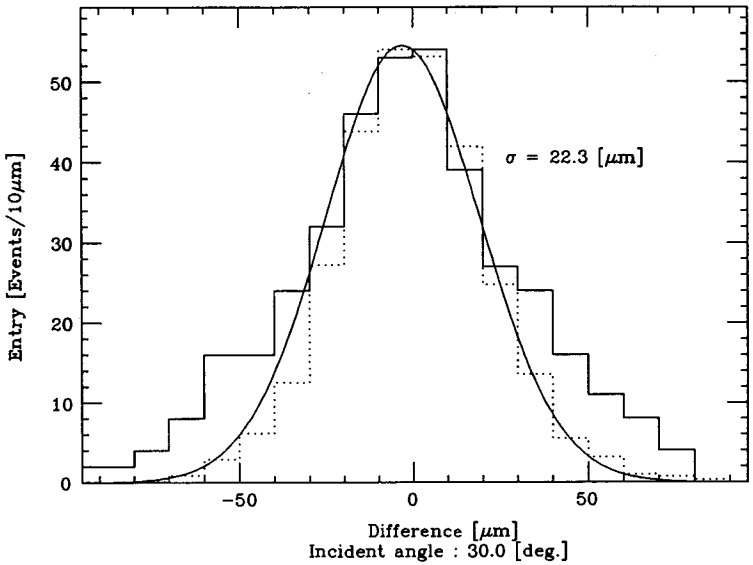

Fig.6 The distribution of the difference between the predicted position and the calcurated position.

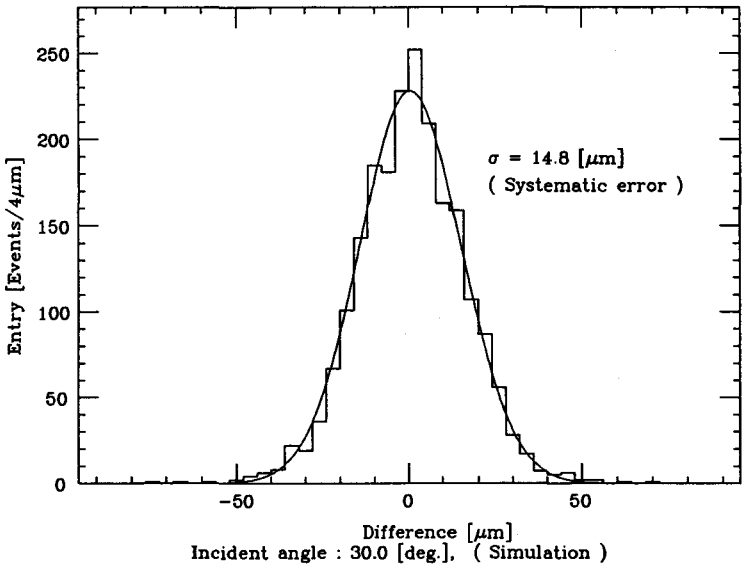

Fig.7 The distribution of the difference between the predicted position and the generated position.

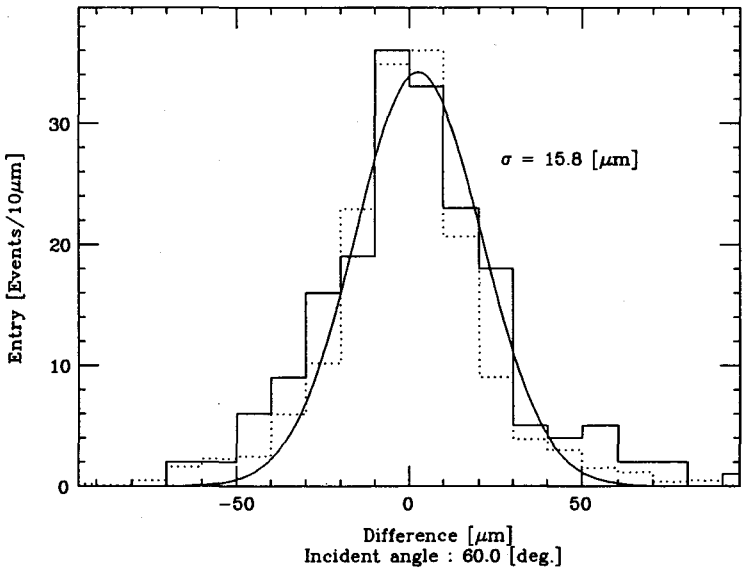

Fig.8 The distribution of the difference between the predicted position and the calcurated position.

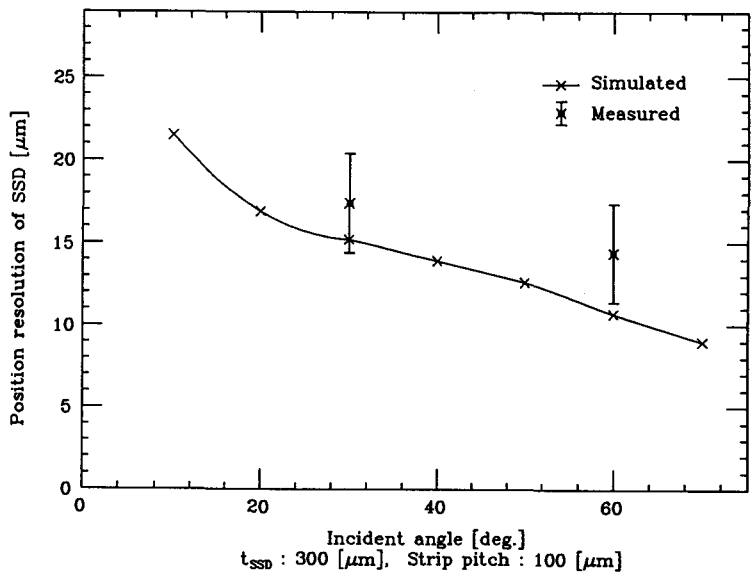

Fig.9 The anguler dependence of the position resolution of SSD.

DEVELOPMENT OF DOUBLE SIDED MICROSTRIP DETECTORS

Saito K, Tajima H., Nakamura M. and Niwa K.
Nagoya University, Nagoya 464-01, JAPAN

(presented by Nakamura M.)

Abstract

We have developed an AC coupled double sided microstrip detector. The developed detector shows a good performance.

1.Introduction

The physical system that we wish to observe is disturbed by the existence of the detector, i.e. by secondary interactions, multiple scatterings, gamma ray conversions and so on. Therefore, we must use a "good-matter-performance" detectors.

In single sided microstrip detector, which has been used in many fixed target experiments, only the hole carriers were used to measure the particle position. The electron carriers were dumped to the cathode electrode. In double sided microstrip detector (DSSD), we can make good use of the electron carriers to measure the particle position in another projection.

The development of double sided microstrip detectors were performed in many laboratories [1-3]. Many important ideas were suggested. But the poor performance of the process of the detectors made it difficult to use DSSD in real experiments and these poor performance obstructed the extensive study, like radiation damage test and so on.

In this time, we have succeeded to obtain a good performance AC coupled DSSD. We will do a systematic study of DSSD based on this success.

2. Characteristics of the DSSD

2-1 Structure and DC characters

The size of the produced device is 1cm*1cm and the thickness is 300 microns. The effective area is 6.4mm*6.4mm. The tested strip pitch is 50 and 100 microns. We will show the results about the device of 100 micron pitch.

The device structure adapted in this time is the same as the one proposed by P.Holl et al[2].

On both sides, AC coupled read out is realized by using the built-in capacitance on the detector. SiO_2 of 2000 A thickness is used as an insulator of the built-in capacitance. The dielectric breakdown voltage of the SiO_2 is estimated to be about 120 V in ideal case, we have not observe any trouble up to 100 V. In order to study DC characters, DC coupled devices were also prepared.

The bias voltage of the P strips are supplied from the bias feed electrode by the method of depletion region overlap. Using the DC coupled device, the bias voltage dependence of the voltage drop caused by the existence of the gap between a strip and the bias feed is measured. The result is shown in Fig.1. At the ordinal operation voltage, i.e. about 70 V, it becomes about 14V. This difference caused no problem in real use.

On N side, the problem caused by the type inversion at the surface that is induced by the positive charge built-up in SiO_2 is expected. This inversion may make a short channel between strips. In order to avoid this, several ideas are proposed[1-3]. In Ref.1 and 2, P isolation strips are suggested. We have adapted this structure. P strip between N strips may compensate the positive charge at SiO_2, then cut the short channel. Fig.2 shows the measured bias voltage dependence of the resistance between strips. This result was obtained by using the DC coupled device. Sudden rise at about 60V may suggest the occurrence of the full depletion. Above this voltage, the resistance becomes about 50 Mohm. This value is large enough to isolate the strips and to suppress the thermal noise. The structure through which the bias voltage of the strips are supplied is constructed from the N bias feed electrode and the narrow surface n channel. The schematic view is shown in Fig.3(b). The width of the n channel is 10 microns and the length is 500 microns. Fig.4 shows the dependence of the resistance of this n channel on the bias voltage. The sudden rise around 60V is also observed, and the value becomes

about 3 Mohm at the normal operation voltage of 70V. This value is also large enough [4].

Concerning about the performance of the process, leakage current of the device is one of the indicators. The measured leakage current is 0.3nA/strip at 70V. This value is small enough. We can say that the double side treatment process is going well.

2-2 AC character

The Infrared ray test and the beam test were performed with the AC coupled device.

(1) Infrared ray test[5]

Using the collimated infrared ray of wave length of 1.1 micron, which is near the absorption edge of silicon, we can create electron-hole pairs almost uniformly along the depth. Therefore, we can check the performance of the detector easily and precisely. Using shorter wave length like 0.830 micron, the generated electron-hole pairs are localized at the surface. Then we can check the charge collection properties at the surface. In this time, the infrared ray was collimated to the spot of 50 micron diameter and irradiated from the N side between the aluminum electrode where the P isolation strip exist. Then we can check the effect of this P isolation strip by shorter wave length.

Fig.5 shows the bias voltage dependence of the collected charge in the case of 1.1 micron and 0.83 micron. In the case of 1.1 micron, full charge collection occurs at about 65V. This is well correspond to the value at that the sudden rise of the interstrip resistance is observed. In the case of 0.83 micron, the saturation is not observed at the normal operation voltage, i.e. 70V. This may indicate the degradation of charge collection efficiency at the surface where the P isolation strip exist. Some charge may be trapped here. The estimated thickness of the dead space is about 2 microns at Vb=70V by supposing that the value at Vb=100V is full charge.

(2) Beam test

Response to the high energy beam was studied with 1 GeV/c minus hadron beam. The beam was exposed perpendicular to the SSD plane. The supplied bias voltage is 70V.

Table.1 shows the distribution of the cluster size of a hit. For the strip pitch is 100 micron, single strip hit is dominant. Using these single hit data, pulse height distributions and pulse height correlation between P and N side were studied. Fig.6(a) shows the pulse height distribution of P side and (b) shows that of N side. There is no significant difference between these distributions. Fig.7 shows the correlations between the pulse height of P and N and shows a quite good correlations.

3. Future Test

As described above, the developed detector shows a quite good performance on DC and AC characters. We will do more extensive study based on this device.

(1) Study with larger size devices.
(2) Study with other methods to cut the N short channel and other methods to supply the bias voltage to strips.
(3) Radiation damage test.
(4) etc.

This development was performed as a Theme of the Center for Cooperative Research in Advanced Science and Technology of NAGOYA university.

We wish to express special thanks to K.Yamamoto, K.Yamamura and K. Miyaguchi.

Reference

[1] G.Bagliesi et al., Paper presented at IEEE 1986 Nuclear Science Symposium. INFN PI/AE 86/10.
G.Batignani et al.,Nucl. Instr. and Meth. A277(1989)147-153.

[2] P.Holl et al., IEEE Trans. on N.S., 36(1989)251.

[3] B.S.Avset et al., Paper presented at IEEE 1989 Nuclear Science Symposium. CERN-EP/90-11.

[4] In real operational condition, N strips are biased to be +70V and the voltage of the read-out aluminum electrode is at the level of the input of the preamplifier. Then the surface under the read-out aluminum becomes depleted and inverted. Therefore, the resistance becomes larger than the measured one.

[5] Y.Tomita et al., Nucl. Instr. and Meth. A270(1988)403-410.

Table 1

Cluster Size (No. of Hit strips per Cluster)	P-Side	N-Side
1	75%	92%
2	20%	8%
3	4%	0%
>= 4	1%	0%

Figure Captions

Fig.1 The dependence of the electric potential of the P strip on the bias voltage.

Fig.2 The dependence of the resistance between N strips on the bias voltage.

Fig.3 The schematic view of the structure of the developed device.
(a) P side, (b) N side.

Fig.4 The dependence of the resistance of the bias N channel on the bias voltage.

Fig.5 The bias voltage dependence of the collected charge which is generated by the infrared ray.
(a) wave length=1.1 micron, (b) 0.83 micron.

Fig.6 The pulse height distribution of the signal of minimum ionizing particle.
(a) P side, (b) N side.

Fig.7 The correlation between the pulse height of P and N.

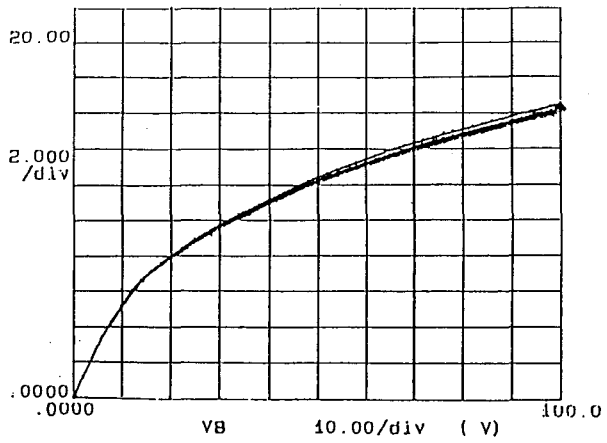

Fig.1 The dependence of the electric potential of the P strip on the bias voltage.

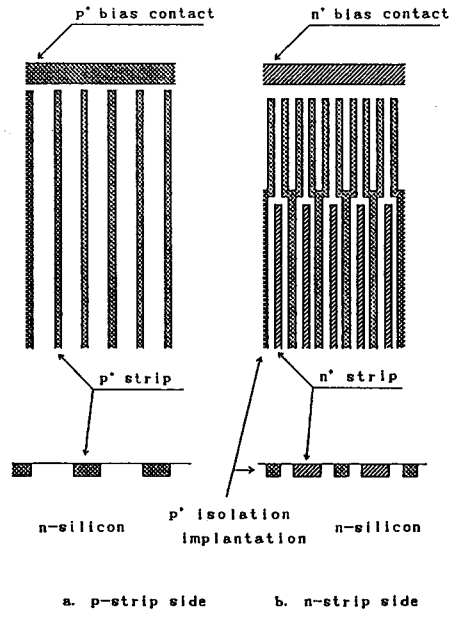

Fig.3 The schematic view of the structure of the developed device.
(a) P side, (b) N side.

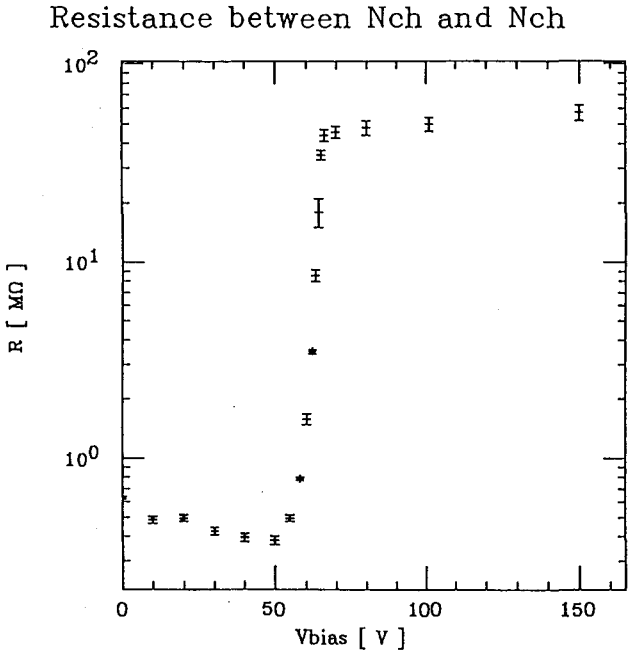

Fig.2 The dependence of the resistance between N strips on the bias voltage.

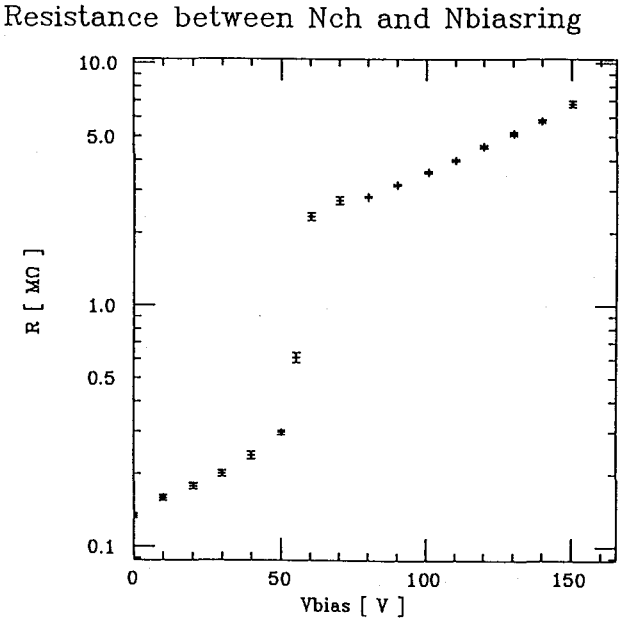

Fig.4 The dependence of the resistance of the bias N channel on the bias voltage.

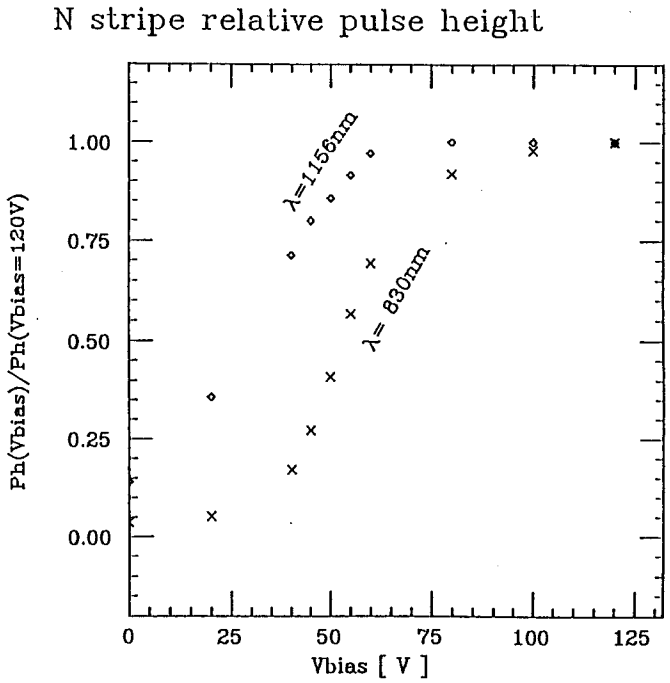

Fig.5 The bias voltage dependence of the collected charge which is generated by the infrared ray.
(a) wave length=1.1 micron, (b) 0.83 micron.

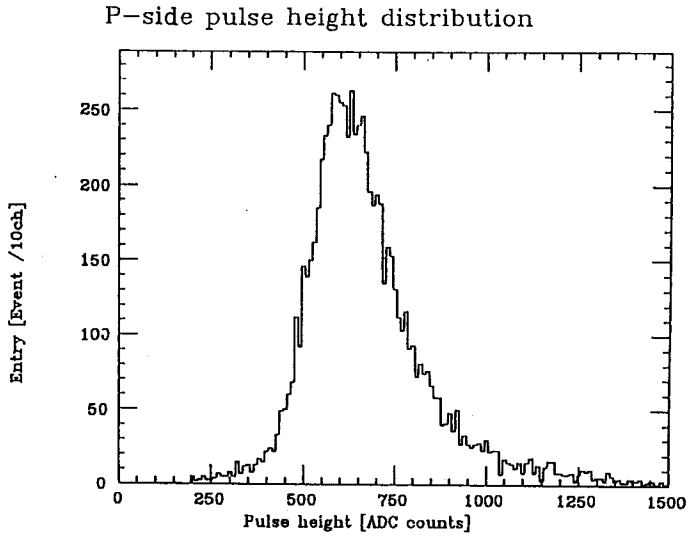

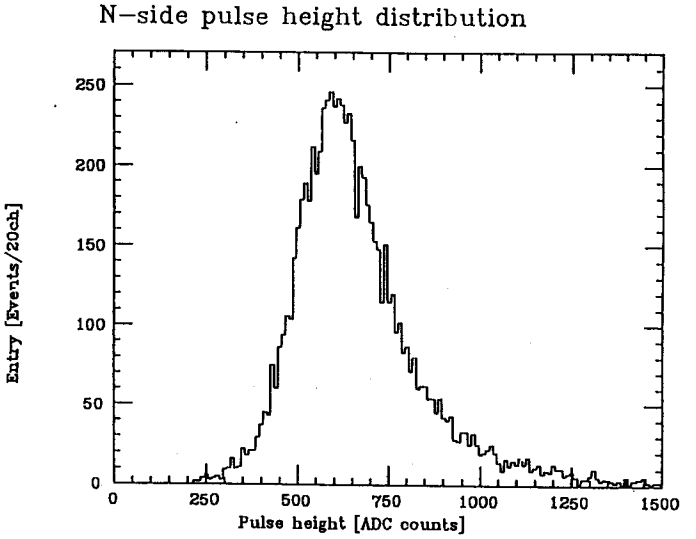

Fig.6 The pulse height distribution of the signal of minimum ionizing particle.
(a) P side, (b) N side.

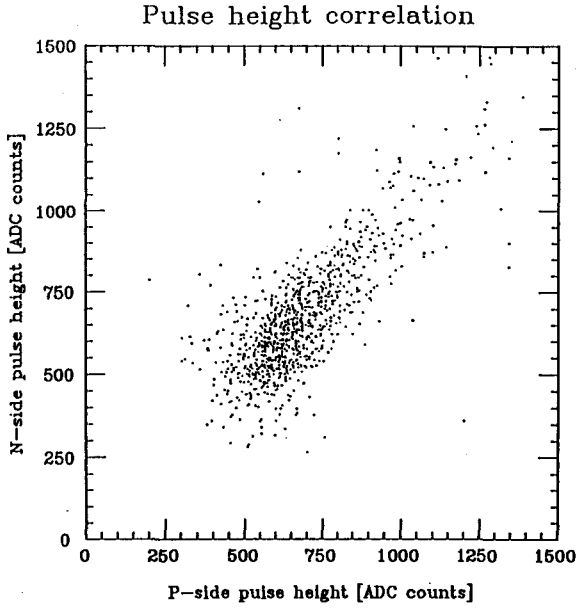

Fig.7 The correlation between the pulse height of P and N.

Silicon Tracker for the SSC

A. SEIDEN
Santa Cruz Institute for Particle Physics
University of California, Santa Cruz, CA 95064

Abstract

This is a status report on the design of a large silicon tracking detector for the SSC. We present our design, the principles on which it is based and initial work on the mechanical support structure for the detectors.

1. Introduction

This is a status report on the design of a large silicon tracking detector for the SSC. We discuss below the principles on which the design is based as well as initial work on the mechanical support structure for the detectors. The work is being done as part of the SSC laboratory subsystem R&D program. The institutions involved in this R&D program are listed at the end of the report.

2. Geometrical Configuration

Figure 1 shows the silicon tracking detector configuration we are proposing. We assume it is made of double-sided detectors using a small stereo angle of 5 milliradians for the second coordinate readout. The primary coordinate readout is the ϕ coordinate in cylindrical coordinates for both barrel and planar detectors. This is the coordinate exhibiting bending in a solenoidal field. The transition from barrel to endcap planar geometry is made at 45° to minimize material. The symmetries of the detector are matched to those of the magnetic field.

The dimensions of the detector planes are given in Table 1. The rapidity coverage for each detector plane is given in Table 2. Figure 2 gives the material budget versus rapidity for the silicon alone. The detectors are assumed to be readout with electronics of 50μm pitch. In the endcap region the detector charge collection strips taper with radius.

3. Design Principles

The goals for the detector are to provide excellent pattern recognition, good momentum resolution in a stand-alone mode and excellent resolution when combined with an outer tracker and excellent vertexing for high $P_\perp$ tracks. It must

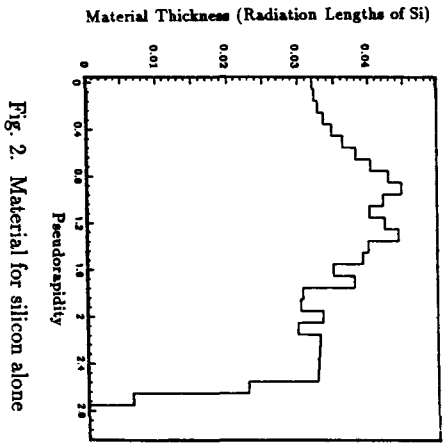

Fig. 2. Material for silicon alone

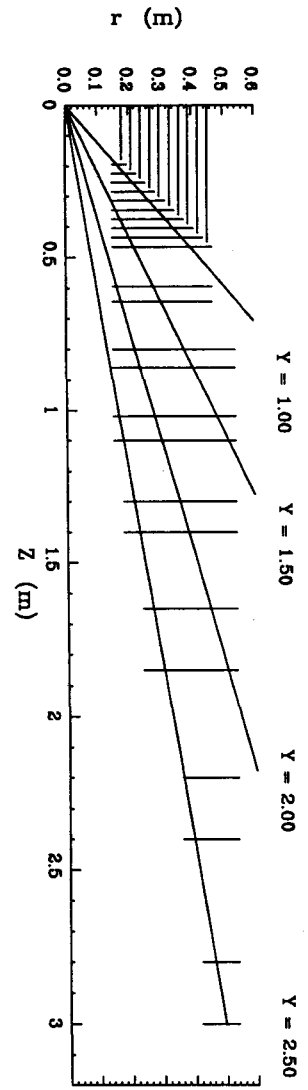

Fig. 1. SSC Silicon Microstrip Tracker

TABLE 1. DETECTOR DIMENSIONS

Cylinder	R	Z	Area
1	0.180	0.180	0.407 m^2
2	0.210	0.210	0.554 m^2
3	0.240	0.240	0.724 m^2
4	0.270	0.270	0.916 m^2
5	0.300	0.300	1.131 m^2
6	0.330	0.330	1.368 m^2
7	0.360	0.360	1.629 m^2
8	0.390	0.390	1.911 m^2
9	0.420	0.420	2.217 m^2
10	0.450	0.450	2.545 m^2
Total area of cylindrical tracker layers			13.402 m^2

Plane	Z	R1	R2	Area
1	0.195	0.150	0.195	0.098 m^2
2	0.225	0.150	0.225	0.177 m^2
3	0.255	0.150	0.255	0.267 m^2
4	0.285	0.150	0.285	0.369 m^2
5	0.315	0.150	0.315	0.482 m^2
6	0.345	0.150	0.345	0.606 m^2
7	0.375	0.150	0.375	0.742 m^2
8	0.405	0.150	0.405	0.889 m^2
9	0.435	0.150	0.435	1.048 m^2
10	0.465	0.150	0.465	1.217 m^2
11	0.595	0.150	0.465	1.217 m^2
12	0.645	0.150	0.465	1.217 m^2
13	0.800	0.150	0.540	1.691 m^2
14	0.860	0.150	0.540	1.691 m^2
15	1.020	0.150	0.540	1.691 m^2
16	1.100	0.150	0.540	1.691 m^2
17	1.300	0.180	0.540	1.629 m^2
18	1.400	0.180	0.540	1.629 m^2
19	1.650	0.240	0.540	1.470 m^2
20	1.850	0.240	0.540	1.470 m^2
21	2.200	0.360	0.540	1.018 m^2
22	2.400	0.360	0.540	1.018 m^2
23	2.800	0.420	0.540	0.724 m^2
24	3.000	0.420	0.540	0.724 m^2
	Total area of planar tracker layers			24.774 m^2
	Total area of silicon tracker layers			**38.176 m^2**

TABLE 2. RAPIDITY COVERAGE OF DETECTOR PLANES

10 Barrel Detectors: $|Y| \leq 0.88$

Planes	Y_{min}	Y_{max}
1	0.88	1.08
2	0.88	1.19
3	0.88	1.30
4	0.88	1.40
5	0.88	1.49
6	0.88	1.57
7	0.88	1.65
8	0.88	1.72
9	0.88	1.79
10	0.88	1.85
11	1.07	2.09
12	1.13	2.17
13	1.18	2.38
14	1.24	2.45
15	1.38	2.62
16	1.45	2.69
17	1.60	2.68
18	1.67	2.75
19	1.83	2.63
20	1.94	2.74
21	2.10	2.51
22	2.19	2.60
23	2.34	2.60
24	2.41	2.66

survive more than 10 years of radiation at the SSC which sets a limit for the allowable inner radius of the detector, and it must have a minimum area because of the large costs involved.

The pattern recognition in silicon involves linking of sparse information. It is therefore critical to understand the pattern recognition technique in advance or else one may get overwhelmed by combinatorial problems when searching for tracks. The method we envision uses local linking of signals into track tangent vectors and then a global linking of the tangents. The local elements are made up of two double-sided detector pairs yielding two ϕ measurements displaced along the track and two stereo measurements with opposite stereo direction. These locally give an excellent measurement of the local bending which is the change in ϕ per unit length

and a coarser measurement of the second coordinate which is the z coordinate in the barrel section and the r coordinate in the forward section (we use cylindrical coordinates r, z, ϕ).

Referring to Fig. 1, we see that the detector planes nearest the interaction region are equally spaced so that we may, except for the first and last detectors, consider a given detector to be part of two pairs involving the two equally spaced neighbors. The detectors spaced further out in z form unique pairs.

The ability to do pattern recognition has been quantified by a set of scaling rules presented in Ref. 1. Table 3 below summarizes the scaling parameters for this design. The relevant detector parameters are given in the table. Note that these rules quantify the resolution and segmentation needed for tracking in 1 TeV jets. Each parameter should be less than or of order 1 for the information to be adequate for recognizing and linking information to form individual tracks. For simpler processes, where tracks are more isolated, the tracking should be very robust.

The detector design shown in Fig. 1 provides 10 double-sided hits and a fixed radial lever arm of about 50 cm for all tracks out to rapidity of 2.5. The actual lever arm varies by about $\pm 10\%$ as a function of rapidity, giving a stand-alone momentum resolution which varies by about $\pm 20\%$ for a given position resolution of the detectors. Note, in the forward direction the silicon provides almost the entire momentum resolution of the detector.

The 10 planes are dictated by pattern recognition requirements. The silicon detector is made of individual pieces which have small dead regions. We estimate a total dead area of about 5% of the total. Table 4 gives the probability of finding a given number of hits out of 10 total for a 5% inefficiency. It is likely that 8 hits is a minimum for robust pattern. We therefore have chosen 10 planes for the design.

For the forward tracking, we measure ϕ as a function of z. Since the amount of bending is controlled by the radial (not z) displacement of a track, the vector elements are progressively spaced further out in z as we go out in rapidity. The goal has been to adjust the z spacing so that on the average a track measurement in the forward paired detectors corresponds to the same 3 cm radial displacement as in the barrel detectors. This allows a measurement of the curvature locally with comparable errors in all the detector pairs.

4. Mechanical Considerations

The detector discussed above will allow position determination with an accuracy of about 15 μm per measurement. To avoid degrading the detector performance it is important that the mechanical system which holds the detectors

TABLE 3. DETECTOR PARAMETERS AND SCALING RULES

Physics Parameters	1 TeV Jets
Track angular separation $\langle\theta\rangle$	0.5 mrad
Jet angular width $\theta_{1/2}$	10 mrad
Track P_T in jet core	50 GeV
Detector Parameters	**Si Tracker**
Magnetic field B	2.0 T
Radius of curvature $\rho = 3.3P_T/B$	82.5 m
Radial detector spacing δ	3 cm
Mean radius r	31.5 cm
Detector length l	15 cm
Double track separation ε_m	100 μm
Stereo angle α	5 mrad
Position resolution σ_m	15 μm
z position resolution $\sigma_z = \sigma_m/\alpha$	3 mm
Scaling Rule Requirements	**Si Tracker**
Resolve hits: $\frac{\varepsilon_m}{r\langle\theta\rangle}$	0.63
Find vector segments: $\frac{\delta}{2\rho\langle\theta\rangle}$	0.36
Link vector segments: $\frac{\sqrt{2}\sigma_m}{\delta\langle\theta\rangle}$	1.40
Match z hits: $\frac{2\sigma_m l\alpha}{(r\langle\theta\rangle)^2}$	0.90
Note: want quantities to be $\lesssim 1$	

TABLE 4

	Probability of Various Numbers of Hits
10 layers	59.9%
9 layers	31.5%
8 layers	7.5%
<8 layers	1.2%

provide position stability of about 5 μm. In addition the amount of material that can be tolerated is at most a few per cent of a radiation length.

Figure 3 shows a picture of the support framework planned for the detectors. The central detector wafers are supported on three cylinders which are held on a large frame which holds the forward planes. Figure 4 shows the units from which the frame is made. Figure 5 shows the frame in more detail. It is made of cylindrical tubes which connect together.

Table 5 provides a list of some potential materials from which the frame can be made. A highly desirable property for the frame would be a negligible coefficient of thermal expansion. This can be achieved by the use of graphite–metal matrix composite materials, which also have adequate strength and reasonably good thermal conductivity. Figure 6 shows the coefficient of thermal expansion versus the composition of the material. A value of zero with mostly graphite, which has a large radiation length, is possible.

A detailed mechanical design, backed up by measurements and radiation tests of materials, is an important goal for the coming year.

REFERENCES

1. J. DeWitt *et al.*, *Proceedings of the Summer Study on High Energy Physics in the 1990s*, Snowmass, Colorado, 1988, edited by S. Jensen (World Scientific, Singapore, 1989), p. 717.

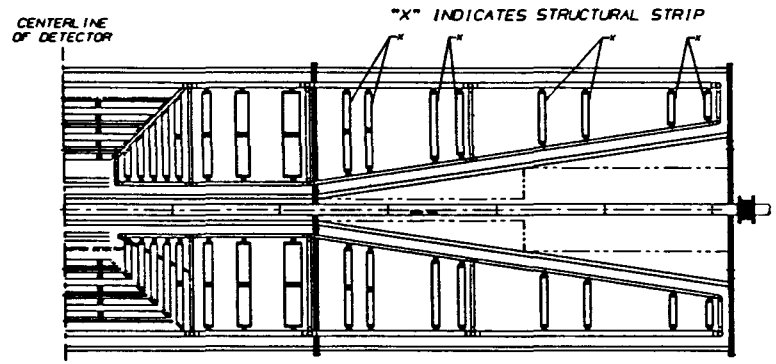

Fig. 3 Schematic drawing of silicon detectors and support members.

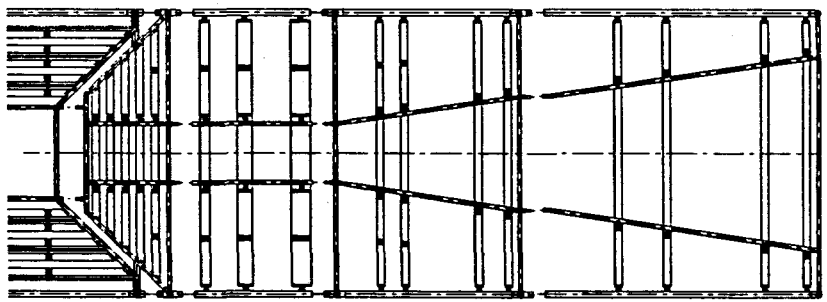

Fig. 4 Schematic drawing of pieces from which the detector is assembled.

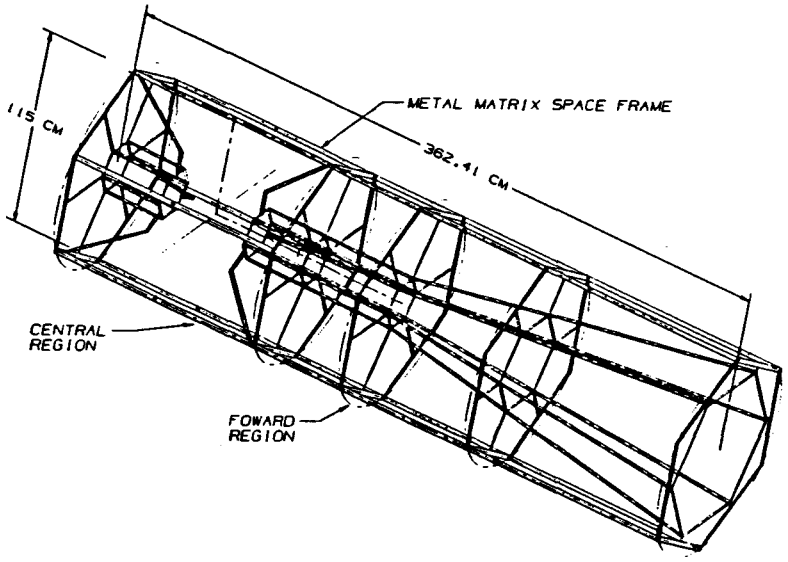

Fig. 5 Support framework for detectors in the forward region.

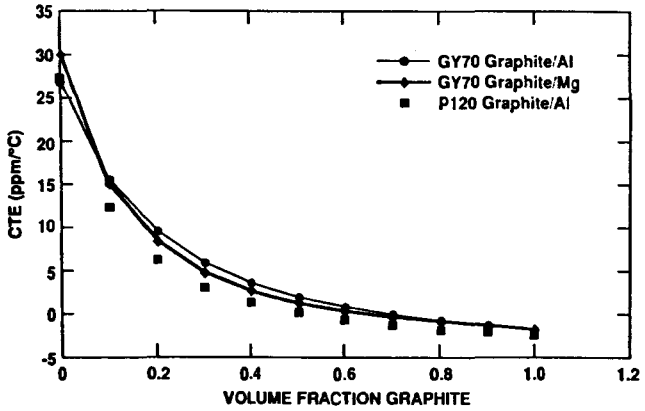

Fig. 6 Isotropic thermal expansion.

TABLE 5. SELECTED MATERIAL PROPERTIES

MATERIAL	ELASTIC MODULUS E- GPa	DENSITY ρ (gm/cm^3)	SPECIFIC STIFFNESS E/ρ-10^8 cm	CTE α ppm/K	THERMAL CONDUCTIVITY k W/M-K	SPECIFIC HEAT c_p J/gm-K	k/α	EFFECTIVE RADIATION LENGTH L-cm
MATERIAL CANDIDATES								
BERYLLIUM	290.0	1.84	16.08	11.60	146.0	1.88	13.0	35.43
BORON CARBIDE (B_4C)	448.2	2.52	18.15	4.73	43.0	0.90	9.0	19.90
CARBON - CARBON**	152.0	1.90	8.16	0.10	246.0	1.00	2460.0	18.80
GRAPHITE and EPOXY**	300.0	1.58	19.37	0.10	52.0	0.90	520.0	24.70 (est)
Mg-MMC (Az91)	177.7	2.02	8.95	0	412.0	?	∞	16.80
Al-MMC* (6061-T6)	196.5	2.39	8.39	0	409.0	?	∞	14.49
REFERENCE MATERIALS								
SILICON (Detector Material)	131.0	2.33	5.74	4.20	129.0	0.70	31.0	9.37
ALUMINUM (6061-T6)	68.9	2.70	2.59	23.58	168.0	0.90	7.1	8.89
BORON	344.7	2.34	15.03	8.30	1.0	1.29	0.2	22.52
FUSED SILICA (SiO_2)	73.0	2.20	3.39	0.50	1.0	0.92	2.0	12.30
COPPER	117.2	8.91	1.34	16.90	400.0	0.39	24.0	
SiC	325.0	3.00	11.05	2.30	200.0	0.89	87.0	8.52

*Graphite Fiber (P-120) MMC - Metal Matrix Composite, quasi-isotropic, ~60% graphite
**Uni-directional properties

The institutions involved in the Silicon R&D are:

California Institute of Technology
University of California, Davis
University of California, Riverside
Santa Cruz Institute for Particle Physics–
University of California, Santa Cruz
University of Hawaii
Johns Hopkins University
University of Pittsburgh
Fermi National Accelerator Laboratory
Lawrence Berkeley Laboratory
Los Alamos National Laboratory
Stanford Center for Integrated Systems
Stanford Liner Accelerator Center
Hiroshima University
Nagoya University
Hiroshima Institute of Technology
KEK, National Laboratory for High Energy Physics
Niigata University
Universities of Pisa and Sassori, and INFN-Pisa
University of Turin
University of Bristol
University of Cambridge
Imperial College
University of Liverpool
University of Oxford
Queen Mary and Westfield College
Rutherford Appleton Laboratory
Krakow Institute of Nuclear Physics
Silicon Dynamics, Inc.
United Technologies Microelectronics Center (UTMC)
Senter for Industriforskning
Messerschmitt-Bölkow-Blohm GmbH
Westinghouse S&T Center

Parallel Session: Calorimeter

April 24, 13:30-17:50

Status Report on Warm Liquid Calorimetry and Preliminary Results from E795 at Fermilab

Presented by M. Pripstein and H. Yuta
WALIC COLLABORATION

B. Aubert, J. Colas, P. Ghez, J. -C. Lacotte, J. -C. Lemarec, and P. Petitpas
Laboratoire d'Annecy-le-Vieux de Physique des Particules

J. Bensinger
Brandeis University

W. Edwards, R. Jared, P. Limon, M. Pripstein*, M. Strovink, W. Thur, T. Weber, and W. A. Wenzel
University of California, Berkeley and Lawrence Berkeley Laboratory

L. Dobrzynski, D.Kryn, J.P. Mendiburu, and P. Salin
Laboratoire de Physique Corpusculaire du College de France

D. Theriot
Fermi National Accelerator Laboratory

J. Womersley
Florida State University

G. Brandenburg, S. Geer, J. Oliver, and E. Sadowski
Harvard University

R. Kikuchi
Kyoto University

K. Miyano
Niigata University

R. Hollebeek, R. VanBerg, M. Newcomer
University of Pennsylvania

Ph. Lavocat, B. Mansoulie, S. Palanque, and J. Teiger
CEN Saclay

K. Masuda
Saitama College of Health

K. Abe, K. Hasegawa, F. Suekane, H. Yuta
Tohoku University

M. Higuchi, Y. Hoshi
Tohoku Gakuin University

J. Busenitz, D. Dibitonto, M. Timko
University of Alabama

§ I. Introduction

Warm liquid calorimetry is being considered as one of the promising new technologies for the SSC calorimeters. The use of warm liquids provides (1) excellent hermeticity without cryostat, (2) smaller mechanical modules with thin walls, (3) shorter read-out cables, and (4) possible compensation with the hydrogenous liquids. Furthermore, it offers (1) excellent calibration stability, (2) excellent uniformity of response, (3) easy segmentation, and (4) less radiation damage. However, it has some disadvantages compared to the liquid argon calorimetry ; (1) lower signal/noise at low voltages, but becomes comparable, even superior at high voltages, (2) purification requirement is much more stringent, and (3) safety issues need more study.

To demonstrate the feasibility of a large-scale warm liquid calorimeter, first we need to study the following problems :

1. liquid purity and long-term stability,
2. material compatibility,
3. search for possible liquids in addition to TMP and TMS,
4. fast signal response with high voltage and ion yield,
5. signal to noise ratio with electrostatic transformer,
6. radiation resistance,
7. e/h compensation,
8. energy resolution,
9. energy calibration and linearity,
10. homogeneity of signal response,
11. stability of operation and
12. hermeticity.

Among these, items (1) through (6) are being studied in each institute in WALIC, and items (7) to (11) are now being carried out in the test beam experiment

(T795) at Fermilab. EG & G is providing the hermeticity, structure and stress analysis for a full size 4π calorimeter.

In addition, before proceeding to the final design of the calorimeter, we need to perform a test beam experiment using a large test beam module of a swimming pool configuration which arranges lead absorbers inside the liquid. The design work for this test beam module is now being carried at LBL intensively. The experimental run is expected in Spring 1991.

§Ⅱ. Electron lifetimes

The lifetime of drifting electrons in the liquid is a sensitive measure of impurities. The relation between the lifetime, τ and impurity, C(mole/ℓ) is :

$$C(\text{mole}/\ell) = 1/(\tau \cdot k),$$

where k is the rate constant of electron attachment. (For O_2 in TMS $k=6.0\times10^{11}$/mole.sec) For instance, the impurity concentration of 81ppb gives $\tau=1\mu$sec for TMS, indicating the stringent requirement of the liquid purity.

Up to now, the institutes in WALIC are studying only a few kind of warm liquids. LBL and Saclay groups are obtaining lifetimes of more than 100μsec for TMP. For TMS, College de France obtained $\tau=100\mu$sec and Pennsylvania and Japanese groups obtained $\tau\sim1\sim10\mu$sec. Recently, Japanese group observed signals from TMG (Fig.1) and confirmed that TMG is also usable for a calorimeter.

§Ⅲ. Material Compatibility and Long-term stability

One of the most important issues for warm liquid calorimetry is the material compatibility, because it has a profound impact on design and costs of large warm liquid calorimeters, especially for the swimming - pool type configuration.

We just started materials tests for a limited numbers of materials. Preliminary results of the test are summarized in Table Ⅰ. Time dependences of the ionization yields are also being studied at several institutes. Fig. 2 shows the results from Pennsylvania for the TMS chamber with lead absorber plates in the liquid. The data were taken for a period of about two months and the ionization yield is falling very slowly [$10^{-0.001t(\text{days})}$]. The measurements have since been extended to a six-month period with the same results. Fig. 3 shows the results from Japan of the TMG with lead plates. The ionization yield at E=6.25keV/cm is falling as $10^{-0.0026t(\text{days})}$ for the period of two weeks, which is faster than the Penn's results. The outgasing from the viton seal, the lead plates or some other materials could cause this declining effect in either case. We need more study for the lead plates, which are going to be placed in the liquid.

§Ⅳ. Radiation Damage

The deteriation of warm liquids due to radiation may not be so important for the swimming-pool design of the calorimeter, since it can be so designed to recirculate and repurify the liquid whenever it is necessary. No systematic study has been carried out on the radiation damage for the warm liquids except the one by Holroyd et al. for TMP. Fig. 4 shows the electron lifetimes for TMP as a function of radiation dosage, indicating strong radiation resistivity upto ~ 10^5 greys.

§Ⅴ. Electrostatic Transformer

To obtain a fast signal response, the electrostatic transformer concept was developed to reduce the tower capacitance by a series connection of the gaps as shown in Fig. 5. This transformer works in magnetic field and the reduced detector capacitance results in a faster signal response and better signal to noise ratio compared with the parallel connection of the gaps.

LBL has been developing the electrostatic transformer by using various test modules. The read-out with this transformer is ready to be tested at LBL using cosmic rays. The critical problem is the increase of cross-talk from tower to tower, but results thus far are encouraging. Further study is being actively pursued.

§Ⅵ. Preliminary Results from T795

The test beam experiment (T795) is being carried out at Fermilab from March 1990, initially using 13 UA1 type thin sealed boxes filled with TMP. Fig. 6 shows the detector setup for this experiment. The experiment primarily aims to measure e/h as a function of (1) absorber-to-TMP thickness and (2) absorber material dependence such as lead and iron. The setup is highly modularized, with the absorber plates and TMP boxes suspended on separated hangers.

Fig. 7 shows the energy spectra for the 50 and 100GeV electron beams obtained from the first run. The preliminary results from this first run show that

1. noise level ~ 2700e per electrode
2. muon signal ~ 1900e per electrode
3. $\sigma/E \sim 20\%\sqrt{E}$

as expected for the 13 TMP boxes.

In the November run, we expect to have the 140 TMP boxes and to complete the study of e/h, including the energy resolution. The results from this experiment will be reflected to some extent in the design of the test beam module expected to be installed in Spring, 1991.

Table I material compatibility for warm liquid ionization chambers

material	LBL	Japan	PENN	Saclay	College de France	UA1
Stainless Steel	◎	◎	◎	◎	◎	◎
Indium		○				
Copper	◎	◎			◎	
Teflon		○				
Viton		○	○			
Macor		○				
Lead	○	○	◎		○	
Aluminium	○					
G10						
Kapton	○					
CERAMIC	◎			◎	◎	◎
Vespel					○	
Peek					○	

◎ : good

○ : tests underway but not completed yet. Preliminary results look promising.

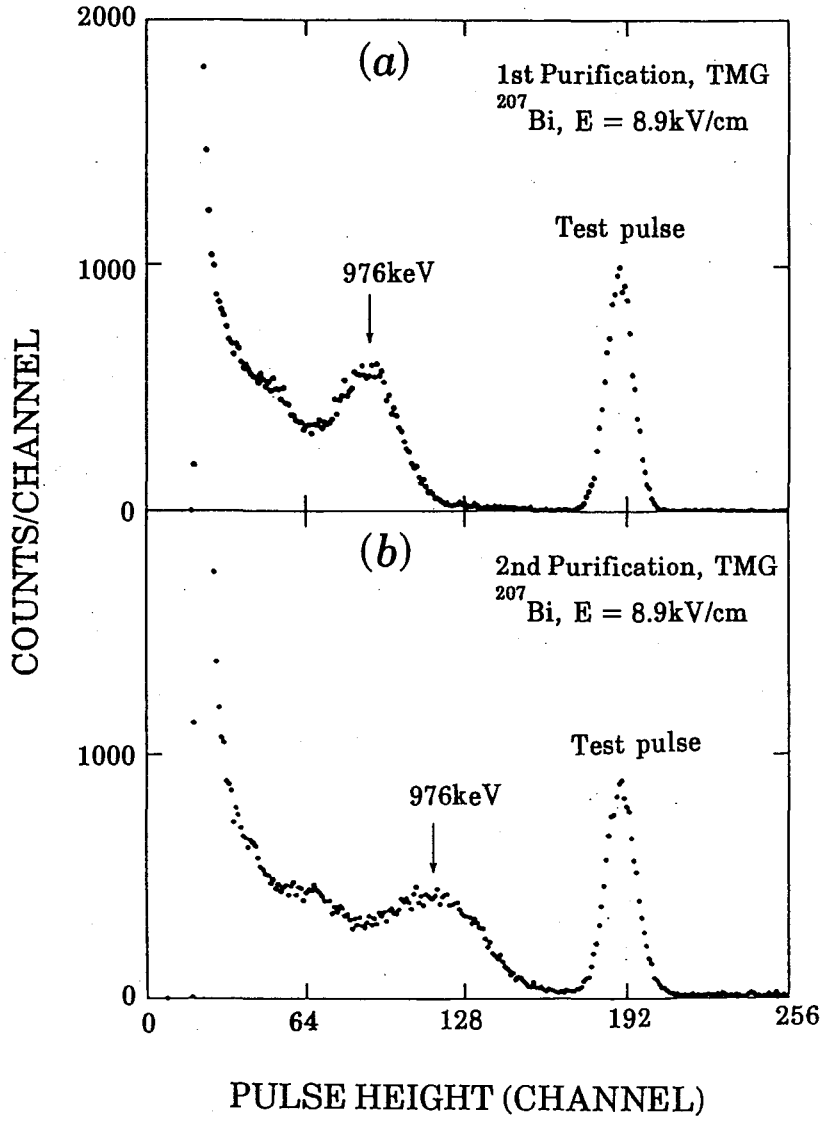

Fig. 1

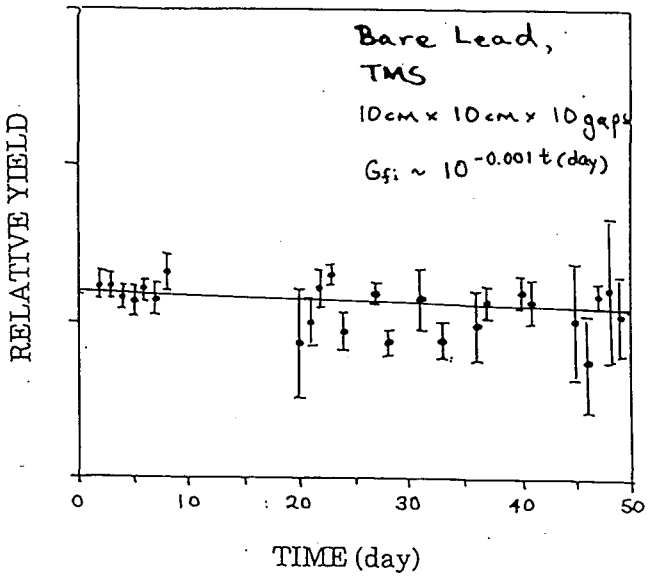

Fig. 2

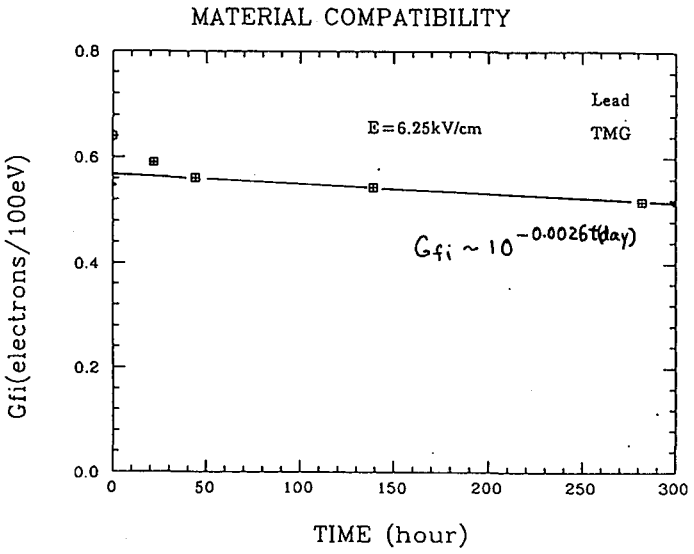

Fig. 3

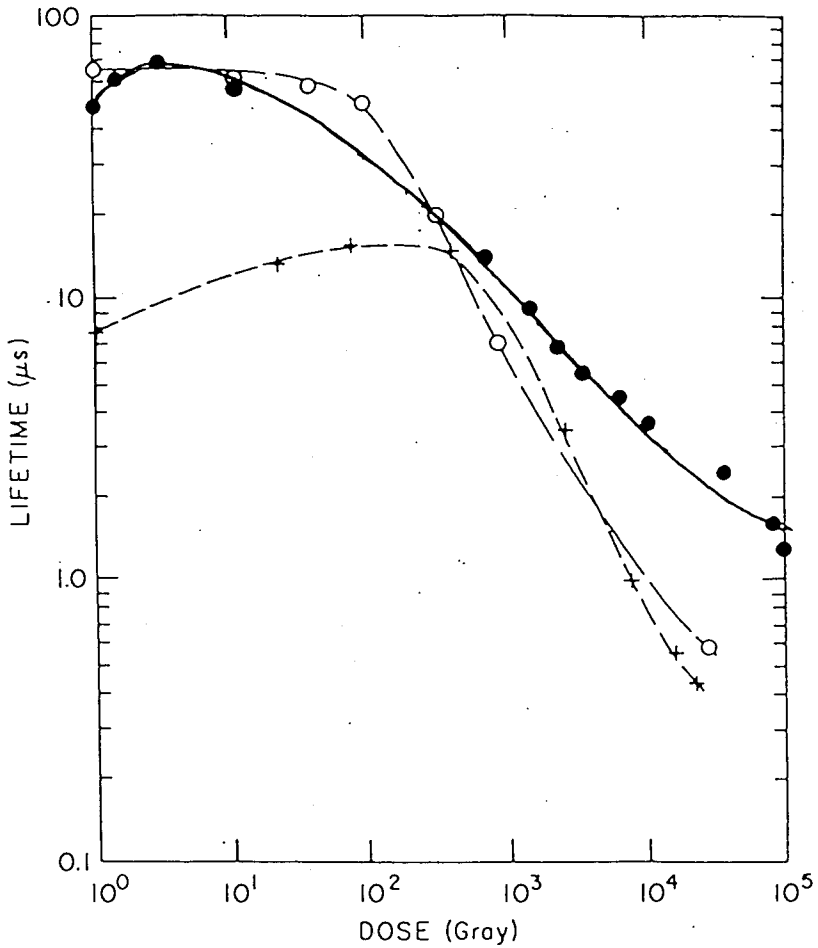

Electron lifetime vs dose for: ···+···, —●— TMP in glass cell with Pt electrodes; and for —○— 2,2,4-trimethylpentane in stainless steel cell.

Fig. 4

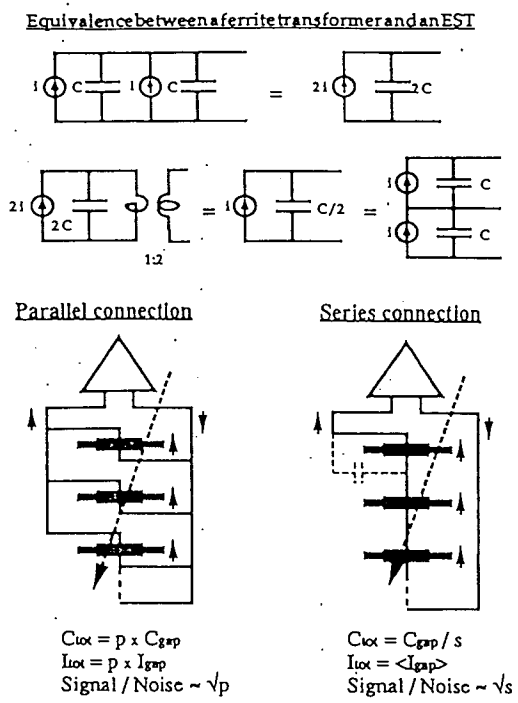

Fig. 5

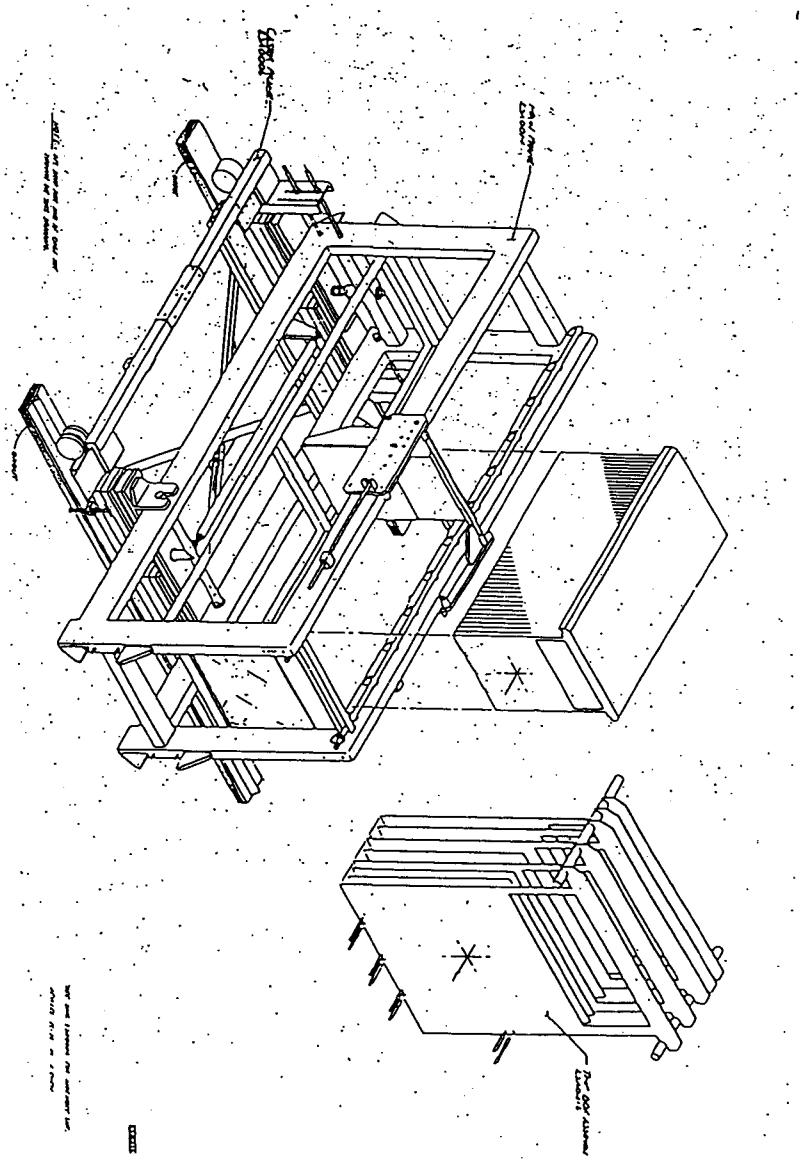

Fig. 6

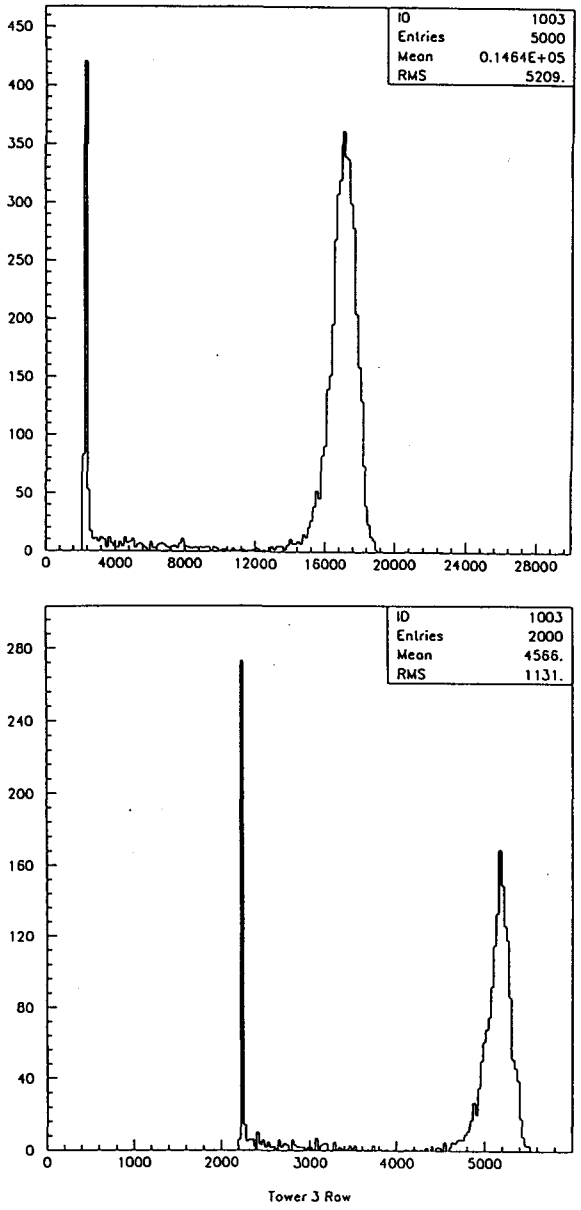
ID 1003
Entries 5000
Mean 0.1464E+05
RMS 5209.
0 50 100 150 200 250 300 350 400 450
0 4000 8000 12000 16000 20000 24000 28000
ID 1003
Entries 2000
Mean 4566.
RMS 1131.
0 40 80 120 160 200 240 280
0 1000 2000 3000 4000 5000
Tower 3 Row

Fig. 7

Liquid Argon R & D for the SSCL

A. Skuja

Department of Physics and Astronomy,

University of Maryland, College Park, Maryland 20742, U.S.A.

ABSTRACT: A brief summary of some of the work being pursued in the United States as part of an R & D project for the SSCL will be presented

Liquid Argon (LAr) sampling calorimeters have been used in high energy physics experiments for over a decade, so that considerable experience and knowledge exists about their performance, strengths and limitations. These attributes - survivability (radiation,etc.), hermiticity - have lead to the conlcusion that LAr calorimetry may be indeed one of the important technologies for SSC experiments.

The R & D work in the US is concentrating on adopting these known technologies to the SSC environment [1]. We wish to establish if Pb-LAr calorimeter can be built with an e/π ratio approximately equal to unity. We wish to establish if charge collection times in LAr can be reduced sufficiently to match the SSC operating environment without jeopardizing calorimeter resolution or $e/\pi = 1$. Finally, we want to establish if calorimeter readout can be devised that will operate in a magnetic field in a sufficiently noise free environment.

We plan to construct and test in a beam of hadrons and electrons a LAr module of sufficient transverse dimensions and deep enough longitudinally to measure:

(a) the energy resolution,

(b) e/π, and

(c) containment

of various absorbers. At present we wish to measure the response of

(a) pure Pb

(b) Pb clad with Fe (or other relatively low Z material) predicted to reduce the electron response

(c) Uranium

These stacks will be exposed to low energy beams (0.5 GeV to 20 GeV) at Brookhaven and eventually to higher energy ones at Fermilab.

Although the e/π and resolution obtained from Uranium and LAr as measured by $D\phi$ and HELIOS at 100nsec measurement time are probably acceptable for an SSC calorimeter, no such measurements exist for Lead. The only full scale Pb/LAr tests have used very shallow stacks and/or have large errors. In addition to the difficulties associated with handling, the cost of Uranium may be prohibitively high to use it for calorimetry at the SSC. We will manufacture at least the two Pb stacks. A Uranium stack will only be manufactured if time and money permit. It should be noted that the existing HELIOS calorimeters will be exposed to low energy particles by that collaboration, so that direct comparisons between Pb and Uranium can be made even if we do not construct a Uranium stack ourselves.

It should be stressed that no reliable measurements exist for Pb stacks. It is possible that an 8λ Pb-LAr calorimeter may yield an e/π reponse well below that measurement of 1.24 by SLD for their calorimeter (2.8λ Pb-LAr backed by 5λ Fe-MWPC). The integration time may also affect this ratio, so that it must be measured with response times appropriate to the SSC (100nsec or less).

The stacks will be built in such a manner that they can use the same electronics. To ensure that the tests can actually be begun during the next running period at Brokhaven (January 1991), the electronics design will be a modification of the HELIOS electrode design and corresponding electronics chain. We will measure the reponse and noise levels for at least three values of the charge collection time t_m: 50, 100 and 150 nsec. Only the pure Pb stack will be tested at this time, but the pulse shaping electronics will be built so that it can be easily modified to measure any of the 3 collection times. A stack of Pb clad with Fe (predicted to reduce the electron response by 5%) will be tested in a later running period. We feel that these two measurements will provide sufficient information to design a true SSC prototype stack.

The module will have a transverse size of $100 \times 100 cm^2$ and a final depth of 10λ. However, to keep the radius of the cryostat to a minimum, the corners of the stack will be removed (making it somewhat octagonal in shape). In addition, there is not enough money in the 1990 SSCL R & D allocation to construct the full 10λ stack,so that one of only 7.5λ will be ready for initial measurements in the low energy beams of Brookhaven.There will be four equal longitudinal divisions in readout, each division consisting of 2.5λ and 80 readout channels (320 for the full 10λ stack). A unit cell within the stack consists of a sheet of Pb, a 2mm argon gap, a signal board(1.6mm) and another 2mm argon gap. The first Pb stack, now under construction BNL, will have 12mm thickness of Pb (chosen because this thickness minimizes the electron reponse as predicted by EGS). The stack is held together longitudinally by 16 tie rods.

The signal boards have 2.54 cm strips with alternately interleaved x and y readout in each section. The interleaving provides redundancy, extra information about transverse profile of the shower, and a measure of the sampling fluctuations. The connection scheme and coupling transformer will follow closely the HELIOS method of achieving low inductance charge transfer to the pramp. The preamps will be based on JFET's on high resistivity silicon being developed jointly by BNL and Interfet Inc. under a different SSCL R & D project. This will allow the preamp hybrid to operate directly in the LAr. Heat dissipation will not cause any problem in the test, since the preamps will be on the outer perimeter of the stack, however, it does leave this problem to be solved for an SSC calorimeter until later. The shaping amplifiers will allow t_m to be canged easily from 50 to 100 or 150 nsec.

The detector capacitance is crucial if we want fast charge transfer, hence the signal boards must be coupled to the amplifiers using transformers. The traditional method used in HELIOS and to be employed in the R & D stack consists of ferrite transformers. These however, cannot operate in magnetic fields. The University of Rochester group is investigating shielding methods based on the "Russian Box" principle. LBL is designing

electrostatic transformers that could be used in any ionizing liquid, again under a different R & D umbrella. The detector capacitance could also be affected by variations in the Pb thickness. However, we have obtained samples from SEAFAB of Seattle that have $\pm 0.009cm$ variations, and would meet our tolerance requirements.

The University of Washington group is building the cryostat. It is similar to the SLD test cryostat which they have already built. The cold signal feedthroughs will be of the MKII / SLD type.

The University of Maryland will be reponsible for the trigger and DAQ for the beam tests. Tile development is being pursued at Michigan State University, radiation hardness tests at Florida State University, and non-conventional electrode schemes at the University of Arizona.

REFERENCES

1. G.S.Abrams, et al., *Proposal for Research and Development of a Liquid Argon Calorimeter for the SSC*, 2 October 1989.

Proceedings of the International Workshop on Solenoidal Detectors for the SSC
KEK, Tsukuba, Japan, April 23-25, 1990

Design of a Liquid Argon Calorimeter for SDC

KEK and Kawasaki Heavy Industry Co. Ltd

Presented by Y.Unno
Department of Physics, KEK
Tsukuba, Ibaraki 305, Japan

Abstract

The structural design of a Liquid Argon Calorimeter for the Solenoidal Detector Collaboration (SDC) has been developed through joint work between KEK and Kawasaki Heavy Industry. Cryostat wall thicknesses, concepts for cold mass support, and close-out of the cryostat are presented. A scheme of lateral and longitudinal segmentation is given and the number of readout channels are presented. Capacitances of the EM and HAD segments are evaluated along with signal speed, limitations of the cables, and thermal noise. Implications for the interleaving of HAD segments and location of preamps are discussed.

1. Introduction

Liquid calorimetry using the liquid argon as an ionization medium of the calorimeter has many advantages such as; 1) durability in a high radiation environment, 2) ease of absorber/readout segmentation, 3) linear, uniform, and stable response, 4) straightforwardness in precision charge injection, 5) simple calibration which is a result of 3) and 4), 6) capability of operation in a magnetic field, and 7) well-established technology.

To establish the liquid argon calorimeter (LAC) as a viable candidate for the SDC detector, we must demonstrate that the physics performance is acceptable despite; a) the presence of dead material due to the cryostat walls and support structures (hermeticity), and b) slow drift speed of electrons in the liquid argon (speed of response).

Recognizing that the engineering issues are critical, KEK and KHI[1] have been working on an engineering model and have proposed a candidate LAC design. Our first presentation was made to the SDC collaboration meeting at Dallas, March 11-13, 1990, and this is a progress report.

2. Design of the cryostat

Although an engineering design study of a LAC for SSC has been done[2], the design is not strictly applicable for the SDC. The superconducting magnet was to be placed outside of the calorimeter. In the ACS design[3], the magnet is inside of the calorimeter. This magnet location offers added flexibility to the design of the calorimeter, but trade-offs are more complex.

Design conditions: Design operating conditions for the cryostat are tabulated in Table 1. The differential pressure on the wall of the inner vessel (LAr vessel), Δp_{LA}, is +3.9kg/cm^2 under the normal operation and -1.0kg/cm^2 when the inside is evacuated to purify the internal volume. The differential pressure on the wall of the outer vessel (Vacuum vessel), Δp_V, is -1.0kg/cm^2 under the normal operation and +0.85kg/cm^2 in case a liquid argon spill occurs due to breakage of the LAr vessel. We assume the same design pressures as in the Martin Marietta engineering study.

The whole calorimeter is composed of one Barrel, and two Endcap calorimeters. We assume lead as the converter, with a calorimeter thickness of approximately 8 interaction lengths (live with lead and liquid argon). The weight of the calorimeter is roughly estimated and tabulated in the table. For the calorimeter vessels, we choose to use 5083 aluminum alloy. This alloy has more than twice the strength per radiation length of Stainless Steel and excellent welding characteristics.

To obtain suitable vessel wall thicknesses and strength, we utilize; (1) the formulae in the ASME Boiler and Pressure Vessel Code Sec. VIII. Div.2; (2) a finite element method (FEM) of analysis for axially symmetric shells developed by KHI; and (3) 3-dimensional FEM analysis. We are in stage (2)

and 3-dimensional analysis has just begun. The vessel's primary stresses are required to be less than the maximum allowable stress (S_m~7kg/mm^2) and the secondary stresses less than $3S_m$. Instability is being evaluated with FEM. Structural analysis is still in progress and the numbers given in this report are preliminary although they are converging.

Table 1. Design conditions for the LAr Calorimeter

Differential pressures:	
LAr vessel (Δp_{LA})	+3.9[(a)] / -1.0[(b)] kg/cm^2
Operating pressure	+0.7 / -1.0
Safety relief pressure	+0.4
LAr liquid head (13m)	+1.8
Vacuum	+1.0 / 0.
Vacuum vessel (Δp_V)	-1.0[(a)] / +0.85[(c)] kg/cm^2
Weight (Pb converter @~8λ) :	
Barrel	3500 tons
Endcap	1000 tons each
Material	Aluminum alloy A5083-O

(a) normal operation, (b) evacuation, (c) liquid argon spill-out

Cryostat structure: We show the cross-sectional view of the calorimeter in Fig.1. The characteristics of the Barrel design are; dished heads, two inner cylinders in the LAr vessel, radial-stay plates connecting the two inner cylinders to the outer-most cylinder of the LAr vessel, and washers penetrating the hadronic (HAD) and the electromagnetic (EM) modules. The Endcaps also have dished heads, inner cylinders (we are discussing to have one or two) and washers. Dished heads are effective to distribute the stress and to make the wall thickness thinner. The two inner module-support cylinders also support the LAr heads, further making the head wall-thickness thinner by reducing the effective vertical span of the wall. The radial-stay plates provides longitudinal strength and assist the inner cylinders in supporting module gravity loads. The washers contribute to both vessel and module support, and help to maintain the whole calorimeter round. The radial-stay plates add dead area in the azimuthal angle (ϕ) obviously, no such plates are used in the EM section. If the plates in the HAD1 section cause serious trouble, we will investigate an alternative plan to remove all the plates in the HAD1 section while the plates in the HAD2 section are kept. We put the thin washer in the EM section to make the inner-most Barrel LAr cylinder thin and yet to be strong against bucking. In this design, the EM and the HAD modules will not contribute to the vessel's structural strength.

This SDC Calorimeter design provides relatively thin vessel walls, convenient module installation and support, and allows dis-assembly access to the modules for maintenance, if necessary. The wall thicknesses we have at present are shown in Fig.2. The most up-to-date radial dimension of the Barrel is given in Fig.3, which are subject to change as SDC subsystem trade-off decisions are made.

Support of the whole calorimeter: A conceptual design for cold mass and vacuum shell supporting legs is given in Fig.4. The LAr vessels of the Barrel and the Endcap calorimeters are supported with the legs on the sides of the vessel cylinder. The calorimeter is placed on a rigid carrier and slides into final position. The carrier also will be an utility housing such as cryogenic valves, vacuum system, etc. The liquid argon calorimeter by itself will need no magnetic-flux return-yoke close to the calorimeter.

Assembly and close-out: A close-out scheme is presented in Fig.5. When modules are being assembled into the LAr vessel, the vessel is reinforced with the steel "girder rings" placed around the outermost LAr cylinder (Fig.5(a)) and the whole vessel will be rotated on the roller-supporter. After the module assembly, the LAr heads will be attached and the weight is transferred from the "girder" to the cold mass support (Fig.5(b)). The LAr vessel, then, slides into the outer Vacuum vessel which is on the rigid carrier (Fig.5(c)). The heads of the Vacuum vessel will then be attached and the close-out is finished.

3. *Design of the modules*

In this section, we present segmentation of the EM and HAD modules in the longitudinal and transverse directions, number of readout channels and the channel capacitances. We discuss the basics of the speed of response and derive requirement for the cable length, etc. We also discuss the basics of the equivalent noise charge and derive level of the thermal noise. Finally, we present electrical readout scheme, cable connections, and location of preamps.

3.1 Segmentation

Segmentation: We show the lateral segmentation of the modules in Fig.6. We employ the basic tower segmentation of $\Delta\eta$=$\Delta\phi$=0.05 in η and ϕ directions. Within a tower, a longitudinal section of the EM module is further subdivided into $\Delta\eta$=$\Delta\phi$=0.025. The finer segmentation is to have a position resolution of less than 5mm for the electromagnetic showers. The segmentation maintains $\Delta\eta$=$\Delta\phi$=0.05 until the physical tower width becomes a value approximately equal to the FWHM EM shower width at shower maximum (about 100mm), after which the tower width remains constant. The ϕ division is set to 128 in 2π in the Barrel. In the Endcap, 2π in ϕ is divided into 1/16 symmetric sectors and segmented into towers in a sector as shown in the fig.6. In the Endcap, 2 meter is the radius for the physical size of a tower be 100mm in ϕ. Over the 2m radius the sector is divided into 8, and inside the 2m radius the sector is divided so that the tower width remains constant (about 100mm) in η and ϕ.

The longitudinal segmentation is shown in Fig.7. A tower is modularized into 3 blocks, EM, HAD1 and HAD2. The EM module is further divided into one "massless" and two EM calorimeter sections. The "massless" gap is made of G10 pc boards only. One EM calorimeter section is subdivided into 4 to have $\Delta\eta$=$\Delta\phi$=0.025 segmentation. HAD1 and HAD2 are not divided further in the sense of readout. They are, however, "interleaved" into several preamps so that failure in a preamp will not kill the whole HAD1 or HAD2 section. The interleaving is also required to have an acceptable capacitance for one preamp. The interleaved outputs are extracted out of the cryostat and ganged into one readout channel.

Number of readout channels: The number of readout channels are counted and summarized in Table 2. When an EM or HAD module of a tower is divided by the washers, we count the channel separately for each modules. We have about 70k EM and 28k HAD, 98k in total, readout channels. These are "Data Acquisition" number of channels. When number of cables from the cryostat are in question, number of "interleaving" should be counted for the HAD sections.

To trigger the calorimeter, we propose an idea of the following trigger tower formation. Since 128 is the number (in ϕ) and 8 is a divisor, we take a sum of 8x8 ($\Delta\eta$x$\Delta\phi$=0.4x0.4) towers as a trigger tower. In η there are 98 towers, including the Endcap, and we form 12 trigger towers. In ϕ we form 16 trigger towers (there is a detail in the Endcap but let's ignore here). We also have triggers for the EM and HAD separately. The number of basic trigger towers is 384. To cover the boundaries between the trigger towers, we further form another 3 layers of the trigger towers, which are half-overlapped. As a result, we will have 1536 trigger channels.

Table 2. Number of readout channels

Cal.	EM modules	HAD modules
Barrel	45568	13312
Endcap	12432x2=24864	7184x2=14368
Total	70432	27680
Grand total	98112	

Detector Capacitances: We have calculated the detector capacitance according to the above segmentation and plotted the values in Fig.8. The inner radius of the EM module was 2.15m for the calculation and is slightly smaller than the proposed 2.25+α(walls, vacuum, clearance...) in the EOI. Typical capacitances of the longitudinal segments are summarized in Table 3.

Table 3. Detector capacitances (nF)

η	"massless"	EM1	EM2	HAD1	HAD2
		Barrel			
0.0	0.30	0.44	4.1	12.0	21.2
0.5	0.35	0.50	4.6	13.7	24.1
0.9	0.44	0.65	5.9	17.5	30.9
		Endcap			
1.5	0.43	0.61	5.2	11.9	16.2
2.0	0.27	0.38	3.2	7.3	9.9
2.5	0.22	0.30	2.6	5.9	8.0

3.2 Speed of response[4]

Basics: A schematic for the response at various stages is shown in Fig.9. Before the charge-amp the vertical axis is the current, and after the amp the voltage. At the detector capacitance the current in time is a triangle with a width of drift time, t_d. It is the best to integrate over the whole drift time, however, it is not necessary to do so because the peak current is at the beginning and effect of cutting the tail enters slowly.

In a real situation, a large electrode capacitance is connected to a preamplifier with a cable or a transmission line. Its effect is to slow down the transfer of the charge from the detector capacitance into the preamplifier due to the inductance of the connection. The peak of the current is now at t_r, named as the charge transfer time. To have a stable integrated charge, it is desirable to have the charge transfer time well less than the peaking time of the impulse response of the shaping, t_p. The requirement for the fast speed is the requirement for the short peaking time, and, then, the requirement for the fast charge transfer time.

Cables have inductance and capacitance. The inductance contributes to the charge transfer time while the cable capacitance contributes to the equivalent noise charge (ENC) due to the thermal noise of the preamplifier. Two choices are possible. One is to require the cable capacitance to be much smaller than the detector capacitance so as ENC to be the smallest, effectively only due to the detector capacitance. The other is to allow a large cable capacitance determined by other requirement such as the required cable length and not to care about its contribution to ENC. The latter is possible if the sum of the detector and the cable capacitance is smaller than the capacitance allowed from the total ENC requirement.

In the following we think of the magnetic transformer coupling (MT) and the electrostatic transformer coupling (EST). The EST coupling is a new idea, in which the detector cells are connected in *series* compared to the conventional parallel ganging. The effect is the reduction of the detector capacitance by $1/n^2$ of parallel ganging when n cells are connected in series. Since detector capacitance is reduced, the requirement for the cable inductance will be relieved and also ENC will be reduced. This is a good news. The bad news is non-linear response in the n cells and large cross-talk to the adjacent towers. In the conventional ganging, the cross-talk is the ratio of the cross-talk capacitance to the high voltage blocking capacitance. The cross-talk capacitance is usually less than 10% of the detector capacitance and the blocking capacitance is more than 10 times larger than the detector capacitance. Thus the cross-talk is usually less than 1%. On the other hand, in the EST, the blocking capacitance is a detector cell seen from the cell in the n cells and the cross talk is about 10%. In reality, the capacitance network of the EST coupling is not as simple as the conventional coupling and requires simulation to have a realistic response[5].

In the MT coupling, the ferrite-core transformer will be placed in front of the preamps. The effect of the MT is not for speeding up the response but for reducing ENC by reducing the total capacitance of detector and cable. We seek the smallest ENC in the MT coupling while in the EST we seek a long cable length, so long we can put the preamps out of the cryostat.

The MT coupling: If the charge transfer time is longer than the propagation time through the line ($t_r > t_{pd}$), the inductance of the line dominates the transmission line effects. The charge transfer time is approximately given as

$$t_r = 3.5\sqrt{LC_D}$$

where C_D is the detector capacitance and L is the sum of inductance in the connection. L is consisting of the inductances between the electrode to the transmission line (L_{DC}), of the transmission line (L_C), and the stray inductance (L_S) as shown in the equivalent circuit. We require;

$$t_r \le t_p/f_r \text{ and } C_c \le C_D/f_c$$

where C_C is the capacitance of the transmission line. The factors f_r and f_c express the requirements for the fast response and for the small contribution of cable capacitance to ENC. We take f_r=2 and f_c=3 for the numerical calculations. The derived characteristics of the transmission line are tabulated in Table 4.

The propagation time through the line, t_{pd}, is given as

$$t_{pd} = \sqrt{L_c(C_c + C_D)} = \frac{t_r}{3.5}\sqrt{1 + \frac{1}{f_c}}.$$

As stated, $t_{pd}<t_r$, and the tabulated relations should be valid for $f_c \ge 0.1$. Since we can not make an infinitely wide transmission line, there is a practical minimum cable inductance (let it be L_O) and we have a limit on the maximum detector capacitance to be connected as;

$$C_D \le \frac{1}{L_{DC} + L_o + L_s}\left(\frac{t_p}{3.5f_r}\right)^2.$$

The EST coupling: We dismiss the f_c relation and, instead, take the cable length l_C as a parameter. The derived characteristics of the transmission line are listed in Table 5. In the expressions the detector capacitance C_D is the capacitance of the parallel ganging and n is the transformer ratio (n cells in series). When C_D becomes small, L_C becomes large and C_C small. Practically, this trends are cut at a limit of a twisted pair cable, e.g. Z_O=110Ω which has a 0.95μH/m unit inductance and a 80pF/m unit capacitance, as an example. Then the propagation time through the line is;

$$t_{pd} = \sqrt{L_c C_c} = 8.7(ns/m)l_c.$$

The range $t_r<t_{pd}$ should be valid for $l_c \le$ 5.7m (@t_p=100ns). For the cable length more than this we require simulations for the response and relations.

Table 4. Derived cable characteristics for the MT coupling

Requirements:

$$t_r \le \frac{t_p}{f_r},\ C_c \le \frac{C_D}{f_c}$$

then,

$$t_r = 3.5\sqrt{LC_D}\ ;\ L = L_{DC} + L_c + L_s$$

$$L_c = \frac{1}{C_D}\left(\frac{t_p}{3.5f_r}\right)^2 - L_{DC} - L_s,\ \left(L_c > L_o \Rightarrow C_D < \frac{1}{L_o + L_{DC} + L_s}\left(\frac{t_p}{3.5f_f}\right)^2\right)$$

$$Z_0 = \sqrt{\frac{L_c}{C_c}} \cong \frac{\sqrt{f_c}}{C_D}\left(\frac{t_p}{3.5f_r}\right)$$

$$l_c = 3 \times 10^8\sqrt{\frac{L_c C_c}{\varepsilon_r}}$$

$$t_{pd} = \sqrt{L_c(C_c + C_D)} = \sqrt{L_c C_c}\sqrt{1 + \frac{C_D}{C_c}} \cong \frac{t_r}{3.5}\sqrt{1 + \frac{1}{f_c}}$$

where

t_r: charge transfer time	t_p: peaking time
L_{DC}: detector-cable inductance	L_C: cable inductance
L_S: stray inductance	Z_O: characteristic impedance
l_C: cable length	t_{pd}: propagation delay
ε_r: relative dielectric constant	L_O: minimum cable inductance

Table 5. Derived cable characteristics for the EST coupling

Requirements:

$t_r \le \frac{t_p}{f_r}$, l_c *fixed*

then

$L = L_{DC} + L_c + L_s \cong L_c$

$L_c = \frac{n^2}{C_D}\left(\frac{t_p}{3.5 f_r}\right)^2 \le 3.8\,\mu H^{(*)}$

$C_c = \left(\frac{l_c}{3\times 10^8}\right)^2 \frac{\varepsilon_r}{L_c} \ge 320 pF^{(*)}$

$Z_o = \sqrt{\frac{L_c}{C_c}}$

$t_{pd} = \sqrt{L_c C_c} = \frac{\sqrt{\varepsilon_r}\, l_c}{3\times 10^8}$

where (*) assumes Z_O=110Ω twist-pair cables (dL/dl=0.95μH/m, dC/dl=80pF/m) and the cable length 4m.

Numerical values of the cable characteristics are summarized in Table 6 for the detector capacitance at C_D=5nF. The numbers are listed for two shaper impulse-response peaking times of 100ns and 50ns. The limitations on the cable length and the detector capacitance are $l_c \le 1.2$m and $C_D \le 12$nF for t_p=100ns, and $l_c \le 0.5$m and $C_D \le 5$nF for t_p=50ns. Although the required speed should be determined from the physics point of view, we take 100ns as the design criteria for the moment.

Table 6. Cable characteristics at C_D=5nF for t_p=100ns and 50ns

	t_p=100ns		t_p=50ns	
	MT	EST[a]	MT	EST[a]
L_c[b]	37nH	1020nH	6nH	255nH
C_c	1.7nF	0.7nF	1.7nF	2.8nF
Z_o	4.7Ω	38Ω	1.9Ω	9.5Ω
t_{pd}	15.9ns	30.3ns	6.4ns	27.6ns
l_c	1.2m	4.0m	0.5m	4.0m
max.C_D	12nF[c]		5nF[d]	

(a) n=5 and l_c=4m are fixed

(b) $L=L_{DC}+L_C+L_S$ where L_{DC}=2nH and L_S=2nH are assumed

(c) L_O=12.6nH (symmetric ground: w/h=10mm/0.2mm and l=1m)

(d) L_O=6.3nH (symmetric ground: w/h=10mm/0.2mm and l=0.5m)

3.3 Thermal noise

Equivalent Noise Charge (ENC): We assume a conventional JFET input charge preamplifier. An equivalent circuit is given in Fig.10. The capacitance C_O is the sum of all the capacitances in front of the preamps, such as detector, cross-talk, and cable. The capacitance C_{GS} is the capacitance of the control electrode of the transistor. We can express the equivalent noise charge due to the intrinsic series noise of the amplifying device as follows. If a charge q_S is induced on the capacitance C_O, then the charge on the control electrode C_{GS} will be $q_S C_{GS}/(C_O+C_{GS})$. Then, the equivalent noise charge induced on the capacitance C_O by the noise charge due to the series noise voltage $\langle v_G^2\rangle = 4kTR_S$ on the capacitance C_{GS} is;

$$\langle q_{sn}^2\rangle = \left(\frac{C_o + C_{GS}}{C_{GS}}\right)^2 \cdot C_{GS}^2\, 4kTR_s = 4kTR_s(C_o + C_{GS})^2 = 4kT\frac{a_n}{g_m}(C_o + C_{GS})^2$$

$$= 4kTa_n\frac{t_{el}}{C_{GS}}(C_o + C_{GS})^2 = 4kTa_n t_{el} C_o\left(\sqrt{\frac{C_o}{C_{GS}}} + \sqrt{\frac{C_{GS}}{C_o}}\right)^2$$

where we have used the relations $R_S=a_n/g_m$ (a_n=2/3 for JFET) and $g_m=C_{GS}/t_{el}$. g_m is the transconductance and t_{el} is the electron channel transit time (t_{el}=0.5ns is being taken).

The factor

$$f=\left(\sqrt{\frac{C_o}{C_{GS}}}+\sqrt{\frac{C_{GS}}{C_o}}\right)$$

is called the capacitance mismatch factor, and the minimum is 2 if matched (C_O=C_{GS}). The matching condition can be achieved with the magnetic transformer or with the eletrostatic transformer by transforming the capacitance C_O into $C_O/n2$ where n is the transformer ratio. The matching ratio is given by $n=\sqrt{C_O/C_{GS}}$.

The optimum noise is the noise passed through the CUSP or approximately the triangular shaping, and $ENC_{opt}^2=<q_{sn}^2>/t_p$ where t_p is the zero-to-peak time (impulse response peaking time). When the bipolar shaping of m integrations is used, ENC is about 1.4 times larger than ENC_{opt} (m=1~4).

The net result is

$$ENC=1.4\sqrt{4kTa_n}\sqrt{\frac{t_{el}}{t_p}}\sqrt{C_o}\cdot\frac{f}{n}=0.658\left(\frac{f}{2}\right)\sqrt{\frac{T(K)}{300}}\frac{1}{n}\sqrt{C_o(nF)}\ fC$$

for t_p=100ns at the input of charge preamp. When matched, the transformer ratio is n=32 at C_o=10nF and C_{GS}=10pF.

In the above argument, the feedback capacitance C_f does not play any role. The equivalent circuit for the charge amplifier can be written as shown in Fig.10. The charge is transferred into the capacitance C_{GS} first, and then it is transferred on to the feedback capacitance C_f within the amplifier response time $R_{in}(C_{GS}+C_O)$.

We have neglected the parallel noises, such as the shot noise, 1/f noise, dielectric noises. Among the available devices, JFET has the best over-all characteristics in the shot and 1/f noises which can be neglected. Bipolar transistors has larger shot noise due to the larger base current. MOSFET or Gallium-arsenide FET (MESFET) or modulation doped FET (MODFET) have larger 1/f noise.

Energy scale: To convert the equivalent noise charge into the equivalent noise energy ("thermal noise in energy unit"), we require the energy scale stating how much of charge is seen at the input of charge preamp by unit incident energy. The general formula is

$$\frac{dQ_o}{dE}=s\cdot\left(\frac{p}{\mu}\right)\cdot\frac{1}{W_i}\cdot\frac{1}{2}\cdot\left(\frac{Q}{Q_o}\right)\cdot\left(\frac{C_B}{C_D+C_b}\right)\cdot\frac{1}{n}$$

where s is the energy-loss sampling fraction in the liquid argon for the minimum ionizing particle, which is specific for the sampling cell structure, (p/μ) is the so-called (e/μ)-ratio for electrons and (h/μ)-ratio for hadrons (e.g. pions), Wi is the energy required to ionize the Ar atoms (the ionization potential), the factor 1/2 is for observing only electrons of the ion-electron pairs, Q/Q_O is the charge collection ratio, $C_B/(C_B+C_D)$ is the charge sharing ratio between the detector and the high voltage blocking capacitances and n is the transformer ratio. The (p/μ)-ratio is also specific for the cell structure but the dependence is small and we assume here (e/μ)=0.6 and (h/μ)=0.4. These are a conservative choice to see less charges. W_i is 25eV. Q/Q_O is $0.9t_p/t_d(2\text{-}t_p/t_d)$ where the factor 0.9 is due to recombination and the latter factor is due to the charge integration up to the peaking time t_p (for $t_p<t_d$). $C_B/(C_B+C_D)$ is 0.9 for C_B being 10 times C_D.

Taking the sampling cell structure as shown in Fig.3, we have the sampling fraction s=0.13 for the EM section and s=0.044 for the HAD section. The resulting energy scales are

$$\frac{dQ_o}{dE}=202\frac{t_p}{t_d}\left(2-\frac{t_p}{t_d}\right)\frac{1}{n}\ fC/GeV=\frac{88.4}{n}fC/GeV\quad(EM)$$

and

$$\frac{dQ_o}{dE}=49\frac{t_p}{t_d}\left(2-\frac{t_p}{t_d}\right)\frac{1}{n}\ fC/GeV=\frac{21.4}{n}fC/GeV\quad(HAD)$$

for t_p=100ns and t_d=400ns.

Thermal noise in energy unit: Combining the equivalent noise charge and the energy scale, we have the thermal noise in energy unit as

$$\sigma_E = 0.00744\left(\frac{f}{2}\right)\sqrt{\frac{T(K)}{300}}\sqrt{C_o(nF)}\ GeV\ \ (EM)$$

and

$$\sigma_E = 0.0308\left(\frac{f}{2}\right)\sqrt{\frac{T(K)}{300}}\sqrt{C_o(nF)}\ GeV\ \ (HAD)$$

for t_{el}=0.5ns (JFET of g_m=20mS and C_{GS}=10pF) and t_p=100ns. We show the noises for the unmatched and matched cases with magnetic transformer (MT) coupling in Fig.11. We take the temperature T=100K assuming the preamps are in the liquid argon, and the capacitance C_o to be the sum of the detector capacitance C_D, the cross-talk capacitance $0.1C_D$, the cable capacitance $C_c=C_D/3$ and the detector-to-cable capacitance C_{DC}=0.2nF. We also show the noises for the EST coupling in Fig.12. In the small detector capacitance region, the noise is dominated by the cable capacitance and is flattened. Further studies are planned to simulate the electric responses and the noises to be more realistic.

3.4 Basic design of the modules

Interleaving: Since a HAD section has a too-large capacitance for the fast response and single preamp for a HAD section has danger to lose the section in case of preamp death, we divide a section into several elements. By alternatively connecting the electrodes to the separate preamps ("interleaving"), the danger of losing a whole HAD section is spread thin. The interleaving is better than dividing the section into longitudinal segments as far as the dividing number is small since in the HAD section the electromagnetic component of the hadronic shower deposits energy in a limited longitudinal depth.

The capacitance of 12nF is the maximum for t_p=100ns. The HAD1 section will be interleaved into 2 and the HAD2 section into 3 in the Barrel (similar in the Endcaps). The signal cables from each preamps are extracted out of the cryostat and the number of cables required are about 2.5 times the number of HAD readout channels.

Connection and location of preamps: In the MT coupling, the maximum cable length is to be less than 1.2m from the electrodes to the preamps. Since the height of the HAD1 and HAD2 modules is about 0.9m, ganging cable will be placed on the both sides of the wedge-shaped modules (a module is made of two towers), and preamps will be placed in the back of the modules in the Barrel calorimeter.

While the modules in the Barrel are tilted 3 degrees to avoid the gap between the modules to be a crack, in the Endcap region the polar angle θ is so small that the tilting will not help. A plan is to have a fan-shaped modules with a height of the fan to be about 1meter. Each readout board of the cell has transmission line to the outer peripheral and ganged at the peripheral where preamps will be located. The transmission lines in cells are ganged in parallel, requirement for the cable inductance can be multiplied by the number of cells. From the point of view of radiation damage, the fan-shaped and peripheral location of preamps is desirable since the radiation decreases rapidly as the angle is going away from the beam axis. Schematics for the Barrel and the Endcap module are shown in Fig.13.

4. Summary

The liquid argon calorimeter has good characteristics such as radiation resistance, ease of calibration, long-term stability, etc. to be a candidate calorimeter in the SSC environment. Recognizing that the engineering issues are critical, we have been working on and have proposed a specific design of the liquid argon calorimeter.

FEM analysis is proceeding for the structure and wall thickness. Support scheme of the whole calorimeter has been emerging, together with the assembly and close-out schemes.

Lateral and longitudinal segmentations are defined and the number of readout channels and capacitances are deduced. The number of readout channels is about 98k.

The slow drift velocity is the fundamental but the critical limiting factor for the fast response is the charge transfer time, t_r, from the detector to the preamps together with the intrinsic thermal noise. Requiring $t_r<t_p/2$

where t_p is the peaking time of the impulse response of the shaper, cable length are required to be less than 1.2m and the maximum detector capacitance to be less than 12nF for the practically smallest thermal noise at t_p=100ns in the magnetic transformer (MT) coupling.

With the matched magnetic transformer coupling and a bipolar shaping, the thermal noises are <4MeV in the "massless" gap, <4MeV in EM1, <15MeV in EM2, <100MeV in HAD1 and <130MeV in HAD2, resulting in the total noise of <165MeV per tower, and <130MeV per 8x8 EM and <1.3GeV per 8x8 HAD trigger tower. The electrostatic transformer coupling (EST) with the transformer ratio of 5 and the cable length of 4m gives twice or more thermal noise, which is dominated by the cable capacitance in the small detector capacitance region (C_D<5nF).

A scheme for a module shape, number of interleaving, connections between detector elements and preamps, and preamp locations are being developed.

---

[1]F.Abe, K.Amako, S.Inaba, H.Ikeda, M.Ikeda, H.Iwasaki, N.Ujiie, Y.Unno(contact person), K.Ogawa, N.Kanematsu, A.Kusumegi, T.Kondo, Y.Sakai, Y.Takaiwa, T.Haruyama, H.Hirayama, A.Maki, K.Tsukada/KEK, Y.Watanabe, T.Tanimori/Tokyo Inst. Tech., K.Nishikawa/INS,Tokyo Univ., K.Kuboyama et al./Kawasaki Heavy Ind.

[2]Summary report on an engineering design study of a hermetic liquid argon calorimeter for the SSC, T.Adams et al, Martin Marietta, Jan.(1990)

[3]An Air-Core Solenoid detector, presented by T.Kondo, KEK-Preprint 89-191

[4]V.Radeka, Ann. Rev. Nucl. Part. Sci. 38(1988)217

[5]M.Levi, LBL memorandum

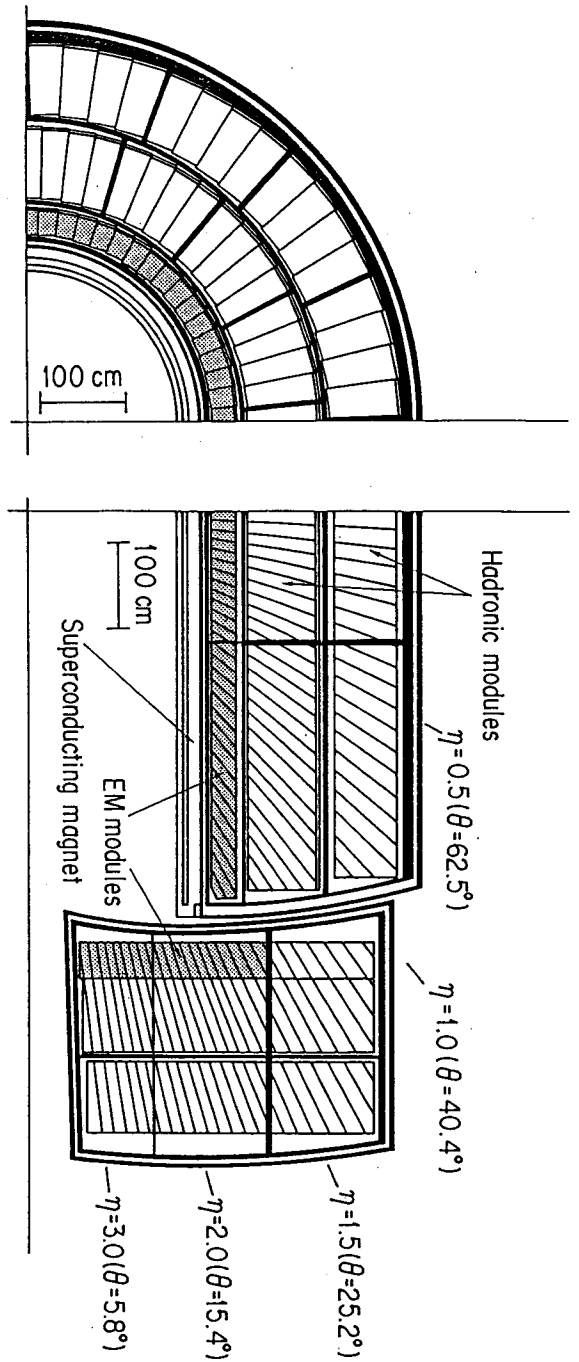

Fig. 1 Cross-sectional view of the LAr Calorimeter

1990.6.20

Cryostat Wall thickness

- Washer / Stays are added
- Positive pressure in the vacuum layer included
  ... and still in progress

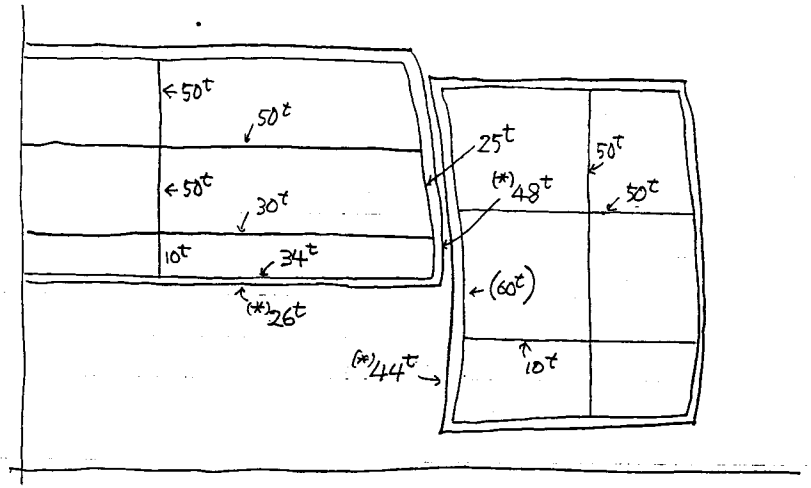

(*) Vacuum layer +0.85 kg/cm² (12 psi) by LAr spill
Instability calculated !

Fig. 2 Cryostat wall thickness (at present)

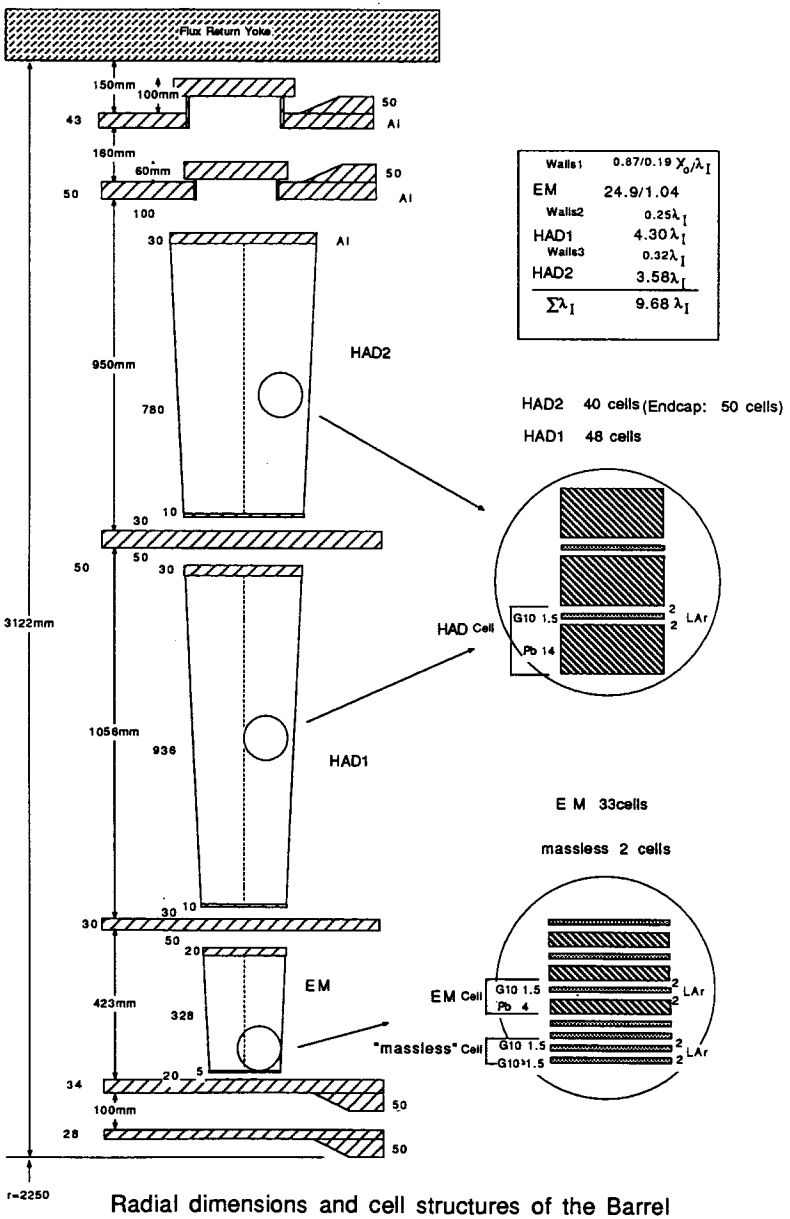

Radial dimensions and cell structures of the Barrel

Fig. 3 Radial dimension of the Barrel

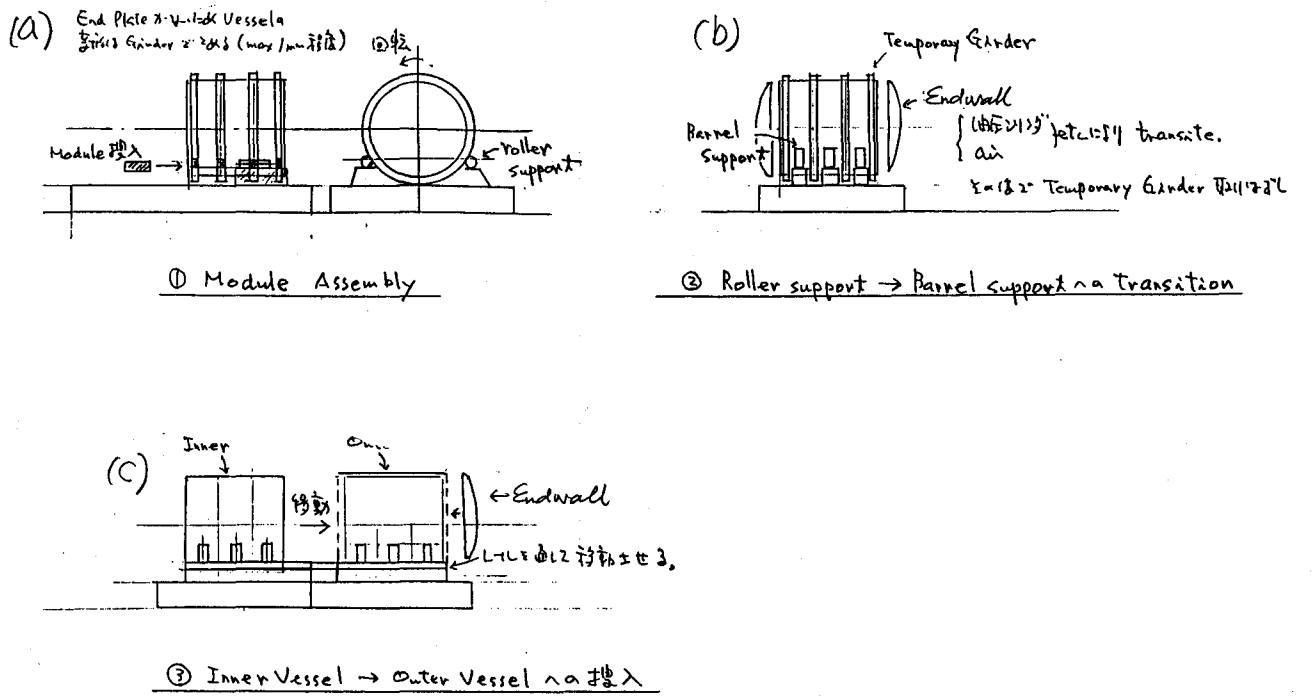

Fig. 5 Concepts for assembly and close-out; (a) module insertion, (b) head assembly and weight transfer from "girder rings" to the cold mass support, and (c) slide-in into the vacuum vessel and attaching heads.

〔参考〕 Assembly 要領概念図(案)

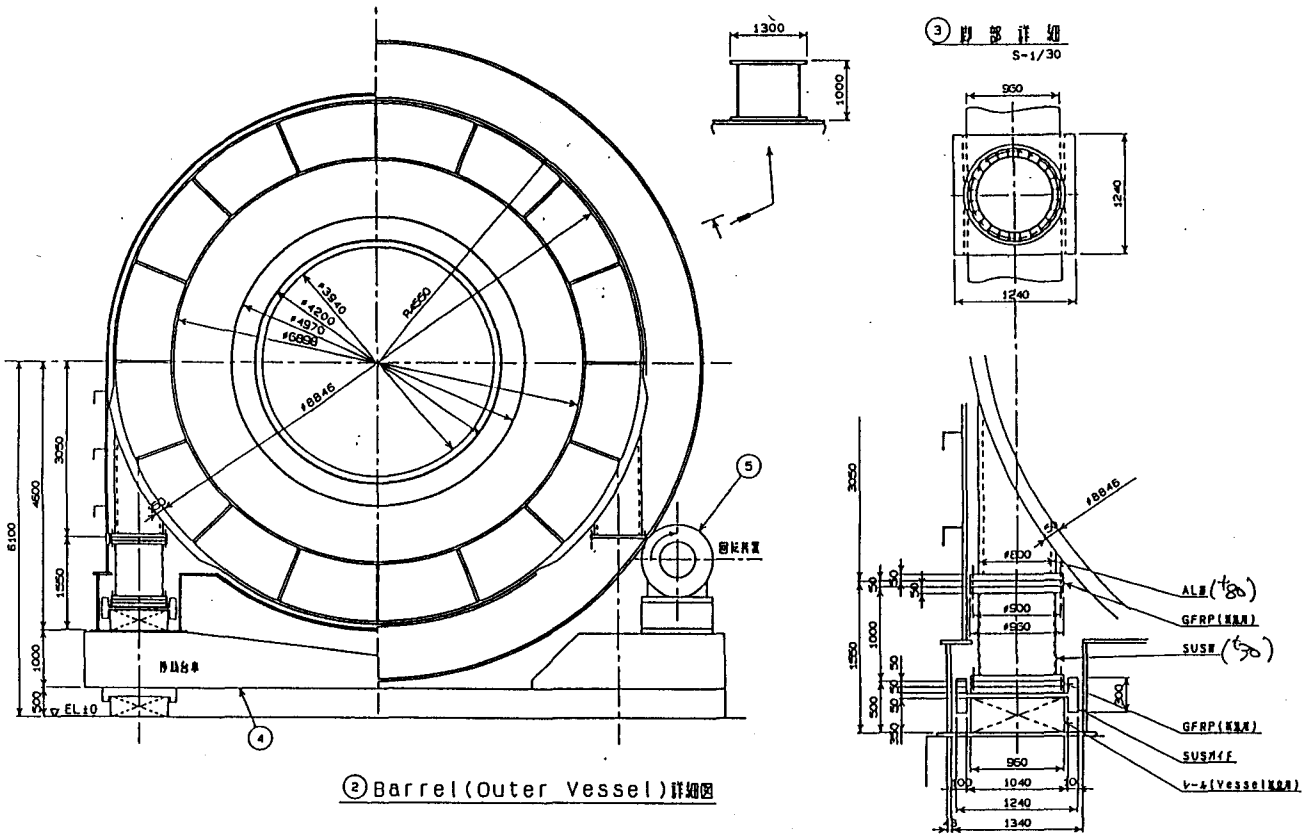

②Barrel(Outer Vessel)詳細図

Fig. 4 A conceptual design for cold mass and vacuum shell supporting

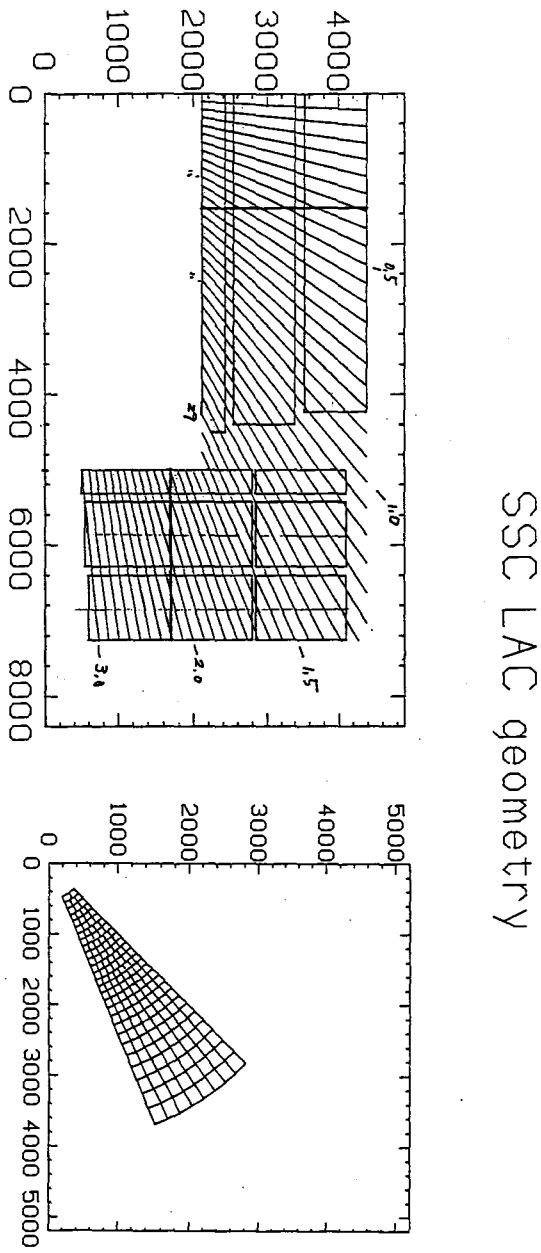

Fig. 6 Lateral segmentation of the modules of the Barrel and the Endcap

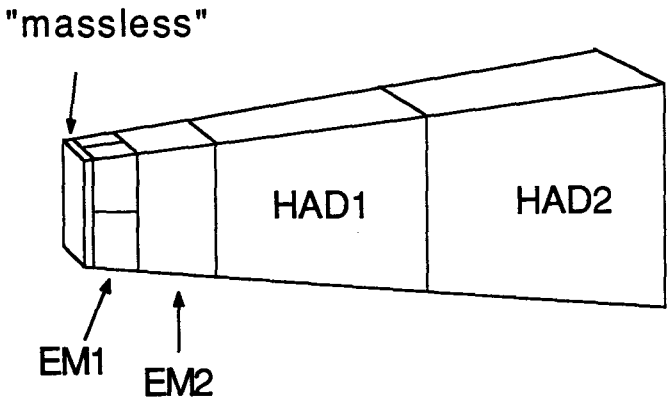

Basic longitudinal segmentation of a tower

Fig. 7 Basic longitudinal segmentation of a tower

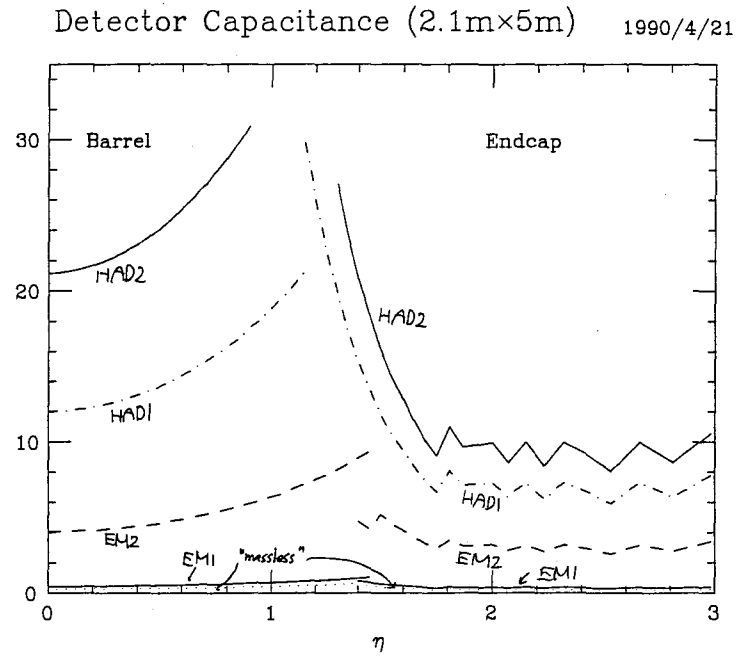

Fig. 8 Detector capacitances as a function of pseudorapidity, η

1990.4.22

Relations between the cable characteristics and the detector capacitance

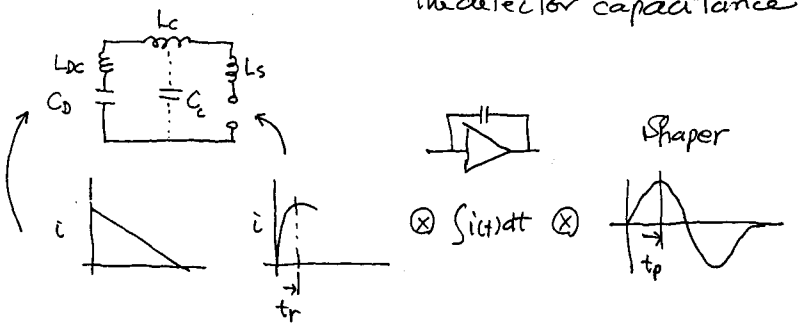

Fig. 9 Speed of response: schematics at various stages

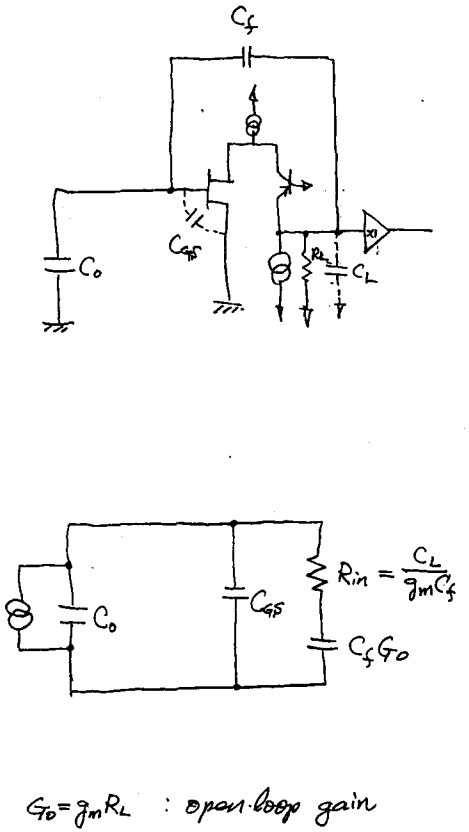

Fig. 10 A schematic of a detector and a charge preamplifier and an equivalent circuit diagram

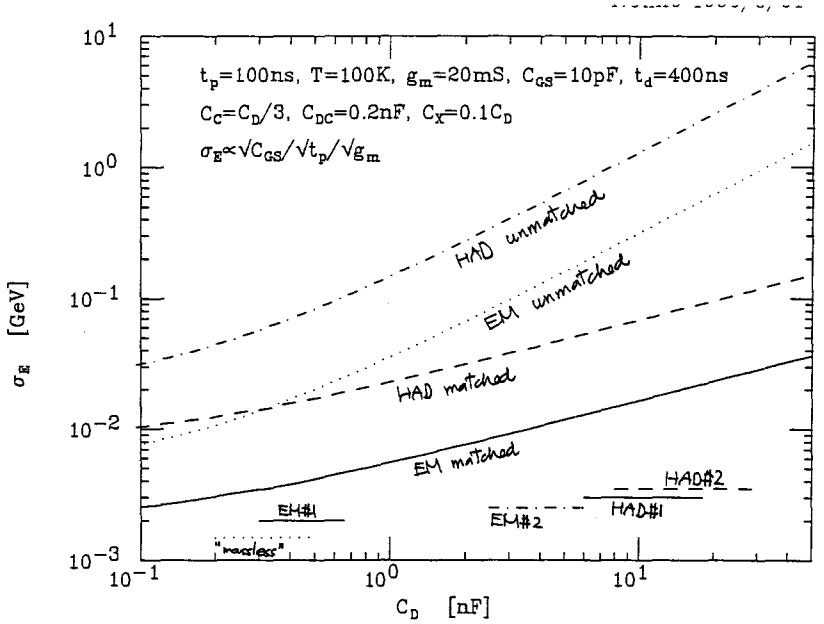

Fig. 11 Thermal noise with magnetic transformer at the EM and HAD sections; matched (solid/EM, dashes/HAD) and unmatched (dots/EM, dotdash/HAD). Capacitance ranges of each segment are also shown.

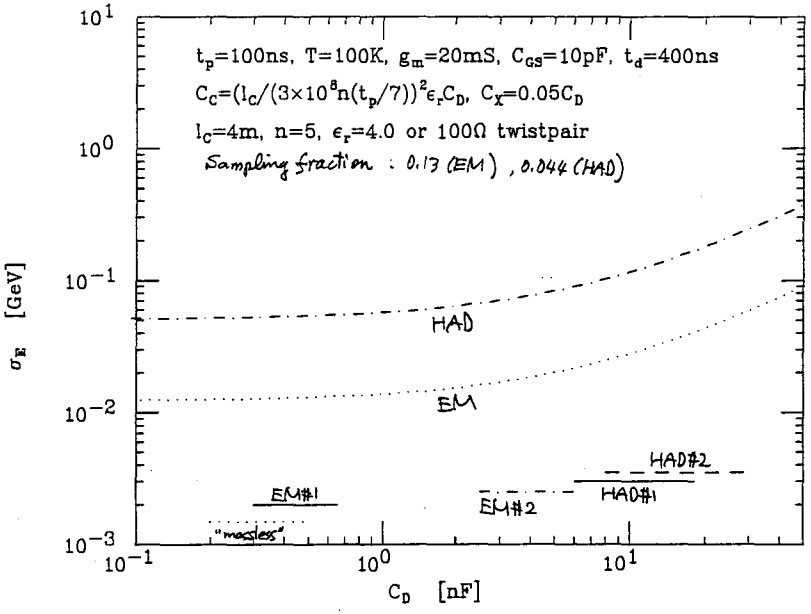

Fig. 12 Thermal noise with electrostatic transformer; dots/EM and dotdash/HAD.

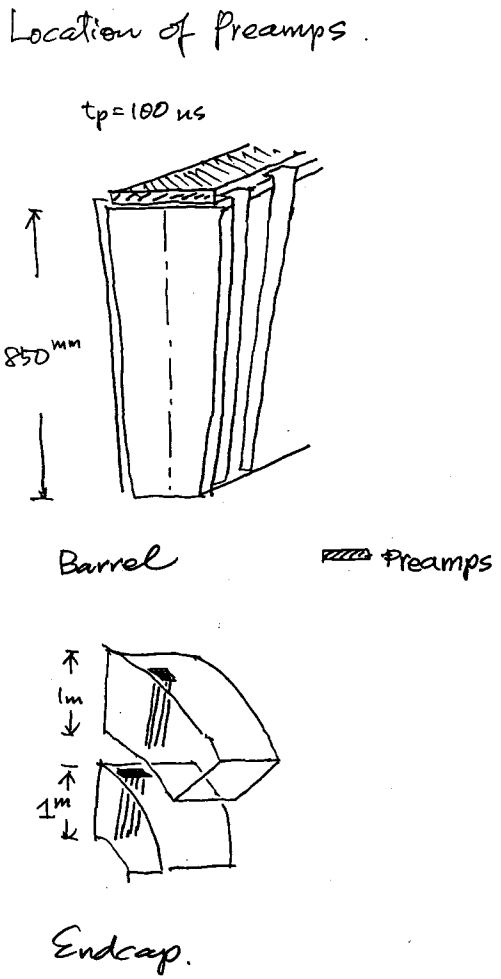

Fig. 13 Concept for the location of preamps and cables from detector elements to preamps

Effects of Dead Material to the Electro-Magnetic Calorimeter and Energy/Resolution Recovery with "Massless Gap"

HIDEO HIRAYAMA

KEK, National Laboratory for High Energy
Physics 1-1 Oho, Tsukuba-shi, Ibaraki, 305 Japan

ABSTRACT

The various dead materials existing in front of the calorimeter affect both the energy and the energy resolution especially of electro-magnetic calorimeter. The possibility of the energy and energy resolution recovery with "massless gap" was studied by using EGS4 Monte Carlo code. Two types of massless gap were considered. The number of the massless gap is changed for the first type and the weight of different values are applied to the fixed massless gap for the second type. The results of both cases showed that the massless gap can recover both the energy and the energy resolution reasonably.

1. Introduction

Various dead materials are exist in front of the calorimeter in the real situation like a inner magnet or a construction material of the calorimeter itself. In some situation, the thickness of these dead materials becomes more than 5 radiation lengths. These materials affect to the energy output and the energy resolution especially of the electro-magnetic calorimeter. It is very important to recover the energy output and the energy resolution as good as possible. In this paper, I report the possibility of the energy output and the resolution recovery of the lead-liquid Ar calorimeter with "massless gap" by using the EGS4 Monte Carlo code[1] . "Massless gap" means the parts without the converter material. Aluminum of various thickness was used as the dead material. Two methods are studied. In the first way, several lead converters from the front of the calorimeter are replaced with liquid Ar but the energy deposition in the liquid Ar in this part is not included as the output. The relation between the number of converters replaced with the liquid Ar and the recovery of the energy or resolution is studied. In the second way, as the more practical method, two lead converters are replaced with G10 and the various weight are applied to this part to recover the energy and the energy resolution. These studies are mainly done for 50 GeV electrons. The dependence of the incident electron energy is also studied for the typical case.

2. Calculation Method

The electron gamma shower Monte Carlo code EGS4 is used to study the effect of the dead material and the recovery of the energy output and the energy resolution of the electro-magnetic calorimeter. The geometrical arrangements of two cases are shown in Figure 1 and Figure 2. In both cases, the dummy material of aluminum having a different thickness is put in front of the calorimeter. Electrons incident on the dummy materials with the angle θ to the normal. In the case 1, the several lead converters from the front are replaced with the liquid Ar. The energy depositions inside the liquid Ar which changes from the lead converter are not counted as the energy output. The effects of the

recovery are studies for the various thickness of the dummy material as the function of the number of the lead converter replaced with the liquid Ar. In the case 2, the two lead converters from the front are replaced with the 1.5-mm G10 plate and this part plays as the massless gap. The whole electromagnetic calorimeter is divided two parts after the massless gap as shown in Figure 2. In this study, however, the recovery by applying the weight to the massless gap was investigated. For this purpose, EGS4 outputs the energy depositions of the massless gap, EM1 and EM2 for each incident electron. The energy output and the energy resolution are calculated by using the EGS4 results by applying the different weight to the massless gap.

3. Results and Discussion

The effects of the dummy aluminum layer are shown in Figure 3 as the energy fraction in the front dummy layer having the different thickness and the various incident angle as the function of the incident electron energy. As the matter of course, the fraction increases drastically as the increase of the thickness and the decrease of the incident energy. More than 20 % of the energy is absorbed for the 5 radiation length of aluminum in the case of normally incident 50 GeV electrons.

The recovery of the energy resolution in case 1 is shown in Figure 4 as the function of the dummy Al layer thickness. For the same thickness of the dummy layer, the energy resolution is recovered as the increase of the replaced number at first but it becomes worse again from the some number. shown in the case of 3 radiation length dummy layer. The pulse height distribution of 50 GeV electrons with the 5 radiation length dummy layer is shown in Figure 5 for without the massless gap and the 12 layers replacement together with that for without the dummy layer. The recovery of the energy resolution can be seen clearly. The energy output with the 5 radiation length dummy layer for 0 and 30 degree incident is shown in Figure 6 when the 12 layers are replaced for the 0 and 30 degree incident. At 50 GeV, the energy output is smaller about 25 % than that without the dummy layer but generally the energy output is recovered well from 10 to 150 GeV. From the results above, it seems possible to recover the energy output and the energy resolution with the massless gap.

As the more realistic way, the recovery of the output energy and the energy resolution for 50 GeV electrons in the case 2 is shown in Figure 7 as the function of the weight of the massless gap in the case of the 3 or 5 radiation length dummy layer of normal incident and the 2 radiation length of 30 degree incident. The weight that gives the same energy output without the dummy layer gives the energy resolution very close to the best one. The weight dependence of the energy resolution is similar to the number dependence of the lead converter replaced with the liquid Ar in the case 1. The pulse height distribution of 50 GeV electrons with the 5 radiation length dummy layer is shown in Figure 8 both with the weight 1 and 5.4 together with that without the dummy layer. The energy resolution and the energy output is recovered well with the weight to the massless gap. The variation of the applied weight to give the same output energy for 50 GeV electrons is shown in Figure 9 for the normal incident and the 60 degree incident. The weight must be applied increases with the increase of the dummy layer thickness. For the same thickness of the dummy layer, the larger weight is needed for the 60 degree incident. The incident electron energy dependence of the corrected energy resolution is shown in Figure 10 in the form of (σ/E_{ab}) x $E^{1/2}$. The large values at 10 and 20 GeV shows the difficulties of the recovery by this method. The increase above 50 GeV shows that the energy resolution has the constant term and can be expressed as follows above 50 GeV if the same weight is applied for all incident energy.

$$\sigma/E_{ab} = 16.7E^{-1/2} + 1.31(\%)$$

In Figure 10, the values obtained with the weight to the massless gap giving the best energy resolution at each incident energy are also ahown together with the applyed weight. The energy output with the weight 5.4 to the massless gap for the 5 radiation length dummy layer is shown in Figure 11. Maximum differences of the output energy from that without dummy layer is 13 % from 10 to 150 GeV and the degree of the recovery is better than the case 1.

4. Conclusion

The effects of the dead materials to the electromagnetic calorimeter and the recovery of the output energy and the energy resolution with the massless gap are studied by using the EGS4 Monte Carlo code. Two types of the massless gap were considered. At first type, the number of the massless gap is changed. The fixed 2 layer was used at the second type but the weight of different values to the massless gap was applied. The results of both case showed that the massless gap can recover both the output energy and the energy resolution reasonably. Before applying this method to the practical electromagnetic calorimeter, it is desired to check the above results with the experiment.

REFERENCES

1. W. R. Nelson, H. Hirayama and D. W. O. Rogers, "The EGS4 Code System", SLAC-265 (December 1985).

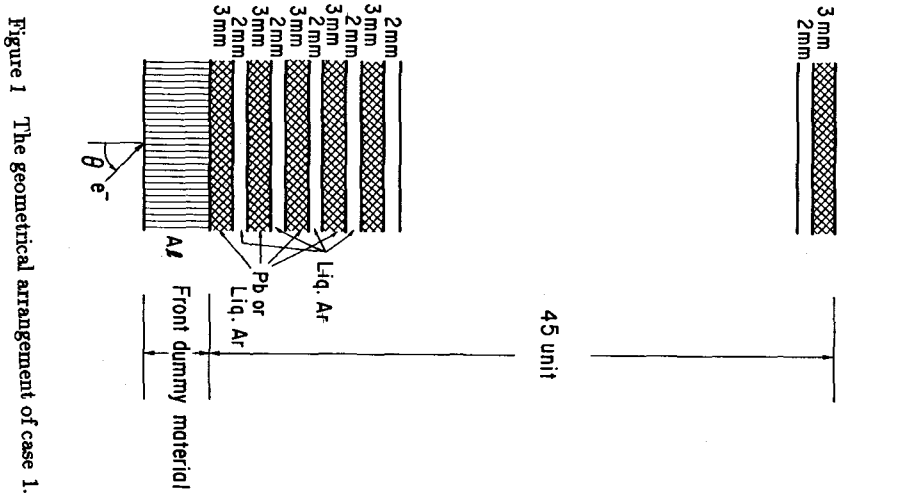

Figure 1 The geometrical arrangement of case 1.

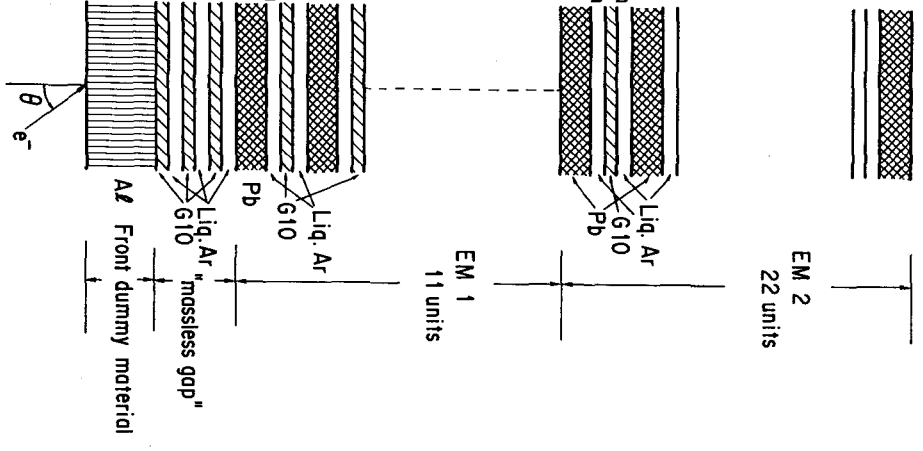

Figure 2 The geometrical arrangement of case 2.

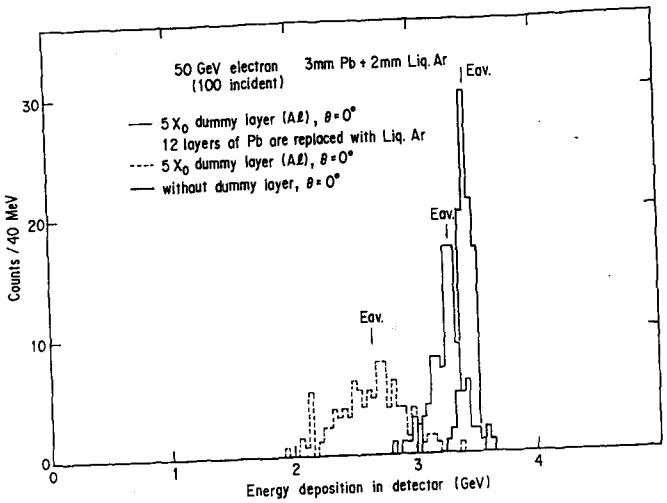

Figure 5 The pulse height distribution of 50 GeV electrons with the 5 radiation length dummy layer for without the massless gap and the 12 layers replacement together with that for without dummy layer.

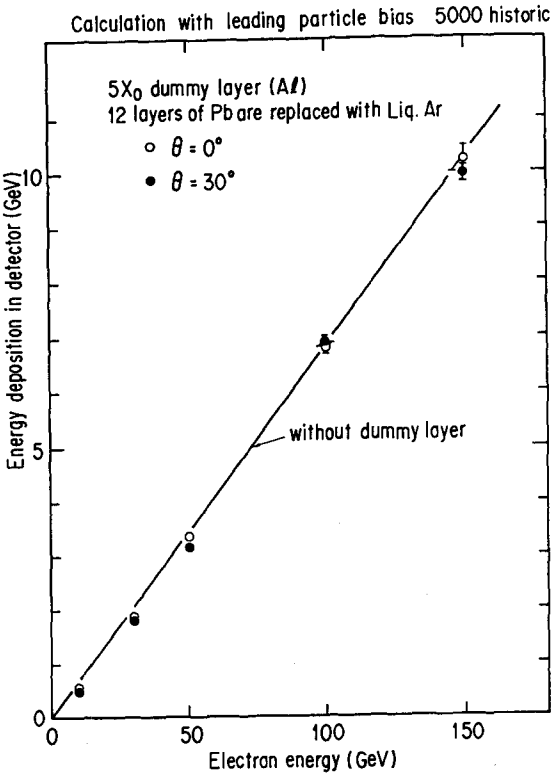

Figure 6 The energy output for the 5 radiation length dummy layer when the 12 layers are replaced for 0 and 30 degree incident as the function of the incident electron energy.

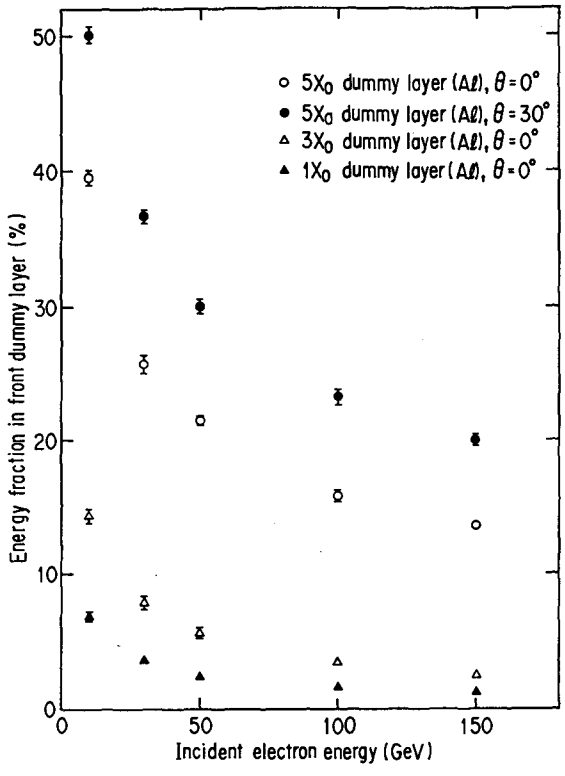

Figure 3 The energy fraction in the front dummy layer having the different thickness and the various incident angle as the function of the incident electron energy.

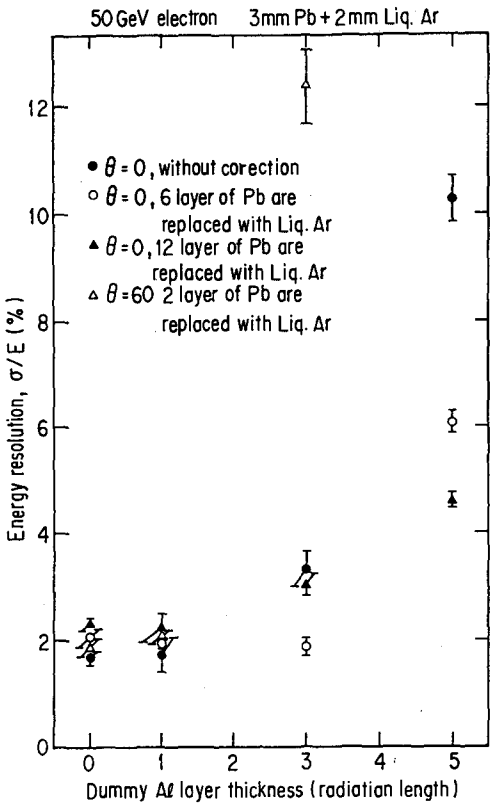

Figure 4 The recovery of the energy resolution in case 1 as the function of the Al dummy layer thickness.

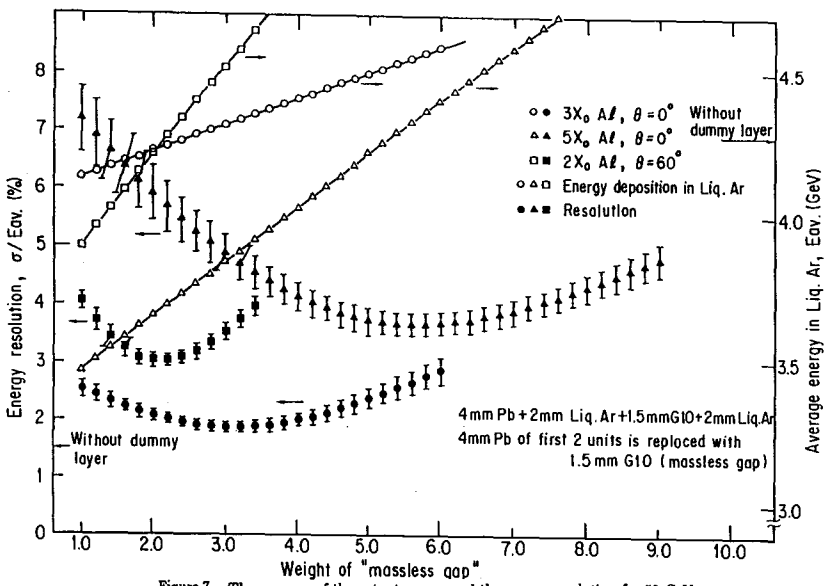

Figure 7 The recovery of the output energy and the energy resolution for 50 GeV electrons in the case 2 as the function of the weight of the massless gap for 3 and 5 radiation length dummy layer of normal incident and the 2 radiation length dummy layer of 30 degree incident.

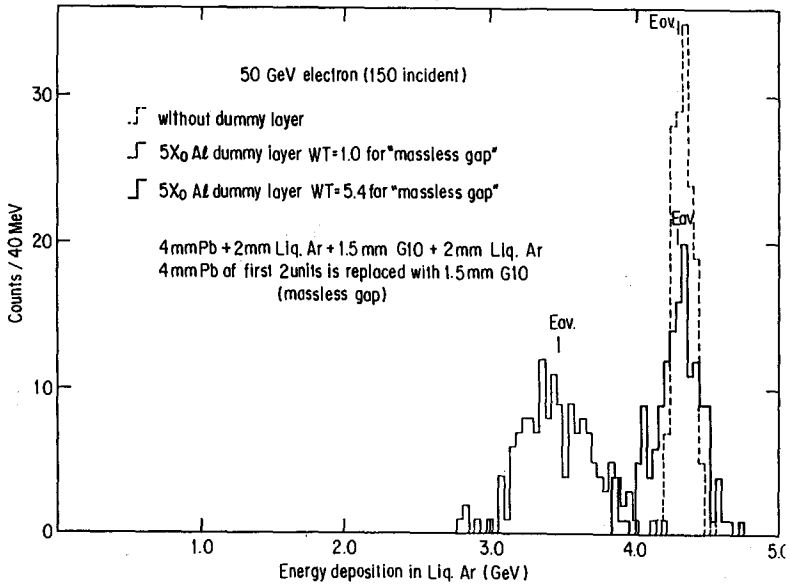

Figure 8 The pulse height distribution of 50 GeV electrons with the 5 radiation length dummy layer both with the weight 1 and 5.4 together with that without the dummy layer.

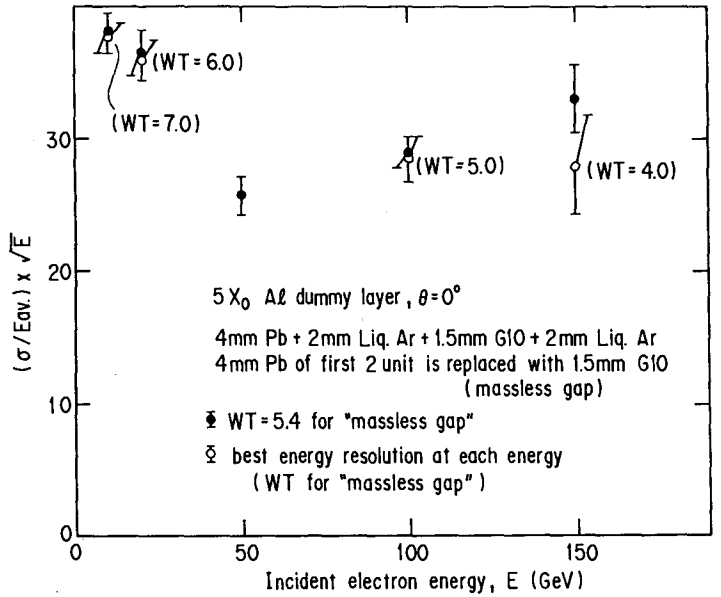

Figure 9 The incident energy dependence of the corrected energy resolution with the 5 radiation length dummy layer.

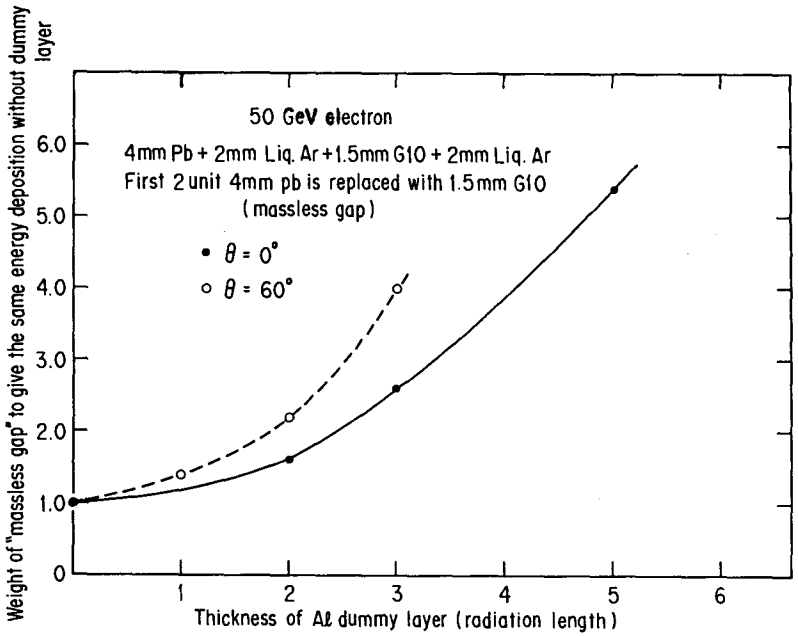

Figure 10 The variation of the applied weight to give the same output energy for 50 GeV electrons for the normal incident and the 60 degree incident.

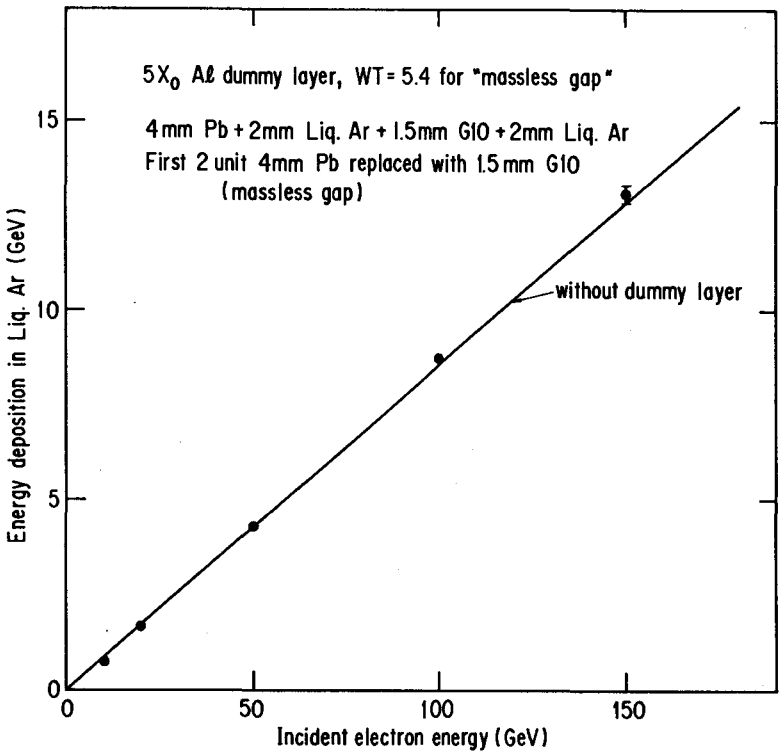

Figure 11 The energy output with the weight 5.4 to the massless gap for the 5 radiation length dummy layer.

Hadronic shower in the liq. Ar calorimeter

M. Asai
Hiroshima Tech

(No written contribution received)

SCINTILLATOR PLATE CALORIMETRY

L. E. Price
Argonne National Laboratory, Argonne, IL 60439

Calorimetry using scintillator plates or tiles alternated with sheets of (usually heavy) passive absorber has been proven over multiple generations of collider detectors. Recent detectors including UA1, CDF, and ZEUS have shown good results from such calorimeters. The advantages offered by scintillator calorimetry for the SSC environment, in particular, are speed (< 10 nsec), excellent energy resolution, low noise, and ease of achieving compensation and hence linearity. On the negative side of the ledger can be placed the historical sensitivity of plastic scintillators to radiation damage, the possibility of nonuniform response because of light attenuation, and the presence of cracks for light collection via wavelength shifting plastic (traditionally in sheet form).

This approach to calorimetry is being investigated for SSC use by a collaboration of Ames Laboratory/Iowa State University, Argonne National Laboratory, Bicron Corporation, Florida State University, Louisiana State University, University of Mississippi, Oak Ridge National Laboratory, Virginia Polytechnic Institute and State University, Westinghouse Electric Corporation, and University of Wisconsin. This group has received funding from SSC Laboratory under the Major Subsystem R&D program. H. Spinka of ANL is the spokesperson of the collaboration. Major tasks have been identified with coordinators as follows: Calorimeter Electronics (E. Rosenberg, W. Smith); Position Measuring System (A. B. Wicklund); Optical Systems and Scintillator Development (R. McNeil, L. Mo); Materials Evaluation (D. Reeder); and Simulation and Mechanical Design (J. Proudfoot, H. Spinka).

The overall layout of a scintillator plate calorimeter is shown in Fig. 1 as presently conceived (the mechanical design is evolving rapidly), set into an overall detector concept. The design will attempt to achieve approximate projectivity in both barrel and endcap regions. The layout of a single module (two towers) is shown in Fig. 2, showing the alternating plate structure, sheets of wavelength shifter alongside the scintillator plates, and photomultiplier tubes in the strong mechanical structure at the outside of the module. An alternative design using wavelength shifting fibers embedded in the scintillator plates is also being developed. This approach was proposed, at least in the SSC context, by an FNAL group and is described in the paper by J. Freeman in these proceedings.

R&D on radiation-hard plastic scintillator is rapidly erasing the concern about darkening of the plastic in the SSC radiation field. Calculations[1] show that the maximum radiation dose, found at electromagnetic shower maximum

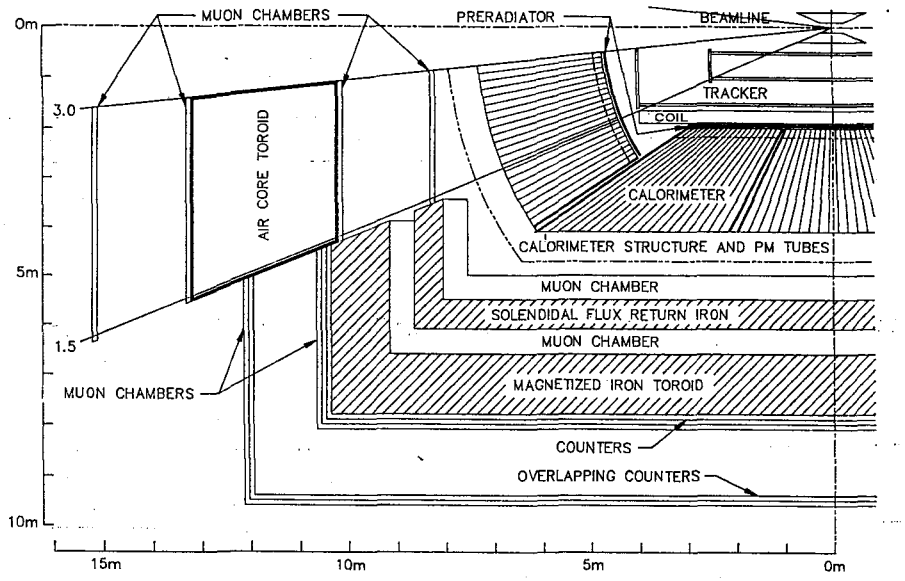

Fig. 1

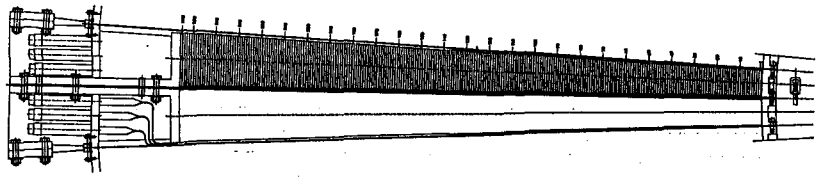

Fig. 2

at the most forward angle ($\eta \leq 3$), amounts to less than 20 Mrad in the 10 year expected lifetime of the detector. Our collaborators in the Bicron Corporation, for instance, have recently produced a blue-emitting scintillator with a modified plastic base called RH-1 whose response to electron irradiation is shown in Fig. 3. After 10 Mrad γ (squares) exposure (and a two-week recovery period) at 20 cm from the source of light (roughly the size of the biggest tiles), only 10% of the light has been lost because of the irradiation. The other curves are 30 Mrad (triangles) and 100 Mrad (open circles). Bicron expects to continue to develop increasingly radiation-tolerant scintillators. Other companies such as Kuraray in Japan and Nanoptics in the US have also made substantial progress in radiation hardness of plastic scintillator.

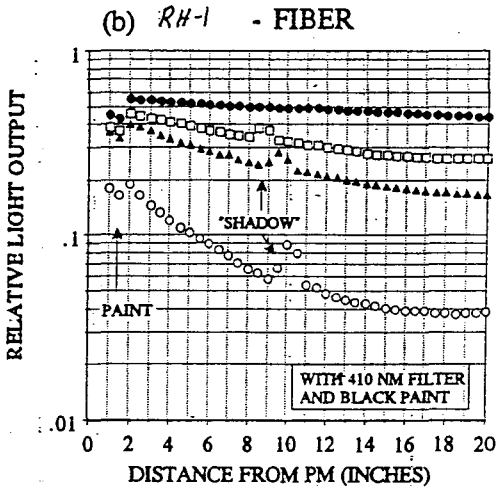

Fig. 3.

Optimization of the unit cell (thicknesses of absorber and scintillator and choice of absorber) is an important early task for the subsystem investigation. The ultimate in resolution is achieved with depleted uranium absorber, where compensation is achieved with relatively thin thicknesses of absorber and sampling fluctuations are minimized. A study of compensation in scintillator calorimeters for varying thicknesses of uranium, lead and iron is shown in Fig. 4 as a function of the ratio of absorber thickness (T_{abs}) to scintillator thickness (T_{sci}). Points are annotated with the thickness in cm. In agreement with a study of Fesefeldt[2] (but not that of Wigmans[3]), the curve for iron shows almost no dependence on absorber thickness, suggesting that there may be no compensating ratio. Iron is of interest to calorimeter designers because of the elegant mechanical solutions that it offers. This

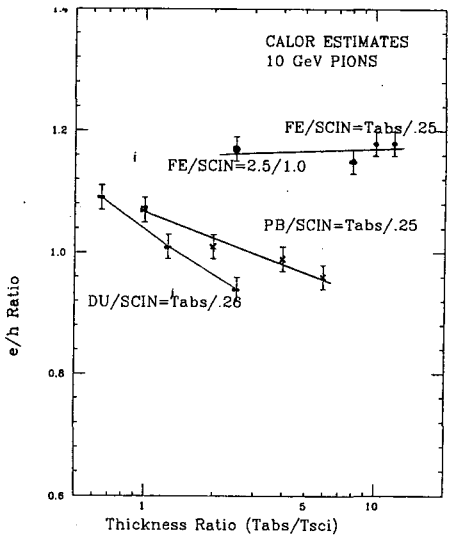

Fig. 4.

subsystem collaboration is focused mostly on lead and uranium absorbers, but we will also investigate iron/lead hybrids.

CDF and ZEUS have shown that optical masking techniques can correct for small amounts of attenuation in scintillator, as long as the attenuation stays approximately constant in time. Cracks for wavelength shifter lightguides, then, remain as a potential problem to be faced in the design. ZEUS has shown that uniformity can be achieved across readout gaps by adding lead between wavelength shifter plates. As shown in Fig. 5 (end view of barrel), we expect to tilt the electromagnetic modules azimuthally by a few degrees to avoid particles that go straight along readout gaps. The problem of readout gaps can be considerably reduced by use of fiber readout, particularly in the electromagnetic section and we will be working with the FNAL group to demonstrate their suitability.

Front end electronics are being developed to take advantage of the fast time response of scintillator and to feed appropriately into a first level trigger system.

Interest in depleted uranium absorber is dampened by the potential cost (ZEUS is paying $12/pound for clad sheets). As a result, one goal of the subsystem R&D is the investigation of alternative methods of production that may be considerably cheaper. Initial investigations suggest that savings of a factor of 2 may be readily achievable. Many of the benefits of uranium

absorber may also be realized with mixtures of uranium and lead or other cheaper material.

Work supported in part by the U.S. Department to Energy, Division of High Energy Physics, under contract W-31-109-ENG-38.

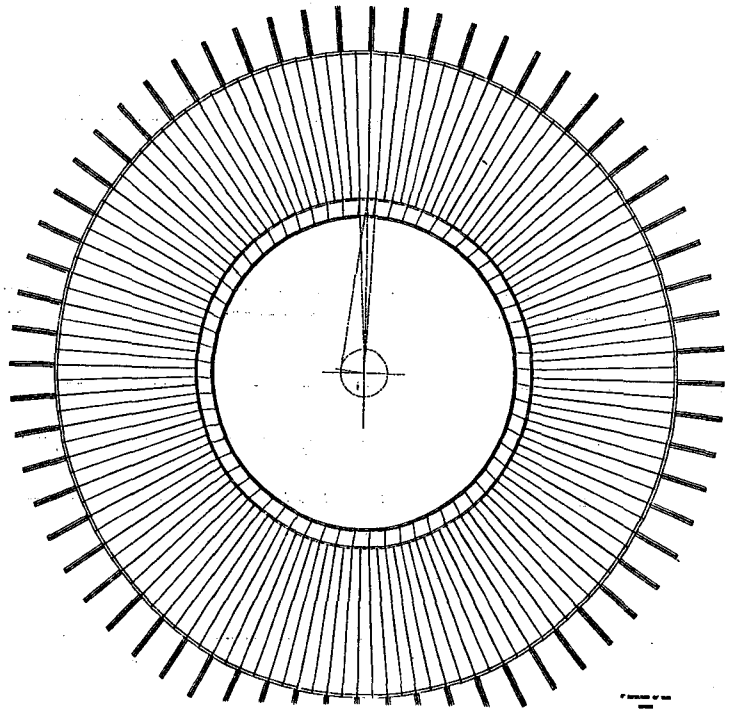

Fig. 5

References

1. D. Groom, SSC-SR-1033.

2. H. Fesefeldt, Nucl. Instr. Meth. in Phys. Res. A263, 114 (1988).

3. R. Wigmans, Nucl. Instr. Meth. in Phys. Res. A259, 389 (1987).

Red-Green-Blue Scintillating Fiber Calorimeter

Koji Takikawa

Institute of Physics, University of Tsukuba

Abstract

The basic design of a new scintillating fiber calorimeter, which utilizes the difference in wavelength of red, green, and blue scintillation light, is described. The calorimeter consists of red-blue jointed fibers embedded uniformly in lead absorber, with red fiber in the electromagnetic section being connected to blue fiber in the hadronic section. Signals are read out entirely in the rear of the calorimeter tower. A green wavelength shifter sheet is used to obtain hadronic energy in a tower. The electromagnetic, red light is detected by a multi-anode phototube behind the wavelength shifter sheet. The calorimeter should provide a uniform spatial response in a tower with no dead space and also a good electron identification capability.

Talk at the International Workshop on Solenoidal Detectors for the SSC, KEK, Tsukuba, Japan, 23-25 April 1990.

Sampling calorimeters using scintillator as a sampling device are suitable for high-energy multi-bunch proton colliders. They are fast in time response. A good energy resolution for hadronic jets is obtained by choosing the thickness ratio of scintillator to absorber such that the electron-hadron signal ratio (e/h) is unity.[1] Recent development of scintillating fiber has led to proposals of the "spaghetti" calorimeter,[2] in which fibers are uniformly embedded in lead absorber along the longitudinal direction of the calorimeter tower and signals are read out in the rear of the tower. The calorimeter of this type has an attractive feature of providing a uniform spatial response within a calorimeter tower and no dead space at the tower boundaries, because scintillating fibers extend to the tower boundary. In this design, however, the separation of electromagnetic and hadronic energies without producing dead space is not trivial and calls for some ingenuity.

In collaboration with Kuraray Co., Ltd., Kondo[3] has recently developed a new plastic scintillator R3 which emits red light of 600 nm in wavelength. The main motivation for going to longer wavelength than that of conventional scintillator was the expectation that red fiber would be stronger against radiation damage and that it would have longer attenuation length. Figure 1 shows absorption and emission spectra of R3 fluor, together with those of other fluors and polystyrene. The blue scintillator SCSN81 is a polystyrene based scintillator doped with P-TP and material "B". The red scintillator SCSNR3 is obtained by doping Y7 and R3 fluors to SCSN81.

On the basis of this development, a new type of scintillating fiber calorimeter has been proposed, which is of "spaghetti" type and yet provides an electromagnetic and hadronic longitudinal segmentation.[4-6] The basic idea is to exploit the difference in wavelength of red, green, and blue scintillation light, so we call it RGB scintillating fiber calorimeter. We note from Fig. 1 that the R3 emission spectrum is completely separated from the absorption spectra of SCSN81 and of Y7. This means that the R3 red light can be transmitted through blue fiber and Y7 wavelength shifter sheet without absorption. The second point to notice in Fig. 1 is that the overlap of Y7 green light and R3 red light is small; it occurs in the wavelength region of R3 self-absorption where the emission and absorption spectra overlap. Since the spectrum of red light traveling through R3 fiber is shifted to wavelength longer than that of the self-absorption region, we will be able to separate red and green effectively by a filter with a cut-off wavelength around 600 nm.

Figure 2 shows a schematic diagram of the RGB calorimeter. We use a red fiber for the electromagnetic section and a blue fiber for the hadronic section. They are glued with a blue-cut, red-pass filter to form a single fiber. The filter is to prevent blue light from entering red fiber and being converted into red. With a Y7 wavelength shifter sheet placed at the rear end of the calorimeter tower, blue light representing hadronic energies is converted into green and it is detected by two conventional phototubes. Red light representing electromagnetic energies is transmitted through the blue fiber and also through the Y7 sheet. It is detected by a multi-anode (8 × 8), red-sensitive phototube. The Y7 sheet is backed with a green-cut, red-pass filter, so that the Y7 green light of hadronic energies does not reach the readout device of red light. The fine-segmented readout of electromagnetic energies allows for measurement of the lateral shower profile as well as the tower energy. This should provide a good electron identification capability as in the CDF central electromagnetic calorimeter.

Two prototype modules of the RGB calorimeter are now under construction to be tested in a beam. The mechanical structure of a prototype module is illustrated in Fig. 3. The module is 2 m long and has a tower shape of 14 cm x 18 cm at the front end, tapered to 23 cm x 28 cm at the rear end. The tower size corresponds to a segmentation of $\Delta\eta = 0.05$ and $\Delta\phi = 0.05$ in a typical configuration of SSC barrel calorimeter. We use scintillating fibers of 1.5 mm in diameter. The fibers are inserted into U-shaped grooves in lead plates, along the longitudinal tower direction. The grooves, 1.8 mm wide and 1.8 mm deep, are cut at intervals of 3.2 mm in the 2.8-mm thick lead plate by extrusion. The volume ratio of scintillating fiber to lead is 1:4 in order to achieve compensation, e/h = 1. An appropriate number of these plates are laminated with glue and are machined to the tower shape.

Along with the prototype fabrication we have been performing a series of bench tests on scintillating fiber in terms of light yield, emission speed, attenuation length, and radiation damage. Most of them were presented in previous SSC calorimeter workshops.[6,7]

One of the concerns often raised against the RGB calorimeter is cross talk or color mixing: can we actually separate electromagnetic and hadronic energies? In order to look at this problem, we have made a bench test measurement. Figure 4 shows the setup. A red SCSFR3 fiber, 1.5 mm in diameter and 25 cm long, was jointed to a blue SCSF81 fiber of the same diameter and 2 m long, through a 2-mm thick blue-cut filter-fiber. The fiber connection was made by Atac's method of thermal fusion.[8] The fiber was scanned by a UV lamp of 365-nm emission. With a 5-mm thick Y7 wavelength shifter sheet, blue light was converted into green and it was detected by a Hamamatsu R329 phototube. Red light was seen by a Hamamatsu R1221 phototube behind the Y7 sheet, through a red-pass filter of 640-nm cutoff. The R1221 has spectral response S-25 with a quantum efficiency of 5-10% in the wavelength region of 600-700 nm. The phototubes were biased only between the photocathode and the first dynode, and the currents were read by picoammeters.

Figure 5 shows the measured red and green light yields as a function of the excitation position. The red light yield remains approximately constant along the red fiber and drops abruptly across the joint to a 3% level in the blue fiber. We do not understand where the 3% red light background in the blue fiber comes from; more study is under way. The green light from red fiber is small and barely detectable above noise. It is about 0.5% of the blue fiber yield.

Using the preliminary results of Fig. 5, we can estimate the separation power of electromagnetic/hadronic energies of the RGB calorimeter. Let an incident particle of energy E deposits energy f(x) at depth x along the calorimeter. Neglecting the effects of finite attenuation lengths, we can write red and green light yields, R and G, as

$$R = C_R (EM + \eta_R HAD) \qquad (1)$$

$$G = C_G (HAD + \eta_G EM) \qquad (2)$$

with

$$EM = \int_{EM} f(x)\, dx , \quad HAD = \int_{HAD} f(x)\, dx , \quad EM + HAD = E ,$$

where EM, HAD are energy depositions in the electromagnetic and hadronic sections of the calorimeter; C_R, C_G are gain constants; η_R, η_G are color mixing factors, where we have $\eta_R \approx 3\%$, $\eta_G \approx 0.5\%$ from Fig. 5. As for electrons, the second term inside the bracket of Eq. (1) can be safely neglected, and we get $R = C_R \times EM$. As for hadrons not interacting in the electromagnetic section, Eq. (2) reduces to $G = C_G \times HAD$. These two relations can be used to calibrate the gain constants. The green light G for electrons is determined mainly by shower leakage into the hadronic section since $\eta_G \approx 0.5\%$. The red light R for hadrons not interacting in the electromagnetic section is determined mainly by the color mixing factor η_R, i.e., about 3% of the red light R for same-momentum electrons.

As for hadrons interacting in the electromagnetic section and for jets, we can determine the electromagnetic and hadronic energies, EM and HAD, and hence the total energy E, by

$$EM = R/C_R - \eta_R\, G/C_G \qquad (3)$$
$$HAD = G/C_G - \eta_G\, R/C_R \qquad (4)$$

where we have assumed e/h = 1. The color mixing effect in the RGB calorimeter is small and can be corrected.

In addition to R3 fluor, Kuraray has developed a new orange fluor O2, whose emission and absorption spectra are shown by the dashed lines in Fig. 1. Use of O2 wavelength shifter sheet and red-green jointed fiber, instead of Y7 wavelength shifter sheet and red-blue jointed fiber, might open the possibility of a red-orange-green (ROG) calorimeter, a variant of the RGB. If the color mixing in the ROG is shown to be manageable, the advantages of the ROG are: (a) Green fiber is less sensitive to radiation damage, (b) Green fiber has a longer attenuation length, so that hadronic shower fluctuation effects are smaller, leading to an improved hadronic-energy resolution. The future of the RGB approach is bright.

References

1) R. Wigmans, Nucl. Instr. and Methods, **A259**(1987)389.
2) R. Wigmans, Proceedings of the Summer Study on High Energy Physics in the 1990's, 798 (1988); F. Takasaki, KEK preprint 88-120 (1989).
3) K. Kondo, Talk at the 9th Japanese Workshop on Physics at Hadron Colliders, University of Tsukuba, September 16-17, 1989.
4) K. Takikawa, Talk at the 9th Japanese Workshop on Physics at Hadron Colliders, University of Tsukuba, September 16-17, 1989.
5) T. Akimoto et al., CDF note No. 1068, November, 1989.
6) K. Yasuoka, Talk at the 1st SDC Collabration Meeting, Fermilab, December 16-18, 1989.
7) K. Yasuoka, Talk at the Workshop on Radiation Hardness of Plastic Scintillator, Florida State University, March 19-21, 1990.
8) M. Atac, Private communication, December, 1989.

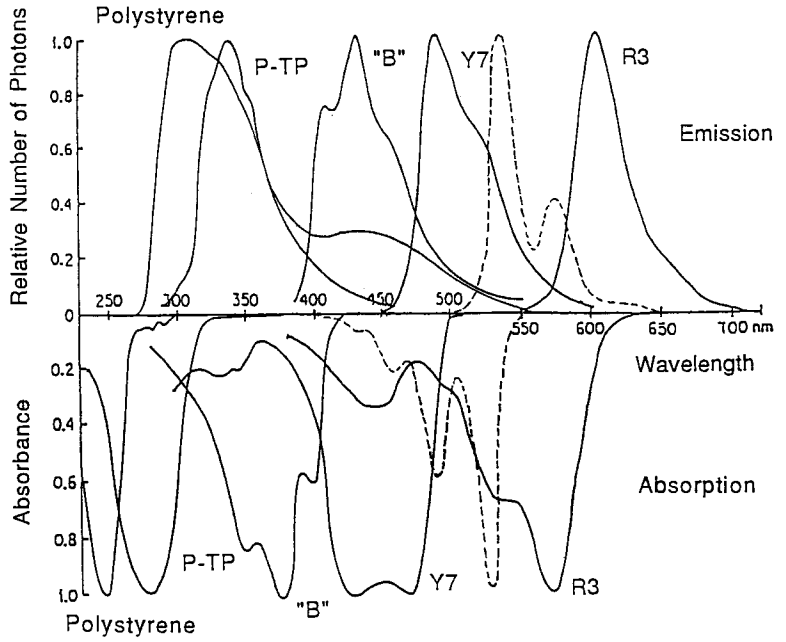

Fig. 1. Absorption and emission spectra of R3, Y7 and SCSN81. The SCSN81 is a polystyrene based scintillator doped with P-TP and material "B". The dashed lines are spectra of O2.

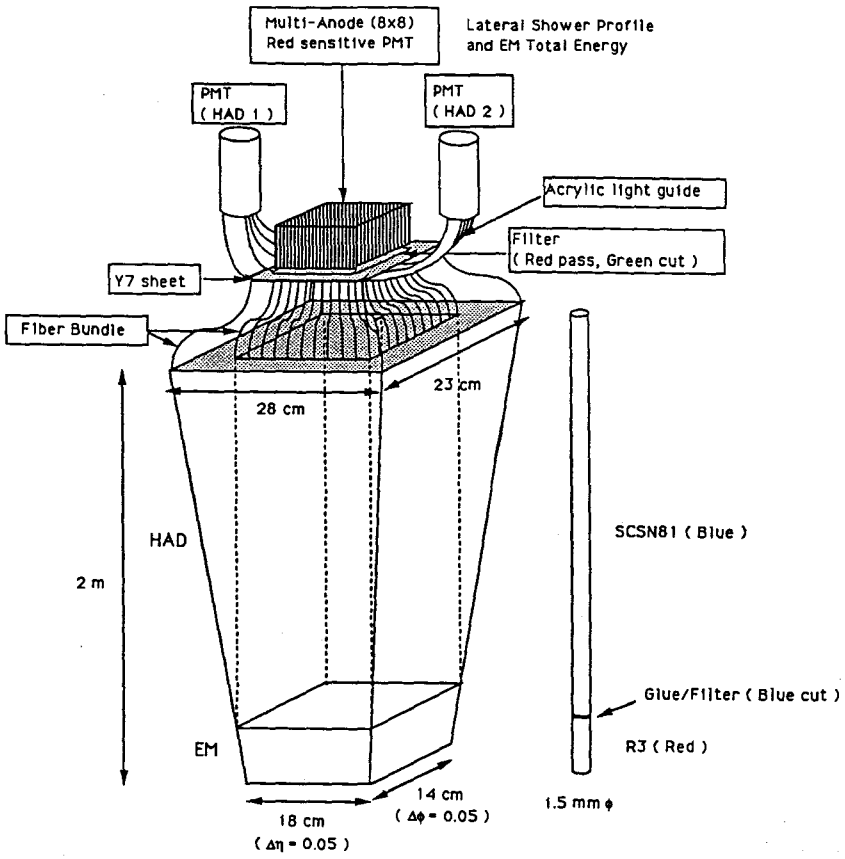

Fig. 2. Schematic diagram of the RGB calorimeter.

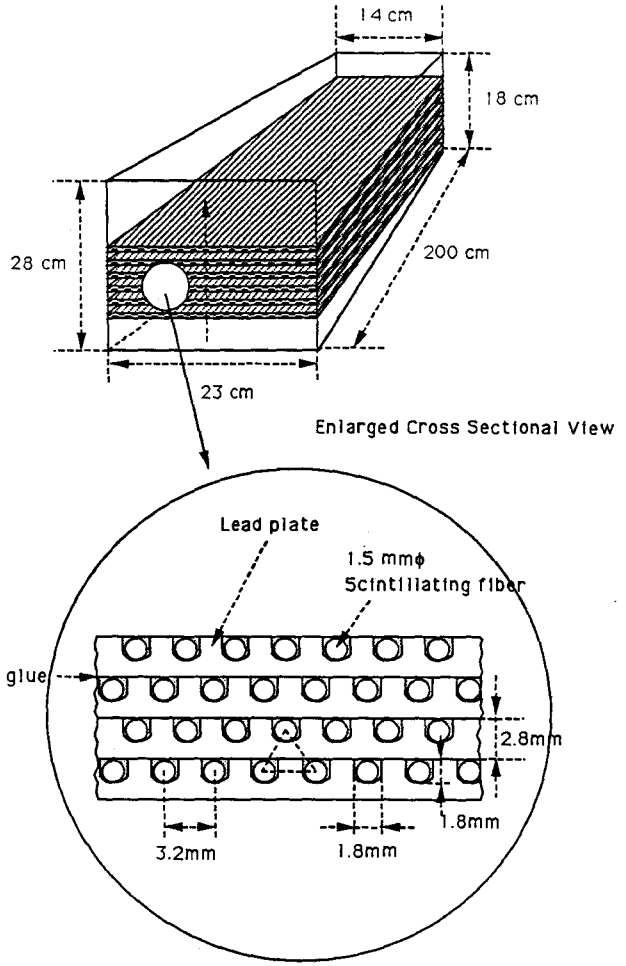

Fig. 3. Mechanical structure of the prototype RGB calorimeter module.

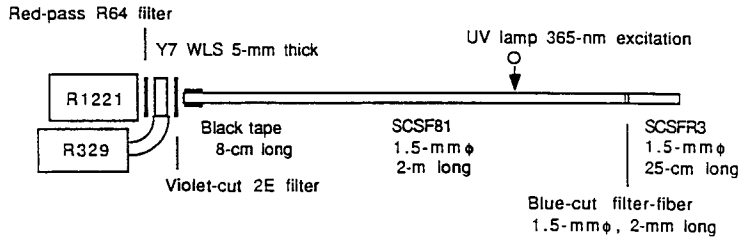

Fig. 4. Testbench setup for measuring color separation in the RGB scheme.

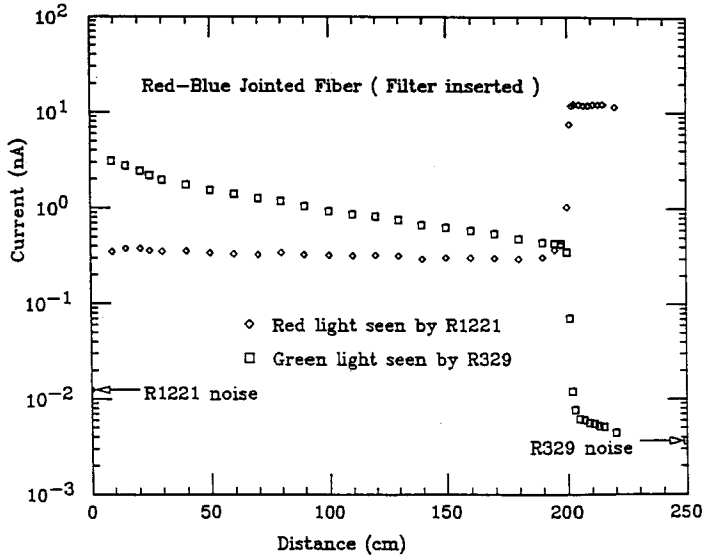

Fig. 5. Red and green light yields of a red-blue jointed fiber as a function of the excitation position.

Radiation damage for scintillation fiber

M. Mishina
KEK

(No written contribution received)

SCINTILLATING TILE/FIBER CALORIMETRY DEVELOPMENT AT FNAL

G. W. FOSTER, J. FREEMAN

Fermi National Accelerator Laboratory Batavia, IL

Presented by J. Freeman

The technique of calorimetry using scintillating tiles with waveshifting fibers imbedded in them for readout has been refined for use in SSC test calorimeters and for the CDF Endplug upgrade. The technique offers high light yield, good spatial uniformity, flexible readout mechanics and a very small "readout crack". Various production techniques have been developed and optimized, including control and correction of scintillator plate uniformity, techniques for splicing plastic fibers with low light losses, and laser-cutting of the groove in which the fiber is placed.

1 Introduction

The technique[1] of imbedding a waveshifting readout fiber into scintillator plate calorimetry has been developed and refined for use in both the CDF End Plug calorimeter upgrade[2] and for SSC calorimetry for the Solenoidal Detector Collaboration [3]. The basic method is illustrated in fig. 1. Scintillating plastic plates ("tiles") are prepared with wavelength-shifter (WLS) optical fibers imbedded in them for readout. Blue scintillation light is produced in the tile and is trapped by a combination of total internal reflection and specular reflection from an aluminized wrapping. Some fraction of it hits a green waveshifter fiber and is shifted. Typically 4% of the shifted light is captured by the fiber (in each direction), and can be transported to the outside of the calorimeter through the fiber. The path of the readout fiber can be either a simple "U" or a serpentine pattern for improved optical coupling. As they leave the plate, the waveshifter fibers are spliced onto transparent readout fibers. These fibers are bundled together with fibers from other plates, and each bundle is taken to a phototube to form the readout for a tower of calorimetry. This pre-assembled and tested tower of scintillators is then inserted into the absorber stack to form the completed module.

Arbitrary lateral and depth segmentation is possible with appropriate bundling of fibers. For example, the transverse granularity of the electromagnetic calorimeter can easily be made finer than that of the hadronic section, and the number of depth segments is unrestricted. The same tile/fiber technology can be used to insert "pre-radiator" and shower-max "strip" detectors into the stack.

2 Advantages of Tile/Fiber

The tile/fiber approach shares many of the features of conventional scintillator tile/wavelength shifter bar calorimetry. These include the "natural" sampling geometry of a scintillator/absorber stack, low cost, a very small "constant term", and a stochastic resolution which is easily tunable by varying the sampling density. This geometry has an established performance in collider detectors. In addition, the tile/fiber technique holds a number of advantages over waveshifter bar readout:

Firstly, the optical segmentation is independent of the mechanical segmentation. In conventional WLS-bar readout, the positions of the readout bars must be placed on the mechanical "cracks" between calorimeter modules. When one contemplates calorimeters with the $\eta - \phi$ segmentation of a typical SSC or LHC detector, one sees that conventional WLS-bar readout will result in several hundred (or more) mechanical subassemblies. In addition, it is very difficult to produce a credible design for a finely segmented endplug calorimeter. With tile/fiber readout, the optical readout path need not coincide with the edges of each tower, and it is possible to place many optical towers in a single mechanical module.

The size of the optical "readout crack" is much smaller in a tile/fiber design, typically $< 0.5\%$ of the tower area vs. several percent of the tower area for WLS-bar readout. Furthermore, the bundle of optical readout fibers can easily be made non-projective, so that neither the average response nor the resolution of the calorimeter will suffer in the vicinity of the readout bundle.

Our ability to reliably splice to a clear readout fiber avoids one of the nagging difficulties of conventional WLS-bar readout, namely the "hot spot" in the response of the calorimeter caused by Cerenkov light from EM showers in the WLS readout bar. The small amount of Cerenkov light which is trapped in the readout fibers has not been waveshifted and is easily filtered.

We find that with a judicious choice of fiber placement and selective masking of a high-quality reflective wrap, we can achieve achieve spatial uniformities of $\sigma \sim 2\%$ across the surface of a tile.

The light yield of the tile/fiber readout system is ~ 4 times higher than WLS bar readout. This is due primarily to the improved coupling of the scintillator light to the waveshifter, and to the long attenuation lengths in the clear readout fibers. Typical light yields are ~ 3 photoelectrons per MIP per 2.5mm plate, using a 1mm readout fiber 2m in length. This factor of ~ 4 can be used in trade for a number of items. One can reduce the diameter of the readout fiber, thereby further decreasing the size of the readout bundle. Alternately, one could switch to more heavily quenched scintillator and shifter dyes with faster decay times but lower light yields. The same result can be achieved by passive clipping of the pulse from the PM tube, a procedure which shortens the pulse but effectively throws away photoelectrons. Finally, one can entertain the notion of using an extremely long (~7m) readout fiber in order to remove the phototubes and electronics completely from the detector. At present we are keeping this factor as a safety margin in the calorimeter designs for the CDF endplug and the SSC prototypes.

Another advantage of the tile/fiber design is that the optical cavities are small (<1ns collection time). This yields a rapid optical pulse for which the time constant is determined mainly by the decay time (~10ns) of the green waveshifting dye. The time dispersion of the readout fiber bundle is also considerably smaller than that of a conventional readout bar, since the cosine of the trapping angle in a typical plastic fiber is 0.95.

The radiation hardness of the tile/fiber design is enhanced with respect to WLS-bar readout schemes due to the shortness of the optical paths for the blue (unshifted) scintillator light. As is well known, radiation damage in scintillator plastics affects the shorter wavelengths first – the plastic turns brown. Transmission of green light is relatively unaffected until much higher doses. Thus, a tile/fiber calorimeter in which the blue light travels 1-2cm before collection will be remain usable a much higher radiation dose that a WLS-bar readout calorimeter in which the collection distance for blue light is 10-20cm.

3 Tile Production Techniques

The basic tile unit (fig.2) is composed of a scintillator plate of dimensions typically 6X6 cm (the pad size of the tower) with a "U" shaped groove formed in it. Tile shapes can be either rectangular for use in a barrel calorimeter, or keystone shaped for en endcap design. Inside the U groove is a wavelength shifter fiber (approximate length of 12 centimeters) spliced on each end to clear optical fibers (length about 3 meters) that carry the light out to phototubes. The construction of a tile unit then consists of 3 principal operations: building the spliced fiber; manufacture of the tile; and gluing the two pieces together.

The tile pieces will be laser cut from plates of the bulk scintillator. The "U" groove of size 1X1 mm is also laser milled by using the beam at a lower power. A small hole of 0.5 mm diameter is drilled thru the tile at the apex of the "U", again by the laser. The fiber is then loaded into the groove, and tape is applied to the top surface of the tile to seal the fiber into place. Glue is then inserted into the cavity formed by the "U" groove and the tape, by injecting through the 0.5mm hole. This procedure eliminates air bubbles in the glue joint and generates a very reproducible optical connection between the tile and fiber. After the tile units are formed, the edges of the tiles are painted white with optical white paint.

First round prototyping (with Laser Services, Westford, MS) have been very successful, generating edge cuts and grooves which are better than can be obtained by diamond fly-cutters. Second round prototyping of 100 tile sets for test beam calorimeters are undergoing assembly and testing.

3.1 Fiber Splicing Technique

The spliced fiber will be constructed by heat-welding wavelength shifter fibers to clear fibers. The techique that we have developed[4] is as follows (fig. 3). Cut the ends of the fibers to be spliced at approximately right angles, using a razor knife or similar tool. Insert the ends of the fibers to be joined into a glass capillary tube of ID the OD of the fiber. A small coil then heats the tube to about 200 degrees F for approximately 1 minute. At this point, the fibers have melted together and fused. As the fibers cool, the differential contraction of the fibers cause them shrink away and release themselves from the glass tube. Initial studies of this simple technique are surprisingly successful: We have made splices with transmission of 95% with splice-to-splice variation of about 2%.

3.2 Uniformity Measurement

The tile uniformity is measured in a computerized test fixture. A 1 milliCurie collimated Sr^{90} source illuminates the tile, and the average current is read out for various positions on the tile surface. A computer controlled XY table drives the tile around the source. The source is collimated to $\sigma \sim 2$mm in order to match the shower size in an EM calorimeter. The response map so generated is used to calculate a correction mask pattern, which is stored in the computer until needed. Tiles that fall outside of selection criteria are discarded. Fig. 4 shows a typical response map for an uncorrected tile. The scans are in the direction crossing the fibers (Y). Each scan line represents a scan at a different X. The fibers generate peaks in light yield which are visible in the figure. These peaks are suppressed by a "masking" technique.

3.3 Masking

Tiles that do not have a completely uniform response can be "flattened" by a masking technique. The tile is wrapped in a reflective metal foil, with the foil blackened in areas where the tile response is too large. This mask pattern is used both correct for both the spatial variations and the piece-to-piece variations in the overall light yield of the tiles. The operating principle of this technique is as follows: Depending on the doping of the scintillator tile, the conversion distance of UV primary scintillation light to blue light is of the order 1mm. Therefore UV light generated near the surface of the tile has a large probability of escaping before being shifted. Placing a UV reflecting surface near the tile will cause the escaping UV light to be reflected back into the tile, which produces a local increase in the light yield. Conversely, a UV black material will cause a local suppression in the light yield. With the polystyrene scintillators that we normally use, there is about a 20-30% dynamic range in the correction, which is sufficient to flatten out any observed nonuniformities. The correction mask of dark patterns is generated using the measured tile response map. This correction mask is applied to a metalized foil[5] with a conventional laser printer.

The resulting mask flattens the tile response to the $\sigma \sim 1\%$ level.

4 Choice of Absorber

The key issues in the choice of an absorber for an SSC calorimeter are performance (energy resolution), cost, speed of response, magnetic properties, mechanical convenience, and neutron albedo in the central tracking volume. Our control of the spatial uniformity of the tile/fiber readout allows us to consider thinner (1-3 mm) scintillator tiles, than would otherwise be practical with conventional tile calorimetry. This allows us the freedom to design a high resolution, compensating calorimeter using lead, iron, uranium, or a wide variety of combinations of the above.

For the electromagnetic calorimeter, we view the resolution as the key parameter. Compensation properties are secondary since it is impossible to deposit a large amount of hadronic energy in the EM calorimeter (unless of course the incoming hadron(s) charge-exchange in the EM calorimeter, in which case the energy is still accurately measured in the EM calorimeter). Thus, for both the CDF upgrade and for SSC prototype work we are following the common choice of Pb as the EM radiator. We choose a Pb:Scintillator ratio of 2:1 by volume, which yields an adequately compensating e/h response ratio of $\sim$1.1. The resolution of the EM calorimeter will be determined primarily by economic considerations (number of samples in depth). We anticipate Pb radiator thicknesses of 0.5mm to yield energy resolutions of $\sim 15\%/\sqrt{E}$, so that at energy ranges of interest at the SSC the 1-2% constant term will dominate the resoluton of the EM calorimeter.

At the SSC, the speed of response is one of the key issues in the design of a hadron calorimeter. Generally speaking, there are two mechanisms for achieving compensation in a samplng calorimeter: The first of these (neutron interactions in the scintillator) yields a slow signal which arrives 50-100ns following the primary energy deposition. In addition to being slow, this neutron "timing tail" fluctuates on an event-to-event basis. This makes it impossible to clip it away in the same manner as the scintillation timing tail, which is purely exponential and is reproducible from pulse to pulse. The second mechanism (suppression of the EM response by alternation of high-Z and low-Z materials) is essentially instantaneous. Clearly, to obtain the fastest possible time response, one would like to use a system with a very low neutron yield and which achieves compensation largely through the suppression of the EM response. The relative neutron yields from U, Pb,and Fe are in the approximate ratio of 5:2:1, suggesting iron as an extremely fast hadron absorber. It is interesting to point out that an iron calorimeter, with its very low neutron yield, will create the smallest neutron flux in the central tracking volume. In addition, iron has other well known advantages in terms of cost and mechanical convenience.

We are prototyping an iron-dominated hadronic calorimeter with the goal of clipping the phototube pulse back to baseline, and achieving approximate compensation, inside a 16ns gate (one crossing time at the SSC). The prototype takes advantage of the ability of the tile/fiber techique to read out large, thin scintillator plates in order to obtain the proper Fe:Scintillator ratio (various computer codes predict the compensating mixture of Fe:Scintilator is between 10:1 and infinity). If necessary, the e/h response will be tuned by the insertion of a small amount of high-Z material (probably lead) into the stack. The purpose of this material is to convert the low-energy γ's from EM showers. Insertion of this material immediately upstream of the scintillator will increase the EM response while leaving the response to MIPs and neutrons essentially unchanged. Conversely, insertion of the lead downstream of the scintillator will suppress the EM response. A similar suppression of the EM response can be obtained by "cladding" the scintillator in a low-Z material (such as aluminum) which will not convert many of the low-energy γ's but will serve to range out the secondaries from γ's which have converted in the iron and thereby shield the scintillator from this EM energy. If some combination of these techniques is successful at reducing the e/h significantly below 1.0, we will then add additional hydrogenous material ("dead plastic") into the stack in order to absorb more of the slow, unwanted neutron signal. These (and other) compensation techniques are being studied for iron hadron calorimeters in the FNAL test beams in 1990-91.

5 Staggered Plate Calorimetry

We have developed a unique mechanical structure and manufacturing technique which is being tested on our SSC hadron calorimeter prototype. The basic concept (fig.5) is to produce each "wedge" of calorimetry in the central barrel which is essentially a solid, keystone-shaped block of iron with a large number of slots cut into it. The slots, which accept the completed scintillator tile assemblies, are staggered in adjacent towers in η so as to maintain the mechanical integrity of the block. The mechanical loads are bypassed locally around each of the scintillator tile slots, and there is no need for large semi-projective structural members to "reach around" the stack to provide mechanical support. In this sense, this design has absconded with one of the main attractive features of "spaghetti" calorimetry, namely that the finished module is a single self-supporting structural unit with no "cracks" needed for mechanical support.

Several fabrication techniques were investigated for the iron block with the slots in it (fig. 5), including casting, water jet cutting, and welding. The method chosen was to laminate the piece together out of a large number of stamped plates, in the manner commonly used to produce large accelerator magnets and industrial transformer cores. The pattern of slots (which determine the pattern of towers in η) is punched into each lamination by a numerically controlled punching machine. The laminations are then stacked and held together by a combination of B-stage epoxy and seam welding. A final machining operation grinds down the faces of both sides of the keystone block, in order to guarantee that the pieces fit together precisely when the complete arch of calorimetry is assem-

bled. Small, non-projective grooves are machined in the side of each block to accept the readout fiber bundles for each tower. The final cost of iron structures manufactured by this method is in the range of \$0.75-\$1/lb.

The last step in the assembly of the calorimeter modules is the insertion (fig. 1) of completed tower assemblies of scintillating tiles into the absorber block. Prior to insertion, each tower assembly will be tested for light yield and uniformity, and the complete assembly will be annealed in it's final configuration to remove internal stresses on all tile and fiber components.

6 Application to CDF Endplug

The tile/fiber system has been presented to the Fermilab PAC as an upgrade proposal to replace the gas proportional calorimetry of the CDF endplug. In this application the tile/fiber system has the unique advantage that the assembled planes of scintillator can be inserted into the gaps of the existing absorber structures, in place of the existing gas proportional chambers. The projective towers are formed by the optical segmentation of the tiles within each scintillator plane.

The clear optical readout fibers from each tile are led to phototubes outside of the calorimeter along the path currently taken by the electrical cables of the gas calorimeters. Thus the small size and flexibility of the readout fibers allows us to retain the absorber structures which were originally designed for use with the gas proportional chambers, thereby avoiding mechanical construction costs, the necessity to re-map the magnetic field, etc. In addition, even in the endplug geometry each tile can be made quite uniform, with an rms variation of light yield with position 1-2%. The spatial uniformity of this technique provides benefits to both electron and jet physics.

Prototypes of both EM and Hadron calorimeters are being evaluated in the current (spring '90) test beam at FNAL, so that results will be available in time for production decision later this year.

References

[1] M.G. Albrow *et al.*, NIM A256 (1987) 23.

[2] The CDF Collaboration, "Proposal For an Upgraded CDF Detector ", Draft: May 1990, Preliminary Version, CDF/DOC/PUBLIC/1172

[3] "Expression of Interest by the Solenoidal Detector Collaboration to Construct and Operate a Detector at the Superconducting Super Collider", submitted to the SSC laboratory, Dallas TX, June 1990.

[4] M. Atac, W.Foster, M. Lundin, "A Simple Method for Fusing Plastic Fibers", Fermilab technical note FN-537, March 1990.

[5] Obtained from Graphic Arts Systems, Inc. Cleveland, OH USA

Figure 1: Schematic Scintillating Tile/Fiber Calorimeter

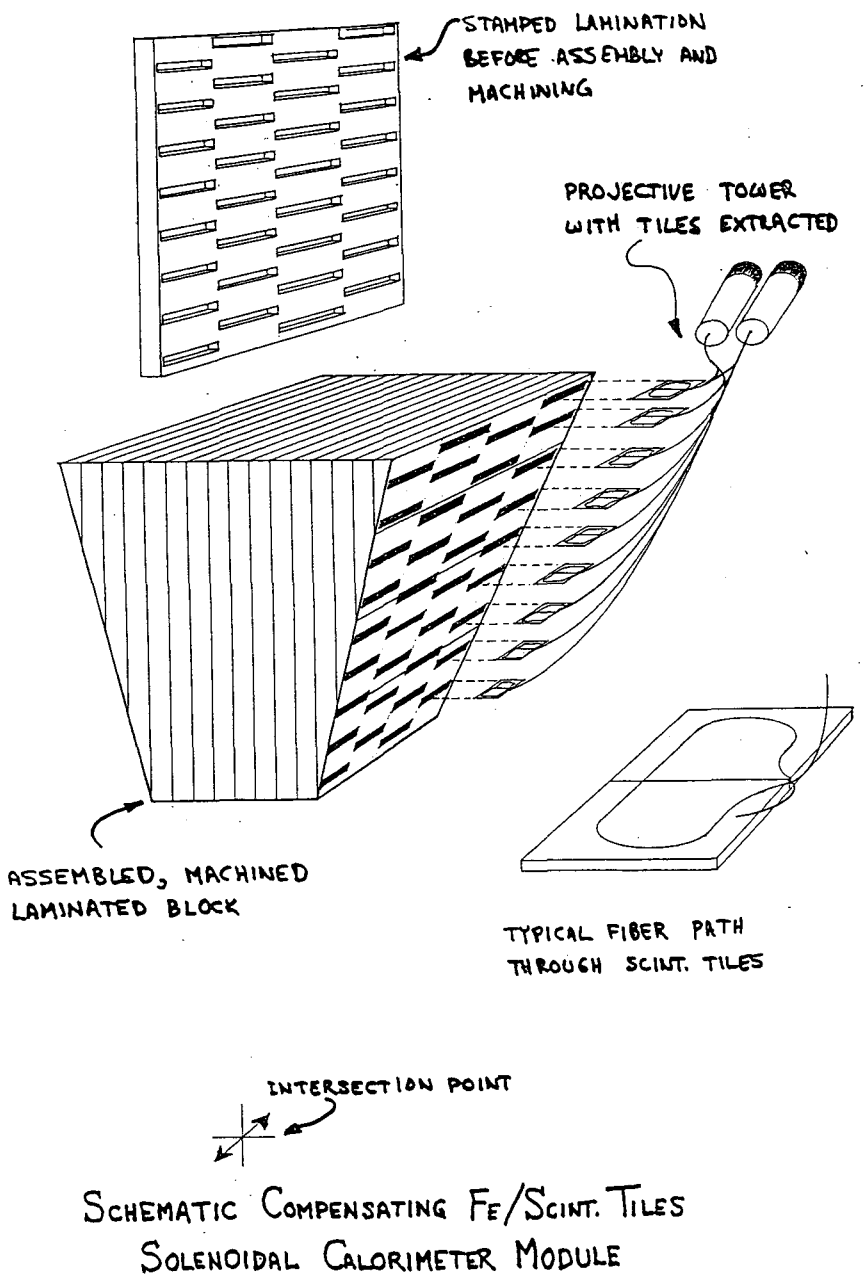

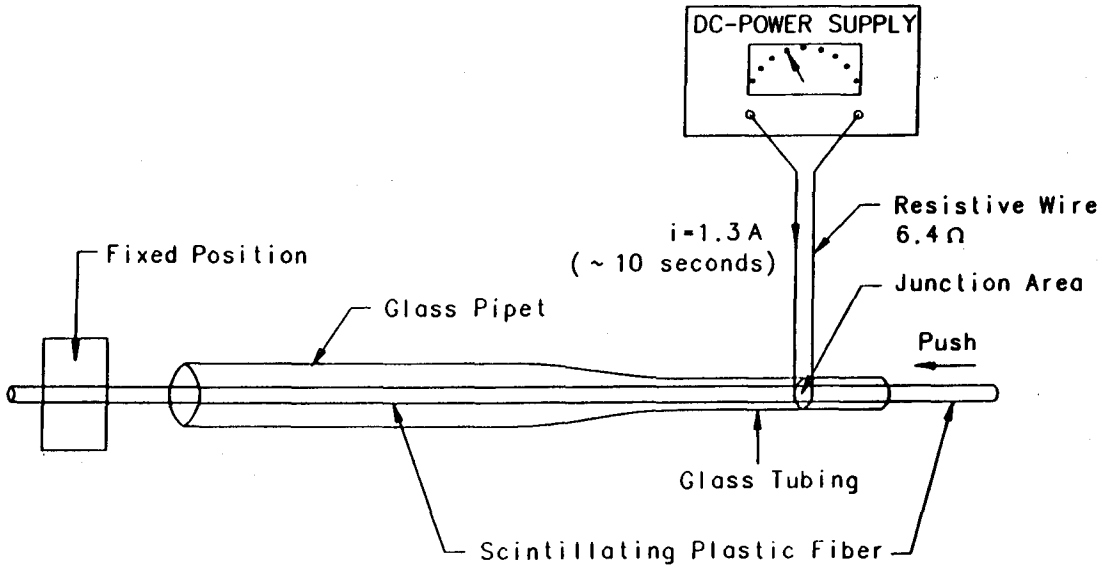

Figure 3: Method for Splicing Plastic Optical Fibers.

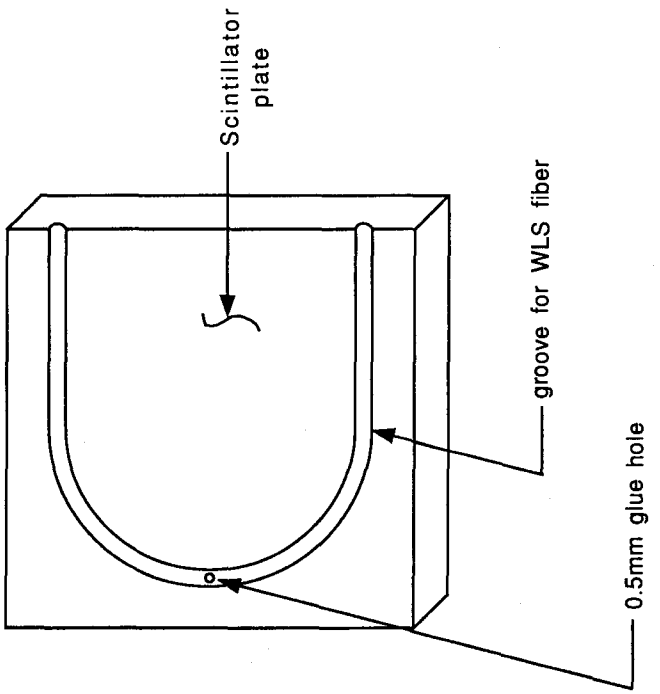

Figure 2: Scintillating Tile/Fiber assembly

Figure 5: Iron Lamination Structure of Prototype Scintillating Tile/Fiber Hadron Calorimeter

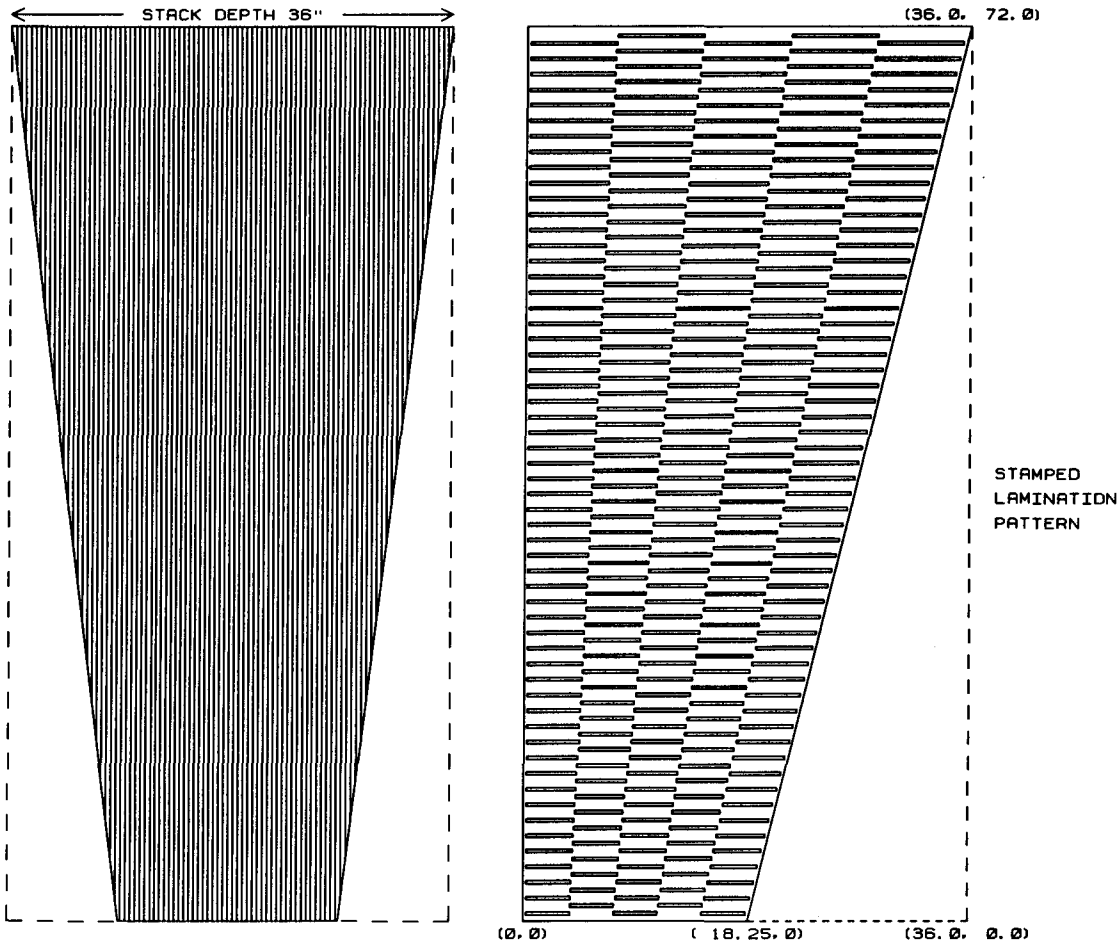

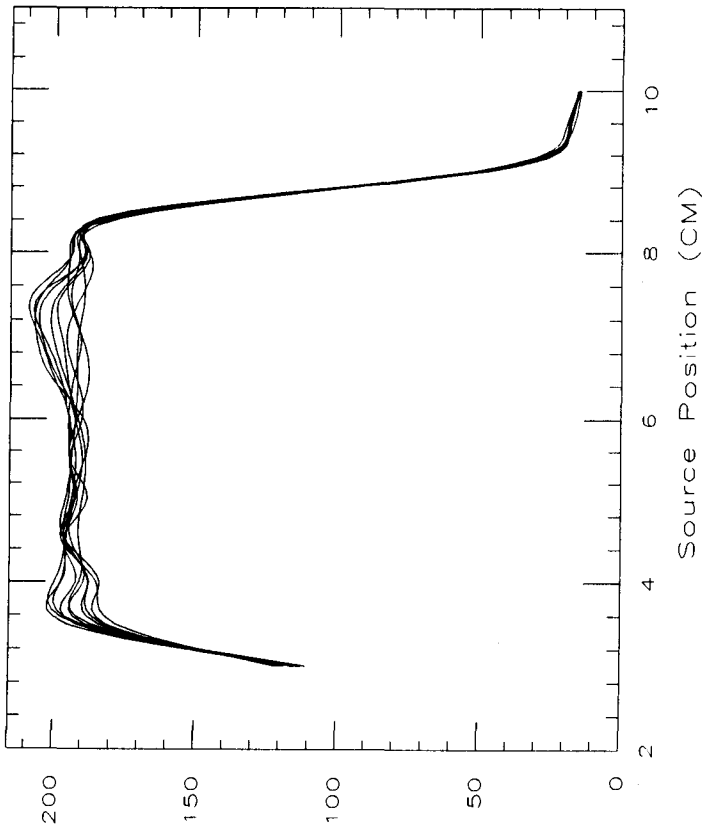

Figure 4: Uncorrected Uniformity of Response of a Typical Scintillating Tile/Fiber Assembly. After a correction mask is applied, the uniformity of response is σ ~2% or less.

Measurement of Radiation Damages in Liquid Scintillators by ^{60}Co γ rays

Masami Chiba, Satoshi Abe
Department of physics, Tokyo Metropolitan University
Setagaya-ku, Tokyo 158, Japan

Hideyuki Kawai
Chiba University
Yayoi-cho, Chiba city 206, Japan

Akihiro Maki, Yasuhiro Sugimoto
National Laboratory for High Energy Physics
O-ho, Tsukuba city, Ibaraki 305, Japan

Norio Tamura
Department of physics, Okayama University
Tsushimanaka, Okayama city 700, Japan

Abstract

A liquid scintillator is considered as an active material in a calorimeter. Radiation damages of five liquid scintillators and container tubes were investigated.

*Presented at the International Workshop
on Solenoidal Detectors for the SSC,
KEK, Tsukuba Japan, April 23-25, 1990.

1. Introduction

We have searched a radiation hard liquid scintillator and a clad material which can be used even in a heavy radiation environment near the beam pipe. We expect e/h approaches unity even in a lead absober when a liquid scintillator with H/C = 2.0 is used. The higher hydrogen content promotes neutron detection in a hadron shower [1]. Features of a liquid scintillator are compared with those of others in table 1. A liquid scintillator has several advantages. The e/h may be equal with unity even with a lead absober. The signal is fast. It is strong in radiation damage and needs no cryogenics. The disadvantage is flammable.

Adding the above features a liquid scintillation calorimeter will satisfy the requirements in the SSC experiment such as good energy and position resolutions with fine segmentaiton and small dead space. Owing to those good features, it is at least suitable for a forward calorimeter in the SSC experiment. A pair will be set at both forward andgles as shown in fig. 1(a). The scintillation light will be measured by mesh tubes, avalanche photodiodes and so on.

We are considering a calorimeter in which the scintillation light is guided by a totally reflecting clad on the inner wall of a hole drilled in the converter like lead to a photosensitive device attached on the end. The clad should have a lower refractive index than that of the liquid scintillator. Many holes are drilled along the calorimeter axis. We are trying to

drill through lead. The way is that thin aluminum pipes with endplugs are put in melted lead. After the lead becomes solid, the pipes are melted away by a chemical process.

Another type is a fibre wavelength shifter readout as shown in fig. 1(b). Lead plates with a thickness of 8 mm are stacked with 2 mm spacing. The surfaces are covered with a sheet made of lower refractive index material. A commercialy available fibre-wavelength shifter is based on polystyrene (n = 1.59) with a clad of PMMA (n = 1.49) which fits NE235 (n = 1.47) and kerosine scintillator (KS) (n = 1.44) concerning the refractive index. The scitillation light can go in the fibre with small reflection loss. The fibre with a diameter of 1 mm is curled in a layer and goes up to the next layer through a hole of the plate. At the end of the electromagnetic part the fibre is connected with an optical fibre which gets through the hadronic part. If this readout scheme works, a photosensitive detector like an avalanche photodiode with a small photosensitive area can be used. The problem is that the radiation hardness is limited by the fibre. But we know that the longer light like R3 transmits rather well than Y7 light against the radiation damage in the fibre wavelength shifter.

2. Radiation damage test of liquid scintillators

Five kinds of liquid scintillators with a plastic scintillator were tested by ^{60}Co γ rays. The characteristics are presented in table 2. KS was made according to ref. 2. NE235 and KS have a maximum hydrogen carbon ratio 2.0. The maximum refractive index is 1.523 for NE216 and the miminum is 1.44 for KS. The light yields are measured and are normalized to 100 % for the plastic scintillator. The mimimum is 45 % for the KS. The irradiated doses are 1.4×10^6 rad, 1.4×10^7 rad and 1.4×10^8 rad for the durations of 1, 17 and 170 hours, respectively. All the irradiation processes, the measurements and the storage were done in air and room temperature. The measured items are variations before and after the irradiation in the light yield, the light transmission spectrum, the light excitation spectrum and the light emission spectrum. The light yield variation up to 30 days after the irradiation was measured.

Figures 2(a) - 2(c) show light yield variation before and after the irradiation up to aroud 33 days. The light yield is normalized 100 % before the irradiation. The 0 day means just after the irradiation. Fig. 2(a), (b) and (c) show the result of the irradiations for 1.4×10^6 rad, 1.4×10^7 rad and 1.4×10^8 rad, respectively. For 1.4×10^6 rad a small recovery is seen for the plastic scintillator SCSN38 as shown in fig. 2(a). All the scintillators keep 80 % light yields. For fig. 2(b), SCSN38 recovers from about 20 to 70 %. The others show no recovery. NE216 and NE224 maintain 80 % light yields. For 1.4×10^8 rad the best was KS which maintained 50 % light yield showing a small recovery. The plastic scintillator still recovers from 10 to 20 %. Fig. 3 shows summary of the light yields against the irradiation doses. KS shows the best at 10^6 rad and 10^8 rad but at 10^7 rad NE216 is the best. KS and NE235 show similar behaviour. SCSN38 shows a remarkable recovery at 10^7 rad.

The light transmissions against the wavelength are shown in fig. 4(a) - (c). The transmission rates are normalized to 100 % at the wavelength of 800 nm. The best liquid scintillator is NE224 as shown in fig 4(a). At 420 nm the transmission deteriorates from 100 to 90 % at 10^8. The worst liquid scintillator is NE213 presented in fig. 4(b). At 440 nm the transmission decreases from 100 to 50 % for 10^8 rad. For the comparison, the plastic scintillator SCSN38 is shown in fig. 4(c). At 420 nm the transmission decreases from 95 to 5 % for 10^8 rad.

The excitation spectrum is the emission intensity measured by setting the emission wavelength at the maximum intensity changing the excitation wavelength. Emission spectrum is the emission intensity fixing the excitation wavelength at the maximum intensity. Excitation and emission spectra with respect to the wavelength are shown in fig. 5(a) - (c). They are normalized to 100 % at the peak wavelength. The smallest change was seen in NE224 as shown in fig. 5(a). The peak emission wavelength does not move appreciably even in 10^8 rad. The largest change seen in the liquid scintillators was KS as shown in fig. 5(b). The peak emission wavelength moves from 410 to 440 nm for 10^8 rad. For the comparison the plastic scintillator SCSN38 is shown in fig. 5(c). The emission spectrum moves longer wavelength for 10^8 rad.

3. Total internal reflection and radiation damages of tubes

We tested 15 different kinds of plastic tubes. Most of them were suffered by the solvent. Four kinds of tubes survived; teflon, viton (transparent), polyimide and urethane. Among them only teflon and viton including fluorine could be used for total internal reflection readout because of their low refractive indeices. We radiated the tubes by ^{60}Co γ ray. Teflon becomes fragile with 10^5 rad and broken into pieces with the dose of 10^7 rad. Viton tube was slightly colored, but no significant mechanical change even with 10^7 rad. Only viton tube satisfies the requirements.

The tube was filled with the liquid scintillator NE224. The light was read by a quantacon photomultiplier R1332 through an optical fibre. The tube was radiated by ^{90}Sr β rays with a trigger counter changing the distance from the tube. Fig. 6 shows the intensity of the scintillation light transmitted through a viton tube. There is a slight degradation after the irradiation of 10^7 rad. The light attenuation length was about 100 cm.

6. Discussion and Conclusion

We find radiation hard liquid scintillator like NE216, NE224, NE235 and KS. Up to the present viton is the best clad. Liquid scintillation calorimeter is hopeful but many works should be done to realize.

1) Drill small long holes in a lead block.
2) Search a more suitable material like Glass Resin which permits total reflection on the hole surface.

3) Test e/h = 1 in a lead absober by H/C = 2.0 liquid scintillators.

4) Make stronger liquid scintillators in radiation damage by lenghthening the fluorescent wavelength.

5) Develope a circulating system to replace damaged liquid scintillator with fresh one.

6) Exploit fibre wavelength shifter readout method.

This work was supported by the US-Japan scientific collaboration program.

Table 1

Features of active materials in a calorimeter. The quality order is presented by A, B and C for each item.

	liq. scinti.	plastic scinti.	warm liq.	liq. argon
e/h=1 with lead	A	B	A	C
signal speed	A	A	B	B
radiation hardness	B	C	B	A
cryogenics	A	A	A	B
flammable	B	A	B	A

Table 2

Features of the liquid scintillators tested

	solvent		H/C	n	light yield
NE224	trimethyl benzen	C_9H_{12}	1.330	1.505	82 %
NE216	?		1.171	1.523	85 %
NE213	xylene	C_8H_{10}	1.213	1.508	85 %
NE235	mineral oil	C_nH_{2n}	2.0	1.47	58 %
kerosine scinti. (KS)	kerosine 3.0 g/l DPO 0.02 g/l POPOP	C_nH_{2n}	2.0	1.44	45 %
Plastic scinti. SCSN38	plystyrene	C_8H_8	1.0	1.58	100 %

References

[1] R.Wigmans, Nucl. Instr. and Meth. A259(1987)389.

[2] K.Yamakoshi, Nucl. Instr. and Meth. 126(1975)407.

Figure captions

1(a) Forward calorimeters at the SSC experiment.

1(b) A fibre wavelength shifter readout scheme.

2 Light yield variations before and after the irradiation.

(a) 1.4 x 10^6 rad

(b) 1.4 x 10^7 rad

(c) 1.4 x 10^8 rad

3 Light yields against the irradiation doses.

4 Light transmission spectra.

(a) NE224

(b) NE213

(c) SCSN38

5 Light excitation and emission spectra

(a) NE224

(b) KS

(c) SCSN38

6 Intensity of the scintillation light of NE224 transmitted through an irradiated Viton tube.

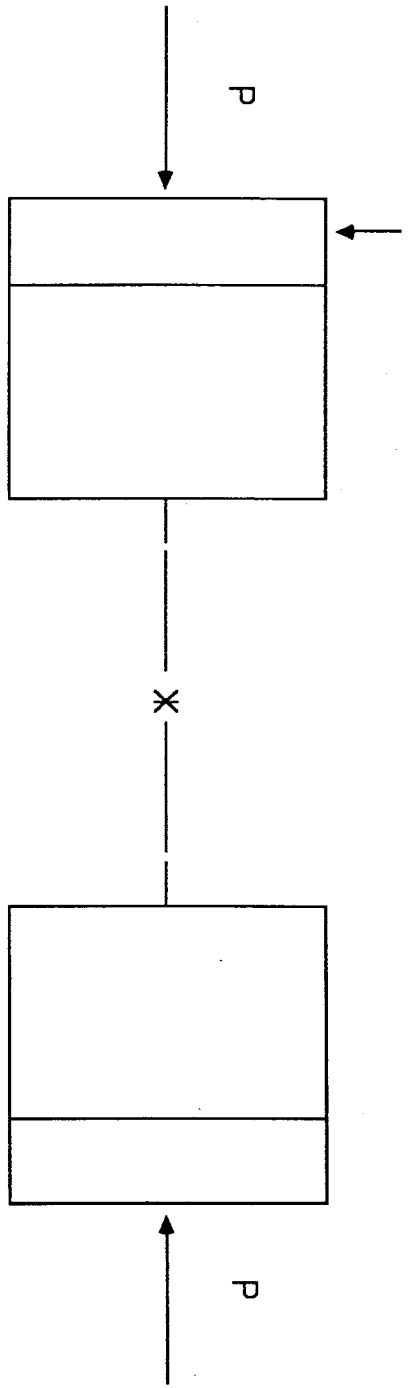

Fig. 1(a)

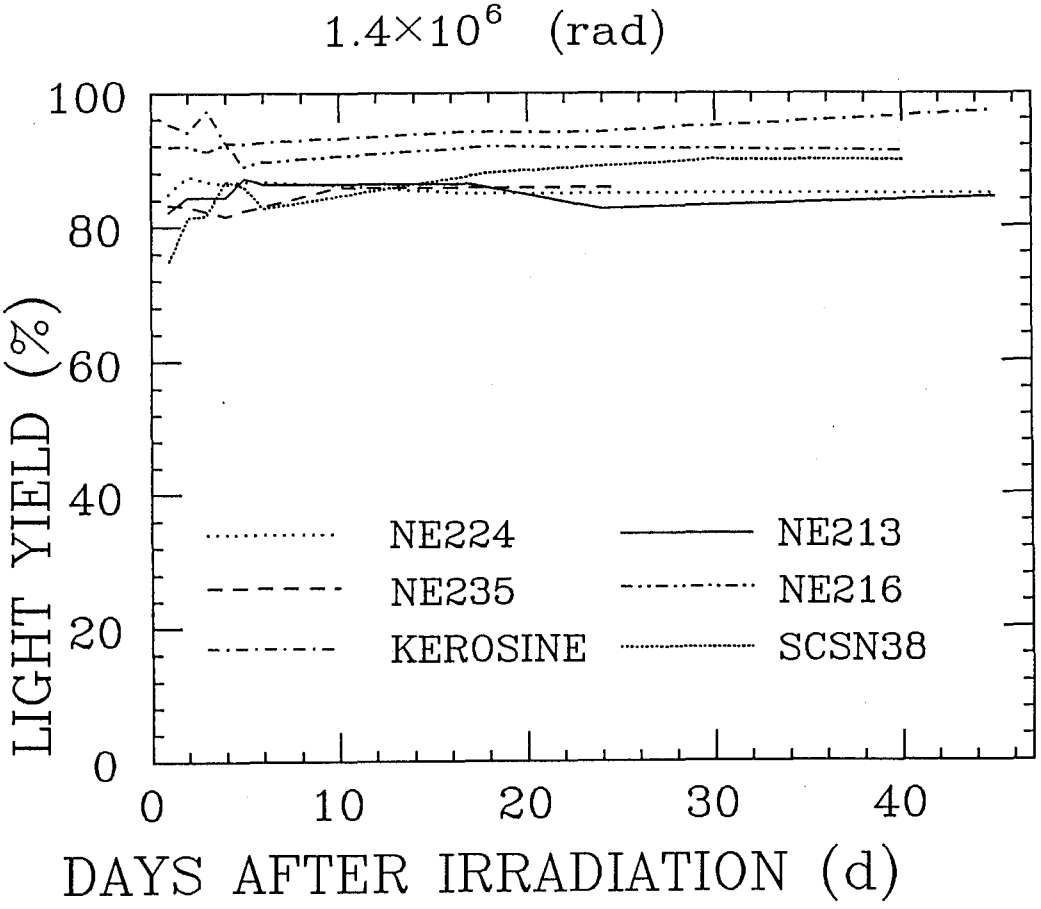
1.4×10^6 (rad)
100
80
60
40
20
0
LIGHT YIELD (%)
0
10
20
30
40
DAYS AFTER IRRADIATION (d)
NE224
NE235
KEROSINE
NE213
NE216
SCSN38

Fig. 2(a)

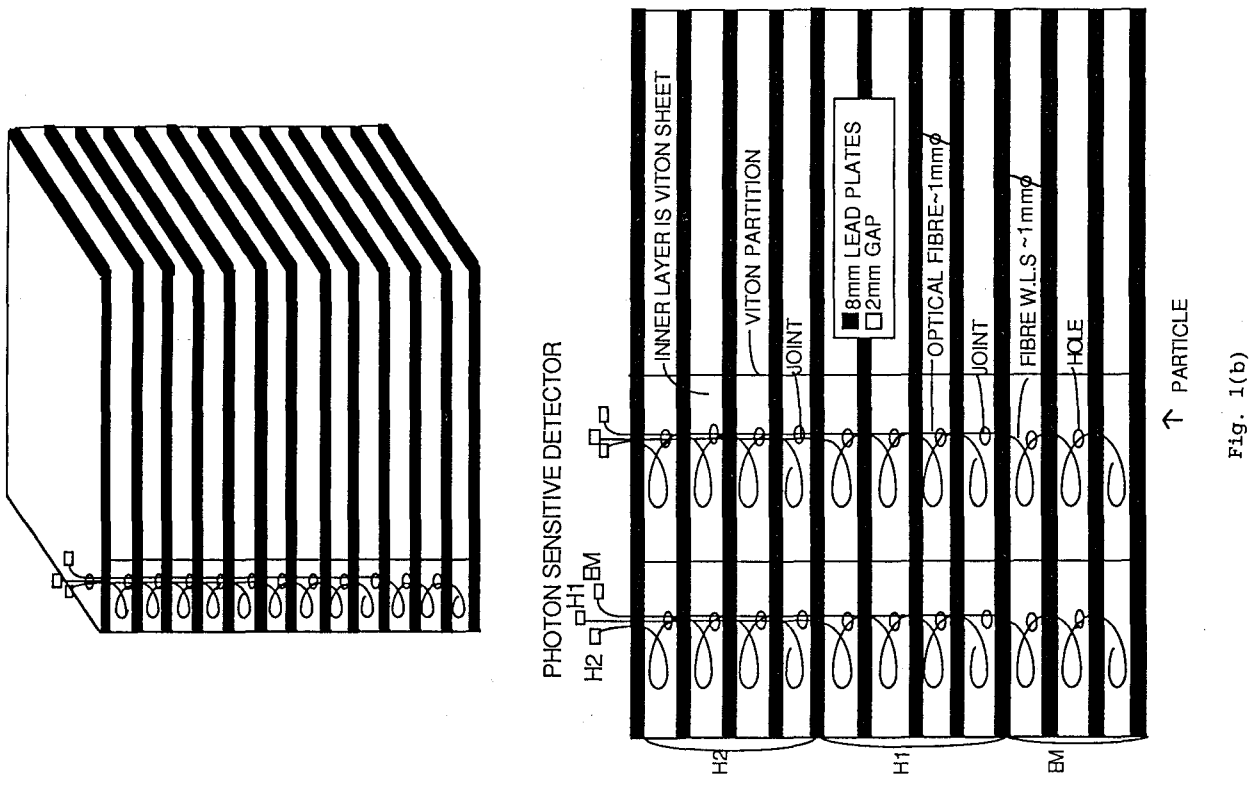
PHOTON SENSITIVE DETECTOR
H2
H1
BM
INNER LAYER IS VITON SHEET
VITON PARTITION
JOINT
8mm LEAD PLATES
2mm GAP
OPTICAL FIBRE~1mmφ
JOINT
FIBRE W.L.S ~1mmφ
HOLE
← PARTICLE
H2
H1
BM

Fig. 1(b)

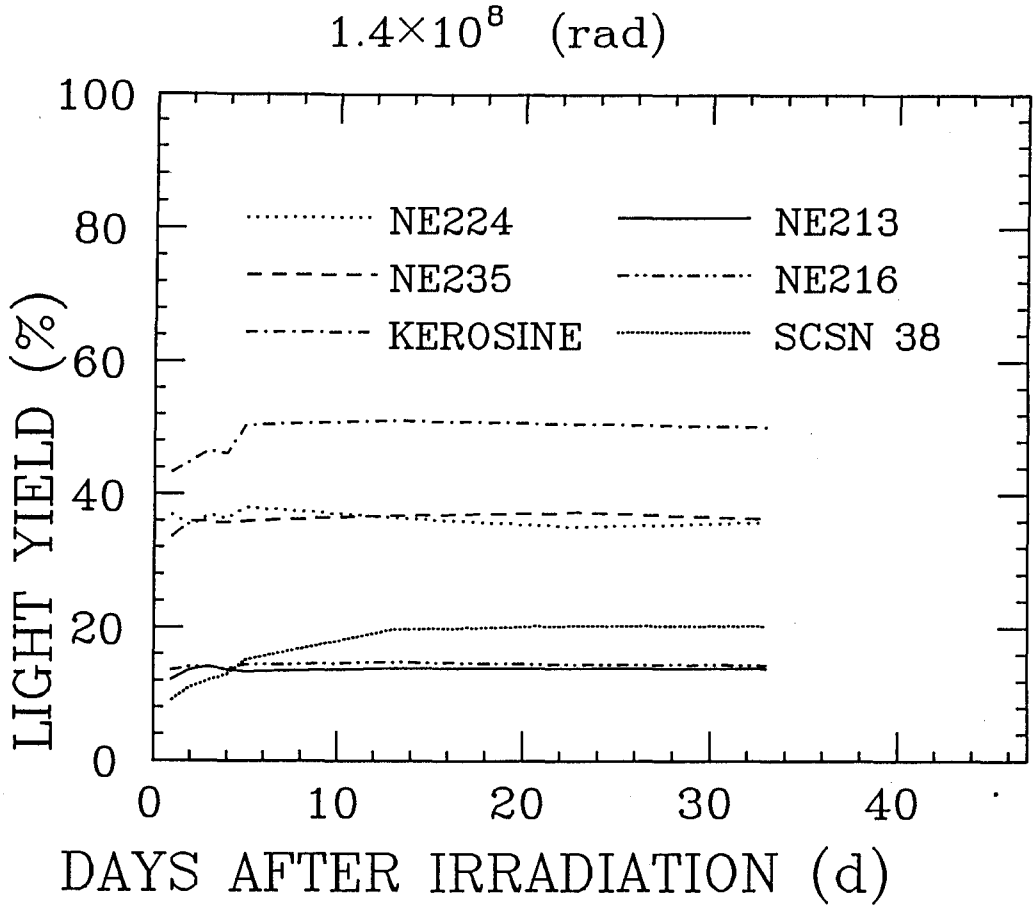
1.4×10^8 (rad)
LIGHT YIELD (%)
100
80
60
40
20
0
0
10
20
30
40
DAYS AFTER IRRADIATION (d)
NE224
NE213
NE235
NE216
KEROSINE
SCSN 38

Fig. 2(c)

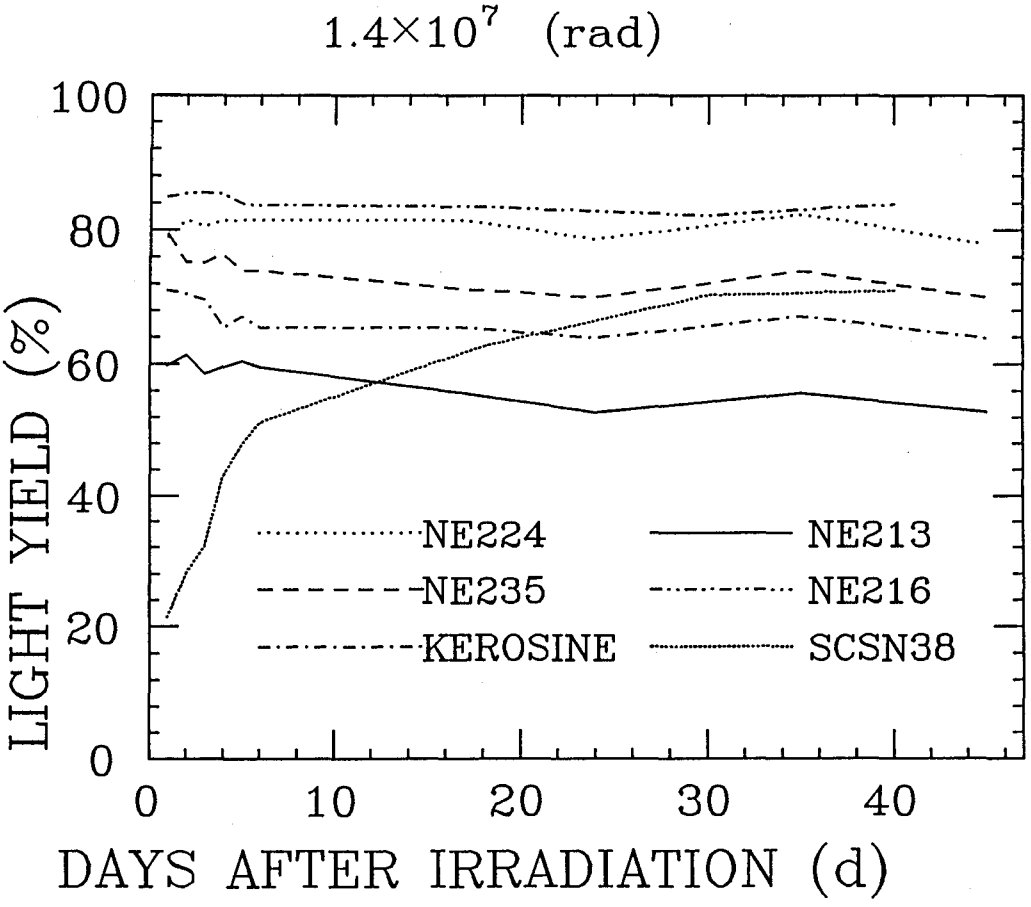
1.4×10^7 (rad)
LIGHT YIELD (%)
100
80
60
40
20
0
0
10
20
30
40
DAYS AFTER IRRADIATION (d)
NE224
NE213
NE235
NE216
KEROSINE
SCSN38

Fig. 2(b)

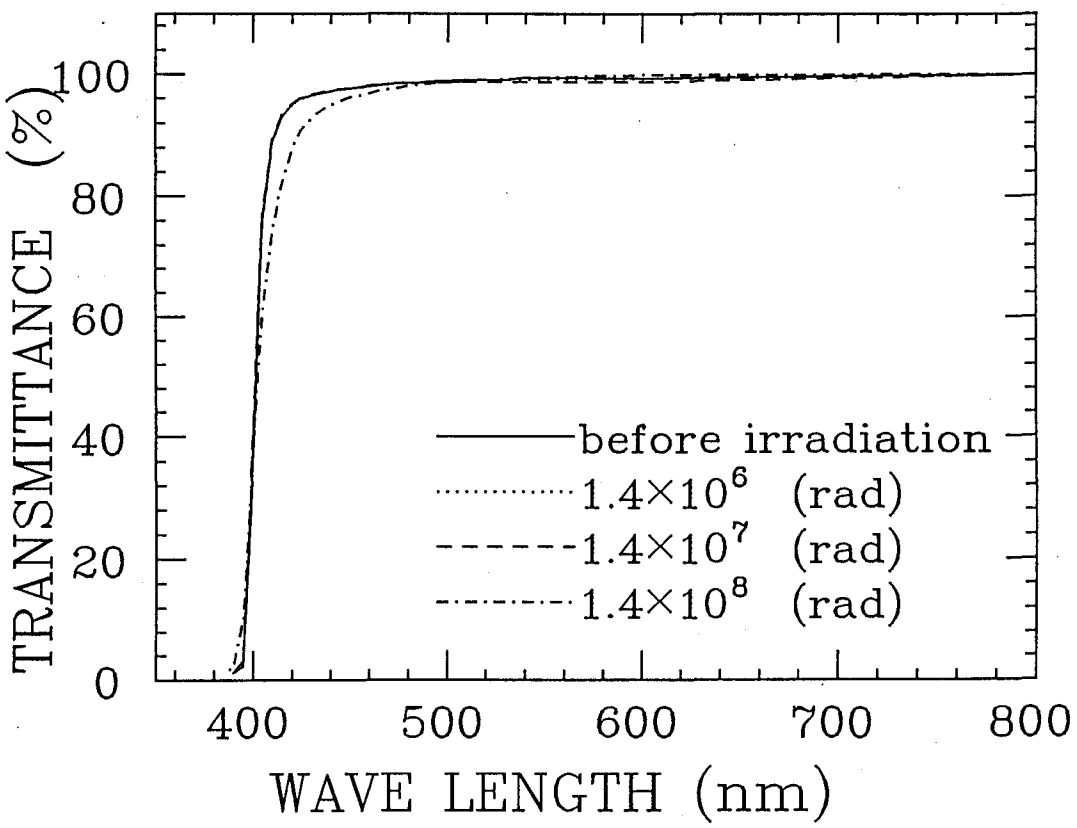
NE224
TRANSMITTANCE (%)
100
80
60
40
20
0
400
500
600
700
800
WAVE LENGTH (nm)
before irradiation
1.4×10^6 (rad)
1.4×10^7 (rad)
1.4×10^8 (rad)

Fig. 4(a)

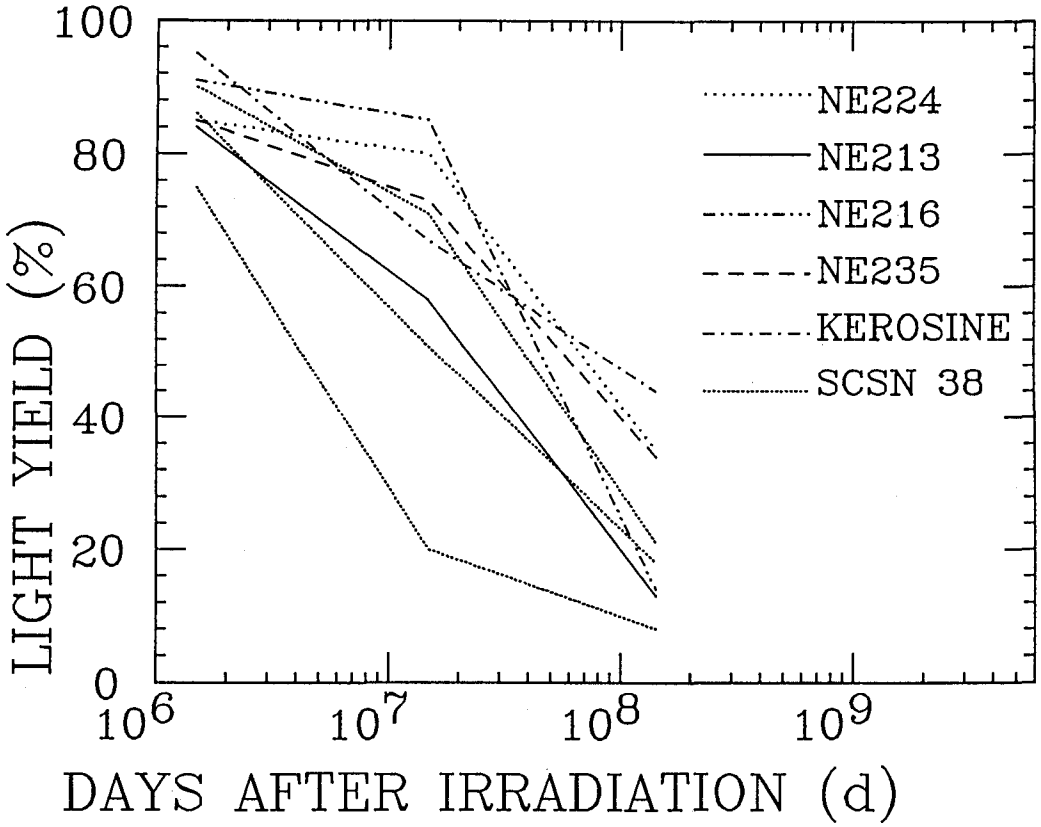
LIGHT YIELD (%)
100
80
60
40
20
0
10^6
10^7
10^8
10^9
DAYS AFTER IRRADIATION (d)
NE224
NE213
NE216
NE235
KEROSINE
SCSN 38

Fig. 3

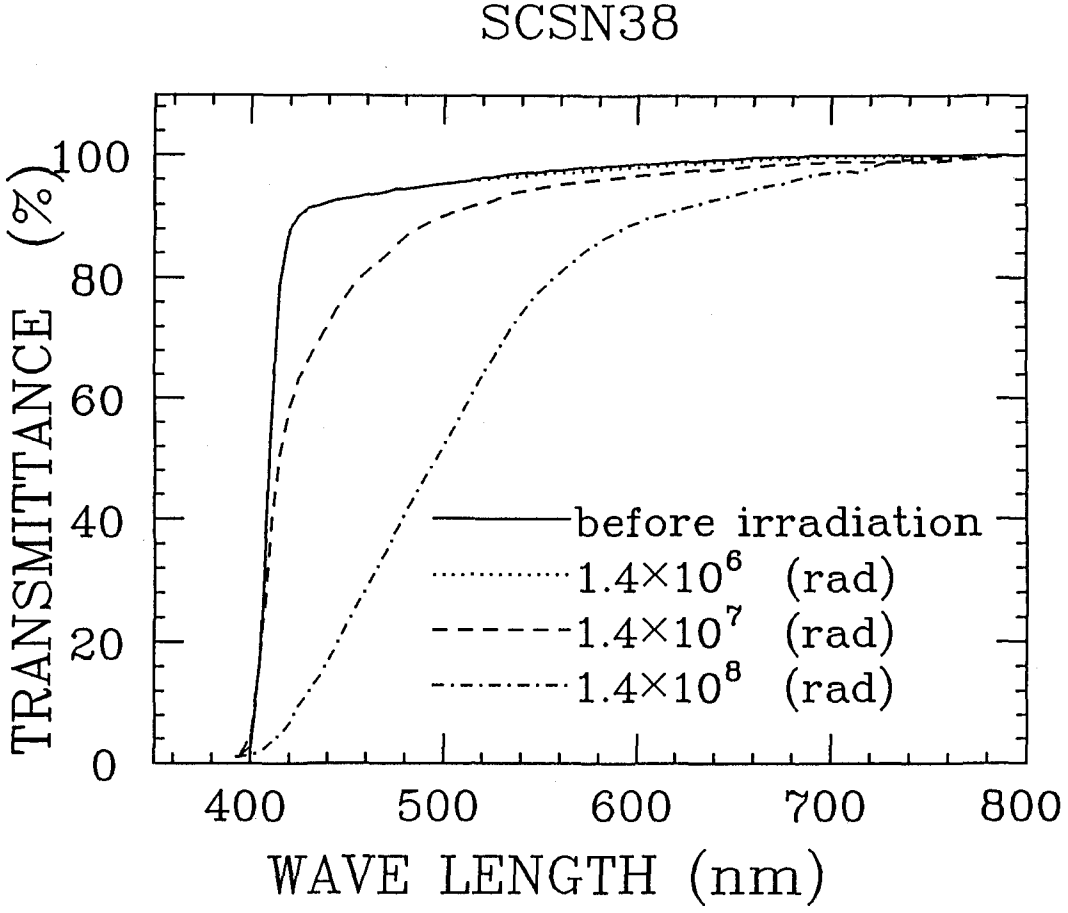
SCSN38
TRANSMITTANCE (%)
100
80
60
40
20
0
400
500
600
700
800
WAVE LENGTH (nm)
before irradiation
1.4×10^6 (rad)
1.4×10^7 (rad)
1.4×10^8 (rad)

Fig. 4(c)

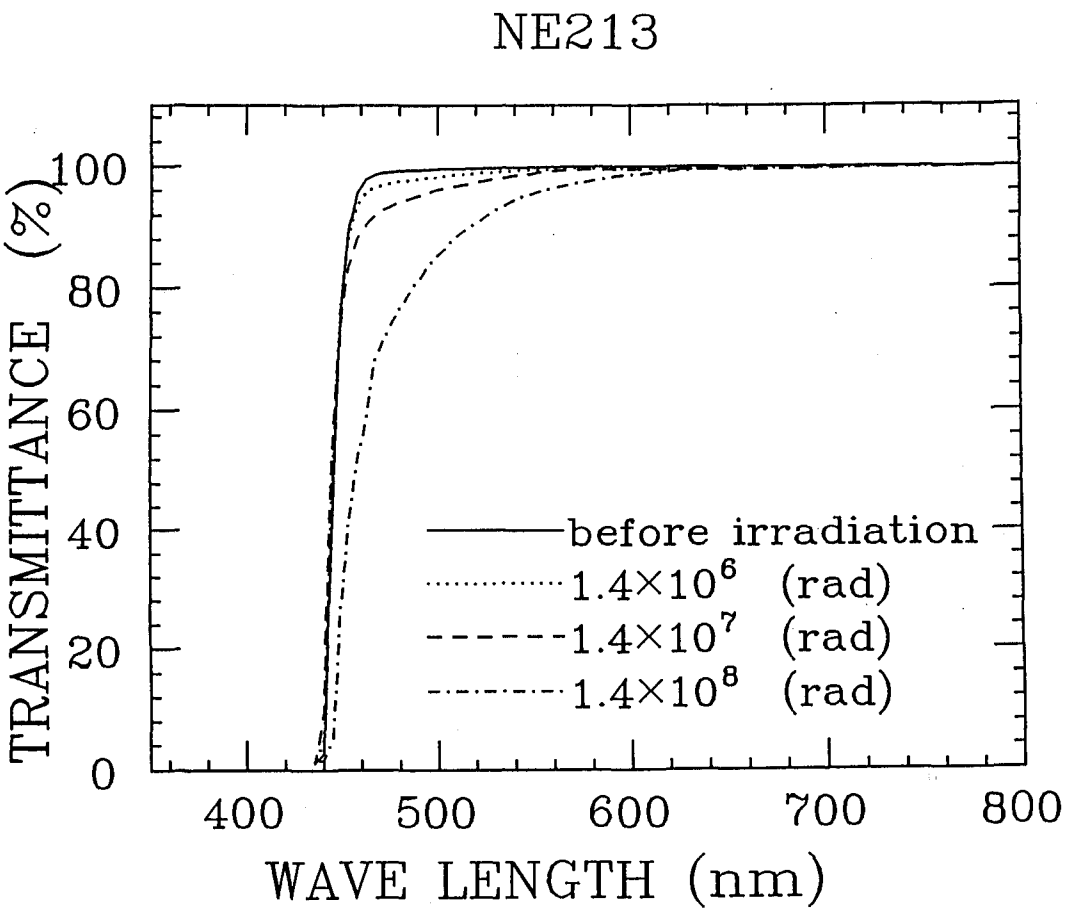
NE213
TRANSMITTANCE (%)
100
80
60
40
20
0
400
500
600
700
800
WAVE LENGTH (nm)
before irradiation
1.4×10^6 (rad)
1.4×10^7 (rad)
1.4×10^8 (rad)

Fig. 4(b)

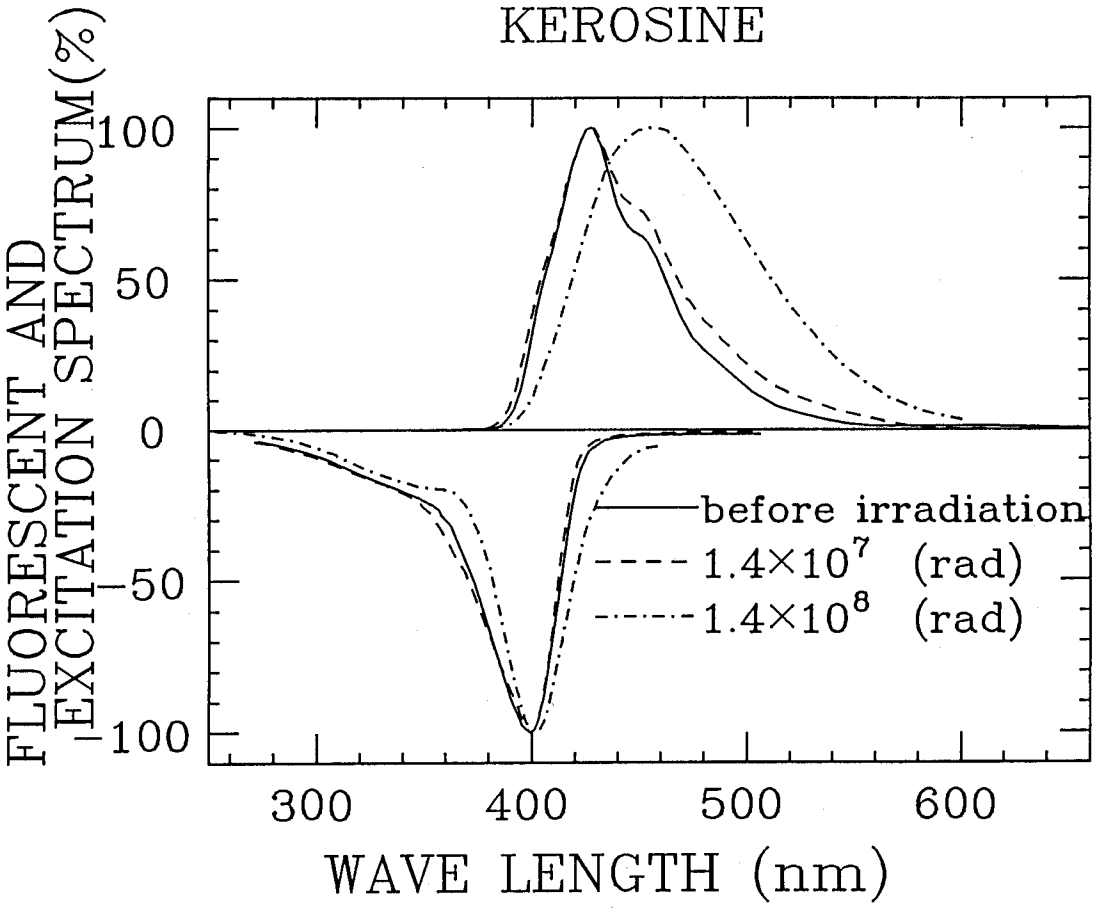
KEROSINE
FLUORESCENT AND EXCITATION SPECTRUM(%)
100
50
0
-50
-100
300
400
500
600
WAVE LENGTH (nm)
before irradiation
1.4×10^7 (rad)
1.4×10^8 (rad)

Fig. 5(b)

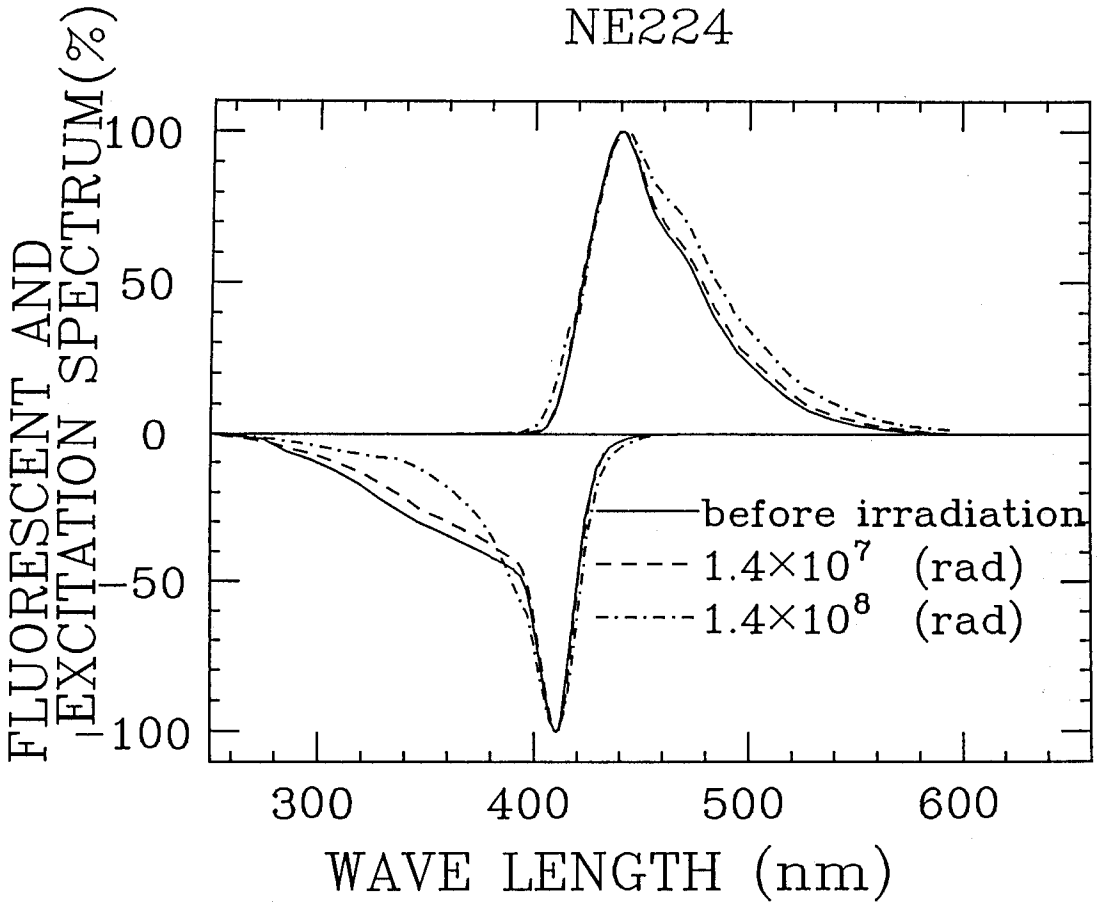
NE224
FLUORESCENT AND EXCITATION SPECTRUM(%)
100
50
0
-50
-100
300
400
500
600
WAVE LENGTH (nm)
before irradiation
1.4×10^7 (rad)
1.4×10^8 (rad)

Fig. 5(a)

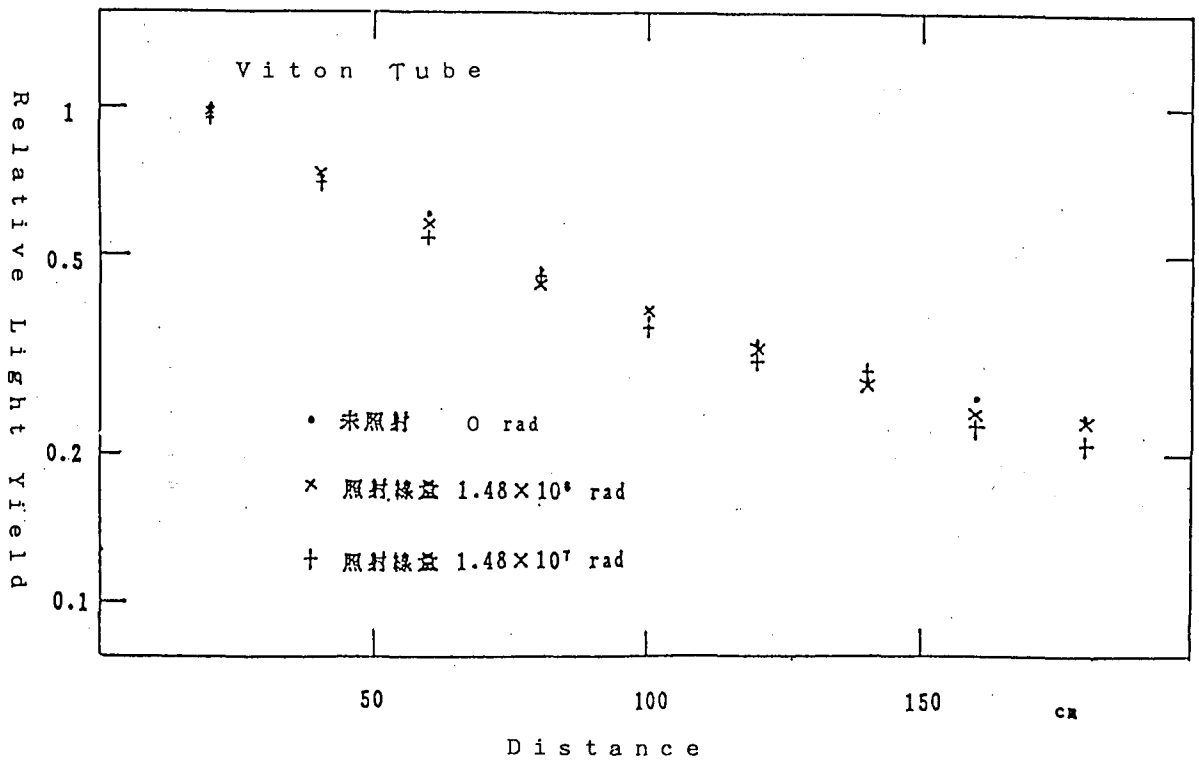
Viton Tube
Relative Light Yield
1
0.5
0.2
0.1
• 未照射 0 rad
× 照射線量 1.48×10⁸ rad
+ 照射線量 1.48×10⁷ rad
50
100
150
cm
Distance

Fig. 6

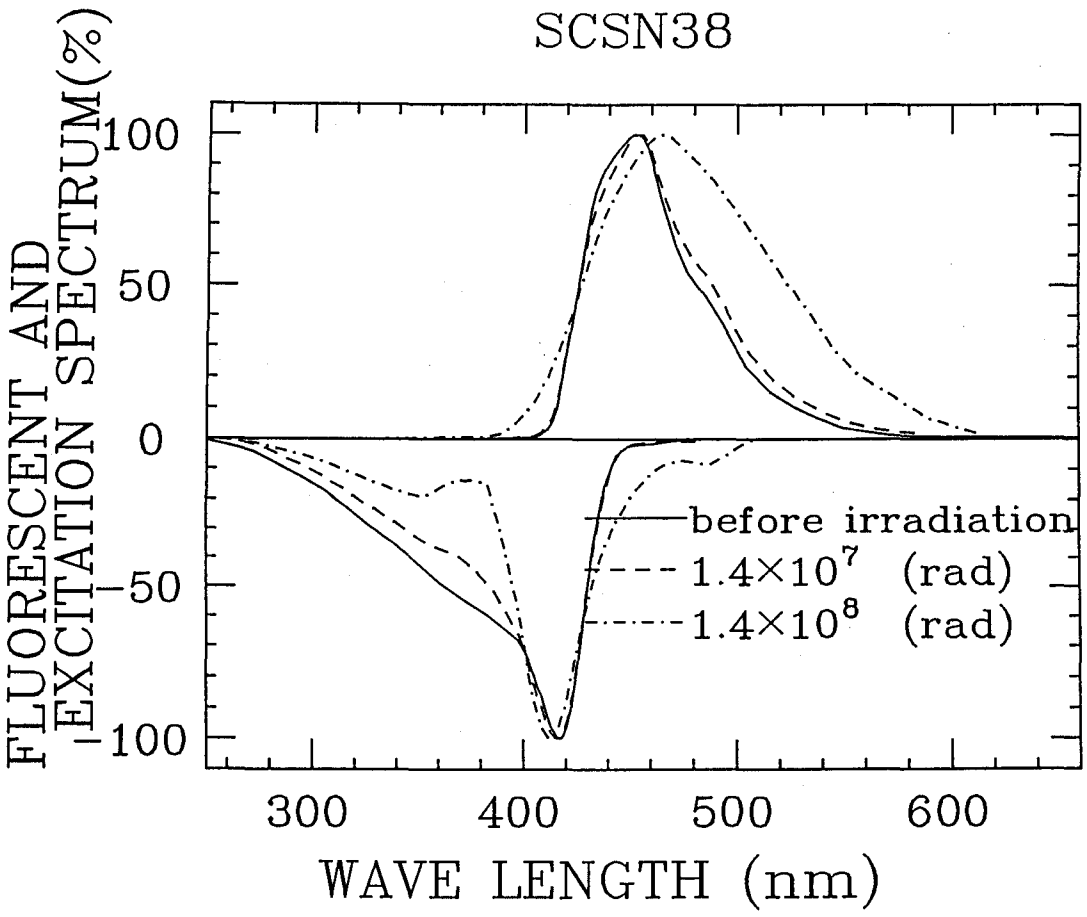
SCSN38
FLUORESCENT AND EXCITATION SPECTRUM(%)
100
50
0
-50
-100
before irradiation
1.4×10⁷ (rad)
1.4×10⁸ (rad)
300
400
500
600
WAVE LENGTH (nm)

Fig. 5(c)

η >3 Calorimeters and W_LW_L Scattering

J.M. Hauptman
Physics Department, Iowa State University
Ames IA 50011 USA

May 1990

Abstract

It is argued that the very forward regions ($3< \eta <6$) of the SDC facility should be instrumented by a liquid scintillator calorimeter capable of triggering on the p_T imbalance between scattered jets, as a means of tagging the WW, ZZ, and WZ initial states.

1. The Importance of WW Scattering

Both K. Hagiwara and F. Gilman have stressed, independently, at this meeting[1] that the study of electroweak symmetry breaking is the most important problem to be addressed at the SSC. That is, we should be designing a facility capable of a detailed study of the scattering processes

$$W_L^{\pm}W_L^{\mp} \rightarrow Z_LZ_L \tag{1.1}$$

$$W_L^{\pm}Z_L \rightarrow W_L^{\pm}Z_L \tag{1.2}$$

$$W_L^{+}W_L^{-} \rightarrow W_L^{+}W_L^{-} \tag{1.3}$$

$$W_L^{\pm}W_L^{\pm} \rightarrow W_L^{\pm}W_L^{\pm} \tag{1.4}$$

As Hagiwara points out, this is the only way to study symmetry breaking in the absence of new particle production. If the Higgs exists, then it will appear as a resonant state in these channels. In either case, whether the Higgs exists or not, the W's and Z's produced will be predominantly longitudinally polarized.

The suggestion to study WW scattering is not new; indeed, theorists for years have spoken of these processes, [2 3 4 5] but we experimentalists have not responded with sufficiently well thought out detectors to perform these measurements. The problem is now known to be much harder than perceived a year ago: the top quark mass limit is now near the W mass, and if its mass happens to be near theoretically expected values (150-180 GeV/c^2), then copious $t\bar{t}$ production followed by $t\rightarrow bW^+$ decay will flood the above channels with background.

[1] These proceedings.

[2] M.K. Gaillard, "Electroweak Interactions at the SSC: Introductory Remarks on Multi W and Z Production", in *$\bar{p}p$ Options for the Supercollider*, 13-17 February 1984, p. 192, Chicago, Illinois.

[3] F. Paige, "Report of the Theoretical Group on Experimental Signatures", in *Physics at the Superconducting Super Collider*, p. 107, Fermilab, June 1984.

[4] R. Cahn, et al., "Transverse Momentum Signatures for Heavy Higgs Bosons", in *Observable Standard Model Physics at the SSC*, UCLA, 15-24 January 1986, and published in PR **D35** (1987) 1626.

[5] M. Chanowitz, M. Gaillard, NP **B261** (1985)379.

2. Experimental Design Studies

Cahn, et al., were the first to point out that, in the WW initial state, the transverse momentum recoil of the quarks which emit the W's is of order M_W, due to the W propagator, and that these quark jets fall in the rapidity range $2< \eta <5$, with a mean η of about 3.5. The geometry of a typical event is shown in Figure 1. A short study at the parton level [6] showed that a discrimination factor of about 50 was possible against the W+jet final states, but this study must be carried through with fragmentation of the partons and a full detector design.

Attempts have been made to separate the final state W's and Z's from Higgs decay (or from V_LV_L scattering, since they will appear in the same selected sample of events) in all combinations of hadronic and leptonic decays. The attempts to use the $WW\rightarrow H\rightarrow WW\rightarrow \bar{q}q\ell\nu$ reaction and decay sequence must now be reassessed, since the $t\rightarrow bW$ possibility was not previously considered. [7]

The leptonic W and Z decays are much cleaner, but the resulting rates are marginal for a 3σ effect in one year of running, assuming that the background is essentially zero, which it may not be.

3. Present Study

There are three discriminators which have not yet been employed, either to full advantage or all at once in the same study,

1. the transverse momemtum *imbalance* between the radiating quarks is a better disciminator that just the magnitude of the either quark's transverse momentum alone;

2. the decaying $W\rightarrow \bar{q}q$ system has lower charged particle multiplicity [8] on average than a QCD gluon jet of the same laboratory momentum as the W; and

3. the processes 1.1 through 1.4 are "quiet" in that the high p_T partons are W's, letpons, and low-multiplicity jets; whereas the hard QCD processes producing $t\bar{t}$ with its decay $t\rightarrow Wb$ yield two high p_T b jets in the event, and possibly other gluon jets radiated from these energetic quarks as well.

There is some hope that even the $WW\rightarrow H\rightarrow WW\rightarrow \bar{q}q\ell\nu$ decay sequence can be useful for WW scattering studies. In the following table we list the potential factors of background rejection against the two largest backgrounds.

[6] L. Gutay, et al., "Intermediate p_T Jet Spectrometers", in *Experiments, Detectors, and Experimental Areas for the SuperCollider*, Berkeley, 7-17 July 1987.

[7] F. Paige, *ibid.*; E. Fernandez, et al., Snowmass 1984, p. 107; S. Protopopescu, Snowmass 1986, p. 180; L. Gutay, et al., *ibid.*; and H-U. Bengtsson, et al., PR **D40**(1989)1465.

[8] H. Sadrozinski, NIM **A277** (1989) 92.

Table. Potential background rejection factors.

Signal Characteristics	Rejection Against QCD→"W"	Rejection Against $t\bar{t}$ →W^+bW^-b
1. $\Delta p_T \approx < p_T > \approx M_{lv}$	≈ 50 (at parton level)	50 ?
2. W→ $\bar{q}q$ pattern in calorimeter	≈ 100	1.0
3. W→ $\bar{q}q$ multiplicity	≈ 20	≈ 20
4. "quiet" events	1.0	≈ 100 ?

The factor of 50 in line 1 was calculated in reference 7, L. Gutay, et al., and the resulting rejection of single W events and elastic scattering events is shown in Figure 2. There is a Higgs signal of about 8 events per 40 GeV/c^2 bin, but a background of W+jet at the 30 event per bin level in the 800 GeV/c^2 mass region. Employing a charged particle multiplicity cut would reduce this background to a negligible level. The QCD elastic background is small, about 5 events per bin.

The factor of 100 in line 2 is from several studies in reference 7, but mostly the Berkeley 1987 Workshop. The factor or 20 is from refernce 8. The $t\bar{t}$ background is the larger of the two considered here, and it is not known if a "quiet" event selection will discriminate against $t\bar{t}$.

A study of these rejection factors is now in progress using Pythia 5.3, a two-dimensional shower simulation (with some GEANT checks), and combining the techniques in references 4, 6, 7, and 8. We are designing a liquid scintillator forward plug calorimeter along the lines suggested by R. Partridge[9]. This device measures E_T directly by masking out the scintillation light proportional to $\sin\theta$, so that E_T is measured directly in slices in ϕ. In a talk in this calorimeter session, M. Chiba demonstrated that liquid scintillator is very radiation resistant.[10]

Acknowledgements

This work was supported mainly by DOE contract DE–AC02–85ER40193, and partially by the Associate Director for Planning and Technology Application, Ames Laboratory, USDOE.

[9]R. Partridge, "Closing the Gap: Forward Detectors for the SSC", Berkeley 1987 Workshop, p. 657.

[10]M. Chiba, "Radiation Damage of Liquid Scintillator", these proceedings.

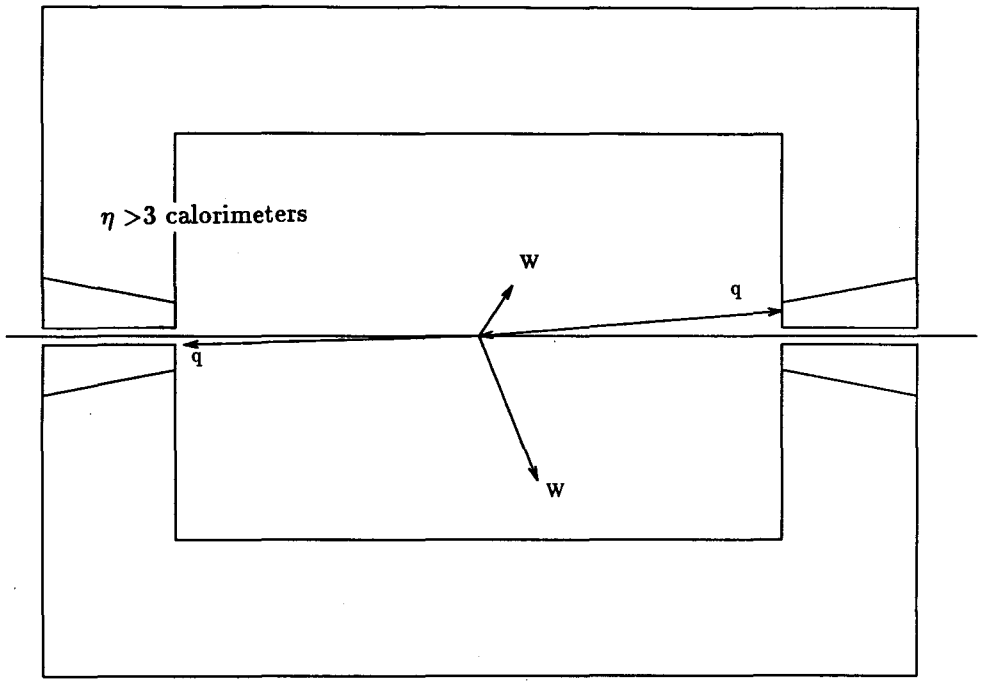

Figure 1. Typical geometry of a WW scattering event. The scattered quarks at $\eta \approx 3.5$ have radiated W's with differing p_T's, hence the WW system has transverse momentum in the laboratory. The typial longitudinal momentum of the quark jets is 1-2 TeV.

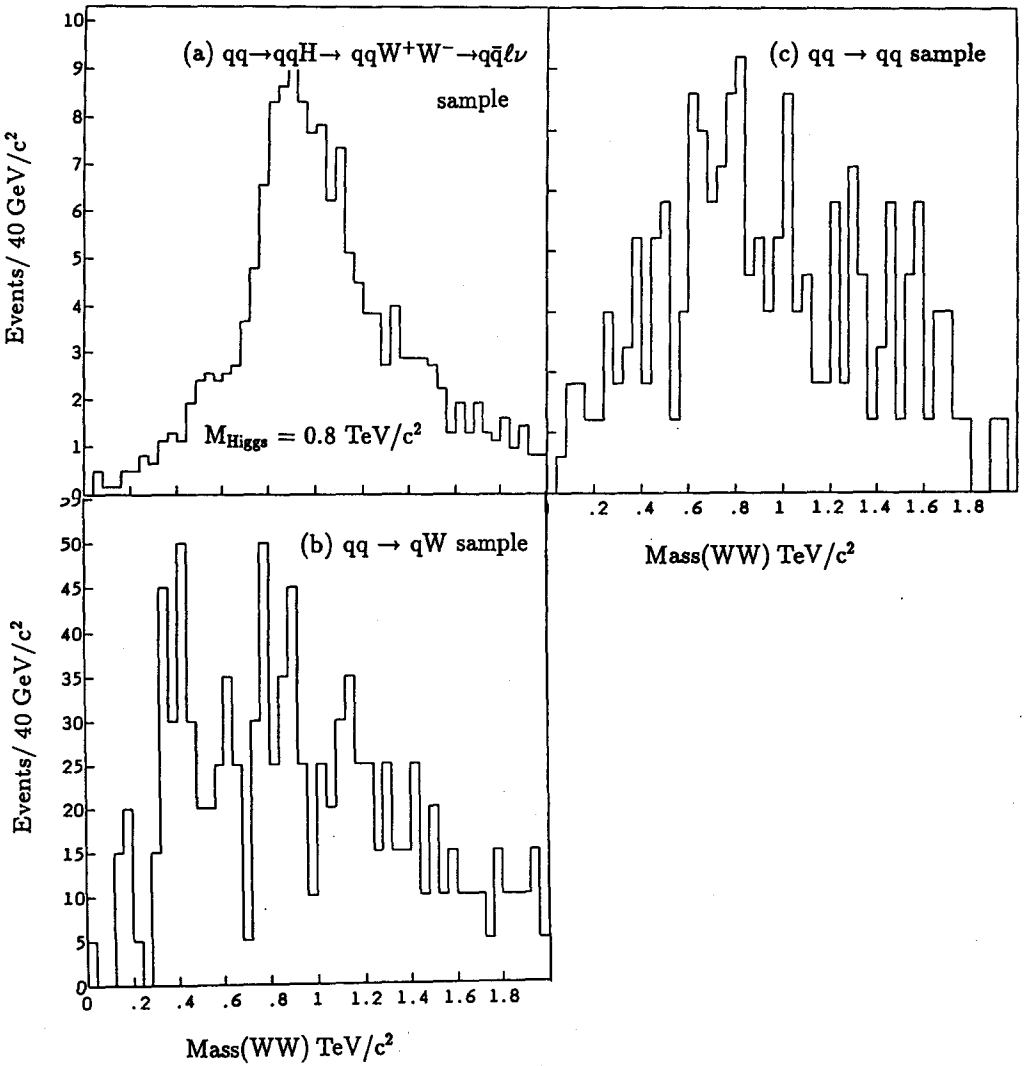

Figure 2. Results of WW mass reconstruction for (a) 800 GeV/c^2 Higgs production, (b) single W+QCD jet production, and (c) QCD elastic scattering.

Parallel Session: Muon System

April 24, 13:30-17:50

MUONS WITH A SOLENOIDAL DETECTOR
An Introduction

K. Heller
School of Physics and Astronomy
University of Minnesota
Minneapolis, Minnesota 55455

The detection of muons will be an important part of any general purpose SSC detector for two very basic reasons: High transverse momentum (p_t) muons signal interesting physics appropriate to the SSC energy scale, and muons are possible to identify and measure in the high rate, high multiplicity environment of the SSC. The recent history of particle physics clearly shows the importance of such muons in discovering new particles. Remember $\psi \rightarrow \mu\mu$, $Z \rightarrow \mu\mu$, $W \rightarrow \mu\nu$. At the SSC, high p_t muons will signal the creation of new heavy particles which decay into at least one Z (i.e. $H \rightarrow ZZ$ or $\rho_T \rightarrow ZW$) or directly into leptons (i.e. $Z' \rightarrow \mu\mu$). These muons can be identified by requiring them to pass through material sufficient to shield the muon detector elements from the vast majority of the particles originating from an SSC collision. Hiding behind this material, the muon detectors will have the highest rate capability in the detector and, thus, the ability to explore the highest luminosity of the SSC. The system described briefly in this report is the product of the continuing work of the many people working together on designing a muon system for a solenoidal detector.

The muon system must provide information which will allow the electronic trigger to reduce an interaction rate of about 100 MHz to a data taking rate of a few Hz. Single muons with p_t above 100 GeV/c occur at a low enough rate to be collected but lower p_t muon signals must be combined with other information in the detector to form a trigger. Off-line, the detector must be able to measure the momenta of muons to a precision necessary to distinguish high mass states from the uninteresting low energy background. A natural scale for this resolution is the width of the Z. Thus a muon must pass through approximately 14 interaction lengths of material for the trigger's particle identification while having its momentum measured with a minimum of multiple scattering for off-line resolution. A solenoidal detector, such as shown in figure 1, accomplishes this in a natural way in the central pseudo-rapidity region (η) by using the inner tracker to provide the high resolution momentum measurement and detectors outside of the calorimetry to provide the other trigger information. Unfortunately, the momentum measuring capability of a solenoid internal tracker degrades as the muon tracks become more parallel to the solenoid field. Thus, the external muon system must also give the precision momentum measurement for muons in the forward pseudo-rapidity region.

The external muon detectors separate into two systems which have slightly different missions. The central muon system ($|\eta| \leq 1.5$) covers the largest area and gives a fast trigger by identifying muons and providing a p_T estimate. This system also gives enough information to identify the interesting muon track in the crowded environment of the inner tracker. Signals from the outer layers of the inner tracker are used to sharpen the muon momentum determination for inclusion in a higher level trigger. The forward muon system ($1.5 \leq |\eta| \leq 2.5$) provides a fast trigger as well as a momentum measurement comparable to that of the inner tracker in the central region.

Because of its large size, the occupancy of the external muon system is low. Conventional detectors such as scintillator or Cherenkov counters and drift tubes will be effective. However, the large size of the external muon system also means that the cost per detector element must be kept low. The difficulty of constructing such a system resides in understanding the technical details of the muon events, the detectors used, and the environment in which the detectors will operate.

The external muon system must be able to tag the interaction giving an interesting muon which implies a time resolution of better than 10 nsec. The first level trigger, muon identification and p_t tagging, must take no longer than about 1 msec to be compatible with a 1.5 μsec electronic pipeline for the detector. The external material used to identify muons gives rise to electromagnetic showers, both hard and soft, which accompany each muon and could confuse a trigger. This material also determines the momentum resolution of the trigger through multiple scattering. The background environment of the external muon detectors is a combination of muons from hadron decay in the internal tracker and calorimeter, cosmic ray muons and their shower products, and low energy neutrons. The total rate of muons as a function of angle and momentum has been calculated by Green and Hadine using both existing data and simulations. These rates are shown in figure 2 as a function of angle for different material thickness and figure 3 as a function of transverse momentum after 14 interaction lengths. After 14 interaction lengths, hadronic punchthrough is no longer important at p_t's of interest and further gains in filtering low energy muons only come as the square root of the thickness of material.

CENTRAL MUON SYSTEM

As shown in figure 1, a possible central muon system consists of 3 banks of scintillation counters and 4 sets of vector drift modules sandwiched around a 1.5 m thick iron toroid (1.8 T). There are 6,000 scintillators distributed around the detector barrel at radii of 7, 9, and 11 meters from the interaction point. No scintillator is longer than 4 meters and each has a phototube on both ends. The purpose of the scintillator is to provide the trigger with muon identification, a

beam interaction tag and an indication that the muon came from the interaction region with a minimum p_t of 10 GeV/c. For a luminosity of $10^{34}/(cm^2s)$ the rate of muons at the outer bank of counters is about 1 MHz from interactions and 0.1 MHz from cosmic rays. A counter coincidence pointing to the interaction region essentially eliminates the cosmic rays and reduces the muon rate to about 10 KHz. The drift modules are then used to give a first order momentum tag to the muon or muons passed by the counters.

The drift modules must have cell sizes no larger than 10 cm (5 cm drift) to acquire the signal in time to use the information in the level 1 trigger. The position of the modules is primarily determined by the configuration of the entire detector and the desired resolution of the preliminary muon momentum tag. Four stations of drift modules are located at radii of 5.5, 7, 9, and 11 meters. Each station has 4 wires along the solenoid axis and 4 in the orthogonal direction giving a total of about 60,000 wires. If each station is aligned to an accuracy of 250 μm the momentum resolution at this level of the trigger is as shown in figure 5. The resolution is about 20%. It is a slowly varying function of momentum with the minimum resolution set by the multiple scattering of the iron toroids. An example of a level 1 trigger is a single muon with a momentum of greater than 140 GeV/c. If one requires that the trigger be 100% efficient at 140 GeV/c, the effectiveness of the trigger is about 1/300 as shown in figure 5. Since rate of 140 GeV/c muons is less than 1 Hz at $10^{34}/(cm^2s)$, this stand-alone trigger rate would be less than 300. This is adequate to pass along to level 2 for refinement. The track from the drift modules is then followed into the inner tracker where an impact parameter measurement can be made using the relevant outer layers. Since multiple scattering is small in the central tracker, the level 2 momentum calculation can be sharp enough to keep this trigger rate at the few Hz level. The multiple scattering dominated external muon momentum determination using the iron toroid is essential to reject hadronic punchthrough. A high momentum hadron in the inner tracker can generate a muon in the calorimeter. This muon can cause a trigger in the external muon system but as the decay product of the hadronic shower has a significantly lower momentum than the parent hadron. A comparison of internal and external momentum measurements with a 25% precision will reject these events.

FORWARD MUON SYSTEM

The forward muon system might also consists of counters, drift modules and a toroid. Using superconducting air core toroids instead of iron in this region matches the off-line resolution of the central tracker. With a per station tracking precision of 100 μm, the resolution will be as shown in figure 6. The multiple scattering dominated minimum resolution of a 5 m long iron toroid is shown for comparison. Because the rates in the forward region are higher than those in the central region, the detectors will have a finer segmentation. Two banks of counters, placed downstream of the toroid at 16 and 18 meters from the interaction region, will be used to identify muons with a minimum p_t of 10 GeV/c. Since the toroid deflects particles radially, these counters will be arranged to detect the radial position of particles as shown in figure 8. At a luminosity of $10^{34}/(cm^2s)$ the rate of muons at the counters is about 10 MHz from interactions. The rate due to production products scraping on upstream elements could be ten times higher. The counter trigger should reduce the muon rate to about 100 KHz, mostly due to junk from scraping. If the rate of neutrons and low energy charged particles is too high, Cherenkov counters might be used instead of scintillator.

Because the drift modules are used to give the final determination of the muon momentum in the forward region, their alignment will need to be known to 100 μm. Air core toroids will make this alignment easier since straight tracks can be used. Multiple scattering makes this impossible with iron toroids. Higher occupancy will require the use of smaller drift cells than in the central region. At this time we estimate that 5 cm cells (2.5 cm drift) should be sufficient. The modules will be arranged parallel to the counters to detect the radial deflection of the muons. The higher accuracy and occupancy will also require at least 6 wires per module with module stations at 10.5, 12.5, 16, and 18 meters. To resolve the ambiguity due to multitrack events, two of the drift module stations will have small angle stereo wires. Instrumenting both forward detectors will take about 40,000 wires.

The superconducting air core toroids used it the forward configuration shown in figure 1 are 3 meters long with a field of 5.5/r Tesla to give the resolution shown in figure 6. The field variation with r gives a uniform p_t resolution as an added bonus. The largest field integral would be 8 T-m at 2.5 m from the beam ($|\eta| = 2.5$) decreasing to 3 T-m at 6 m from the beam ($|\eta| = 1.5$). No magnet of this type has ever been constructed in this size. Tom Fields will give the status of preliminary engineering studies for this magnet in this session.

ISSUES

The muon system outlined above is large, ambitious, and expensive but certainly within our technical and financial capability. Much work is now going on to determine the real parameters of a muon system design. A drift module design must be chosen. This design will be optimized to reduce the effects of the soft electrons and photons accompanying a high energy muon emerging from material. By comparing shower simulations with beam tests we must decide whether to use an open or closed cell design, whether it is useful to build the modules out of low Z material, and how to space the wires inside the module. A trigger counter design must also be chosen. Simulations and beam tests will determine the extent of the problem of soft neutron albedo. A high neutron flux

will preclude the use of hydrogen based detectors such as scintillator. Work is still needed on the optimal drift module design to give as sharp as possible p_t trigger threshold and to facilitate the link to the central tracker. The configuration of the forward muon system needs investigation to see if one can shield against the high rate of particles which will scatter off the inner edge of the forward calorimeter. Much engineering work is ahead to design a workable and affordable air core toroid with the specifications needed. An inexpensive alignment system is needed to give a 250 μm resolution in the central muon system and a 100 μm resolution in the forward. The layout of the muon system must take into account the important reality of plumbing and wires which can create dead regions in the detector. Schemes must be devised for access to the detectors for replacement and repairs. Finally in such a large system, we must consider clever ideas to reduce the number of detectors and the cost per detector.

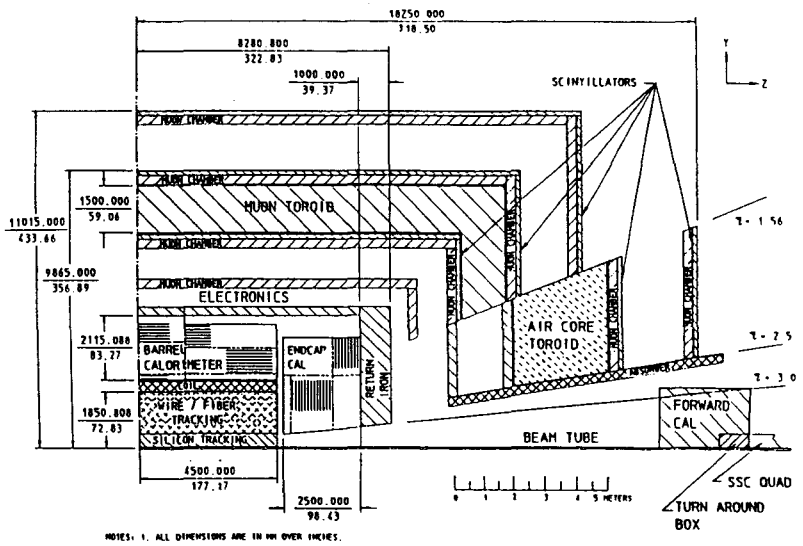

FIGURE 1-- A possible configuration of a muon system for a solenoidal detector. The central external muon system consists of 4 drift module stations (labeled muon chamber), 3 banks of counters (labeled scintillators), and an iron toroid. The forward external muon system consists of 4 drift module stations, 2 banks of counters, and a superconducting air core toroid. One half of the detector is shown.

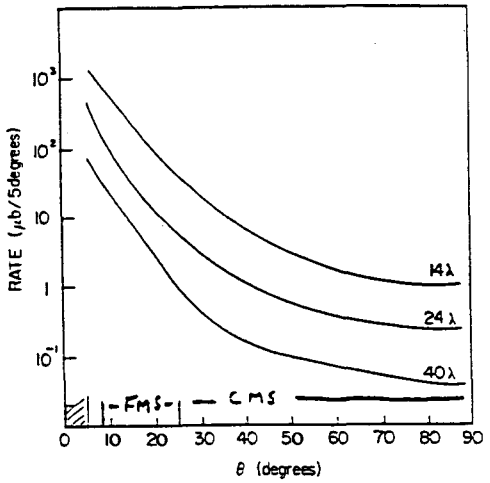

FIGURE 2-- Muon rates from the interaction as a function of angle. The region covered by the central muon system (CMS) and forward muon system (FMS) is shown.

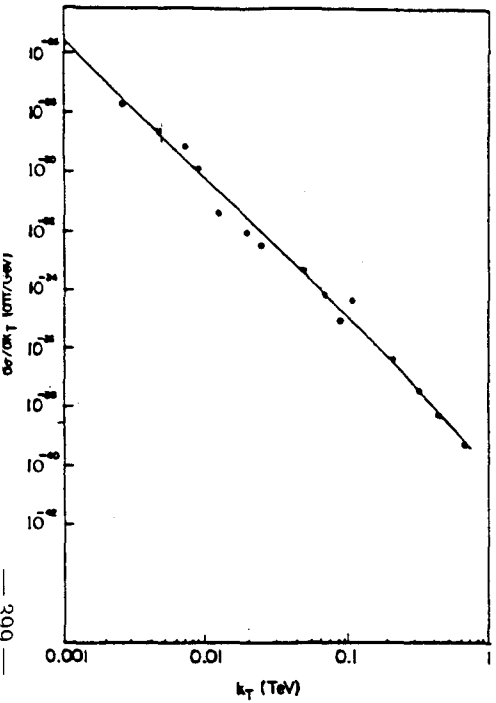

FIGURE 3-- Muon rates from the interaction as a function of transverse momentum after 14 interaction lengths of material.

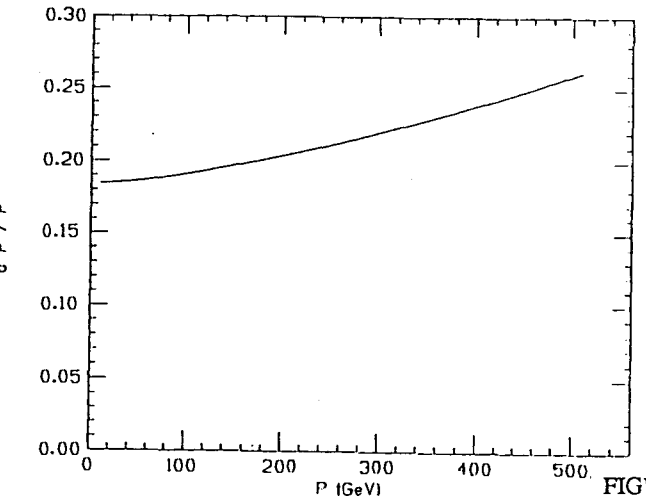

FIGURE 4-- Momentum resolution of the external central muon system.

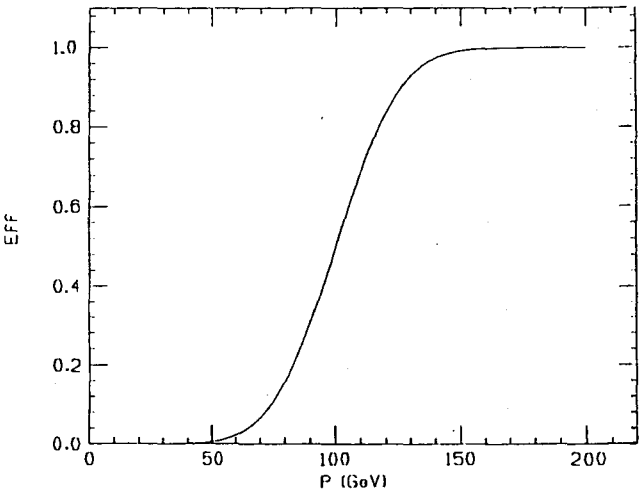

FIGURE 5-- Efficiency of the muon momentum identification using the external central muon system to tag 140 GeV muons.

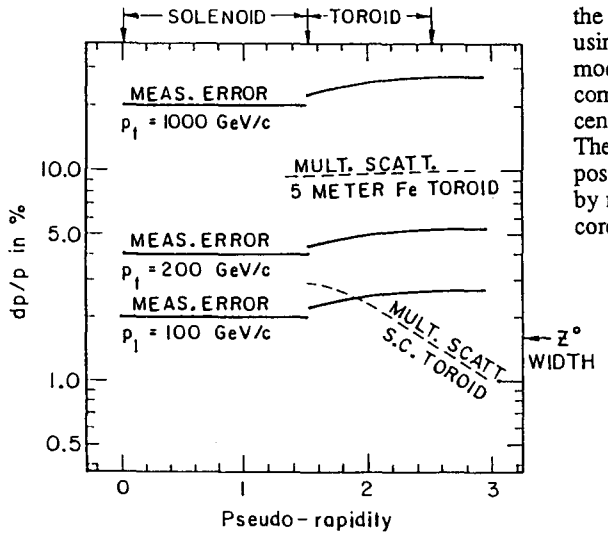

FIGURE 6-- Momentum resolution of the forward external muon system using the air core toroid and drift module system described in the text compared to the resolution in the central region of the inner tracker. The dashed lines show the best possible momentum resolution, set by multiple scattering, for the air core toroid and a 5 meter iron toroid.

Beam test EM

H. Lubatti
U Washington

(No written contribution received)

A Proposal to Measure EM-Showers Associated with High Energy Muons in Iron Absorber

Takuo Yoshida
Osaka City University, Osaka 558, Japan

Abstract

A Monte Carlo study on the electromagnetic showers caused by high energy muons penetrating the iron absorber has been made. An experiment to confirm the Monte Carlo results is proposed.

The muon tracks are usually identified by observing the tracks penetrating a thick absorber without creating showers. However, if the muon energy is larger than a few hundred GeV as expected for SSC experiment, it is known in the framework of QED that the muons passing through the absorber loose more energy due to radiative processes rather than ionization. This effect will increase the probability that high energy muons penetrating the absorber are accompanied by the electromagnetic showers. Such showers may disturb the muon chambers behind the absorber. Therefore, understanding this electromagnetic behaviour of high energy muons both theoretically and experimentally is important to determine the design parameters of the muon chambers. The theoretical study on this subject is reviewed by J. J. Eastman and S. C. Loken (Proceedings of the Workshop on Experiments, Detectors, and Experimental Areas for the Super Collider, Berkeley, CA., 1987, p. 542).

Using GEANT3 software library, high energy muons going through an iron absorber have been simulated, and the showers associated with the muons have been observed at the absorber end. The tracks in the showers were traced until 100 KeV. For 500 GeV muons penetrating 40 cm iron absorber, the average number of associated e^+ or e^- at the absorber end was 1.6 per muon track. The average number of associated photons was 14 per muon track. Much more photons than charged tracks emerge from the absorber.

Fig. 1a and Fig. 1b show the GEANT3 calculated probability that a muon is accompanied by at least one charged background particle at the absorber end. Fig. 1a shows it as a function of muon energy. The absorber thickness was 1 m. More than 30 % of the muons are accompanied by charged background particles at the muon energies above 500 GeV. Fig. 1b shows the probability as a function of absorber thickness. The muon energy was 1 TeV. The probability satulates above the thickness of 25 cm. The result calculated with 2 tesla magnetic field in the iron, which is indicated by a cross in Fig. 1b, shows that the magnetic field does not help to reduce the probability. This is because most of those charged background particles are created within a thin layer near the absorber end.

For the Monte Carlo events with 500 GeV muons incident on 40 cm thick iron, Fig. 2a shows a distance distribution between muon tracks and the charged background tracks exactly at the absorber end. Most of those charged background tracks are within 5 mm from the parent muons. Fig. 2b shows an angle distribution of the charged background tracks with respect to the parent muon direction. The directions of those background tracks are wide spread around the parent muon direction. The kinematic energy distributions of the charged background particles and the background photons are given in Fig. 3a and Fig. 3b, respectively. Most of those charged particle energies are less than 20 MeV. Photons are much softer than charged particles.

Based on the Monte Carlo study mentioned above, a simple experiment to confirm the Monte Carlo results has been designed, supposing that Fermilab 500 GeV muon beam are available. As sketched in Fig. 4, the apparatus consists of an iron absorber, 1 mm step MWPCs behind the absorber, and several scintillation trigger counters placed at appropriate locations along the beam line. The trajectories of the charged background particles associated with high energy muons are measured by the 1 mm step MWPCs. Four planes of MWPCs are available for this experiment for the time being. They are placed in a same wire direction to measure one side view of the events. The sensitive area of each MWPC plane is 10 cm by 10 cm.

There is a suggestion that covering the absorber end with a material which has a larger critical energy than that of iron may help to absorb the soft background particles rather than creating additional showers. The experiment proposed here can also confirm this effect by inserting between the iron absorber and the MWPCs various materials such as aluminum, plastic, and so on.

Typical Monte Carlo events are shown in Fig. 6, where the parent muon tracks and the charged background tracks emerging from the absorber are shown with 1 mm step vertically and 5 mm step holizontally according to the MWPC resolution. These events suggest that the MWPCs have to be placed at least 10 cm downstream of the absorber end. Placing the MWPCs too close to the absorber makes it difficult to distinguish each track.

The experiment thus proposed can be expected to present some basic data useful to design the SSC muon system.

The author would like to thank Dr. Lubatti for his useful advices on the muon beam experiment at Fermilab. The author would also like to thank Dr. A. Masaike and Dr. K. Imai, who are so kind as to devote their MWPCs for this experiment.

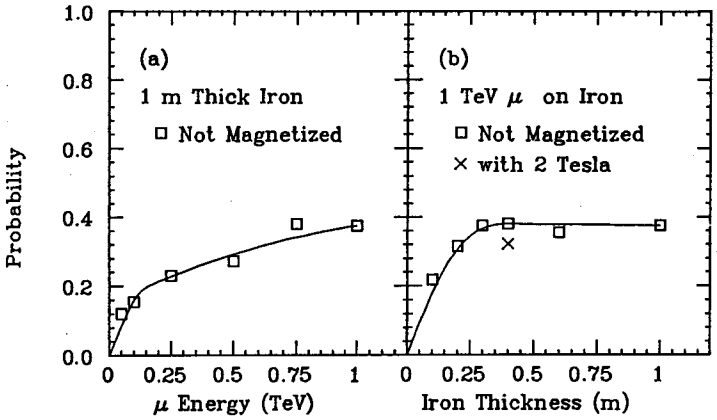

Fig. 1. Probability that a muon is accompanied by at least one associated charged track at the absorber end: (a) as a function of muon energy, (b) as a function of absorber thickness.

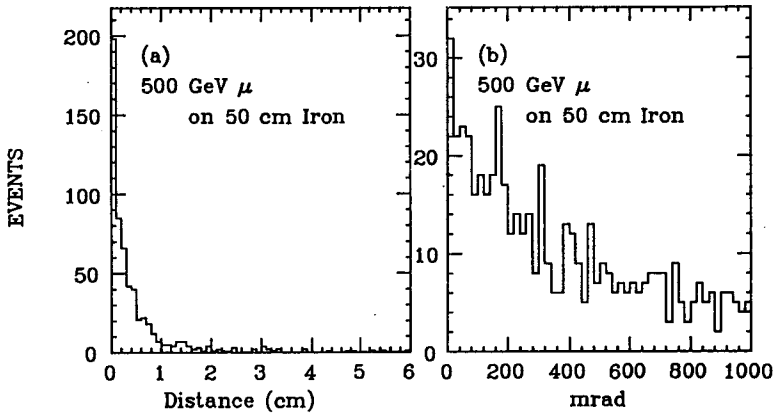

Fig. 2. (a) Distance between muons and the associated charged particles at the absorber end, and (b) angle of the associated charged particles with respect to the muons.

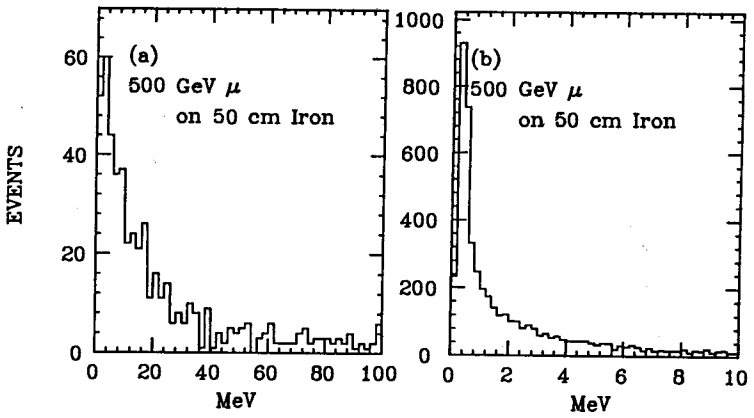

Fig. 3. Kinematic energy distributions of the particles associated with muons: (a) e^+ or e^-, (b) photons.

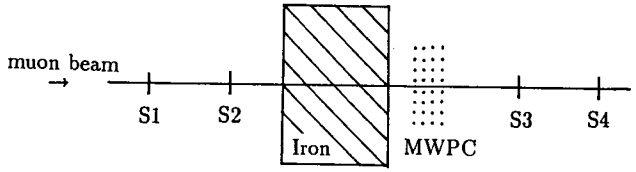

Fig. 4. Apparatus proposed.

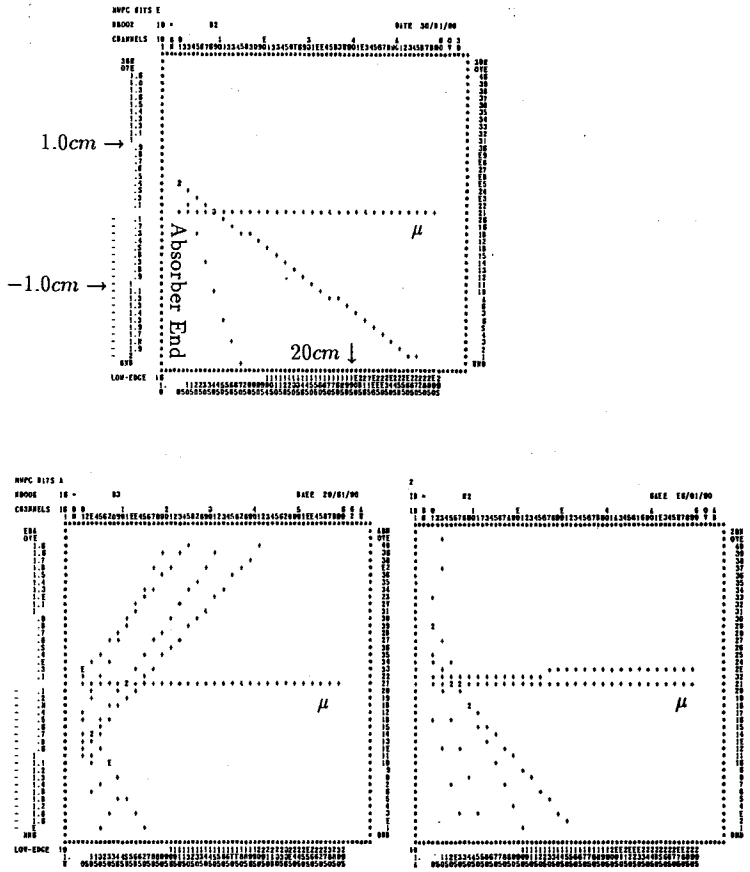

Fig. 5. Typical Monte Carlo events.

NEUTRON BACKGROUND TESTS AT FERMILAB

by

Dan Green
Fermi National Accelerator Laboratory

and

Ken Johns
University of Arizona

As part of the Muon System Level R&D proposal, the Muon Group has decided to measure neutron yields in the vicinity of thick (10 - 14 λ_o) absorbers. These measurements will be made during the 1990-91 Fermilab Fixed-target run. The main question for the Muon Group is whether or not muon trigger rates are effected by n counts in the trigger scintillators. At higher trigger levels, the question is whether tracking in wire chambers is effected by the "sea" of punchthrough neutrons. In particular, one wishes to see if $Ar:CO_2$ is less sensitive to the neutron background, as expected, than $Ar:C_2H_6$.

The aim of the tests is to measure the flux and energy spectrum of neutrons from 14 λ_o of both steel and uranium. This yield will be measured both in front of (albedo) and behind (punchthrough) the absorber. The albedo measurement is crucial for tracking issues, while the punchthrough measurement is important for the Muon System. Specifically, the data will be collected in the NWA beam, since D$\emptyset$ resides there with a U/LA calorimeter. Unfortunately, the minimum momentum is about 20 GeV. Since the momenta of interest are, $P \sim \langle P_\perp \rangle / \sin\theta$, with $\langle P_\perp \rangle \sim 0.6$ GeV and $|\eta| < 3$ ($\sin\theta \geq 0.1$), the match in momenta is not very good.

The expected spectrum[1] has been measured in several places. A recent set of data[2] was taken in D$\emptyset$ with a layout as shown in Fig. 1. Halo protons showering in steel magnets lead to neutrons which are measured with pin diodes and Bonner spheres (discussed later). The resulting spectrum of neutrons is shown in Fig. 2. There are a large number of thermal ($\lesssim$ 1 eV) neutrons, and a prominant peak of ~ 1 MeV neutrons.

This ~ 1 MeV peak is characteristic of all measurements taken during shielding studies. The reason for the peak is straightforward. A hadron shower develops, leading to de-excitation neutrons from nuclei. The inelastic n-Fe cross section falls precipitiously at ~ 1 MeV. The neutrons then "decouple," since at ~ 1 MeV the steel is transparent to neutrons. At that energy the neutrons leak out of the shielding pile. Uranium,[1] with its fission neutrons, is expected to be considerably worse than steel. We wish to make a quantitative measurement of the difference between U and Fe.

Subsequent detection of these ~ 1 MeV neutrons requires an understanding of elastic scattering kinematics for the reaction $n + A \rightarrow n + A$. All inelastic processes have died out. The fractional energy loss in an elastic collision is roughly: for initial kinetic energy T_o, final kinetic energy T.

$$T \sim T_o \, (A-1)/(A+1). \qquad (1)$$

Thus for large A (say steel), neutrons leak out at the "decoupling" energy, $T|_{A>>1} \sim T_o$. However, off free hydrogen, the neutrons can deposit a significant fraction of their energy.

This kinematic fact leads one to conclude that scintillator as a calorimetric detection element will result in decreased albedo and punchthrough. As part of the test beam measurements, we will place various thicknesses of plastic moderator between the absorber (U or Fe) and the detectors (scintillation counters or proportional drift tubes) in order to measure the counting rate as a function of moderator thickness. The scintillators will be calibrated with neutron sources; ^{22}Na - 1.275 MeV, ^{137}Cs - 0.662 MeV and AmBe - 4-5 MeV. Various thicknesses of hydrogenous plastic will be interposed between the material (U or Fe) and the detectors (scintillators or chambers filled with various gases). The question is; can we moderate the neutrons?

The absolute flux and energy spectrum of neutrons emitted from U or Fe absorbers will be measured in two ways. The first employs an NE-213 liquid scintillator counter (~ 1 liter) viewed by a 5" photomultiplier. NE-213 has been used for many years as a neutron detector and provides good neutron/gamma separation based on pulse height discrimination. A similarly sized plastic scintillation counter will also be used. It suffers, however, from poor neutron/gamma separation. Lead sheets will be used as a pre-converter.

The other class of instrumentation we plan to use in NWA are Bonner spheres, which consist of polyethylene moderator material of various diameters. The detector at the center is sensitive to thermal neutrons via the capture reaction:

$$n + {}^6_3Li \rightarrow \alpha + {}^3_1H, \; Q = 4.8 \text{ MeV} \qquad (2)$$

Clearly, (see Eq. 1) successive elastic scatters in light material will reduce the neutron energy substantially. That is why different radii spheres are sensitive to different n energies, as shown in Fig. 3. Clearly, a 5" sphere is well matched to the appropriate spectrum of neutrons, (Fig. 2). A set of these spheres will be used in the NWA measurements in order to unfold the n energy spectrum.

In the temporary absence of data from NWA, an appeal to Monte Carlo results is made. Shown in Fig. 4 is the yield of neutrons/GeV incident energy as a function of depth of material for various incident energies. Clearly, the yield is about 6 n/E_π near shower maximum, $\lambda/\lambda o \simeq 2$. For the purposes of extrapolation, the curves are "eyeball fit" to,

$$\langle n \rangle \sim 6[E(GeV)]\ EXP\{(\lambda - 2\lambda o)/\lambda_{EFF}\}$$
$$\lambda_{EFF}/\lambda o \sim 0.67[E(GeV)]^{0.33}. \qquad (3)$$

The punchthrough probability for neutrons of 5 GeV, at a depth 14 λo, is then estimated to be 5.5×10^{-4}.

The elastic cross section for neutrons off protons in the range 10 - 300 MeV can be fit to:

$$\sigma_{np} \simeq 7\ barn/[E(MeV)]^{0.84}. \qquad (4)$$

For a 1 cm plastic scintillator, $(dE/dX)\ \Delta X \sim 2$ MeV. For neutrons of 1 MeV, $(N_o \rho L \sigma np)/A \sim 0.4$. Thus, a large fraction of the 1 MeV punchthrough neutrons elastically scatter in a scintillator, depositing enough energy (see Eq. 1) to count. An overestimate, used in what follows, is to assume that the recoils all count.

At the SSC, for $L = 10^{33}/cm^2 sec$ there is a 100 MHz interaction rate. With 6 particles of $P_\perp = \langle P_\perp \rangle$ per unit of rapidity, one has 600 MHz of pions at 5.7° (y=3) with momenta of 5 GeV in a counter covering $\Delta y = 1$, $\Delta\phi = 2\pi$. At a depth of 14 λo, this flux results in ~ 130 kHz of singles rate if all the elastic scatters in the scintillator result in a count. Assuming one counter covering $\Delta y = 1$, the two-fold accidental rate is < 100 Hz for a 20 nsec resolving time.

Thus, the preliminary indication is that neutrons are not a problem. Corroboration comes from test data on punchthrough in a steel liquid scintillator stack[3]. The data for punchthrough probability as a function of depth for various momenta are shown in Fig. 5. The "punchthrough" consists of shower hadrons, neutrons, and muons. A function $EXP\{(\lambda - \lambda')/\lambda_{EFF}\}$ is used to represent the data. Extrapolating to 5 GeV (again, a poor test beam momentum match), at 15 λo the total punchthrough probability (which counts as ≥ 0.25 MIP[3] in liquid scintillator) is $\leq 2 \times 10^{-4}$. These data confirm our rough calculation, made above.

Although it is expected that neutron punchthrough is not a problem, albedo may be. In any case, these measurements will be of wide utility, and will be made soon.

References

[1]D.E. Groom, "Radiation Levels in the SSC Interaction Regions," SSC-SR-1033 (1988).

[2]P.M. Yurista et al., "Neutron Spectral Measurements in the DØ Collision Hall, Fermilab TM-1594, DØ Note 852.

[3]F.S. Merritt et al., Nucl. Inst. Meth. **A245**, 27 (1986).

Figure Captions

Fig. 1. Layout for n studies in the DØ Collision Hall showing magnets and instrumentation.

Fig. 2. Measured n spectrum from the DØ study.

Fig. 3. Response of Bonner spheres of various radii as a function of incident neutron energy.

Fig. 4. Neutron yield/energy of the incident pion as a function of depth for various incident energies.

Fig. 5. Punchthrough probability using scintillation counters in a steel stack as a function of longitudinal depth for various incident hadron energies.

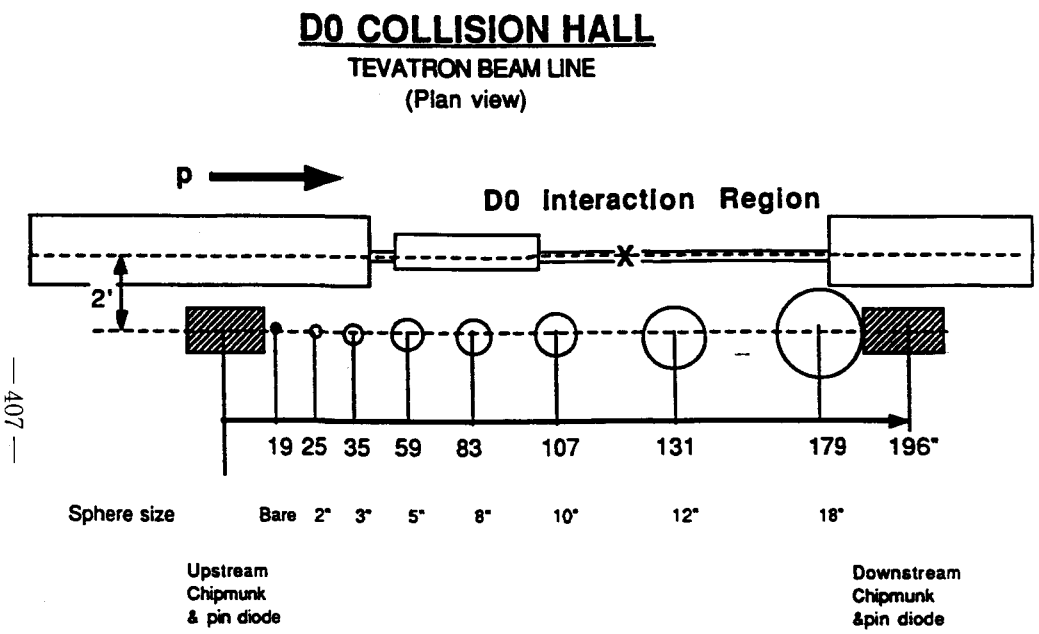

Fig. 1. Layout for n studies in the DØ Collision Hall showing magnets and instrumentation.

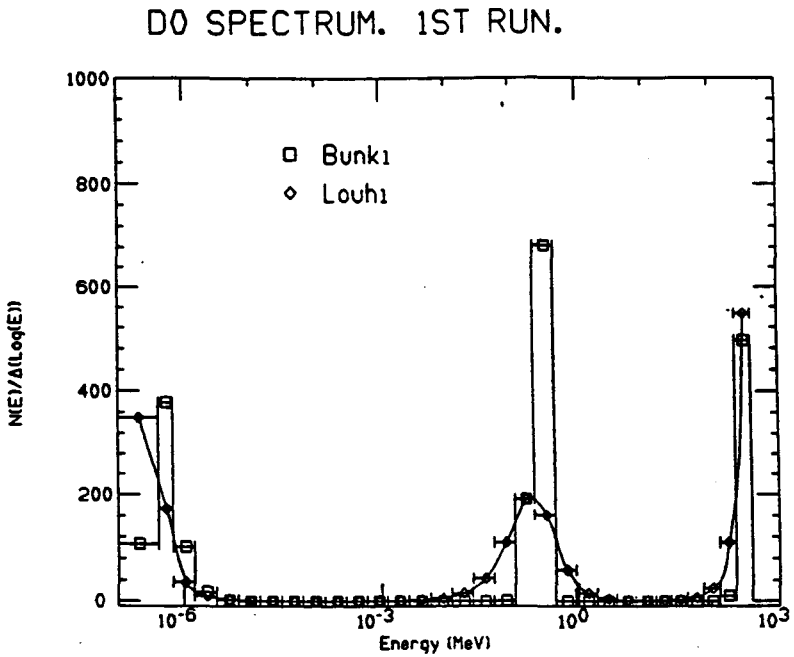

Fig. 2. Measured n spectrum from the DØ study.

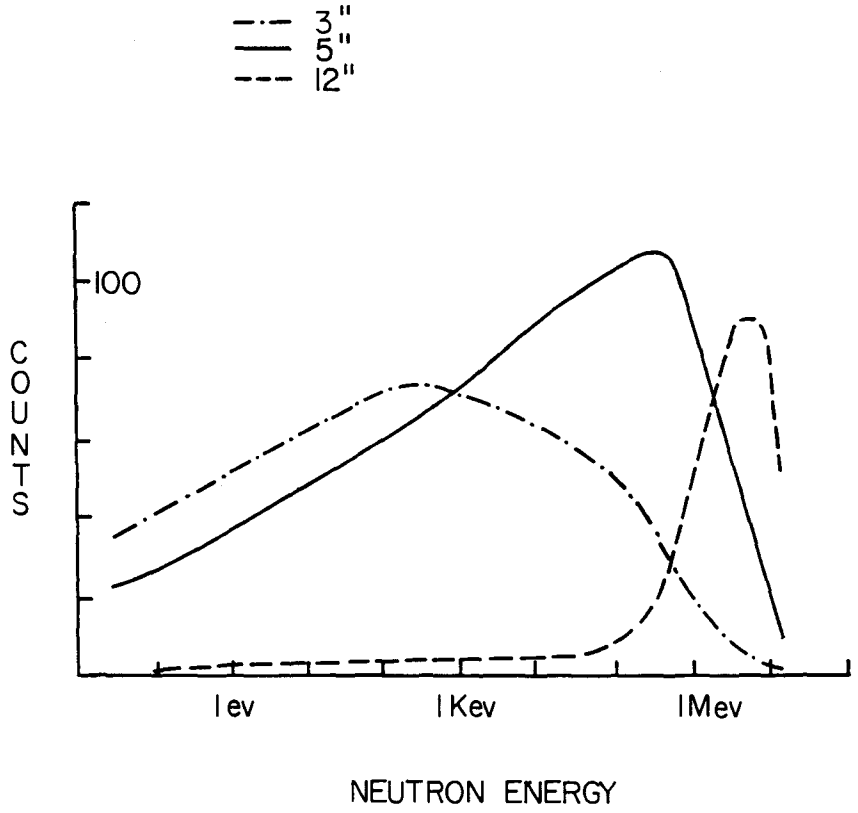

Fig. 3. Response of Bonner spheres of various radii as a function of incident neutron energy.

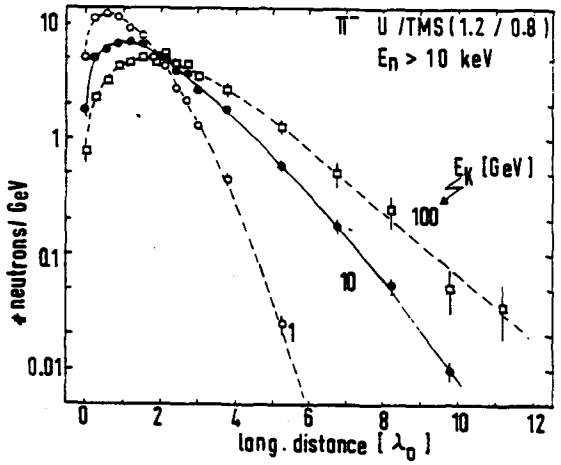

Fig. 4. Neutron yield/energy of the incident pion as a function of depth for various incident energies.

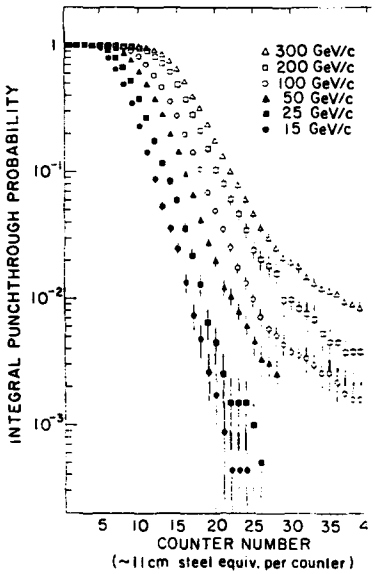

Fig. 5. Punchthrough probability using scintillation counters in a steel stack as a function of longitudinal depth for various incident hadron energies.

Japanese muon group activities I

Activities at University of Tsukuba

Yuzo Asano
Inst. of Applied Physics
Univ. of Tsukuba

Here I briefly introduce the muon group activities at Univ. of Tsukuba, which have been done so far and which are going. First I introduce some of the works done by our students. Mr. Hashimoto (first year graduate student) did calculations on the momentum resolution for the iron-toroid spectrometer in various configurations. Muon trajectories were generated using GEANT program, so that the effect of energy losses other than the usual ionization process is taken care of. A measuring station consists of 5 drift chambers with a thickness of 5cm. Fig. 1 shows the results for the case of 1 iron toroid of 85cm in thickness and for the case where the incoming momentum vector of the muon is assumed to be known (a perfect interaction-point constraint). Resolutions are given as a function of incoming muon momentum, for various chamber resolutions and chamber separations. Chamber separation is more important than the resolution at higher momenta, as can be seen in the figures for D=50cm and D=150cm. The momentum resolution is limited to 20 % due to the multiple scattering in the iron almost independent of momenta and chamber resolution. Fig. 2 shows the case for 3 iron toroids with a perfect interaction-point constraint. The resolution is limited to about 10% almost independent of momenta and chamber resolution and chamber separation. Fig. 3 shows the case for 3 iron toroids without interaction-point constraint. Here the chamber resolution is very important. In order to measure the sign of 2 TeV muons, the resolution must be better than about 300 microns. Fig. 4 shows the comparison between the calculation using the closed formula given by Voss and Zapančić for the momentum resolution in the iron toroid and the Monte Carlo calculation. They agree if the approximation condition is satisfied, but the closed formula underestimates the resolution if the condition is not satisfied. The region where this condition is satisfied is shown in momenta and chamber resolutions.

Mr. Itoh (first year graduate student) is studying the spatial resolution of drift tubes with a circular cross section of 3cm in diameter in cosmic ray tests. Fig. 5 shows the residuals when the trajectory of a cosmic ray is fitted with a straight line as a function of a timing offset value. The minimum value of the residuals give the right offset value. Fig. 6 shows the distribution of residuals, from which rms resolution of 470 micron is obtained. In order to improve this resolution, an improvement of the discriminator is under consideration. Fig. 7 shows the calculated induced current for different positions of a track from the anode wire. Also shown are the calculated shaped-signals to be obtained from the pre-amplifier with rise time 25.3ns and fall time 76.9ns (these values were measured for the first batch of ICs, which are being developed, by Mr. Kawaguchi).The calculated pulse shapes are very similar to the experimentally obtained ones. By using this simulation, a designing effort of a constant-fraction timing discriminator ICs is under way.

Mr. Hara (second year graduate student) is studying the effect of secondary particles produced by a high energy muon, using GEANT program. Fig. 8 shows the assumed configuration of detector set-up. For simplicity, only two drift tubes are arranged behind the magnetized iron of 1m in thickness. Table I summarizes the origins of the secondary particle production for 1000 of 100 GeV muons incident on the iron block. The detector wall-thickness is assumed to be 1mm. Most of electrons and almost all of positrons and gammas are produced in the iron. The effect of 3mm thick aluminum behind the iron is not appreciable. Table II shows the single hit probability for the tubes and the probability that the secondary particle gives a signal more than 100ns after muon signal (case I) and that it gives a signal before 100 ns (case II). The effect of electron range in the wall is not properly taken into consideration. And there are some ambiguities in the calculation, so this work should be continued and refined in the near future.

Mr. Kawaguchi (second year graduate student) is measuring the properties of IC chips which are being developed. The results are presented in the other session, but in the cosmic ray test by Mr. Itoh, the chips were successfully used as the

pre-amplifier for the drift tubes.

Finally I present my own work, which is already shown elsewhere. First, the simulation of Higgs (500 GeV) reconstruction through ZZ going into 2-jets and 2 muons. Fig. 9 shows the reconstruction of Z through 2 jets. Assumed resolution of the calorimeter is 0.2/sqrt(E) for EM, 0.5/sqrt(E) for hadrons, the granularity being 0.06x0.06. Fig. 10 shows the reconstructed Higgs. This channel is more favorable than the 4-lepton channel because of its larger branching ratio, provided the background in the 2jet mode is manageable. (In the case of 4-lepton channel, the Higgs signal is only barely visible for integrated luminosity of 10 to 40). The isolation of muons gives a rejection factor of 300 against top (200 GeV) pair events. Other cuts must be carefully applied to reject QCD background. Next, the results of Higgs reconstruction efficiency are applied to the iron-toroid vs air-core-toroid option for the forward muon detector. The conclusion is that as far as the Higgs reconstruction through 4-mu is concerned the air-core toroid has only a limited amount of advantage, perfectly in agreement with Thun's conclusion (R. Thun, IMPACT OF VARIOUS MAGNET OPTIONS ON HIGGS PHYSICS, 12 April 90). Fig. 11 shows the Higgs reconstruction efficiency for various detector resolutions through 4 muon-channel (the width of Z is not taken into consideration, the mass cut of Z is 88 GeV-100 GeV, the Z mass is a little higher than the present value, but does not affect the conclusion). 'Mix' means that the central tracker measures the muon momenta up to pseudo rapidity 1.6 and the iron toroid measures it for pseudo rapidity from 1.6 through 3. Fig. 12 shows the Higgs reconstruction efficiency through 4-mu channel for various coverage of central tracker. For example, y_b=2 means the central tracker measures the muon momenta up to pseudo rapidity 2, the iron-toroid measures the muon momenta from y=2 through y=3. This figure may be interpreted in the following way: as the resolution of air-core toroid is very similar to the central tracker, y_b=3 corresponds to the case of central tracker+air core toroid, y_b=1.5 corresponds to the case of central tracker+iron toroid, and y_b=0 corresponds to the case of iron toroid only (stand alone system, where the central tracker does not work, as in the case of luminosity 10 to 34). Air core toroid improves the efficiency only by 15%. Table 3 is taken from R. Thun's paper as mentioned above. Here his results and mine are combined to give the following values. Air core toroid improves the Higgs reconstruction efficiency by, 12% for Z mass cut of 81-101 GeV, 0.3% for Z mass cut of 71-111 GeV, 15% for Z mass cut of 88-100 GeV. Of course, if the mass-cut is enlarged more background will enter the signal region, although the detector efficiency becomes less sensitive to the reconstruction efficiency.

HASHIMOTO

Fig. 1

検出器 I

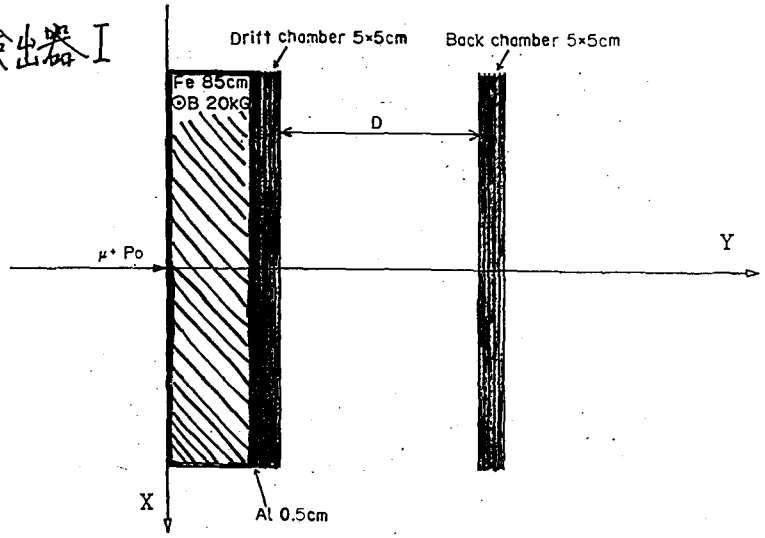

Muon Momentum Resolution

85cm Fe with 0.5cm Al θ=0mrad

D : Gap for Back Chamber

θ : Incident Angle

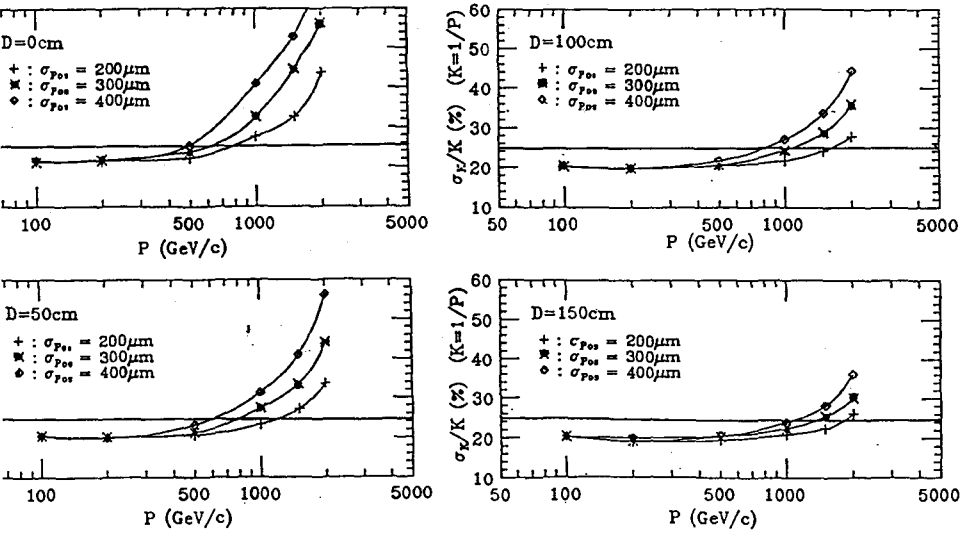

Fig. 2

検出器 II

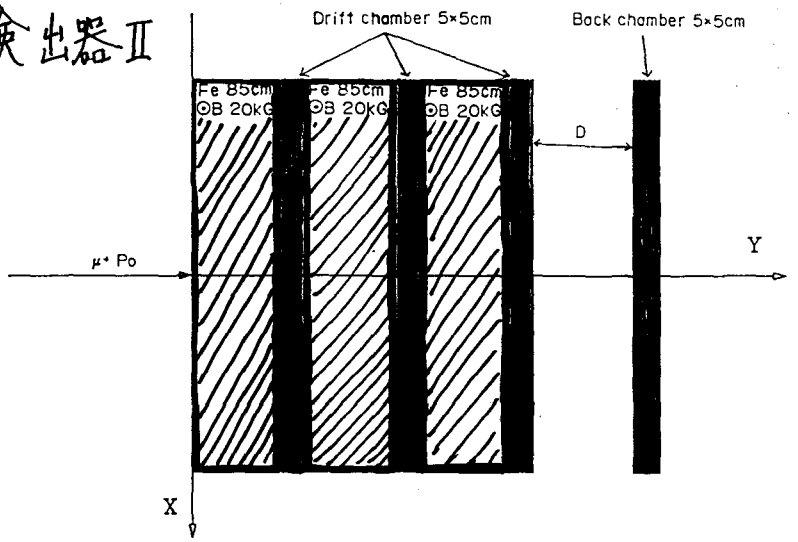

Muon Momentum Resolution

3 × 85cm Fe with 25cm Gaps θ=0mrad

D : Gap for Back Chamber

θ : Incident Angle

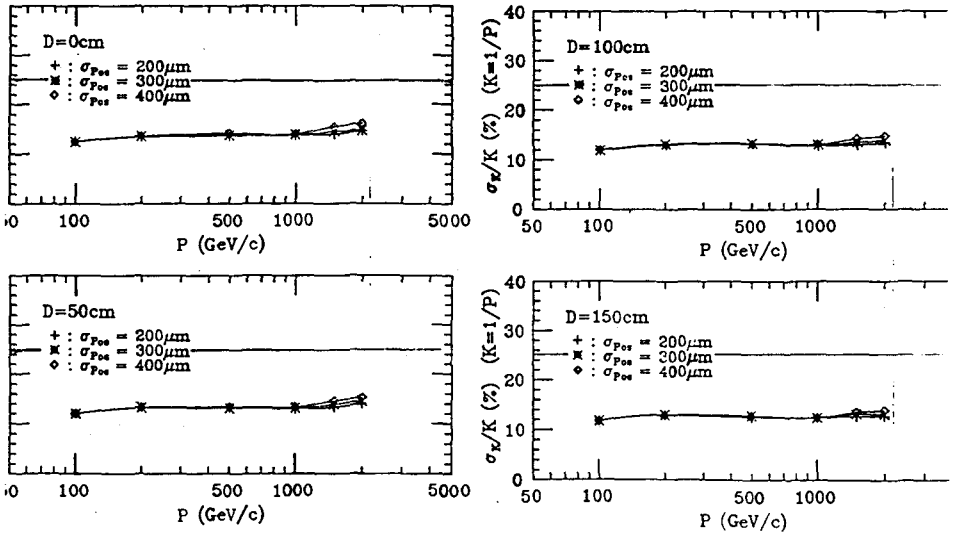

Fig. 3

検出器Ⅲ

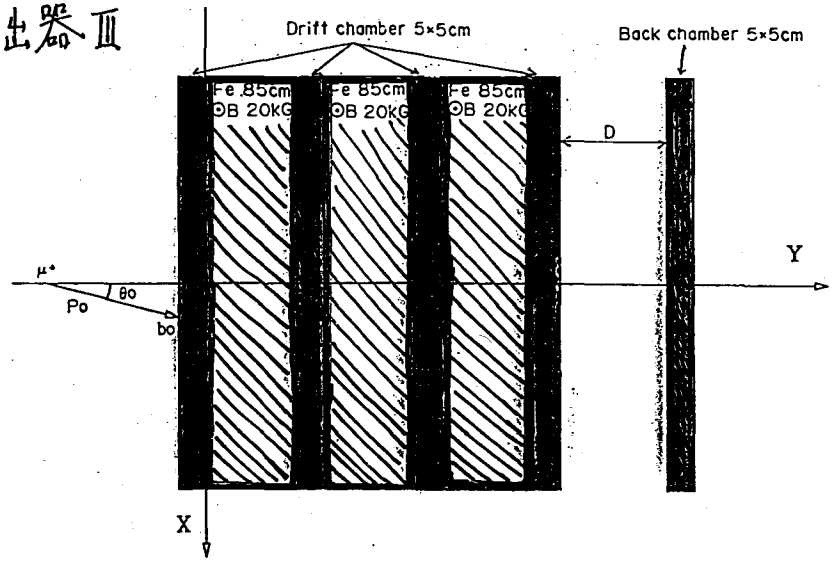

Muon Momentum Resolution

3 × 85cm Fe with 25cm Gaps θ=10mrad

D : Gap for Back Chamber

θ : Incident Angle

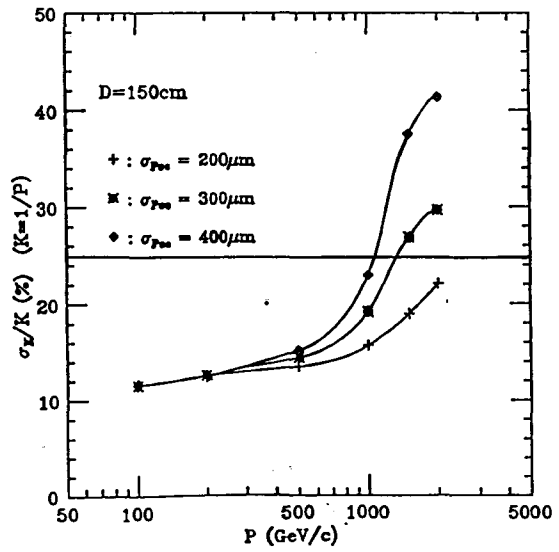

Fig. 4

R. Voss and Č. Zupančič

Proc. of the ECFA-CERN workshop March 1984

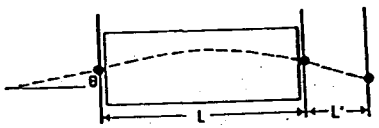

$$\left(\frac{\sigma_K}{K}\right)^2 \simeq \psi^2 + \Phi^2 + 2\Sigma'^2 \quad \text{if } \psi^2 \gg \Phi^2, \Sigma^2, \Sigma'^2$$

$$\psi^2 = \frac{1}{2}\left(\frac{E_s}{eBL}\right)^2 \frac{L}{l_r}$$

$$\Sigma^2 = \left(\frac{\sigma}{L}\right)^2 \left(\frac{p_0}{eBL}\right)^2 \qquad \Sigma'^2 = \left(\frac{\sigma}{L'}\right)^2 \left(\frac{p_0}{eBL}\right)^2$$

$$\Phi^2 = \sigma^2_{\theta,e} \left(\frac{p_0}{eBL}\right)^2$$

E_s = 20 MeV
B = Magnetic field , e = elementary charge
l_r = radiation length
σ = spatial detector resolution
$\sigma_{\theta,e}$ = resolution of external slope measurement
p_0 = incident muon momentum , $K = 1/p_0$

Muon Momentum Resolution D=100cm

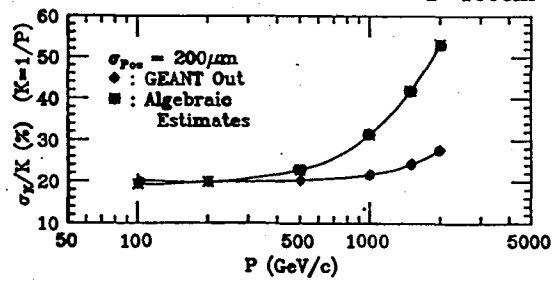

Requirements of Algebraic Estimates

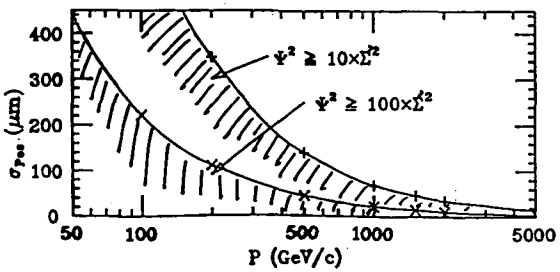

Itoh

Fig. 5

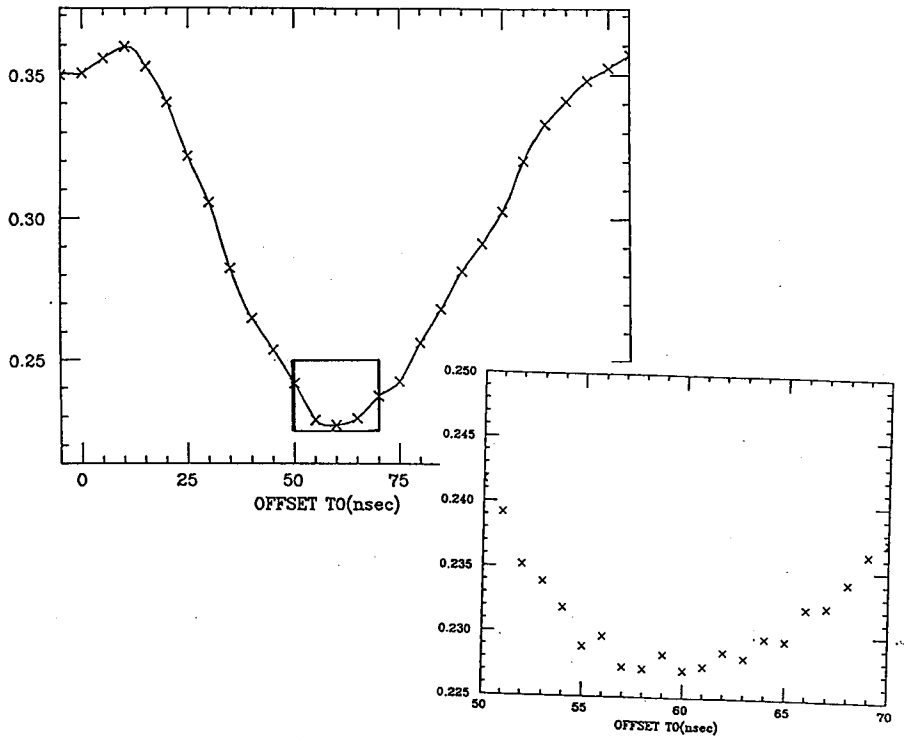

オフセット

H. V.	2. 4kV	2. 5kV	2. 6kV
tube#1	78ns?	73ns	58ns
tube#2	82ns?	60ns	50ns

2．4kVでは、データの数が減ってしまい、上図のような残差二乗和の平均の谷ができなかったので、上の表に示す2．4kVのオフセット値は正確な値ではない。

Fig. 6 宇宙線テストによる位置分解能

treshold −90. 0mV

H. V.	2. 4kV	2. 5kV	2. 6kV
tube#1	659±18μm	555±8μm	518±8μm
tube#2	612±17μm	470±7μm	420±6μm

H. V. 2. 5kV

threshold	-30.0mV	-50.0mV	-70.0mV	-90.0mV
tube#1	556±9μm	575μm±9	574μm±9	555±8μm
tube#2	538±9μm	508±8μm	491±7μm	470μm±7

ドリフトチューブの分解能

400～600μm > 300μm

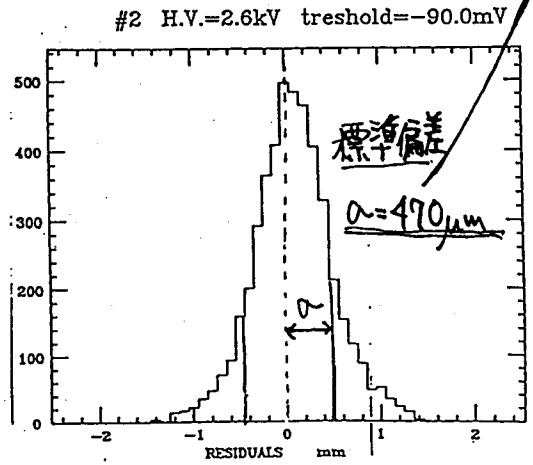

Fig. 7

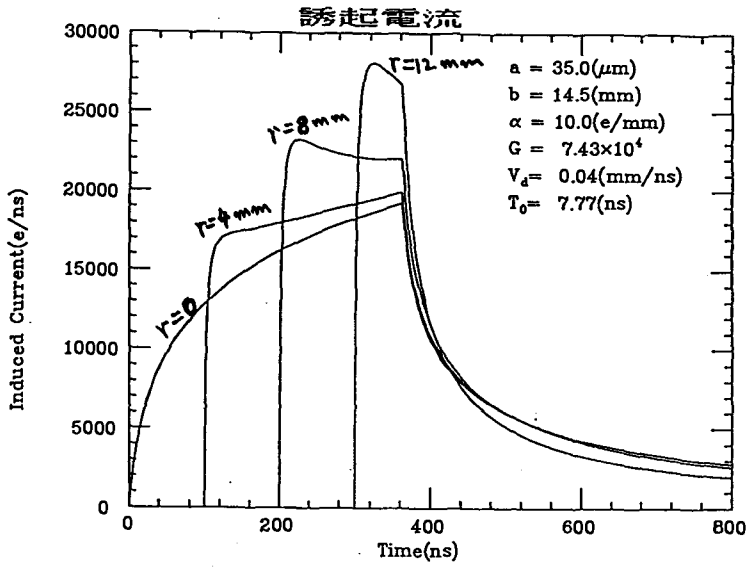

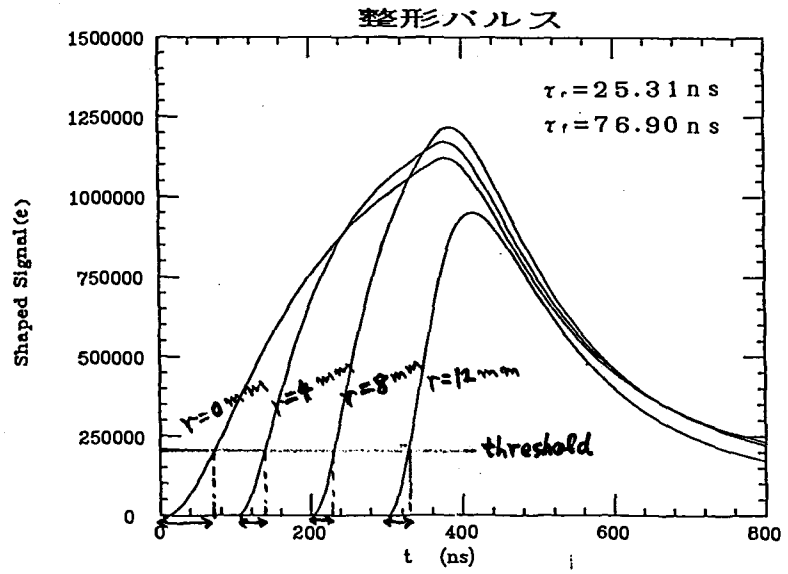

H. HARA

Fig. 8

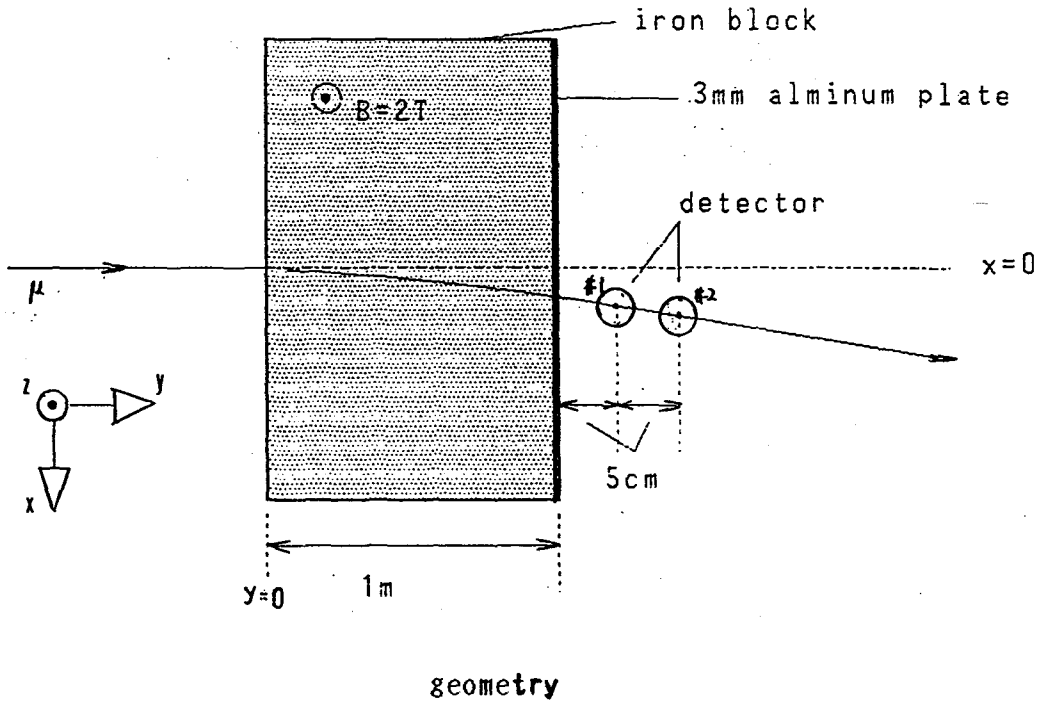

Table 1

Table 1

d(cm)	aluminum plate	particle	original vertex: iron block	original vertex: detector #1	original vertex: detector #2	< p > (MeV/c)
1	○	e^-	156	7	8	50.89
		e^+	107	0	0	61.35
		γ	2532	0	0	12.89
1	×	e^-	91	15	6	39.37
		e^+	59	0	0	64.67
		γ	1284	1	0	10.94
3	○	e^-	373	119	103	23.33
		e^+	231	1	1	57.13
		γ	5647	14	12	9.11
3	×	e^-	232	108	77	20.91
		e^+	117	1	2	41.71
		γ	3070	1	4	8.83

Table 2

Table 2

d(cm)	aluminum plate	single-hit (%) #1	single-hit (%) #2	number of secondary #1	number of secondary #2	case I (%)	case II (%)
1	○	94.4	95.5	0.68	0.62	0.4	5.3
1	×	95.1	95.8	0.61	0.58	0.4	4.5
3	○	87.2	89.3	0.88	0.82	2.3	11.8
3	×	87.3	89.6	0.81	0.75	3.5	10.3

Y. ASANO

Fig. 9

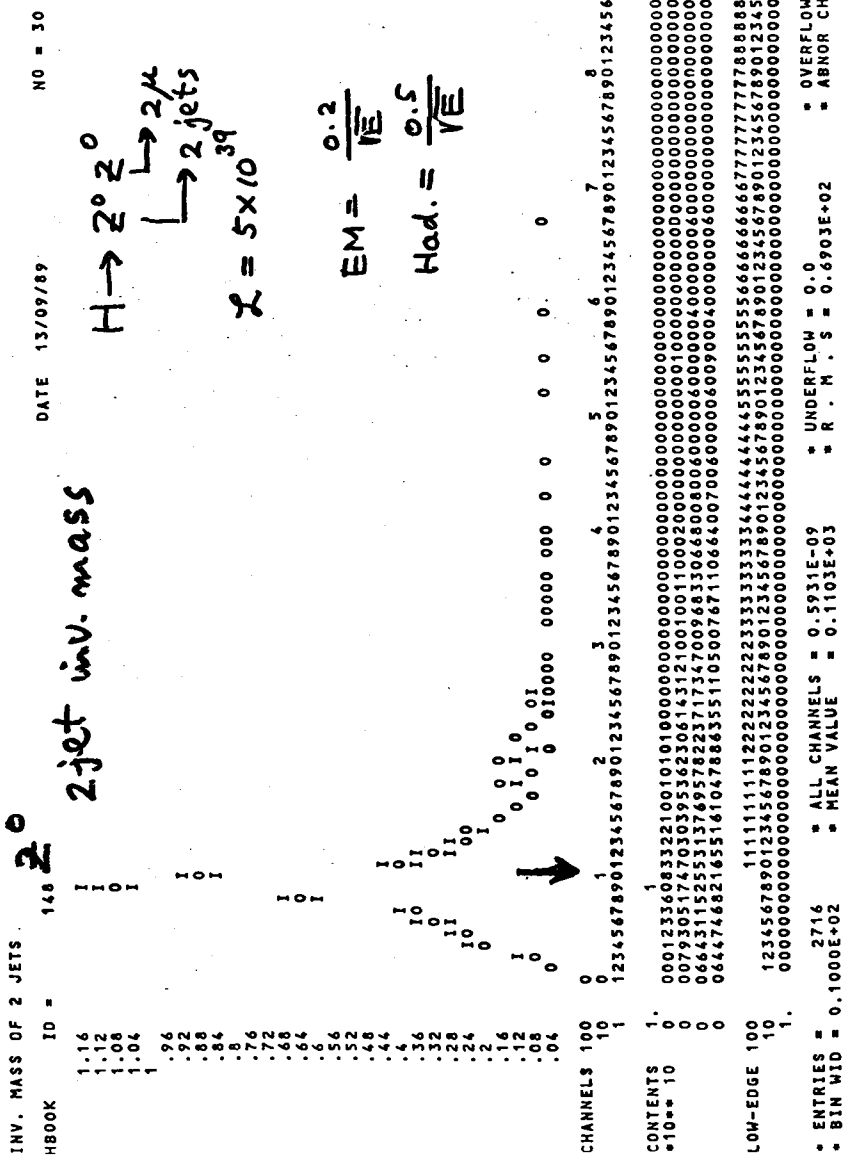

Fig. 10

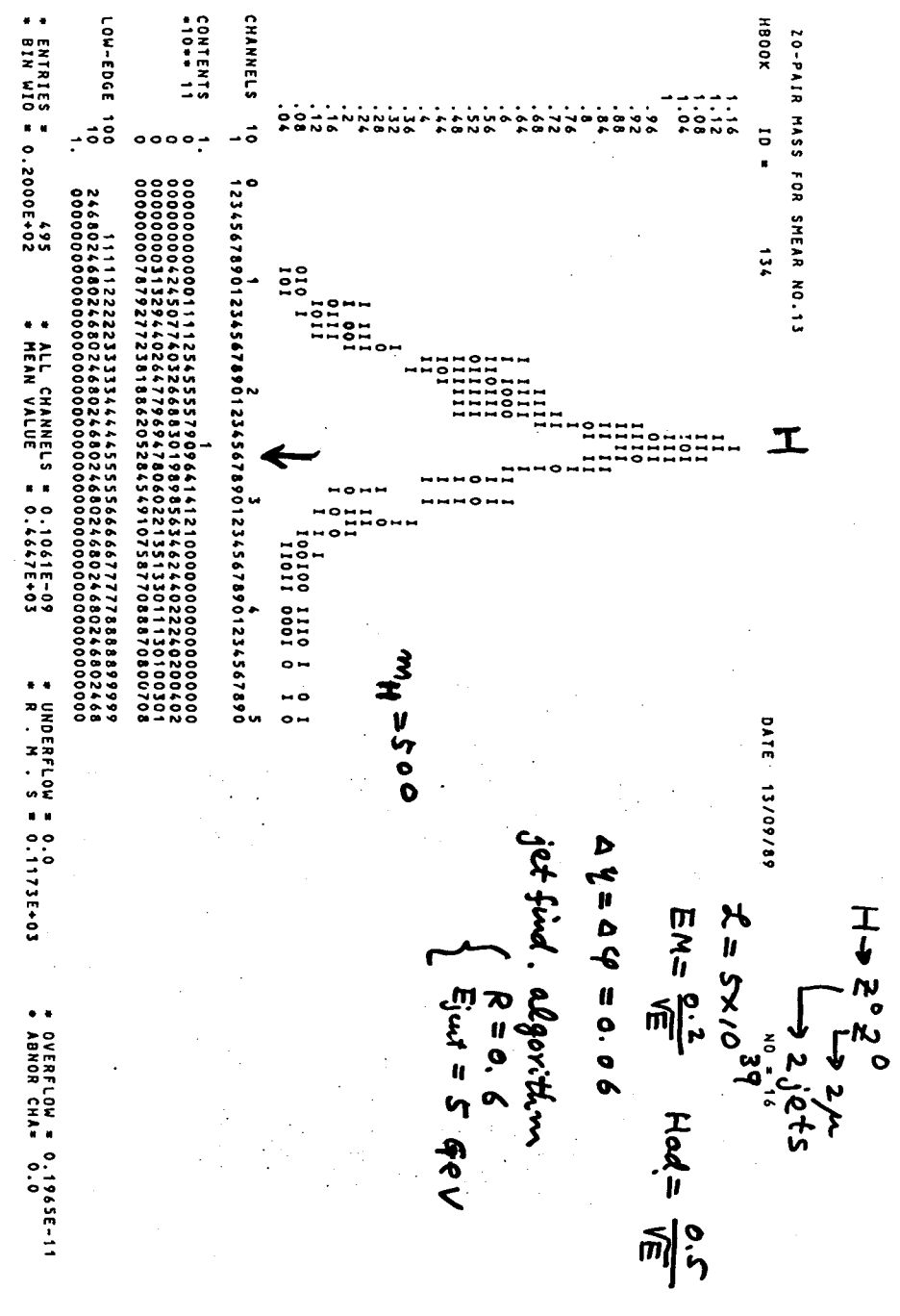

Fig. 11

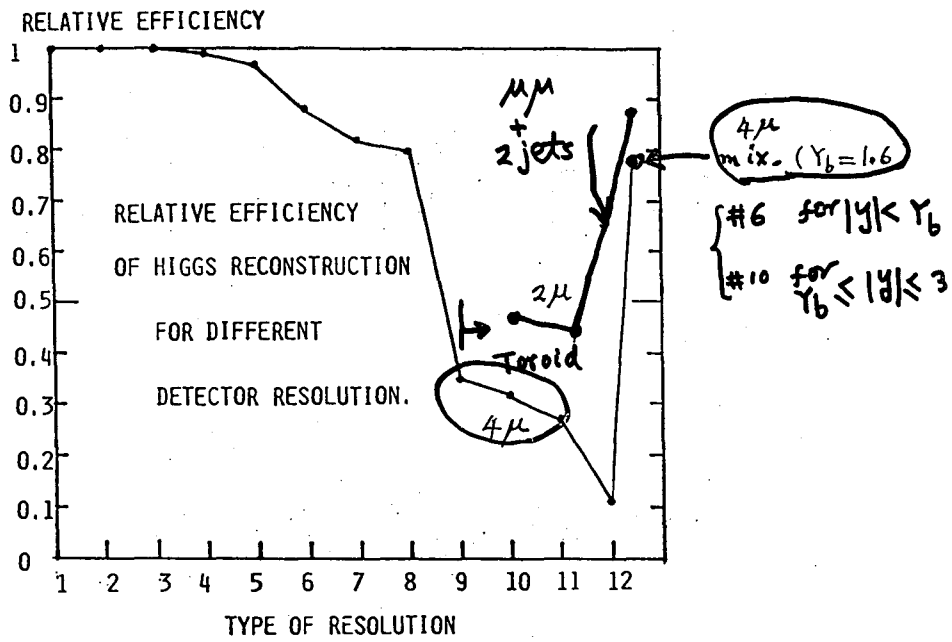

TYPE NO.	RESOLUTION ΔP/P
1	Perfect
2	2%
3	0.15/sqrt(E)
4	$0.3P_T$
5	4%
6	$0.14P+0.01$) central tracker
7	$0.54P_T$)
8	0.02 for ABS(y) .LT.1, 0.02+(ABS(y)-1)*0.06 for ly| .GT.1 and .LT.3) L3+I
9	($0.1+0.1P_T$ (TeV/c) Iron Toroid
10	(Toroid case 3 (Amako program #3...muon vector is measured at the exit of the filter.)
11	Toroid case 2 (Amako program #2...only position of the mu is measured at the exit of the filter.)
12	20%

Fig. 12

Y. ASANO

Contr. paper to Vancouver 1989

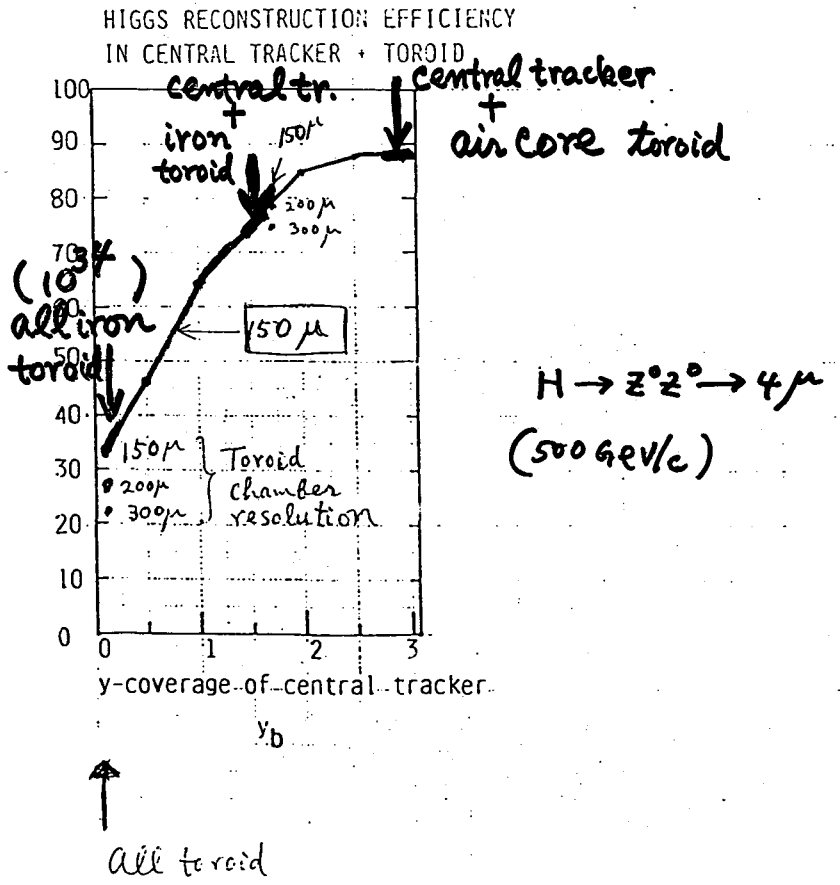

TABLE 1. Higgs Event Properties.

M(higgs) (GeV)	Width (GeV)	Width/(2M) (higgs)	muon tracks y<1.5 fraction (GeV/c)	y<1.5 <p>	y>1.5 fraction (GeV/c)	y>1.5 <p>
300	8.95	0.015	0.70	88	0.30	265
500	63.0	0.063	0.67	151	0.33	424
800	261	0.163	0.71	253	0.29	605

Table 3

TABLE 2. Resolution Results.

M(higgs) (GeV)	Magnet Config.	dM/M dp/p (rms) y<1.5	y>1.5	all y	f(ZZ) (higgs) rms	71-111 GeV	81-101 GeV
300	"Iron"	0.016	0.120	0.067	0.038	0.997	0.923
	"Air 1"	0.016	0.050	0.030	0.018	1.000	0.999
	"Air 2"	0.016	0.025	0.019	0.012	1.000	1.000
	"All Iron"	0.138	0.120	0.133	0.072	0.968	0.674
500	"Iron"	0.026	0.121	0.073	0.042	0.997	0.881
	"Air 1"	0.026	0.065	0.043	0.028	1.000	0.992
	"Air 2"	0.026	0.033	0.029	0.019	1.000	1.000
	"All Iron"	0.139	0.121	0.134	0.078	0.941	0.586
800	"Iron"	0.041	0.126	0.076	0.049	0.986	0.871
	"Air 1"	0.041	0.097	0.063	0.045	0.989	0.927
	"Air 2"	0.041	0.049	0.043	0.030	1.000	0.984
	"All Iron"	0.140	0.126	0.136	0.079	0.940	0.577

12%

NOTES:

(1) One expects very roughly dM/M(higgs) = <dp/p>/2
dM/M(Z) = <dp/p>/sqrt(2)

(2) f(ZZ) is the fraction of Higgs events in which at least two mu+mu- pairs have effective masses in the indicated intervals of 71<m<111 GeV and 81<m<101 GeV.

$.3 > |\eta| > 1.5$ Iron Toroid → Air core toroid

$81 < m_Z < 101$ 12% increase in efficiency

$71 < m_Z < 111$ 0.3% increase "

mycase $88 < m_Z < 100$ 15% increase "

Activities at Osaka City University

Yoshiki Teramoto[1]

Department of Physics, Osaka City University
3-3-138 Sugimoto, Sumiyoshi, Osaka 558, Japan

The experiences of the TOPAZ muon chambers will be briefly described. From these experiences, we propose "chain connections" of "permanently-sealed-disposable modules" to be used as the SSC muon chambers. Though the status of this proposal is still at the conceptual design stage, this scheme has a potential of solving major difficulties specific to muon chambers, by enabling low production cost, easiness of mass production and maintenance.

1. Experiences of TOPAZ

Osaka City University has been committed to the TOPAZ muon chambers in the last several years. Here we briefly present the experiences of TOPAZ. Though the SSC muon chambers are different from the TOPAZ muon chambers at various aspects, they share the main feature which comes from their hugeness of sizes, namely (1) how to cover the large area at the moderate cost, (2) difficulty in construction and maintenance due to their sizes. The TOPAZ muon chambers are made of rectangular-shaped-extruded-aluminum tubes with the cell size: 10 cm x 5 cm. The extrusion was done in four-cell units. Then the eight-cell unit was made by welding of the two four-cell units with a half cell staggered. This basic eight-cell structure is common to all TOPAZ muon chambers. In the production process, however, these weldings of aluminum caused difficulties. The dimensions of the TOPAZ muon detector are summarized in Table 1. The construction cost of the TOPAZ muon detector is listed in Table 2.

Though the TOPAZ muon chambers have been operated successfully, there are several points that could be done better in the next time if we build the chambers for SSC. These are,

1. **Chamber gas:** Gas supply systems for the large number of chambers always have the possible problems of gas leaks. The cost of the chamber gas in TOPAZ is about $ 40K/year without a gas circulation system, though we use the low cost $Ar/CH_4 = 90/10$ mixture. If we use expensive gas as CF_4, this cost will be more than ten fold. Safety is probably a bigger concern, since we use flammable gas in the underground. It is also cumbersome to change gas cylinders frequently.

2. **Installation scheme:** The muon chambers were installed between iron absorber. This structure together with the crowdedness at the both ends of the chambers with cables and gas tubing makes us hard to remove the muon chambers after they were installed.

3. **Insensitive regions:** We have two types of insensitive regions,

   - **Cell walls:** Cell walls(2.6mm) and the regions about 2 – 3 mm from the cell walls are insensitive, resulting of about 5 % dead regions in the geometrical coverage.
   - **Sector boundaries:** TOPAZ is an octagonal shaped detector and each octant is called a "sector". Between these sectors have small gaps in detector coverage referred as "sector boundaries". In the muon chambers, these sector boundaries account about 3 % dead regions.

[1] Representing Osaka City University: T.Okusawa, T.Takahashi, Y.Teramoto and T.Yoshida.

2. Permanently-sealed modules

In order to be free from the gas supply problems and to achieve the easiness of mass-production and operations, we propose "permanently-sealed-modules" which are somewhat similar to "florescent light tubes". Fig. 1 shows the schematics of a proposed permanently-sealed chamber. The chamber body is made of a thin($\sim$ 0.5mm) stainless steel tube. At both ends, the high-voltage-insulator plugs made of ceramic with kober[2] disks are welded to the body. A rigid feed-through and a gas port are integrated in the ceramic insulator plug. These feed-throughes are used to fix the chamber both mechanically and electrically. The gas port is used to pump out airs from the chamber and fill the gas to the chamber at production. After the gas was filled, this port will be sealed permanently. Though the status of this project is still at the conceptual design stage, they could solve the major problems in the mass-production and operations, if they are realized. Their features are listed below,

1. **Safety:** There will be no gas flow in the system, hence they are free from gas leaks.

2. **Low operation cost:** Since the volume of the muon chambers are by far the largest among the sub-detectors, the ordinary muon chambers will be the biggest gas-guzzler in SDC.

3. **Easiness of maintenance:** Since the major task in the maintenance of ordinary chambers is the constant supply of the chamber gas and since the permanently-sealed chambers are free from this, it will be as easy as florescent light tubes to maintain the sealed chambers.

4. **Easiness of mass production:** The simpleness of the modules make them suitable for mass production. In addition, since the chambers can be tested fully at the production line after the gas filling, quality control of the chambers should be easier than the ordinary chambers.

5. **Disposable option:** Radiation damage by a high flux of neutrons as well as charged particles may be a serious problem in the SSC muon chambers in general. Using CF_4 may prolong their lives in some extent, since this gas has no hydrogen in its molecular structure. It is believed that high gas-flows will extend the chamber's life and since the permanently-sealed chamber certainly lacks of this remedy, the life of a permanently-sealed chamber may be shorter than the ordinary chamber. To overcome this possible shortcomings, we propose to make the chambers as disposable and keep the production line running even after the initial completion of the muon chambers. This will push the operation cost higher, but if we can make the cost of one module in less than $ 100 and its life to be 3 – 5 years, this option is realistic as long as the cost is concerned. To avoid the mess of alignment work after each replacement of aged chambers, however, chambers and their support frames should be designed as alignment free or at least "alignment friendly".

In order to save the total cost of the muon detector, we are also working on the "chain connection" of modules. There are two ways to lower the number of readout channels. One is to make the cell size larger, but this causes longer delays in triggers as its draw backs. The other is to extend the other coordinate, i.e. make the chambers longer. To build very long chambers, however, is not easy, because of wire stability, wire sagging, etc. To overcome this difficulty, we propose to connect chambers serially as shown in Fig. 2. The initial test of this external "chain connection" of two chambers shows no problem so far. This configuration reduces the number of electronics channels without suffering the triggers. This configuration also makes us possible to build shorter modules, which are much easier to be build than the full size modules and hence are suitable to be mass-produced. Moreover, this also enables us to measure the wire directional readout by using the time difference of signals at the both ends of the chain, by adding one extra pair of front-end electronics and TDC. Our preliminary test shows that we can get the space resolution of 2 cm along the wire direction without using any special techniques[3].

[2] Metal alloy of iron, nickel and chrome.

[3] Time resolution of TDC is the main cause of the limitation of this resolution

In order to achieve the easiness of replacing chambers and alignment friendliness, we propose a mounting scheme using cartridges as carriers of the chambers, which is illustrated in Fig. 3. All the electrical connections as well as mechanical alignment should be done and guaranteed by the cartridges. The required mechanical precision of the cartridge is order of $\sim$ 100 μm.

3. Conclusion

The "chain-connections" of "permanently-sealed-disposable modules" using cartridges as the carriers have a potential to solve the major difficulties specific to muon chambers – easiness of mass production and quality control, low production cost, reduction of readout channels, easiness of maintenance, alignment friendliness, and safety from possible gas explosions. At Osaka City University, we also work on the beam test project to measure electromagnetic soft associates of high momentum muons. This subject, however, will not be mentioned here, since they are presented in the separate article in this proceedings.

Table 1. The dimensions of the TOPAZ muon detector.

region	area(m^2/plane)	# of planes	# of channels
Barrel	160	8	2.3K
Forward-backward	150	4	1.7K

Table 2. The construction cost of the TOPAZ muon detector.

item	cost	cost/ch
Chamber		
• Al extrusion (a) – (c)		
(a) Barrel – azimuth	\$ 320 K	\$ 250 (\$ 350/m^2)*
(b) Barrel – polar	\$ 190 K	\$ 170 (\$ 570/m^2)*
(c) FB	\$ 300 K	\$ 180 (\$ 550/m^2)*
• FB structure	\$ 70 K	\$ 42
• Wire string and miscellaneous	\$ 100 K	\$ 25
• Installation	\$ 70 K	\$ 18
total	\$ 1050 K	**\$ 260**
Electronics		
• Front end	\$ 270/8ch	\$ 34
• Intermediate	\$ 8600/crate	\$ 12
• TDC/CAMAC		\$ 64
TDC	\$ 1400/32ch	
Controller	\$ 7000/crate	
Crate	\$ 7000/crate	
• Cables	\$ 64/8ch	\$ 8
• P.S.	\$ 5700/crate	\$ 8
total		**\$ 126**
Grand total		**\$ 390**

1 crate = 704 ch
140 yens = 1 U.S. dollar
Fe absorber cost = \$ 1.8 / pound
H.V. etc = small cost
(*) cost per plane.

Fig. 1 Conceptual design of a permanently-sealed module

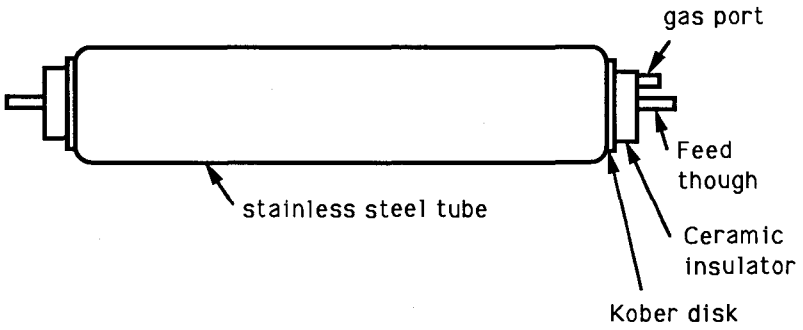

Fig. 2 Chain connections of modules

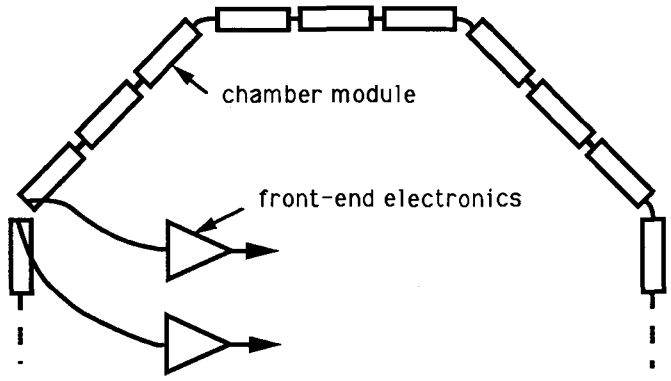

A view along the beam axis.

Fig. 3 Mounting scheme using cartridges

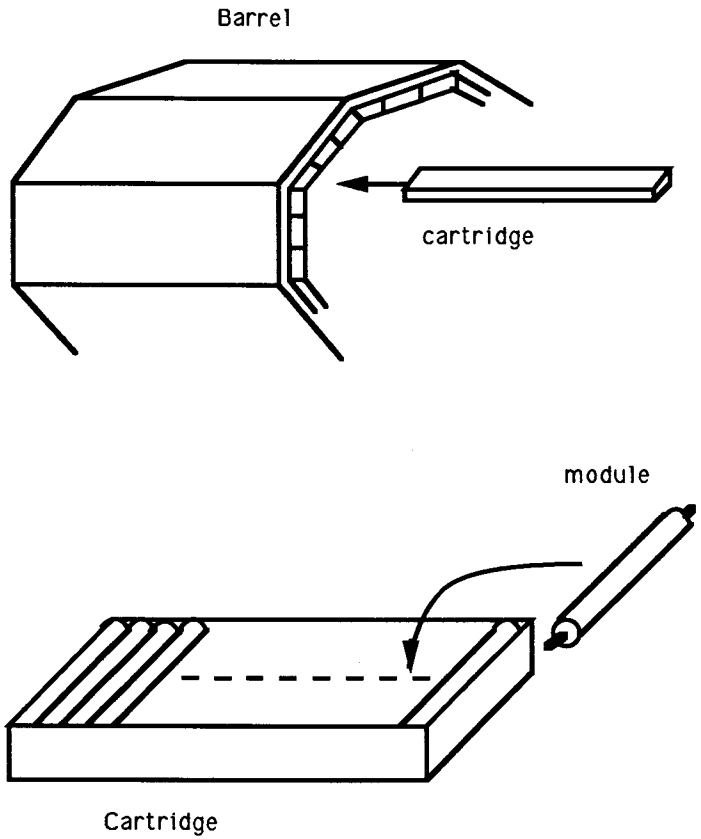

Muon Trigger Rates and Momentum Resolution Calculations

Yoshihide Sakai

KEK, National Laboratory for High Energy Physics
Tsukuba, Ibaraki, Japan 305

ABSTRACT

The muon rates and momentum resolution for muon detectors are calculated. The muon rates are calculated at exit of the calorimeter and the muon filter using a simple detector geometry for the SSC at $\sqrt{s} = 40$ TeV with $L = 10^{33}cm^{-2}sec^{-1}$. Contributions from prompt, decay, and punchthrough are presented as a function of various muon quantities. Also, the efficiencies for typical physics process are calculated for corresponding muon quantities. The momentum resolution for muon toroid system is calculated by a simple simulation and track fitting for various configurations and parameters. The result of simple simulation which include only multiple scattering effect is compared with that of full simulation by GEANT and they have resonable agreement.

MUON TRIGGER RATES CALCULATIONS

At the SSC, many of the new physics signatures involve leptons. Since some of the processes, such as Higgs $\rightarrow Z^0Z^0 \rightarrow 4\mu$ and $Z' \rightarrow \mu^+\mu^-$, involve only muons and no other activities, the muon trigger is quite important (especially at 1st level trigger) to catch those events. Here, the muon rates exiting the calorimeter and the muon filter are calculated for various quantities which might be used in the trigger.

Detector Geometry

In order to calculate the rate of muons, at least the geometry of absorber material should be specified. A simple geometry shown in Fig. 1 is used in the calculation described in the following. A simple cylindrical geometry is assumed: The barrel calorimeter starts from R = 2 meters and is treated just as 2 meter thick iron block. A 2.5 meter thick iron muon filter is placed just outside of the calorimeter; The endcap calorimeter starts from Z = 4 meters with same thickness of barrel part (2 meter thick iron). A 3.5 meter thick iron muon filter follows it. The inner corner between barrel and endcap corresponds to rapidity y = 1.5.

Event Generation

The background events are generated using ISAJET[1] (version 6.21) at $\sqrt{s}$ = 40 TeV. In order to estimate background rates in the region relevant to the consideration here (mainly 1st level trigger) including minimum bias events, the process 'TWOJET' in ISAJET are used with wide rapidity range and low p_t limit for primary jets. The ranges used here are: $-8 < y < 8$ and $5 < p_t < 200$GeV/c. This gives a total cross section of 90 mb which is about same as the expected total cross section ($\sim$ 100 mb). In order to get enough statistics for full range of consideration, events are generated in 6 steps of p_t ranges.

Muon sources

The following three sources are considered for the muon rate associated with the beam interactions.

i) Prompt muons: prompt muons are defined as particle which has muon particle ID in the generated events by ISAJET. These muons come from decays of heavy quarks (c and b). The mass of top quark is set to 160 GeV/c^2 in the program and the contribution to the background muon rate from top quark is negligible in the first level trigger.

ii) Decay muons: muons produced by decay in flight of stable hadrons. The decay probability is given by

$$\text{Prob.} = [1 - \exp(-L/c\tau\gamma)] \times \text{Br}(\text{had} \rightarrow \mu x)$$

where L is distance to the surface of calorimeter from the interaction point, $\gamma = E/m_h$, and Br(had$\rightarrow \mu$x) is a branching ratio for muonic decay. Only $\pi^{\pm}$ and $K^{\pm}$ are considered as decay source for simplicity (3-body decay of K_L is neglected). Decay muons coming from two body decay of hadrons with $\beta \sim 1$ have flat energy distribution:

$$E_\mu \cong \gamma(E^*_\mu + p^*_\mu \cos\theta^*), \qquad \text{with} -1 < \cos\theta^* < 1$$

iii) Punchthrough: There are several empirical parametrization formula which were obtained by fitting experimental data. However, the range of the data in fit is limited and sometimes 2 formula give quite different answers. For example, WA1 parametrization was used in the muon rate calculation at Snowmass 86:[2]

$$\text{Prob.} = \exp - [(\lambda - 1.53E^{0.33})/(0.89E^{0.165})]$$

Ref. 3 gives following formula:

$$\text{UA1 Fit}: \quad \text{Prob.} = 0.13p^{1.62}\exp(-x/23\text{cm})$$

Bodek Fit : Prob. = $(p/350) \times 0.0095 \times \exp[-1.42(\sqrt{R}-2)] \times 0.81$

Lang Fit : Prob. = $10^{-4} a \cdot p^{b} \exp[-(c/p+d)R']$

(for the detail of formula, see ref. 3). These formula are compared in Fig. 2 for Fe thickness of (a) 2 meters and (b) 4.5 meters. They differ orders of magnitude. relatively low energy and thin Fe data are used in WA1 and UA1 fits, while relatively high energy and thick Fe data are used in Bodek and Lang fits. In the calculation here, probabilities are calculated both for WA1 and Lang fits and the higher probability is taken for given energy and Fe thickness. This is illustrated in Fig. 3. Basically, WA1 fit is used at thin Fe and Lang fit is used at thick Fe.

Rate calculation

The muon rates are calculated in two ways for decay and punchthrough:

A) Simulate decay/punchthrough muons according to the calculated probability using random number.

B) Multiply decay/punchthrough probability as weight for each particle and accumulate histograms for various quantities.

Method A) is more realistic but statistics is much lower than B). Most of the plots shown below is using method B).

Results

The results are presented in terms of the rate (Hz) which is converted from the cross section assuming $L = 10^{33} cm^{-1} sec^{-1}$ (i.e. 1 mb corresponds to 10^6 Hz). The overall muon rates for each source are shown in Table 1. The decay muons are dominant source for all cases and the punchthrough gives only small contribution especially after the muon filter.

Table 1. Overall muon rates

y range	Exit at	Prompt(Hz)	Decay(Hz)	Punch(Hz)	Total(Hz)
$\|y\| < 3$	CAL	1.3×10^5	1.1×10^7	5.3×10^5	1.2×10^7
$\|y\| < 3$	Mu Filter	1.1×10^5	5.3×10^5	3×10^3	6.4×10^5
$\|y\| < 1.5$	CAL	1.5×10^4	2.8×10^5	4×10^3	3×10^5
$\|y\| < 1.5$	Mu Filter	2.6×10^3	9×10^3	5×10^1	1.2×10^4

Fig. 4 shows muon multiplicity rates. The rate of multiplicity 2 is an accidental rate of single muons in the same bunch. Therefore, if muon trigger can not separate N bunches the 'dimuon' rate is N times higher. Fig. 5 - 8 show muon rate vs Polar angle and y of muons for each muon source component at the exit of the calorimeter and the muon filter. The rates are presented in two plots for each case: a) The (differential) rate at given quantity value; b) The trigger rate with given threshold value for the quantity. This is given by integrating the differential rate a) from threshold value to infinite. In order to minimize statistical effect, the integration was done after smoothing the distribution shown in a). The values at the lowest point gives total rate. Fig. 9 - 12 show muon rate vs p_t and p for rapidity range $|y| < 3$ and Fig. 13 - 16 shows those for $|y| < 1.5$. For p_t and p plots, momenta of decay muons are used rather than momenta of parent hadrons, since momenta measured by the muon detector would be relevant to the muon triggers for early stage. For punchthrough muons, momenta of hadron are used for convenience. Fig. 17 compares the total muon rates vs p_t/p threshold values for various cases.

Most of new physics signatures give leptons to be isolated. A simple isolation algorithm is considered here. The calorimeter energy deposit around muon track are checked for single, 9 (3 × 3), and 25 (5 × 5) calorimeter towers. The calorimeter energy deposit is simulated using simple calorimeter simulation program CALSIM[4] with tower size $\Delta y \times \Delta\phi = 0.15 \times 2\pi/32$. Fig. 18 (a),(b) show energy deposit distributions of the calorimeter towers. Fig. 19 show trigger rate versus calorimeter isolation energy threshold E_{CAL} where if calorimeter towers have energy deposit more than E_{CAL}, the events are rejected. It shows rate does not decrease so much. Probably, without muon momentum cut, majority of muon rates are due to low momentum particles and already away from the hard component of the jet.

Efficiency for Physics Events

For any quantity, the trigger rate can be reduced to any value by raising the threshold. However, the threshold should be kept low enough to keep the efficiency of the interesting physics events to be good enough. As an example, the Higgs production process ($H \rightarrow W^+W^- \rightarrow \mu + \nu$+jets) is chosen. The mass of Higgs is chosen to be 400 GeV/c^2. The events are generated using ISAJET program. The total cross section of the process is 0.46 pb including branching ratios.

The results are shown in Fig. 20-23. Now a) shows the differential cross section and b) shows the efficiency vs threshold value for each set.

From the background distributions, it is important to have p_t or p threshold in the first level trigger in order to reduce the muon trigger rate to comfortable level. p_t (or p) threshold of 20 (40) GeV/c is enough to reduce background rates to the level of 10^3, while the efficiency for Higgs production process still kept more than 80%.

MUON MOMENTUM RESOLUTION CALCULATION

It is important to estimate the muon momentum resolution in designing detectors for the SSC. It is possible to calculate resolution using empirical formula,[5] but sometimes it is not straightforward to apply it to different and complicated configurations. Therefore, it is useful to calculate resolutions with more realistic procedures for various detector configurations. For this purpose, a simple simulation and fitting program was made.

Geometrical Configurations

A planar geometry of muon chambers and filter material is assumed in the program and calculation is made two-dimensionally in the bending plane. The general configuration and coordinate system is illustrated in Fig. 24. For each layer of material, magnetic field and radiation length are are assigned. The magnetic field is assumed to be uniform. Calculation can be done for given numbers and positions of material layers and chambers.

Procedures

The calculation is made in the following procedures:

1) A track trajectory is produced through the material layers for given momentum (p), $\sin\theta$, and y position at x=0 ($\sin\theta_0$, y_0). A multiple scattering is taken into account by tracing trajectory with small steps (1 radiation length). Simple formalism with Gaussian distribution is used for multiple scattering calculation.[6]
2) Hit position at each chamber is calculated from a trajectory. The positions are smeared with Gaussian distribution with given chamber position resolutions.
3) A track fit to chamber hit positions is performed with p, $\sin\theta_0$, and y_0 being free parameters. A fit was done in a 'brute force' manner using program MINUIT as follows: Since only uniform field is considered, the position at each chamber can be calculated analytically (without multiple scattering effect) for given p, $\sin\theta_0$, and y_0. Then, $\chi^2 = \sum(y_i - y_{fit})^2/\sigma_i^2$ is calculated and fed into MINUIT. Note that this program is not intended to develop a track fitting algorithm used in a analysis but just to estimate the momentum resolution which would be obtained by a reasonable fitting program.

Procedures 1) - 3) are repeated for each events and $(K_{fit} - K_0)/K_0$ ($K = 1/p$) is accumulated in histogram. The momentum resolution ($\sigma_K/K = \sigma_p/p$) is obtained by fitting histogram with Gaussian distribution.

Trajectory points can be supplied from the file so that the fully simulated trajectory by GEANT can be also used for resolution calculation.

Results

In the following, calculations are done for configurations based on the muon toroid system of the ACS detector.[7] Fig. 25 (a) and (b) show the barrel and end cap configurations used in the calculation. The barrel (end cap) part consists of 3 (4) layers of magnetized iron filters with thickness of 85 cm and 15 cm gaps between them. 3 chambers with 3 cm apart are always treated as one set in the calculation for convenience, which is different from actual design. Two sets of chambers are placed before and after muon toroid and one set of chambers is place each gap between iron. For two set of chambers after muon toroid, three different gaps between chamber sets are considered: (A) 40 cm, (B) 1 meter, (C) 2 meters. 40 cm gap is taken if it is noted otherwise. The magnetic field in iron is assumed to be 2 Tesla.

In Fig. 26, results from simple track simulation in step 1) (multiple scattering only) are compared with full simulation by GEANT (provided by M.Asai) for barrel part with chamber resolution of 300 μm. In GEANT simulation case, $(K_{fit} - K_0)/K_0$ distribution shows long tail for high end as shown in Fig. 27. This is due to the energy loss by bremsstrahlung and reflected in large difference in resolutions taken from width of Gaussian fit (×) and from RMS of distribution (+). Except this long tail, the effects to resolution due to energy loss by dE/dx and bremsstrahlung in full simulation is not so large (about 10%) and simple simulation gives good estimate for resolution. Also shown in figure (by *) are average shift of fitted momentum from originally produced momentum (in unit of %).

All the results described in the following are obtained by simple simulation with multiple scattering only.

Shown in Fig. 28 and 29 are the dependence of momentum resolution on chamber position resolution and on the gap between the last 2 set of chambers after iron toroid for barrel part. Fig. 30 shows the dependence of momentum resolution on chamber position resolution for end cap part.

Fig. 31 shows momentum resolution for 3 different configurations are compared for barrel part with 1 m gap for the last 2 sets of chambers. (×) shows configuration with no chambers in gap between iron filter and is compared with that with chambers in iron gaps. In order to keep the number of chambers to be same, chambers in iron gaps are moved between first and last 2 sets of chambers for the former case. The chambers in iron gaps improve the resolution considerably. (+) shows the resolution with vertex constraint which is supposed to given by central tracking detector in addition to the muon chamber information. The vertex constraint is given by one additional measured point at x=0 with 200 μm position resolution. Further improvement is seen.

Fig. 32 shows momentum resolution as a function of pseudo rapidity η with ACS muon toroid configurations for p = 1 TeV (o) and 2 TeV (+) with (doted lines) and without (solid lines) the vertex constraint. 1 m gap for the last 2 set

of chambers is taken for both barrel and end cap part. For $\eta = 1.25$ and 1.5, trajectory pass through boundary region between barrel and end cap part. This effect is taken into account by taking iron and chamber positions along the muon trajectory (assumed to be a straight line), as well as taking effective chamber resolutions.

The author wishes to thank Dr. Y.Takaiwa for providing ISAJET program package and help and discussions for proceeding the calculations.

REFERENCES

1) F.E.Paige and S.D.Protopopescu, BNL-37066 (1985).

2) "SSC Muon Detector Group Report", page 405 in Snowmass 1986 Proceedings.

3) A.Bodek, UR911 ER13065-412 (1985).

4) F.E.Paige, Proceedings of the Workshop on Triggering, Data Acquisition and Computing for the High Energy/High Luminosity Hadron - Hadron colliders, Fermilab (1985), Page 51.

5) C.Zupancic, "Physical and Statistical Foundations of TeV Muon Spectroscopy", CERN-EP/85-144

6) Particle Properties Data Booklet, 1988.

7) T.Kondo, "ACS Detector", KEK preprint 89-191, JSD-NOTE-1990-005.

FIGURE CAPTIONS

Fig. 1. Geometry used in the calculation.

Fig. 2. Comparison of punchthrough probability given by different parametrizations for iron thickness of (a) 2 meters and (b) 4.5 meters.

Fig. 3. illustration of punchthrough probability use in the calculation.

Fig. 4. Muon multiplicity rate at exit of calorimeter and muon filter.

Fig. 5. Muon rate vs polar angle of muons at exit of calorimeter.

Fig. 6. Muon rate vs polar angle of muons at exit of muon filter.

Fig. 7. Muon rate vs rapidity of muons at exit of calorimeter.

Fig. 8. Muon rate vs rapidity of muons at exit of muon filter.

Fig. 9. Muon rate vs p_t of muons at exit of calorimeter for $|y| < 3$.

Fig. 10. Muon rate vs p_t of muons at exit of muon filter. for $|y| < 3$.

Fig. 11. Muon rate vs p of muons at exit of calorimeter for $|y| < 3$.

Fig. 12. Muon rate vs p of muons at exit of muon filter. for $|y| < 3$.

Fig. 13. Muon rate vs p_t of muons at exit of calorimeter for $|y| < 1.5$.

Fig. 14. Muon rate vs p_t of muons at exit of muon filter. for $|y| < 1.5$.

Fig. 15. Muon rate vs p of muons at exit of calorimeter for $|y| < 1.5$.

Fig. 16. Muon rate vs p of muons at exit of muon filter. for $|y| < 1.5$.

Fig. 17. Comparison of total muon rate vs (a) p_t and (b) p of muons for: at exit of calorimeter and muon filter; and $|y| < 3$ and 1.5.

Fig. 18. Distribution of energy deposit corresponding muon position with single, 9, and 25 calorimeter towers for muons exiting calorimeter (a) and exiting muon filter (b).

Fig. 19. Rate vs E_{CAL} for isolation requirement for rapidity range $|y| < 3$ (a) and $|y| < 1.5$ (b).

Fig. 20. Muon rate vs polar angle of muons at exit of muon filter for Higgs production: H(400 GeV) $\rightarrow W^+W^- \rightarrow \mu + \nu +$ jets.

Fig. 21. Muon rate vs p_t of muons at exit of muon filter for Higgs production: H(400 GeV) $\rightarrow W^+W^- \rightarrow \mu + \nu +$ jets.

Fig. 22. Muon rate vs p of muons at exit of muon filter for Higgs production: H(400 GeV) $\rightarrow W^+W^- \rightarrow \mu + \nu +$ jets.

Fig. 23. (a) Distribution of energy deposit corresponding muon position with single, 9, and 25 calorimeter towers for muons exiting muon filter with $|y| < 3$ for

Higgs production: H(400 GeV) $\rightarrow W^+W^- \rightarrow \mu + \nu +$ jets. (b) Rate vs E_{CAL} for isolation requirement for (a).

Fig. 24. General configuration and coordinate system used in momentum resolution calculation.

Fig. 25. Detailed configuration used in the momentum resolution calculation. (a) Barrel muon detector and (b) end cap muon detector.

Fig. 26. Comparison of result from simple track simulation and full GEANT simulation.

Fig. 27. $K_{fit} - K_0)/K_0$ distribution for GEANT simulation.

Fig. 28. Dependence of momentum resolution on chamber position resolution for barrel part.

Fig. 29. Dependence of momentum resolution on the gap between the last 2 set of chambers after iron toroid for barrel part.

Fig. 30. Dependence of momentum resolution on the gap between the last 2 set of chambers after iron toroid for end cap part.

Fig. 31. Momentum resolution for 3 different configurations.

Fig. 32. Momentum resolution as a function of η with ACS muon toroid configuration.

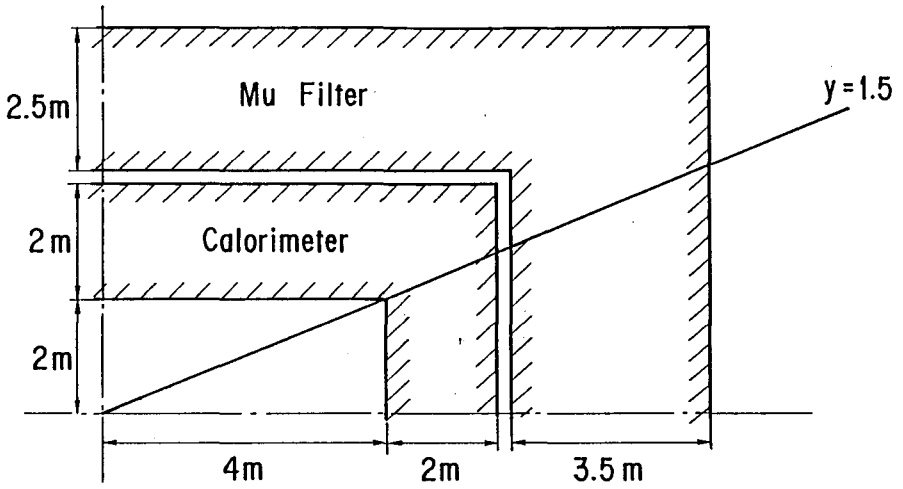

Fig. 1

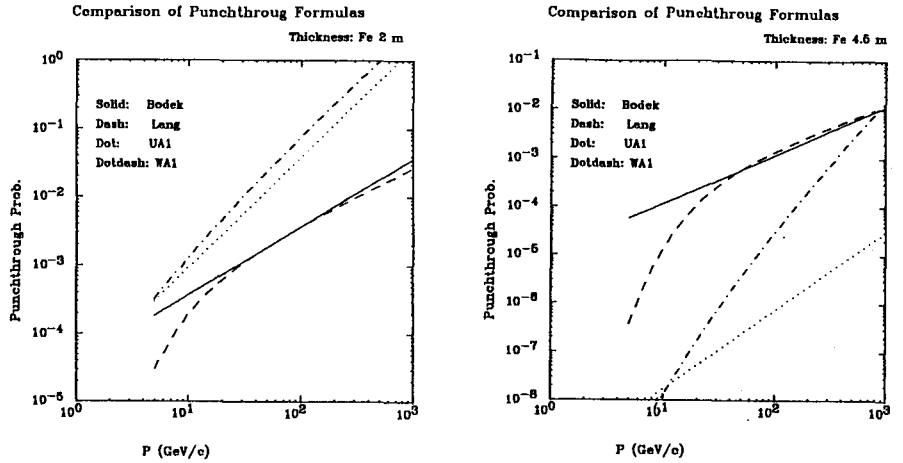

Fig. 2

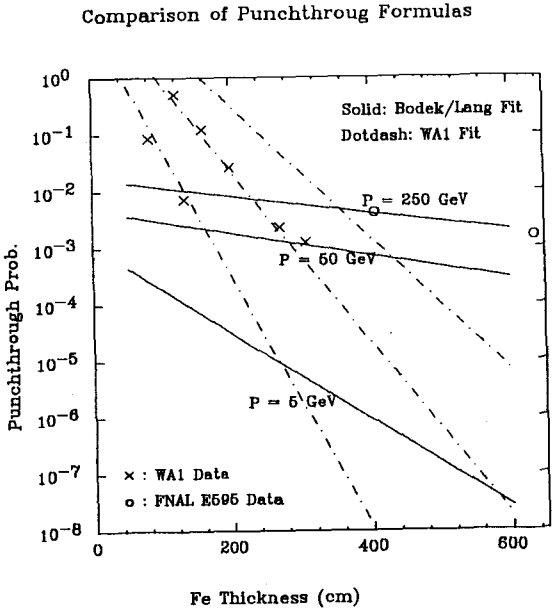

Fig. 3

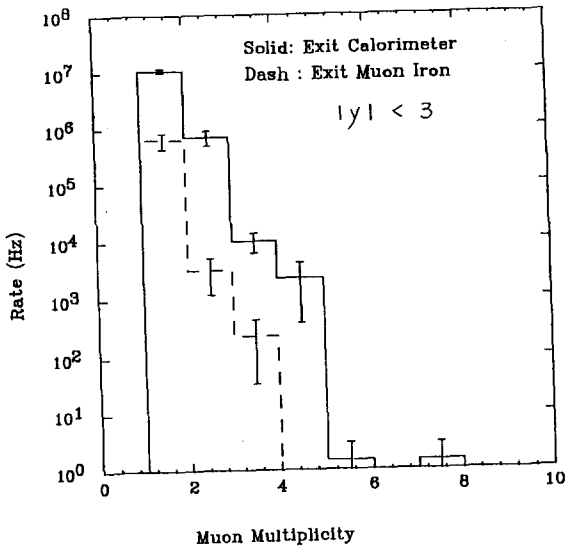

Fig. 4

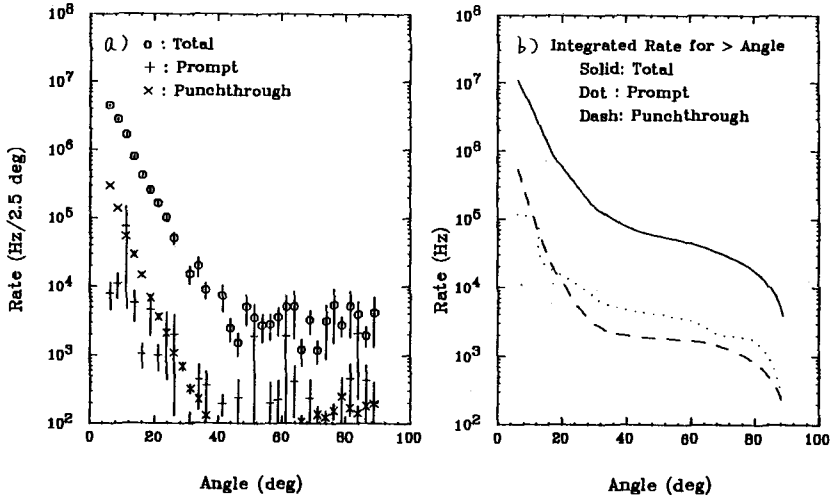

Fig. 5

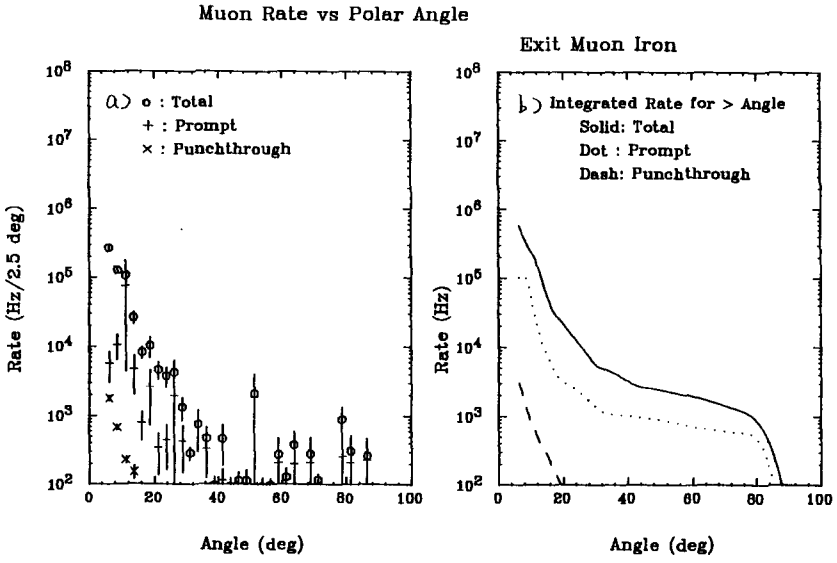

Fig. 6

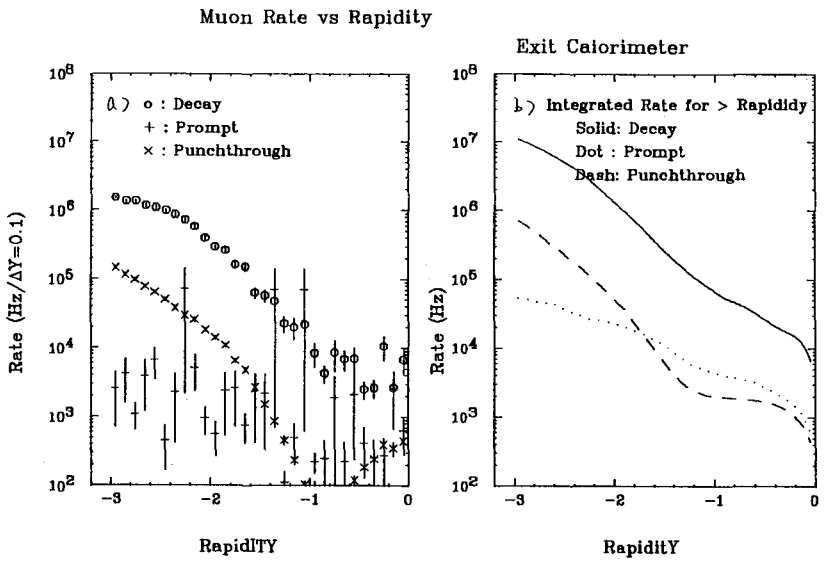

Fig. 7

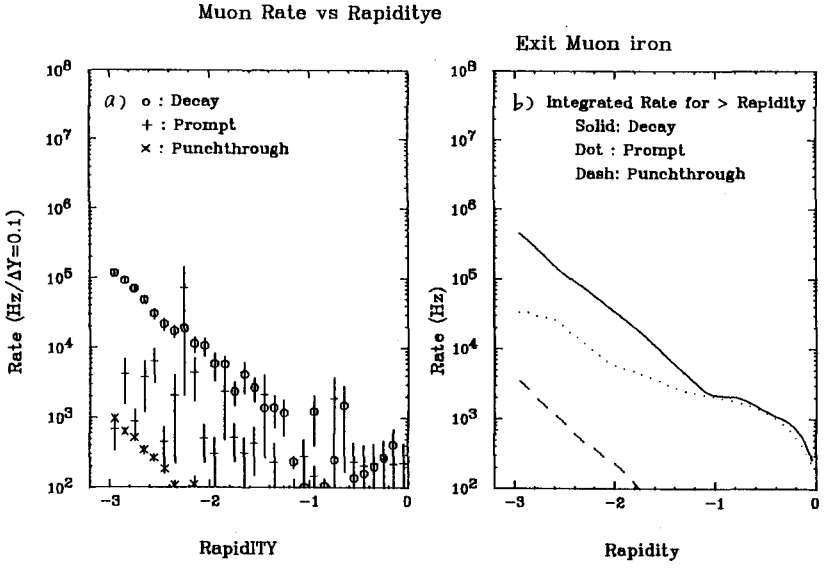

Fig. 8

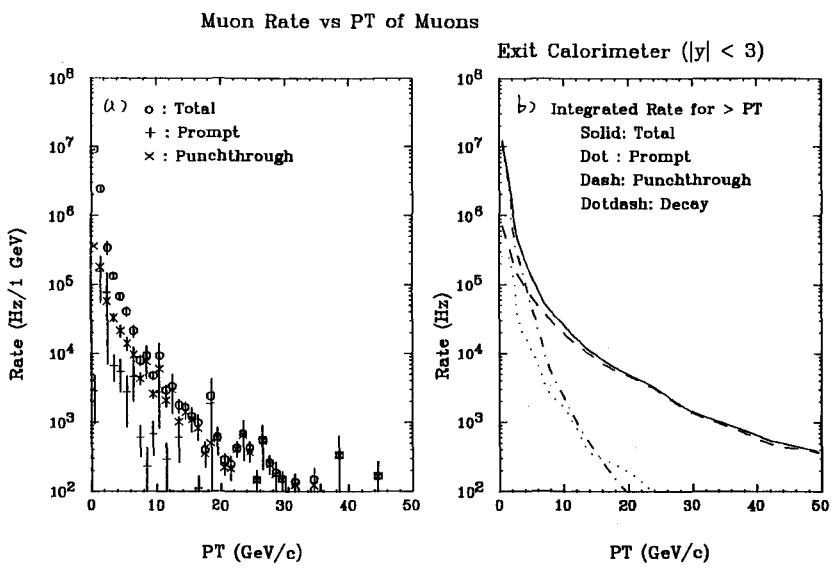

Fig. 9

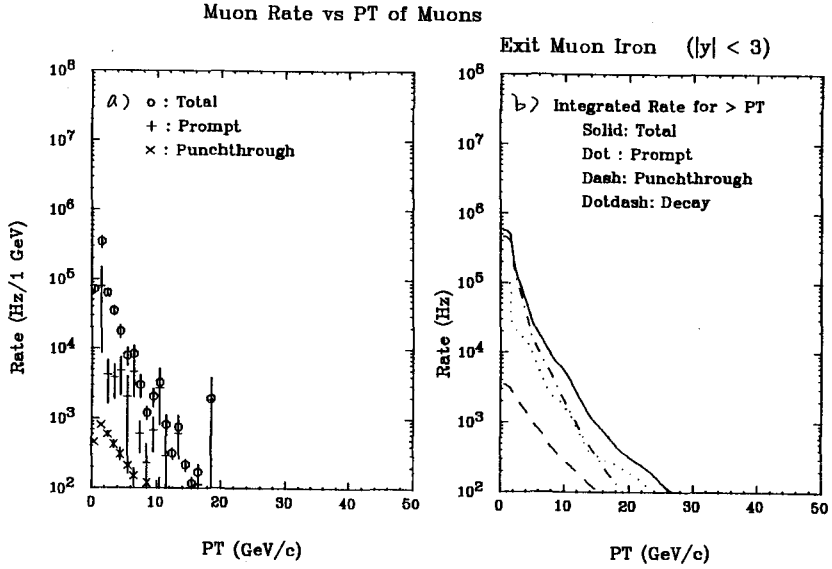

Fig. 10

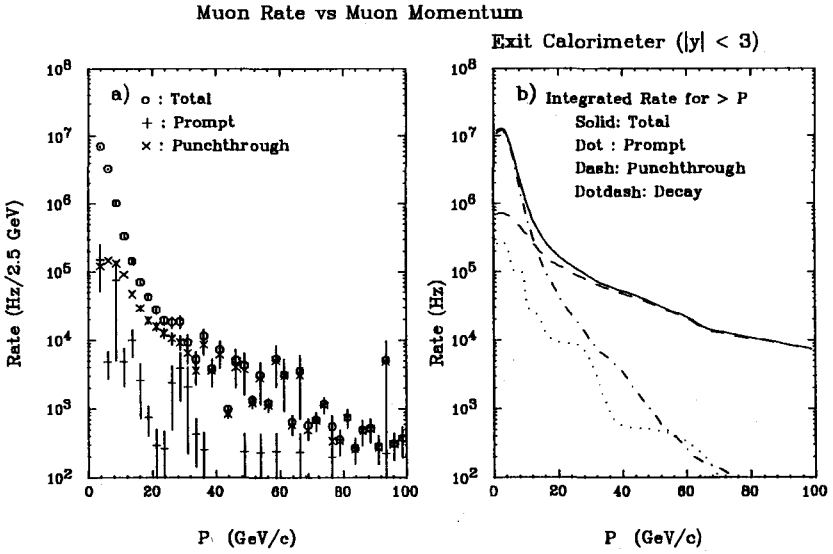

Fig. 11

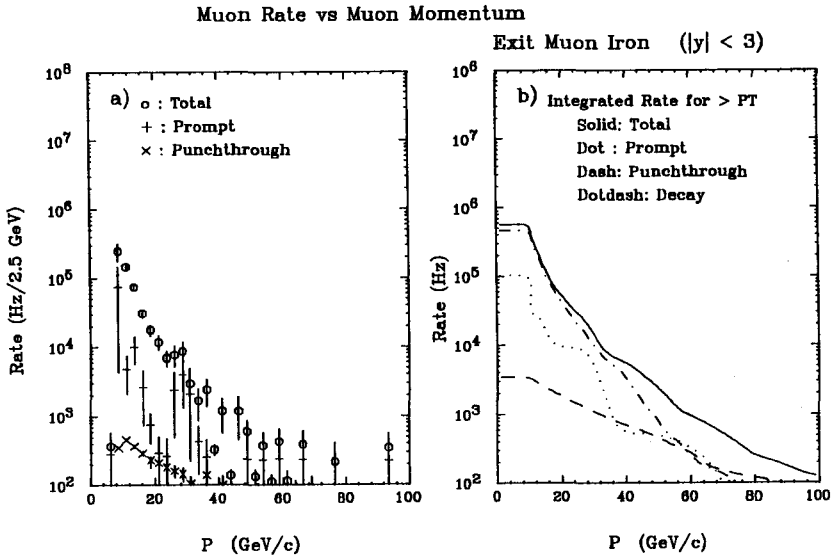

Fig. 12

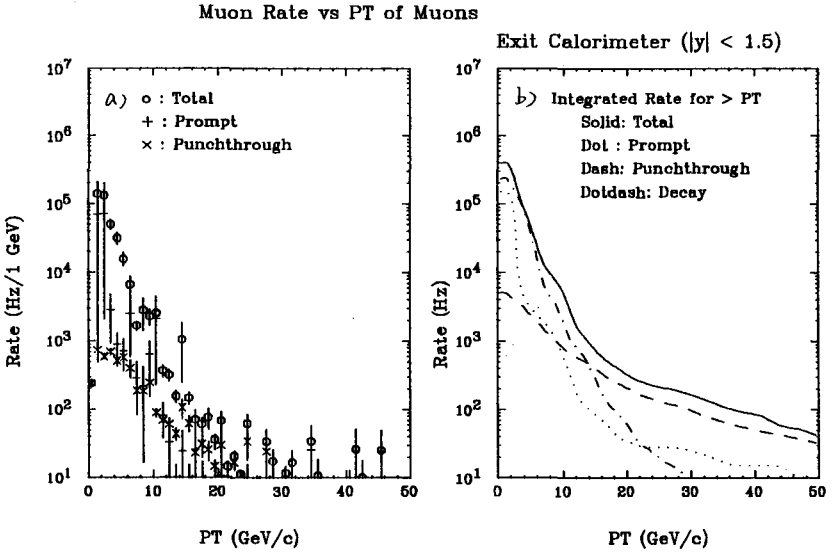

Fig. 13

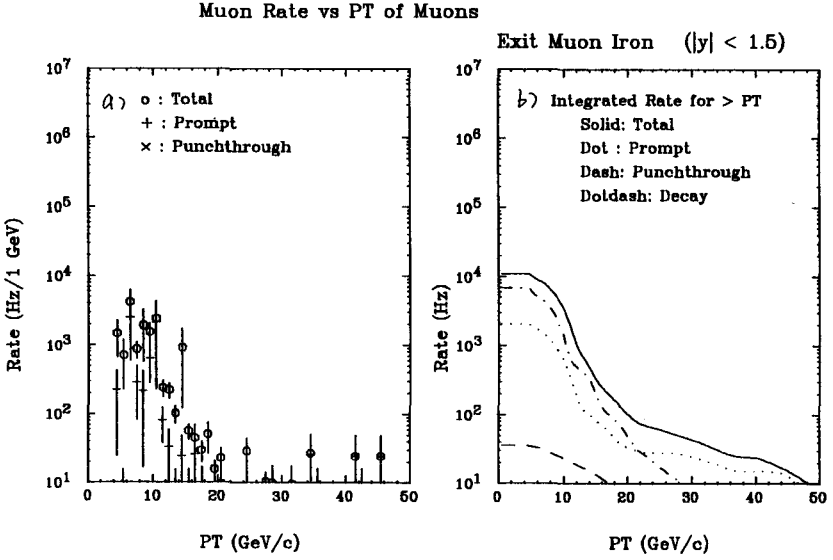

Fig. 14

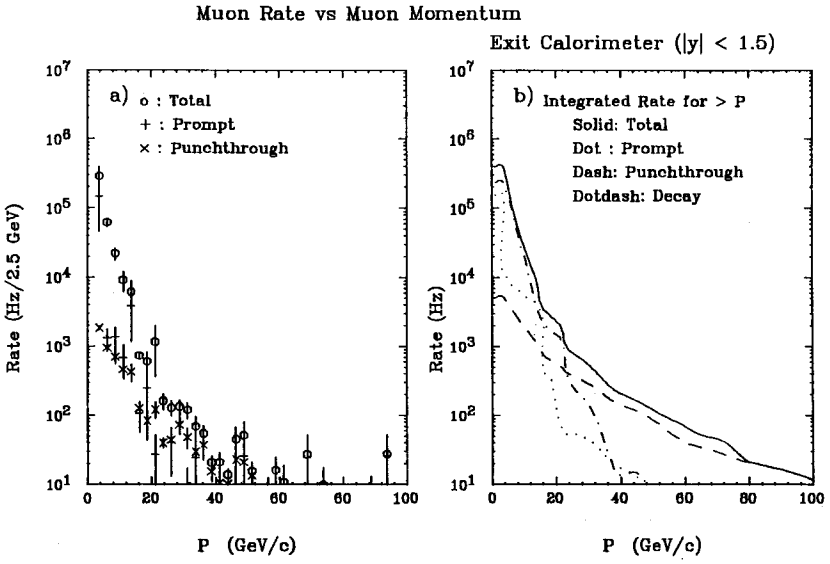

Fig. 15

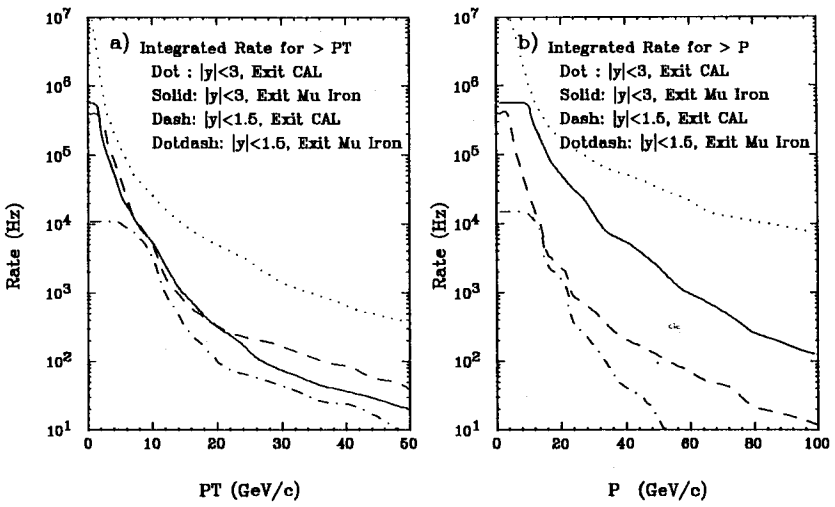

Fig. 17

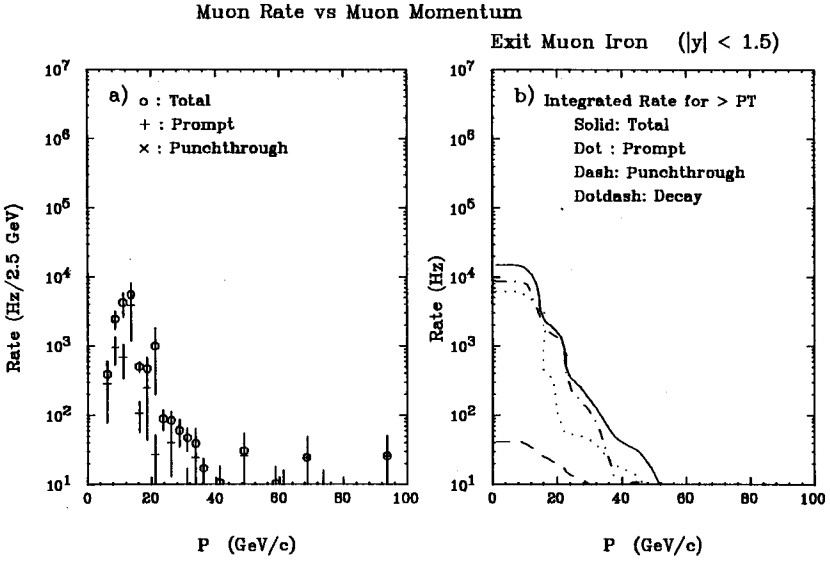

Fig. 16

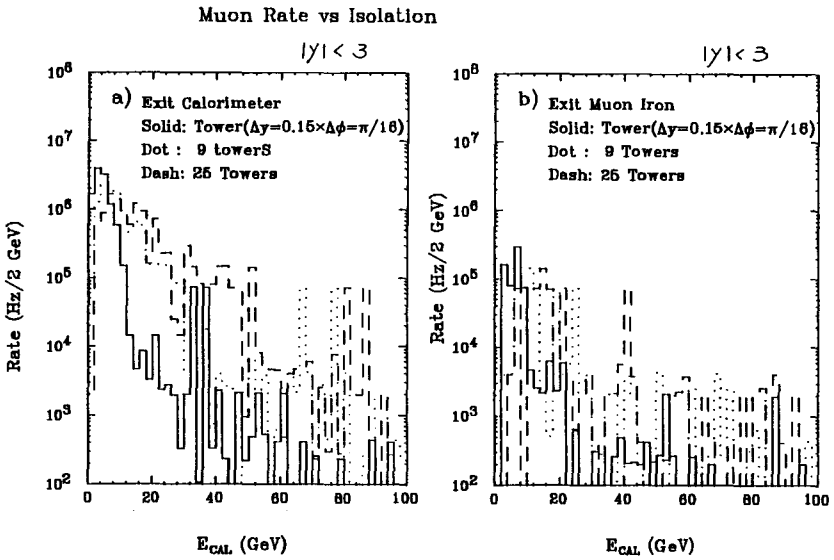

Fig. 18

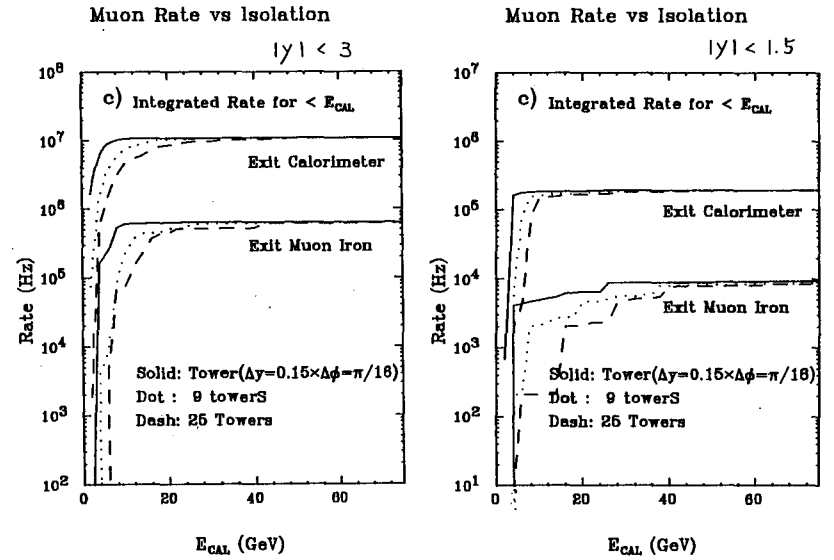

Fig. 19

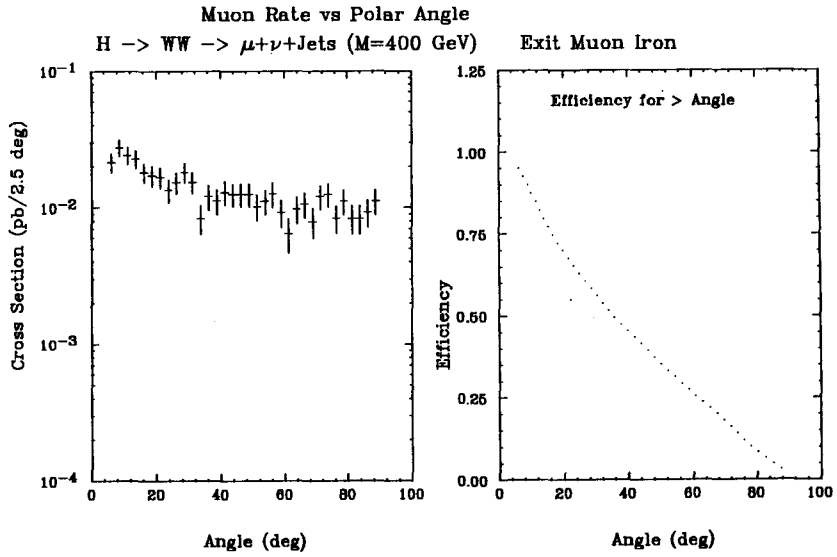

Fig. 20

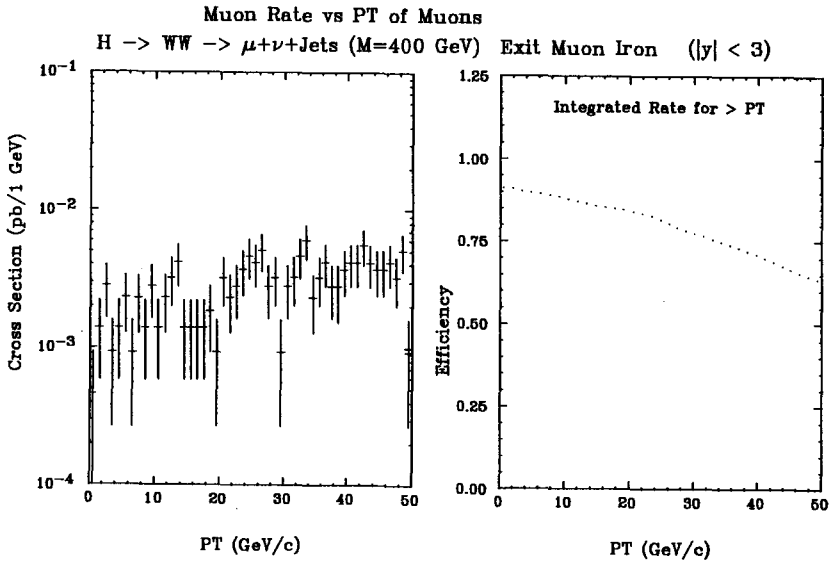

Fig. 21

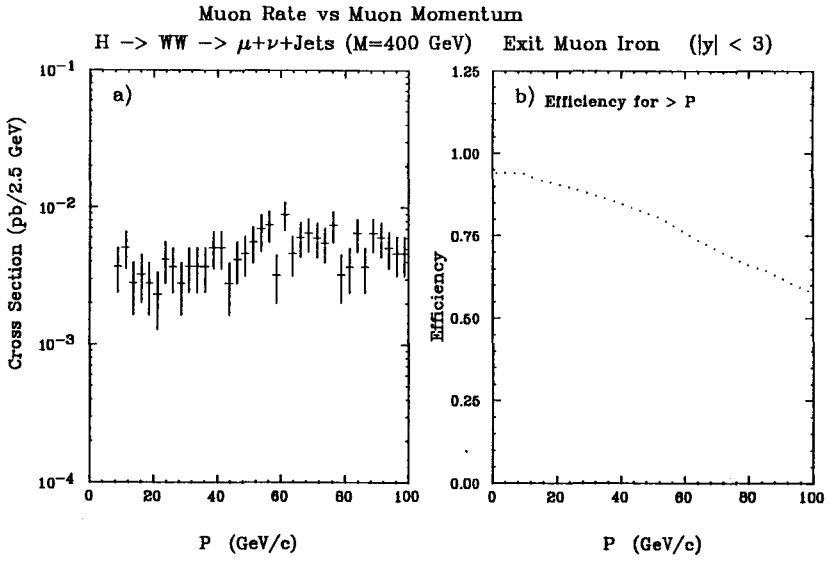

Fig. 22

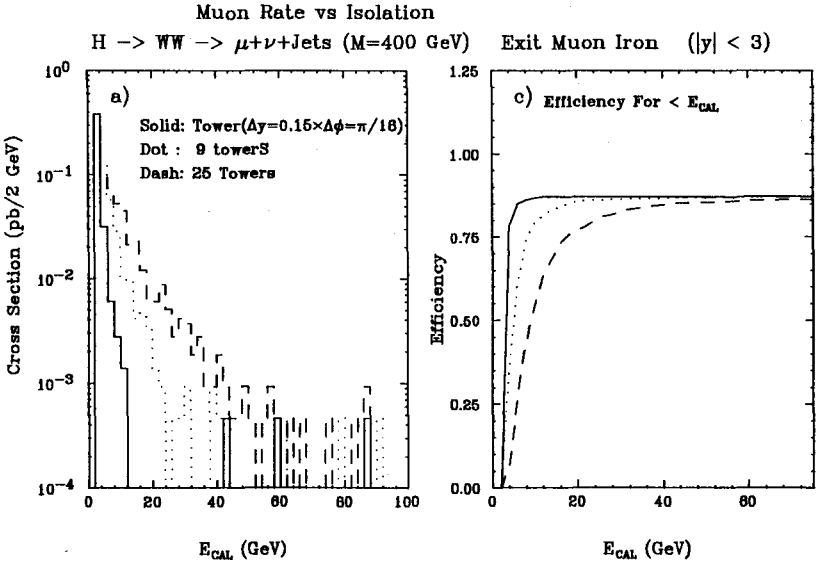

Fig. 23

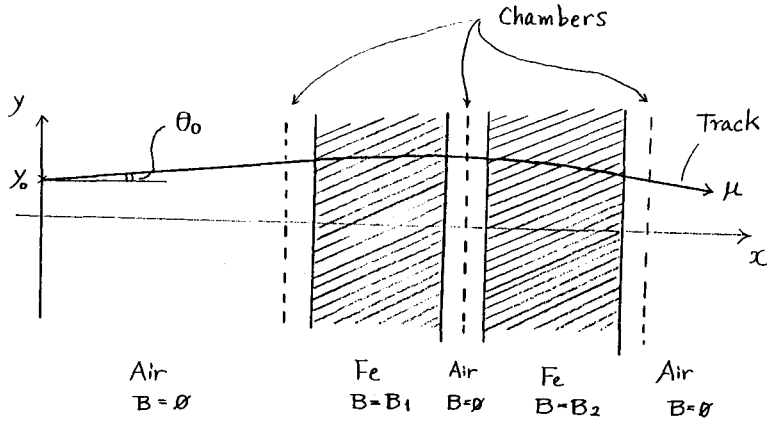

Fig. 24

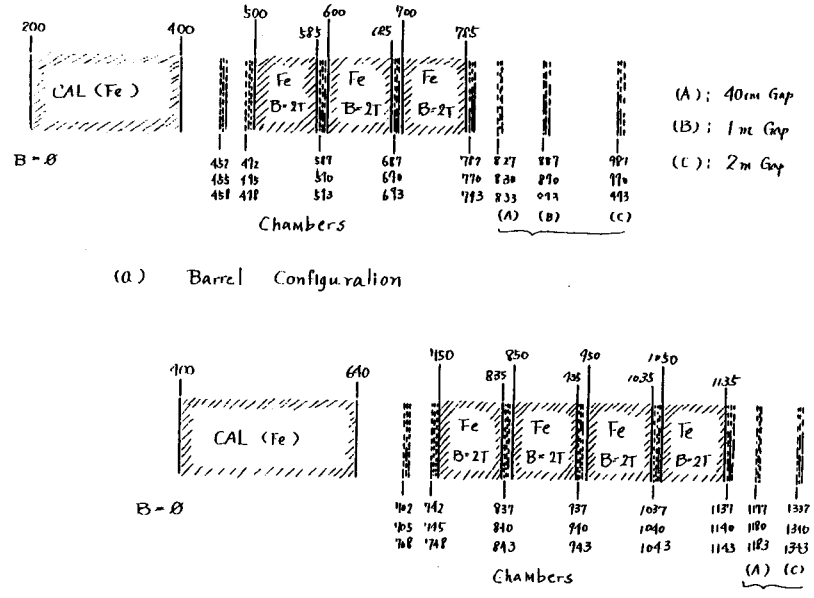

Fig. 25

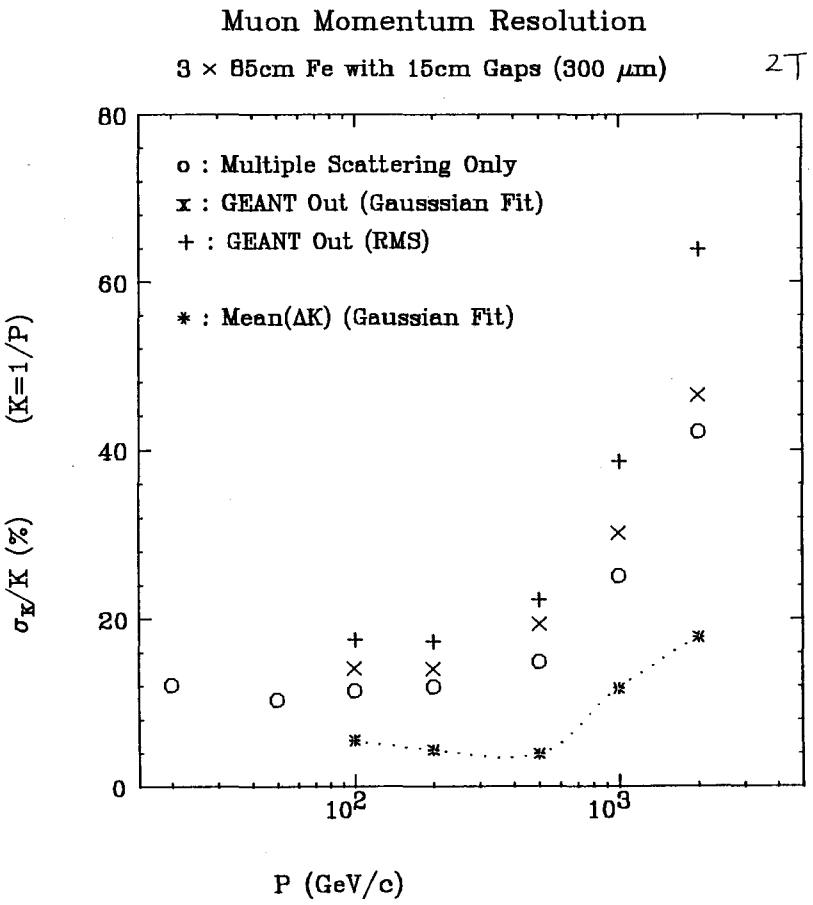
Muon Momentum Resolution
3 × 85cm Fe with 15cm Gaps (300 μm)
2T
o : Multiple Scattering Only
x : GEANT Out (Gausssian Fit)
+ : GEANT Out (RMS)
* : Mean(ΔK) (Gaussian Fit)
σK/K (%) (K=1/P)
P (GeV/c)
0
20
40
60
80
10^2
10^3

Fig. 26

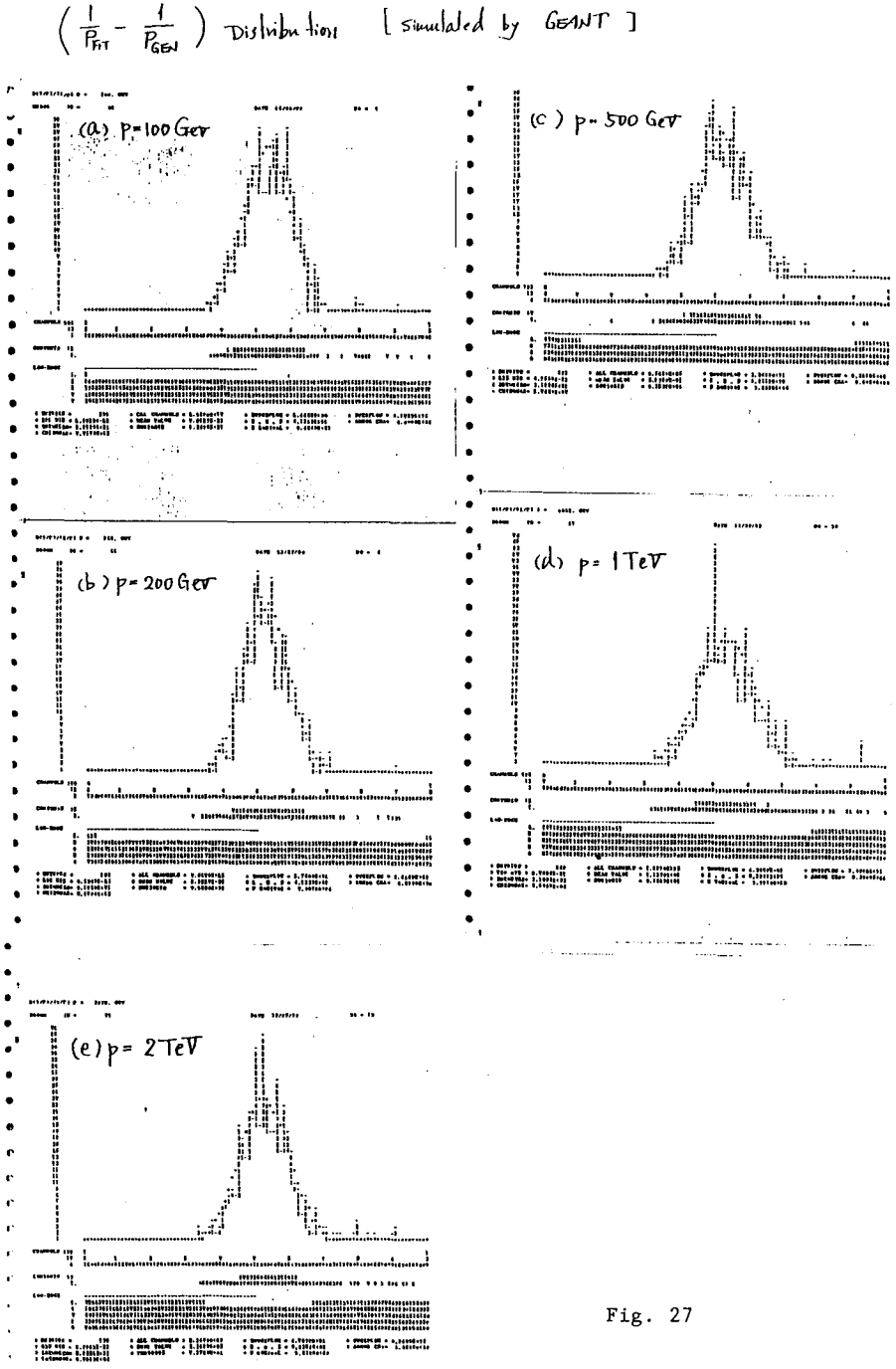
(1/P_FIT - 1/P_GEN) Distribution [simulated by GEANT]
(a) P=100 Gev
(b) p=200 Gev
(c) p=500 GeV
(d) p=1 TeV
(e) p=2 TeV

Fig. 27

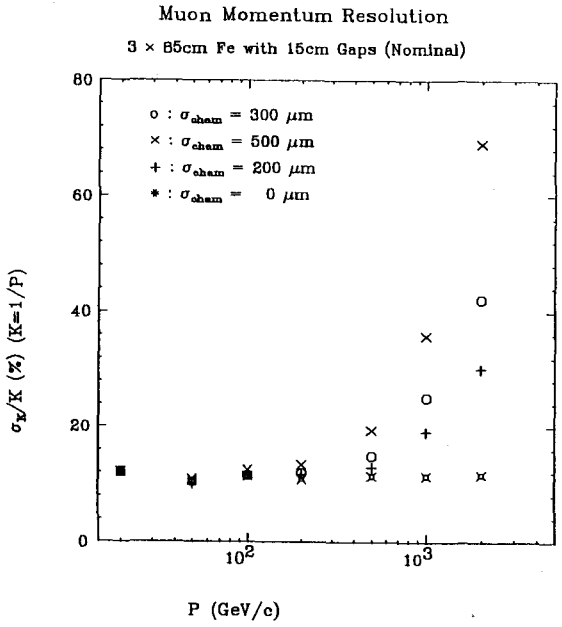

Fig. 28

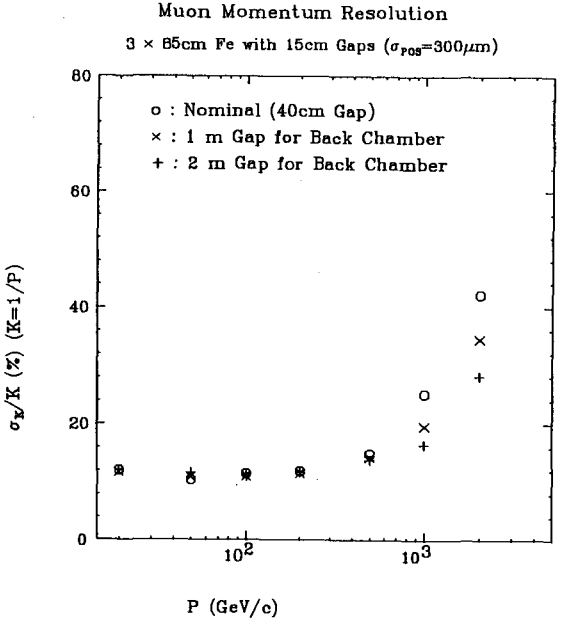

Fig. 29

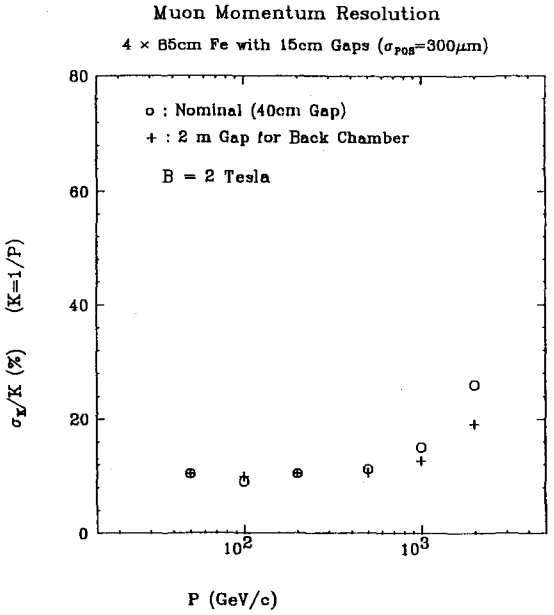

Fig. 30

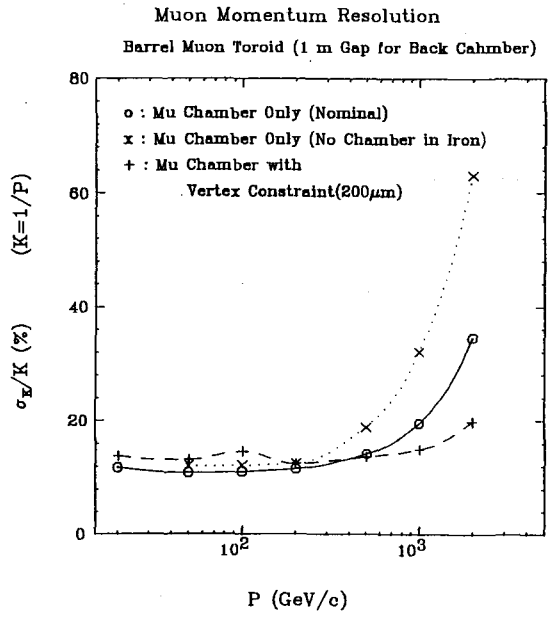

Fig. 31

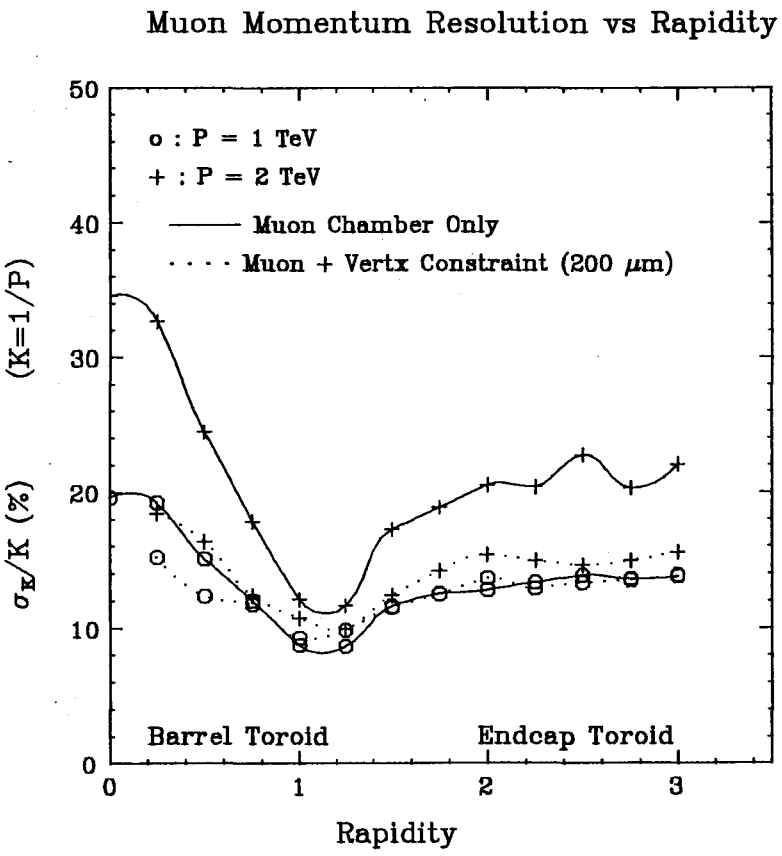
Muon Momentum Resolution vs Rapidity
o : P = 1 TeV
+ : P = 2 TeV
Muon Chamber Only
Muon + Vertx Constraint (200 μm)
σK/K (%) (K=1/P)
Barrel Toroid
Endcap Toroid
Rapidity
0
10
20
30
40
50
0
1
2
3

Fig. 32

ANL-HEP-CP-90-45
May 22, 1990

Conceptual Design for a Superconducting Toroid

T. Fields
Argonne National Laboratory

Introduction

By having a toroidal magnetic field in the forward angle region, momenta of forward-going muons can be measured more accurately than by using the solenoid central tracker alone. Such a capability can substantially increase the detection efficiency and momentum accuracy for multimuon events which are likely to be important in SSC experiments, such as Higgs $\rightarrow Z^{\circ}Z^{\circ} \rightarrow \mu^{+}\mu^{-}\mu^{+}\mu^{-}$.

If this toroidal field is obtained using iron magnetized to 1.8 Tesla, a 5 meter path length in iron will allow momentum measurement to no better accuracy than $dp/p \approx 10\%$. This limitation is due to multiple Coulomb scattering in the iron. A possible alternative choice is to generate the toroidal field by using a superconducting coil, as was pointed out several years ago by Jones[1]. In this talk, I shall present a status report on the conceptual engineering design of such a superconducting toroid. Its measurement accuracy is limited by multiple Coulomb scattering to about 2.5%, and is also very well matched to the accuracy expected for central muon tracks in the solenoid tracker system.

Specifications

The specifications which defined the physics design requirements are listed in Table 1. These were chosen on the basis of (SDC) detector designs which were under consideration several months ago. In a current (EOI) SDC

To appear in the Proceedings of the KEK International Workshop on Solenoidal Detectors for the SSC (April 23-26, 1990).

design which is shown in Fig. 1, the toroid distance from the interaction point is 14 m, rather than the 11 m used here. However, most engineering features of this conceptual design should also be applicable to superconducting toroids whose specifications are not too different from those in Table 1.

Design Goals

Next I shall briefly describe the status of the conceptual design work which is being done by John Purcell and Lew Creeden of Advanced Cryo Magnetics, Inc. They have used the specifications of Table 1, and have designed a magnet of conservative mechanical and electrical properties, low cost, and simple fabrication. In addition, they have attempted to avoid the use of new technology which would require extensive R&D work.

Design Features

The principal features of the Advanced Cryo Magnetics design are: the use of aluminum stabilized Nb Ti conductor that is bath cooled, fabrication of almost the entire structure from welded aluminum plates, and the use of carbon fiber loops to carry the axial magnetic forces. Fig. 2 shows the geometry of the coil and the aluminum shells which form the helium vessel, as well as of the heat shield and the vacuum vessel.

The carbon fiber tension loops run parallel to the axial (beam) direction, and support the outward axial magnetic pressure which is felt by the upstream and downstream ends of the coil. This magnet has a complicated topology and considerable effort was devoted to specifying practical, low-cost assembly procedures.

Table 2 shows some of the parameters of this conceptual design.

Cost

Cost estimating work is still underway, so that only a very preliminary result of ten million dollars (± 30%) per toroid can be given now.

Future Work

The completed conceptual design work and cost estimating information will be documented soon in a report from Advanced Cryo Magnetics, Inc.

Before proceeding to more detailed engineering work on a superconducting toroid for the SDC detector, three steps should be taken:

1. This design and cost estimate should be scaled up to the most recent (EOI) dimensions and field integral.
2. Physics and cost trade-offs between using a forward superconducting toroid as opposed to using a forward iron toroid should be evaluated by the SDC collaboration.
3. A comparison with other proposed superconducting toroid designs, such as those using forced-cooled superconductors, should be made.

These three steps can hopefully be completed in time to allow more detailed toroid engineering design work to begin within the next six months.

Work supported by the U.S. Department of Energy, Division of High Energy Physics, Contract W-31-109-ENG-38

Reference

1. L. W. Jones, Snowmass 1986 Proceedings, P462.

Table 1

Physics Specifications for Advanced Cryo Magnetics Design

Inner radius	1 m
Outer radius	5.5 m
$\int Bdz$ at inner radius	10 Tesla meter
Distance from i.p.	11 m
Pseudorapidity coverage	1.5-3.0
Total thickness near outer radius	$\lesssim$ 3 R.L.
Total thickness near inner radius	$\lesssim$ 6 R.L.

Table 2

Parameters of Advanced Cryo Magnetics Conceptual Design

Length in z direction	3.3 m
Field at inner radius	3 Tesla
Stored energy	130 MJ
Operating current	7000 Amp
Conductor size	0.39 x 2.0 cm^2
Ampere turns	15×10^6
Conductor length	32000 m
Cold weight	98,000 lb
Warm weight	28,000 lb
Liquid helium volume	15,000 liter

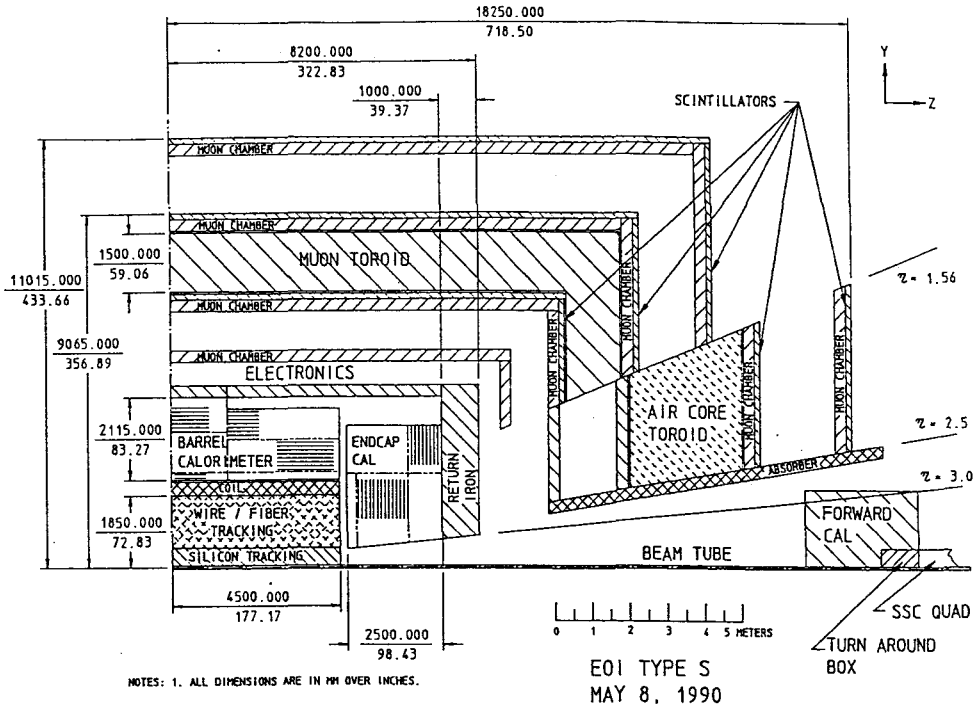

Fig. 1. SDC detector, with a superconducting air core toroid at 14 meters, covering η = 1.5 to 2.5.

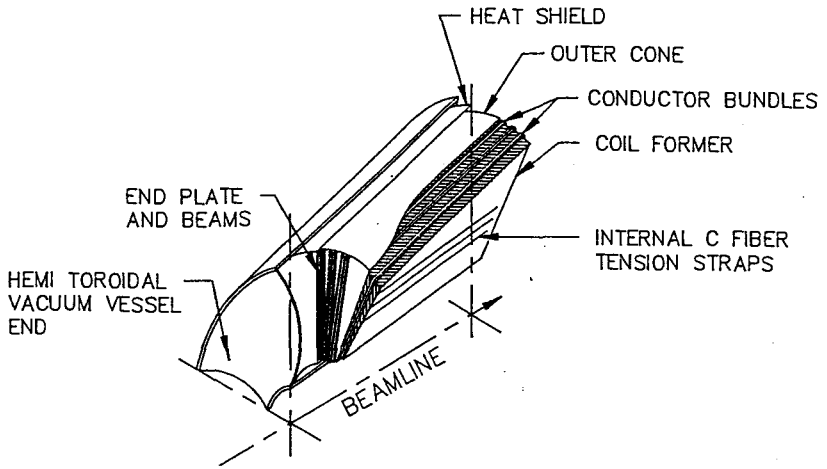

Fig. 2. The air core toroid designed by Advanced Cryo Magnetics, Inc.

The Muon System for the EOI of the SDC

A. Skuja

Department of Physics and Astronomy,

University of Maryland, College Park, Maryland 20742, U.S.A.

I led a twenty minute discussion about the Status of the EOI for the Muon System of the Solenoidal Detector Collaboration. The EOI is now finished and those interested should consult this document [1].

REFERENCES

1. Solenoidal Detector Collaboration, *Expression of Interest*, 24 May, 1990.

Parallel Session: Electronics, Trigger, and Data Acquisition

April 24, 13:30-21:00

R & D on front end electronics in US

H. H. Williams
U Penn

(No written contribution received)

Radiation hardened electronics

D.Dorfan
UC Santa C

(No written contribution received)

EVALUATION OF BIPOLAR AMPLIFIER CHIPSET FOR SILICON STRIP READOUT

HIROKAZU IKEDA AND NORIHIKO UJIIE

National Laboratory for High Energy Physics
1-1 Oho, Tsukuba, Ibaraki-ken, 305 Japan

KOICHI KAWAGUCHI

Department of Applied Physics, University of Tsukuba, Tsukuba, 305 Japan

YUKIO AKAZAWA

NTT LSI Laboratories, Atsugi, Kanagawa, 243-01 Japan

ABSTRACT

Monolithic amplifier circuits have been designed for a head amplifier of the silicon strip detector for the SSC. Experimental chips, including preamplifiers and/or shapers, were fabricated for practical evaluation. The basic properties of this amplifier chips were examined in terms of pulse response and noise characteristics

★ Contribution to INTERNATIONAL WORKSHOP ON SOLENOIDAL DETECTORS FOR THE SSC, April 23-25, 1990, at KEK, Tsukuba, Japan

1. INTRODUCTION

In order to resolve complex track configurations and reconstruct vertices, microstrip detector has been developed for recent high energy experiment. In order to put it into use for the SSC detector, bipolar amplifier circuits were designed and fabricated in a monolithic process. General goal for the amplifier chain is to achieve:

1. Low noise amplifier chain
2. Low power consumption
3. High density integration of microcircuit

Additional requirements for hadron-hadron collider experiments are:

1. Radiation hardness up to 10^6 rads/year and 10^{13} neutrons/cm^2/year.
2. Wide frequency bandwidth to be compatible with high rate of particle flux.
3. Short shaping time to suppress the shot noise from the detector damaged by radiation.

Our compromise is to design the frontend amplifier chain in bipolar process achieving a high frequency bandwidth and possibly radiation hardness. The amplifier head is a current sensitive preamplifier, followed by a low pass filter that determines noise frequency bandwidth. Finally the signals are fed into a discriminator and then a Digital Time Slice Chip (DTSC)[1] that stores hit information temporarily until a low-level trigger decision is completed. The design work of the DTSC chip is in progress at UC Santa Cruz. In order to examine the scheme, a TEG version of the amplifier was designed and fabricated at the research fabrication line of NTT LSI Laboratories. The results were presented in 1988 NSS symposium[2]. The preamplifier based on bipolar SST process[3][4] showed high frequency bandwidth; the feature has been demonstrated by NTT people with advanced circuit technologies[5][6]. The radiation hardness is a big issue for practical application of the amplifiers in the radiation environment of the SSC. Studies about radiation hardness of the bipolar SST has been done to show that the transistors are reasonably rad-hard[7][8][9][10] to be used in the SSC environment. Based on the studies of the previous version of TEG design, new series of experimental chips were fabricated as a step towards the realistic scale of integration. This work describes basic properties of these experimental chips in terms of pulse response and noise characteristics. The standing current of the preamplifier was varied to examine design parameters about open-loop gain and to extract quantitative nature of equivalent noise generators of i_p^2 andv_s^2.

2. CIRCUIT CONFIGURATION

Preamplifier The input stage of the current sensitive preamplifier is a common emitter npn transistor whose quiescent current is 100 μA. The collector signal is fed into a cascode transistor to be followed by emitter followers. The output of the preamplifier is buffered by an unity gain buffer, which can drive 50 Ω coaxial cable. The trans-impedance is 20 $K\Omega$. Three versions of 5 channels preamplifier chips were fabricated for evaluation; the transistor of the common emitter input stage was chosen for three different $I_{c(maz)}$'s: 2 mA, 4mA and 8 mA.

Shaper In order to define frequency band width for noise and to obtain reasonable S/N ratio, we designed also a low pass filter, shaper amplifier. The shaper amplifier designed here is a second order low pass filter that satisfies a critical damping condition. The filter amplifier has a transfer function

$$1./(1. + S * T_M)^2 \tag{2.1}$$

in Laplace transform, where S is a frequency variable and T_M is a measurement time of the shaping function. The impulse response is

$$(t/T_M) * exp(-t/T_M) \tag{2.2}$$

The design value of T_M was 15 nsec, however, the actual peaking time was longer than this value. That is due to that the preamplifier and shaper amplifier were fabricated separately. The stray capacitance existing at the junction of the preamplifier and shaper brought additional time constant to the total peking time. The output of the preamplifier was once fed into 50 Ω load. The same amount of current flowing into 50 Ω load was also fed into shaper amplifier. The input impedance of the shaper amplifier is 1 $K\Omega$. Here we have voltage gain of 20. The output of the shaper amplifier was about 30 mV for an impulse charge input of 25000 electrons at nominal operating conditions. The noise level of the amplifier chain was evaluated as a fluctuation of the peak voltage for a standard amount of input charge for the preamplifier.

3. OPERATION FOR EVALUATION

A low power operation is also the serious issue for the silicon strip detector application of the bipolar circuit. Small current operation exhibits three features:

1. The input impedance couples with a detector capacitance to make slower the rise time of the output signal.
2. The trans-conductance of the input transistor is decreased; so the noise associated with v_s^2 becomes worse.
3. The base current of the input transistor is decreased; so the noise associated with i_p^2 is improved.

The latter two features are in fact coupled intimately with the first feature. Figure 1 shows pulse shape variation due to $C_{detector}$ and I_c in terms of peak pulse height (Figure 1 (a)) and rise time (Figure 1(b)). The data shown here are for the amplifier version with input transistors of $I_{c(maz)}$=2mA. There can be seen that for small value of I_c the rise time is increased, hence, the effective peaking time of the output time is delayed. We measured also the noise characteristics over wide range of I_c and $C_{detector}$. Figure 2 is a plot of input equivalent noise electrons versus standing current of the input transistor. The parameter is $C_{detector}$. A typical noise level with $C_{detector}$ = 10 pF was 1000 electrons for $I_c > 50$ μA . The feature is again shown in different view in Figure 3, where input noise electrons are plotted versus $C_{detector}$. The parameter is I_c. We can clearly see that there is a trade-off between noise and power consumption. We can state that 50 μA is sufficient enough for operation as long as noise and/or pulse shaper are concerned. However there exists another trade-off between radiation damage and power consumption. The transistor with small standing current is easy to be degraded in h_{fe} by radiation damage. We have a plan to make a new implementation of narrow pitch amplifier array VLSI, where standing current is set as 100 μA .

4. CONCLUSIONS

Experimental preamplifier and shaper amplifier chips were fabricated in bipolar SST technology to investigate circuit stabilities and noise properties under low power operation. We have confirmed that the preamplifier shaper amplifier chain achieved a low noise feature with low power operation and fast shaping scheme.

ACKNOWLEDGEMENTS

We would like to acknowledge supports and suggestions of T. Kondo, T. Ohsugi, Y.Asano, and Y. Watase. We appreciate encouragement of Prof's S. Mori, S. Iwata, T. Takahashi, and M. Kobayashi. This work is partially supported by US-Japan Scientific collaboration program and a Grant in Aid from Japanese Ministry of Education, Science, and Culture.

REFERENCES

1. Joel DeWitt, "The Digital Time Slice Chip", private communication
2. H.Ikeda, N.Ujiie, and Y.Akazawa, "Monolithic Preamplifier with Bipolar SST for Silicon Strip Readout", KEK Preprint 88-71, Nov 1988, IEEE Trans. on Nucl. Sci. NS-36, Feb, 1989
3. S.Konaka, Y.Yamamoto, and T.Sakai,"A 30 ps Si Bipolar IC using super self-aligned process technology", Proc. of 16th conf. on solid state devices and materials, Kobe, Japan, 1984, pp.209-212
4. N.Ohnuki, A.Kayanuma, A.Asano, H.Hayashi, and M.Noda, IEDM '84 Dig. Tech. Paper, 1983, p. 55
5. Y.Akazawa, A.Iwata, T.Wakimoto, T.Kamoto, H.Nakamura, and H.Ikawa, " A 400 Msps 8 b flash AD conversion LSI", ISSCC Dig. Tech. Paper (1987)98-99
6. Y.Akazawa, N.Ishihara, T.Wakimoto, K.Kawarada and S.Konaka,"A design and packaging technique for a high-gain, giga-hertz-band single chip amplifier", IEEE Journal of Solid-State Circuits SC-21(1986) 417-423
7. M.Umehira, H.Kikuchi, S.Konaka, and S.Kato,"High-speed and Precise Monolithic Multiplier with Radiation Hardness Using Silicon Bipolar SST", Elec. Lett. 3rd July Vol.22 No.14 pp.744-746
8. H. Ikeda and N. Ujiie,"Radiation Damage of Bipolar SST Due to Fast neutrons", Nucl. Instr. and Methods A281(1989)508-511
9. H. Ikeda and N. Ujiie, "Radiation Damage of Bipolar SST Due to γ Ray of ^{60}Co", to be published in Nucl. Instr. and Methods (1990)"
10. N. Ujiie and H. Ikeda, in this proceedings

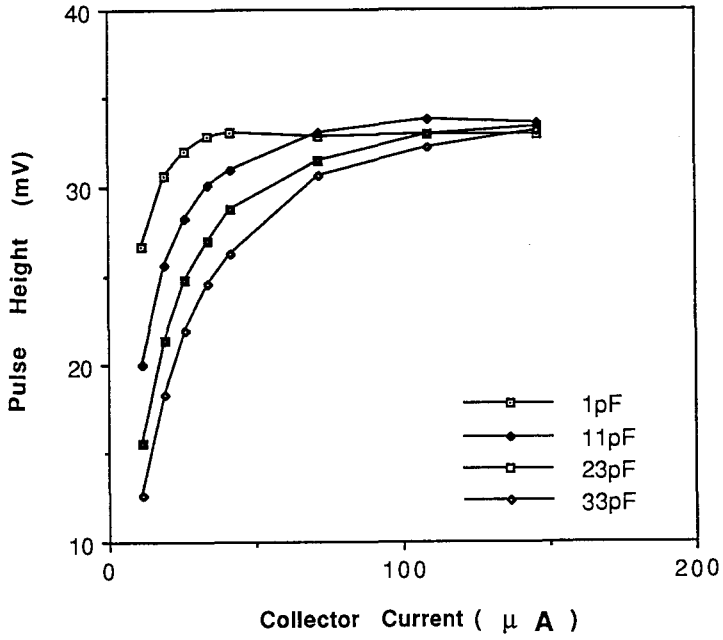

Fig . 1 - a PULSE HEIGHT

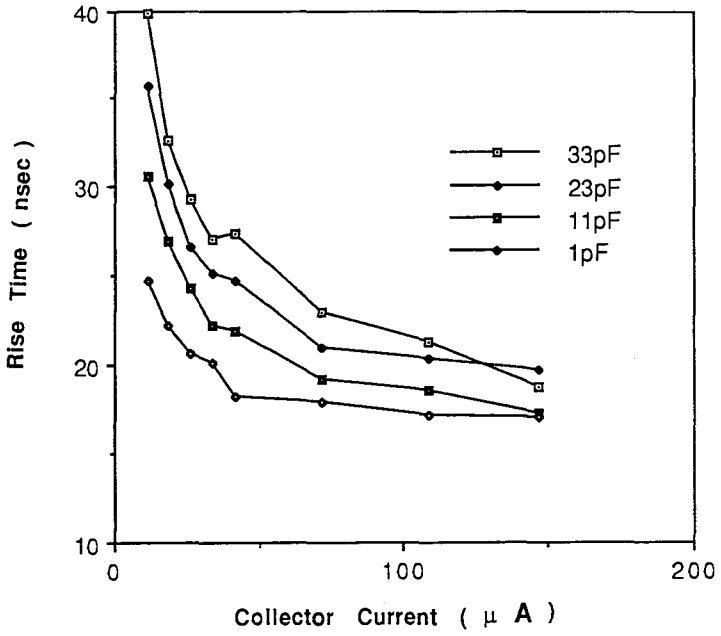

Fig 1- b Rise Time

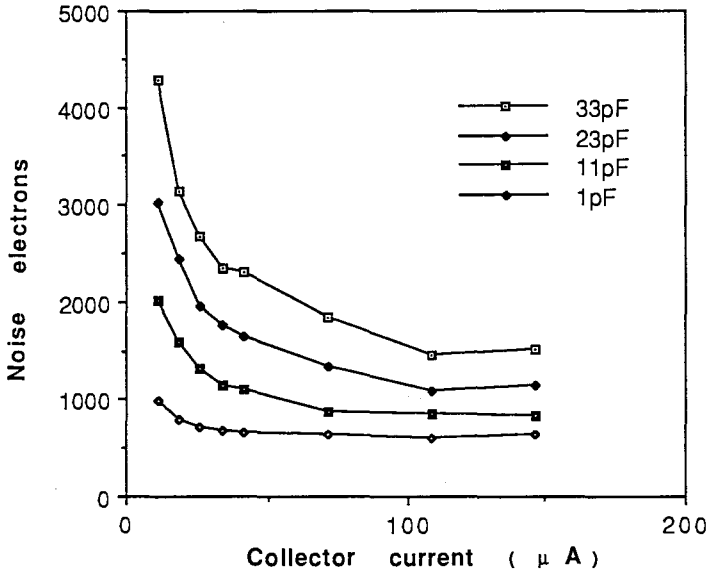

Fig. 2 Equivalent input noise electrons due to collector current .

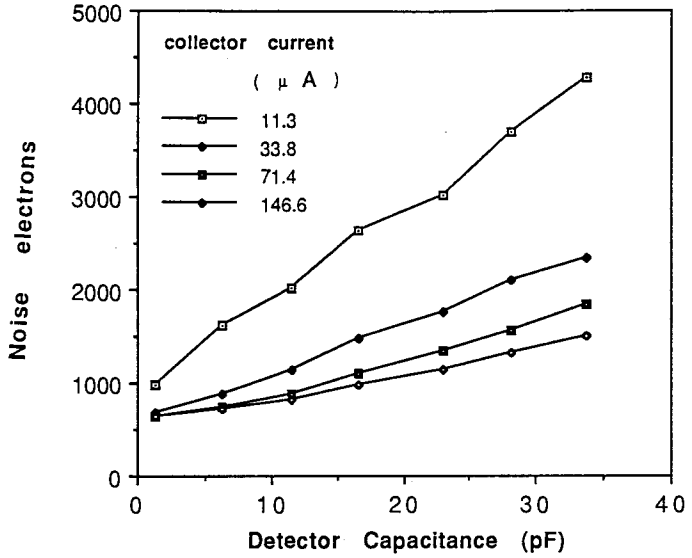

Fig. 3 Equivalent input noise electrons due to detector capacitance .

Radiation Damage to a very fast Bipolar SST Transistor

Norihiko Ujiie and Hirokazu Ikeda

National Laboratory for High Energy Physics, KEK
1-1, Oho, Tukuba-city, Ibaraki, 305 JAPAN

ABSTRACT

In order to investigate the radiation hardness of a bipolar SST transistor, samples were exposed to fast neutrons from a nuclear reactor. The obtained degradiation coefficient, $\Delta(h_{FE}^{-1})$, was equivalent to $\approx$ 0.0001 for 10^{13} neutrons cm^{-2}. Other transistor chips were exposed to intense γ-rays from a ^{60}Co source; they withstood a total dose of the order of 10^4 Gy(equivalent to $\approx 10^7$ Roentgen).

1. Introduction

The bipolar super self-aligned technology (SST) transistor is a component of high-frequency integrated circuits. Its properties are described in Ref.[1]. This technology has been applied to a silicon strip readout amplifier VLSI [2] to be used for an experiment at the SSC. In the SSC environment, the front end integrated circuits are irradiated by fast neutrons, γ-rays [3], and other particles. We expect severe damage to semiconductor detectors and front end circuits [4]. The transistors should be radiation-hard in order to survive more than one year of operation. In this work, SST transistors were exposed to fast neutrons from a nuclear reactor and to γ-rays from a ^{60}Co source in order to investigate their degradiation and hardness, respectively. The radiation effect of fast neutrons on bipolar SST transistors was studied last year [5]. It was proven that transistors made of bipolar SST process technology can withstand 10^{13} neutrons cm^{-2} as well as 10^4 Gy γ-rays.

2. Damage to a Bipolar SST Transistor due to Fast Neutrons

2.1. Neutron flux

The reactor TRIGA MARKII has a maximum output power of 100 kW. At this power a fast neutron flux of 10^{11} neutrons $cm^{-2}s^{-1}$ can be expected. The fast neutrons from this reactor have an energy spectrum peaked around 1 MeV. The operation conditions were arranged so as to obtain information concerning both the total dose effect and the dose rate effect. The irradiated transistors were the T1M200, T2M400, and T4M8EE types, listed in Table 1. Table 2 gives a summary of the operation points and transistors irradiated at these points. Thermal neutrons were eliminated by a cadmium sheet covering the samples. The fast-neutron flux was monitored by an activation method for each operation point. The reactions used for the foil-activation method are summarised Table 3. Gamma-ray contamination was measured using cobalt glass. The γ-ray dose was $2.5 * 10^5$ R during a neutron exposure of $1.1 * 10^{13}$ neutrons cm^{-2}. Thouth γ-ray contamination is believed to induce substantial effects on MOS transistors, its effect induce substantial effects on MOS transistors , its effect on bipolar SST transistors is believed to be small [6].

Table 1. Transistor Family for Bipolar SST

Transistor	$I_c(max)$	Emitter Size
T1M200	2.0 mA	0.5μm*16μm*1
T2M400	4.0 mA	0.5μm*16μm*2
T4M8EE	8.0 mA	0.5μm*16μm*4

Table 3. Monitor Foils

Monitor	Threshold Energy	Reaction
Ti	2.2 MeV	$Ti^{47}(n,p)Sc^{47}$
Ni	2.8 MeV	$Ni^{58}(n,p)Co^{58}$

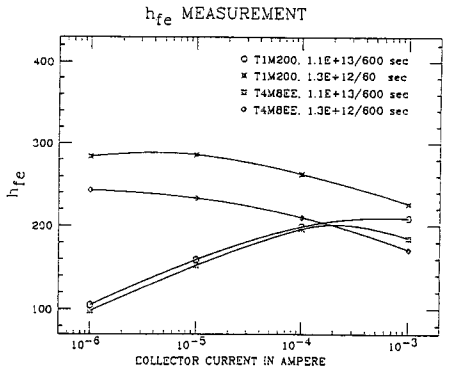

Fig.1. The h_{FE} degradiation of raw data

Table 2. Neutron Flux and Transistors

Output power of the reactor [kW]	~ 10^{11} n/cm^2	~ 10^{12} n/cm^2	~ 10^{13} n/cm^2
4		1.2×10^{12}/500 s T1M200 T2M400 T4M844	
10		1.4×10^{12}/200 s T1M200 T2M400 T4M8EE	
33	1.5×10^{11}/6 s T1M200 T4M844	1.3×10^{12}/60 s T1M200 T4M8EE	1.1×10^{13}/600 s T1M200 T4M8EE
100		1.5×10^{12}/20 s T1M200 T4M8EE	

2.2. Total dose effect on h_{FE}

The total dose effect for fast neutrons was studied in terms of the degradiation of the common emitter current gain, h_{FE} . Figure 1 shows raw data plots for h_{FE} after irradiation ; h_{FE} was measured with V_{CE}=2.0 V. The initial h_{FE} before irradiation ranged from about 200 to 300. It was observed that the transistors still showed a high h_{FE} value after irradiation . In order to obtain a more general view concerning degradiation it is common to use the following equation [7]:

$$\Delta(h_{FE}^{-1}) = \frac{1}{h_{FE}(after-exposure)} - \frac{1}{h_{FE}(before-exposure)} = \frac{\Phi_n}{2\pi * f_t * K}, \quad (1)$$

where Φ_n is the neutron flux, f_t the cut off frequency of the transistor , and K the damage constant. It is evident from this equation that high-frequency transistors are less damaged. Figure 2 shows h_{FE} degradiation using the $\Delta(h_{FE}^{-1})$ equation for a neutron fluence of $10^{11} \sim 10^{13}$ neutrons cm^{-2}. Between the curves for 10^{12} and 10^{13} neutrons cm^{-2} , one can write the ratio

$$\Delta(h_{FE}^{-1})_{\Phi_n=10^{13}} / \Delta(h_{FE}^{-1})_{\Phi_n=10^{12}} \leq 10. \quad (2)$$

This is a consistent with eq.(1). For data points between 10^{11} and 10^{12} neutrons cm^{-2}, the ratio $\Delta(h_{FE}^{-1})$ is much smaller than 10. This is due to some offset that has nothing to do with neutron fluence, such as a temperature change, which can be expressed as

$$\Delta(h_{FE}^{-1})_{Temperature} \simeq -h_{FE}^{-1}\left(1 - \frac{1}{(1+\Delta(T)/T_o)^2}\right), \quad (3)$$

where Δ(T)=T-T_o, and T_o is the initial ambient temperature.

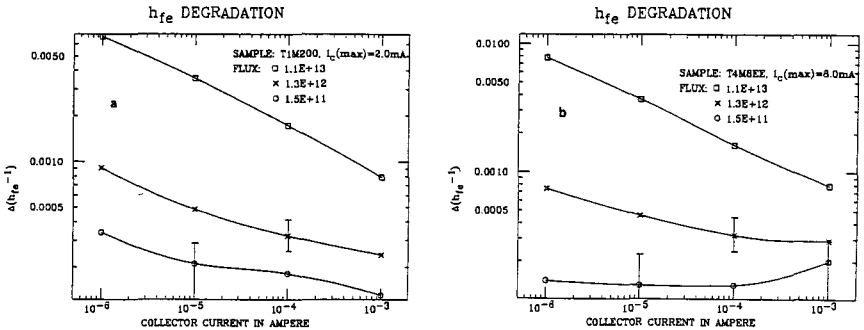

Fig.2. Total dose effect for T1M200; (a), and T4M8EE; (b)

2.3. Dose rate effect on h_{FE}

Because the neutron flux from the reactor was more intense than the practical SSC environment by an order of $10^4 \sim 10^5$ Gy, we had a chance to observe an effect that was inherent to this experiment at the reactor. In order to check this possibility, the neutron dose rate was swept from 10^{12}/500-second to 10^{12}/20-second. Figure 3 shows plots for two kinds of transistors . Thouth in Fig 2.(a) it appears that there exists some dose-rate effect, Fig 2.(b) shows no such effect. It is fair to say that the ordering the dose rate in Fig 2.(a) is quite accidental. There may be some effect which depends on the dose rate which contributes to the degradiation coefficient by no more than 0.0001, and which is compatible with a systematic error due to temperature ambiguity.

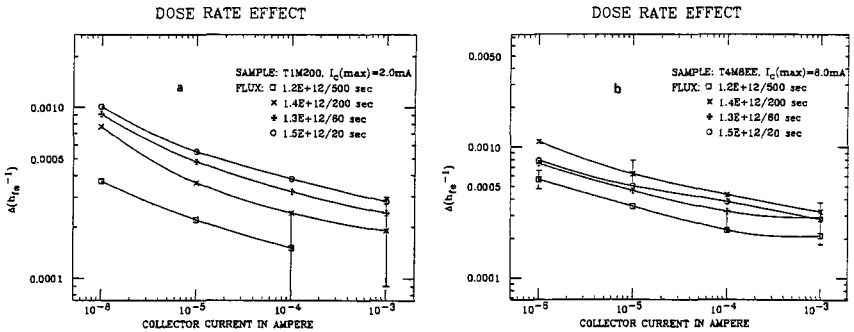

Fig.3. Dose rate effect for T1M200; (a), and T4M8EE; (b)

2.4. Effect on V_{BE}

Thouth we observed a V_{BE} shift of about +10mV (Fig.4), it was insensitive to the total dose. Thus, the observed V_{BE} shift was not due to the irradiation of neutrons but, rather, to an ambient junction temperature change. The base-emitter junction voltage is insensitive to the neutron fluence, which is a good feature regarding circuit design.

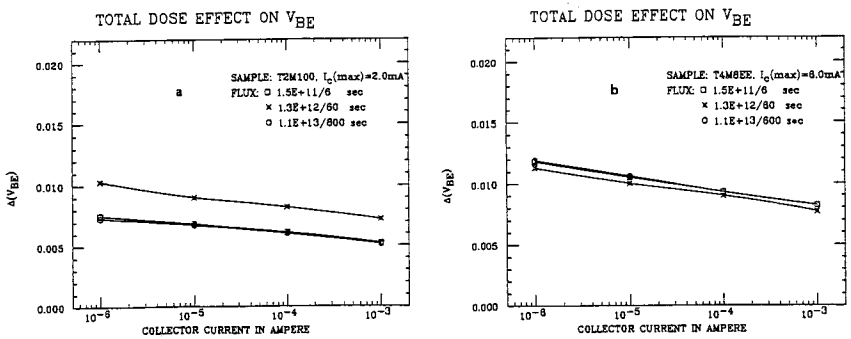

Fig.4. Total dose effect on V_{BE} for T1M200; (a), and T4M8EE; (b)

2.5. Annealing effect for room temperature and forced annealing

We have kept track of long-term room-temperature annealing for over 2000 hours, during which we observed a small fluctuation of $\Delta(h_{FE}^{-1})$ (Fig.5). This fluctuation was about $\pm$ 0.0001, which is consistent with the temperature change of the ambient. We can thus say that there was no significant long-term annealing effect. In order to accelerate annealing we warmed the transistors to 100°C and maintained this condition for 9 hours. A slight recovery of h_{FE} was observed at a lower collector current, I_c, region, i.e. I_c=100 μA, but not in the practical operation region, i.e. I_c=100 μA.

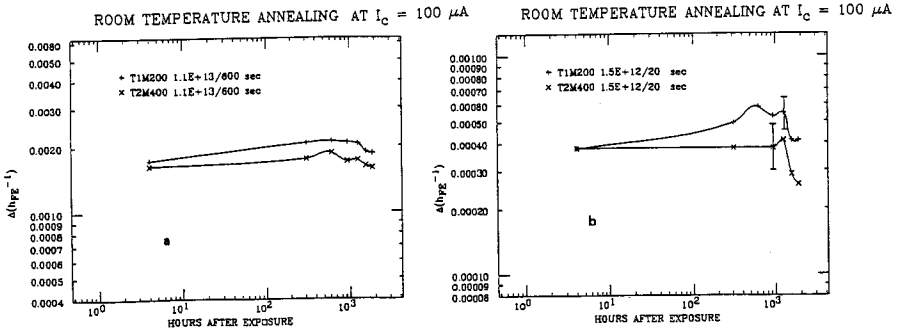

Fig.5. Room temperature annealing for high fluence sample ; (a) and high dose rate; (b)

3. Damage of a bipolar SST transistor due to $^{60}C_o$ γ-rays

3.1. Exposure Conditions

3.1.1 Test chips

The chips used for exposure tests had an area of 2.5 mm^2, on which 10 transistors were located with a common emitter configuration; the emitters were grounded in common, and both the collectors and bases were bonded separately to the package pins for measurements. Table 4 shows a list of all the transistors on a test chip. The largest transistor had an $I_{c(max)}$ of 8 mA; the smallest had an $I_{c(max)}$ of 0.625 mA.

3.1.2 Dose level for exposure

The exposure was carried out at the $^{60}C_o$ facility of JAERI(Japan Atomic Energy Reserch Institute), at Tokai. Transistor samples were packed within a glass test tube 16 mm in inner diameter and 15 cm in height. The glass test tubes were located for each test stand which was calibrated for the radiation level. The radiation level ambiguity was 10 % or less. The dose level and the elapsed time for exposure are listed in Table 5. The dose coverage was from 10^2 to 10^4 Gy. In the following disscussion the actual dose levels are intentionally designated in Roentgen instead of Gy [8].

Table 4. Transistors on Test Chips

Transistor	I_c(max)	Emitter Size
T05MS1	0.625mA	5.0 μm^2
T05M1M	1.0 mA	8.0 μm^2
T1M200	2.0 mA	16.0 μm^2
T2M400	4.0 mA	32.0 μm^2
T4M8EE	8.0 mA	64.0 μm^2

Table 5. Dose Level and Exposure Time

Dose (Roentgen)	Time for exposure (hour)
$1.0 * 10^4$	1
$1.2 * 10^5$	1
$1.1 * 10^6$	1
$3.3 * 10^6$	3
$1.0 * 10^7$	2

3.2. Gain Degradiation

The common emitter current gain was measured for a collector current ranging from 10 μA to 2.0 mA. Figure 6.(a) shows the degradiation of h_{FE} for T1M200. It is evident that h_{FE} is reduced much for a lower current range. The degradiation of h_{FE} was evaluated using equation (1). Figure 6.(b) shows a plot of the $\Delta(h_{FE}^{-1})$ equation for the degradiation of the current gain of T1M200. It is apparent that the degradiation decreses linearly for a larger collector current on a log-log plot, implying that $\Delta(h_{FE}^{-1})$ can be formulated as

$$\Delta(h_{FE}^{-1}) = F(D_\gamma) * (I_c/I_{c(max)})^m, \tag{4}$$

where I_c is the collector current, $I_{c(max)}$ the maximum collector current (listed in Table 4) and F(D_γ) a function of the radiation dose. F(D_γ) is often denoted as

$$F(D_\gamma) = A * D_\gamma^n, \tag{5}$$

where A is a constant and D_γ is the radiation dose. We tried to determine the experimental values of m, n, and A in order to qualify the radiation effects on bipolar SST transistors .

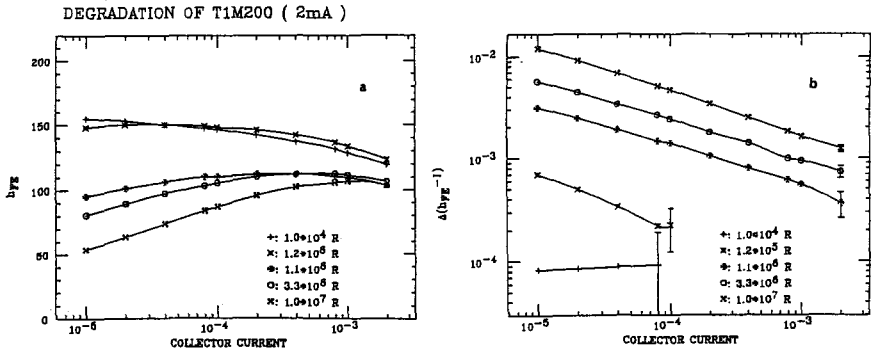

Fig.6. Degradiation of current gain of T1M200; (a) , and $\Delta(h_{FE}^{-1})$ plot; (b)

3.2.1 Dependence on the Collector Current

The degradiation from Fig 6.(b) seems to be proportional to

$$(I_c/I_{c(max)})^m. \tag{6}$$

The degradiation curves were fit for radiation doses of $1.1 * 10^6$ R, $3.3 * 10^6$ R, and $1.0 * 10^7$ R. The values for each curve are shown in Fig.7. The exponent of I_c was constant for all of the transistors and radiation doses investigated: quite close to -0.4, with data points scattered around $\pm$ 0.04.

3.2.2 Dependence on the Radiation Dose

The dependence on the radiation dose was investigated at a collector current of

$$I_c = I_{c(max)}. \tag{7}$$

The degradiation curves were extrapolated to $I_{c(max)}$ along the fit curve determined by equation (4), and can be expressed as

$$\Delta(h_{FE}^{-1}) = A * (D_\gamma^n). \tag{8}$$

Figure 8 shows the data points; the straight line shows a data fit with equation (8). The exponent for the radiation dose was 0.45, with an estimated error of $\pm$ 0.01. Coefficient A was determined as being $1.0*10^{-6}$, with an estimated error of $2.0*10^{-7}$. In order to estimated the error, a measurement error of 0.0001 was assumed for each $\Delta(h_{FE}^{-1})$ data point. We have thus obtained an experimental formula for predicting the degradiation of bipolar SST transistor ,

$$\Delta(h_{FE}^{-1}) = \frac{1.0 * 10^{-6} * D_\gamma^{0.45}}{(I_c/I_{c(max)})^{0.40}}. \tag{9}$$

Assuming that transistors are operated at 10 % of the maximum current, the degradiation is 0.0013; this value is very close to the degradiation level for 10^{13} neutrons cm^{-2}.

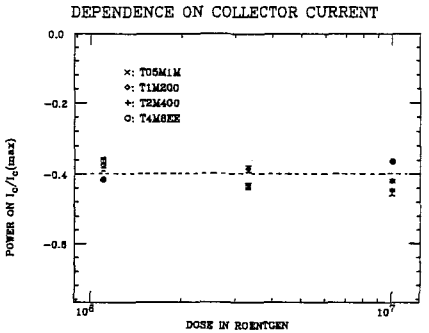

Fig.7. Dependence on collector current

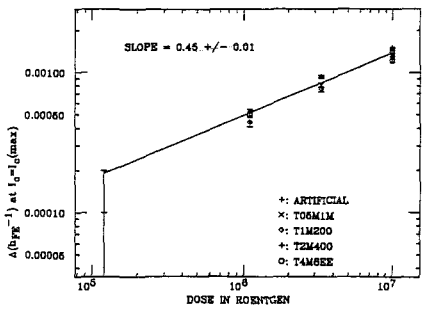

Fig.8. Dependence on radiation dose

3.3. Increase in the Leakage Current

The radiation induces a surface ionization charge, which results in a leakage current at the base-collector current junction. Since the leakage current can vary over many orders of magnitude, depending on the type structure, I_{CBO} is usefull in qualifying the rad-hard process of a bipolar transistor. Figures 9(a) and (b) show the I_{CBO} of T1M200 and T2M400 for each radiation dose. The following characteristics were obaerved:

- The leakage current is a slow function of V_{CB} .
- Thouth the leakage current increases monotonously for increasing radiation dose, it appears to saturate at higher dose, around 10^7 R.
- The leakage current is correlated with $I_{c(max)}$, which is proportional to the emitter size of the transistor .

In order to investigate the last feature, data regarding three kinds of transistor samples are plotted together in Fig.10. The straight lines are least-square fits to the data. The straight lines appear to represent a hypothetical zero emitter current transistor. This feature is clear at a radiation dose of 10^7 R. The data points shown in Fig.10.(b) were fit with

$$I_{CBO} = I_0 + G * I_{c(max)}. \tag{10}$$

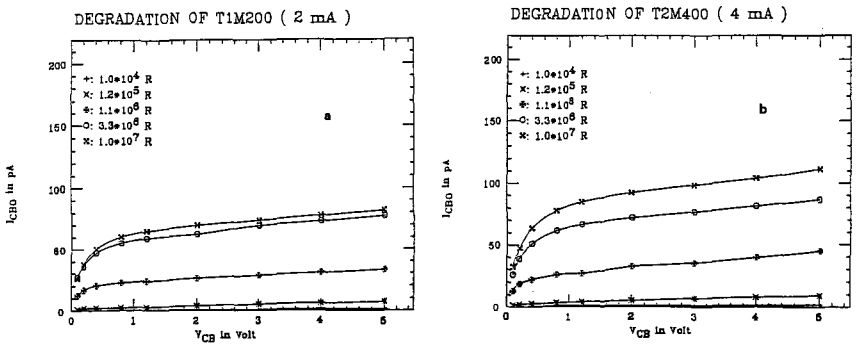

Fig.9. Leakage current of T1M200; (a), and T2M400; (b)

Figure 11 shows I_0 and G separately. It is very clear that I_0 is flat for a wide range of V_{CB} and that G increase monotonously for V_{CB} . It is reasonable to interpret the feature that there are two components of the leakage current:

- One is independent of the transistor size and V_{CB} .
- The other is proportional to the transistor size and V_{CB} .

One possible interpretation is that the former comes from an induced leakage channel around the peripheral area of the transistor ; the other comes from the base-collector depletion area, which is a generation-recombination current. The ionization charge trapped at the interface of S_i-S_iO_2 is a possible origin of unnecessary electric field that induced an FET-like conduction channel between the collector and the base region. For small-size transistors the leakage current around the peripheral area dominates over the leakage current due to bulk damage of the collector-base junction area. We obserbed that there were some smallest-size transistor samples which did not work at all; we considered this to represent a deterioration of the break down voltage due to an increase in a field-induced current.

3.4. Increase in Noise

It is said that γ-ray exposure beyound 10^2 Gy manifests increasing levels of 1/f noise. The noise spectrum in the low-frequency region is due to 1/f noise and a generation-recombination current; both of them increase with the radiation dose. In the present study this effect was not investigated.

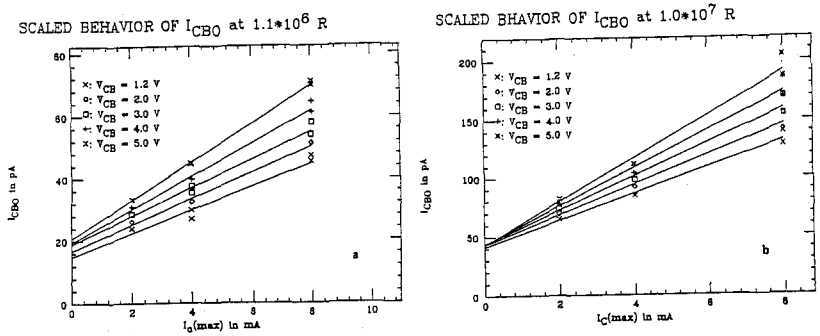

Fig.10. Scaled behavior of I_{CBO} at $1.1 * 10^6$ R; (a), and $1.0 * 10^7$ R; (b)

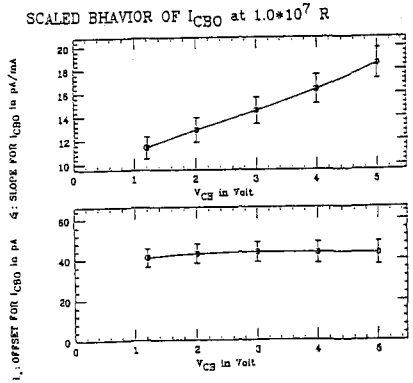

Fig.11. The coefficient for fit of leakage current

4. Summary and Conclusion

Bipolar SST transistors were examined for their hardess against fast neutrons. We obtained a degradiation coefficient, $\Delta(h_{FE}^{-1})$, of $\simeq 0.001$ for 10^{13} neutrons cm^{-2}. This small degradiation of SST is due to its high-frequency feature and high-current density at the base-emitter region, even under low-power operation. Moreover, on behalf of the high value of the initial h_{FE} , SST transistors maintain an h_{FE} greater than 100, which is practical for designing a practical circuit. We observed neither a dose-rate effect nor a room-temperature annealing effect on h_{FE} . An acceleration of annealing with high temperature achieved a small recovery of h_{FE} in a low-I_c region. V_{BE} was insensitive to the neutron fluence.

The degradiation of h_{FE} for γ-rays is 0.001 in terms of $\Delta(h_{FE}^{-1})$ for an irradiation level of 10^4 Gy, confirming an earlier irradiation test of NTT [6]. In conjunction with the hardness regarding neutron damage, we are convinced that preamplifier VLSIs made of SST bipolar process technology have a good chance to survive longer than one year of operation near the interaction point of the detector.

ACKNOWLEDGEMENT

We thank Y. Akazawa, NTT LSI Laboratories, and H. Ikawa, NTT Electronics technology Corpolation, for their advice during this work. We also thank M. Shiraishi for his advice regarding the nuclear reactor at Rikkyo university. Y. Oki, Radiation safety division, KEK, provided the opportunity to expose transistor samples to γ-rays exposure. This work was supported partially by the US-Japan Scientific collaboration program and grant-in-aid of Japanease Ministry of Education, Science and Culture.

REFERENCES

[1]. S. Konaka, Y. Yamamoto and T. Sakai, Proc. 16th Conf. on solid state Devices and Materials, Kobe, Japan, (1984), 209-212.

[2]. H. Ikeda, N. Ujiie and Y. Akazawa, IEEE Trans. Nucl. Sci. NS-36, (1989), 502.

[3]. D.E. Groom, ed., Radiation levels in the SSC Interaction Region, SSC-SR-1033, (1988).

[4]. M.G.D Gilchriese, ed. Radiation effects At the SSC, SSC-SR-1035,(1988).

[5]. H. Ikeda, N. Ujiie. Nucl. Instr. and Meth. A281(1989), 508-511.

[6]. M. Umehira, H. Kikuchi, S. Konaka and S. Kato, Electron Lett. 22, (1986), 744.

[7]. G.C. Messenger and M.S. Ash, The effects of Radiation on Electronic Systems (van Nostrand Rheinhold), New York, (1986), 183.

[8]. H. Ikeda and N. Ujiie, Nucl. Instr. and Meth. A290(1990), 462-468.

GaAs Custom Integrated Circuit

Tokio K. OHSKA, KEK (*)

We have been working on developing custom-made ICs for various data acquisition electronics. One project that is now complete is to develop a shift register (depth 256) that works at 1GHz clock speed for a pipeline TDC application. We spent almost one year to decide what type of IC family and which production process to be used for our application. There are number of IC production processes that would possibly operate at 1GHz. Through consultation with several IC manufacturers, we ended up with a GaAs IC, mainly because it would require lowest power among many possible candidate. However, a practical consideration such as the willingness of an industry to produce such ICs for us and a mass-producibility of such IC turned out to be quite important in the selection process. With R&D group of OKI Electric Industry Co.,LTD., we started with required conditions for the readout electronics. It turned out that the required number of gates for such IC (requires close to 2000 gates per channel) far exceeds that of a typical GaAs ICs in production, so that we had to start with smaller scale shift registers for production study. Shift registers of smaller depth were tried with various types of inner structure that would achieve high reliability and high production yield. It took almost 2 years until we reached the final design for mass production since the day one when we started from a scratch. Final mass production (6000 pieces) is under way and we are already getting a few thousand of them. The shift register can operate at up to 1.2GHz and consumes 1 watt which is significantly less than that of other types of ICs. During the cource of circuit development, we realized the importance of a 1GHz clock driver ICs and OKI Electronic Industry Co. also started production of such ICs. There are number of ICs that is capable of driving 1GHz clock signals, but we also needed a circuit that will start and stop the clock signal at the appropriate timing so that the shift registers will receive only full-width clock signals. If a clock signal was interrupted in the middle of a full cycle, last clock pulse may not have sufficient pulse width so that the shift register ICs may or may not responded to it, thus produce ambiguity in timing.
It turned out that such circuit built with available ICs demands power and space on board more that we would like. The new clock driver ICs have this feature built-in so that there are significant saving in board space, power and cost for the pipeline TDC module. The pipeline TDC module in TKO system is now ready for mass production with the ICs. We have learned a few things during the course of the development for such ICs.

(1)Unless the production process is within a reach of present production technique, it would take more than a couple of years for a sure mass production.

(2)We do need a standard supply voltage(s) for next generation ICs that would be used for next generation experiments such as the SSC project. Plus 5 volts and minus 5.2 volts for TTLs and ECLs are well accepted and built into many electronics systems. We used plus 1.8volts power supply for the GaAs ICs for lower power consumption. The input logic level swing of the ICs is set to 600mV for faster speed. It would be nice if we knew what the next standard voltage(s) when we will be designing a readout system so that we can incorporate it on the backplane. Some GaAs IC manufactures are adding I/O sections to make the IC compatible with an ECL logic ICs. It is quite understandable as an industrial practice to do so. We have seen it for CMOS ICs as well. However,we would be spending extra cost and power for nothing. I think if a large scale enterprise, such as SSC, would take responsibility in leading the effort to determine the third standard voltage levels for power supplies (5th, if we count for +/- 15 volts) and design everything around it, it might become the next industrial standard. We would save power, cost and God knows what. Smaller project could not make enough impact. I would like to see other people join me in this respect. Remember, large voltage swing requires large power and slower speed. My recommendation is +2 volts. It should not be the worst possible choice. Most GaAs ICs should be able to conform to such supply voltage and, as I see it, the GaAs IC families would play an important role in SSC project. Be brave!

* O.Sasaki did most of the work in this pipeline TDC project.

Development of TMC Chip and On-Chip Processing

Y. Arai
KEK, National Laboratory for High Energy Physics
1-1 Oho, Tsukuba, Ibaraki 305, Japan

Introduction

In the time measurement system of drift chambers at SSC, low-power and high-density TDC chip is required for frontend electronics. If the circuit is composed of mostly digital circuit, further processing within the chip will be possible. Particularly in large scale electronics system, digital circuit is preferable compared with small voltage analogue electronics. Furthermore, it will be easier to buffer and move the data in multi-level trigger scheme.

To realize the above functions, idea of the TMC was born in 1986 [1] and a test chip was produced in 1988[2,3]. Encouraged at the success of the test chip, a first useful chip (TMC1004) was designed and will be available soon. The TMC1004 includes 4 channels of circuits and each channel has 1024 bits time memories. Timing resolution of the chip is 1 ns and stores 1 μs data inside the chip. Technology used for TMC is 0.8 μm Bi-CMOS process, and about 100,000 transistors are implemented in 5.0 mm by 5.6 mm chip area. Total power consumption for a channel is estimated at about 7 mW for 100 kHz trigger rate.

There are many directions to extend the ability of the TMC chip. One direction is to include data processing capability such as track finding and T0 finding. Another direction is to improve performance; increase the number of channels in a chip, improve timing resolution, extend capacity of the memory. In addition to these possibility, it may be possible to include preamp / shaper / discriminator circuits in the same chip as the TMC, because the present process already has excellent bipolar transistors.

In this paper, I will describe about the design and expected performance of the TMC1004 chip. I will also discuss about future possibility of the trigger and data processing within TMC chip.

Design of TMC

Detailed descriptions of the TMC circuit are presented in several places[1,2,3,4], so only a brief description is given here. Main components of the TMC are memories and controlled delay elements as shown in Fig.1. Write signal for the memories are delayed 1 ns for each memory, so the input signal transition is recorded in the memory. Block diagram of the TMC 1004 is shown in Fig.2. The chip has 4 channel of circuit and each channel has 32 rows times 32 columns time memory cells. To point write row and read row, there are two counters which are counted up with external clock. Initial offset of these counter , which is set through CSR registers, is corresponds to trigger decision time.

Each delay element is controlled by referencing external clock of 32 ns period. Fig.3 shows the characteristics of the delay element. If the delay time is not controlled, the delay value will change more than 20% with variation of power supply voltage, temperature and transistor threshold. By controlling a gate voltage (Vg) of the delay element by the feedback circuit, the delay time will be kept within 3%.

Data are readout in 32 bit parallel and encoded to 6 bit in 32 ns pipeline cycle. This enables us to write and read the data at the same time, that is, deadtimeless operation is possible. Data is encoded as shown in Table 1. The "0" to "1" position is encoded to 5 bit and first bit in a row appears in bit 5 to distinguish the signal transition between row. Timing diagram of readout cycle is shown in Fig.4. After receiving the trigger signal (DS* assert), readout address is given from the read pointer, then the data are sensed, encodeed and output to external device. Readout cycle will continue during the DS* signal is kept low level. For example, if we need to read out 96 ns data for each trigger, DS* signal is kept low for 3 cycle. If the next trigger comes before finishing the readout, the DS* signal has to be extended to cover the necessary data. This mechanism enables to take events within a detector response time.

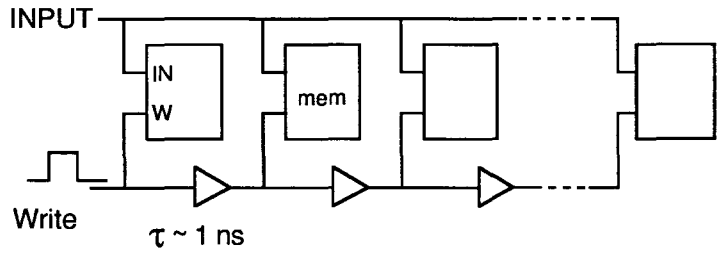

Fig.1 Basic configuration of the TMC

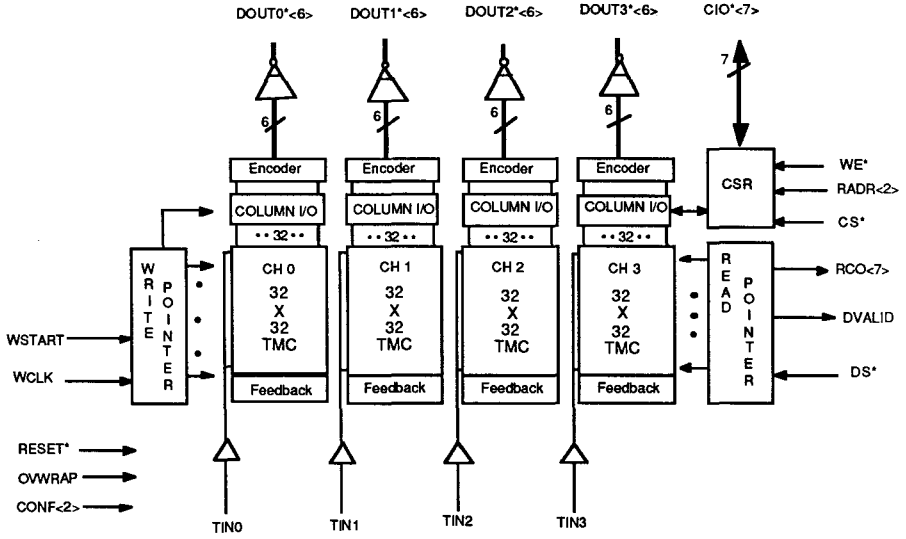

Fig.2 Block Diagram of the TMC1004

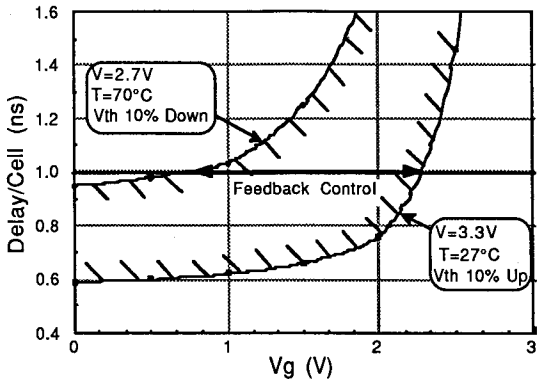

Fig.3 Delay characteristics of the delay element.

Table 1 Data Encoding Logic. Detect 0 to 1 position, and encode the position.
Bit 5 of the encoded data represents the contents of the bit 0 data.

Bit Pattern	Encoded Data
3322222222221111111111 1098765432109876543210987654321 0	5 4 3 2 1 0
00000000000000000000000000000000	0 0 0 0 0 0
xxxxxxxxxxxxxxxxxxxxxxxxxxxxxx10	0 0 0 0 0 1
xxxxxxxxxxxxxxxxxxxxxxxxxxxxx100	0 0 0 0 1 0
xxxxxxxxxxxxxxxxxxxxxxxxxxxx1000	0 0 0 0 1 1
:	:
10000000000000000000000000000000	0 1 1 1 1 1
11111111111111111111111111111111	1 0 0 0 0 0
xxxxxxxxxxxxxxxxxxxxxxxxxxxxx101	1 0 0 0 1 0
1xxxxxxxxxxxxxxxxxxxxxxxxxxx10x1	1 0 0 0 1 1
:	:
10xxxxxxxxxxxxxxxxxxxxxxxxxxxxx1	1 1 1 1 1 1

(x..xx..x = 1..10..0)

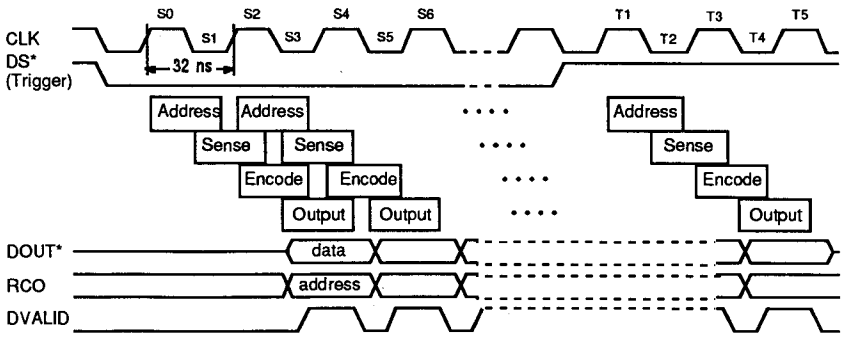

Fig. 4. TMC Readout Timing

Most power consuming part of the TMC is sense amp circuit. Because each channel has 32 sense amps, there are 128 sense amps in a chip. Sense amp has DC current path, and consumes about 2 mW, so in total it consumes about 256 mW. As the readout operation is required only when trigger comes, the DC current path is cut while not reading. Power consumption was estimated and plotted as shown in Fig.5. The power consumption is depend on trigger (read out) rate. For 100 kHz trigger rate and read out data in 4 rows (128 bit), power consumption of a channel is estimated at about 7 mW. This is order 2 less than the ordinary shift register circuit.

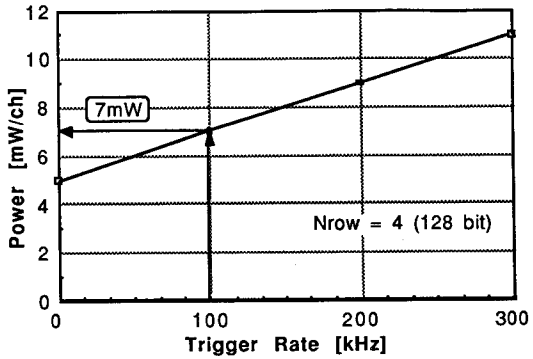

Fig.5 Estimated power consumption vs Trigger rate

Although the TMC1004 is designed to have 1 ns time resolution, it will be possible to improve time resolution. Direct way is to use more fine lithography such as 0.5 μm technology. Another method is to construct the TMC cell using bipolar and CMOS transistor, or use two delay lines and take the difference of these lines. These technique will enable us to get 0.5 ns time resolution.

The area of the present chip is only 5 mm by 5.6 mm. Even if we double the number of channels (8 channel), and expand the memory capacity to 4 times larger (4 k bit), the circuit can be contained in a 10 mm by 12 mm chip.

Trigger / Readout Processing

One attractive feature of using the VLSI chip in frontend is the possibility to include trigger logic in the chip. Here I will show some examples for stiff track finding and T0 (track passing time) finding inside the TMC chip combined with the straw tube central tracker.

Track trigger in central tracker and muon chamber has been extensively studied by J. Chapman[5] by using track synchronizer method. He used analog method in which current source/sink and capacitor are used to calculate T0 timing. This T0 finding method can be implemented more easily in digital way by using controlled delay element of the TMC. Fig. 6 and 7 shows the simplified scheme of Stiff track and T0 finding method.

Stiff track can be found by taking coincidence in a superlayer of straw tubes. If we take 3 out of 4 coincidence in a half side of the superlayer, track with less than a few GeV fails this coincidence. To increase the momentum threshold, coincidence window has to be reduced. To lower the threshold further, we have to include neighboring cells and configure the appropriate coincidence logic. Stiff track information can be used not only for trigger purpose but also for data reduction. M. Asai has made simulation [6] for straw tube central tracker with 3 out of 4 coincidence, and he showed the data size will be reduced down to an order of magnitude.

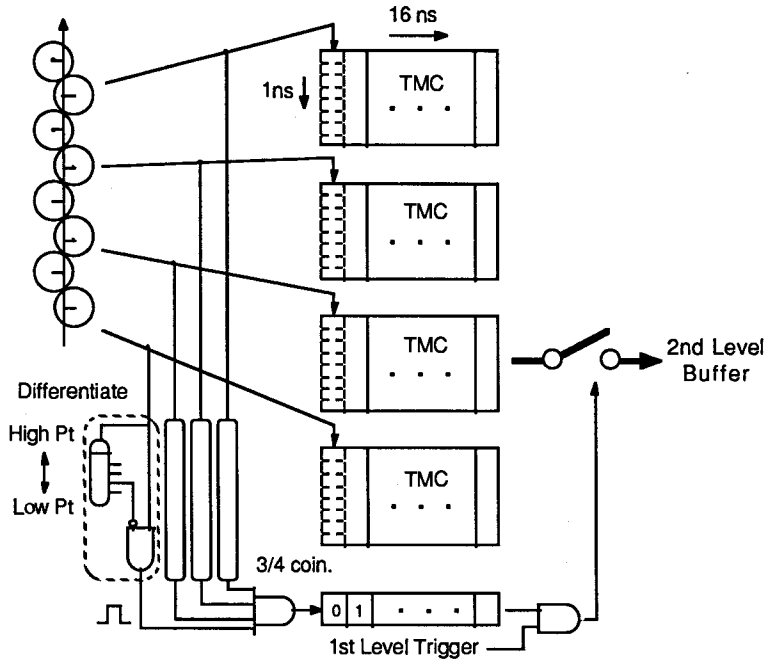

Fig.6 Stiff Track Readout Scheme

To get T0 information in the first level trigger, we can use the fact that sum of the drift time for left and right side (T_L and T_R) is almost constant for high momentum track (Fig.7). By implementing two delay line of which length is same as the maximum drift time of the tube, left and right signal coincidence at $T_{OUT} = T0 + T_L + T_R$. Because the sum of the T_L and T_R is equals to maximum drift time (T_{Drift}), T0 value is available as position of coincidence bit. T0 finding may be combined with stiff track finding, and one T0 value can be get for a track in a superlayer.

This method is also applicable for Z position finding by measuring the timing at the both ends of the tube. Z coordinate measurement by time difference has several advantage from stereo wire method. At first, the number of layers can be reduced to half. This also reduce the material in the central tracker. The number of total electronics channel is almost same. As the same readout electronics will be implemented at both sides, the electronics has redundancy. So even if one side of electronics has broken, we still be able to get r-phi information from the tube. Timing accuracy can be improved, because the pulse height variation is compensated for both ends signal. To get Z information in the first level trigger is very attractive feature, but it may be difficult how to get signals from both ends and combine with logics. Although the time difference method has less Z position resolution than stereo wire method, Z resolution of 10 cm will be achieved for a tube by using information from both ends and 0.5 ns timing resolution electronics. By combining the data in a superlayer, Z resolution of less than 5 cm can be achieved. This value is enough for pointing calorimeter tower , and it is usually easy to solve z position by time difference.

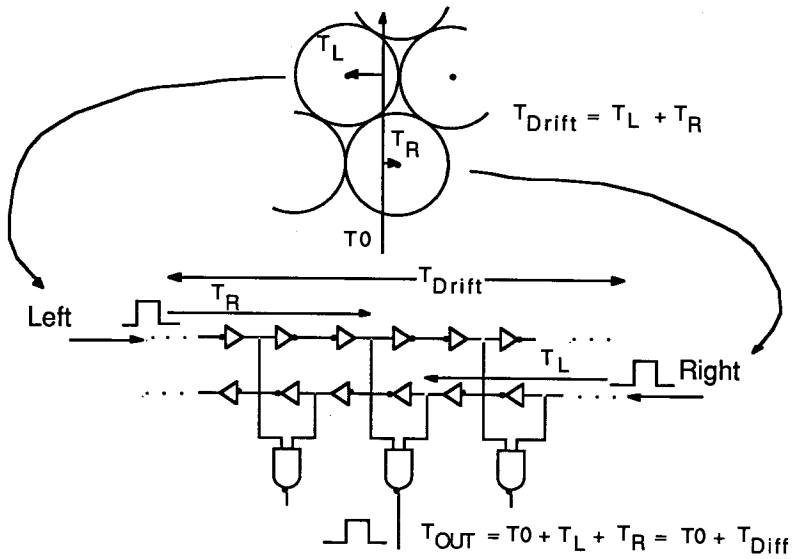

Fig.7 T0 Finding scheme

In table 2, characteristic figures of straw tube central tracker is shown. Hit rate was taken from the simulation of M. Asai[7]. Rapidity coverage of the chamber is assumed to be η=1.65 and maximum length of tube is 3 m. Each tube is divided in 2 at z=0. Time jitter and walk are calculated from naive approximation of initial signal. Jitter and walk seems to be manageable value due to the dividing of tube and using of low noise preamplifier[8]. However, the hit rate seems still to be high.

Summary

A new TDC chip which can be used in SSC environment was developed and available soon. The chip was designed to work in deadtimeless readout scheme and multiple trigger in a detector response time. The chip also has many possible features to include local trigger / data processing.

Table 2. 4 mmϕ Straw characteristic figures. (xd : track distance from anode wire)

r [cm]		60	80	100	120	140	160
Hit Rate [MHz]		4.5	3.9	2.7	1.5	0.84	0.27
Length [m]		1.77	2.35	2.94	3.0	3.0	3.0
I/wire [mA]		1.38	1.20	0.83	0.46	0.26	0.08
Charge [C/cm/5year]		0.39	0.26	0.14	0.08	0.04	0.01
Capacitance [pF]		19.4	25.8	32.2	32.9	32.9	32.9
ENC [e]		1530	1800	2100	2100	2100	2100
xd=0mm	Jitter [ns]	0.26	0.31	0.35	0.36	0.36	0.36
	Walk [ns]	0.47	0.55	0.63	0.64	0.64	0.64
xd=1mm	Jitter [ns]	0.12	0.14	0.16	0.17	0.17	0.17
	Walk [ns]	0.21	0.25	0.29	0.30	0.30	0.30

(Gain=4×10^4, measuring time=5ns, Qs(xd=0mm)=30000e, Qs(xd=1mm)=67000e, Fast Gas (100μm/ns), 25μϕ wire, ATT Preamp, No magnetic Field)

References

[1] Y. Arai and T. Ohsugi; "An Idea of Deadtimeless Readout System by Using Time Memory Cell", Proceedings of the Summer Study on the Physics of the Superconducting Supercollider, Snowmass, (1986)455.

[2] Y. Arai and T. Baba, "A CMOS Time to Digital Converter VLSI for High-Energy Physics", 1988 Symposium on VLSI Circuits, Aug. 1988/Tokyo, IEEE CAT.No. 88, TH 0227-9, p121.

[3] Y. Arai and T. Ohsugi, "TMC - A CMOS Time to Digital Converter VLSI", IEEE Trans. on Nucl. Sci. Vol.36, No.1 (1989)528

[4] Y. Arai, "Time Measurement System at the SSC", Workshop on Triggering and Data Acquisition for Experiments at the Supercollider", Toronto, (1989)125. SSC-SR-1039.

[5] J. Chapman, in this workshop.

[6] T. Ohsugi, M. Asai and Y. Arai, "On-chip Filtering of Low Pt Track with Straw-Tube Chamber", HUPD-9003, JSD-NOTE-1990-3.

[7] M. Asai, in this workshop.

[8] F. M. Newcomer, private communication.

R & D on data acquisition in US

I. Gains
FNAL

(No written contribution received)

Fiberoptics data transfer protocol

KEK online group
Masaharu NOMACHI

Introduction

Fiberoptics data transfer has been studied for high speed data link. TAXI chip set, which is developed for FDDI, has been tested. It can send data with 12.5 M byte / second at maximum speed. Recently new chip set has been developed by Gazelle. It can send 40 bit data with 125 M byte / second at maximum speed.

Simple but high speed data transfer interface is designed for experiments in high energy physics. They need data transfer with 16 bit word or 32 bit word. 32 bit data plus 8 bit control can be a good solution for data transfer protocol, and meets to Gazelle chip set. It is optimized to one way data transfer.

40 bit data transfer

information field

Lower 32 bit is information field. It can be data, word counts, status code etc.

control code field

Most significant 8 bits in 40 bits are used for control code. Up to 256 control codes are possible to be assigned. Most of the codes are reserved. Control codes are classified to the following four categories.

General command code.

The codes force some reaction to receiver are called "command code". This general command codes and the next general information codes are assigned to first 16 codes in 256 codes. Meaning of control and response are defined.

Data transfer mode initialize: It is sent after power up or reset. Receiver must be initialized and must send back *status information* with *initialized* status code.

Inquire: It request status information to receiver. Receiver must send back *status information* with certain status code.

General information tags

These codes are used to send informations commonly used in data transfer. These control doesn't request any response in the protocol. The response is fully up to applications.

DATA: 32 bit information is a data.

Null No information, no command.

Status: Status information must be sent on request by *inquire* command. Status can be sent at any time. Details are defined in later paragraph.

Beginning of packet (packet number): It declares the beginning of the packet. Packet might correspond to "event". It can have packet sequence number in its 32 bit information field.

End of packet: It declares the end of packet. It can have word count in its information field.

Reserved codes

Control codes from 16 (0F in hex) to 63 (3F in hex) are reserved for data transfer mode protocol. Control codes from 128 (80 in hex) to 255 (FF in hex) are reserved for other mode such as FASTBUS protocol.

User area

Control codes from 64 (40 in hex) to 127 (7F in hex) are user area. Users can assign their own command or information in this area.

Status information

General format

Status information has 32 bit information field. 32 bit status code is possible but it makes difficult to decoding. Most of application doesn't need so many status code. Here in this protocol, simplest status byte assignment is defined. 16 bit status code or 24 bit status code might be possible in some complicated application. Several code sets are possible to be assigned with 32 bit information field. 8 bit status is distinguished by bit 8 to bit 31. If those 24 bits are zero that status information has 8 bit status byte in least significant byte. Other status code must be assigned to be able to be distinguished from 8 bit code. All code sets must have "initialized", "ready" and "not ready" codes.

8 bit status

Lower 4 bit filed is status code. Higher 4 bits are error bits or reserved for extension. 16 status can be assigned for "Ready", "Not ready" etc.

Reduced data transfer mode

Experimental data flows one direction, from front-end module to computer. Only status is needed to be sent back from downstream to upstream of data flow. Most of application doesn't need full 32 bit status information. 40 bit status code is not necessary.

Assuming higher 32 bit is 8 bit control code for status information and 24 bits are zeros, lower 8 bit is enough to be sent. It saves number of chips and pins.

8 bit data transfer

Status information transfer is assumed without sending control code. Upper 24 bits in information field is assumed to be zero. Thus, in 8 bit data transfer mode, only status information with byte status mode can be sent. Other control code or other status code mode can be sent with full 40 bit data transfer mode.

Fiberoptics data transfer auxiliary module

Fiberoptics data transfer auxiliary modules will be designed. Physical protocol between auxiliary module and main module is the protocol designed in this report. It is 40 bit data transfer mode or 8 bit status transfer mode. Protocols on the fiberoptic depends on hardware. It is defined in the next paragraph. Auxiliary module on transmitter side and receiver side must use same protocol on the fiber. However pair of auxiliary modules can be replaced to another pair of auxiliary module with different hardware.

Hardware implementation

Gazelle chip

Gazelle chip can send 40 bit at the same time. 40 bit mode can be used without any modification. 8 bit mode is implemented just by ignoring higher 32 bits.

Taxi chip

TAXI can send only 8, 9 or 10 bits at the same time. 40 bit data needs to be send with 4-5 transmission. Addition to that, control nibble or tag bit must be send to put a mark on most significant byte or word.

40 bit data transfer is done by sending a non zero control nibble followed by five 8 bit data words. Six nibbles must be transfered. TAXI can send one nibble per 80 nsec in 8 bit mode. Then, 40 bit data is sent with 480 nsec.

Four TAXI chip

Four fiber with four TAXI is much faster than one TAXI. 40 bit is divided into four 10 bit data. Each 10 bit fraction is sent with one TAXI. No control nibble is sent. Maximum data transfer speed for 10 bit data mode is 96 nsec for each nibble. 40 bit data word in every 96 nsec is maximum. It may be designed with 10 MHz clock. Then 40 bit data per 100 nsec or 40MB/sec data transfer rate.

40 bit transmitter and receiver

An auxiliary module which has only transmitter or receiver with 40 bit mode.

40 bit transmitter and receiver with 8 bit status return

Data transmitter auxiliary module has 40 bit mode transmitter and 8 bit mode receiver. Data receiver auxiliary module has 40 bit mode receiver and 8 bit mode transmitter. 40 bit mode is used for data transfer. 8 bit mode is used for status return.

TRANSPUTER ARRAY TRIGGER
– A Second Level Trigger Based on A Microprocessor array –

H. Sakamoto and Y. Watase

National Laboratory for High Energy Physics, KEK
1-1 Oho, Tsukuba, Ibaraki 305, Japan

T. Korhonen

Department of High Energy Physics, Helsinki University
Siltavuorenpenger 20 D, 00170 Helsinki, Finland

A. Taketani

Department of Physics, Hiroshima University
Higashi-senda-machi, Naka-ku, Hiroshima 730, Japan

ABSTRACT

A second level trigger system is going to be introduced to the VENUS experiment at TRISTAN. The system consists of two parts, i.e. an IMS T800 Transputer array and interface modules which are also based on the Transputer. The trigger data are all transferred via the Transputer links. Track finding is performed on the array in a few miliseconds and the result is sent to a FASTBUS master. The performance was studied using Monte Carlo and real experimental data.

INTRODUCTION

In recent collider experiments, the sizes and the channel density of the detectors become so large and requirements to the trigger system become so sophisticated that it is very difficult to cover the requirements only by the first level trigger logic. Thus, it is natural consequence to introduce the second level trigger scheme.

The VENUS detector began its operation in 1986 and at the early stage of the experiment, only the first level trigger was used. All the trigger signals were processed using analog signal discriminators or memory lookup tables to determine whether the event should be taken or not. Due to the implemetation limitation on the number of signals or the size of the lookup tables, the resolution of the trigger system was not so good. For example, the central drift

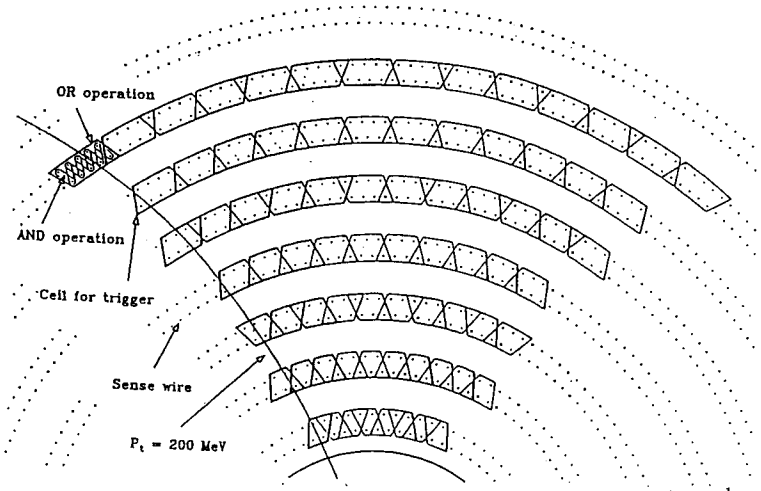

Fig. 1: First level trigger cell pattern of VENUS CDC. Dots represent anode wires and signals nearest in the neighbouring layes are ANDed and then ORed together in each rectangle to make input signals for RAM lookup tables.

chamber (CDC) has 7104 anode wires in 29 cylindrical layers, and the signals of these wires were logically AND-ORed as shown in Fig. 1 to reduce the number to 768 which was acceptable by 12 bit address RAM lookup tables.[1] This means that the resolution of the CDC track finder becomes 10 times worse due to this signal bundling. According to a study using verious experimental data, if all the 7104 wires are used without the AND-OR bundling, the momentum and vertex resolutions are dramatically improved for low momentum tracks which have large curvature. Such low momentum tracks come mainly from background events like beam-gas or beam-beampipe interactions, so by sharply cutting off the low momentum tracks, a 10 times better S/N ratio than now is expected.

Recently, a 68020 FASTBUS Processor Interface (FPI) was employed[2] as the front-end master instead of our old VAX11/780. The FPI unit can access the FASTBUS modules much more easily and quickly without a large overhead which the VAX FPI used to have. As the 68020 FPI gathers data and builds up them into an event record, it can also make a second level decision of triggering using the data. It takes abount 10 miliseconds from the first level trigger to the completion of the event building. So our second level decision must be done in this time interval. But the CPU power of FPI is not enough to perform pattern recognition on tracking devices so in order to improve the trigger resolution, an external computing unit or an accelerator is necessary.

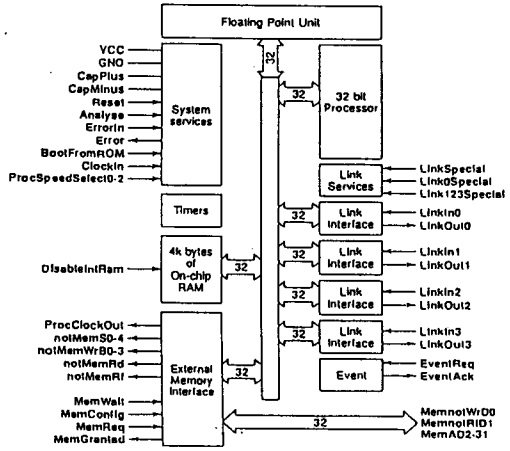

Fig. 2: Block diagram of IMS T800 TRANSPUTER.

MICROPROCESSOR ARRAY

T800 transputer chips[3] made by INMOS were chosen for our microprocessor array. T800 is a 32 bit wide microprocessor which involves a floating point unit, 4 kB on-chip RAM, timers and 4 communication links. The architecture is shown in Fig. 2. These links transfer messages from one to another transputers at the rate of 20 MHz. Using these 4 links, a 2 dimensional lattice of transputers is constructed.

Performance of this T800 was evaluated using a WHETSTONE benchmark test[4]. The result is shown in Fig. 3. Access time of onchip RAM is 50 nsec while 150 nsec is required for external memory so the performance depends on the code size whether the instruction codes or data frequently accessed are allocated on the onchip RAM or not. The difference of results among OCCAM, C and FORTRAN may be due to the code size. Anyway, a single T800 has a remarkable computing power comparable to small VAXes.

Transputer modules (TRAMs) are commercially available which mount T800 chips and DRAM of 1 MB or so. These modules are small DIL boards and 8 modules can be mounted on one VME board. Several tens of TRAMs can be installed in a single VME crate. So what we had to do was to develop interfaces between the experimental readout system and these modules.

SYSTEM INSTALLATION

Block diagram of this system is shown in Fig. 4. Trigger data are read via trigger interface cards (TRICs) mounted on the FASTBUS auxiliary card

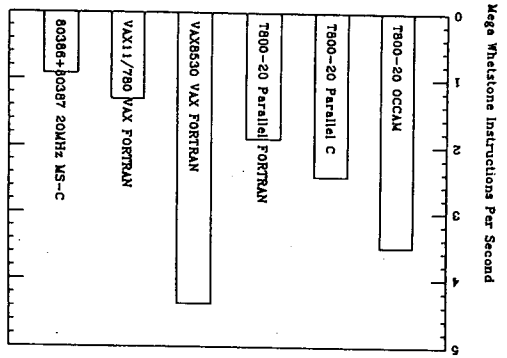

Fig. 3: Result of Whetstone benchmark test on several languages on T800 and other computers. For OCCAM and C version, the original FORTRAN source was converted by hand.

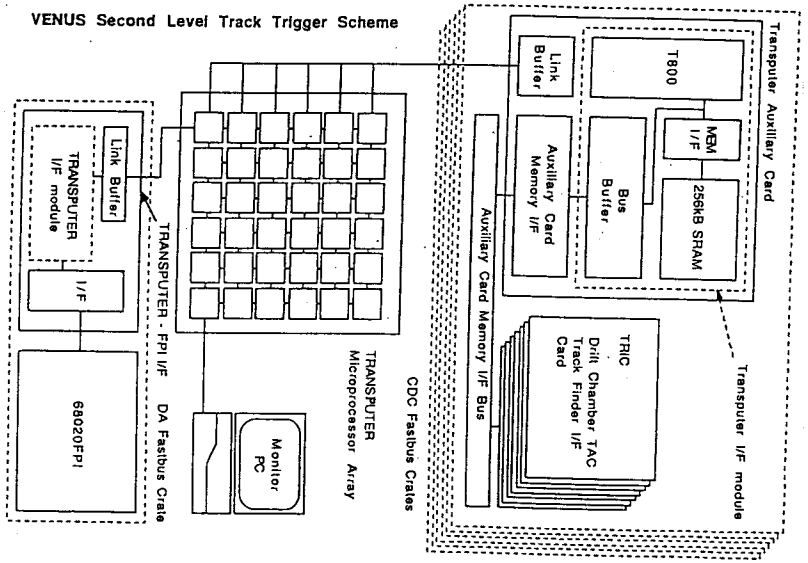

Fig. 4: Conceptual view of the second level track trigger system for VENUS. Trigger data are taken via axiliary connectors of CDC time to analog converters (TACs). A data collection module on each crate reads the data and sends them to a processor array. Result of tracking is sent to FPI to make the second level trigger decision.

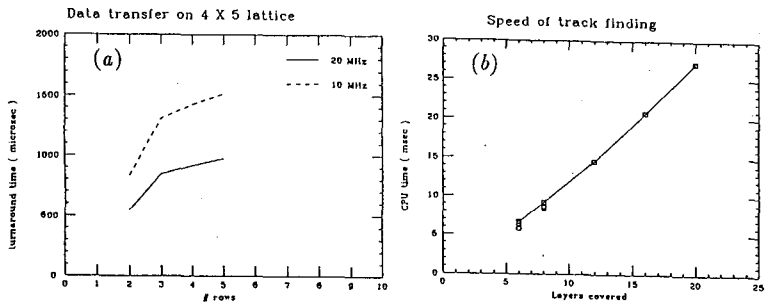

Fig. 5: (*a*). Average time to distribute trigger data into the transputer network of 4 $\times n$ lattice. (*b*). Average computing time to find a track staring from one innermost hit wire of CDC. The number of layers assigned to one processor was changed.

of time to analogue converter (TAC) modules of the CDC readout. A data collection module of auxiliary card size is mounted on each crate which reads hit wire information through its private bus. This module is divided into two parts, i.e., a general purpose transputer interface module (TRIM) and a private bus driver. The TRIM module is a small DIL board through whose connector all the memory bus signals of the T800 are extracted. The private bus driver interfaces the transputer memory bus and the data collection bus which is dedicated for the trigger data collection. The trigger data are formated by a T800 on the crate and are sent to the microprocessor array through its communication link. At present this array consists of 20 TRAMs which form a 4 $\times$ 5 two-dimensional lattice and this number can be easily increased by merely adding transputer modules. Configuration of the transputers is freely modified by a software. On this array, tracking is done by sharing the hit wire data. The tracking procedure is divided so as that a sector is covered by a row of the lattice and each element of the row is assigned to several layers of the anode wires. The element searchs a track using a condition common to the row and sends the result to one end of the row. The element at the end compares the result to find a track passing through the all layers. These results are gathered and sent to the host 68020 FPI through a link. At the auxiliary connector of FPI, there is also provided a transputer module which communicates with the 68020 CPU via a parallel interface.

The speed to distribute the trigger data was measured using typical experimental data and the result is shown in Fig. 5-a. In this measurement, no track finding was done and pure transfer speed was observed by changing the number of cooperating rows. As the links and the elements work as a pipeline, excess of turn around time produced by increasing a row is substantially small in the case of more than 3 rows. Time consumed to find a track using an example algorithm was also measured by changing the number of searching layers. It is seen in Fig. 5-b. that the CPU time increases proportionally as the layer count increases and the absolute time is larger than the overall transfer speed of 1 msec. It means that this application is a good example of distributed calculation where a data transfer does not bring a large overhead. According to these results, when a lattice of 5 $\times$ 10 elements or so is introduced, the track finding is able to be completed in a few seconds which is of the same order of the A/D conversion.

SUMMARY

Construction of the hardware components has been done and they are going to be installed in the next shutdown of the experiment. Several kinds of track finding algorithms are now being evaluated using the processor array. At the same time, a general purpose monitor program is being developed to provide a convenient environment for development and maintenance. Though the decision time of a few miliseconds may be too long for a future hadron collider experiment, it is announced that a new product of TRANSPUTER, which works 10 times faster than T800, will become available at the end of 1991 and accumulated software for T800 is all valid for the new TRANSPUTER. This research and development should be continued.

REFERENCES

[1] T. Ohsugi et al., Nucl. Instr. and Meth. A269(1988)522.

[2] Y. Arai et al., private communication.

[3] *The Transputer Databook*, INMOS Limited, First Edition, November 1988.

[4] *A Synthetic Benchmark*, Curnow H.J., and Wichmann B.A., Computer Journal 19 no 1, February 1976.

Computer farm

A. Manabe
KEK

(No written contribution received)

Isolated High Pt Track Trigger with a Scintillating Strip Tracker

S.Kim and K.Kondo

University of Tsukuba

Abstarct

The trigger with the SSC scintillating strip tracker was studied to estimate the ability of reducing the QCD background at an early stage of trigger (Level 1) at $\sqrt{s} = 40$ TeV with $L = 10^{33}$ cm^{-2} sec^{-1} . The trigger rate and the efficiency of the signal events were calculated for an isolated high Pt track trigger. This isolated high Pt track trigger picks up W and Z leptonic decay at high efficiency and reduces the QCD background significantly.

1. Introduction

We studied the isolated high Pt track trigger with the SSC scintillating strip tracker. This scintillating strip tracker has the following special features:

(a) To suppress signals from low Pt charged particle tracks.

(b) To output signals fast enough to make a Level 1 trigger.

We can compose an isolated high Pt track trigger making use of these special features. This trigger picks up the isolated lepton signal such as Higgs → ZZ → 4 leptons, Higgs → ZZ → 2 leptons + jets, Higgs → WW → lepton + jets and W/Z inclusive production, while it rejects the QCD background.

2. Scintillating Strip Tracker

We assumed the scintillating strip tracker in solenoidal magnetic field of 15 kG as the SSC central tracking detector. The structure of this tracker is described in detail elsewhere.[1] The geometry of the tracker is shown in Fig.1. It consists of 6 layers with radii of 50, 75, 100, 125, 150 and 175 cm. All layers cover the pseudorapidity range between -1.25 and 1.25. A dimension of a scintillating strip cross section is 2mm x 0.2mm . The light output from the scintillator is transmitted to a multianode photomultiplier via a wavelength shifter fiber. With this tracker, the straighter a track is, the longer is the track path length in a scintillating strip. Thus the signals from low momentum tracks are suppressed by setting the pulse height threshold higher. This tracker was intended to have signals only from high Pt tracks. It makes the track reconstruction and the trigger simple.

We calculated the path lengths of charged particle tracks as the signal magnitude, neglecting the fluctuation of energy loss in a scintillating strip and light signal attenuation. The path length in a single strip is plotted as a function of the transverse momentum of a leading charged particle which passed the scintillating strip for each layer in Fig. 2. The path length above 2mm is caused by tracks with Pt > 2 GeV/c in the first layer, and by tracks with Pt > 4 GeV/c in the sixth layer.

Here we set the threshold of the path length to 2 mm.

We generated QCD background events using ISAJET6.21[2] with minimum jet Pt's of 10GeV/c, 100GeV/c and 1TeV/c. When we set the threshold of the path length to 2 mm, the hit points for typical jet events with Pt = 10, 100 and 1,000 GeV/c are shown in Fig.3, together with generated charged particle tracks. A hit occupancy is defined to be the number of hit strips divided by the total number of strips in a layer. The hit occupancy in each layer for 1 TeV/c jet events is shown in Fig.4. It is 1.6% in the first layer and 0.5% in the sixth layer.

3. Isolated high Pt track trigger

We made the following trigger simulation:

(1) We divide the tracker into 24 segments each of which covers 15 degrees in azimuth and has 6 layers of scintillating strips.

(2) If we have only one hit in a layer of a segment, we call it a single hit layer. If we have at least 5 single hits in a segment, we call it an isolated track.

(3) We required that there should be at least one isolated track (Single isolated high Pt track

trigger)

3-A Trigger Rate

We generated the QCD background events using ISAJET6.21 with a minimum jet Pt of 10 GeV/c. The maximum number of layers with a single hit in a segment ($N_{S.H.}$) is shown in Fig.5. 85% of the QCD background events fail the cut of $N_{S.H.} > 4$. The event rates from the QCD background at $\sqrt{s} = 40$ TeV with $L = 10^{33}$ cm^{-2} sec^{-1} is shown as a function of a leading charged particle Pt in Fig. 6a with no trigger requirement, and in Fig. 6b with the isolated high Pt track trigger. The integrated event rates from the QCD background are also shown against the Pt threshold of a leading charged particle in Fig. 6c with no trigger requirement, and in Fig. 6d with the isolated high Pt track trigger. The rejection factor with the isolated high Pt track trigger is about 10.

3-B Efficiency for Higgs/W/Z events

The efficiencies of the isolated track trigger are calculated for the following processes:

(1) Higgs $\rightarrow$ ZZ $\rightarrow$ 4 μ's

(2) W + jets $\rightarrow$ e + ν + jets

(3) Z + jets $\rightarrow$ e + e + jets

These events were generated using ISAJET6.21 with M_{Higgs} of 500 GeV/c^2 in the process (1), and with Pt of W or Z > 3 GeV/c in the processes (2) and (3). Hit points and charged particle tracks are shown for a typical event of Higgs $\rightarrow$ ZZ $\rightarrow$ 4 μ's in Figs. 7a and 7b, respectively.

The maximum number of layers with a single hit in a segment ($N_{S.H.}$) is shown for the processes (1) to (3) in Figs. 7a - 7c. They show that the trigger efficiencies for the processes (1) to (3) are 99.5%, 96.1% and 98.5% for the cut of $N_{S.H.} > 3$, and are 99.5%, 86.3% and 94.4% for the cut of $N_{S.H.} > 4$.

References

1. K.Kondo et.al. "Scintillation Strip Tracker " in the Japan Solenoidal Group Report (1989).

2. F.E.Paige and S.D.Protopopescu, BNL-37066 (1985)

Figure Captions

Fig.1. The geometry of the scintillating strip tracker.

Fig.2. The path length in a scintillating strip is plotted against Pt of leading charged particle traversing the strip in (a) the first, (b) the second, (c) the third, (d) the fourth, (e) the fifth and (f) the sixth layers.

Fig.3. Charged particle tracks and hit points are shown for typical jet events:
(a) Pt > 10GeV/c, charged particle tracks
(b) Pt > 10GeV/c, hit points
(c) Pt > 100GeV/c, charged particle tracks
(d) Pt > 100GeV/c, hit points
(e) Pt > 1TeV/c, charged particle tracks
(f) Pt > 1TeV/c, hit points

Fig.4. The hit occupancy is shown for 1TeV/c jet events in (a) the first, (b) the second, (c) the third, (d) the fourth, (e) the fifth and (f) the sixth layers.

Fig.5. The maximum number of layers with a single hit in a segment ($N_{S.H.}$) is shown for QCD jet events with Pt (jet) > 10 GeV/c.

Fig.6. Event rates of the QCD background with a jet Pt > 10 GeV/c are shown as a function of a leading charged particle Pt with and without the isolated high Pt track trigger:
(a) Event rate with no trigger
(b) Event rate with the isolated high Pt track trigger
(c) Integrated event rate with no trigger

Fig.1. The Geometry of the Scintillation Strip Tracker

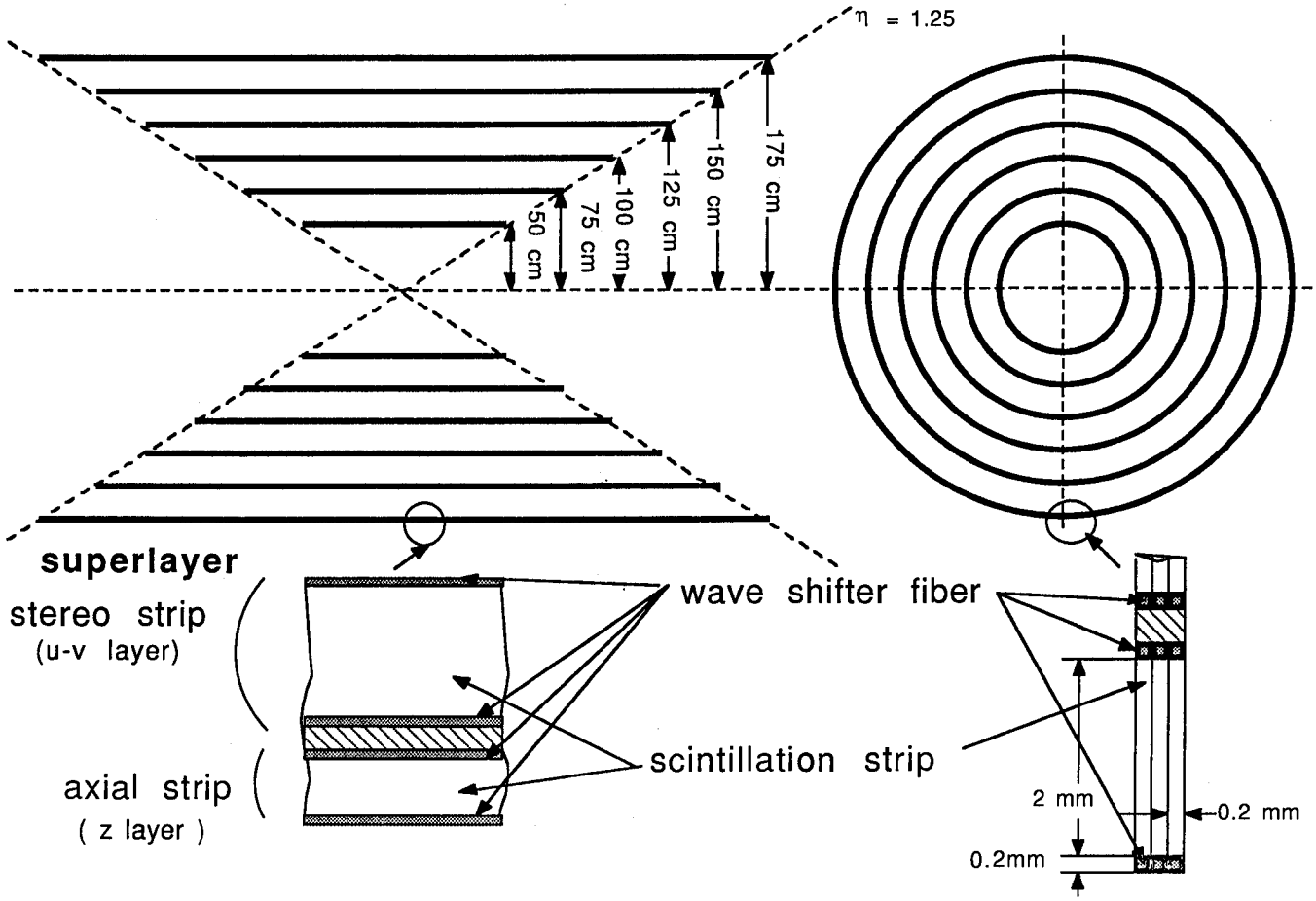

(d) Integrated event rate with the isolated high Pt track trigger

Fig.7. For a typical event of Higgs → ZZ → 4 μ's, (a) hit points and (b) charged particle tracks are shown.

Fig.8. The maximum numbers of layers with a single hit in a segment are shown for (a) Higgs → ZZ → 4 μ's, (b) W → e + ν , and (c) Z → e + e events.

Track Path Length vs. Pt of Leading Charged Particle Traversing the Scintillation Strip

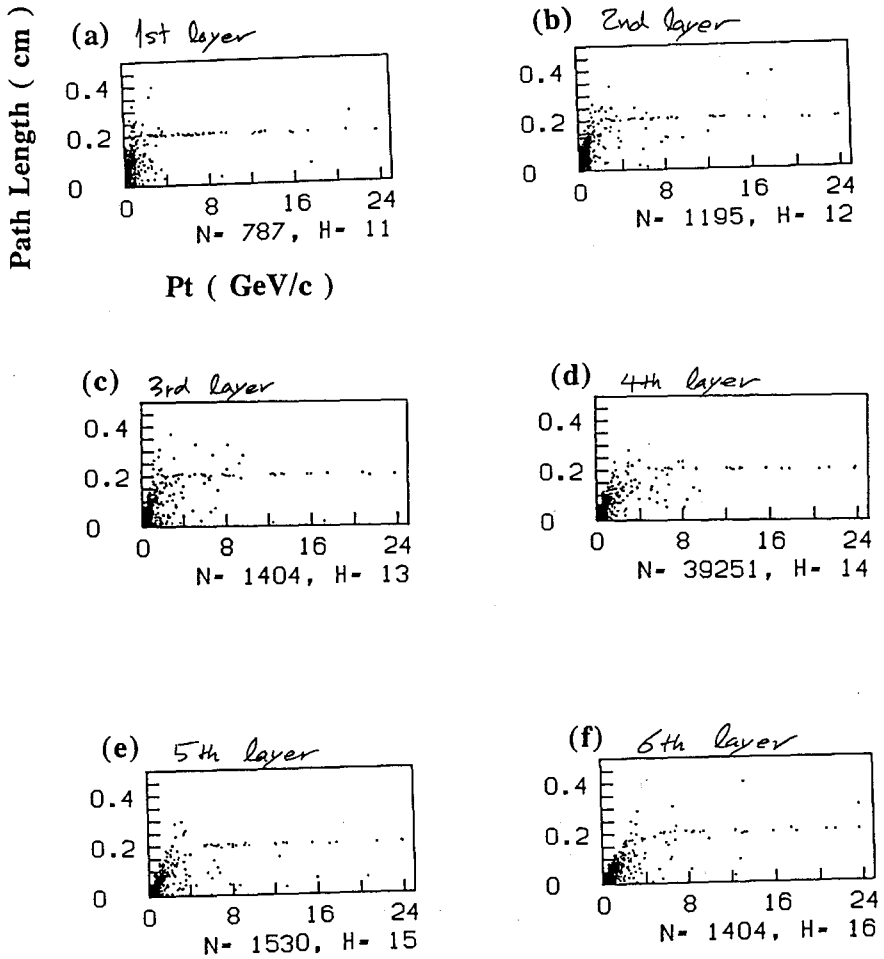

Fig.2

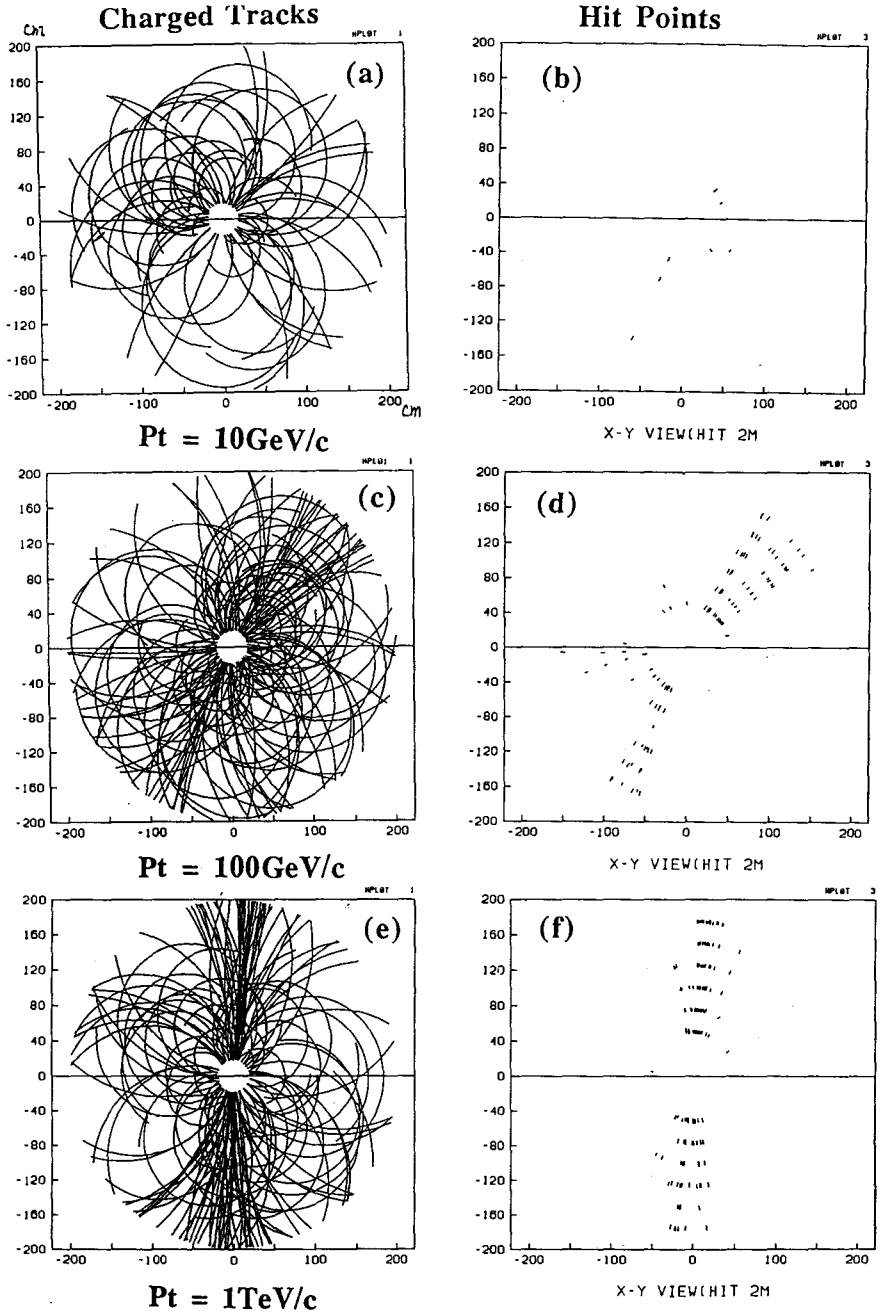

Fig.3

Hit Occupancy for QCD jet events with Pt(jet) > 1TeV/c

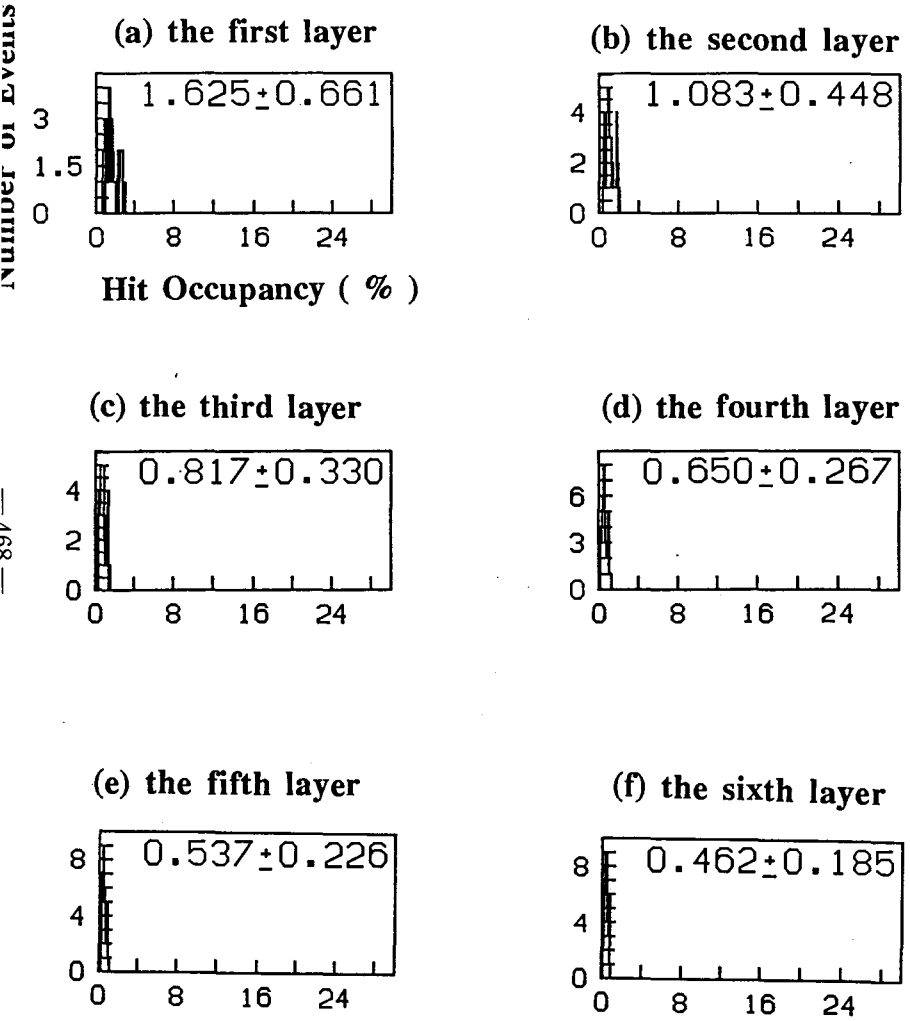

Fig.4

Maximum Number of Single Hits in a Segment for the QCD background events with Pt(jet) > 10 GeV/c

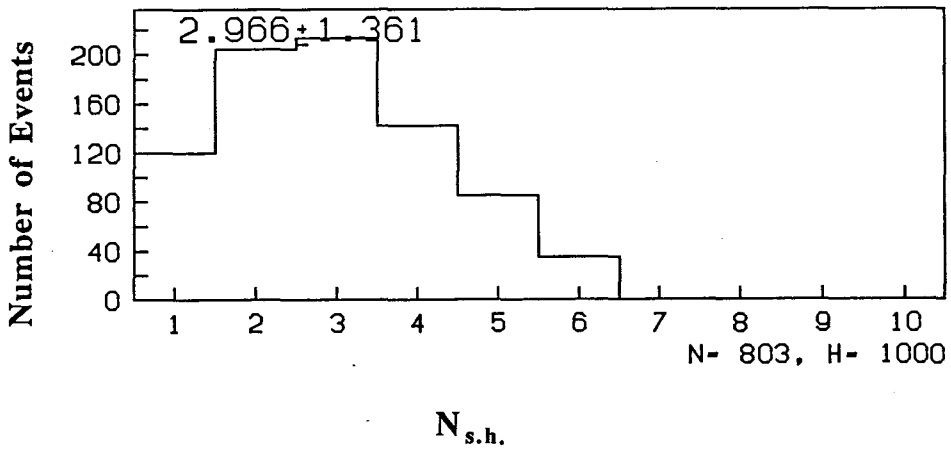

Fig.5

Event Rates with and without Isolated Track Trigger

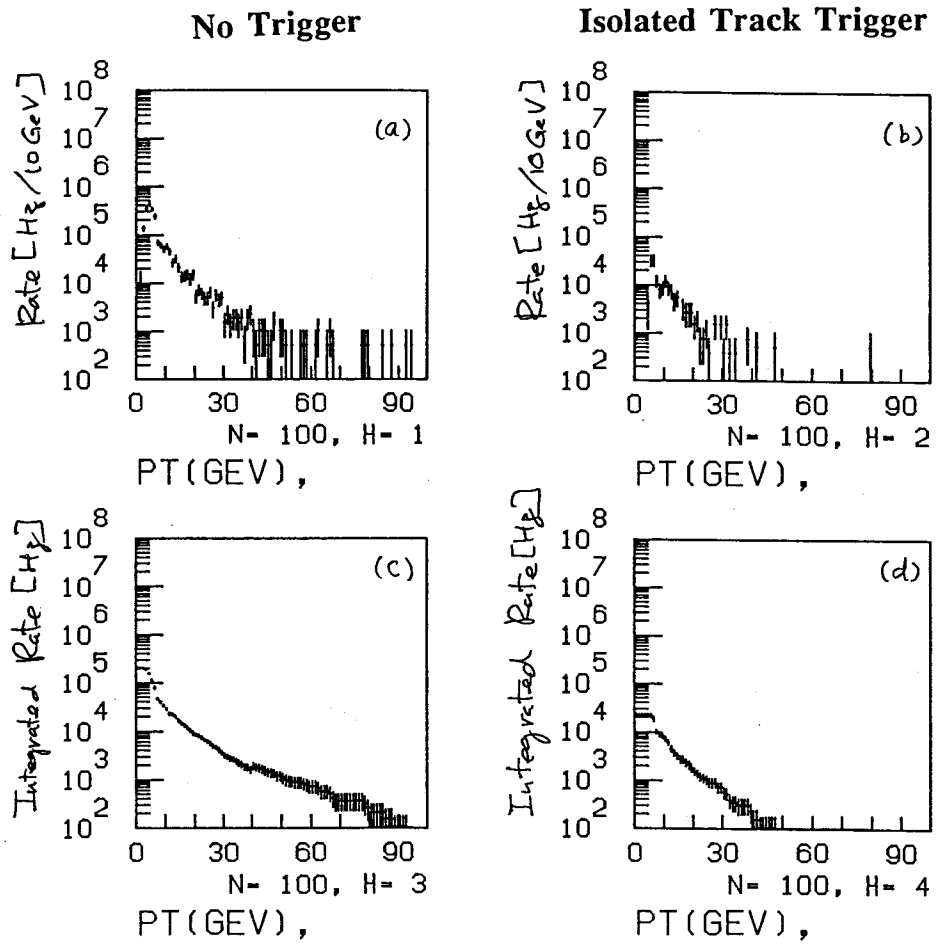

Fig.6

Higgs -> ZZ -> 4 μ's

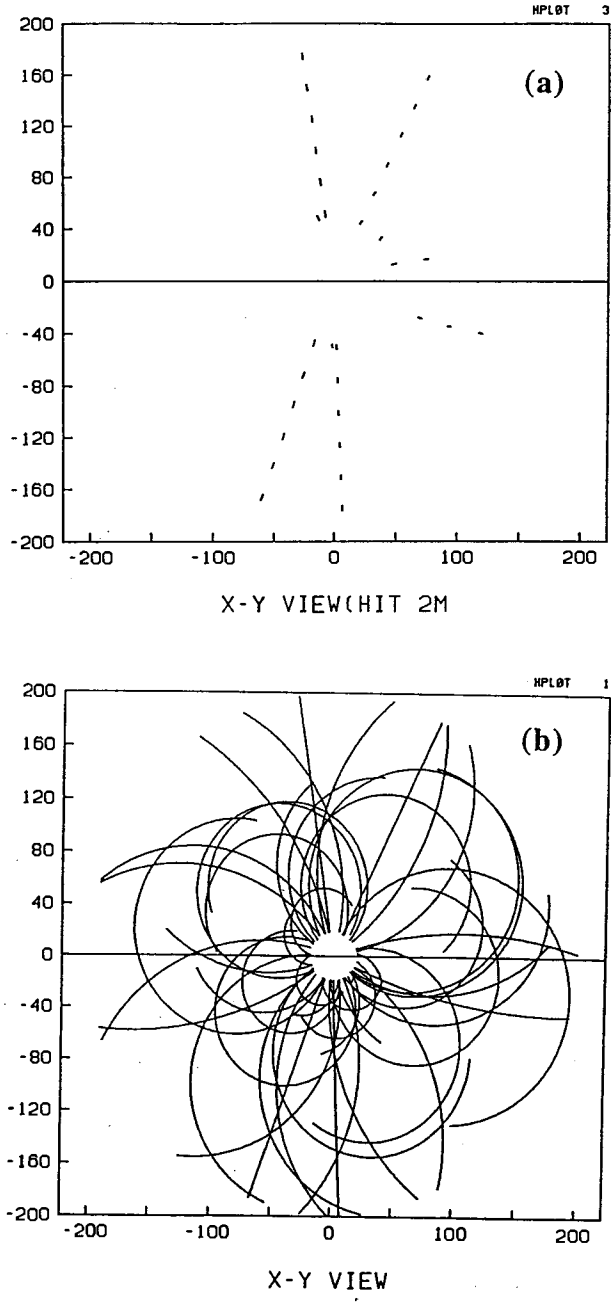

Fig.7

The Maximum Number of Single Hits in a Segment

(a) Higgs -> ZZ -> 4 μ's

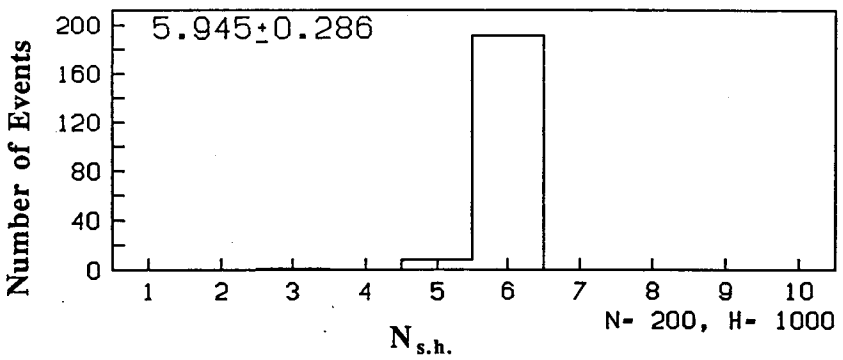

(b) W -> e ν

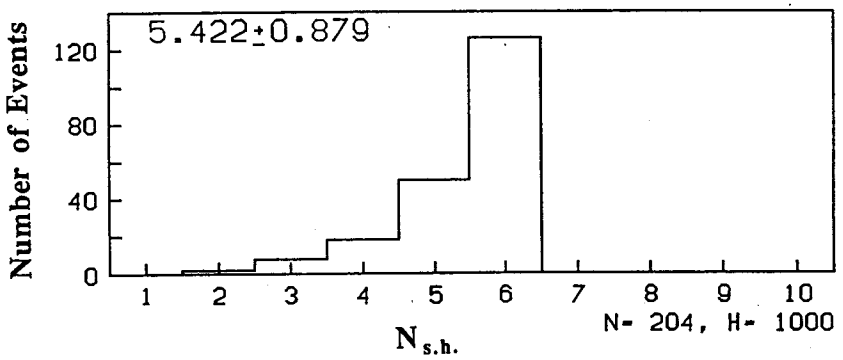

(c) Z -> e e

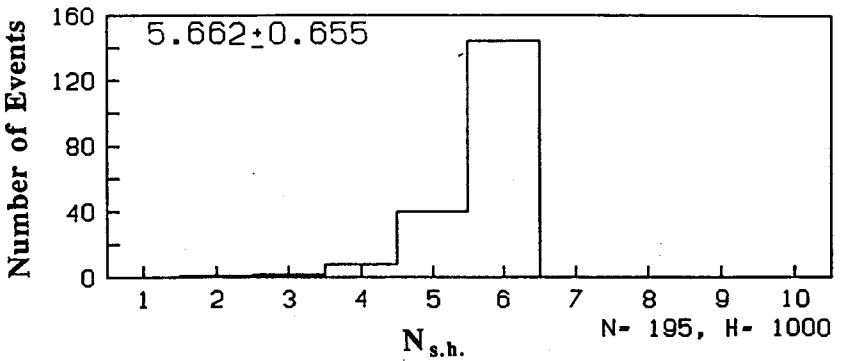

Fig.8

Synchronizer Development Update

J. Chapman
University of Michigan
Ann Arbor, MI 48109 USA

Introduction

As an outgrowth of work on the question of tracking and triggering options for drift tube devices in the SSC environments[1] , I discovered that very simple circuits could be implemented that held promise for first level triggering at the SSC[2] . These circuits were named "Synchronizers"[3] since they output a signal that is synchronized with the particle passage after a delay time equal to the maximum drift time of the cells used. This synchronized signal makes fast coincidence possible between axial and stereo layers for z determination and collision tagging for crossing determination. This presentation us an update of the program to explore the usefulness of these circuits and to construct versions of the circuit in Application Specific Integrated Circuits, ASICs. We have fabricated and tested at the most preliminary level, the first version of the circuit.

Circuit Concept

I will first review the features of the synchronizer circuit and then summarize the work of the past 8 months. The circuit accepts input from three 1/2 cell staggered layers of drift tubes. See figure 1 for two patterns of such tubes, the first (a) show the pattern as constructed from closely packed straw tubes and (b) shows the pattern manifest from rectangular tubes. The extreme pair of the three tubes are assumed to be radially aligned. In both cases the drift times that result from the passage of a straight track can be mathematically related. In the case of a linear drift-time distance relationship, the equation takes on the simple form;

$$t_2 + \frac{t_1 + t_3}{2} = T$$

where t_n is the drift time for the n_{th} tube and T is the maximum drift time. This equation relates the times from particle passage to the arrival of a signal at each wire. The goal of the synchronizer is to electronically determine and wait a time, t_{wait}, from the arrival of the last wire signal so that the total time from particle passage to the end of the wait period is always equal to a fixed time. This is electronically possible since the wait time can be calculated from the equation above using only drift time differences. When rewritten by adding and subtracting terms, the time equation takes on a form that exhibits a one to one relation to components of the synchronizer. This difference equation is of the form;

$$\frac{|t_3 - t_1|}{2} + |t_2 - \text{largest of}(t_3, t_1)| + 2t_{wait} = T$$

where t_{wait} is the time to wait from the last wire signal until the maximum drift time has been reached. The circuit to accomplish the synchronizer is shown in figure 2. The inputs labeled 1, 2, and 3 are assumed to be digital signals from the individual wire amplifier-discriminator circuits. They each set a flip-flop that retains the hit condition until reset. A discussion of the reset conditions appears later.

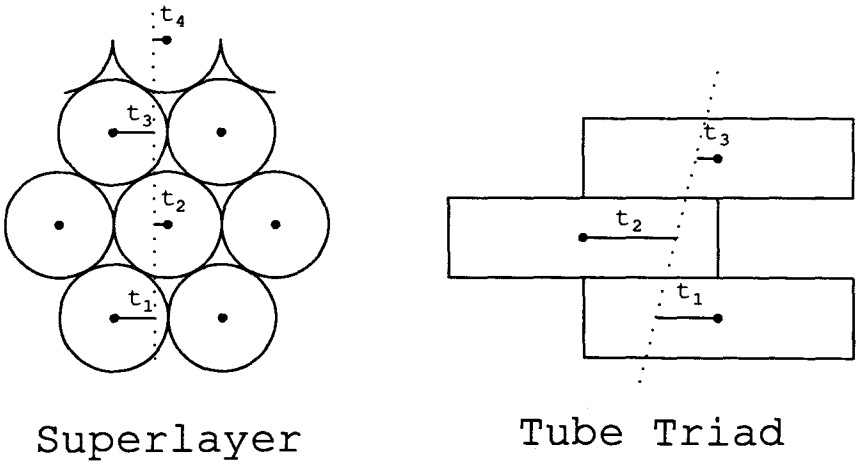

Figure1. Two forms of 1/2 cell staggered drift tubes, a) Part of a superlayer of straw tubes. b) Large high aspect ratio tubes typical of μ detectors at colliding beam machines.

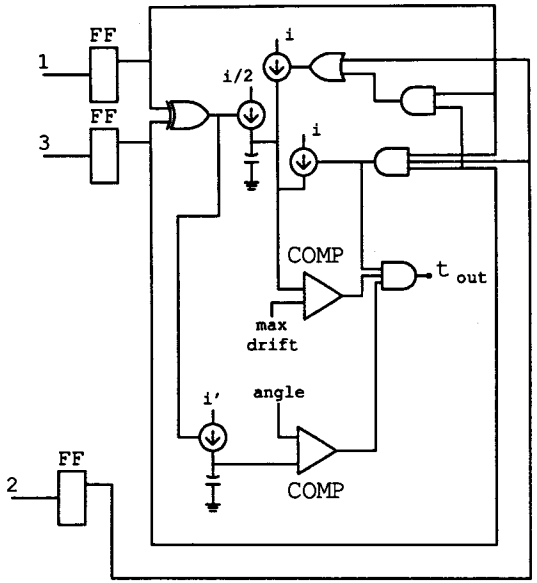

Figure2. The schematic of a synchronizer with circuitry for momentum selection. The auto-reset and auto-calibration are not shown.

The three terms on the left of the difference equation are computed separately by integrating current sources onto a common capacitor. The testing that the equation is satisfied is performed by the comparator that reaches its trigger threshold when the left terms equal the constant represented on the right of the equation. The three terms on the left have multipliers 1/2, 1, and 2 respectively. These terms will manifest as three different currents i/2, i, and 2i. As explained below, the current 2i is developed by adding i to an already active current i rather than switching off i and on 2i. The circuit is a generalization of a mean timer.

The time difference of the radially aligned pair is measured by integrating a current i/2 on a capacitor for the time between the arrival of the first of the pair and the second as given by the exclusive-or circuit. (Note also that this difference signal is used to gate the current i' onto a separate capacitor.) This part of the synchronizer computes the first term in the difference equations. The solution of the drift time equation is further pursued by the accumulation of the current i on the same capacitor beginning at the first of a) the middle wire signal or b) the last of the radially aligned wires. This corresponds to the second term in the difference equation. Logically this current should cease when the second of a) and b) arrives. However, for electronic convenience the current is left on so that the third term in the difference equation can be accomplished by the addition of a second current i rather than by the introduction of a current 2i accompanyed by the cessation of the current i. The calculation of the third term begins when all three signals have arrived. The comparator sampling the voltage on the capacitor reaches its threshold when the equation is solved. This occurs when the circuit has waited the appropriate time to extend the arrivals one maximum drift time from the particle passage.

Momentum Restriction and Auto-Reset

The second capacitor and its current i' provide for a programmable momentum restriction. The timing difference of signals on the radially aligned wires measures the track angle with respect to the chamber normal. This angle is linearly related to the track momentum for constant solenoidal fields. If the time difference between these aligned wires exceeds the threshold represented by the label "angle", then the output from the equation solution is blocked and no external signal is generated. The synchronizer will therefore output only when "stiff" tracks pass trough the tubes. The circuit resets , *i.e.*, the flip-flops are reset whenever the currently developing conditions are such that no output pulse will be generated. This occurs when the computation of the left terms reaches the threshold of the comparator without having all the tube signal flip-flops set and when the angle (momentum) inhibit has reached the blocking condition. Immediate activation of the reset clears uninteresting conditions and increases the live time for the high momentum tracks.

Auto Calibration

One potential problem associated with fast triggering with drift tubes in such great numbers as is implied in SSC detectors is the large number of circuits and the calibration

accuracy required. Another potential problem is the variability of the synchronized timing. Variations in gas pressure and temperature will change the drift time slightly. Circuit variations will also lead to output signal variations. The presence of non-linearity in the drift-time to distance relationship of gas tube detectors will also induce variations in the timing output of the synchronizers since the circuit is based on a linear relationship. To minimize the effect of these variations, a scheme of auto calibration has been proposed for the synchronizer and studied in simulation. In this scheme the two currents, i, are permitted to vary in a closed loop convergence cycle. Each current is modified until a specific condition is met.

A simultaneous pulse on the radially aligned pair of wires followed by a pulse on the 1/2 cell staggered wire at the maximum drift time later corresponds to a radially aligned track passing through the radially aligned pair. Such a pattern activates only the first current i. Adjustment of this first current to give the output at the maximum drift time (delay slightly through the circuit) represents the first step of the auto-calibration cycle. The simultaneous arrival of all three tube signals corresponds to a radial track positioned halfway between the wires. The timing of this track is representative of the half-cell drift time. In the circuit the two currents, i, are both active for the time from the half-cell time to the full-cell drift time. Adjustment of the second of the currents, i, to establish the output at the desired maximum drift time is the second step in the auto-calibration cycle. Adjustment of the currents for precise timing at the half-cell and full-cell drift time effectively removes all circuit non-uniformities and detector non-linearities as concerns. Figure 3 shows the effect of this current optimization. With the nominal currents the output timing variation rises with the fractional non-linearity in the drift-time distance relationship. With the optimized currents, it remains small up to non-linearity of 40%. The fractional non-linearity shown in figure 3 is parameterized as the magnitude of a quadratic term at the largest drift distance. The figure is for round tubes with 50ns maximum drift time.

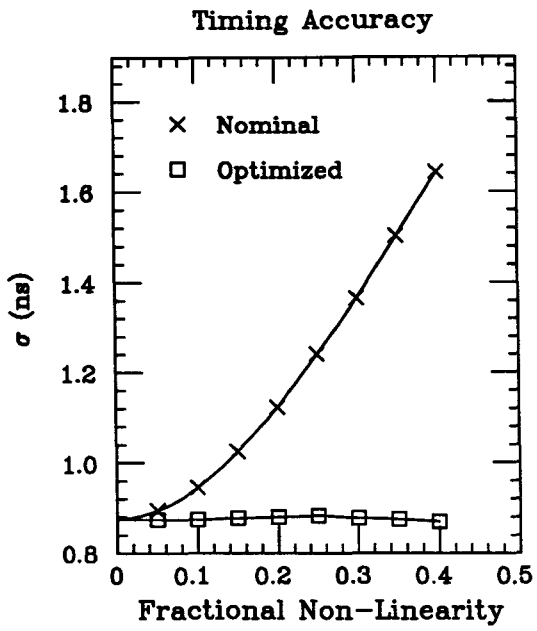

Figure3. The effect of drift-time distance non-linearities is shown for nominal currents and for auto-calibration adjusted currents. While the timing jitter shows a growth of σ with non-linearity in the case of nominal currents, no such growth is seen for the circuit where the currents are adjusted to minimize the timing variation for non-linear terms up to 40%.

Circuit Fabrication

The first fabrication of the synchronizer circuit includes auto-reset but does not include auto-calibration electronics. The currents are derived from external supplied voltages so that auto-calibration can be investigated through the use of external electronics. The circuit was developed on the Mentor Graphics CAD station and submitted to MOSIS for fabrication in 1.6μ CMOS. Figure 4 shows a simulation of the chip from MSpice on the Mentor for the case when all three wire signals occur simultaneously. Several internal points are shown in addition to the synchronizer output t_0. Upon return of the fabricated units the same signal conditions were applied to the inputs and the output signal measured

on the oscilloscope. Figure 5 exhibits the scope traces for this condition. The results track with amazing precision the simulation.

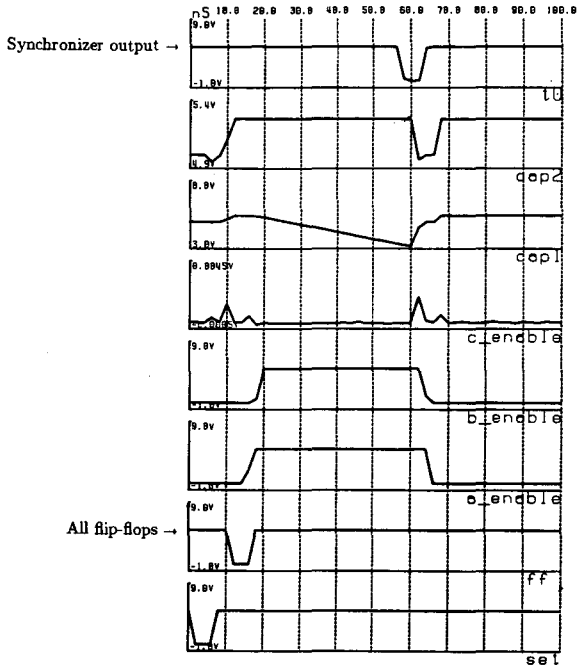

Figure4. An MSpice simulation of the synchronizer on the Mentor Graphics CAD station.

Future Plans

We will test the first versions of the synchronizers over a wide range of track positions and angles. In addition we will establish external logic for evaluating the auto-calibration requirement and from the results design an internal version of the auto-calibration electronics. The current version of the chip is designed for the short drift times of straw tubes. A second version of the chip designed to operate with long drift times up to a μsecond will be developed in parallel. This latter form will be tested with large high aspect ratio tubes of the kind used in μ detector systems. We plan to operate both long and short drift time synchronizers with real chambers in a cosmic ray stand.

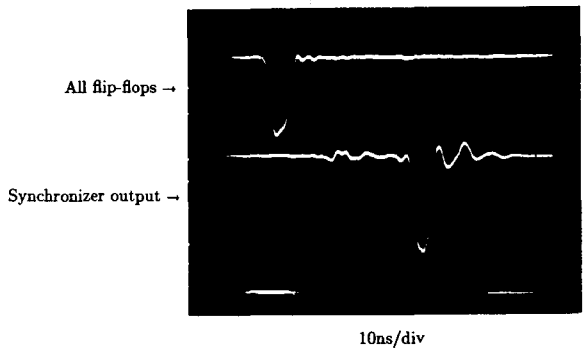

Figure5. A comparative measurement of the chip performance under the same conditions as in figure 4. The actual timing is essentially identical to that of the simulation.

REFERENCES

1. J. Chapman, Measurement of the Third Coordinate, Berkeley Workshop on Front-End Electronics for the SSC, March 6-8, 1989

2. J. Chapman, Drift Tube Synchronizers, Berkeley Workshop on Triggering for the SSC, June 13-16, 1989

3. Drift Tube Synchronizers, J. Chapman, University of Michigan Preprint, UM-HE-89-10, June, 1989

Let's Our Farm Grow
— on Its Scalability —

Minato Kawaguti Hajime Yoshida
Fukui University

May 31, 1990

1 Introduction

How can we grow our computer farm and get fruitful products?

1.1 Gazing into a crystal ball

Though it is hardly possible to "predict" future development of computer technologies, some common understandings on future efforts and trends may be shared[1].

- speedups of cpu chips
- development of parallel computing
  1. hardware technology
     - architecture, shared/local memory MIMD etc.
     - network communications
     - new technologies like Data Flow machines etc.
  2. software technology
     - operating systems after Unix
     - automatic parallel compilers (Fortran and C)
     - new parallel programming languages
     - CASE tools etc.
     - distributed operating system

In this note, we first have a sketch of our future farm, how it looks like in hardware's point of view. Then, we will discuss on its tools with which to cultivate the farm : operating systems and programming languages. Problems on software scalability will be discussed.

[1] See, for example, "Forcast of Electronic Technologies in the Nineties" edited by MITI Japan.
It is important to learn from the past. Almasi & Gottlieb : "Highly Parallel Computing". Benjamin.

2 Our Farm , Its Hardware

Speed requires that our farm will inevitably be a *multi-processor* and/or *multi-computer* system.

2.1 Words on multi-cpu systems

2.1.1 Multi-processor: UMA and NUMA

Multi-processor systems are those in which many cpus are co-working on a *shared memory*. They are further classified into two categories, according to their memory architecture :

- Uniform Memory Access (UMA)
  Single shared and global memory is implemented by a common bus or by a network of cross-bar switches. All processors have equal rights to access the shared memory.
- Non-Uniform Memory Access (NUMA)
  This system has a mixed memory architecture ; global memory to which all processors have a right to access and local memories private to individual processors. Usually it is implemented with a network of cross-bar switches to accommodate more cpus than in UMA.

2.1.2 Multi-computer: NORMA

Multi-computer is a set of node computers, each of which may be either a single-processor or a multi-processor with *independent local memory*. There is no global memory. It is also called NORMA (No Remote Access Memory Architecture). Relatively speaking, communication between the node computers is slow. If communication is implemented by Local Area Network (LAN), such multi-computers are now called distributed computers. But it is no longer true that communication speed is slower than the speed of bus, due to recent progress in optical fiber communications.

2.1.3 Why multi-X?

Our problems have well-known large-grain parallelism, which requires no such parallel computing if single cpu with its local memory can do the job within a limited time. The fastest RISC chips available now and easy to implement in mass (like R3000 and 88000) have about 20 MIPS (or about 15 VAX MIPS equivalent). They are apparently too slow for our processing unit. Some benchmark data will be shown later. Ten times faster chips will be available in the near future, though they require much harder implementation technology.

Our farm will be a kind of multi-computer which is composed of a network of node computers, each of which is, in turn, a multi-processor.

2.2 A Sketch of our Farm

2.2.1 Architecture

The farm will be a kind of *multi-computer*. Aggregate computing power of our farm is expected to be of the order of *one million Vaxen*. It will be true in 1995 that such a computing power cannot be provided by single or multi-processor UMA or NUMA. Multi-computer systems (NORMA) of loosely-coupled node processors will be required, even if communication among nodes will not be critical.

A possible architecture of the farm will be ;

- a node computer equivalent to about 1000 Vaxen, which is either
  - powerful single processor (improbable) or
  - a multi-processor system UMA (the candidate), NUMA
- connection among node computers, which will be implemented with either
  - industrial standard LAN like FDDI (desirable) or
  - specific methods like hypercube etc. or
  - SSC-specific faster connections
- connections to fast concurrent I/O.

  Scalable connections of the farm to fast I/O channels will be one of the most important and critical issues of hardware design. This should be completely transparent to the software of the farm. We assume this and will not touch on it here.

2.2.2 Hardware scalability

We expect that the dimension and power of our farm will expand in proportion to technological progresses and number of processors and/or computers to be added.

We can find typical examples of hardware scalability in some commercial systems of the second generation; Alliant's FX/2000 (UMA), BBN's TC2000 (NUMA) and Intel's iPSC/860 (NORMA). They all have scalable hardware: the number of cpus and I/O bandwidth (not for all). They are the second generation multi-processors or multi-computers in the sense that they are no more experimental but are targeted to general (though restricted) uses.

UMA type machines with peak scalar power of about several hundred MFLOPS are close at hand. This trend is and will be accelerated by speed-ups of cpu chips and multi-processor technologies. It is almost certain that we can get commercial GIPS-grade machines in the near future.

2.2.3 Scaling Factors

Computing power of our farm will scale up with three factors :

- Speed-up of cpu and memory chips
- Number of cpus of a node computer
  We hope that a node computer will be at least one thousand Vaxen equivalent. This may be attained with UMA.
- Number of nodes
  If node's power doesn't suffice to handle an event within a limited time delay, we will have to choose another architecture for our farm. This will be NORMA.

Now let's look into some of the above factors in more details.

2.3 Speed-up of CPU chips

From a users' or system-builders' point of view, this is the most profitable and the most efficient factor of power-up. From the point of view of software transparency and speed-up, we expect much of it.

2.3.1 Present RISC-based systems

Technologies developed on the mainframe machines and super-computers are and will be integrated on silicon ; pipeline, array processing, memory management and cache snooping etc..

Here are some results of simple benchmarks of cpu-bound jobs on available Unix systems. The systems visited by us are as follows:

- RISC NEWS : R3000 64 KB(Inst.) + 64 KB(Data) cache, 16MB Main Memory 4.3 BSD
- Titan II : (1 cpu) R2000 20 MHz (16 MIPS), 16 KB(Data) + 16 KB(Inst.) cache, 2K × 64 bit-word register file, 32 MB main mem. peak 16 MFLOPS (vector) System V + BSD
- IRIS 4D/220S : R3000 ×2 25 MHz UMA, 64 KB (Inst) + 64 KB (Data) cache/cpu System V + BSD
- Luna-88K : 88100 ×2 25 MHz UMA, 16 KB(Inst) + 16 KB(Data) cache/cpu, 16 MB main memory 20 MIPS/cpu 4.3 BSD under Mach, beta test version without Fortran compiler
- Sun 3/60 : 68020 16.7 MHz, 3 MIPS

Some additional data for Fortran programs are referred with respect to the following systems:

- Titan III : (UMA-type 4 cpus, vector processors) [2]
- NEWS 1750 : (68030 + 68882) 4.3 BSD [3]
- FACOM M-760/6 [4]

Multiplication of two matrices

Two matrices of 100 × 100 to 800 × 800 elements of floating-point numbers are multiplied. This is an optimistic case for vectorization as well as parallelization. Fortran compilers are used with available optimizers, including vectorizer(-O2) and parallelizer(-O3) for Titan III. For a large matrix, not only the cpu's speed but also the performance of Memory Management are relevant. User and system times are added for Risc News and News 1750.

dimension of a matrix	100^2	200^2	300^2	400^2	500^2	600^2	700^2	800^2
Risc News total time (sec)	0.6	5.1	22.5	65.4	137.4	228.6	381.2	623.7
Titan III -O1(1 cpu) (sec)	0.51	6.05	23.34	62.0	129.8	340.1	519.2	1222.9
Titan III -O2 (sec)	0.20	1.62	5.35	12.7	24.6	42.9	67.3	101.2
Titan III -O3 (sec)	0.12	0.62	1.91	4.5	8.6	14.6	23.4	35.1
M-760/6 cpu time (sec)	0.66	5.22	17.74	45.91	85.27	145.8	237.9	976.0
News 1750 total time (sec)	11.7	96.5	366.1	882.5	1766.1			

It is interesting to see that for some systems and for some compilers, measured times do not obey anticipated proportionality to the cube of the dimension of a matrix.

Function calls

This fortran code calculates $\sqrt{\sin^2 x + \cos^2 x}$ repetitively 10^6 times. Parallelization is easier than vectorization.

machine	time(sec)
Risc News usr time (sec)	14.1
Risc News sys time (sec)	1.7
Titan III -O1 (sec)	7.7
Titan III -O2 (vectorization) (sec)	3.7
Titan III -O3 (parallelization) (sec)	0.9
M-760/6 usr time (sec)	9.604

On the above examples, a system with R3000 is as fast as M-760/6, whose cpu power is about one fifth of M-780/2, same as a part of the Tristan main computer.

Mach system

Mach system (Luna-88K) is compared with Unix systems. Since the system we used is a beta test version, lacking a Fortran compiler C compilers are used.

[2]Data by Kubota Computer. Thanks to Dr. K. Asada for communicating these results

[3]Data by T. Takahama, Fukui University

[4]Data by T. Takahama and S. Iwahara, Fukui University

- *pi.c* evaluates π with the Monte Carlo method. One million pairs of uniform random numbers are generated, using random() function.
- *matinv.c* inverts a randomly generated matrix of 100 × 100 double precision elements with the sweep-out method.
- *vfft.c* is the Very Fast Fourier Transform of R.D. Preuss.

In the table below, all numbers are in seconds. Numbers in parentheses are indices of relative performance, where Sun-3/60's usr time is normalized to one. Also listed are the figures from the article on *IEEE MICRO* [5]. Dodoc measures scalar performance, where IBM 370/168's power is normalized to 100.

	pi.c	matinv.c	vfft.c	average	Dodoc
Risc NEWS	6.87 (14.3)	0.88 (23.6)	0.07 (19)	(19)	443 (26)
Titan II	17.77 (5.5)	3.15 (6.6)	0.27 (4.9)	(5.7)	nd
IRIS	9.22 (10.6)	1.05 (19.8)	nd	(15.2)	443 (26)
Luna-88K	12.28 (8.)	1.68 (12.4)	0.08 (17)	(12.3)	nd
Sun 3/60	98.0 (1.0)	20.77 (1.0)	1.33 (1.0)	(1.0)	17(1.0)

Luna-88K's results are obtained with single cpu, since no parallelizer is available now. We had no problem to compile and execute C codes on Mach (exactly speaking, Release 2.0). With its full implementation of 4 cpus, it will provide the peak scalar performance equivalent to M-780.

2.3.2 Future of RISC

RISC chips with super-scalar architecture provides us about 10 MFLOPS now. Further speed-up of C-MOS chips and those using ECL and/or Bi-CMOS technologies is announced by many chip makers. This trend is expected to continue for several years till saturation at about 200 MIPS will be attained.

Chips implementing technologies such as super-pipeline, super-scalar and VLIW (very long instruction word) are emerging, though software development and compatibility are a little left behind. We refer some RISC chips announced by manufacturers only to see the hot trends (these informations were gathered progressively. Some of the following project have been delayed already or abandoned):

- MIPS, R6000 (55 MIPS, working now), R8000 (160 MIPS, 1991), NEC
- Motorola 88110 (80 MIPS, 1990), 88K-compatible ECL (140 MIPS, end 1990)
- Sun SPARC BIT (50 MIPS?; 200 MIPS, 1993), Fujitsu
- HP PRISM(100 MIPS, 1991?),PA (1990), Hitachi(1991?)
- Intel N11 etc.

[5]"A Benchmark Tutorial", W.J. Price, *IEEE MICRO* pp. 28–43 October 1989

The most serious problem on implementation of ECL is thermal dissipation[6]. If ECL RISC will not be used massively in office environments, impetus to ECL will be weakened down and CMOS and Bi-CMOS will be prevailing. We hope that CMOS chips with 100 MIPS will be sufficient for us, if used in UMA type system.

Chips of GaAs may not be so superior to silicon chips [7].

2.3.3 Multi-cpus on a wafer

Speed-up of cpu chips realized mainly by silicon technology and technological transfer of large machines will be saturated before about 1995 at about 200 MIPS. Further progress will be searched in parallelizing cpus on a ECL bus on a wafer. Project such as MIPS-X and Intel's MICRO 2000 are very interesting, when auto-parallelizing compilers will be developed for practical use.

2.3.4 CISC

Architectural borders between RISC and CISC become more and more indistinct. Though slowly, CISC chips are catching up RISCs' speed. As technology of several millions of gates is and will be available, we will have CISC chips with top RISC's speed. The most appealing point of CISC chips is their software compatibility.

2.3.5 Direction of our efforts

Progress of chip technology will assure us with the single largest factor we can expect in the near future. Thus, it is and will be the most critical point where our *hardware efforts* should be concentrated. For implementation of such ultra-fast cpus, many technical mastery such as fast cache memory (maybe two stages or even more complex), fast bus (specific ECL bus or standard futurebus+ etc.) is imperative. As speedup will be severely limited by power consumption, cooling problem must be attacked very seriously.

2.4 Multi-processors

In our farm, a node computer should be capable of processing one event within a specified time delay. When main factor of speedups come from exploiting medium and fine grained parallelisms, they are implemented only within a UMA or NUMA multi-processor node.

[6] We have heard that air flow cooling is efficient under around 20W/chip, while convection by liquid is adequate up to about 50W/chip. New cooling technologies is required above.

[7] According to Amdahl's paper, GaAs HEMT, compared with Silicon, is slower than Si-ECL at room temperature, consumes more energy at equivalent speed, is more radiation-resistant, and works at liquid nitrogen temperature. So GaAs is expected to find its fields in harsh environment. So, SSC is not a harsh environment for computers?

2.4.1 UMA

Current UMA multi-processors are implemented on common buses or cross-bar switch networks. Multi-processor systems may offer us a factor of several tens improvement over a single processor performance. The limit comes from bus saturation, shared memory contention, inter-process communications and/or by the nature of the problems to be solved (algorithms). But it is based on a well-proven technology and will provide us with a reasonable speed-up factor. Important technological elements of UMA-type multi-processor are memory management and cache coherency. Recent cpus like 88K and 68040 have fairly large cache and cache snooping mechanism as well as advanced memory management for multi-processor applications. VME boards with four cpus are available now.

UMA-type workstations with more than 60 MIPS are commercially available now. So, we have UMA computers which are connected via LAN. This may be a starting model of our farm. We expect that many commercial systems are to come in the near future. When wafer-scale integrations of multi-cpus and shared memories will be implemented, such *UMA-on-a-chip* will be an important component of our node. All experiences on present UMA machines will be applicable to it.

2.4.2 NUMA

NUMA-type machines (like BBN TC2000) are also interesting due to large number of cpus connected via network. But they are certainly much more difficult to build and program.

2.5 Multi-computer

In NORMA machine, number of nodes is not difficult to increase, when inter-connection is well-designed. Scalability depend on the speed of inter-connections, too. Communication speed must be proportional to node's power, so that NORMA can execute fine-grained parallelisms. We hope that

- Heavy-duty NORMA system will not be necessary.
- Present trend in "distributed computing" on LANed workstations will provide us useful experiences.
- Future development of communication like FDDI and HPX will offer natural extensions of LANed "distributed programming".

3 Our Farm, Its Software

3.1 Problems on portability

First of all, big real programs must run on the farm. They are developed on a workbench which is offered by Unix and cross-developed codes are ported to the farm. As the on-line filtering

programs are demanded to be more powerful and yet error-free and their development is only possible on a large machines with full computing power and playback capabilities, *portability* is the real problem. Such a cross-development procedure will be best facilitated, when the farm and the workbench use the same cpus. It should be noticed here that our farm cannot be a kind of embedded systems without operating system.

The ***absolute minimum*** requirement to the farm is that it should be run under the same operating system as the workbench.

This requirement poses us two problems.

- The first problem is the choice of the platform, i.e., the operating system.
- Second is the way of programming.

3.2 Issues on software scalability

To be scalable, users programs should be independent on hardware "details" such as :

- the number of processors and computers
- how the processors are connected
  - tightly coupled multi-processors
  - multi-computers
  - LANed computers

Such a scalability should be supported by

- run-time libraries of distributed or parallel operating systems and/or
- "intelligent" programming languages[8] and/or
- "intelligent" programmers (last choice!)

If such a programming environment exists, any program written for single processor can run on any type of multi-computers without rewriting it (recompiling may be required). This does not necessarily mean that existing Fortran programs can run on multi-computers. A program written following some specifications can be scalable under such an environment, which is a common situation for parallel computing.

We can see the most successful examples of such environments in some commercial multi-processors (UMA or NUMA). They have, for example, symmetrical Unix and automatic parallelizing compilers. Unix offers only user interfaces. Switching of processes and mapping of processes on processors are performed automatically by hardware. After the success of automatic vectorizing compilers, much efforts are devoted to automatic parallelizer also. Such a compiler permit us to realize parallelism at a fine grain level, such as parallelizing a do loop body, without modifying existing codes. As is usually the case, some touch-ups or larger modifications are required to achieve better performance gain.

[8] H. E. Bal. J. G. Steiner and A. S. Tanenbaum Programming Languages for Distributed Computing Systems *ACM Computing Surveys*, Vol. 21 No. 3 (1989)

3.3 Platform : The Operating system

We have proposed to choose Mach as our common software platform[9].

3.3.1 Unix

All supercomputers and mini-supercomputers are run under Unix. For program development and verifications requiring cpu powers, we have no choice but to use Unix. Unfortunately, Unix is not only ill-suited for on-line programming but also is now suffering for its old design (optimized for a small memory and single cpu system). Its monolithic, centralized design and implementation are now a heavy burden.

3.3.2 Mach

New operating system designed intentionally for multi-processors, large address spaces and networking is now available; Mach[10].

- support of networks of processors
- message-based efficient IPC (Inter Process Communication)
- advanced and efficient VM (Virtual Memory) system
- perfect compatibility with 4.3BSD Unix
- small-sized kernel (kernelized kernel)

The most important aspect of Mach is, without doubt, its advanced VM system. It provides open interfaces so that even the pager is implemented as a user program. With Mach's open policy, this sort of hardware independence is quite useful for the farm. We can imagine a private pager with which full sparse data space can be efficiently addressed.

Mach offers a user interface which is pure 4.3BSD. So we can shift from Unix to pure Mach gracefully. Though the situation around the future Unix is unpleasantly confused for users. OSF/1 has adopted Mach Release 2.5 as its kernel and products are awaited soon. This fact guarantees nothing, but the commercial acceptance of Mach is a good news for us, since it is lacking many tools.

Mach offers us basic tools of programming UMA type systems and provides basic functions for NORMA systems. Now we are working on a two-cpu (88K) Mach system with Release

[9] "Software for the Processor Farm" September 1989

[10] M. Acetta et al., "A New Kernel Foundation for UNIX Development" 1986. Technical Report. School of Computer Science. CMU

2.0 (soon 2.5). In 1991 when Mach release 3.0 will be available, this Mach will become the so-called kernelized (or de-kernelized) kernel. Many functions, traditionally included in the operating system, are to be implemented as user tasks. Unix 4.3BSD interface will be served by multi-task Unix servers. Network services will be done by another task running on the kernel as a user task. Then, we will have all basic tools (such as network server, RPC services etc.) for UMA as well as NORMA process communications.

Its real-time (RT-Mach) and fault-tolerant (T-Mach) versions will be available in 1991. We propose to commit ourselves now to this promising platform.

3.4 Parallel programming

Second problem is the way of programming. People have been working over past thirty years to use parallel systems. Vector machines demonstrated their capabilities as well as their limits. Parallel machines are also well-known for its software non-scalability. Amdahl's law on parallel computing is the pessimistic case[11]. However, in such fields as Computational Fluid Dynamics, this spell was broken by encouraging examples. We have now a much more optimistic prediction; Moler's Law[12]. He says that sequential part of a big program may become smaller as its size increases. Thus, software scalability is not a dream but a reality for some kind of problems which require fine-grained parallelism.

We are not allowed to expect such happy cases. However, there may be cases where vectorization is difficult but parallelization is efficient. We hope that a modest gain of speed of about ten may not be very difficult for our problems, if we use UMA type machines.

All second generation UMA, NUMA machines are equipped with auto-parallelizing compilers. Recent progress in parallel programming is an advent of CASE tools and new languages for NUMA and NORMA type machines with a large number of processors. NORMA type machines are expected to become less difficult to program with such tools.

3.5 Software scalability

For speed-up, we will have to go further to exploit smaller-grain parallelism. However, software is hard to scale. This is a challenging job with a high reward. So, the most important motif: *software scalability and transparency.* How can we achieve scalable programs and software transparency to hardware's expansion? In another word, programs written on present-day computers can be run on our future multi-computer farms without any modifications and thus gain speed-up accordingly?

3.5.1 Speed-up of single-cpu computers

This factor has a very strong merit : almost 100 % [13] *transparent to software.* It also provides a *completely proportional scaling* in software without any modifications. As seen already, we can expect as much as a few to several hundreds MIPS in about five years to come.

[11] *Int. Jour. Supercomputer Applications* Vol.2 No.1 1988, *Limits of Expectation*

[12] *Communications ACM* Vol.31 pp532 1988

[13] If manufacturers are always vigilant for it.

3.5.2 Auto-parallelizer on UMA

Then, we think of moderately multi-processor UMA. The number of cpus sharing a global memory may be limited to about ten. This sector has been and is the favorite target of research and commercial implementations of cheaper super-computers. One can observe that many multi-processor systems have been implemented to be overwhelmed by much more powerful single processors. Nevertheless, this will be certainly our option, since speedups of single cpu chips will be saturated sooner or later.

Software transparency is a serious problem to be solved. Many valuable experiences have been reported on this type of machines which are to be studied carefully not to repeat errors and not to fall into many pitfalls.

Commercial systems such as IRIS, FX/2800 and others have modified Unix into a symmetrical one. Mach is now a promising operating system best suited for UMA, though it has not yet implemented symmetrical Unix interfaces[14] .

Automatic parallelizer may be available on commercial machines. On UMA multi-processors equipped with auto-parallelizer, we have little hesitation to step forth in this direction of parallel programming. We have many works to do in this respect. Though execution speed may not scale completely in proportion to the number of cpus, modest gain may be expected.

3.5.3 NUMA

As for NUMA machines, scalability is usually much more difficult to achieve. In this respect, a pioneering work of W. Celmaster of BBN of parallelizing EGS4 codes for TC2000 is interesting[15].

3.5.4 NORMA

As for NORMA machines, way is certainly long. Do we really need such a difficult-to-program machine? We will wait and see courageous users of the second generation NORMA machines?

We will have to implement about a thousand of nodes to achieve one million Vaxen. Progress in hardware for NORMA machines is promising, while software can catch it up with pains. The nature of parallel computation of NORMA systems is quite different from that of UMA multi-processors. Fine and medium grain parallelism will be difficult to achieve. Such a situation is changing with faster communication between nodes.

There are plenty of business to be completed on it. We have no operating system available now. We can even say that our aim of processor (node) utilization by processes is not similar to that of operating systems. Equal right among processes is not our business. We demand

[14] D.L. Black "The Mach cpu_server: An Implementation of Processor Allocation" CMU August 1989

[15] See "Interactive Radiation Transport Simulation on the BBN $TC2000^{TM}$ Parallel Computer EGS4: A Case-History" March 7, 1990.

the fastest turn-around time. For that, some processes will be blocked without available resources.

Then, we have a problem of mapping : mapping of processes to processors. Clustering of computers and burden sharing are important software problems. Whether the mapping is transparent to programmers or is to be handled directly by programmers? When transparent, mapping is under OS's control and is optimally used for OS's sake. If we demand hand-made mapping, we must devise some method of software scalability to be independent on the number of nodes.

Large-grained parallelisms such as macro-pipeline and macro-data flow can be treated therein without communication burdens, though such a parallelism will not involve many computers. So, if a node's power is not enough to handle an event within a limited time, a cluster of nodes can cooperate. This kind of programming will be also our important business. We need powerful software tools for that. Automatic RPC generators, program analyzer etc. Again, the second generation commercial NORMA systems are equipped with modern CASE tools for parallelizing codes.

After all these thinks on NORMA machines, we will finally make our mind that we should use "de facto" industrial standard. We have as yet no standard "distributed operating systems". In this field too, the situation is rapidly evolving. It is likely that NCS will be the industrial standard for network computing. It is the standard of OSF/1, at least. NCS is based on RPC (Remote Procedure Call). Mach has basic interfaces to implement RPC between independent computers. We can start with LANed workstations for such a study.

Another subject to keep watching is Linda[16]. It supports "shared data" on NORMA-type systems. Its transparency to hardware and ease of realizing parallelism for a certain class of problems (many workers doing similar jobs etc.) may be interesting, if I/O to the Tuple Space become much faster.

4 Let's Grow Our Farm

In any way, parallelism is the way we go. We have and will have to get necessary tools which are and will be the (de facto) industrial standards.

And then, let's cultivate our farm and fill it with parallel programs.

[16] "Domesticating Parallelism" D. Galerntner *IEEE Computer* p. 12 August 1986

Summary of Discussions on Strategies of R&D efforts

19:50 - 22:30 April 24, 1990

Y. Watase (KEK)

After the parallel session of the electronics, trigger and data acquisition subgroup, a meeting has been arranged for further discussion on strategies of R&D for electronics and data acquisition. About 25 people gathered on the evening of April 24. Two discussion leaders chaired the following major topics.

Thema 1. Strategy for R&D of the frontend electronics .. Hugh H. Williams (Pennsylvania)

Thema 2. Strategy for R&D of computer farm ..... Irwing Gaines (FNAL)

The following is the short summary of the discussions.

1. Strategy of R&D for the frontend electronics (LSI)

S.Inaba(KEK) made a short comment on an analog sampling chip under development at KEK with a switched capacitor scheme.
M. Tanaka(KEK) also reported on various ASIC activities at KEK, such as shaping amplifier for multi-anode PMT, time to analog converter, charge to amplitude converter, and constant fraction discriminator using various analog master slice.

The many efforts for LSI developments are under way in US, Japan as well as in Europe. These include the readout chips of silicon strip detector, straw tube detector, various types of calorimeters. Some of them are showing promising performance electronically. The others are under process of improvement. There are, however, no coordination for the individual development so far. The information exchange and some coordination were remarked to be necessary for the future integration. On the point of view of radiation damage of the frontend electronics, several trials of the radiation hardened process have been reported. And possible silicon foundries are under collaboration in US. Some frontend chips of bipolar can survive for the radiation dose of order of Mega rad..

In conclusion, the development of individual readout LSI is under progress at the right pace. But these have been desinged as a part of the real frontend from pre-amplifiers to the first level buffers. For the further development of LSI's which include the second level buffers, the data acquisition architecture and system integration scheme must be designed in detail in cooperation with data acquisition and trigger subgroups.

2. Strategy of R&D for the computer farm

H. Yoshida (Fukui) talked about development of the computer farm with the title of "Let's our Farm Grow on Hardware and Software Scalability".

The computer farm is one of the key elements of the data acquisition and processing in the SSC experiments. The farm for high energy physics experiments has been built in SLAC and FNAL in the 1980's. But in the recent years, various companies provide multi-CPU parallel computer system based on the high performance microprocessors. The rapid and continuous R&D must be required to keep the up-to-date technology in our use. However, the reality is that it is impossible to use currently advanced CPU chips within a comparable leading time with the venders. For example, Intel will release 100,000 MIPS parallel computer system within two years. Then, one of the things to be done by ourself is a development of the software system to utilize the parallel computer farm efficiently. For the accumulation of the know-how, we need to use extensively various parallel computer farms.

The large capacity of the data I/O is a specific requirement for the farm system in the application to high energy physics experiments; online and offline data processing. The I/O capability is greatly dependent on the hardware design and the communication software. This point should be discussed in future and some type of R&D will be required.

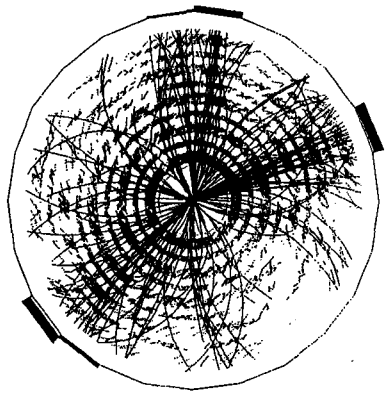

Parallel Session: Physics, Computing, and Simulation

April 24, 13:30-17:45

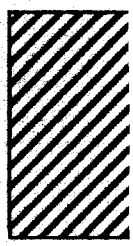

Simulation activities in US

L. Price
ANL

(No written contribution received)

MINIMUM BIAS AT 40 TEV

Michelangelo L. MANGANO

Istituto Nazionale di Fisica Nucleare
Scuola Normale Superiore and
Dipartimento di Fisica, Pisa, ITALY

The total rate of inelastic interactions at 40 TeV will be of the order of 100 *mb*. At the nominal luminosity of $10^{33} cm^{-2} sec{-}1$ this implies an interaction rate of 10^8 Hz, or 1.6 interactions per bunch crossing, with the nominal bunch spacing of $16ns$. At higher luminosities, the average number of overlapping events will increase accordingly.

Even though one can argue that this physics is not interesting *per sé* (and this conviction is by no means universally accepted), the structure of these so called minimum-bias (MB) events has important consequences on the performance of the apparatus, on the feasibility of important measurements and on the features of important new physics signals.

We still cannot predict in a fully credible way the properties of MB physics from first principles, and we have to rely on phenomenological models arising from the analysis of currently available data. It is important to understand how far our predictions are from reality, in order to understand the margins we have in detector development and in planning important measurements.

Pile-up of events within one bunch crossing, or integration of events over various bunch crossings could in principle deteriorate energy resolution, electron identification, lepton triggers and so on. These issues require an understanding of the transverse energy distributions and fluctuations in the MB events that will overlap on top of the interesting physics. The large multiplicities associated to the presence of multiple interactions make tracking in a solenoidal field problematic, both online (triggers) and offline. This issue requires understanding the multiplicity distribution and p_T spectrum of the charged particles. The p_T spectrum, in particular, will define the radius of maximum occupancy in the tracking system of a solenoidal detector.

During this Workshop [1] we saw how with reasonable assumptions on the structure of the pile-up events and on the wave form simulation most of these problems can be avoided with luminosities of the order of 10^{33}, and can be kept under control perhaps up to the 10^{34} threshold. How far one can go before running into serious problems will depend, among other things, on the precise features of the MB events.

One sector which can still be seriously affected by our ignorance of the MB is the understanding of the underlying event in high-p_T processes. When the hadrons collide giving rise to a large Q^2 process (say Higgs production), in addition to the radiation emitted by the evolution of the initial- and possibly final-state partons we will have the particles coming from the interactions of the left-overs of the hadrons themselves. If the energy released in the hard process is, say, 2 TeV (as would be reasonable for the production of a heavy Higgs with some kinetic energy and initial-state radiation), the energy available to the remnants of the hadrons for their collision is 38 TeV, still a remarkable amount. It is reasonable to assume that this interaction is analogous to a MB interaction, even though it is by no means proved. The ability to apply cuts on the underlying event, such as cuts on the total multiplicity, in order to eliminate possible backgrounds, rests on the ability we have to properly predict the structure of the underlying event itself. As an example in which these cuts can be useful and have been studied, we indicate the separation of the $H \to ZZ \to e^+e^- jets$ signal from the ordinary QCD $Z + jets$ background [2].

Today's common lore on MB events indicates the existence of two components, one soft and one *semi-hard*. The soft component obeys KNO scaling as far as multiplicities go, and predict an exponential spectrum for the p_T distributions. The rapidity distribution has a large plateau, which is mostly of kinematical origin. Total cross section, $dN/d\eta$, $\langle p_T \rangle$, etc. evolve with s in a logarithmic way.

The semi-hard component originates from partonic processes with a Q^2 scale large enough to justify the use of parton models, but small enough to give rates of the order of the *mb*. It is usually described by QCD $2 \to 2$ scattering with a partonic p_T larger than a given threshold p_T^{min}. This component violates KNO scaling, as multiplicity distributions in QCD behave like negative binomials, and gives a power-like decay of the p_T distributions.

It is believed that all of the hadronic inelastic cross-section can actually be described by these semi-hard processes, already at energies like ISR, $Sp\bar{p}S$ and Tevatron [3]. KNO scaling and exponential decay of the p_T spectrum observed at these lower energies are due to saturation effects which inhibit the otherwise diverging growth of the semi-hard cross-section at very small p_T. These effects are understood within the study of the small-x behaviour of QCD.

If this picture is correct, we can predict the structure of MB events, and then of the underlying event in high-p_T processes, by just studying QCD scattering with p_T^{min} of the order of the saturation threshold, which for SSC energy is of the order of 5 GeV. For this value of the transverse momentum the semi-hard cross section is of the order of 100 *mb*.

In this note I will collect some important inclusive distributions for MB events obtained by assuming the two extreme cases in which MB is either totally dominated by a soft component, or totally dominated by the semi-hard component. Reality will probably sit in-between, and therefore a reasonable range of expectations can be obtained by superimposing the distributions for the soft component with those for the semi-hard one with the proper relative weights.

The description of the soft component is obtained by a phenomenological model developed by Marchesini and Webber [4] and inspired by the UA5 Montecarlo. The parameters fit low energy MB data, and evolve logarithmically with s. The generation and evolution of the semi-hard processes is obtained by running QCD $2 \rightarrow 2$ scattering on the Marchesini-Webber Montecarlo Herwig [4]. Even though this hadronic MC has been shown to reproduce well Collider data at current energies, there is no reason to believe that the MC is suited to properly describe the critical small-x behaviour which is important in understanding these low-p_T phenomena. A new version of Herwig is being developed , which will contain the most recent understanding of small-x evolution. It will be important to check how the results presented here will change when this new MC will be available.

To start with, in Table 1 I give the values of the total inclusive cross-sections for QCD $2 \rightarrow 2$ processes with different p_T^{min} thresholds. These numbers are only indicative, as different choices of structure functions, corresponding to different choices of gluon parametrizations and small-x evolution, will give results varying within factors of 2 or more. The structure functions chosen here were EHLQ set 1.

p_T^{min}(GeV)	3	4	5	6	7
σ_{tot}(mb)	200	120	80	55	40

Table 1: Inclusive semi-hard cross-sections

In the following Figures I will display distributions for three different choices of underlying event: the soft component described earlier (dotted histograms), a semi-hard component generated with p_T^{min}=4GeV (solid histogram) and with p_T^{min}=5GeV (diamonds).

In Fig. 1 I show the charged multiplicity distributions (all charged particles within ± 5 units of pseudorapidity and with no p_T cut).

Fig. 2 shows the p_T spectrum of these charged particles.

Fig. 3 shows the multiplicity distribution of charged particles as a function of rapidity. In this case, apart from a scale normalization factor due to the larger multiplicities of the semi-hard component, the shape of the distribution are similar for soft and semi-hard component, a reflection of the kinematical nature of this variable.

Fig. 4 contains the distribution of average transverse energy as a function of rapidity. The rapidity is parametrized by the 'tower' number, from 1 to 15, corresponding to 15 annuli covering the full azimuth and 0.4 units of rapidity wide each.

Fig. 5 shows the average energy deposited in towers of size 0.4×0.4 in $\eta - \phi$ space. This tower size correponds to the a typical cone size used for electron isolation cuts, *i.e.* $\Delta R < 0.2$.

Fig. 6, finally, shows the transverse energy density per unit of rapidity per radiant, averaged within ± 3 units of rapidity. Notice that the semi-hard component has more than twice the amount of transverse energy as the soft component. Furthermore the distributions are rather wide, and one would expect fluctuations of the order of the GeV per unit of rapidity per radiant per event. Therefore 10 overlapping events would give rise to fluctuations of the order of 1.5 GeV within a cone of radius 0.2. If the 10 events were to belong to the same bunch crossing, as is the case at luminosities above $5 \times 10^3 3cm^{-2}s^{-1}$ these fluctuations could deteriorate electron isolation.

References

[1] See talks by H. Iwasaki, H.H. Williams and Y. Sakai at this Workshop.

[2] H.F. Sadrozinski, A. Seiden and A.J. Weinstein, in *Proceedings of the 1988 Snowmass Summer Study*, p. 124, ed. S. Jensen, World Scientific, (1989).

[3] E.M. Levin and M.G. Ryskin, Sov. Phys. Usp. **32** (1989), 479.

[4] G. Marchesini and B.R. Webber, *Nucl. Phys.* **B310** (1988), 461.

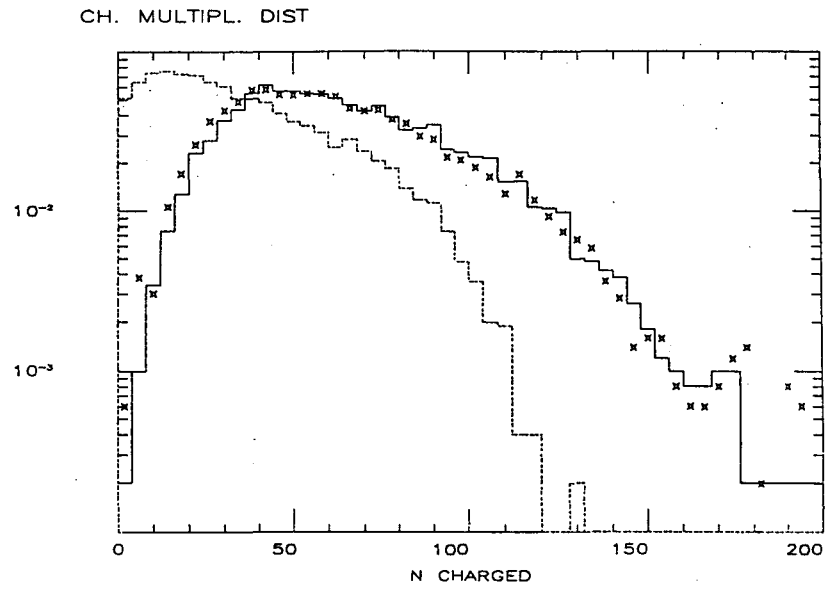

Figure 1

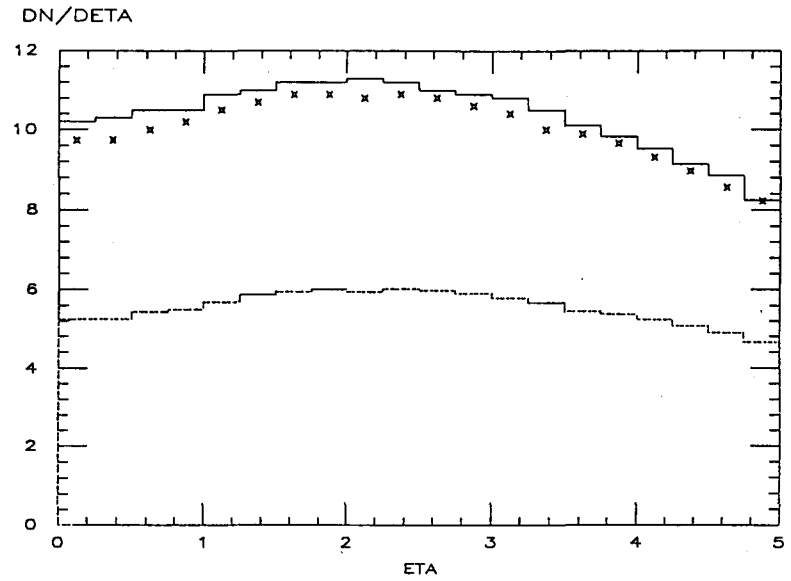

Figure 3

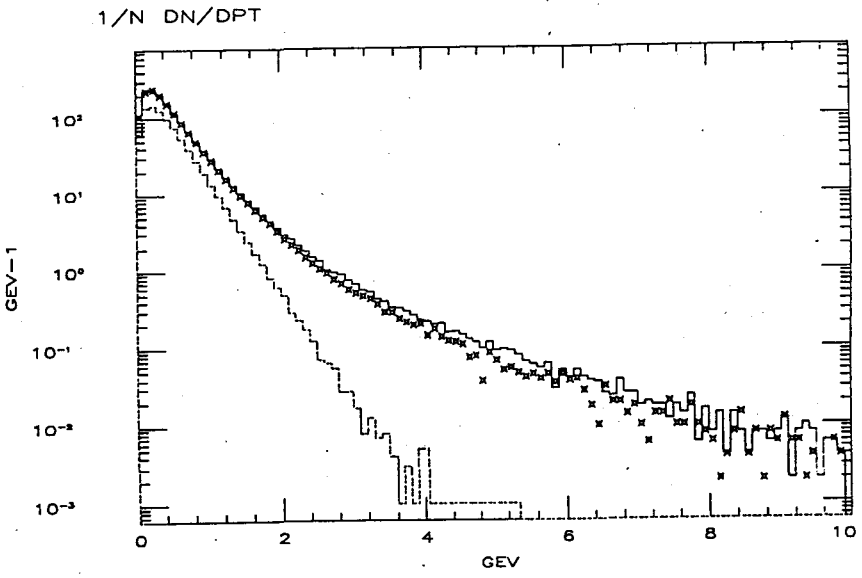

Figure 2

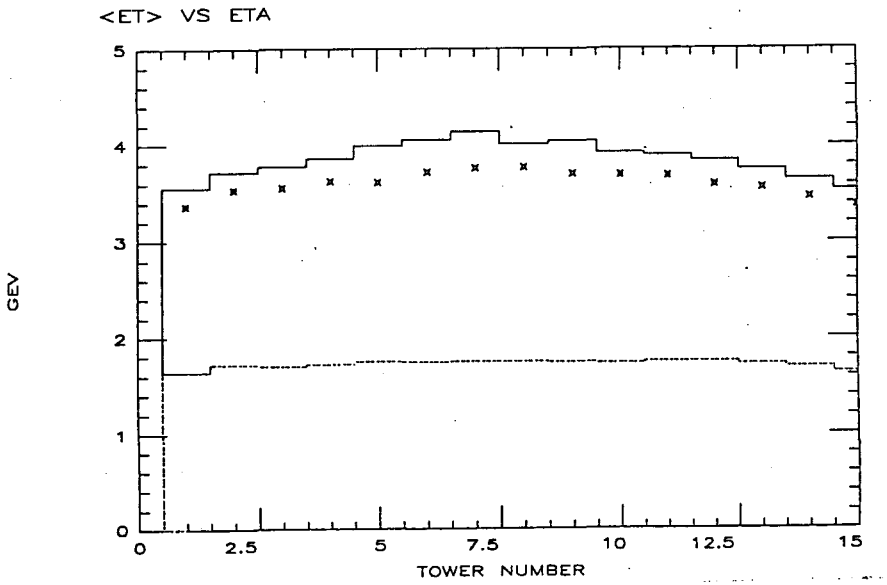

Figure 4

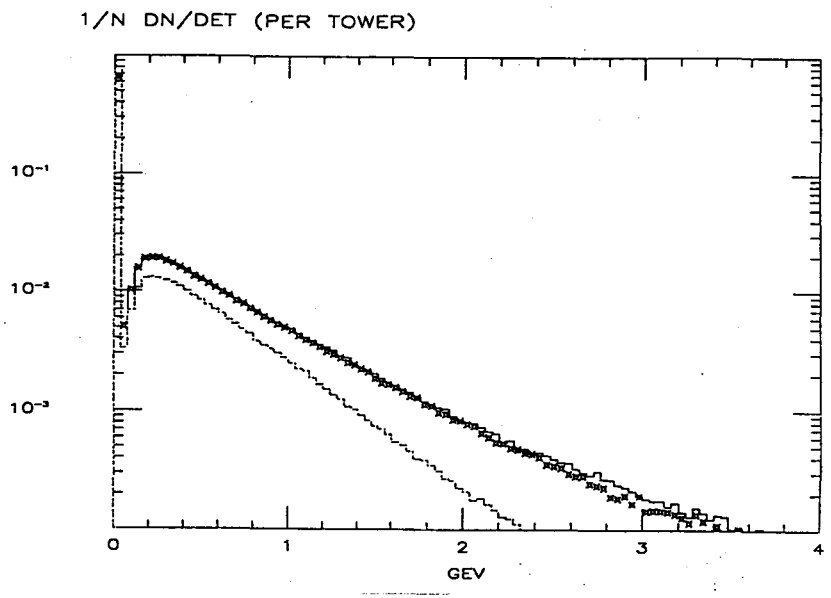

Figure 5

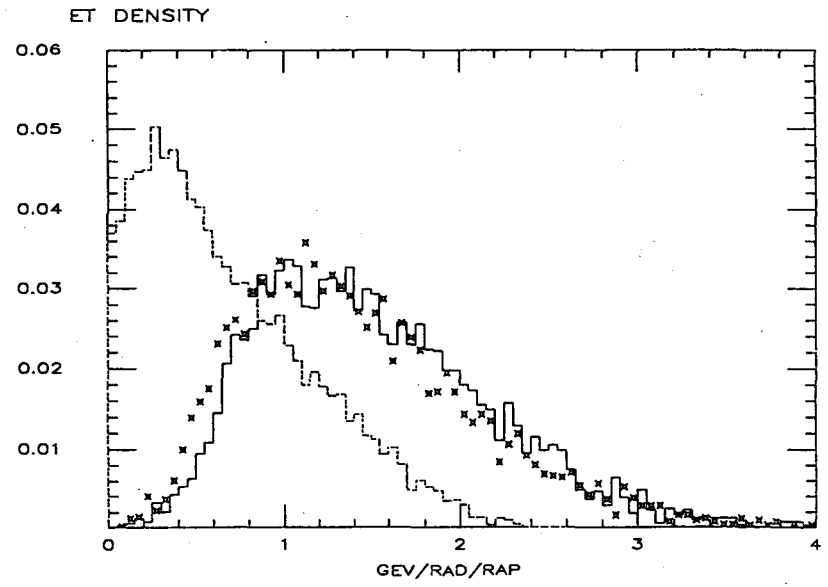

Figure 6

Background estimation in Higgs search with GFLASH

S. Sugimoto
Osaka U

(No written contribution received)

Pattern Recognition Study for the ACS detector

F. Abe, K. Amako, and Y. Takaiwa

National Laboratory for High Energy Physics, KEK
Oho 1-1, Tsukuba, Ibaraki 305, Japan

M. Asai

Hiroshima Institute of Technology
Miake 725, Itsukaichi, Saheki, Hiroshima,
Hiroshima 731-51, Japan

ABSTRACT

A program to reconstruct high-P_T tracks in r-ϕ plane have been developed. The program is applied to $H^0 \rightarrow 4\mu$ and $H^0 \rightarrow 4$ jet events in the ACS configuration. The processing speed is very fast: 185 ms/event for $H^0 \rightarrow 4\mu$ and 320 ms/event for $H^0 \rightarrow 4$ jets. However the current version of the program does not have sufficiently high tracking efficiency for extremely collimated jets. In this note, we describe the algorithm of the pattern recognition program and the progress of the analysis.

1. Introduction

One of the big problem on the SSC tracking system is how we can really find the tracks from the hit pattern by a software. Several efforts have been made to reconstruct the events using conventional link-and-tree method[1]. This approach, however, seems not applicable to highly collimated jets due to the bad resolutions of the track segments in the angle-curvature space. We used a histograming method with a matrix approximation[2] to find high-P_T tracks only. Using this algorithm, better separation of the tracks and reduction of the CPU time are expected.

In this note, we describe the overview of the simulation system in Sec. 2. The algorithm of the pattern recognition program is described in Sec. 3. The results for the $H^0 \rightarrow 4\mu$ and $H^0 \rightarrow 4$ jet events are presented in Sec. 4. Summary is given in Sec. 5.

2. Overview of the simulation system

The present tracking simulation and pattern recognition programs are working on the KEK HITAC M680-H computer which computing power is about 30 MIPS. Figure 1 shows the total simulation system for the ACS tracking schematically. Higgs events are generated by PYTHIA Monte Carlo event generator with the 40 TeV center-of-mass energy of the protons. The Higgs mass is assumed to be 500 GeV. The decay modes are selected to be

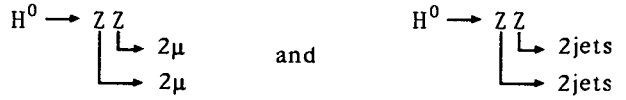

Generated event data are processed by a detector simulator GEANT. The simulator traces charged particle trajectories through the central trackers and calculates the particle positions at each layer. A uniform solenoidal magnetic field of 2 Tesla along the beam axis is assumed in this process. The multiple Coulomb scattering by the detector material is taken into account. The present simulation system cannot include the event pile-up effect.

The traced data are converted to the detector output data by a converter. The sizes of the silicon detector pads and the Gaussian type resolutions of 250 μm of the straw chambers are taken into account. The uniform chamber efficiency is assumed to each layer. The resolution and the efficiency for each layer are summarized in Table 1. The converted data are processed by a pattern recognition program. This program uses PYTHIA output data to evaluate the reconstruction efficiency.

3. Pattern recognition procedure

This pattern recognition program uses the matrix approximation technique to find high-P_T track fast. The original idea and the detailed formulations of the matrix approximation can be found in Ref. 3. We discuss here mainly about the algorithm of the track finding program.

Figure 2 shows the flow chart of the program. At the initialization process, setting geometrical parameters and calculations of the matrices A_i, B_i, and G_i are made. The matrix A_i is the transfer matrix from the origin to layer i with vertex constraint,

$$\begin{bmatrix} \phi_i \\ \cdot \\ \phi_i \\ C \end{bmatrix} = A_i \begin{bmatrix} \phi_0 \\ C \end{bmatrix}, \qquad (1)$$

and the matrix B_i is the transfer matrix from layer to layer without vertex constraint,

$$\begin{bmatrix} \phi_{i+1} \\ \cdot \\ \phi_{i+1} \\ C \end{bmatrix} = B_i \begin{bmatrix} \phi_i \\ \cdot \\ \phi_i \\ C \end{bmatrix}. \qquad (2)$$

We have not attempted to calculate matrices E's at the initialization; the matrix E is the matrix for the least squares fit,

$$\begin{bmatrix} \phi_i \\ \cdot \\ \phi_i \\ C \end{bmatrix} = E \begin{bmatrix} \phi_1 \\ \phi_2 \\ \vdots \\ \phi_n \end{bmatrix}. \qquad (3)$$

The storing of the matrices E for most of the combinations of the layers requires too much memory space. After initializing, the event analysis is started. The simulated data are read from a disk file, then they are converted to the ϕ values. The current program does not attempt to solve left-right ambiguity of the straw chambers at this step. Then the program starts to find $P_T > 30$ GeV/c tracks.

At first, one of the hit points at outermost silicon layer is selected. Then the points in a relatively wide road which is determined by $P_T > 30$ GeV/c and the chamber resolutions are selected. The selected points are processed by a histograming method. The ϕ_0 and C are calculated by the outermost silicon point and one of the other points using matrix G. A two-dimensional histogram in ϕ_0-C space is accumulated for all combinations. Figure 3 shows a histogram around the peak. This histogram essentially has only single peak if the outermost silicon point belongs to a $P_T > 30$ GeV/c track.

Using the peak of the histogram, relatively narrow road is determined with the chamber resolutions; the present program takes 4 standard deviations of the resolutions. The selected points are processed by the least squares fit. Sometimes several hits can be found in a layer. Trying all combinations takes lots of time to process. The following self-feedback iteration process is used to obtain quick convergence. The initial track obtained from the peak of the histogram is traced to obtain a combinations of the closest points. The obtained points are fitted by the least squares fit. Then the track is traced to obtain the closest points again. If the closest combination is the same as the previous one, the iteration is finished. The present program allows up to 5 times iteration, but it converges within 2-3 times in most case. The points used for the fitting and the corresponding goast points caused by the left-right ambiguity are tagged to remove the subsequent analysis. After these processes, the next outermost silicon point is selected to find the corresponding high-P_T track.

After finding $P_T > 30$ GeV/c tracks, retry to find $P_T > 5$ GeV/c tracks is made. The algorithm of this process is the same as that for $P_T > 30$ GeV/c tracks except for the width of the initial road and the histogram bin size. During these process, searching peak and initializing histogram may be time consuming. In most process, however, the distribution of the histogram is sparse. Most of the bins are 0. To avoid searching all of the bins, we used a pointer technique. During the accumulation, the program watches whether the bin exceeds a threshold by the accumulation. If an accumulation causes to exceed the threshold, the indexes of the bins are recorded in arrays. When searching the peak, the arrays are used as the pointers to search only the bins above the threshold.

4. Results

Figures 4(a)-4(c) show a typical $H^0 \rightarrow 4$ jet event. All tracks traced by GEANT are shown in Fig. 4(a). Many curling tracks can be found. Fig. 4(b) shows the tracks which are $P_T > 5$ GeV/c and $|\eta| < 1.5$, and Fig. 4(c) shows the processed result by the pattern recognition program. The dashed lines in Fig. 4(b) show the tracks which cannot be found by the pattern recognition. As shown in Fig. 4, the present program sometimes loses high-P_T tracks although most of the the high-P_T tracks can be found correctly. For about 52 % of $H^0 \rightarrow 4\,\mu$ and 40% for $H^0 \rightarrow 4$ jet events, this program finds all high-P_T tracks; the track finding efficiencies are 84 % for $H^0 \rightarrow 4\,\mu$ and 79 % for $H^0 \rightarrow 4$ jet events. Figures 5 shows the example of the correctly reconstructed events. The CPU time to process an event is about 185 ms/event for $H^0 \rightarrow 4\,\mu$ and 320 ms/event for $H^0 \rightarrow 4$ jets.

The problem in the present program is the relatively low reconstruction efficiency. To understand the reason of the inefficiency, each 40 of $H^0 \rightarrow 4\,\mu$ and $H^0 \rightarrow 4$ jet events have been scanned. One of the reason of the misfiring of the reference layer. The present program requires the hit on the outermost silicon layer, so the tracks cannot be found if the outermost silicon layer misfired. Figures 6 shows example of the misfiring of the output silicon layer.

Another reason of inefficiency is the decay-inflight of the short lived particles. Figure 7 is an example of the decay-in-flight. We cannot find the corresponding hits on the dashed line. If the tracks are close to each other, the program confuses these tracks. In Fig. 8(a), the hit points corresponding to the dashed line which is pointed by an arrow are slightly displaced. This is probably due to the multiple scattering or decay-in-flight. The pattern recognition program looks find the track quite reasonably (see Fig. 8(b)). The constraints used to evaluate whether the tracks are correctly reconstructed or not my be too severe for low-P_T tracks. An example of such a confusion is shown in Figs. 9(a) and 9(b); Fig 9(a) shows the

simulated tracks, and Fig. 9(b) shows the reconstructed tracks. The dashed line in Fig. 9(a) is not found correctly. A low-P_T track passed close to the dashed line, so the program confused. The extreme case of such a confusion is highly collimated jet. Figure 10 shows the worst example we have studied. For such a collimated jet the program cannot find the tracks efficiently unless the resolution of the chambers become better.

As described above, the present program and the evaluation method of the tracking efficiency have several problems. Further modifications are necessary to obtain better efficiency. The present program does not have capability to reconstruct tracks three-dimensionary. Development of the three-dimensional reconstruction program is necessry for the next step.

5. Summary

A pattern recognition program to reconstruct $P_T \rangle 5$ GeV/c tracks in r-ϕ plane have been developed for ACS configuration. To achieve fast processing speed, a new technique matrix approximation is used. The program applied to reconstruct $H^0 \rightarrow 4\,\mu$ and $H^0 \rightarrow 4$ jet events. The track reconstruction efficiencies for $P_T \rangle 5$ GeV/c tracks are 84 % for $H^0 \rightarrow 4\,\mu$ and 79 % for $H^0 \rightarrow 4$ jets. The efficiencies to reconstruct all high-P_T track of the event are 52 % for $H^0 \rightarrow 4\,\mu$ and 40 % for $H^0 \rightarrow 4$ jets. Studies of the inefficiencies have been made to improve algorithm and the evaluation method. The development of the three-dimensional reconstruction program are in progress.

References

[1] D. G. Cassel and H. Kowalski, Nucl. Instr. and Meth. 185 (1981) 235.

[2] F. Abe, "Matrix Approximation in Track Finding", Design Studies and Detector R & D for Super High Energy Hadron Colliders in Japan, edited by T. Ohsugi and T. Kondo (1990) 274.

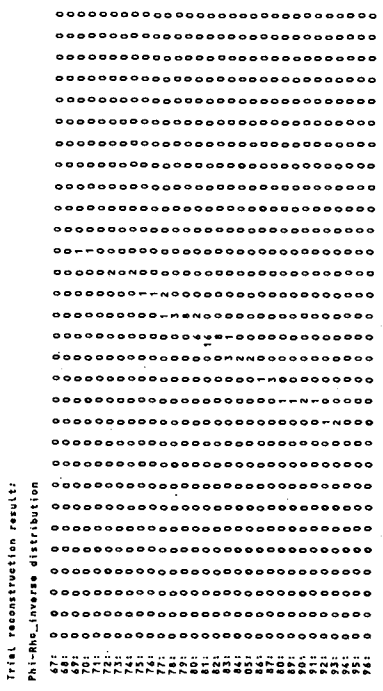

Fig. 3 Typical ϕ_0-C distribution arround the peak

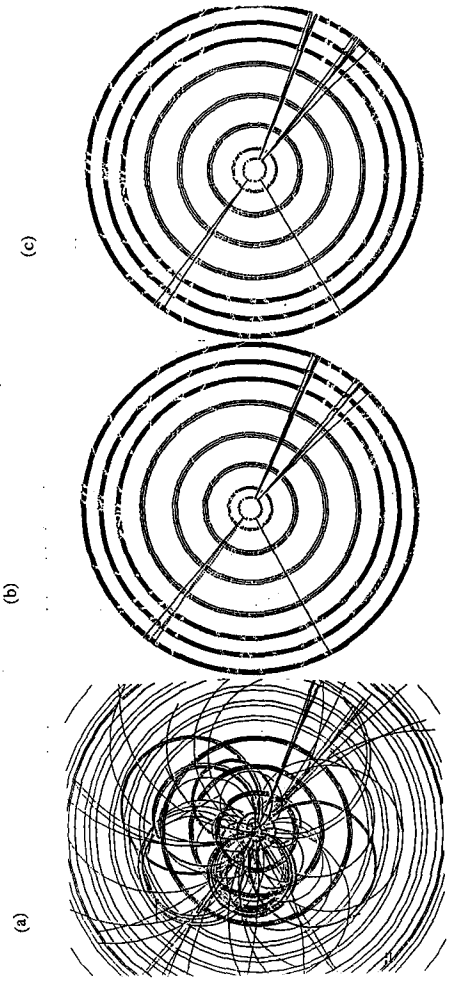

Fig. 4 Reconstruction of a $H^0 \rightarrow 4$jet event

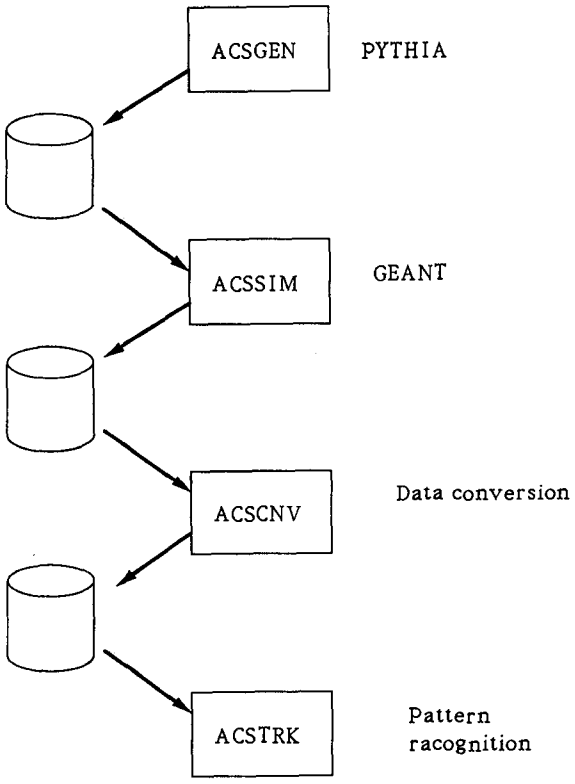

Fig. 1 Tracking Simulation/Analysis System

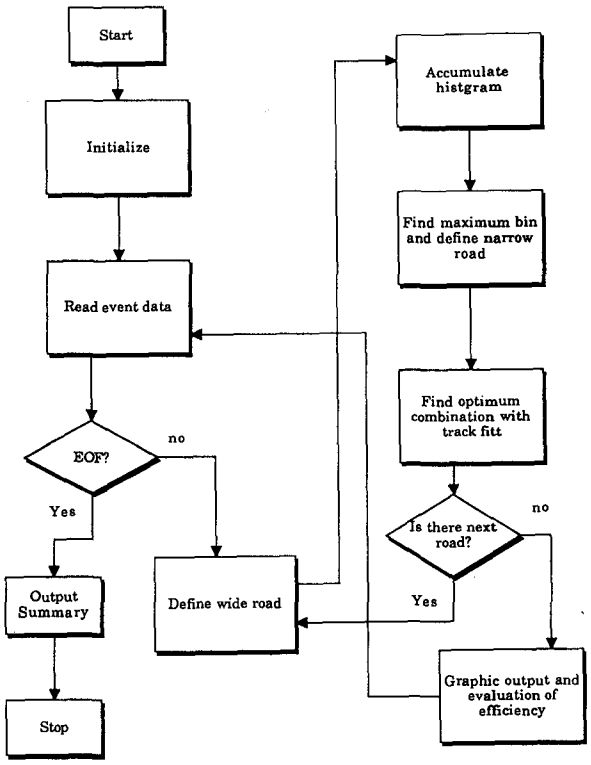

Fig. 2 Flow chart of the pattern recognition program

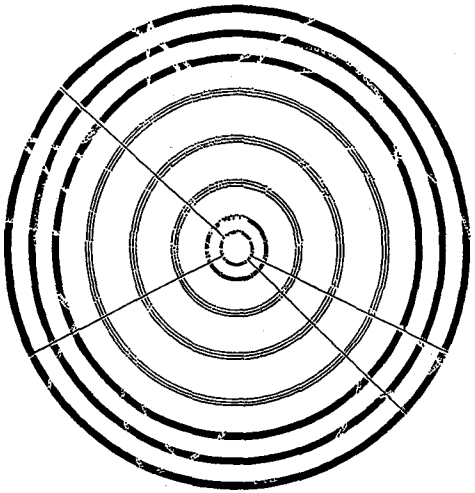

Fig. 5 Completely reconstructed $H^0 \rightarrow 4\mu$ event

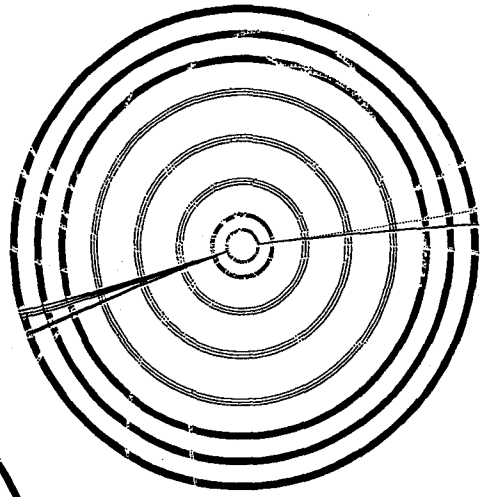

Fig. 6 $H^0 \rightarrow 4\mu$ event; the reference layer misfired

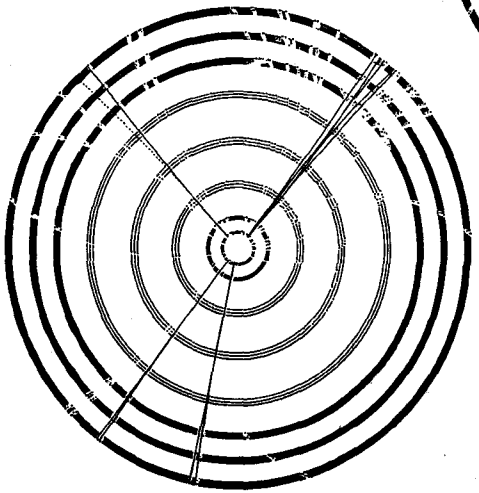

Fig. 7 $H^0 \rightarrow 4$jets; decay in flight

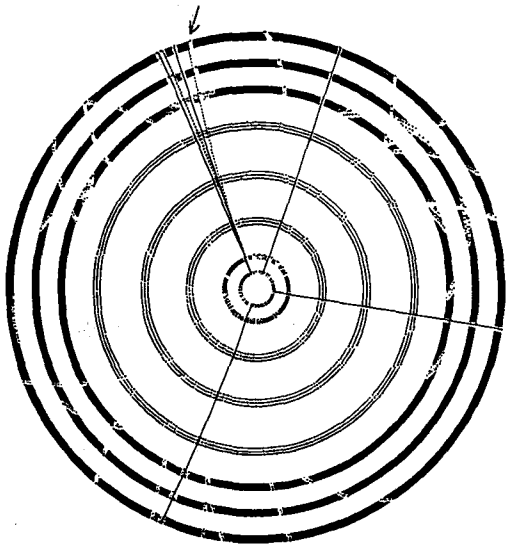

Fig. 8(a) $H^0 \rightarrow 4\mu$ event; multiple scattering

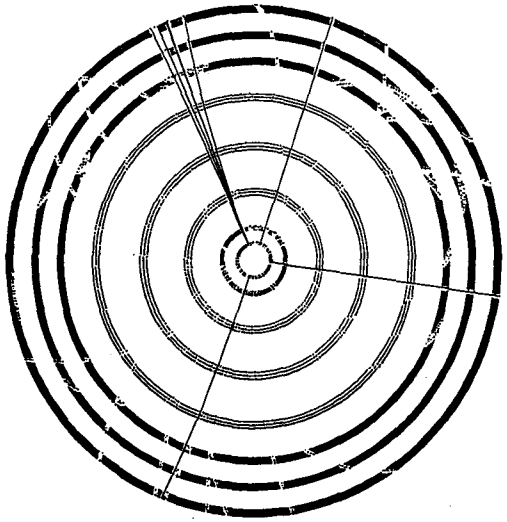

Fig. 8(b) Reconstructed same event

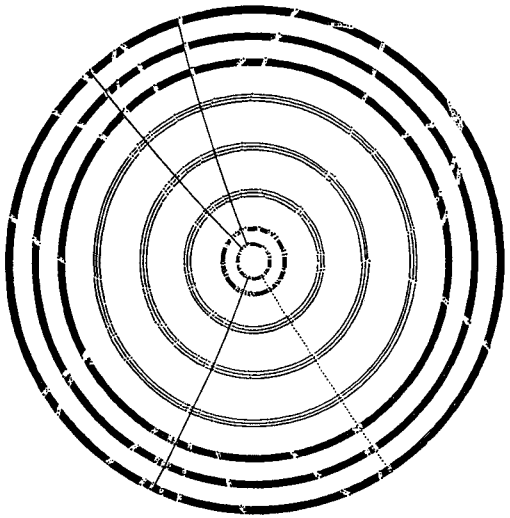

Fig. 9(a) $H^0 \rightarrow 4$jets; confused by low-p_T track

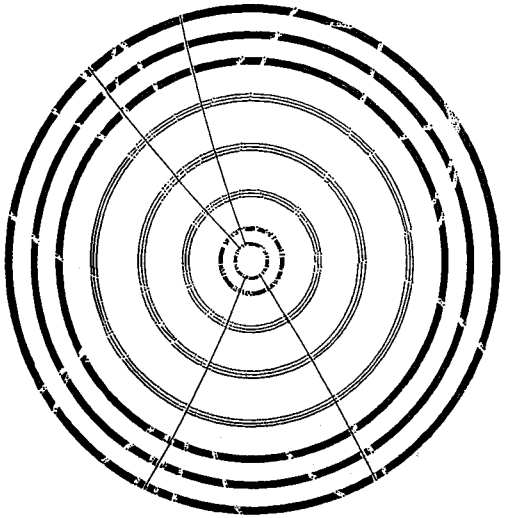

Fig. 9(b) Reconstructed same event

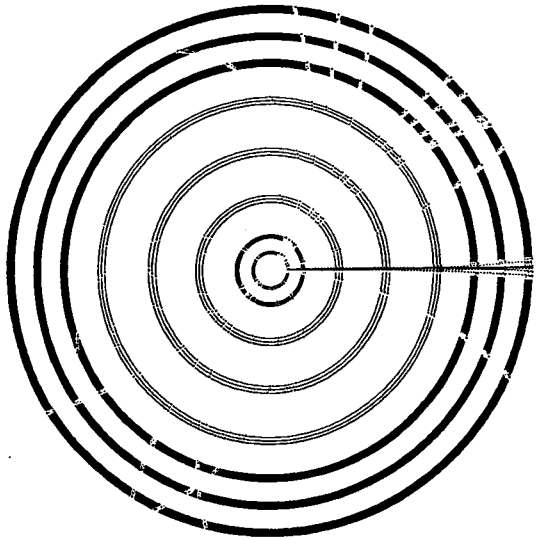

Fig. 10 $H^0 \rightarrow 4$jets; extremely collimated jet

Experience of CDF data analysis in Japan

S. Kim
U Tsukuba

(No written contribution received)

SSCL COMPUTER PLANNING

L. E. Price
Argonne National Laboratory, Argonne, IL 60439

The SSC Laboratory is in the process of planning the acquisition of a substantial computing system to support the design of detectors. Advice has been sought from users and computer experts in several stages.

A Computer Planning Committee was convened in December, 1988, under the chairmanship of Joe Ballam, to make recommendations to the Laboratory on initial needs for computing to support the experimental program and related theoretical calculations. Their report[1] constructed a scenario based primarily on detector simulation. It recommended that the SSCL provide by March, 1992, a system with 4000 VAX 780 equivalents of processing power, 400 Gbytes of disk space, and 6 Tbytes of accessible tertiary storage such as jukeboxes of optical disks or video cassettes. The committee also made that point that substantial computing was needed early and called for 1/8 of the system to be installed by October, 1990. The Computer Planning Committee also recommended that the SSCL Computer Department should structure itself to be a major resource for HEP computing. It endorsed a distributed-function computing model based on open systems (UNIX or variations) with separated compute engines, file servers, and batch job schedulers connected by a high speed local-area network and accessible to outside users by fast wide-area networks. The wide area networking now being provided by ESNET (4 T1 links to different points in the US) was considered adequate for the near future, but would need to be upgraded to T3 (45 Mbits/sec) or some intermediate value by 1992. It was expected that remote users would increasingly use workstations running a version of X-windows to access the SSCL system.

SSCL has largely accepted the recommendations of the Computer Planning Committee, and has established a Computer Acquisition Committee, chaired by Laird Cormell, to plan the initial acquisition of about 500 VAX 11/780 equivalents and corresponding amounts of storage. An example design of the initial system developed by the Acquisition Committee is shown in Fig. 1. The committee is developing a statement of requirements[2] to become part of a Request for Proposals to vendors, which is expected to be released in June, 1990. SSCL hopes to take delivery of the initial system in the Fall and to have it running for initial use by users around the end of 1990.

A major issue for the Computer Acquisition Committee is the operating system and scheduler to be run by this initial system. It is thought desirable to allow convenient use of multiple CPU's for a single job, in order to allow concentrations of computing for a single user's job. Many people,

particularly in computer science departments of universities, have thought about ways to implement such scheduling systems, but a standard way to proceed has not yet emerged. Hence, the SSCL will inevitably be involved in at least a partial development of an operating system/scheduler. In order to be educated on recent developments in the field, a Workshop on Distributed Unix Computing was held in February, with experts from universities and laboratories invited to talk. Proceedings are available[3].

In addition to planning a short term acquisition, the Laboratory has convened a Computer Policy Committee, chaired by Stewart Loken, to make longer term recommendations on the organization and goals of computing at SSCL. Questions put to the committee include the desirability of a concentrated central computing facility as opposed to a model where each major detector provides its own computing and attendant organization. The committee was also asked to make recommendations on the extent to which the SSCL computing organization should take as one of its goals the development of needed software for general use in the SSC and broader HEP community. The committee met in May, 1990, and is expected to make a report by the end of the Summer.

Work supported by the U.S. Department of Energy, Division of High Energy Physics, under contract W-31-109-ENG-38.

References

1. L. Price, ed., SSCL-N-691 (Dec. 1989).

2. "Physics and Detector Simulation Facility Specifications", SSCL-275 (1990).

3. G. Yost, ed., SSCL-SR-1050 (Feb. 1990).

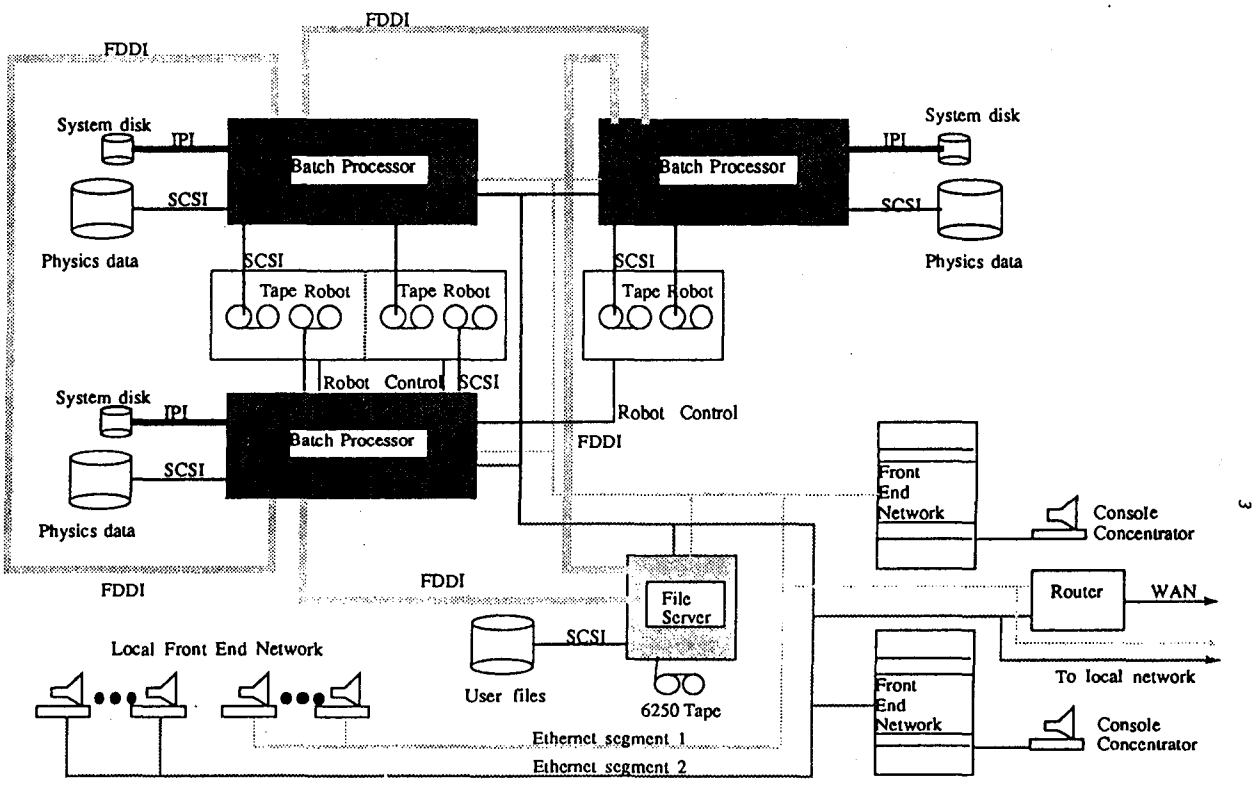

Functional diagram (block diagram) of the simulation facility.

Fig. 1

Network between Japan and US

Y. Karita
KEK

(No written contribution received)

Experiences of Computer Networking System Between U.S. and Japan in SLD Experiment

Katsuo Hasegawa

Tohoku University

Abstract.*The author has been working both at SLAC and at his home institute and likes to explain his various experience of computing using many machines of both sites via various networking systems among Japan and U.S. HEPnet has been placed and historical development and computer environment are presented. New TCP/IP networking system is discussed.*

§1.Introduction

The auther is visiting back and forth to SLAC, Stanford, U.S., for the research and development of the SLD experiment from Tohoku University, Sendai, Japan. There are lots of computing facilities both at Tohoku University and at SLAC. These computing machines are getting easier to be accessed from far places through the various kinds of new networking systems. Especially most of major networking systems are now running TCP/IP including the HEPnet. The author has been contributing the establishment of the first academic LAN(Local Area Network) in his home institute finacially backed up by the Japan Mistry of Education having prepared the situation he would be to have. He likes to explain the status and the environmental networking system of his institute relating with the efforts and progress of the KEK networking group. Also he likes to mention how the Japan networking systems would look to Japanese physicists from abroad when they might travel abroad for research. It would be quite conceivable the similar situation would occur when many Japanese and foreign physicists would come and go out between their home institutes and SSCL as well as other institutes in a couples of years.

§2.History and development

2.1.High energy physics at Tohoku

The high energy physics group of Tohoku University had been working mainly on bubble chamber film analysis for the various kinds of film taken at many laboratories in the world since erarly 1960's. It started the laboratory with a TOSBAC computer which was a unique machine for online measurement in Japan at that time. The laboratory computers have been upgraded several times from it to, ACOS 700, 900, 1000, and eventually ACOS 2000 which is the same model as one of the main frames of the Tohoku University Computer Center that owns ACOS 2040 and SX-II. The group has been involved in various experiments with the finantial support by the U.S.-Japan collaboration for more than ten years. As many other bubble chamber physicists moved out from fim analysis to different types of experiments, the group has had a same tendency, splitting into some sub-groups joining the TRISTAN experiment, SLD, SSC, DUMAND, etc., besides still continuing the film analysis and the last exposure at Fermilab. Many big collaborations has been requiring a lot of data exchanges between different institutes, different machines, different formats and different media. The author has joined the SLD since 1988 and working on the CRID(Cerenkov Ring Image Detector) from both sites of Tohoku and SLAC since then. These years were and still are remarkable ones for new technology of remote communication using various networking systems. Every institute has been exposed to the new requirement of installation of communication tools not only for high energy physics. The geometrical distance between any two institutes is getting shorter and shorter electronically. The Education Center for Information Processing(ECIP) of Tohoku University had placed the BITNET line to Science University of Tokyo(SUT) which has the next node of CUNY, New York. Tohoku University has started a University LAN named TAINS(Tohoku University Academic/Advanced Network System) since 1988 and is now running TCP/IP, DECnet, XNS and newly developed OSI(Open System Interconnection) type protocols. Numerous number of personal computers, engineering work stations are connected and there are many projects to make use of TAINS.

2.2 Networking at KEK

As the proceedings of the conferences held at KEK [(1)] describe in detail, KEK has been developing new networking systems all over Japan offering useful services to KEK users distributed in Japan. The Ministry of Education of Japan has started the new project to place the scientific information network through all Japan named SINET. KEK has cleverly moved over this SINET to run HEPNET-J(High Energy Physics Network in Japan) distributing Cisco gateways which hand

pass DECnet, TCP/IP and XNS, from NTT(Nippon Telegram Telephone Company) lines. KEK has also placed the oversea network with LBL connecting HEPNET-J to the world-wide HEPNET. KEK is also a BITNET node connected to SUT.

2.3 Networking at SLAC

SLAC has recently upgraded its main frame from the IBM 3081 VM system to new IBM 3090 XA system. BITNET has been running and another VAX 8800 is linked to various networking systems such as SUNET(Stanford University Network), ESnet, etc. via various protocols. As described above, the TCP/IP protocol is getting popular and majour machines seem to be coneected via TCP/IP. The documents of the Stanford networking systems could be found elsewhere.

§3. Computer and network environment

The computers and various networking machines of Tohoku University high energy physics laboratory as well as the Tohoku University network environment is shown in Fig. 1. The main characteristics are the 100 Mbps optical fibre link rounding six campuses, and each Ethernet of the speed of 10 Mbps making an in-hous network for every building. The optical fibre is magnificent against the lightning thunder noise and for digital data transmission. Tohoku University has developed OSI type protocol for the RS-232C connection which are common in personal computers. Other features may be understood directly from Fig. 1.

§4. Usages

As seen from Fig. 1, various protocols are running on TAINS and throu some gateways, some of them can be extended to outside of TAINS back and forth. When a user stays at Tohoku, it can log in the SLAC machines in various ways. There is a DECNET connection between THKAWA or THKVAX and SLD. Once it logs in KEKVAX, it can use TCP/IP connection to SLACVM or SLD through KEKUX. When it stays at SLAC, the reverse ways are possible. Possible, should be possible, the author had expected. However, he found it was impossible to reach Tohoku from the U.S. via TCP/IP commands such as *telnet* or *ftp*. It was quite recent why it had been impossible. He had found it possible to reach Kyoto University or University of Tokyo from SLAC and therefore had expected the same to Tohoku. He had to make a number of inquiries to investigate why he did not succeed.

It turned out that another gateway exists at University of Tokyo controling handpassing packets. There were two projects of new network at the time to interconnect Japan to University of Hawaii. And also there was another project testing the interconnection of universities in Japan using the science information network(SINET). So the time was just the transition period. He expects now it would be soon to use the TCP/IP commands on the 48kbps SINET riding one of these projects.

§5. Experiences

It was December of 1989 when the Cisco gateway was delivered from KEK to Tohoku. The author went to SLAC at the end of January, 1990, staying till mid March and could have some experiences. At Tohoku he can use various terminals like VAX station 3100, Macintosh II, JSTAR and PC9801 running various emulators. As TAINS is getting popular and more common, the Japanese language is getting to overwhelm the English or Roman ones. The VAX can handle Japanese, and can TelnetJ on MAC-II. The KEK version of KERMIT also does on PC9801's. JSTAR is an extension of STAR to Japanese and does handle it. In the U.S., he had to meet the difficulty to use the Japanese Kanji codes. He had his students to teach during his stay in the U.S. and they prefered Japanese to communicate in both the classes and their private communication. Actually the communication in Japanese letters or mails were magnificent and quite fluent, making the author realize the fact that mother languages are instinctively important for human communication though the young are getting better to speak English than the old.

§6. Future projects

The author thinks electronic mails or even electronic chattering using character strings by typing messages would not be enough to establish an instant and sufficient communication. It would be very close to use the new technology of Television conference to the face to face communication. Therefore the author wishes to speed up the

K.Hasegawa
May 16, 1990

Fig.1 Tohoku University High Energy Physics Lab Network Environment

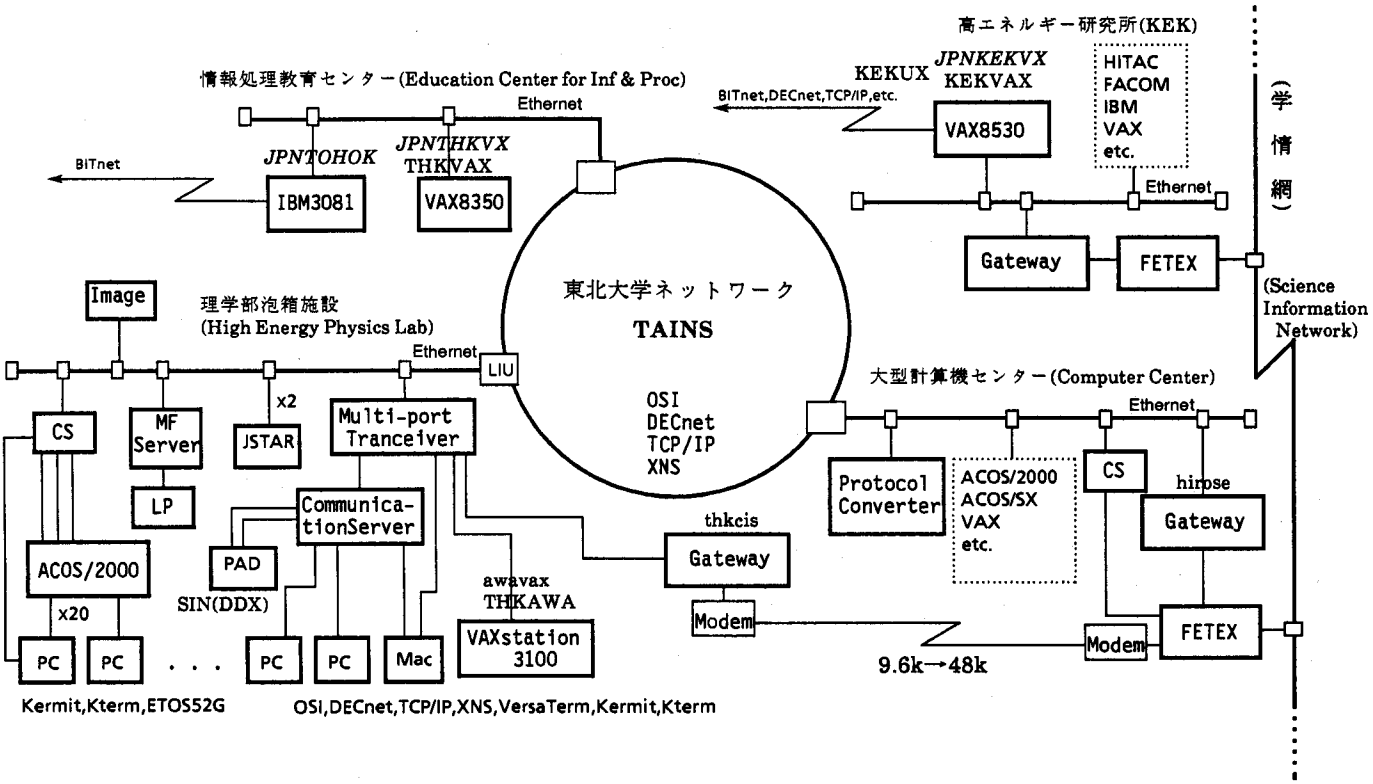

line speed and also the TV-forum or conferences to get together even people are busy staying at different far places.

References

1.Proceedings of the Symposium on Networking, KEK Report 89-3; Proceedings of the Workshop on the Japanese Hepnet, KEK Report 90-8.

R & D of computing tools required in SSC experiment

I. Gains
FNAL

(No written contribution received)

A New Architecture of Parallel Processors for SSC Experiment

Katsuo Hasegawa

Tohoku University

Abstract. *A new architecture of parallel processors is introduced and a feasibility to apply the architecture to the SSC, especially the high luminosity experiments is discussed.*

§1.Introduction

The author has interests to new types of computers which might have intellect and been involved himself in the neuro science as well as neuro computers. Inevitably he had to meet various new architectures in order to improve these present computers in performance. In the section 2, the reasons why new architectures would be required will be discussed.

§2.Why new architecture is required

Many discussions about the electronics, triggering, and data acquisition at high luminosity SSC have been reported[(1)]. Frequently, high luminosity of $\sim 10^{33}$ has been required to get as many events as to be sensitive to many of the processes of greatest interest. This luminosity corresponds to an interaction rate of order 10^8 events per second. Most of high energy physicists who have been using various fast computers seem to have vague misgivings that even the fastest one at the future time of SSC might not be fast enough for triggering or data acquisition. By the way, the present fastest computer has a speed of ~210 MFPS. Some readers might think it as just a foreboding or a presentiment expecting various new developments of the faster machines. Also in various fields many super computers are being used for those calculations that fit the vector type processing.

In SSC experiments, most computer power would be used for data reduction, Monte Carlo simulations, online calibrations, online monitoring, online control, online diagnosis, development, and to make everything fail safe. Will the super computers fit these requirements? The author likes to propose to take a bit careful look at the parallel processing in the next session.

§3. Parallel processing

There would be many elements that make up the whole big detectors for the SSC experiments, like vertex chambers, central drift chambers, electro-magnetic and hadronic calorimeters, muon detectors, and some particle identifiers. As of computing corresponding to these elements, there would be tracking calculation, both electro-magnetic and hadronic shower calculation comparing with simulating, magnetic field strength calculation, calibration calculation, etc. You might easily imagine some messy events elsewhere obtained from some Monte Carlo simulation program like ISAJET. It seems to the author very good timing to call up some newly developed architecture of typical parallel processing computer named Connection Machine(CM)[(3)]. CM is a massively parallel computer which can have up to 2^{16}(=65,536) processors, and has been developed by Thinking Machine Corporation, Cambridge, Massachusetts, U.S.A., now having the models of CM-1 and new CM-2 which is announced to have the peak performance of the largest systems of more than 10 GFlops. Fig. 1 shows the evolution of supercomputers. This is achieved by using increasingly sophisticated VLSI technology.

§4. Control and data parallelism

It would be certain for those messy events to have similar algorithm to analyze most of the input data from the segments of each detector. In such a case, it would be nice to at least have the option of using the power of all the processors on a single application. One way of doing this under a serial programming paradigm, is to break up a standard program into more or less independent subsets of instructions and to assign one such subset to each processor. That is called *multi-tasking* or *control-parallelism*. It is used by vector supercomputers, as well as by the numerous multiple-instruction multiple-data (MIMD) computers currently on the market. Synchronization and load balancing between the workings of different subunits is a real problem.

SSC would be the case that data are much more parallelizable than instructions, and like current trends in computational physics and engineering. Then it would be possible to handle data in the context of multitasking. Part of the multitasking procedure might be to split an

array in half, and treat half in one processor and half in another. This, however, retains all the disadvantages of the MIMD paradigm with regard to synchronization, and only hints at what is possible. If we assign one processor broadcasting a single instruction stream to all the processors (SIMD), we could develop a programming paradigm that avoids synchronization problems and which is in many ways simpler than the usual serial computer programming paradigm. This is the new architecture of CM.

§5. Computational model

As decribed in the previous section, the SIMD architecture can have at least two features for the interprocessor communication. First, data can be transfered logically in the two-dimensional space. Second, It can make use of advanced high-band-width communication technologies. Clearly these features are applicable to many computational physics problems, such as three-dimensional viscous fluid flow that manipulate tens of millions of pieses of data. Reportedly CM attaches physically to an ordinary memory bus of the front-end computer, and, in fact, one of the best ways to think of CM is as "smart memory." As shown in Fig. 2, the front end can read (write) data from (to) the local memories of the CM-2's processors. In addition, however, the front end can issue instructions to the processors via a microcontroller, asking them to manipulate their data in some specified way. In addition to purely local (on-processor) operations, this might include each processor getting (sending) data from (to) another processor. In the latter case, the processors utilize the very sophisticated communications network hardware by which they are linked. These characteristics seem to be very attractive to develop the new analyzing method for the messy events from SSC.

§6. Conclusion

We have started thinking of the Thinking Machines. The architecture seems applicable to SSC. Research and development(R and D) is necessary with the progress of the simulation groups. Some cooperation with academic and/or commercial development may be necessary.

References

1.Proceedings of the Snowmass 1986, and 1988.
2.B.M.Boghosian,Computers in Physics, American Institute of Physics, January/February 1990.

Figure captions

1.Supercomputer evolution, courtesy of COMPUTERS IN PHYSICS.
.2.CM-2 Computational Model, same as above.

Fig. 1. Supercomputer evolution

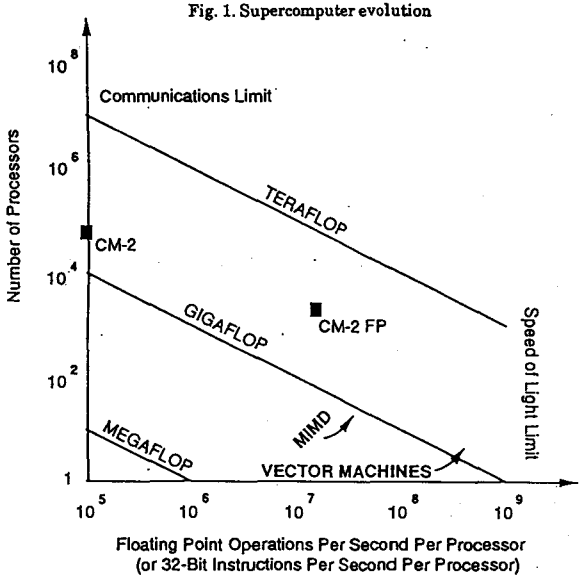

Fig. 2. The Computational Model

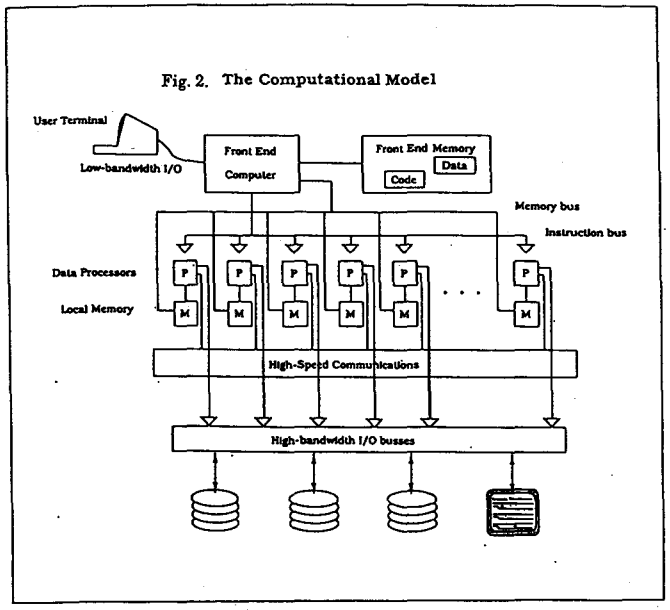

Fast hadronic shower simulation

M. Asai
Hiroshima Tech

(No written contribution received)

Summary Talk

April 25, 11:50-12:10

Y. Nagashima

Osaka University

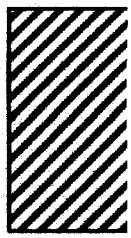

Summary talk

Y. Nagashima
Osaka Universtiy.

Physics opportunity.

_In exploring a new frontier beyond the standard model, SSC accelerator provides a fale safe experiments. Combined features that the SSC provides in terms of the attainable energy ($s=(4o\ TeV)^2$) and the luminosity ($L=2x10^{32}/cm^2/sec$) enable us to find a Higgs with mass less than 800 GeV and to study the nature of of symmetry breaking. If the coupling of the Higgs is so strong that the width of the Higgs is too broad to be detected as a sharp resonance, it also means the coupling of the longitudinal component of the gauge bosons is strong. Then we can expect a rich sturucture in the scattering cross sections of the guage bosons. Since the origins of the Higgs mass and the longitudinal component of the gauge bosons is the same, it also provides clues to the nature of the symmetry breaking. The question is can we do it? It was discussed in Hagiwaras' talk. It is certainly possible but by no means convincing.

Reachable mass limit could be doubled with x10 luminosity and detector feasibility at x10 intensity was discussed by Green. A simple considerations is that at r>1.5 meter the environment is no worse than that of standard luminosity at any part of the detector.

Magnet coil configuration

After a long work, we have boiled down to three options, type **S**(air core version similar to AMY or HERA), type **L**(in which the coil penetrates all the way down to the return yoke) and type **I**(where the coil size is similar to type S, but iron part of the endcap calorimeter provides a partial return path to the magnetic flux)(Mori,Yamamoto,). While type S provides a nice uniform coverage of the

all important calorimeter, there are some concerns about compression force caused by the radial component of the magnetic field. The disturbance that it gives to the tracking has also to be addressed(Takaiwa,Hauptman). Type L is the most conservative approach from engineering point of view, but a possible crack in the angle between the barrel and the endcap calorimeter may be a serious problem(Iwasaki). The uniformity of the field is good so that from tracking viewpoint this is the best option. Type I falls somewhere in between. Undoubtedly the choice of the magnet type and its dimension is one of the urgent questions to be addressed quickly, since it affects all other components.

With regard to the tracking ability, beautiful pictures of J/psi and upsiron reconstruction were presented by CDF group(Mishina) setting a standard we may aim at.

Some other topics are:

Electronics pile up should be no problem(Williams,Sakai) if proper care is taken.

Cadel presented an overall engineering effort for the whole sturucutre at LBL. Another version restricted mainly to muon section was provided by Watanabe.

In many ways , SDC can be considered as a logical extension of CDF experiment. A great experience on large scale international experience, successful cooperation with large insustry will be extended further and we hope the SDC collaboratiaon follow that good example.

Appendix :
Excerpts from parallel sessions. The sentences are based on the summary of the session leader, but are edited by the present author. Therefore, mistakes ,if any, are solely the present author's responsibility.

Calorimeter session (Yuta)
1. Warm liq.
*Promising first results from warm liquid(Beam test run at Fermilab, T-798)
Noise level is as low as hoped for ~2700e.
myu- signal/noise/sampling gap ~0.7
myu- signal/noise/200 sampling gaps ~10/1
E.M. calorimeter(partially installed) ~25%/routeE
Developing swimming pool type module as proof of principle
2. Liq Argon
Proposal for a beam test at BNL
Design work and various aspect of M.C. calculation is being developed at KEK.
3. Scintillater
*Tile, test and proposal are repoted(R & D work)
*Fiber, Radiation damage was discussed.
*Both scint. tile/fiber type are promissing.
*Liquid scintillator seems to have higher radiation resistivity than solid scintillator.

Muon session(Asano)
1)Beam test using 500 GeV muon at Fermilab is planned to tune GEANT.
2)Air core toroid vs iron toroid in the forward region($1.5<y<2.5$)
$B \sim 1/r$, (0.6T at the outer edge, 3T at the inner edge) so is $p \sim 1/r$ with fixed PT
H->ZZ->4mu is not a good test bench(only 10 % increase in efficiency)

*Comparison air core vs iron core

$\delta P_T/P_T$	~ $0.25P_T$ 0.1	<1 TeV, 0.2 @ 2TeV
@ low momentum	good	dominated by multiscattering
weight (ton)	~ 100	3000
add. cost	~ $10M? need study	enough experience
δ ray	OK	problem
chamber configuration	need study	easy

Electronics, data acquisition, and trigger(Watase)

1)Front end electronics status both in US and Japan was summarized.

2)Functionality and radiation hardness of VLSI at component level seems OK. System level functions have to be discussed further.

3)Sytem design, simulation, modelling and other items on data acquistion were reported.

4)Computer farm discussion: 100-105 VAX system will be available within a few years. Establish software structure of the farm including the user environment. Data I/O mechanism has to be specified to the requirement of the HEP application.

5)Possible trigger schemes of the first level for scintillatiing strip and drift chamber were addressed.

Physics/Computing/Simulation(Amako)

1)Activities in US.

Summary of physics benchmaraks for each componet, software tools, and some results.

2)Minimum bias at 40GeV

Two components, soft and semi-hard, exist. Event shapes are different.

3)GEANT +GFLASH is 300 times faster than GEANT+GHEISHA and can be used for the first level simulation.

Matrix approximation in track finding
Fast shower simulation. with new parametrizaton, a factor 30~50 gain(GEANP)
4)Experience of CDF experiment.
5)General discussion of computing tools for SSC
*SSCL computer plan
4000MIPS CPU, 400GB disk, GTB tapes by March'92.
Push UNIX OS
Upgrade of network(T1->T3) by FY'92.
6)Network between Japan and US
proposal for the KEK-SSCL direct line 128Kbps(--> 1.5Mbps) for VIDEO conferencing(cost 1.5 Myen/month for each lab.).
proposal for KEK-Hawaii(PACCOM),(64 Kbps -->?)for data communication.
7)General discussion on computing tools required for SSC experiments.

List of Participants

1	**Tom Fields**	Argonne National Lab.
2	**Thomas Kirk**	Argonne National Lab.
3	**Lawrence Price**	Argonne National Lab.
4	**Seog Oh**	Duke University
5	**John W. Cooper**	Fermilab
6	**John Elias**	Fermilab
7	**Jim Freeman**	Fermilab
8	**Irwin Gaines**	Fermilab
9	**Dan Green**	Fermilab
10	**Minato Kawaguchi**	Fukui University
11	**Hajime Yoshida**	Fukui University
12	**Hidehiro Kume**	Hamamatsu Photonics Co. Ltd.
13	**Junnichi Takeuchi**	Hamamatsu Photonics Co. Ltd.
14	**Makoto Asai**	Hiroshima Institute of Technology
15	**Takashi Ohsugi**	Hiroshima University
16	**Kawamura**	Hitachi-Kasei-Shoji Co. Ltd.
17	**Ryou Shirai**	Hitachi-Kasei-Shoji Co. Ltd.
18	**Masaomi Shioden**	Ibaraki College of Technology
19	**Hideo Kakui**	IHI Co. Ltd.
20	**Gail G. Hanson**	Indiana University
21	**Harold Ogren**	Indiana University
22	**Enrico Iacopini**	INFN, Sez. di Pisa
23	**Aldo Menzione**	INFN, Sez. di Pisa
24	**Minghan Ye**	Institute of High Energy Physics, Beijing
25	**Koichiro Nishikawa**	Institute of Nuclear Study, University of Tokyo
26	**Hideki Okuno**	Institute of Nuclear Study, University of Tokyo
27	**John Hauptman**	Iowa State University
28	**Takeshi Suzaki**	Kawasaki-Zukogyo Co. Ltd.
29	**Yoshitaka Yanagishima**	Kawasaki-Zukogyo Co. Ltd.
30	**Fumio Abe**	KEK
31	**Kazuo Abe**	KEK
32	**Katsuya Amako**	KEK
33	**Yasuo Arai**	KEK
34	**Yoshikuni Doi**	KEK
35	**Hirofumi Fujii**	KEK
36	**Kaoru Hagiwara**	KEK
37	**Hideo Hirayama**	KEK
38	**Hirokazu Ikeda**	KEK
39	**Hiroyuki Iwasaki**	KEK
40	**Seiji Kabe**	KEK
41	**Takahiko Kondo**	KEK
42	**Asao Kusumegi**	KEK
43	**Akihiro Maki**	KEK
44	**Masanori Mishina**	KEK
45	**Kazuo Ogawa**	KEK
46	**Tokio K. Ohska**	KEK
47	**Yoshihide Sakai**	KEK
48	**Hiroshi Sakamoto**	KEK

List of Participants

49	**Takao Shinkawa**	KEK
50	**Kasuke Takahashi**	KEK
51	**Yoshinobu Takaiwa**	KEK
52	**Susumu Terada**	KEK
53	**Toru Tsuboyama**	KEK
54	**Norihiko Ujiie**	KEK
55	**Yoshinobu Unno**	KEK
56	**Yoshiyuki Watase**	KEK
57	**Akira Yamamoto**	KEK
58	**Yoshiji Yasu**	KEK
59	**Alan Fry**	KEK / Univ of Rochester
60	**Hiroshi Harima**	Kurary Co. Ltd.
61	**Tohru Shimizu**	Kurary Co. Ltd.
62	**Osamu Shinji**	Kurary Co. Ltd.
63	**Kozo Miyake**	Kyoto University
64	**Murdock Gilchriese**	Lawrence Berkeley Lab.
65	**Richard Kadel**	Lawrence Berkeley Lab.
66	**Morris Pripstein**	Lawrence Berkeley Lab.
67	**George Trilling**	Lawrence Berkeley Lab.
68	**Teruo Nakamura**	Miyazaki University
69	**Mitsuhiro Nakamura**	Nagoya University
70	**Kimio Niwa**	Nagoya University
71	**Hiroyasu Tajima**	Nagoya University
72	**Tsuguyuki Kawai**	Nippon Steel Coporation
73	**Toru Okusawa**	Osaka City Univeristy
74	**Yoshiki Teramoto**	Osaka City Univeristy
75	**Tamotsu Takahashi**	Osaka City Univeristy
76	**Takuo Yoshida**	Osaka City Univeristy
77	**Yorikiyo Nagashima**	Osaka University
78	**Shojiro Sugimoto**	Osaka University
79	**David Koltick**	Purdue University
80	**Akira Murakami**	Saga Univeristy
81	**Kimiaki Masuda**	Saitama College of Health
82	**Michelangelo Mangano**	Sculoa Normale Superiore
83	**Tsunehiro Mizuuchi**	Shinnihon Seitetsu Co. Ltd.
84	**David L. Bintinger**	SSC Laboratory
85	**Fred Gilman**	SSC Laboratory
86	**Peter M. McIntyre**	Texas A&M University
87	**Masato Higuchi**	Tohoku Gakuin Univeristy
88	**Yoshimoto Hoshi**	Tohoku Gakuin Univeristy
89	**Katsuo Hasegawa**	Tohoku University
90	**Haruo Yuta**	Tohoku University
91	**Keisho Hidaka**	Tokyo Gakugei University
92	**Yasushi Watanabe**	Tokyo Institute of Technology
93	**Masami Chiba**	Tokyo Metropolitan University
94	**Tachishige Hirose**	Tokyo Metropolitan University
95	**Tuneyoshi Kamae**	Univeristy of Tokyo
96	**Richard Breedon**	University of California, Davis

List of Participants

97	**David Dorfan**	University of California	Santa Cruz
98	**Winston Ko**	University of California,	Davis
99	**Richard Lander**	University of California,	Davis
100	**Abraham Seiden**	University of California	Santa Cruz
101	**Andris Skuja**	University of Maryland	
102	**Jay Chapman**	University of Michigan	
103	**Kenneth Heller**	University of Minnesota	
104	**Tim Thomas**	University of Minnesota	
105	**Hugh H. Williams**	University of Pennsylvania	
106	**Hisashi Harada**	University of Rochester	
107	**Yuzo Asano**	University of Tsukuba	
108	**Takeshi Chikamatsu**	University of Tsukuba	
109	**Ikuo Fujiwara**	University of Tsukuba	
110	**Yoshimi Funayama**	University of Tsukuba	
111	**Hiroyuki Hagura**	University of Tsukuba	
112	**Koichi Kawaguchi**	University of Tsukuba	
113	**Shinhong Kim**	University of Tsukuba	
114	**Kunitaka Kondo**	University of Tsukuba	
115	**Hisafumi Mitsushio**	University of Tsukuba	
116	**Shigeyuki Miyashita**	University of Tsukuba	
117	**Shigeki Mori**	University of Tsukuba	
118	**Itsuo Nakano**	University of Tsukuba	
119	**Ryutaro Oishi**	University of Tsukuba	
120	**Makoto Shimojima**	University of Tsukuba	
121	**Yoshihisa Takada**	University of Tsukuba	
122	**Koji Takikawa**	University of Tsukuba	
123	**Kiyoshi Yasuoka**	University of Tsukuba	
124	**Henry Lubatti**	University of Washington	
125	**Eva H. Low**	Varginia Polytechnic Inst.	